DEUTSCHES ELEKTRONEN–SYNCHROTRON

DESY-PRC 00/04
October 2000

HERA – B

Report on Status and Prospects
October 2000

The HERA – B Collaboration

HERA – B

Report on Status and Prospects

Department of Physics, University of Texas, Austin, TX 78712, USA

University of Barcelona, Dept.E.C.M., Facultat de Fisica(U.B.), E-08028 Barcelona, Spain

Institute for High Energy Physics, Beijing, P.R. China

Institute of Engineering Physics, Tsinghua University, Beijing 100084, P.R. China

Institut für Physik, Humboldt-Universität zu Berlin, Germany

Dipartimento di Fisica, Università di Bologna and INFN, Bologna, Italy

Physics Dept., University of Cincinnati, Cincinnati, Ohio 45221, USA

LIP Coimbra and Lisboa, Portugal

Wayne State University, Dept. of Physics and Astronomy, Detroit, MI 48202, USA

Institut für Physik, Universität Dortmund, Germany

Northwestern University, Evanston, Il 60208, USA

DESY, Hamburg, Germany

II. Institut für Experimentalphysik, Universität Hamburg, Germany

Max-Planck-Institut für Kernphysik, Heidelberg, Germany

Physikalisches Institut, Universität Heidelberg, Germany

Physics Department, University of Houston, Houston, TX77204, USA

Institute for Nuclear Research, Ukrainian Academy of Science, Kiev, Ukraine

Niels Bohr Institutet, DK 2100 København, Danmark

Institut J. Stefan and Oddelek za fiziko, Univerza v Ljubljani, Ljubljana, Slovenia

University of California, Los Angeles, CA 90024, USA

Lehrstuhl für Informatik V, Universität Mannheim, Germany

Institute of Theoretical and Experimental Physics, Moscow, Russia

Joint Institute for Nuclear Research Dubna, Moscow, Russia

Moscow Physical Engineering Institute, Moscow, Russia

Max-Planck-Institut für Physik, Werner-Heisenberg-Institut, München, Germany

Dept. of Physics, University of Oslo, Oslo, Norway

Universität Rostock,Fachbereich Physik, Germany

Institut für Physik, Universität Siegen, Germany

Universiteit Utrecht/NIKHEF Amsterdam, 3584 CB Utrecht, The Netherlands

DESY–Institut für Hochenergiephysik, Zeuthen, Germany

Physikalisches Institut der Universität Zürich, Zürich, Switzerland

Contents

1 Executive Summary **1**

1.1 Introduction 1

1.2 Detector Status and Plans 2

1.2.1 Introduction 2

1.2.2 Inner Tracker 3

1.2.3 Outer Tracker 4

1.2.4 High-p_T Chambers 6

1.2.5 Muon 8

1.3 Trigger Status and Plans 9

1.3.1 Calorimeter Pretrigger 9

1.3.2 Muon Pretrigger 9

1.3.3 High-Pt Pretrigger 10

1.3.4 Optical Links 11

1.3.5 First Level Trigger 11

1.3.6 Trigger Efficiency Estimates 12

1.3.7 FLT Track Finding Efficiency Estimate (OTR) 12

1.3.8 Trigger Efficiency for $J/\psi \to e^+e^-$ 14

1.3.9 Trigger Efficiency for $J/\psi \to \mu^+\mu^-$ 15

1.4 Run 2000 17

1.5 Physics Prospects 19

1.5.1 CP Violation in $B^0 \to J/\psi\, K^0_S$ Decays 23

1.5.2 The FCNC Decay $B^0 \to \mu^+\mu^- K^{*0}$ 25

1.5.3 B^0_s–$\overline{B^0_s}$ Mixing 27

1.6 Conclusions 30

2 Detector Status and Plans for the Shutdown 2000/2001 **33**

2.1 Target 33

2.1.1 Requirements, Setup and Basic Rationale of the HERA – B Target 33

2.1.2 Status and Run Experience 37

2.1.3 HERA and Beam Related Topics 45

2.1.4 Shutdown Plans: Hardware Upgrades & Repairs 49
2.1.5 Shutdown Plans: Software Setup 51
2.1.6 Target Setup & Commissioning Plans for the Year 2001 51
2.2 Beam-Pipe 53
2.2.1 Introduction 53
2.2.2 Previous Upgrade Plans 54
2.2.3 Plans for the Shut-down 56
2.3 Vertex Detector System 58
2.3.1 Status 59
2.3.2 Performance 59
2.3.3 Radiation Damage 65
2.3.4 Material Budget 66
2.3.5 Improvements 66
2.3.6 Module Production and Installation Plan for the Year 2001 68
2.4 Inner Tracking 69
2.4.1 Status of Installation and Subsystems 69
2.4.2 Detector Operation 71
2.4.3 Tracking 71
2.4.4 Trigger Signals 74
2.4.5 Improvements of the Inner Tracking Detector during Shutdown 75
2.4.6 Summary 75
2.5 Outer Tracker 76
2.5.1 Hardware Status 76
2.5.2 Track Reconstruction Software 84
2.5.3 Detector Performance 87
2.5.4 Repairs and Upgrades During the Shutdown 92
2.5.5 Outer Tracker Summary 95
2.6 Status of the High-p_T Trigger 97
2.6.1 Overview 97
2.6.2 Performance of Inner Chambers during the 2000 Run 98
2.6.3 Status of Outer Chambers during the 2000 Run 105

2.6.4 Status of Pretrigger Electronics 105
2.7 The HERA – B RICH 109
2.7.1 Expected Performance 109
2.7.2 Measured Single-photon Angular Resolution 110
2.7.3 Measured Photon Yield 110
2.7.4 Stability of Operation 111
2.7.5 Tracking Capabilities 111
2.7.6 Particle Identification Capabilities 114
2.7.7 Plans for the Shut-down 118
2.8 Transition Radiation Detector 124
2.8.1 Status 124
2.8.2 Detector Performance 125
2.8.3 Shutdown Plans 2000-2001 126
2.9 Electromagnetic Calorimeter 128
2.9.1 General Remarks 128
2.9.2 Radiation Hardness 128
2.9.3 Noise Problem 129
2.9.4 Readout Electronics 129
2.9.5 Slow Control 130
2.9.6 Calibration 130
2.9.7 Monitoring 131
2.9.8 Performance 131
2.9.9 Upgrade/Repair Plans 132
2.10 Muon System 137
2.10.1 Status of Muon System Hardware 137
2.10.2 Performance and Running Experience 138
2.10.3 Chamber Aging Studies 143
2.10.4 Shutdown Plans 144

3 The Trigger System: Status and Prospects 147

3.1 The First Level Trigger 147

3.1.1 Introduction . . . 147
3.1.2 Operation . . . 149
3.1.3 Performance . . . 162
3.1.4 Conclusions . . . 173
3.2 The ECAL Pretrigger system . . . 176
3.2.1 Technical Description . . . 177
3.2.2 Present Status and Performances . . . 179
3.2.3 Future Plans . . . 183
3.3 The Muon Pretrigger System . . . 184
3.3.1 Requirements and Coincidence Algorithm . . . 184
3.3.2 System Overview and Latency . . . 184
3.3.3 Efficiency Measurements . . . 188
3.3.4 Software and Monitoring . . . 188
3.3.5 Future Improvements . . . 190
3.4 High-P_T Pretrigger . . . 191
3.4.1 Introduction . . . 191
3.4.2 Pretrigger Logic . . . 191
3.4.3 Electronics Overview . . . 192
3.4.4 The Link Board . . . 192
3.4.5 The Pretrigger Board . . . 193
3.4.6 The Message Generator . . . 193
3.4.7 Status . . . 193
3.4.8 Plan for Luminosity Shutdown . . . 194
3.5 Second Level Trigger . . . 195
3.5.1 Introduction . . . 195
3.5.2 SLT hardware . . . 195
3.5.3 SLT Algorithm . . . 197
3.5.4 The Use of SLT in 1998–2000 . . . 198
3.5.5 The SLT Performance in August 2000 . . . 200
3.6 Third Level Trigger . . . 205
3.6.1 Changes since the Technical Design Report . . . 205

3.6.2 System Status 205
3.6.3 Monte Carlo Studies for a TLT using the VDS 205
3.6.4 Plans for the Luminosity Shutdown 206
3.7 Farm 208
3.7.1 Introduction 208
3.7.2 Concept 208
3.7.3 Implementation 209
3.7.4 Status in 2000 210
3.7.5 Data Handling 211
3.7.6 Perspectives 212
3.8 Data Acquisition System 215
3.8.1 Introduction 215
3.8.2 The SHARC Cluster Board 215
3.8.3 Second Level Trigger Switch and Data Buffering 215
3.8.4 Logging 216
3.8.5 Status and Performance 217
3.8.6 Event Building 217
3.8.7 Prospects 219
3.9 Online Calibration and Alignment (CnA) 221
3.9.1 Description and Implementation 221
3.9.2 Status and Performance 221

4 Achievements of the Physics Run 2000 223
4.1 Introduction 223
4.2 Minimum Bias Triggers 223
4.2.1 Luminosity Monitoring 223
4.2.2 Single Particle Inclusive Distributions 225
4.2.3 Strangeness Production 229
4.2.4 Multiplicities 230
4.2.5 Particle Fractions 231
4.3 Double Lepton Triggers 232

4.3.1 Electron Triggers . . . 233
4.3.2 Muon Triggers . . . 235
4.4 Single High-p_T Lepton Triggers . . . 237
4.5 Summary . . . 239

5 HERA-B Physics Beyond the Shutdown 241

5.1 Physics of Proton-Nucleus Interactions . . . 244
5.1.1 Normal Inelastic Proton-Nucleus Interactions . . . 244
5.1.2 High p_T Physics and QCD Tests . . . 250
5.2 Physics of High Mass Lepton Pair Triggers . . . 259
5.2.1 Drell-Yan Pair Production . . . 259
5.2.2 Heavy Quarkonium Production . . . 260
5.2.3 Beauty Production Cross Section in Proton Nucleus Interactions . . . 266
5.2.4 CP Violation in $B^0 \to J/\psi\ K^0_S$ Decays . . . 270
5.2.5 CP Violation in $B^0_s \to J/\psi\ \Phi$ Decays . . . 272
5.2.6 Exclusive Lifetimes of Beauty Hadrons . . . 274
5.2.7 Measurement of $\Delta\Gamma_s$ from $B^0_s \to J/\psi\Phi$ Decays . . . 276
5.2.8 Rare Decays $B^0 \to \ell^+\ell^-(X_s)$ . . . 277
5.3 Physics of Triggers Based on High p_T Leptons . . . 285
5.3.1 $B^0 - \overline{B^0}$ Mixing . . . 285
5.3.2 $D^0 - \overline{D^0}$ Mixing . . . 285
5.3.3 Measurement of $\Delta\Gamma_s$ from Semi-Leptonic Decays . . . 291
5.3.4 Charm Physics . . . 292
5.4 Physics of Triggers Using High p_T Hadrons . . . 294
5.4.1 High p_T Hadron Production and QCD . . . 294
5.4.2 $B^0_s - \overline{B^0_s}$ Mixing . . . 294
5.4.3 Measurement of CKM Angles α and γ . . . 302
5.4.4 Hadronic Rare B Decays . . . 315

References 320

1 Executive Summary

1.1 Introduction

HERA − B was approved in February, 1995 to carry out a study of the physics of B meson production and decay. According the Design Report, "HERA − B is an experiment designed primarily to search for CP violation in decays of B mesons into the "gold plated" decay mode $B^0 \to J/\psi\, K^0_S$".

The ambitious schedule, calling for completion of the detector by the beginning of 1998, was not to be met. The proposed technologies for the main tracker were proven to fail quickly when confronted with the high radiation environment required for HERA − B operation. Vigorous R&D programs for both the inner and outer trackers were launched and eventually solutions were found. The detector was finally completed [1] only in February, 2000 – a two year delay.

The schedule established to build and commission the sophisticated First Level Trigger system of HERA − B also proved to be seriously over-optimistic. Production finished in 1999 and installation was largely completed by January 2000. System-level commissioning began in 1999 and continued through to the end of this year's run in late August. The trigger system is now able to find tracks starting from pretrigger seeds and map them through the tracker stations behind the magnet, as designed, but is not yet fully commissioned. There is, however, good reason to hope that the remaining problems can be solved during the present shutdown.

In the meantime, the new e^+e^-machines at KEK and SLAC have held to their (also ambitious) schedules and the associated detectors, BELLE and BABAR have reported first physics results this summer, including preliminary measurements of CP violation in the $B^0 \to J/\psi\, K^0_S$ decay mode: our primary goal according to the Design Report.

It is therefore necessary to ask if HERA − B can be reasonably expected to contribute in a meaningful way to the physics topics for which it was designed and if it is possible to use what is arguably the most sophisticated fixed-target multiparticle spectrometer and trigger system ever built for other, perhaps more mundane, physics topics. To answer these questions we must first summarize the state of the detector and estimate the efficiencies and sensitivities we can hope to achieve. Next, a survey of potential physics topics and HERA − B's competitiveness must be estimated.

The collaboration has produced a lengthy report ($\approx$ 300 pages) which attempts the answer to these questions on a rather short time scale, particularly given that the primary goal during most of this period had to be to make best of the available beam-time before the start of the long HERA upgrade shutdown. We apologize in advance for any omissions, inconsistencies and rough edges still present in the report.

This summary will first review the status of the detector and triggering systems, with emphasis on problem areas. We will then give a brief description of the data taken during the year 2000 run and finally summarize the studies of potential physics topics.

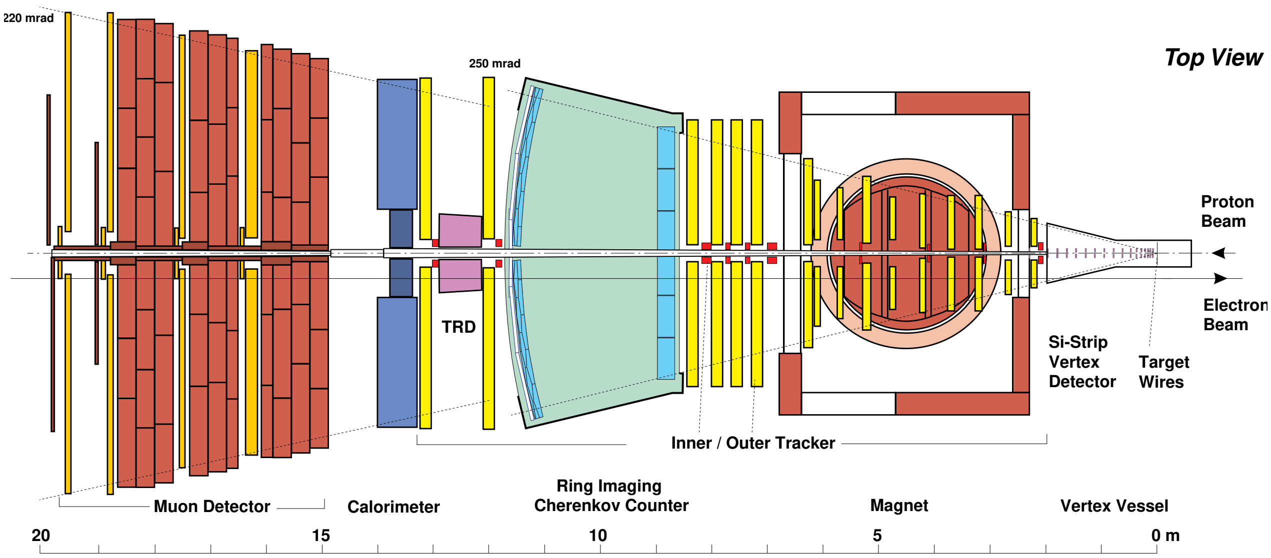

Figure 1: *The HERA – B spectrometer*

1.2 Detector Status and Plans

1.2.1 Introduction

The HERA – B spectrometer is shown in Fig. 1. We start with a very brief summary of the subsystems. Those systems in need of a more detailed status report are deferred to the following sections.

- **Target and beam:** The target has been operating regularly already since 1997. In 2000, the target was in operation during 94% of HERA luminosity periods, usually at rates between 5 and 10 MHz. Beam conditions were for the most part acceptable. Remaining problems include a large contribution to the interaction rate from unbunched beam when operating with outer and above wires and rate instability at high interaction rates. Both of these problems are being addressed together with the machine group.

- **Vertex Detector System:** The vertex detector installation was largely completed in December, 1999 (and fully completed in March 2000 with the installation of the remaining 8 modules outside the vacuum vessel). The detectors were positioned close to the beam for the majority of luminosity time during the 2000 run. The performance is as designed with signal/noise ratios of 15 – 25 (p-side, n-side), overall efficiencies >97%. Secondary vertex resolution is about a factor of two worse than expected (630 μm vs. 300 μm). This discrepancy is under study.

- **Inner Tracker:** See Section 1.2.2.

- **Outer Tracker:** See Section 1.2.3.

- **High-Pt system:** See Section 1.2.4.

- **RICH:** Installation of the RICH was completed in Spring, 1998. Since then, the system has been in stable operation. Studies show that the RICH has fully reached design specifications.

[1] With the exception of the "High-pt" system, two inner tracker stations and the TRD.

- **Transition Radiation Detector:** The TRD was installed in summer 1999 but has yet to be equipped with more than a few channels of readout electronics for budgetary reasons. The detector was powered to full high-voltage for most of the running period and operated stably. We plan to complete the installation and commissioning of this device in 2001.
- **Electromagnetic Calorimeter:** The calorimeter installation was completed in the Winter shutdown of 1997/1998. Production and installation of readout electronics lagged behind due to problems in the production and testing. By the end of the run, inner and middle regions had been equipped and the installation of electronics for the outer region had begun. The system is now complete. Energy and spatial resolutions are close to design values.
- **Muon Detector:** See Section 1.2.5.
- **First Level Trigger:** See Section 1.3.
- **DAQ and Second Level Trigger:** The hardware and software of the DAQ and the SLT are intimately intertwined since both systems use the second level buffer system, the switch and the second level processing nodes. These systems are fully installed and operating stably. A major activity of the DAQ group was growing the system as channels were added and digging out subtle bugs exposed by this growth. The DAQ/SLT system has been shown to be capable of stable operation for periods of many hours at input event rates up to 22 kHz. The second level trigger algorithm was used as a stand-in for the incomplete First Level Trigger. By the end of the run, the algorithm was close to that envisaged in the design. Suppressions and timing depend sensitively on input.
- **Fourth Level:** The 4th level hardware is complete. The farm was used for event reconstruction in the latter part of run 2000. The reconstruction time depends sensitively on interaction rate and trigger conditions. For triggered runs at 5 MHz, an average time of 4s/event was achieved. The data rates from the second level and to the computer center exceed design specifications.

1.2.2 Inner Tracker

The inner tracking system provides coverage in the area around the beam pipe up to distances of 25 cm. It provides tracking at small radii, for about 40% of all tracks from B-decays and provides input for the First Level Trigger. The Inner Tracker uses a total of 184 MSGC/GEM detectors, each with 768 anode strips organized into 10 tracking stations.

All but two (the furthest downstream) of the stations were installed and commissioned in the course of run 2000. Because of problems with the trigger outputs which precluded use in the First Level Trigger and because they are of little use for pattern recognition, the final two were not installed.

In general, the chambers and ancillary systems have run for several months and worked well, apart from some problems with the low voltage power supplies which we are investigating, together with the manufacturer. During operation, a few problems appeared which affected $\approx 2\%$ of installed chambers. All broken detectors will be repaired or replaced during the shutdown. At this point, remaining problems will be limited to defective anodes at the level of 1%.

The efficiencies of the chambers in the first inner tracking station (MS01) were determined using vertex detector tracks. The results for 7 detectors are shown in Fig. 2 as a function of GEM voltage. After individual adjustment of GEM voltages, efficiencies in the range $.91 - .98$ were achieved. We have recently learned that the gain variations between GEM foils (leading to the spread in efficiencies) is most likely due to a mismatch between electrodes on the two sides of the foil. An efficiency study for the entire system awaits tuning of the alignment and general track-finding code.

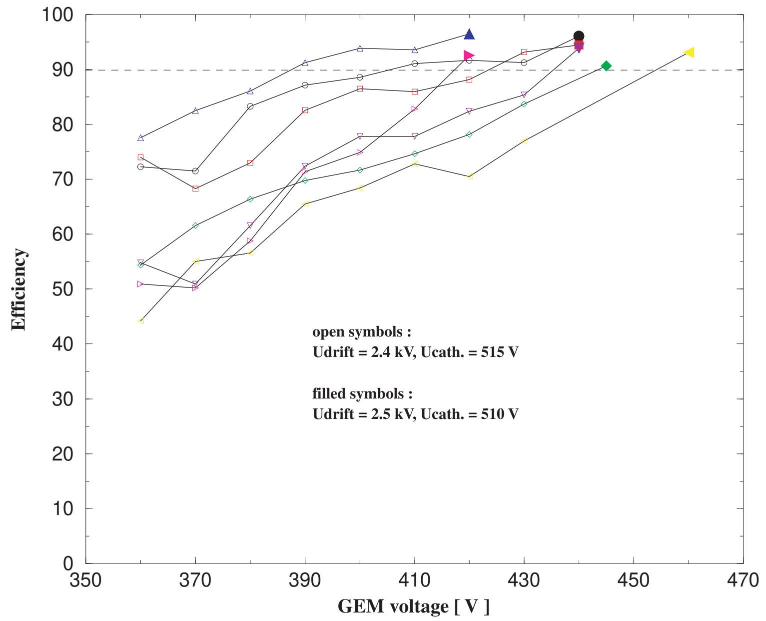

Figure 2: *Efficiency of 7 detectors of station MS01 versus GEM voltage for fixed cathode and drift voltages. The filled symbols show the efficiencies for the current voltage settings after individual gain adjustments.*

Four of the tracking stations behind the magnet will have to provide hit information for the First Level Trigger. To guarantee high efficiency, each of these stations has two layers per view whose trigger outputs are ORed in the front-end electronics. Hit information comes from discriminating the analog signal for each strip and subsequent ORing of 4 neighbors. Each readout chip delivers 32 hit/no-hit signals for each event.

The present trigger installation cycles correctly but, because the discriminator threshold had to be raised to prevent oscillation, it does not give adequate efficiency. By reducing the voltage swing of the trigger output drivers and reworking the grounding scheme, the oscillation could be overcome. Three double trigger layers were installed and operated in August. The measured efficiency is at least 90% and compatible with 100%.

During the shutdown, all detectors will be taken out of the experiment. Broken ones will be repaired or replaced. All front end cards for trigger layers will receive a new version of the readout chip to correct an error with the analog pipeline length. New trigger driver boards will be installed and the path to the First Level Trigger will be commissioned during the shutdown. By the end of the shutdown, the system will be fully installed, including the remaining two trigger stations.

1.2.3 Outer Tracker

The Outer Tracker provides coverage starting from about 25 cm from the beam pipe up to the full aperture of the spectrometer (220 $\times$ 160 mrad). The Outer Tracker is organized into 13 super-layers extending from the vertex vessel to the calorimeter. Each super-layer is logically segmented into 12 sectors of varying dimensions. The Outer Tracker is built from honey-comb drift cells with a wire pitch of either 5 mm or 10 mm, depending on sector. Four of the super-layers behind the magnet are used in the First Level Trigger. The trigger layers are doubled for high efficiency.

The installation of the Outer Tracker was completed in January 2000. Since then, the system has been available >90% of the time. The high voltage and gas systems are operational and fully integrated with the global HERA – B slow control.

Apart from a potentially serious problem with high voltage stability (described below), only relatively minor and solvable problems were encountered:

- On two occasions, the system was out of operation due to leaks in the gas system. Finding the leaks proved to be a difficult and time consuming operation, resulting in a total downtime of about two weeks. The failure modes have been identified: dirt in bellows of pumps and loosening of gas fittings and measures have been taken to eliminate them.
- 138 (of 7200) readout boards were not giving signals. Most of these failures probably occurred at assembly (cables coming loose). Improvements in assembly procedures are expected to reduce this problem to a negligible level.
- The thresholds of the four super-layers used in the First Level Trigger had to be raised because of additional noise induced by connections between the TDC boards and trigger electronics. We are studying ways to reduce or eliminate this additional noise.

From the beginning of Outer Tracker operation in July 1999, high voltage groups[2] started to fail. The average failure rate was one group per 5 hours of operation. By the end of the run, 6.9% of high voltage groups had failed.

The failure rate was particularly high in the first assembled super-layer. It was suspected that the reason for the failures was mechanical instability since the modules of this super-layer had not been reinforced with carbon fiber stiffener rods. This super-layer was removed and overhauled in December 1999, then reinstalled. Since the repair, the failure rate decreased by a factor of 10, one of the lowest rates in the system.

Several initial tests and observations indicated that discharges and mechanical module imperfections might have been responsible. After the end of the run in September 2000, inspection of damaged modules revealed a completely unexpected source of failure. Of the modules inspected, 39 of the 49 "shorts" were caused by burnt-in carbon traces of varying resistance in residue left over from the soldering process across either of two capacitors on the bottom side of the high-voltage board responsible for distribution to a 16-wire group. A total of 17 capacitors are mounted on this board, 15 on the top and 2 on the bottom. Failures were seen only in connection with the 2 capacitors mounted on the bottom. This systematic difference is most likely due to differing mounting techniques.

While it is clear that shorts across the capacitors are implicated in the vast majority of the failures, we are concerned about remaining failure modes which might by a first indication of future problems. We are currently working to understand the experimental findings and making tests to try to reproduce the failures on a test bench.

During the shutdown, all bottom-side capacitors will be exchanged using a clean soldering technique. Also all modules which have not yet already received carbon fiber stiffeners will be reinforced

[2]A high voltage group consists of 16 channels.

(mainly 2 half super-layers). All modules will be subjected to a rigorous high voltage test to identify short and hot wires, while mechanically exercising them. Improved assembly and test procedures should reduce the number of unplugged readout boards to nearly zero.

We have determined the Outer Tracker cell efficiency for data taken at various times throughout the run. As an example, Fig. 3(a) shows the efficiency of cells in one 5 mm module of one sector of one super-layer, near the end of the run. From the fitted curve, the efficiency in the plateau was determined to be 0.93. The region has a radius of about 2 mm around the wire. Outside the plateau region, (near the edges of the hexagonal cell), the efficiency drops to zero[3]. The efficiencies of the 128 cells of the same module sector are mainly above 0.90, as shown in Fig. 3(b).

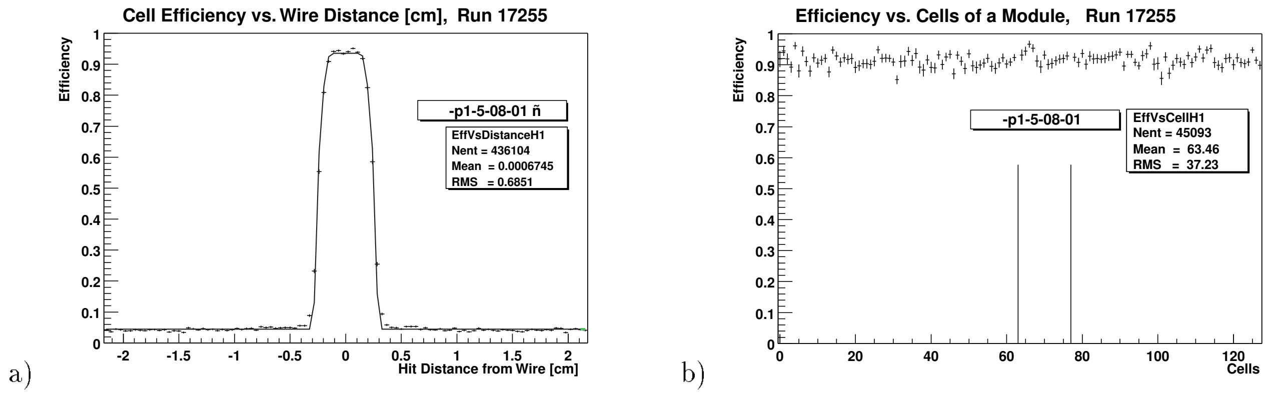

Figure 3: *a) Dependence of the cell efficiency on the distance from the anode wire (5 mm cell) for module 8 in sector 1 in stereo layer 5 of super-layer PC1−. b) Efficiency of the 128 cells of the same module.*

The results of the same analysis applied to 8 super-layer halves in the main tracker behind the magnet for two runs are shown in Fig. 4, as a function of the discriminator threshold setting averaged over the super-layer half. A clear threshold dependence is seen. The runs 17255 and 17254 were taken nearby in time and differ only in high voltage settings and therefore gain. Most of the data taken during year 2000 run was taken with settings similar to those of run 17255 because of the high-voltage stability problem described above. It now seems likely that we will be able to run with the increased gain settings of run 17254 and thus benefit from the increased efficiency.

Two methods were used to check the resolution of the chambers. One method estimated a "local" resolution by comparing the hit positions of hits on adjacent double layers. The method has the advantage of being insensitive to alignment effects and extrapolation errors. A resolution of 240 μm – 300 μm was found, compared to a value of 500 μm – 700 μm, estimated using found tracks. The discrepancy is most likely due to our still preliminary alignment.

1.2.4 High-p_T Chambers

The concept of the high-p_T trigger is as follows: tracking chambers with a pad-type readout are placed within the spectrometer magnet. Pad hits are input to dedicated processors, and high-p_T tracks are selected based on the hit patterns. Such tracks tend to bend little or make larger angles with respect to the beam, and their hit-patterns are distinct from those caused by minimum bias tracks.

[3]By construction, the neighboring cell overlaps sufficiently to ensure negligible efficiency drop in the edge region.

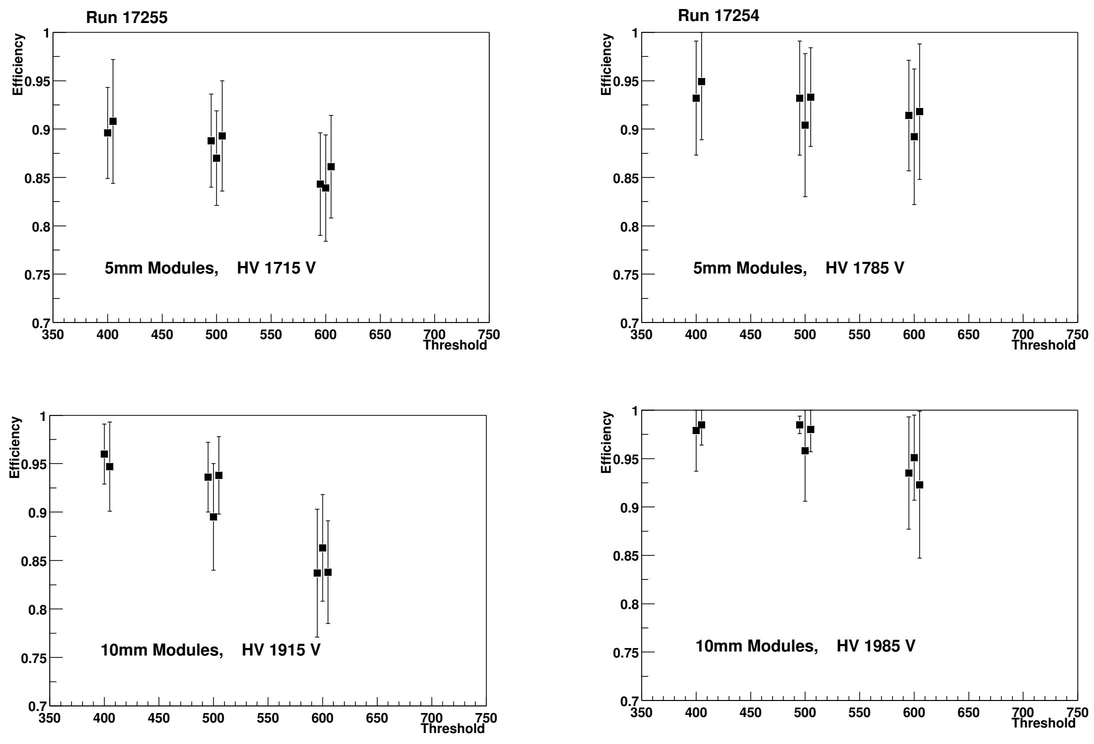

Figure 4: *Average efficiency of the PC super-layer halves for runs 17255 and 17254 taken under identical conditions, except the high voltage. The corresponding gains are 1.17 and 1.46. The horizontal axis is the preamplifier threshold voltage in millivolts.*

The tracking chambers with pad readout come in two types: gas-pixel chambers for the region nearest the beam, and straw-tube chambers with "pickup-pads" for the larger outer region.

The gas-pixel chambers use short anode wires oriented parallel to the beam. The tracks going from the main vertex to the inner high-p_T chambers are almost parallel to the wires resulting in large primary ionization and sharp rise times.

The straw tube chambers utilize straw tubes against which are positioned printed circuits consisting of a pad pattern. These pads are positioned very close to, or in contact with, the outer surface of the straw tubes. A gas avalanche occurring at an anode wire then induces an image charge on the pad directly above the avalanche.

There are a total of 12 chamber halves organized into 3 super-layers: six gas-pixel chambers for the inner region and six straw tube chambers for the outer region.

Status of Inner Chambers: All inner chambers were installed during the 2000 running period and were operational at a voltage setting at least 50 V above the value corresponding to the beginning of the efficiency plateau. During the last month of data taking, the chambers were operated routinely along with the rest of the HERA – B detector. The number of dead channels is relatively small: out of 11 960 channels, 18 are dead due to missing wires or disconnected cables and 12 have lost one wire (of two in the cell) resulting in an efficiency loss of about 30%.

The single-cell efficiency was determined using tracks defined by matching VDS, ECAL, and RICH segments and two of the three high-p_T stations (e.g., PT1 and PT3). All known dead and hot channels were excluded. The efficiencies obtained for different chambers and cell sizes are shown in Fig. 5.

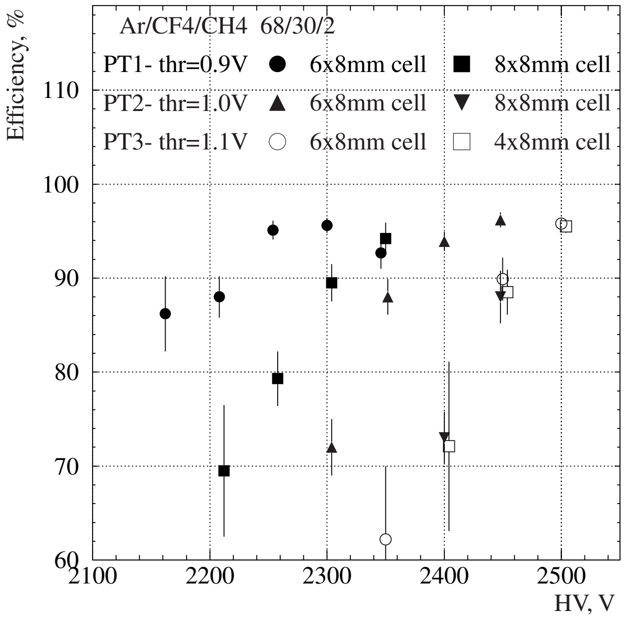

Figure 5: *Efficiencies measured for inner high-p_T chambers during the 2000 run using VDS-ECAL-RICH tracks.*

The efficiency measured reaches a plateau of about 96% and does not increase further. This could indicate that some fraction of the reference tracks are ghosts; alternatively, there may exist a timing problem or an electronics inefficiency with large signals. Previous tests at the ITEP synchrotron yielded a single-cell efficiency higher than 99% for fluxes up to about 5×10^5 particles/cm^2-s. These measurements, however, were performed without a magnetic field.

Status of Outer Chambers: During the 2000 running period, four of six outer high-p_T chambers were installed and run regularly at nominal high voltage. All but two of 1488 straw tubes were active. The very limited access to the detector precluded installation of the remaining two chambers, they will be installed during the present shutdown.

The installed chambers were partially instrumented with front-end cards and read out. Substantial intermittent noise and oscillations were seen on the front-end ASD-8 cards which prevented us from measuring chamber efficiencies or inputting meaningful signals to the pretrigger electronics. During the present shutdown, we will attempt to trace the sources and eliminate the oscillations.

1.2.5 Muon

The muon system provides a pretrigger signal for the First Level Trigger and is used for muon identification in the offline analysis. It consists of a muon filter and four super-layers of muon chambers. Each super-layer has pixel chambers covering the area near the beam pipe. The outer regions are covered by a combination of tube and pad chambers. The outer regions of the first two super-layers consist of three layers of muon tube chambers with 0^o and $\pm 20^o$ views. The outer regions of the third and fourth super-layers consist of one 0^o layer with both anode and pad readout. The pads (and pixels) of these layers are used in the muon pretrigger. The First Level Trigger also relies on the tube chambers of the first, third and fourth layers for tracking.

All 342 tube chambers, 132 pad chambers and 16 pixel chambers are installed and running. Chamber operation has been smooth and reliable.

The major cause for concern in the muon system is the efficiency of the pad chambers. The measured efficiencies for the MU3 and MU4 pads are 75% and 68% respectively. Since one pad from each chamber is required in the muon pretrigger, the efficiency per track is just 51% and since most triggers require two tracks, the pretrigger efficiency is just 26%. Studies are underway to understand how to improve on this. Foreseen improvements including a better grounding scheme, installation of additional filter capacitors, a modified termination scheme, repair of high-voltage problems and broken readout channels, and operation at higher chamber bias (high voltage) are expected to improve the efficiency to $\approx$90%, resulting in an overall 2-track pretrigger efficiency of 66%. Improvements beyond this will almost certainly require replacement of the front-end amplifier board (ASD-8). The ASD-8 amplifier has a shaping time of 6 ns which is a poor match to the 25 ns rise time of the pad pulses. We are looking into the feasibility of designing, producing and installing new amplifier cards in the present shutdown.

The efficiency of the tube chambers is also somewhat uncertain. A tube efficiency of $> 99\%$ was measured in a test beam, however a measurement in situ shows efficiencies in a range from 96.6% – 98.3%, depending on super-layer, despite the fact that we are running the chambers well above the knee of the plateau curve. The discrepancy between the test beam result and the in situ measurement has not been fully tracked down however it is due in part to some residual broken channels ($\approx$ 1%) which we expect to repair during the shutdown. We also suspect that the sample of reference tracks includes some ghosts.

1.3 Trigger Status and Plans

We first briefly review the status of the pretrigger systems and the First Level Trigger. An extended discussion of the trigger efficiency of the pretrigger/FLT system follows.

1.3.1 Calorimeter Pretrigger

The calorimeter pretrigger system has been in operation since the beginning of the 1999 run, providing a high-E_T trigger which allowed detection of the J/ψ in its e^+e^-decay mode. During the course of the 1999, 2000 runs, the system grew and was finally completed near the end of run 2000. By Summer 2000, the majority of the system ($\approx$ 80% by end July) was fully integrated with the DAQ and running reliably. The intrinsic efficiency of the system was determined by comparing clusters found in the offline analysis with those generated by the pretrigger system and inserted into the event stream via the FLT electronics. The average efficiency for working cells is 95%.

1.3.2 Muon Pretrigger

The muon pretrigger has been in operation and supplying pretriggers since July of this year. Coverage of the muon pad chambers is complete. The efficiency of the system was measured using a technique similar to that used to measure calorimeter pretrigger efficiency. Half of the system was found to have an efficiency >99% while 28% showed efficiencies between 95% and 99% and 7% have efficiencies between 80% and 95%. The remaining channels suffered from hardware failures in the readout chain. A major reason for the inefficiencies has been traced to bit errors in the pretrigger messages. The errors most likely occur in a single FLT module in the transmission chain. (If this turns out to be the case, this module will be repaired or replaced.) The electronics needed to cover the pixel chambers exists and has been tested. The installation will be completed during the shutdown.

1.3.3 High-Pt Pretrigger

A small test setup consisting of six link boards and four pretrigger boards was installed in the experiment and, after considerable effort to tune the optical links, worked essentially error-free during periods without target operation. During data taking, bit errors occurred occasionally, presumably due to the larger number of hits in the data streams. This may imply that the DC offset for the optical receivers should be increased at higher interaction rates. The problem is under study (see Sect 1.3.4.

Using data from the inner chambers collected during minimum bias runs at various interaction rates, we have estimated the pretrigger rate. This rate as a function of interaction rate is shown in Fig. 6 (for inner chambers only). All channels with occupancy larger than 20% have been masked out. The average number of pretriggers is 0.18/BX at an interaction rate of 5 MHz, about 60% larger than the Monte Carlo prediction of 0.11/BX. The contributions from the $+x$ and $-x$ sides are equal. The pretrigger rate drops if one makes more stringent cuts on noisy channels. The pretrigger rate is 1.06/BX at an interaction rate of 20 MHz, again somewhat larger than the Monte Carlo prediction of 0.61/BX. The rate of the high-p_T pretriggers in coincidence with the electron (FLT-SLT trigger with $p_t > 1.5\,(1.0)$ GeV/c is 0.82/BX at 2 MHz. This is a factor of two larger than the Monte Carlo prediction.

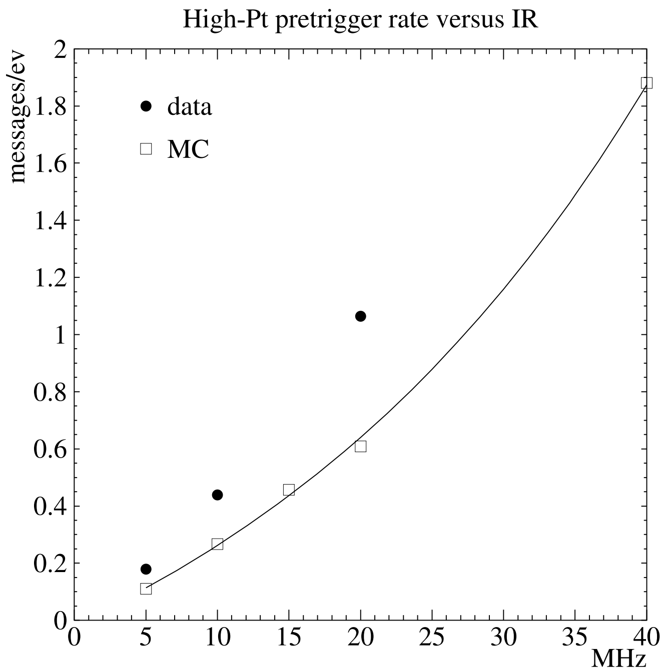

Figure 6: *High-p_T system pretrigger rate as a function of interaction rate.*

1.3.4 Optical Links

Optical links are used for transmitting hit data from the trackers to the pretrigger systems and the TFUs. A serious concern is whether the present optical links can provide the required stability over an extended period of time. In the present scheme, offset and modulation currents are adjusted with potentiometers. Because of different attenuation for the different optical fibers, temperature drifts and other effects, the pre-adjusted values have often proven to be outside the dynamic range of the receiver. The potentiometers are not accessible once the boards are installed. Hence any adjustment requires removal of the board which is a delicate and lengthy procedure. Thus we are considering adding the capability to adjust the offset and bias currents remotely. A new optical transmitter piggy-back is being designed and the feasibility of producing and replacing some or all of the links installed in the experiment is being evaluated.

1.3.5 First Level Trigger

The FLT attempts to find tracks in the tracking super-layers behind the magnet starting from seeds defined by the pretrigger systems (4 main-tracker super-layers and, for the muons, also 3 muon super-layers). It is capable of making cuts on kinematical properties of tracks, of requiring any number of tracks from combinations of pretrigger sources and of combining tracks pair-wise, and imposing cuts on the pair mass.

The track finding is done in an array of 82 interconnected purpose-built processors (called Track Finding Units). Each processor takes input from one section of one super-layer. Messages containing track parameters pass from pretrigger systems to TFUs and then from TFU to TFU and finally (for accepted tracks) into Track Parameter Units which calculate and cut on kinematical parameters, passing on accepted tracks to the Trigger Decision Unit which is responsible for the final trigger decision.

By the beginning of 2000, the FLT electronics had been largely installed and was undergoing system tests. Many problems were yet to be solved, among them:

- The optical links were not working properly and had to be hand-tuned. Eventually most optical links (96%) were made to work and those with significant error rates ($> 10^{-6}$) were set "on" meaning that all channels serviced by that link showed hits for all events.
- Other system level hardware problems had to be corrected to stabilize the system, such as cooling in the TFU crates and unstable "repeater boards" between TFUs.
- The Outer Tracker was not behaving at performance levels: many channels were being lost due to high voltage problems. The resulting inefficiencies were large enough to kill any hope of using the FLT as a trigger until a way had been found to mask ON the dead areas.
- The cell spacing of the Outer Tracker was found to be less uniform than expected, due to the modular construction. A new software tool had to be written to minimize the resulting inefficiencies.
- Links between pretriggers and the track-finding units were flaky and had to be stabilized.
- Many of the tools needed to control, monitor and simulate the FLT were found to be either missing or inadequate and had to be either written or rewritten.

Nonetheless, by the end of the run, the system was working at the level of finding tracks with fair efficiency (see below) and producing messages containing lists of triggered tracks and their coordinates for the second level trigger. The FLT was also used as a trigger in the last days of the run, with mixed success. This is further discussed in the next section.

1.3.6 Trigger Efficiency Estimates

In the remainder of Section 1.3, we go into quite some detail to explain our present understanding of the trigger efficiency of the complete triggering chain based on data taken during the year 2000 run and our expectations for startup in 2001. Readers not interested in the details are invited to skip to tables 2 and 4.

1.3.7 FLT Track Finding Efficiency Estimate (OTR)

Table 1: *Efficiency factors needed to calculate the track finding efficiency of the First Level Trigger. Row 13 is the calculated efficiency based on the given figures. The upper limit of the range given in the last line under "present" has been increased to accommodate a measurement not consistent with the model of 74% (see text).*

		Efficiency model	
		Present	**Potential**
1	Working-cell efficiency	0.90	0.95
2	Dead single cells	0.08	0.015
3	Dead double cells	0.08	0
4	Masking efficiency	0.8	1
5	Partially working optical links	0.04	0
6	Efficiency TDC-TLB links	1.00	1
7	Efficiency optical links TLB-TFU	1.00	1
8	Hit efficiency	0.968	0.997
9	All trigger layers hit, 1 track	0.68	0.96
10	Lookup table coding problems	0.97	>0.97
11	Understood geometrical effects	0.95	>0.95
12	Other geometrical effects	0.92	>0.92
13	Tracking efficiency (model)	0.58	>0.81
14	Adjusted track efficiency	0.58 - 0.74	0.81 - 0.96

In this subsection we summarize our present understanding of the FLT tracking efficiency in the four Outer Tracker super-layers. There are several ways to arrive at efficiency estimates using data sets taken under different conditions, using simulation and paper models based on known efficiencies. We find inconsistencies when comparing the various estimates which we are working to resolve.

We start with a paper model. The input numbers are given in the column labeled "Present" of Table 1. Row 1 of this table is the measured single-cell plateau efficiency (see the Outer Tracker section). Most dead single cells (row 2) are due to disconnected high voltage groups. Dead double cells (row 3) are mainly due to malfunctions of ASD8 preamplifier cards or misplugged cables from chamber to preamplifers.

As described in the paragraph entitled "Optical link performance tests" of the FLT report, a comparison was made of occupancy distributions as seen in the wire memory of the TFUs and in the offline analysis. Discrepancies at the level of 1.5% are seen. Most of these errors can be attributed to failures in the masking technique. If we assume that the entire 1.5% is due to such failures, the fraction of successfully masked channels must be 0.8 (row 4) since the total number of dead double layers is 8.0%.

At run startup, the optical links connecting the detector to the TFUs are checked and if a significant bit error rate is found ($> 10^{-6}$), the corresponding cells are switched on (i.e. the TFU sees a hit for each cell). Typically, 4% of the links were switched on (row 5). Since they were on, no inefficiency is incurred (we list them in the table for completeness). The remainder of the links were 100% effective (rows 6,7).

To first order, the hit efficiency is:

$$P_{hit} = P_3 \cdot P_4 + (1 - P_3) \cdot (P_2 \cdot P_1 + (1 - P_2) \cdot P_1 \cdot (2 - P_1))$$

The numbers refer to the rows in Table 1. Plugging those numbers into the formula yields a hit efficiency of 96.8%. Thus the probability that all hits needed to find a track are present is $P_{hit}^{12} =$ 68%, since 12 hits are required.

Next, we turn to the results of a simulation. The simulator does a "bit-wise" identical emulation of the FLT hardware and can take input from either Monte Carlo or data, in this case we use Monte Carlo. The Monte Carlo takes into account the Outer Tracker single-cell efficiency as well as the complete map of dead and hot channels. The simulator also uses the dead/hot channel map to turn on dead channels but assumes 100% masking efficiency in place of the 80% given in the table. The simulator result of 80% for percentage of tracks with all hits becomes 67% after a global correction for the non-masked (1.5%) channels is applied, in good agreement with row 9.

The next factor to consider is the track-finding efficiency of the FLT itself, given that the hits are present. The simulator shows a total drop in efficiency of 15% from "algorithmic" effects. We separate these effects into 3 factors in the table:

- Lookup table coding problems: The algorithm used to generate the lookup tables uses an oversimplified geometrical model of the detector. Most of this inefficiency can be recovered with a more realistic model.
- Understood geometrical effects: These are mainly due to irregularities in the cell spacing of the Outer Tracker arising from its modular structure. It is in principle possible to recover most of this ineffeciency by treating the position of each wire individually when generating the lookup tables.
- Other geometrical effects: These effects are not yet understood.

When these effects are taken into account, an overall tracking efficiency of 58% is found. This can be compared with measured values derived from other studies:

- Data was taken while triggering on the calorimeter. The FLT was in "transparent" mode, i.e. found tracks were recorded but the FLT decision did not actually produce triggers. Reference tracks were defined using reconstructed ECAL-RICH-VDS matches. The reference tracks were matched to tracks in the FLT output record 74% of the time.
- Compare the same set of reference tracks with the simulator output (rather than the recorded FLT record) on an event by event basis. The measured efficiency is found to be 59%.

- Run the simulator on the sample of J/$\psi \to \mu^+\mu^-$ events accumulated over the summer. The result is 59%. (Additional inefficiencies in the muon tracking are not included in this estimate.) The estimate is clearly somewhat biased by the trigger selection which should, if anything, lead to an overestimate.

The discrepancy between these values is not understood. Until the inconsistency is resolved, we use the lowest and highest measured values to indicate the range: 58% – 74% (line 14).

We also list in Table 1 the numbers we expect to achieve by the end of the present shutdown. Improvements in the Outer Tracker's single-cell efficiency and dead channel count will result in a findable track (i.e. all hits present) efficiency of 96%. After losses in the FLT algorithm are taken into account, this will be reduced to between 81% and 96%. Finally, we adjust the lower end of the range to the lower limit of the present range multiplied by the ratio of the values given in line 9. We hope to reduce the errors on this estimate in the near future.

1.3.8 Trigger Efficiency for J/$\psi \to e^+e^-$

Table 2: *Efficiency for J/$\psi \to e^+e^-$. All rows are event level efficiencies.*

		Model		**Design**
		Present	**Potential**	
1	Geo., ktrig 500, m > 2 GeV	0.34*	0.34*	0.45
2	Missing low angle coverage	0.44*	1	1
3	ECAL pretrig eff. (incl coverage)	0.62	0.95	1
4	Tracking efficiency (2 tracks)	0.34 - 0.55	0.66 - 0.92	1
5	Frontend pipeline overflows	1	1	1
6	Total efficiency	0.032 - 0.051	0.21 - 0.30	0.45
7	Ratio to design	0.07 - 0.11	0.47 - 0.67	1
Triggered rates (5 MHz)				
8	direct J/$\psi \to e^+e^-$ / hour	1000 - 1700	7000 - 10000	15000
9	B $\to$ J/$\psi \to e + e-$ / hour	.7 - 1.2	5 - 7	10

* to be verified

In Table 2 we summarize our understanding of the geometrical and trigger efficiency for J/$\psi \to e^+e^-$ as seen near the end of Run 2000, what we expect to achieve and a comparison of these to the values given in the Design Report. Rows 1 and 2 of the table come from the FLT simulation[4]. Row 3, the pretrigger efficiency was, at the time of this estimate (end July), dominated by missing calorimeter readout and pretrigger coverage but also includes an intrinsic inefficiency of 5% when compared to the offline calorimeter reconstruction (hence the 95% in the "Potential" column). Row 4 is explained in section 1.3.7.

Row 5 gives that the efficiency factor due to the loss of triggers which arrive after the event data has left the frontend pipelines is zero. Since the trigger decision is made in the required time when the processor network is unloaded, the number can always be adjusted to 1 by adjusting the

[4]We believe these numbers to be correct, however we were unable to dispel all doubts before the deadline for publication.

interaction rate. The issue then is the maximum interaction rate imposed by congestion in the processor network. By design, the processor network is intended to cope with interaction rates up to 40 MHz. A conclusive measurement has not yet been made.

Over the lumi upgrade shutdown we expect to complete the low angle coverage by introducing the Inner Tracker into the trigger, utilize the complete calorimeter coverage, improve the Outer Tracker and work to better understand and improve the FLT efficiency. Row 7 shows that we expect the final efficiency to lie between a third and two thirds of the design value. Much of the difference between the Design Report and present estimates comes from the geometric and kinematical factors shown in row 1. The number given in the Proposal (32%) is much closer to the presently accepted value. The figure given in the Design Report is clearly over-optimistic.

Note that, as in the Design Report, we have not included SLT efficiency in this table since it is highly correlated with reconstruction efficiency. The estimates of reconstruction efficiency given throughout the document include SLT efficiency, except when specifically itemized. A discussion of the observed and simulated SLT efficiency can be found in the SLT report.

1.3.9 Trigger Efficiency for $J/\psi \to \mu^+\mu^-$

Table 3 shows factors entering into the calculation of the muon pretrigger efficiency for a single muon as well as additional factors needed to determine tracking efficiency in the muon system. The numbers in the 2nd column refer to the present setup, those in the 3rd to the setup at startup in 2001.

The pad and pixel chambers (super-layers 3 and 4) are used to define pretrigger candidates and three of the four muon tube chambers (super-layers 1,3,4) are used to define track seeds in preparation for tracking through the tracker super-layers. At present, only the pad chambers have been used in the pretrigger. The average pad efficiency is 71%, implying a coincidence efficiency of 51% (row 1). Some losses are measured in the pretrigger and peripheral electronics (row 3). The overall per-track efficiency of the pretrigger system is given in row 4.

Pretrigger candidates initiate track-finding in the FLT processors dedicated to muon tracking. The tracks are followed through 3 of the 4 muon super-layers before being passed into the main Outer Tracker processors, thus the efficiency of the muon tube chambers also affects the trigger efficiency. Since 5 tracking layers are used, the effective hit efficiency is raised to the fifth power, leading to an overall probability that all hits needed to find a track are present of between 86% and 95%. (row 10).

The factors pertaining to intrinsic FLT efficiencies (rows 11 - 13) are closely related to the corresponding factors in Table 1. See Section 1.3.7 for explanations.

The full tracking efficiency (including Outer Tracker) is obtained by multiplying the values from row 14 of Table 1 for tracking in the Outer Tracker: 39% to 56%. This can be compared to two other efficiency estimates:

- A data set was accumulated using a trigger which required a single track at the first level. The second level then looked for two tracks using the same algorithm used for the bulk of the muon-triggered running. A (somewhat biased) tracking efficiency can be derived by comparing the rate of J/ψs found in this data with that seen with the SLT-only runs taken nearby in time. The resulting efficiency is 19% per track.

Table 3: *Efficiency factors needed to calculate the muon pretrigger efficiency and track finding efficiency in the muon system. Row 15 is the calculated track-finding efficiency in the muon chambers, based on the given figures. The values given in line 16 refer to the full efficiency for finding a track in both the muon and outer tracker chambers. Line 16 has been adjusted to accommodate all of the measurements.*

		Efficiency Model	
		Present	**Potential**
1	MU3 · MU4 pad efficiency	0.51	> 0.90
2	Dead/hot channels (muon pads)	0.01	0.01
3	Pretrigger system efficiency	0.92	1
4	Overall pretrigger efficiency/trk	0.46	0.90 - 0.98
5	Tube efficiency (working cells)	0.85 - 0.90	0.85 - 0.90
6	Double layer tube efficiency	0.97 - 0.99	0.97 - 0.99
7	Dead/hot muon tubes (single layer)	0.06	0.02
8	Link efficiency	1.00	1
9	Effective hit efficiency	0.97 - 0.99	0.97 - 0.99
10	Hits in all tube chambers/trk	0.86 - 0.95	0.86 - 0.95
11	Lookup table coding problems	0.94	>0.94
12	Understood geometrical effects	0.95	>0.95
13	Other geometrical effects	0.89	>0.89
14	Muon system tracking	0.68 - 0.76	0.68 - 0.95
15	Complete Muon + OTR tracking	0.39 - 0.56	0.55 - 0.91
16	Adjusted complete tracking	0.19 - 0.56	0.27 - 0.91
17	Pretrigger & tracking(adjusted)	0.09 - 0.26	0.24 - 0.89

- A data set with a 2-track FLT trigger and 2-track SLT trigger was accumulated in the last days of the run. No J/ψ was seen so no efficiency can be derived. However an upper limit of 28% efficiency per track can be inferred by comparing with SLT-triggered runs taken nearby in time.

The first of these measurements is not consistent with the range given on line 15. We are therefore, once again, forced to adjust the range to accommodate this lower value (line 16). Finally, we multiply in the pretrigger efficiency given on line 4 and obtain our final estimate of pretrigger + FLT efficiency for a single track of 9% – 26% for the current setup.

The efficiency estimates for $J/\psi \to \mu^+\mu^-$ are given in Table 4. The uncertainties in both the muon tracking and the main tracker tracking lead to a large uncertainty in the total J/ψ efficiency. In the present setup, the maximum efficiency estimate is 2.7% of the design value. Foreseeable improvements should bring the efficiency up to near 79% of the design value. Most of the uncertainty lies in the "algorithmic" problems of the First Level Trigger and inconsistencies between the various efficiency measures. We are working on narrowing down the errors on these estimates with high priority.

Some losses are seen due to triggers arriving too late (row 5) even at an interaction rate of 5 MHz, implying an upper limit on the interaction rate somewhat less than 5 MHz for the present setup. Foreseen improvements will reduce these losses to at most 8% at 5 MHz interaction rate. At least part of the reason for the present high latency is congestion in the FLT network stemming from the large number of switched on channels. We expect improvements after the number of masked

Table 4: *Efficiency for $J/\psi \to \mu^+\mu^-$. All rows are event level efficiencies (i.e. 2 tracks).*

		Model		**Design**
		Present	**Potential**	
1	Geometry, p > 5 GeV	0.62	0.62	0.62
2	Missing low angle coverage	0.44*	1	1
3	Pretrig, tracking efficiency (2 tks)	0.008 - 0.07	0.06 - 0.79	1
4	Frontend pipeline overflows	0.77 - 0.88	0.92 - 1	1
5	Total efficiency	0.002 - 0.017	0.03 - 0.49	0.62
6	Ratio to design	0.003 - 0.027	0.06 - 0.79	1
Triggered rates (5 MHz)				
7	direct $J/\psi \to \mu^+\mu^-$ / hour	70 - 560	1000 - 16000	21000
8	$B \to J/\psi \to \mu^+\mu^-$ / hour	0 - 0.4	0.7 - 12	15

* to be verified

channels is reduced to the number given in line 2 of Table 1 and the the 4% of non-working optical links are repaired. Further ways to decrease the trigger latency are under study (e.g. using 2 rather than 3 muon super-layers in the track propagation).

1.4 Run 2000

A summary of the major data sets taken since April of this year is given in Table 5. The FLT tracking was under intense development during the run and was not available for taking production data, except at the very end. We therefore triggered using calorimeter and muon pretriggers and the Second Level Trigger. The Trigger Decision Unit of the FLT received the pretrigger messages and issued a trigger if a required number (one or two) of pretrigger candidates were seen. The second level made further cuts on p_T and possibly mass then attempted to find tracks associated with the pretrigger candidates.

After a short run with a minimum bias trigger, we concentrated on developing the Di-lepton trigger. At first, we triggered with the electron pretriggers and the SLT. During this period, the SLT projected pretrigger candidates directly into the vertex detector, with no intermediate tracking in the OTR. The bulk of the data of the year 2000 sample was taken with these conditions. When the Outer Tracker stabilized and an alignment became available in mid-June, the second-level algorithm for tracking behind the magnet was commissioned. At the end of June, we introduced muon pretriggers and ran simultaneously with both electron and muon pretriggers. Finally, in the last two weeks of the run, we turned on tracking at the first level and took data with both single and double track conditions at the FLT and both single and double track requirements at the SLT. Most of the di-lepton data was taken with an interaction rate of 5 MHz. The single lepton data was taken with a 2 MHz interaction rate. Higher rate running (up to 40 Mhz) was tested on a weekly basis.

The invariant cross section per event, as derived from the minimum bias sample, is shown in Fig. 7 together with the reconstructed Monte Carlo. The Monte Carlo agrees with the data to about 20% except for the high p_T region where the measured spectra are somewhat harder. For the charge ratio shown in the bottom of the figure, most acceptance corrections cancel and, for $p_T > 0.5$ GeV/c, the data and Monte Carlo are in good agreement. The relative deficit of low-p_T positive particles in

Table 5: *The major data sets taken during the year 2000 run. The active pretriggers (E = ECAL, μ = Muon) are shown in the "pre" column. The "FLT" column distinguishes between runs with no tracking requirements and a requirement of 1 track or 2 tracks. The "SLT" column gives the SLT requirements: 1 $\Rightarrow$ 1 track, 2 $\Rightarrow$ 2 tracks, V $\Rightarrow$ Vertex detector tracking, O $\Rightarrow$ Outer tracker tracking.*

Type	Start	Stop	Trigger			Events	Time(min)	
			Pre	FLT	SLT	$\cdot 10^{-6}$	total	live
Min Bias	10 Apr	14 Apr	-	-	-	2	2000	-
Di-lepton	29 Apr	13 Jun	E	-	V,2	12	10387	7508
Di-lepton	15 Jun	27 Jun	E	-	OV,2	1	1385	953
Di-lepton	28 Jun	16 Aug	Eμ	-	OV,2	3.7	9363	4853
Hard γ	17 Aug	17 Aug	E	-	-	0.6	390	375
Single lepton	17 Aug	18 Aug	μ	1	OV,1	1.4	362	116
Di-lepton	18 Aug	18 Aug	Eμ	2	OV,2	0.4	470	390
Di-lepton	18 Aug	22 Aug	Eμ	1	OV,2	1.0	1297	995
Single lepton	24 Aug	25 Aug	Eμ	1	OV,1	3.1	831	465

the data is not yet understood.

The left hand side of Fig. 8 shows the e^+e^-invariant mass spectrum from a preliminary analysis of a subsample of 2 million events of the electron-triggered di-lepton sample. The analysis defines tracks by matching calorimeter clusters with track segments in the vertex detector. To eliminate background, each electron candidate is required to have an associated bremsstrahlung cluster in the calorimeter from radiation in front of the magnet. The analysis yields a preliminary value for the J/ψ production cross section of 270 ± 128 nb/nucleon. The error is currently dominated by the simulation of calorimeter acceptance which was still evolving while the data was being accumulated in April and May. Analysis of the full sample is underway.

The right hand plot in Fig. 8 shows the $\mu^+\mu^-$ mass spectrum from $\approx 80\%$ of the di-muon sample. The peak is some 30 MeV lower than the accepted value of the J/ψ and has a width of 75 MeV, compared to a Monte Carlo value of 60 MeV. The total J/ψ sample of 3000 events is being used to tune vertex packages. The final goal of the analysis is to detect displaced vertices which can then be used to determine the $b\overline{b}$ cross section.

The left hand plot in Fig. 9 shows the distribution of the z difference between primary vertex and $\mu^+\mu^-$ vertex for selected $\mu^+\mu^-$ pairs in the J/ψ region. The right hand plot in Fig. 9 shows the same distribution but with the additional requirement that at least one extra track is consistent with having originated at the $\mu^+\mu^-$ vertex. Despite the low statistics, the plots demonstrate the capacity to reconstruct detached vertices. A $b\overline{b}$ cross section of 12 nbarn would contribute about two $\mu^+\mu^-$ pairs. We expect that ongoing optimization of software tools and alignment will further decrease the background on these plots in the near future.

It is evident that a measurement of the $b\overline{b}$ cross section can only come from an analysis of the full J/ψ sample collected with the electron trigger. We estimate that the sample contains about 30,000 reconstructible J/ψ's without bremsstrahlung cut, about 20 of which come from b decay. The bremsstrahlung cut would reduce this to 3000 J/ψ's, not enough for a cross section measurement. However, other combinations of cuts, including a secondary vertex cut may allow a signal to emerge. The analysis is in progress.

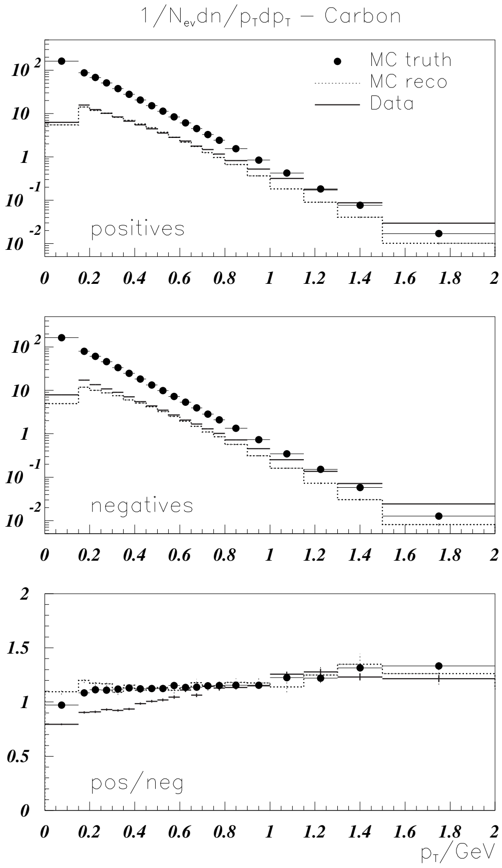

Figure 7: *Transverse momentum spectra for inelastic interactions in proton-carbon scattering. The data for positives and negatives are compared to Monte Carlo predictions after reconstruction and on the generator level ("truth"). Also shown is the ratio of positives to negatives.*

Finally, in Fig. 10, we show the $\pi^{\pm}K^{\mp}$ mass spectrum from the 1.2 million event sample collected with a single muon high-p_T ($p_T > 1.2\,\mathrm{GeV}$) trigger requirement run of Aug. 17. The $\pi^{\pm}K^{\mp}$ candidates were required to have a vertex separation of at least 2 mm. The candidates were required to have a RICH identification consistent with a pion hypothesis and the kaon candidates were required to be both consistent with a kaon hypothesis and inconsistent with a pion hypothesis. A D^0 signal is also seen in all of the hard-triggered (single lepton and di-lepton) data samples.

1.5 Physics Prospects

The chapter entitled "HERA – B Physics Beyond the Shutdown" is a compilation of 16 contributions by 20 authors. Each section evaluates the HERA – B potential to contribute to particular physics topics. The topics fall into 3 main categories: B physics, charm physics and QCD studies. The level of simulation ranges from the generator level through to complete detector simulation and reconstruction using the standard reconstruction software.

We have chosen to delve into three topics in the field of B physics in more detail in this summary:

- CP Violation in $B^0 \to J/\psi\, K^0_S$ Decays: It now appears unlikely that HERA – B will contribute

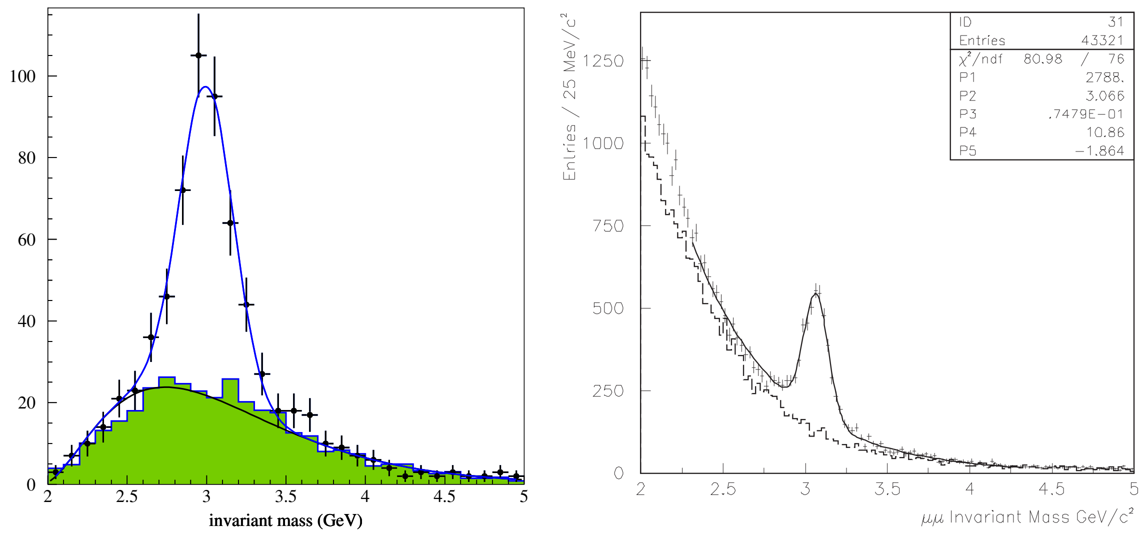

Figure 8: *The left hand plot shows the* e^+e^- *invariant mass spectrum from 10% of the electron-triggered data. The right hand plot shows the* $\mu^+\mu^-$ *and* $\mu^\pm\mu^\pm$ *(histogram) invariant mass spectra from 80% of the muon triggered data.*

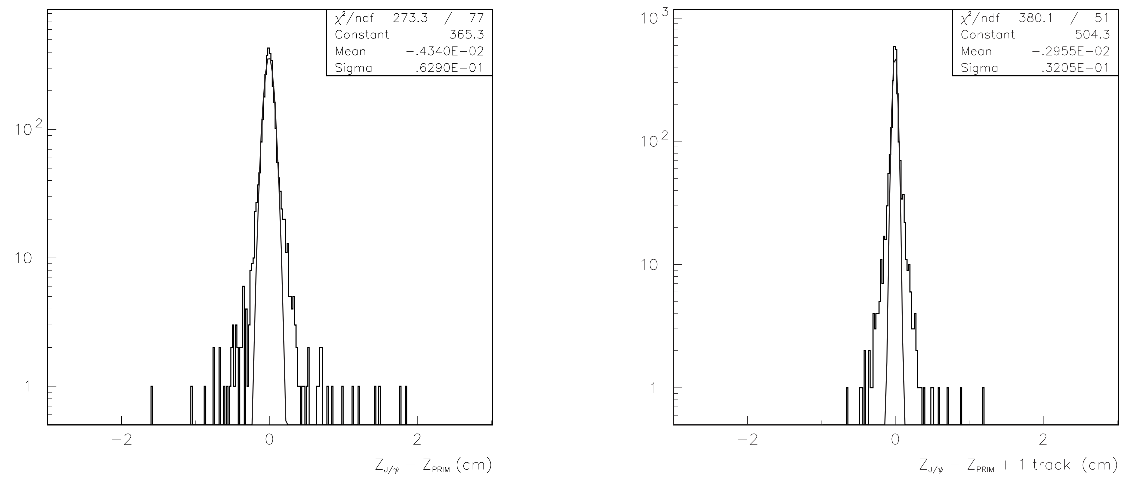

Figure 9: *The left hand plot shows the distribution of the* z *difference between primary vertex and* $\mu^+\mu^-$ *vertex for selected* $\mu^+\mu^-$ *pairs in the* J/ψ *region. The right hand plot shows the same distribution but with the additional requirement that at least one extra track is consistent with having originated at the* $\mu^+\mu^-$ *vertex.*

to this measurement at a level comparable to the e^+e^-experiments. Nonetheless, a significant measurement is still possible. Furthermore, a new visit to this topic gives the opportunity to update sensitivity estimates made at the time of the proposal in the light of a much more detailed simulation and full reconstruction.

- The flavor changing neutral current decay: $B^0 \to \mu^+\mu^- K^{*0}$. The Standard Model offers testable predictions for the decay rate of this process which is highly sensitive to new physics, such as charged Higgs bosons or heavy supersymmetric particles. HERA − B has the potential to compete

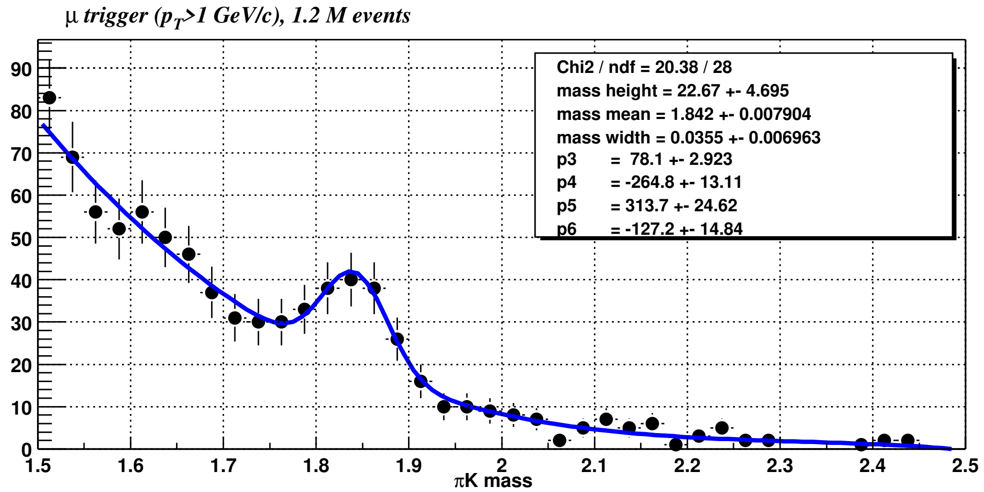

Figure 10: *Invariant mass spectrum of $\pi^{\pm}K^{\mp}$ candidates from a run taken with a trigger requiring a single high-p_T muon with p_T > 1.2 GeV.*

in this field with both e^+e^-machines and the TEV II experiments. $B^0 \to \mu^+\mu^- K^{*0}$ is but one of several exclusive final states relevant for FCNC studies.

- B^0_s–$\overline{B^0_s}$ Mixing: This very challenging measurement can provide important constraints on parameters of the CKM matrix.

Before turning to these topics, we first comment in general on HERA – B potential for the topics studied. For most of the B physics measurements considered here, our most serious potential competition comes from the Tevatron RUN II program, depending on how quickly the Tevatron and the collider experiments reach design performance. Since we are unable to judge this, we offer two evaluations. The first, in Table 6, compares HERA – B's physics reach to existing measurements and extrapolations of existing experiments. The second, in Table 7 assumes that the TEV II experiments quickly reach design performance. Most likely, the situation by mid-2002 will be somewhere in between the scenarios.

In both tables, we indicate competitiveness for a baseline scenario which assumes a 20 MHz interaction rate, a single-track reconstruction efficiency of 80%, full trigger functionality and a $b\overline{b}$ cross section of 12 nb. We also indicate what would happen if the rate of accepted $b\overline{b}$ events falls below the baseline by a factor of 10. Once again, reality will most likely lie between these limits.

In the scenario of Table 6, it can be seen that, even for relatively modest assumptions on the performance of HERA – B, much of the field of heavy flavor physics is open to us. Even with optimistic assumptions on the capabilities of competing experiments, Table 7 shows that HERA – B can produce competitive or at least interesting and significant results in some areas of heavy flavor physics, but only if the baseline scenario is reached.

The interesting topics in the field of charm physics require a relaxation of trigger thresholds (invariant masses, transverse momenta etc.) and therefore greater demands are placed on the second and higher trigger levels. The feasibility is yet to be evaluated. Most likely a charm physics program can not be carried out in parallel with a B physics program in a transparent way.

It is noteworthy that the very preliminary study of measuring CP violation in $B^0 \to \pi^+\pi^-$ decays in this report shows promise. Assuming the branching fraction recently measured by the BABAR

Table 6: *Summary of requirements and performances of* HERA – B *for the main physics topics, measured against the presently available experimental results and extrapolations of existing experiments (excluding the TEV II experiments). Needed triggers are indicated by a cross. A double-cross indicates that the trigger must be operated at reduced thresholds (invariant masses, transverse momenta etc.). The assessment of competitiveness is made for a baseline scenario which assumes an interaction rate of* 20 MHz, *a conservative single-track reconstruction efficiency of* 80%, *and the full trigger functionality. A second scenario is included which assumes that the reconstructed* $b\overline{b}$ *rate is 10% of the baseline. The* $b\overline{b}$ *production cross section is assumed to be* 12 nb *per nucleon for the baseline scenario (more precisely, a* $b\overline{b}$ *production rate of* 18 Hz *is assumed), a value which is at the lower end of the range allowed by existing measurements. This cross section could be larger by up to a factor* 5.

Topic	Trigger Requirements μ	e	hpt	FLT	Competition	Potential (% of baseline) 100%	10%
B physics							
$\sigma_{b\overline{b}}$	×	×	–	×	-	***	***
$\sin(2\beta)$	×	×	–	×	e^+e^-,TEV I	*	–
$CP(B_s^0 \to J/\psi\Phi)$	×	×	–	×	LEP,SLC,TEV I	*	–
b lifetimes	×	×	–	×	LEP,SLC,TEV I	***	**
$\Delta\Gamma_s$	×	×	–	×	LEP,SLC,TEV I	***	*
$B_s^0 \to \mu^+\mu^-$	×	–	–	×	CLEO,TEV I	***	**
$B^0 \to K^{*0}\mu^+\mu^-$	×	–	–	×	e^+e^-,TEV I	***	**
$B^0 - \overline{B^0}$ Mixing	×	×	–	×	e^+e^-,TEV I	*	–
$B_s^0 - \overline{B_s^0}$ Mixing	×	×	×	×	LEP,SLC,TEV I	***	–
α, γ	×	×	×	×	e^+e^-	*** (?)	–
rare $B \to$ hadrons	×	×	×	×	e^+e^-,TEV I	*** (?)	–
Charm physics							
$D^0 - \overline{D^0}$ Mixing	×	–	–	××	e^+e^-	**	*
$D^0 \to \mu^+\mu^-$	×	–	–	××	E771,e^+e^-	***	**
$D^0 \to e\mu$	×	(×)	–	××	E789,e^+e^-	***	**
QCD physics							
Drell-Yan	×	×	–	×	E866	***	**
Quarkonia	×	×	–	×	E866	***	**
soft pN	–	–	–	–	-	***	***
hard pN	–	×	(×)	(×)	-	***	***

*** Possible to perform the first or best measurement.
** Sensitivity worse than extrapolated values of competition but still interesting.
* Sensitivity comparable to existing measurements attainable.

experiment and that the FLT is operational with an overall trigger efficiency of 0.6, we obtain a surprisingly favorable result. Obviously this would be an important measurement and we are now investigating this possibility more carefully with a full simulation of the detector performance. It is worth noting that this measurement depends critically on K - π separation, as $B^0 \to \pi^+\pi^-$ decays must be distinguished from more copious $B^0 \to K^+\pi^-$. Such K - π separation is expected to be substantially better at HERA-B than at, e.g., CDF.

Table 7: *Assessment of the HERA – B physics potential as in Tab. 6, however measured against the full design performance of present and future competition, including the TEV II program.*

Topic	Trigger Requirements μ	e	hpt	FLT	Competition	Potential (% of baseline) 100%	10%
B physics							
$\sigma_{b\overline{b}}$	×	×	–	×	-	***	***
$\sin(2\beta)$	×	×	–	×	e^+e^-,TEV II	*	–
$CP(B_s^0 \to J/\psi\Phi)$	×	×	–	×	TEVII	*	–
b lifetimes	×	×	–	×	TEVII	**	*
$\Delta\Gamma_s$	×	×	–	×	TEVII	**	–
$B_s^0 \to \mu^+\mu^-$	×	–	–	×	TEVII	**	–
$B^0 \to K^{*0}\mu^+\mu^-$	×	–	–	×	e^+e^-,TEV II	***	–
$B^0 - \overline{B^0}$ Mixing	×	×	–	×	e^+e^-,TEV II	*	–
$B_s^0 - \overline{B_s^0}$ Mixing	×	×	×	×	TEVII	**	–
α, γ	×	×	×	×	e^+e^-,TEV II	** (?)	–
rare $B \to$ hadrons	×	×	×	×	e^+e^-,TEV II	** (?)	–
Charm physics							
$D^0 - \overline{D^0}$ Mixing	×	–	–	××	e^+e^-	**	*
$D^0 \to \mu^+\mu^-$	×	–	–	××	E771,e^+e^-	***	**
$D^0 \to e\mu$	×	(×)	–	××	E789,e^+e^-	***	**
QCD physics							
Drell-Yan	×	×	–	×	E866	***	**
Quarkonia	×	×	–	×	E866	***	**
soft pN	–	–	–	–	-	***	***
hard pN	–	×	(×)	(×)	-	***	***

*** Possible to perform the first or best measurement.
** Sensitivity worse than extrapolated values of competition but still interesting.
* Sensitivity comparable to existing measurements attainable.

For completeness, we note that HERA – B can make significant contributions in the areas of heavy quarkonium production and spectroscopy, and of the physics of soft and hard proton-nucleus interactions even in the most pessimistic scenario.

1.5.1 CP Violation in $B^0 \to J/\psi\ K_S^0$ Decays

The HERA – B detector was designed to reconstruct the final states $\mu^+\mu^-\ \pi^+\pi^-$ and $e^+e^-\ \pi^+\pi^-$ of the golden decay mode $B^0 \to J/\psi\ K_S^0$. At the time of the Design Report [1] many idealistic assumptions had to be made to estimate the reconstruction efficiencies for these decay modes. Since then software became available for track reconstruction and trigger simulation. Several studies have been performed using these programs [2, 3, 4]. The numbers presented here are based on the most recent ones [5].

Tab. 8 lists the current estimates of the reconstruction efficiencies for the muon and the electron channel in comparison to the Design Report. The L1 trigger efficiencies are the upper limit efficiencies given in Tables 2 and 4. The reconstruction efficiencies are smaller now for various reasons. The actual mechanical constraints in the fabrication of the Outer Tracker and the compensation coil of the electron beam pipe lead to holes in the acceptance and to an increase in multiple scattering. The lifetime cut was increased in ref. [5] to improve background suppression. This reduces the efficiency by 18% but has practically no impact on the measurement error of $\sin(2\beta)$ since the CP asymmetry only builds up during the mean lifetime of the B meson and can hence anyway not be measured at very small decay times. The geometrical acceptance for pions from K^0_S decays is smaller due to fewer Inner and Outer Tracker super-layers in the magnet.

Table 8: *Reconstruction efficiencies for the golden decay mode in comparison to the Design Report. The K^0_S reconstruction in ref. [5] is too small due to a bug in the Monte Carlo simulation which was found recently [6]. The number listed here is the corrected one.*

	$B^0 \to J/\psi\ K^0_S \to \mu^+\mu^-\ \pi^+\pi^-$		$B^0 \to J/\psi\ K^0_S \to e^+e^-\ \pi^+\pi^-$	
	Design	ref. [5]	Design	ref. [5]
L1 trigger efficiency*	62%	49%	45%	30%
lepton tracking in PC	89%	87%	89%	87%
J/ψ vertex+mass	99%	91%	99%	92%
pion tracks (geometry, reconstr.)	63%	50%	63%	55%
K^0_S vertex+mass	97%	93%	97%	93%
B^0 vertex+mass	94%	88%	73%	56%
main vertex	-	92%	-	87%
vertex detector tracking	-	90%	-	90%
lepton particle ID	94%	94%	85%	85%
decay kinematics	80%	-	80%	-
lifetime cut	69%	57%	69%	71%
total	16%	7.1%	8.3%	3.3%

* The numbers in columns 3 and 5 are the upper efficiency bounds from Tables 2 and 4.

For the measurement of CP violation the flavor of the B meson at production time has to be determined (tagged). Several tagging methods have been developed by other experiments and their applicability in HERA – B has been studied repeatedly [4, 7, 8].

Every method has a certain efficiency ϵ for finding a tag and a probability χ of correctly measuring the b quark charge. Hence the measured asymmetry is smaller by the dilution factor $D = 2\chi - 1$ and the error on $\sin(2\beta)$ scales with the tagging power $P = D\sqrt{\epsilon}$. All studies yield similar results of $P \simeq 0.3$.

The "same side tagging" method has successfully been used by CDF [9] and was a powerful tag in their analysis of the golden decay mode [10]. So far this method was not studied by HERA – B. Hence it is conceivable that the achievable tagging power can be increased.

Tab. 9 lists the expected statistical error on $\sin(2\beta)$ for one and four years of running (10^7 s per year) for different scenarios: for the nominal detector at an interaction rate of 20 MHz, and for a 20% reduced single track reconstruction efficiency. The assumed $b\bar{b}$ production cross section is 12 nb/nucleon. Note that this number is at the lower end of the expectations from measurements [11, 12] ranging from 8 nb/nucleon to about 60 nb/nucleon when scaled to 920 GeV/c proton beam energy.

In the worst case the achievable error on $\sin(2\beta)$ is 0.22 for four years of nominal running of

Table 9: *The CP reach of HERA – B , assuming a 20 MHz interaction rate and efficiencies as given in Table 8 (nominal) and when an additional factor of 0.80 per track is applied to the efficiency estimates given in Table 8.*

	nominal	80% tracking eff.
$b\overline{b}$/year	1.8×10^8	1.8×10^8
$B^0 + \overline{B^0}$	1.5×10^8	1.5×10^8
golden decays	74000	74000
produced $\mu^+\mu^-\ \pi^+\pi^-$ evts	3060	3060
produced $e^+e^-\ \pi^+\pi^-$ evts	3060	3060
reconstr. $\mu^+\mu^-\ \pi^+\pi^-$ evts	220	90
reconstr. $e^+e^-\ \pi^+\pi^-$ evts	100	40
backgr. fraction in $\mu^+\mu^-$ channel	0	0
backgr. fraction in e^+e^- channel	0.1	0.1
tagging power	0.3	.28
error on $\sin(2\beta)$ after 1 year	0.24	0.40
error on $\sin(2\beta)$ after 4 years	0.13	0.22

HERA – B. In comparison BABAR, Belle and CDF plan to achieve an error around 0.11 for one year [13, 14, 15]. Even though the situation is less favorable for HERA – B our result will still be valuable. The value of $\sin(2\beta)$ is a fundamental number of the SM and several measurements obtained with different experimental techniques are obligatory, especially if the current central values of CDF on one hand ($\sin(2\beta) = 0.79 \pm 0.44$ [10]) and preliminary results from BABAR ($\sin(2\beta) = 0.12 \pm 0.35$ [16]) and Belle ($\sin(2\beta) = 0.45 \pm 0.45$ [17]) on the other hand sustain with increased statistics. An additional measurement even with lower precision could become important.

It has to be realized, of course, that the above projections assume a First Level Trigger running near the upper limit of the range allowed by the present understanding of the trigger efficiency. Should the trigger performance stay much below design, HERA – B will not be able to make a significant measurement in this field.

1.5.2 The FCNC Decay $B^0 \to \mu^+\mu^- K^{*0}$

One of the dominant mechanisms in the $B^0 \to \mu^+\mu^- + X_s$ decay is a flavor changing neutral current (FCNC) penguin diagram with an intermediate top quark $b \to t \to s$, and a W-boson loop. Because of the heavy intermediate particles the process is very sensitive to the presence of new physics. From the theoretical point of view, a measurement of the fully inclusive non-resonant FCNC decay $B^0 \to \mu^+\mu^- + X_s$ represents an ideal testing ground for the standard model due to the absence of uncertainties from the hadronic final state.

The exclusive decay channel $B^0 \to \mu^+\mu^- K^{*0}$, chosen to characterize the HERA – B potential in searching for FCNC decays, is theoretically more difficult to treat but has a very clean experimental signature, giving powerful handles for background suppression. The decay has a large predicted branching fraction[5][18, 19]: $(2.0 \pm 0.7) \cdot 10^{-6}$) compared to $(5.7 \pm 0.7) \cdot 10^{-6}$ for $B^0 \to \mu^+\mu^- + X$.

[5]This more recent estimate of the branching fraction is somewhat larger than that ($1.5 \cdot 10^{-6}$) given later in this report. See also [20]

An important observable in this decay is the di-muon invariant mass spectrum or equivalently the differential decay rate as a function of s, the squared invariant mass of the di-muon system. The SM prediction, as well as the predictions for two other models, for the differential decay rate is shown in Fig. 11 (for details refer to [21]).

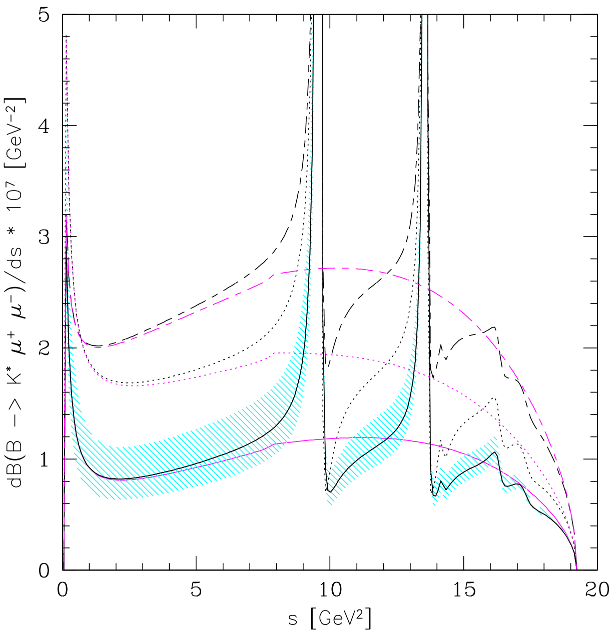

Figure 11: *The dilepton invariant mass distribution in* $\mathrm{B}^0 \to \mu^+\mu^-\mathrm{K}^{*0}$ *decays[21], using the form factors from LCSR as a function of s. The solid lines represents the SM and the shaded area depicts the form factor related uncertainties. The dotted lines corresponds to the SUGRA model. The long-short dashed lines correspond to an allowed point in the parameter space of the MIA-SUSY model. The corresponding pure SD spectra are shown as the lower curves in each case.*

Estimates for HERA – B acceptance and reconstruction efficiency for $\mathrm{B}^0 \to \mu^+\mu^-\mathrm{K}^{*0}$ are derived from an estimate of $\mathrm{B}^0 \to \mathrm{J}/\psi\mathrm{K}^{*0}$ efficiency, based on a GEANT simulation and reconstruction using existing software packages. The trigger will be less efficient for $\mathrm{B}^0 \to \mu^+\mu^-\mathrm{K}^{*0}$ compared to $\mathrm{B}^0 \to \mathrm{J}/\psi\mathrm{K}^{*0}$ because of p_T and mass cuts. Based on Fig. 11, we estimate that a 2 GeV mass cut will cut an additional 25% of the signal after p_T cuts.

The efficiency estimates are summarized in Tab. 10, assuming a (reduced) total interaction rate of 20 MHz and a conservative reconstruction efficiency of 80% per track. The First Level Trigger efficiency is the upper limit efficiency given in Table 4. Combining all factors, the total efficiency for detection and reconstruction of the FCNC decay $\mathrm{B}^0 \to \mathrm{K}^{*0}\mu^+\mu^- \to \mathrm{K}^+\pi^-\mu^+\mu^-$ is about 6% corresponding to about 13 observed events per year. At the same time, roughly 1000 examples of the $\mathrm{B}^0 \to \mathrm{J}/\psi\mathrm{K}^{*0}$ would be collected.

The decay $\mathrm{B}^0 \to \mathrm{K}^{*0}\mu^+\mu^-$ has been studied extensively by the BABAR collaboration (cf. [22] and references therein). BABAR expects a final statistics of 8 events[23] in a full year run with a nominal integrated luminosity of $30\,\mathrm{fb}^{-1}$. The CDF collaboration quotes a similar sensitivity, down to a branching fraction of 2×10^{-7} (corresponding to roughly 10 events) with the expected integrated luminosity of $2\,\mathrm{fb}^{-1}$ for Tevatron RUN II [24]. To gain enough statistics to measure the mass spectrum and a predicted forward-backward asymmetry in the $\mu^+\mu^-$system[18, 19], however, an integrated luminosity of $\mathcal{O}(10\,\mathrm{fb}^{-1})$ would be needed [25]. Any potential of HERA – B to measure

Table 10: *Estimate of* HERA − B *sensitivity for the non-resonant FCNC decay* $B^0 \rightarrow K^{*0}\mu^+\mu^- \rightarrow K^+\pi^-\mu^+\mu^-$ *for one year of running at a (reduced) interaction rate of* 20 MHz *and an assumed conservative single track reconstruction efficiency of* 80%. *The total trigger efficiency is denoted by* ϵ_{trig}.

Production per Year:	
$b\overline{b}$ per year	1.8×10^8
$B^0 + \overline{B^0}$ per year	1.5×10^8
$B^0 \rightarrow K^{*0}\mu^+\mu^- \rightarrow K^+\pi^-\mu^+\mu^-$	210
Acquisition and Reconstruction:	
FLT efficiency (incl. Geo, p,p_T cuts, tracking)(Table 4)	49%
FLT mass cut	75%
reconstruction efficiency $\mu^+\mu^-$	64%
geometrical acceptance $K^{*0} \rightarrow K^+\pi^-$	84%
reconstruction efficiency $K^{*0} \rightarrow K^+\pi^-$	64%
Background Cleaning:	
$J\psi$, ψ' mass cuts ($\pm$ 150 MeV)	75%
decay vertex cut ($\Delta z > 5$ mm)	62%
total efficiency	0.06
$B^0 \rightarrow K^{*0}\mu^+\mu^- \rightarrow K^+\pi^-\mu^+\mu^-$ per year	12.6

this FCNC process is therefore important in order to increase the world statistics necessary for sensitive tests of the standard model.

In conclusion, HERA − B has a chance to contribute in a significant way to the world statistics expected for the next years, provided that the di-muon trigger is running close to the upper limit of the range given in Table 4. So far, study of the HERA − B capability to measure this decay mode has been limited to efficiency estimates. An in depth analysis of possible background sources is beginning. HERA − B's excellent vertex detection and particle identification capabilities are powerful tools for background suppression which may also allow study of the inclusive process $B^0 \rightarrow \mu^+\mu^- + X_s$. It is perhaps also worth pointing out that many of the final states in the "X_s" system will also be reconstructible, such as $B^0 \rightarrow K^{*0}\pi^+\pi^-\mu^+\mu^-$, as well as decays of the charged B mesons: $B^+ \rightarrow K^+\pi^+\pi^-\mu^+\mu^-$. Channels such as $B^0 \rightarrow K^{*0}\pi^0\mu^+\mu^-$ may also be accessible.

1.5.3 B_s^0–$\overline{B_s^0}$ Mixing

The measurement of the B_s^0 oscillation frequency, Δm_s, provides important constraints on parameters described by the unitarity triangle. Present lower limits on Δm_s are set by LEP experiments, SLD and CDF, all using semi-leptonic B_s^0 decays. Because of the missing neutrino, the proper time resolution for B_s^0 decays in these experiments is not sufficient to discern the very rapid oscillations that are expected. To improve the Δm_s reach, one needs fully reconstructed B_s^0 decays. Among the most promising decay modes are $B_s^0 \rightarrow D_s^-\pi^+$ and $B_s^0 \rightarrow D_s^-\pi^+\pi^+\pi^-$. These final states have relatively large branching ratios and low multiplicities. The CDF group realized the importance of these decays and is constructing a special all-hadronic trigger for RUN II in order to accept them. These decays can also be detected at HERA − B.

B_s^0 decays to $D_s^-\pi^+$ and $D_s^-\pi^+\pi^+\pi^-$ can be accepted by a hadron-lepton trigger [1]. The requirements we consider at the first-level of the HERA − B trigger are a high-p_T charged track

($p_T > 1.5\,\mathrm{GeV/c}$) and a high-$p_T$ lepton ($p_T > 1.0\,\mathrm{GeV/c}$ for muons and $p_T > 1.4\,\mathrm{GeV/c}$ for electrons). The high-p_T lepton is produced in the semi-leptonic decay of the second B hadron present in the event. The charge of the lepton track provides a high quality tag.

Using data taken in the year 2000 run and Monte Carlo, we estimate a combined suppression from pretriggers and FLT of 3000 for electron/high-p_T triggers and 290 for muon/high-p_T triggers, corresponding in an SLT input rate of 35 kHz. This is somewhat lower than the SLT design input rate of 50 kHz. The SLT suppression from tracking, an impact parameter cut on the pion and lepton identification is estimated to be a factor of 100. This leads to an output rate of 350 Hz. At the third level, the presence of a second B meson in the event can be used to further suppress background. This is under study.

As shown in Table 11, we plan to reconstruct $\mathrm{B_s^0}$ mesons in 9 decay modes, most of which were reconstructed by LEP experiments. We expect that the excellent vertex resolution and kaon identification at HERA – B will allow sufficient suppression of combinatorial background also in high multiplicity modes.

The result of efficiency studies are summarized in Table 11. The high-p_T pretrigger efficiency was estimated using a full Monte Carlo simulation. The efficiencies of the muon and ECAL pretriggers as well as the FLT are provisionally assumed to be 1 (more below). SLT efficiencies are based on currently achieved values. The reconstruction efficiency is based on performance studies of the tracking algorithms for $1+4$ interactions. In addition, the 17% of tracks which interact in the material of the spectrometer are assumed to be lost. The number of events reconstructed with this standard technique are listed in Table 11.

The efficiency can be improved considerably if one starts reconstruction in the vertex detector and does not require that the track passes the full tracking system. Moreover, if the track direction is determined in the vertex detector, its momentum can be obtained from kinematical constraints. Such a procedure does not deteriorate the proper time resolution significantly. The numbers of events reconstructed with this method are shown in Tab. 11.

The tagging power is larger than the P $\approx$ .3 (see Sec. 1.5.1) derived in other HERA – B studies because the triggering lepton is used for a tag. The tagging efficiency is therefore 1 and the high-p_T lepton requirement assures a high quality. We estimate a tagging power P $\approx$ 0.6.

Two background sources were studied: inelastic events where the tagging lepton is fake and both reconstructed $\mathrm{D_s^-}$ and $\mathrm{B_s^0}$ are fake, and $c\bar{c}$ events where the tagging lepton is real while the reconstructed $\mathrm{D_s^-}$ meson is either real or fake and the reconstructed $\mathrm{B_s^0}$ meson is fake. The estimated signal-to-background ratio (S/B) from these sources is about 20.

The $\mathrm{B_s^0}$ proper time resolution is dominated by vertex resolution which we estimate at $\sigma_z = 356\,\mu\mathrm{m}$ for the $\mathrm{D_s^-}\pi^+$ and $\sigma_z = 338\,\mu\mathrm{m}$ for $\mathrm{D_s^-}\pi^+\pi^+\pi^-$. Using the target wire constraint, the primary vertex resolution is $150\,\mu\mathrm{m}$. The resulting proper time resolution is $\sigma_t = 0.060$ ps and $\sigma_t = 0.057$ ps for the $\mathrm{D_s^-}\pi^+$ and the $\mathrm{D_s^-}\pi^+\pi^+\pi^-$ decay modes, respectively.

In addition to the events listed in Table 11, we expect to collect 56 (22) reconstructed $\mathrm{B_s^0} \to \mathrm{D_s^{*-}}\pi^+(\pi^+\pi^-)$ decays in the same period of time. The $\mathrm{B_s^0}$ invariant mass distribution for the $\mathrm{D_s^{*-}}$ modes with a missing photon is estimated to be five times wider than that for the fully reconstructed $\mathrm{D_s^-}$ modes and the background is expected to be correspondingly larger, but still we expect a large signal-to-background ratio. In addition we expect to collect 34 (20) $\mathrm{B_s^0} \to \mathrm{D_s^{*-}}\pi^+(\pi^+\pi^-)$ decays with kinematically determined momentum of one of the tracks reconstructed in the VDS only.

Fig. 12 shows the expected significance of our measurement of $\mathrm{B_s^0}$ oscillations, using both the

Table 11: *Expected fraction of signal events per inelastic (minimum bias) event.*

	$B_s^0 \to D_s^- \pi^+$	$B_s^0 \to D_s^- \pi^+\pi^+\pi^-$
Physics:		
$\sigma_{bb}/\sigma_{inel.}$	10^{-6}	10^{-6}
$b\overline{b} \to B_s^0$ (or $\overline{B_s^0}$)	0.16	0.16
$B_s^0 \to D_s^- \pi^+(\pi^+\pi^-)$	3.0×10^{-3}	8.0×10^{-3}
$D_s^+ \to \phi\pi^+ \to K^+K^-\pi^+$	0.018	0.018
$K^+\overline{K^{*0}} \to K^+K^-\pi^+$	0.022	0.022
$(K^+K^-\pi^+)_{nonres.}$	0.009	—
$K^+\pi^-\pi^+$	0.010	—
$\pi^+\pi^+\pi^-$	0.010	—
$K^{*+}\overline{K^{*0}} \to K_S^0\pi^+K^-\pi^+$	0.009	—
$\phi\pi^+\pi^+\pi^- \to K^+K^-\pi^+\pi^+\pi^-$	0.006	—
Total D_s^+ branching fraction	0.084	0.040
Trigger:		
Geometry, $p_T(\mu) > 1.0$ or $p_T(e) > 1.4$ GeV/c	0.095	0.095
Pretrigger, $p_T(\text{had}) > 1.5$ GeV/c	0.70	0.38
μ Pretrigger	1.0	1.0
e Pretrigger	1.0	1.0
FLT	1.0	1.0
SLT Slicer/Refit	0.9	0.9
Lepton ID	0.95	0.95
Geometrical acceptance	0.68	0.51
Track reconstruction (0.965×0.83 per track)	0.41	0.30
Main vertex	0.94	0.94
B_s^0 and D_s^- vertices	0.81	0.81
$VX(B_s^0) > 3.0$ mm	0.66	0.66
$VX(D_s^-) > 4.5$ mm	0.95	0.95
Summary	3.0×10^{-13}	1.1×10^{-13}
$B_s^0 \to D_s^- \pi^+(\pi^+\pi^-)$:		
#events/year	61	23
#events/year, 1 track reconstr. in VDS only	37	21
$B_s^0 \to D_s^{*-} \pi^+(\pi^+\pi^-)$:		
#events/year	56	22
#events/year, 1 track reconstr. in VDS only	34	20
Total number of events	188	86

$D_s^{(*)-}\pi^+$ and the $D_s^{(*)-}\pi^+\pi^+\pi^-$ decay modes modes, as a function of the oscillation parameter $x_s = \Delta m_s \cdot \Gamma_s$. Using the fully reconstructed $B_s^0 \to D_s^{(*)-}\pi^+(\pi^+\pi^-)$ decays, x_s values up to 24 can be measured at a $3\,\sigma$ level within one year of operation at 20 MHz interaction rate. We expect that we will find handles against the larger backgrounds[20] in the partially reconstructed decays. This would allow HERA – B to cover the complete range allowed by the Standard Model, assuming full pretrigger and FLT performance.

This conclusion is not significantly modified when the upper-limit trigger and pretrigger efficiencies arrived at in Sect. 1.3 are taken into account. The upper-limit efficiency for triggering on a single muon (electron) and tracking it with the FLT algorithm is 89% (91%). Track-finding of the pion from the high-p_T pretrigger contributes another factor of 96% for a total efficiency of 86%. The statistical significance scales as the square root of the number of events, implying a loss of significance of just 7%.

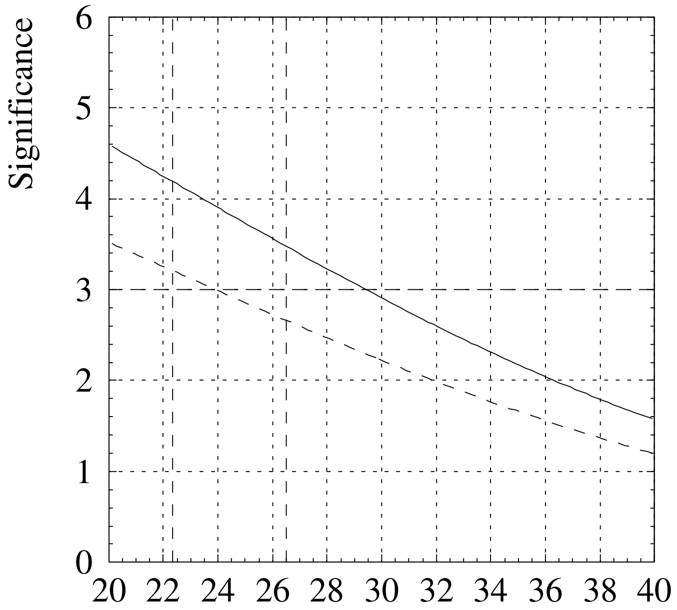

Figure 12: *Significance of* B_s^0 *oscillation measurements as function of* x_s*, expected to be achieved after one year of operation at an interaction rate of* 20 MHz*, using the* $D_s^{(*)-}\pi^+(\pi^+\pi^-)$ *decay modes (dashed line). The solid line shows the expected significance, if a kinematical reconstruction for the momentum of one of the tracks is also used. The present experimental lower limit and the upper limit from Standard Model fits are also indicated by vertical dashed lines.*

1.6 Conclusions

The HERA – B detector was completed in February of this year and has, for the most part, behaved stably. With some exceptions, the subsystems are either operating close to design or can be reasonably expected to approach design specifications with improvements already underway. Still, some work has yet to be finished and some concerns remain:

- The Outer Tracker was losing high-voltage channels at a high rate during the year 2000 run. The causes of this are believed to be understood and a remedy has been found. Investigations continue to determine if any of the observed failure modes are indicative of possible future problems.
- The efficiency of the muon system's pad chambers is low. Steps are being taken to improve it but full efficiency can probably only be reached if the preamplifiers are replaced. We are looking into the feasibility of doing so during the present shutdown.
- The optical links connecting chamber output to FLT are probably not sufficiently stable. A new link is being designed and the feasibility of replacing all or part of the system is under study.

- The readout electronics of outer chambers of the high-p_T system suffer from induced oscillations and noise pickup from an unknown source. This is not likely to be fatal since several similar systems have been made to work in the experimental hall but some additional experience with beam will most likely be necessary to fully debug the system.
- The capabilities of the FLT are not well known. Many tests have been performed but the results are not fully consistent. We expect that additional study of the data taken and of the simulation code will allow a clear picture to emerge on a time scale of several weeks. Until then, we cannot guarantee that the system will work close to design specifications.
- The ultimate rate capability of HERA – B is not yet known. The design calls for 40 MHz. To be more conservative, we have made the sensitivity estimates for this study assuming a 20 MHz interaction rate. It is not yet established that the trigger can operate without deadtime at even this rate.
- One item totally beyond our control but nonetheless relevant is the value of the $\mathrm{b\overline{b}}$ cross section at 920 GeV which is still uncertain by nearly a factor of 8. (Our estimates assume a value of 12 nb, close to the low end (8 nb) of this range.

Many uncertainties remain but we have not found any fundamental flaw which would prevent HERA – B from working near to design.

The year 2000 run was used for commissioning the detector and triggering system. Data samples were accumulated with a combination of pretriggers and second level trigger. The data is under analysis and may be of sufficient quality to allow determination of the $\mathrm{b\overline{b}}$ cross section. While the J/ψ signal in the $\mu^+\mu^-$mode is fairly clean, the signal can only be seen in the $\mathrm{e^+e^-}$when inefficient particle id cuts are applied. We are looking into more efficient ways of reducing background (RICH cuts, improved E/p) but if none are found the utility of the $\mathrm{e^+e^-}$decay mode for B studies will be limited.

Studies were performed to evaluate the potential of HERA – B to contribute to several areas of B-physics as well as charm-physics and QCD studies. The results are summarized in Tables 6 and 7. The general conclusion is that HERA – B can still be competitive in some areas such as a measurement of the $\mathrm{B}^0 \to \mu^+\mu^-\mathrm{K}^{*0}$ provided we succeed in operating close to design potential. Given the uncertainties listed above, this must be regarded as an "optimistic" scenario. In any case, there remains a good chance that HERA – B can provide meaningful and solid data in the area of B-physics, possibly charm physics and certainly QCD studies.

2 Detector Status and Plans for the Shutdown 2000/2001

2.1 Target

The HERA − B target is designed to produce the required large number of B-mesons for the HERA − B experiment in proton nucleon interactions. It is realized as a multi-wire fixed target which operates in the halo of the 920 GeV HERA proton beam in parallel to the usual HERA e-p luminosity operation.

This section describing the HERA − B target is structured as follows. After a brief review of the basic requirements and rationales in section 2.1.1 the status and achievements obtained by the end of the last run period in August 2000 are summarized in section 2.1.2. Beam related topics are briefly reviewed and discussed in section 2.1.3. The shutdown plans which include upgrades, repairs, maintenance work, improvements and modifications of the setup etc. are divided into two subsections: foreseen hardware upgrades are discussed in 2.1.4 and software related improvements are considered in 2.1.5. Finally the anticipated target setup and configuration together with the (re-)commissioning plans during the HERA and HERA − B start-up phase in the autumn of the year 2001 are sketched in section 2.1.6.

2.1.1 Requirements, Setup and Basic Rationale of the HERA − B Target

Fig. 13 shows a simplified sketch of the HERA − B halo target. The main idea is rather simple: protons leaving the beam core interact on the wires before getting lost on any aperture limitation. In the

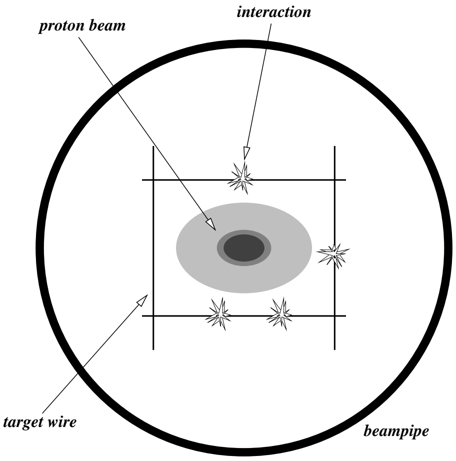

Figure 13: *Sketch showing the basic idea of a halo target. Protons leaving the beam core interact on the target (typical interaction points are indicated by stars) before getting lost on aperture limitations.*

following section the most important design requests are summarized and the basic construction, layout and functionality is described.

Rates, Luminosity & Target Efficiency

An interaction rate R_{ia} of around 40 MHz is required to achieve the HERA − B physics goals [26]. For a titanium target with an inelastic cross section per nucleon of $\sigma_{nucl}(Ti) \approx 13.3\,\mathrm{mb}$ [27] one gets therefore the following produced luminosity[6] $\mathcal{L}$ per second:

$$\mathcal{L}/\mathrm{s} = \frac{R_{ia}}{\sigma_{nucl}(Ti)} = \frac{4 \cdot 10^7/\mathrm{s}}{13.3\,\mathrm{mb}} = \frac{3.0}{\mathrm{nb\,s}} = 3.0 \cdot 10^{33}\mathrm{cm}^{-2}\mathrm{s}^{-1} \quad (1)$$

[6]The luminosity is given per nucleon. For comparison: the value corresponds exactly to the PEP/BaBar design luminosity.

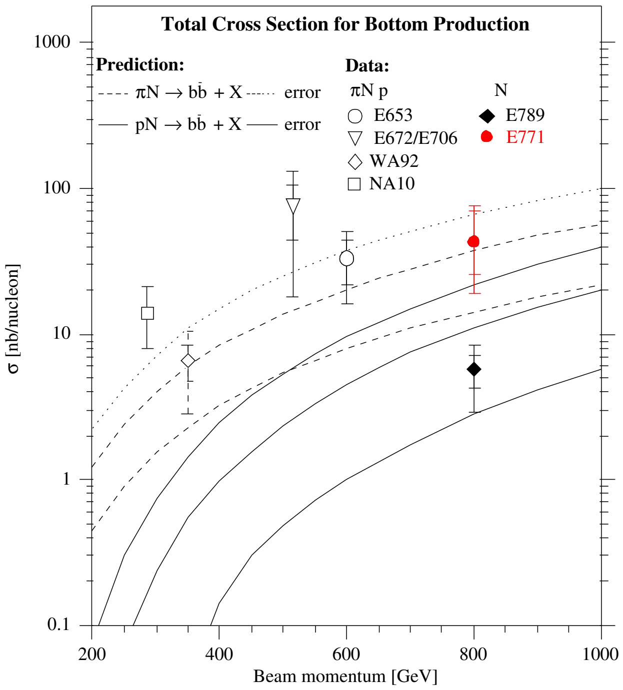

Figure 14: *QCD prediction for the $b\bar{b}$ cross section and experimental results[11].*

The 920 GeV HERA protons hitting a fixed target leads to a center of mass energy $\sqrt{s} \approx 40\,\mathrm{GeV}$, here the $b\bar{b}$ cross section is suppressed by six orders of magnitudes compared to the inelastic cross section. Figure 14 shows the result of QCD calculations up to α_s^3 [28]; they predict for 920 GeV protons a cross section $\sigma_{b\bar{b}} \approx 17$ nb but with large uncertainties. Also shown are experimental data on $b\bar{b}$ production. The results of the two Fermilab experiments E771 [11] and E789[12] which are obtained at an energy range very similar to the HERA – B target differ by nearly one order of magnitude - but they are still consistent within their large errors.

Assuming the QCD predictions for the $b\bar{b}$ cross section one gets at design luminosity the following number of produced $b\bar{b}$ pairs at the HERA – B target:

$$N_{b\bar{b}}/\mathrm{s} = \sigma_{b\bar{b}} \cdot \mathcal{L}/\mathrm{s} \approx 17\,\mathrm{nb} \cdot \frac{3.0}{\mathrm{nb\,s}} \approx 50\mathrm{Hz}\,. \tag{2}$$

This leads to a yield of around 40 B_0 or $\bar{B}_0$ mesons per seconds. The b-yield depends slightly on the choice of the target material [26].

The target efficiency ϵ_T is a very important number to judge on the performance of the target operation, especially at high rates. It describes the ratio between the number of protons interacting with the HERA – B target and the total number of protons which are lost inside the complete HERA p-ring:

$$\epsilon_T = \frac{\text{Interaction Rate}}{\text{Proton Loss Rate}} = \frac{\tau_p}{N_p} \cdot R_{ia} \tag{3}$$

The proton loss rate is determined by the number of protons N_p or the proton current and the proton lifetime τ_p, e.g. a proton beam with a current of $I_p = 100$ mA and a still acceptable lifetime $\tau_p = 50$ h has a loss rate of roughly 72 MHz. This example demonstrates that it is quite important to catch up the main fraction of protons inside the target, before they get lost anywhere else. To limit the impact on the proton lifetime to an acceptable level it is therefore quite important to achieve a target efficiency $\epsilon_T > 50\%$, particular if the target is operated at higher rates.

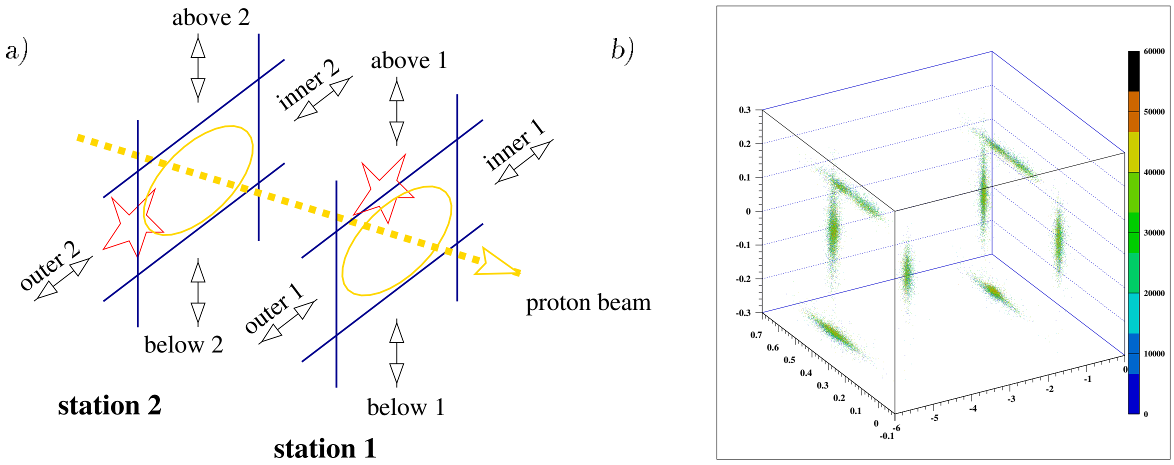

Figure 15: *a) Schematic drawing of the eight target wires surrounding the HERA proton beam. b) Reconstructed vertices while all eight target wires are operated simultaneously at the beam.*

Continuous Operation

A reliable and regular target operation is required to accumulate the necessary statistics for the HERA – B experiment. An operation time of around 10^7 seconds per year is anticipated, something what has to be achieved in parallel to the HERA e-p luminosity operation. This requires a continuous and very efficient target operation which uses more than 90% of the HERA e-p luminosity time. On the one side this demands a save, reliable and easy procedure to operate the HERA – B target. On the other side the interference with the e-p luminosity operation has to be small, something what is strongly correlated with the HERA operation and here mainly to the settings of the proton collimator system and the beam orbit. The HERA proton collimator system was extended during the shutdown in the year 1996 to minimize the impact of target induced background on the other HERA experiments [29]. Since that time the system has proven that a reasonable optimized working point can be established which allows the operation of the HERA – B target at design rate without interfering seriously with the other experiments [30].

Multiple Interactions, Separated Vertices & Target Geometry

The bunch crossing rate of the filled HERA proton bunches is approximately 8.5 MHz[7]. This leads to multiple interactions which are in first order distributed according to the Poisson statistics:

$$P_\mu(n) = \frac{\mu^n}{n!} \exp\left(-\mu\right), \quad n = 0, 1, 2, 3, ... \tag{4}$$

where $P_\mu(n)$ describes the probability to get n interactions during one bunch crossing (bx) if the mean number of interactions per bx is μ. The variance of the Poisson distribution is equal to its mean value μ, i.e. one gets a broad distribution.
To simplify and improve the reconstruction of the events it is necessary to obtain a reasonable spatial separation of these multiple simultaneous interactions. Therefore HERA – B uses a multi-wire setup with eight target wires (see Fig. 15)[8]. They are mounted and operated in two stations separated by approximately 4 cm along the beam axis. The typical operation point in radial direction is between 3 to 6 beam sigma, with a typical beam sigma of around 400 μm.

[7] 180 out of 220 buckets are filled - the bunch distance is 96 ns: $f_{bx-filled} = 180/220 * (1/96\text{ns}) \approx 8.5\,\text{MHz}$.

[8] The naming convention (inner, outer, above, below) was chosen with respect to the HERA storage ring. The 1.station is closer to the HERA – B VDS (Vertex Detector System).

Until now the target wires are usually small ribbons with a thickness of 500 μm along the beam axis and a radial width of 50 μm. These dimensions are chosen in such a way that the geometrical defined location[9] of the main interaction vertex on the target is smaller than the expected vertex resolution[10] of the HERA – B detector. The dimensions of the target wires have been not yet decreased further to have a reasonable large amount of material close to the beam in order to be on the safe side with respect to the required large target efficiency. Protons with a betatron amplitude large enough to reach the target usually hit the target each $\mathcal{O}(100)$ turns [39]. Before the protons interact they have to pass in the mean one interaction length λ_{int} of target material (see Table 12), i.e. with the actually used geometrical setup several ten thousand up to a few hundred thousand turns are required. This time scales with the geometrical target dimensions. Hence using smaller target wires the required time increases - and with time also the probability that the proton gets lost somewhere else, e.g. due to diffusion or other scattering processes[11].

Table 12: *Atomic number Z, mass A, interaction length λ_{int}, radiation length X_{rad} and mean angular smearing Θ_{sc} at 920 GeV for various target materials.*

Material	C	Al	Ti	Fe	Cu	W
Z	6	13	22	26	29	74
A	12.	27.	47.9	55.9	63.6	184.9
λ_{int}/cm	38.1	39.4	27.5	16.8	15.1	9.6
X_{rad}/cm	18.8	8.9	3.56	1.76	1.43	0.35
Θ_{sc}/μrad	23.	34.	45.	49.	52.	80.

Stable Rates & Target Steering

To achieve an efficient triggering and an effective data taking and reconstruction with the HERA – B detector[12] it is necessary to provide a reasonable stable interaction rate equally distributed among the various wires in use. This is the task of the target control system (TaCoS). All target wires can be moved in radial direction by stepping motors. The main steering loop operates with a frequency of around 10 Hz and a minimal step-size of 50 nm to stabilize the interaction rate. It retracts the wires in case the actual measured interaction rate is too large or moves them closer to the beam in case the rate is too low. The interaction rate is measured with a hodoscope, which consists of four pairs of scintillating counters. These are equipped with fast electronics, allowing a dead-time less rate measurement. A measurement of the interaction rate on the individual wires is performed by means of integrating the charge produced by δ electron generation inside the target wires [31]. This provides the information for a proper wire selection in a multi-wire operation mode.

Rate Performance & Beam Properties

An efficient triggering and data taking demands that several additional conditions have to be met by the produced target interactions. They are closely related or even defined by the HERA beam properties. The following list summarizes briefly the main topics, which are then discussed in more details in section 2.1.3:

[9]dimension divided by $\sqrt{12}$.

[10]$\approx 25\ \mu$m in transversal direction and $\approx 500\ \mu$m in longitudinal direction.

[11]Due to the high intrinsic proton lifetime and the positive experience with a thin test wire we intend to use in the future thinner wires - as discussed in section 2.1.6.

[12]The HERA – B detector with its trigger and reconstruction is basically occupancy limited.

1. The timing of interactions should be within 1 ns out of the 96 ns between two consecutive bunches. Observed problems are coasting beam and side-bunch contributions.

2. One is aiming for a uniform bunch structure, i.e. all filled proton bunches should contribute equally to the interaction rate.

3. The global rate stability also depends on HERA. It is correlated with the settings (e.g. collimators) and stability (e.g. beam orbit) of the machine and HERA has measures to increase the beam halo population which improves the HERA – B rate stability.

2.1.2 Status and Run Experience

First tests of a halo target operation at the HERA proton ring have been performed already in the year 1992. The basic layout, requirements and general principles of operation are discussed in the HERA – B proposal [26] and the HERA – B Design Report [1]. A target test experiment with a reduced and simplified setup was operated in the HERA west right straight section[13] until the year 1995[32]. During that time period the main operation and steering concepts for the target have been developed and the basic properties of the target have been studied. During the shutdown in the year 1996 the final target mechanics was installed at their final position in the HERA – B experiment[14]. Four target mechanics stations are mounted from four sides on the HERA – B VDS vessel, each containing two wire targets which are separated along the beam axis by 40 mm. Since the year 1997 the HERA – B target is in regular and nearly continuous operation. Details of the target commissioning are documented e.g. in [30, 33, 34] and in several Diploma & PHD theses [35, 36, 37, 38, 39, 40, 41, 42, 43, 44, 45].

The target environment is handled regularly by the HERA – B shift crew and worked very stable, reliable and secure. Therefore the maintenance effort could be kept on a reasonable low level since 1998. Most of the basic requirements are obtained regular and a high level in understanding the rationale and the main impacts on the performance and the various dependencies has been achieved so far. In the following section the most important achievements and the performance of the target operation are summarized together with considerations of remaining problems and open questions.

Run Statistic & Reliability of the Target System

Fig. 16 shows the target operation statistics for the last two years. The total number of produced interactions within the years 1999 and 2000 are around $N_{int} \approx 33,000\,\mathrm{MHz\,h} \approx 1.2 \cdot 10^{14}$. In some months the target operation time is even slightly higher than the HERA e-p luminosity time due to the fact that the target was sometimes operated during periods without e-p luminosity (no positrons available, HERMES 12 GeV running, ...).

- The target operation time in the year 1999 was 84 % and in the year 2000 94 % compared to the HERA e-p luminosity time. The main losses are caused by waiting for the permission from the other HERA experiments to insert the target. In the year 2000 this was mainly the time until the HERMES detector was switched on. The lower run efficiency in the year 1999 was mainly caused by the interferences with the ZEUS-LPS [46] detector and the correlated intensive task force studies (details are discussed in section2.1.3).

[13] at WR118 - i.e. in the **W**est **R**ight HERA octant, 118 m upstream of the center of the HERA West Hall.

[14] The location is approximately at z=0 m in the HERA – B coordinate system, which corresponds to WR009 in the HERA coordinate system.

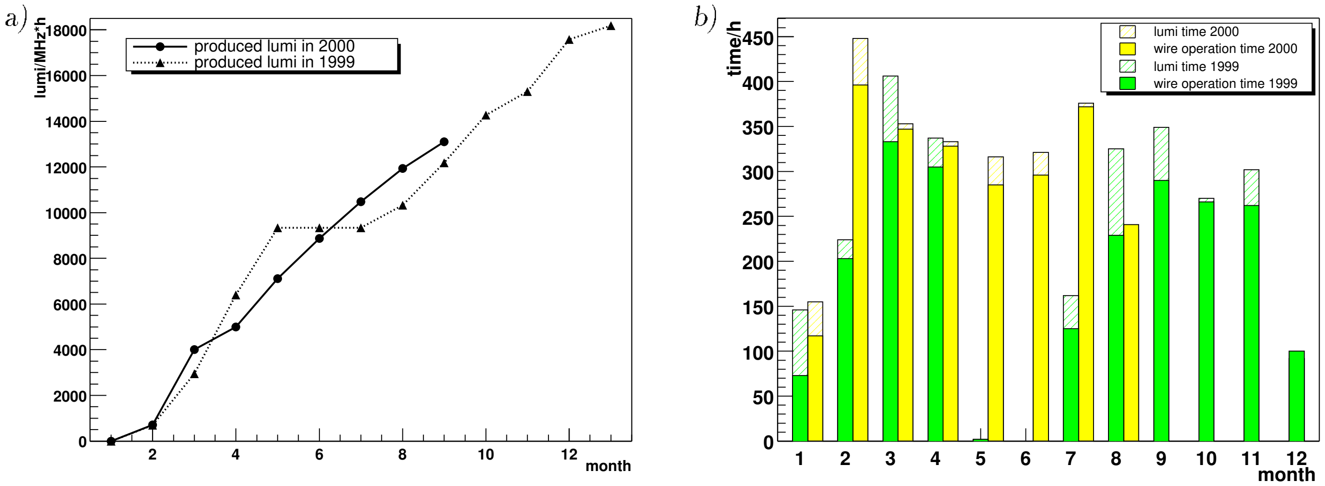

Figure 16: *Target operation statistics for the years 1999 and 2000: a) Number of interactions produced at the* HERA – B *target in the years 1999 and 2000. b) HERA luminosity time and target operation time for each month in the years 1999 and 2000.*

- Losses due to technical problems account for $\mathcal{O}(< 1\,\%)$. They have been mainly due to: crashes of the target database server, failure of the HV or stepping motor controller, break of electronics components, ...
- Problems to insert wires or a very unstable and non proper target operation also accounts to losses of $\mathcal{O}(1\,\%)$. They are usually correlated with bad beam conditions, e.g. high and spiky background. Therefore this behavior should be considered more as a feature than a bug. Nevertheless serious considerations has started to adopt inside the target control more automated to unstable beam conditions.
- The reliable and smooth operation allowed to schedule on call target experts for periods of two week. Their main effort during these 14 day periods went into:
  - visiting meetings and coordination tasks (HERA and dedicated target studies)
  - ≈ 2 working days to provide run overviews, including the handling and accounting of data base files and the preparation of summary pictures
  - the communication with the shift crews, give them instructions and advice. This accounts for less than one day.
  - fixing technical problems demands usually less than 10 % of their time

Target Operation in the Year 2000: Wires, Rates & Operation Point

Fig. 17 shows how often the individual wires have been used and at which rate the target was operated during the run period in the year 2000. The running was dominated by the operation of the single wire *Inner2* at a rate of 4 or 5 MHz. During 26.7 % of the runtime a multi-wire configuration was used. This was typically a two-wire setup (14 %). Four wires have been operated during 8.1 % and more than four wires just during 0.13 % of the run time.

As shown in Fig. 18a) the various target wires operate usually at a distance of 3 – 5 rms beam width[15] from the center of the beam. One observes systematic differences between the various

[15]The typical beam size of the HERA proton beam at the target wires is $\sigma_x \approx \sigma_y \approx 400\,\mu$m.

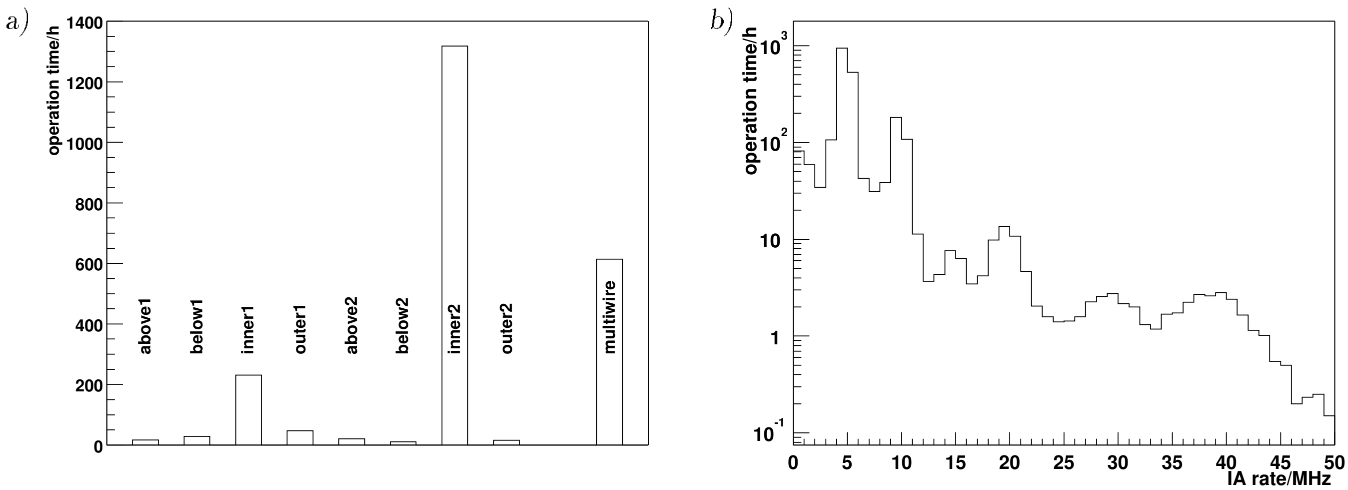

Figure 17: *Overview about the usage of the individual wires (a) and the target rate (b) during the run period in the year 2000.*

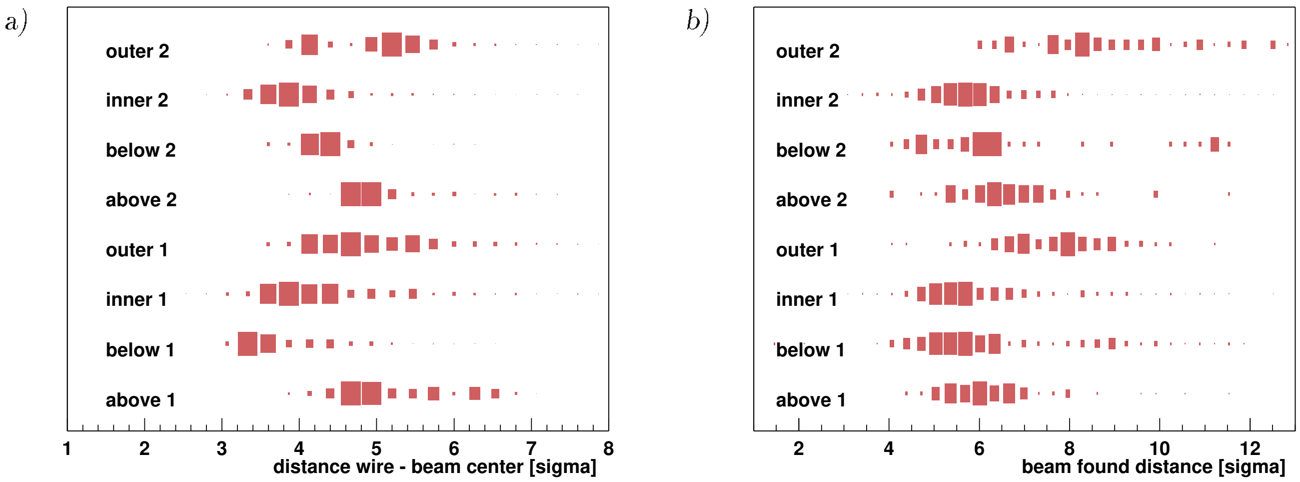

Figure 18: *a) Distance of the various used target wires from the beam center during rate operation in the year 2000. b) Distance δ_{bf} of the various wires when they "found" the beam (cp. text).*

wires. The most obvious and dominating impact arises from coasting beam protons which causes due to the dispersion $D_{x/y}$ in the target area broad transverse tail on the outer and above side (see section 2.1.3). Other reasons for the differences are e.g. due to varying values for the beam sigma, influenced by the operation conditions (collimators, rates, new or old fill, statistics) or due to errors in the alignment or the measurement of the target and the beam position. Fig. 18b) shows the distance from the beam center at which the target wires reached the beam halo. This *beam found position* δ_{bf} is calculated by the first significant increase of the target rate and is determined by the aperture limitation A which is mainly defined by the HERA p collimator-system. One gets rather tight settings[16]: the mean value of δ_{bf} is around $6.5\,\sigma$ and the most probable value around $5.5\,\sigma$. Transverse coasting beam tails are again the main source for systematic deviations; these tails are very distinct on the outer side and causes there the high values of δ_{bf}. Evaluating the collimator settings one gets similar close aperture limitations for the HERA proton beam. Such tight aperture

[16] Values larger than $10\,\sigma$ are usually unreasonable and should be neglected. They are mainly due to measurement errors e.g. unstable background rates which makes it difficult to define in an automated way the beam found position.

limitations causes a problem for the target operation[17], it reduces the target efficiency and leads to less stable rate as discussed in the next sections.

Under the actual HERA operation conditions with a very high intrinsic proton lifetime the impact of diffusion processes on the target efficiency ϵ_T is small. ϵ_T is dominated by the multiple scattering inside the target which is described by the mean scattering angle Θ_{sc} within one interaction length λ_{int} of target material (cp. Tab. 12):

$$\Theta_{sc}^2 \approx \left(\frac{14\,\mathrm{MeV}}{p}\right)^2 \cdot \frac{\lambda_{int}}{X_{rad}} \tag{5}$$

with p the momentum of the protons hitting the target. The scattering angle is large compared to the beam divergence $\sigma_{x'/y'} = \sqrt{\epsilon/\beta} \approx 10\mu$rad at the target. This angular smearing leads therefore to a significant broadening of the betatron amplitude of these protons and to their potential loss on collimator jaws or other aperture limitations. Very tight proton collimator settings results therefore in a small target efficiency ϵ_T. The distance between the target position and the aperture should be at least two sigmas to achieve the requested target efficiency of more than 50 %. Actually the mean distance is just around $1.5\,\sigma$. The better understanding of coasting beam properties at HERA-p also improved the understanding of its impact to the target efficiency. Depending on the used wire configuration one has to distinguish between bunched and non bunched loss rates. Unbunched coasting protons are shifted due to the dispersion in the target area mainly to the outer side. If one operates just a target wire on the inner side then these protons have nearly no possibility to interact with the target wire. The analysis of rate scan data allows here to distinguish between two loss rates, a bunched beam loss rate which generates the target interactions and an independent coasting beam loss rate. One gets then even with the actual tight collimator settings a mean value for the target efficiency of around 45% with respect to the bunched loss rate. The estimated coasting beam loss rates are typically $\mathcal{O}(10$ MHz).

Rate Stability

All kind of rate fluctuations[18] leads to a frequency distribution of the number of produced interactions which is broader than the optimal Poisson distribution. One gets therefore an enhanced probability for events with less and events with more interactions than aspired. The low multiplicity events reduce directly the available statistics and the high multiplicity events are usually rejected within the trigger or reconstruction chain[19]. The measurement of rate fluctuations depends on the chosen frequency or time range, details can be found in [42, 45]. Most of the pictures and numbers quoted within this section uses the important short term rate fluctuations σ_s which are evaluated by means of the normalized difference between two consecutive measured hodoscope rates; they are measured approximately every 100 ms[20]. Fig. 19 shows these short term fluctuations for the complete run period in the years 1999 and 2000 as a function of the time within a week. One obtains a mean value for the rate fluctuations of approximately 8 % with a very pronounced structure. The target rate gets much more unstable during usual working hours, i.e. Monday to Friday between 7h and 16h, revealing a strong impact of civic noise on the target performance. The overall rate stability is reasonable good[21], but there are time periods with larger fluctuations which leads to an efficiency loss for the HERA − B experiment.

[17] The usual conditions are now significant tighter than the initially requested and assumed $\geq 3\,\sigma$ free space between target and collimator position.
[18] Also the later on discussed bunch to bunch variations.
[19] The trigger system even selects dominantly high multiplicity events, which might then even spoil up the system.
[20] The short term fluctuations here are obtained by calculating the sigma per each half hour of stable target operation.
[21] Fluctuations smaller than 10 % are considered as good.

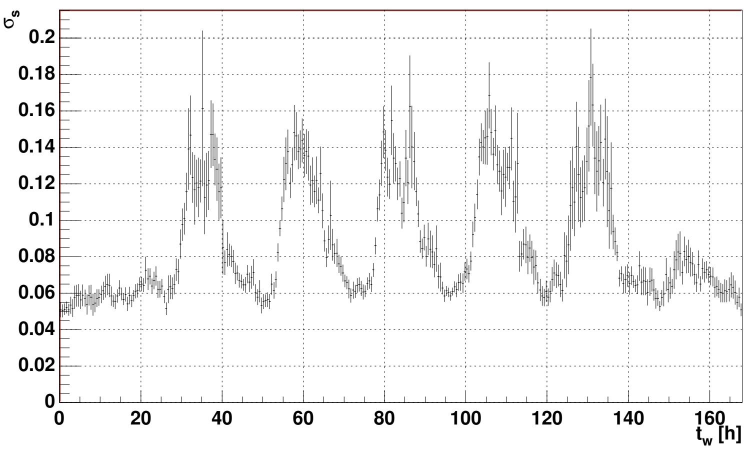

Figure 19: *Short term rate fluctuations σ_s during the run period in the years 1999 and 2000 plotted versus the time in hours of a week (starting on Sunday 0h up to Saturday 24h).*

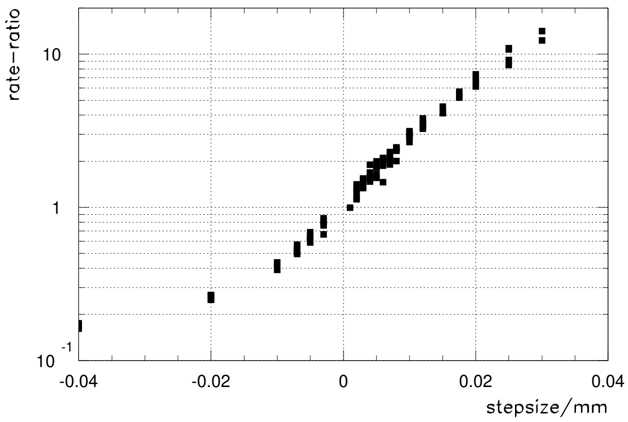

Figure 20: *Step functions measurement: ratio of the interaction rate as function of the applied step size.*

One important investigation in the understanding of rate fluctuations is the analysis of step function measurements. Such a measurement is shown in Fig. 20: it indicates the ratio between the obtained interaction rate after and before the target was moved with a well defined step size. These measurements reveals typically a rate sensitivity of a factor two per $10\,\mu$m. This indicates that the target rate stability is sensitive to beam orbit fluctuations. Fig. 21 shows the fluctuations of the beam orbit close to the HERA − B target for the run period during the years 1999 and 2000 also as a function of the time within a week. They show the same systematic increase during usual working hours as the rate fluctuations in Fig. 19. Assuming the rate sensitivity obtained from step function measurements then the level of the observed rate fluctuations is compatible with what one expects from these beam orbit fluctuations [45]. During the run-period in the end of the year 1998 and in the beginning of the year 1999 several extreme examples have been observed which emphasizes the close correlation between civic noise and rate stability. During this time period an ongoing heavy ground work in the Volkspark stadion close to DESY took place which spoiled up sometimes the target operation completely. This was strongly correlated with an increased ground motion[34, 42].

Other important systematic impacts to the rate stability are shown in Fig. 22:
(a) - tighter apertures leads to increased fluctuation
(b) - a low ϵ_T is correlated with tight apertures and results in larger fluctuations.
Fig. 23 shows the obtained rate fluctuations for all eight target wires during the run period in the year 2000. One observes several systematic dependencies:

Target Orientation: Wires moving in vertical direction deliver a more unstable rate than the wires in the horizontal direction. This is correlated with the larger beam fluctuations in the y direction (cp. Fig. 21).

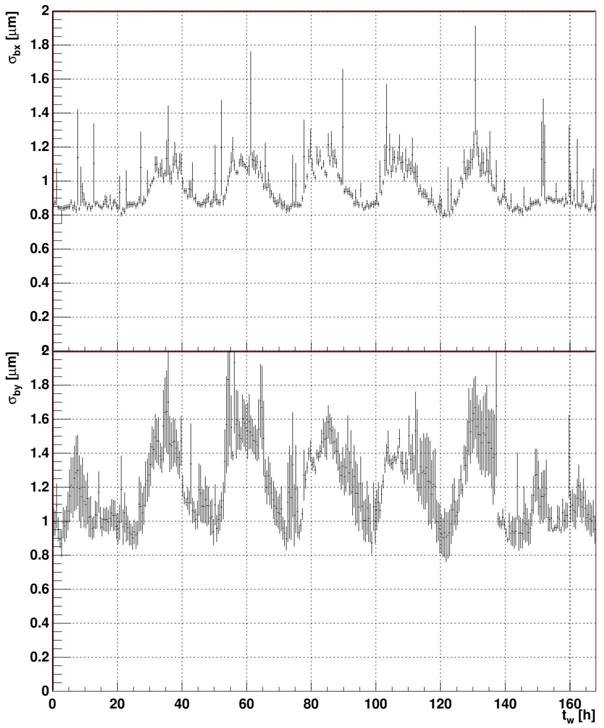

Figure 21: *Short term beam orbit fluctuations in horizontal (σ_{bx}) and vertical (σ_{by}) direction for the run period in the years 1999 and 2000 plotted versus the time in hours of a week (starting on Sunday 0h up to Saturday 24h).*

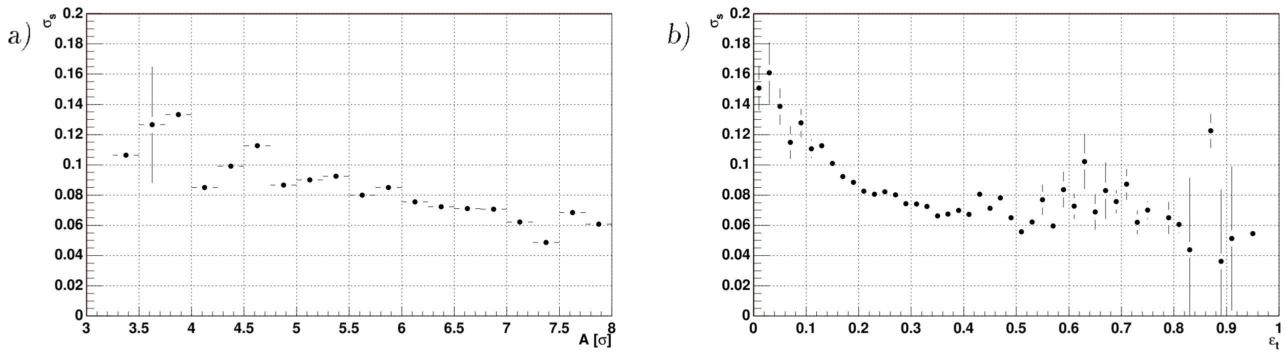

Figure 22: *Short term rate fluctuations σ_s as a function of the measured aperture A (which corresponds to the beam found position δ_{bf}) (a) and the target efficiency ϵ_T(b).*

Target Material: The tungsten wire at the position Below-2 ($n_w = 5$) gives the largest rate fluctuations. This is presumably due to the large scattering inside the heavy target material (cp. Tab. 12 and Eq. 5) which leads to a low target efficiency ϵ_T. This target ribbon has in addition a nearly "perfect" geometrical shape without small edges and roughness of the surface. Even if this target moves just by a small step towards the beam a large amount of even heavy material arises where the protons scatters. One assumes that targets consisting of lighter material and with non perfect geometrical properties or with a round shape enables a smoother "beam scraping" (cp. section 2.1.3).

Outer Wires: Their operation is dominated by coasting beam properties which results usually in very unstable rate while one scrapes off transversal coasting beam tails (which accounts for a considerable fraction of the operation time for the Outer-1 target) and rather stable rates after that at the bunched beam (presumably due to the larger transversal "diffusion" rate).

Target Shape: For the Outer-2 target ($n_w = 7$) a 50 μm round wire was used. This target shows the smallest fluctuations.

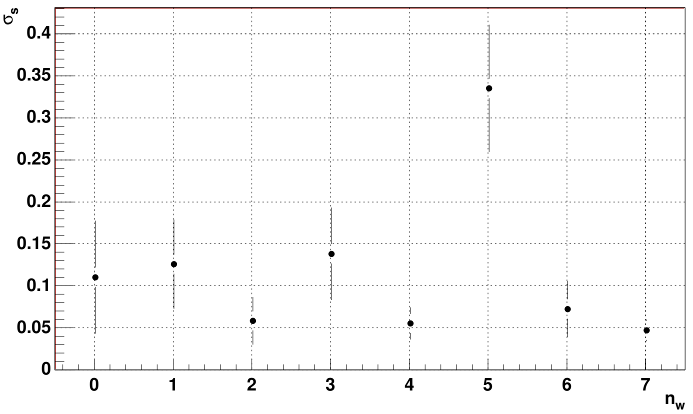

Figure 23: *Short term rate fluctuations σ_s for the different target wires. The wire number n_w from 0 to 7 corresponds to the above, below, inner and outer targets of the 1. station (0 to 3) then of the 2. station (4 to 7).*

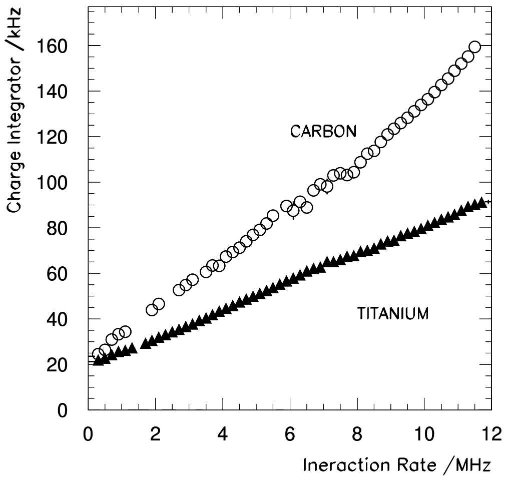

Figure 24: *Example of two calibration curves for the charge integrators connected to the target wires Inner-1 (Ti) and Inner-2 (C).*

Multi-wire Operation

A big improvement in the hardware setup for multi-wire operation has been achieved in the last run period. During the Xmas shutdown 1999/2000 the charge integrator electronics was completely replaced[22]. The sensitivity of the electronics is increased by more than two orders of magnitude[23], it works very reliable and gives an improved stability and linearity. Fig. 24 shows an example of the correlation between the interaction rates measured with the hodoscopes and the values obtained by the charge integrator measurement. With this setup one obtains a very reasonable multi-wire operation performance. The main cross check comes from the analysis of vertex detector data. Fig. 15b) shows the reconstructed vertices for a run where all eight target wires have been operated simultaneously and contribute rather equally to the interaction rate[24]. A more quantitative event by event based analysis is summarized in Fig. 25. It shows for a four wire operation the correlation between the number of wires on which a vertex was found and the total number of reconstructed vertices for real data and Monte-Carlo data. The agreement is remarkable good and indicates a very homogeneous illumination of the four used wires.

[22]Thanks to the common effort of the MPI Heidelberg and KINR Kiev.

[23]compared to the previous used first generation of electronics.

[24]this describes the time integrated properties. The more often tested four wire operation leads to a contribution of $\approx 25 \pm 3\,\%$ for each individual targets.

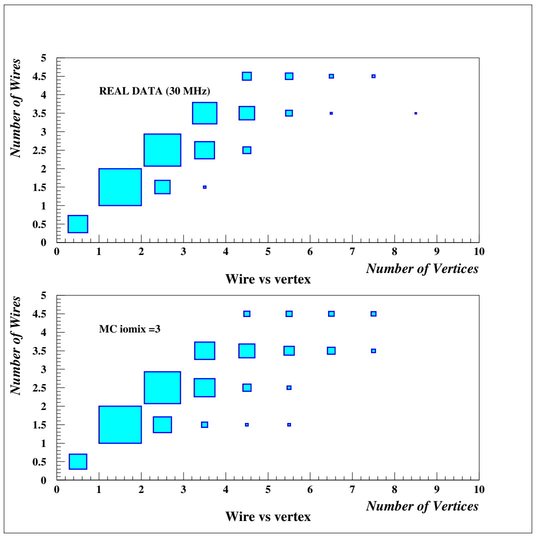

Figure 25: *Four wire operation: number of wires on which a vertex was found as function of the total number of reconstructed vertices for real data and MC data. The left lowermost point corresponds to (0,0), the neighboring point (1,1) has the highest probability.*

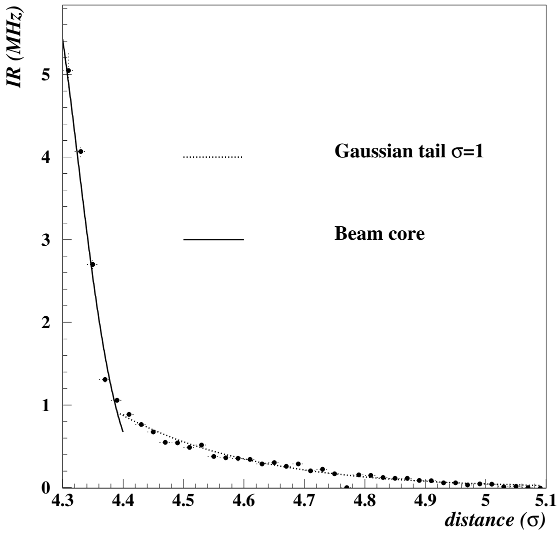

Figure 26: *Interaction rate produced on the Below-1 target as a function of the distance to the beam core during a two wire operation at a constant total rate of 10 MHz.*

Several studies have been carried out to investigate the impacts and to reveal the sensitivity of the multi-wire operation. One example where two target wires (Inner-1 and Below-1) have been in operation is shown in Fig. 26. The Below-1 target was retracted and reinserted (typically using $10\,\mu$m steps) while the total interaction rate was kept constant at 10 MHz[25]. During the first few retraction steps the contribution of the Below-1 wires drops steeply. Already after four steps the relative rate contribution decreased from the initial 50 % to roughly 10 %. This reveals a similar sensitivity as the step function measurements shown in Fig. 20. The further decrease can be well described by a Gaussian distribution with the sigma of the proton beam.

Even if the general multi-wire operation performance looks quite promising some problems have been observed. The baseline of the charge integrator electronics[26] is not very stable. Variations are observed which correspond to an interaction rate of several hundred kHz (or even more). This makes the calibration difficult and might lead especially at lower rates to non equal contribution of the various wires. These base line variations are most likely caused by the RF field of the charged p-beam[27] and cross talk between the different channels. Therefore several potential improvements

[25]The Inner-1 target was moved by the automatic slightly ($< 0.1\,\sigma$) closer to the beam.
[26]Defined by a calibration current.
[27]mirror currents, pickup or wake fields - that's not yet finally understood.

for the next run period are under considerations. The charge integrator cabling including the various connections, grounding and shielding will be improved. A more complicated tube wire configuration[28] is as test setup for one single wire under discussion. Additional improvements might come from the online analysis of the vertex detector data. The number of vertices per wire found in the second or third level trigger could be used as a feedback to readjust the calibration constants.

Another problem was occasionally observed at the operation at higher rates, the rate stability got worse and screwed up the multi-wire performance. The main improvement here has to come from measures applied by HERA (as discussed in the next section) to increase the rate stability. The long term multi-wire operation, especially at higher interaction rates, is not yet finally commissioned. That is mainly due to the fact that the target operation during the last two run periods have been dominated by a low rate single wire operation.

2.1.3 HERA and Beam Related Topics

The performance of the target operation and the quality of the produced interaction rate are closely related to the HERA operation and the properties of the p-beam.

Background and Interference with other Experiments

During the last years the potential interference of the HERA – B target operation with the other HERA experiments was seriously considered. Protons scattered elastically at larger angles inside the target might cause increased backgrounds at the other experiments. In addition it was realized that a second important background source at HERA arises from coasting beam protons. This lead to more complicated conditions, because this coasting beam background shows a different behavior: it develops with time during a fill and depend very strongly on the used wire configuration; here the target operation can even improve significantly the background situation.

In the beginning of the run period which started in July 1999 the ZEUS LPS[29]-detector[46] suffered under serious background problems which were partially correlated to the target operation. This lead to the formation of a task force group which investigated the overall background situation and finally managed to establish good running conditions for all HERA experiments [48]:

- A key point is the understanding of aperture limitations and the operation point of detectors or devices which are moved close to the beam[30].
- The main background reduction has to come from the collimator system. The system is able to fulfill this task, but this requires optimized settings. E.g. the jaws should not be set too close to the beam, because this reduces the target efficiency ϵ_T and increases therefore the number of scattered protons which get lost without interacting in the target.
- The smooth operation of all experiments with their various requirements relies on an optimized and very stable and reproducible operation of HERA.
- Any measure to reduce the coasting beam content at HERA helps to improve the background situation.

[28] target wire with thin insulator surface and one additional shielding surface - which would be connected to a second voltage to increase the gain further.
[29] Leading Proton Spectrometer
[30] e.g. it was initially tried to operate the LPS detector too close to the beam [48].

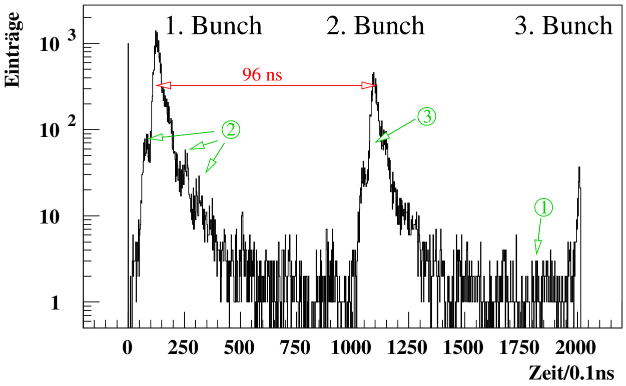

Figure 27: *TDC measurement of the interaction rate: (1) - coasting beam contributions, (2) - side bunch contributions and (3) contributions from the main bunch.*

After that optimization the usual HERA – B low rate running was performed without any serious interferences. Even during the several shorter test operations at our design rate no critical background problems has been observed. H1 observed sometimes a non critical increase of several rates inside their central detector. Due to the fact that the HERA – B detector and trigger commissioning required a low rate operation no systematic studies and attempts to improve the situation further has been performed.

Timing of the Interactions & Coasting Beam

The generated interactions in the HERA – B target should be due to protons in a narrow time window of approximately 1 ns length around the main bunch. Fig. 27 shows a TDC measurement of the interaction rate over two consecutive bunch crossing, which reveals this requirements together with the observed deviations. Two problems are obvious, which are observed on a regular basis:

Side Bunch Contributions: a significant amount of interactions are coming out of the ± 5 ns side bunches. These buckets are generated by the 208 MHz RF-system and filled with protons from the main bunch. Their existence is well known since long time and they are regularly observed e.g. inside the LOPEZ monitor measurements[47]. Different HERA – B measurements reveals side bunch contributions in the 10...20% level[31] [43]. All potential measures to reduce the side bunch population relies on HERA, it depends on details of the timing, synchronization and the RF system operation during the HERA filling procedure. The problem could be reduced if it would be possible to provide shorter bunches, but there exists serious limitation inside the HERA pre accelerator chain. The side bunch population is presumably correlated with the coasting beam generation inside HERA.

Coasting Beam: especially on the outer and above targets a significant amount of unbunched coasting beam contributions to the interaction rate are observed. Typical values are between a few MHz up to more than 10 MHz. Details concerning coasting beam are discussed e.g. in[33, 38, 44, 49]. Protons with an energy deviation $|\Delta E/E| > 2...3 \cdot 10^{-4}$ start to cross the separatrix in the longitudinal phase space and travel now freely (unbunched) around the proton ring. At HERA one usually just observes protons with negative energy deviation, the main reason for that are presumably the energy losses due to synchrotron radiation which accounts for approximately 10 eV/turn. Due to the dispersion $D_{x/y}$ in the target area these protons are displaced in the horizontal phase space to the outer and above side: $\Delta x/y = D_{x/y} \cdot \Delta E/E$. The production

[31] target hodoscopes, RICH and OTR. There are some uncertainties e.g. with the time resolution properties of the counters - thats one reason to build a new set of scintillator counters.

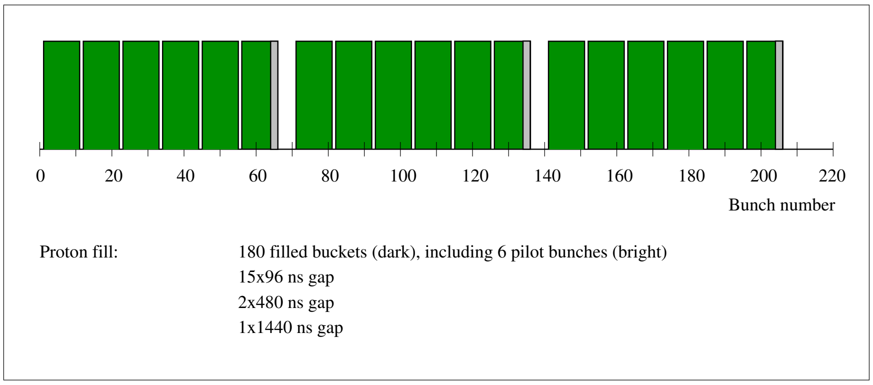

Figure 28: *Bunch scheme of the HERA proton ring.*

mechanism, which forces the protons to cross the separatrix, is not yet finally understood, several potential reasons are under discussions:

- **Intra Beam Scattering:** is most likely the main reason for the observed longitudinal lengthening of the main bunch
- **RF settings:** tests which has been performed during the summer of the year 2000 indicates that the production depends e.g. on the amplitude of the 52 MHz system.
- **RF noise:** noise in the RF system is supposed to generate chaotic behavior and to increase the longitudinal instability. Until yet it is not verified whether the actual low level of noise in the HERA RF-system leads to any significant impact.
- **Energy loss inside the target:** from all actual considerations and observations one concludes that the energy loss of protons inside the target is not the main source [33].

To reduce the impact of the coasting beam HERA has invented a system which excites the coasting beam protons transversally inside the dump gap with the intention to kick them effectively out of the proton ring [44]. In Fig. 28 the bunch scheme of HERA is presented, the last 1440 ns long gap is required to ensure a save dump of the protons. The coasting beam kicker was in nearly regular operation during the last run period. It helped to keep the coasting beam related background under control and to reduce slightly the level of coasting beam target interactions on the outer and above side[32]. Unfortunately it causes other problems, the excitation of several filled bunches, which lead to nonuniform contributing bunches. This is discussed in the next section.

Equal Contributions of all Bunches

A measurement how regular all $N = 180$ filled proton bunches contribute to the interaction rate is performed by calculating the RMS from the distribution of the relative contributions λ_i of the 180 filled bunches [38, 44]:

$$\sigma^2_{bx,rel} = \sigma^2_{bx}/\bar{\lambda}^2 = 1/\bar{\lambda}^2 \cdot \frac{1}{N}\sum_{i=1}^{N}(\lambda_i^2 - \bar{\lambda}^2) \ . \tag{6}$$

The RMS value is directly correlated to the number of effectively contributing bunches n_{eff}:

$$n_{eff} = \frac{(\sum_{i=1}^{N}\lambda_i)^2}{\sum_{i=1}^{N}\lambda_i^2} = \frac{180}{1+\sigma^2_{bx,rel}} \tag{7}$$

[32]Due to the rare operation of these wires it is difficult to judge quantitatively about the achievements. An analysis of the data is underway.

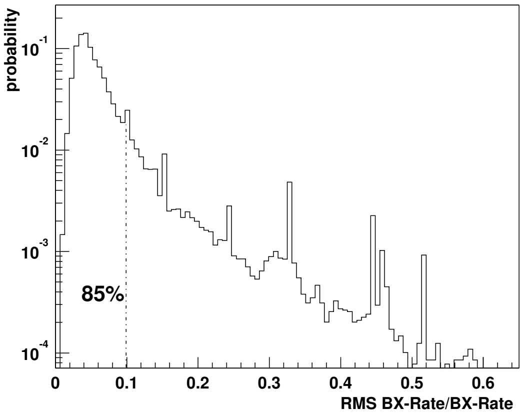

Figure 29: *Measured bunch to bunch variation $\sigma_{bx,rel}$ for the year 2000.*

In Fig. 29 the measured bunch to bunch variations for the run period in the year 2000 are plotted. During 85 % of the time the variations are smaller than 10 %, a value which is considered as limit for good running condition. More non uniform contributions are usually due to one of the following reasons:

- Reflections of the coasting beam kicker leads sometimes to a characteristic excitation of several bunches within the first 20 filled bunches. This problem can be usually significantly reduced by separating the HERA tunes from the kicker frequency.
- The tune control on a certain positron bunch increases usually the contribution of the corresponding proton bunch due to beam beam interaction drastically. Switching off the tune control is the measure which improves or even cures the situation[33]. The important impact of the beam beam interaction on the halo population of the proton bunches is also in other examples obvious, e.g. the six non colliding proton pilot bunches contribute usually much less to the interaction rate compared to the other bunches and quite often differences in the positron bunch currents are reflected in the bunch contribution to the HERA – B interaction rate [49].
- Another source for non-homogeneous bunch contributions arises sometimes from timing problems during the injection.

Rate Stability and Beam Tail Shaping

Also the global rate stability depends on HERA. Due to the intrinsic high proton lifetime of several hundred up to a few thousand hours there are not enough protons diffusing into the beam halo for the target operation. Therefore the target has to scrape away protons from the beam tails. This leads to a large sensitivity of the rate stability to all kind of beam fluctuations as shown e.g. in Fig. 19 and Fig. 21.

Several proposals to broaden the beam tails and to increase the halo population without disturbing the emittance of the beam core[34] has been discussed and tested during the last years. These measures to improve the HERA – B rate stability are called "beam tail shaping". A very promising attempt is the application of a tune modulation. First successful tests has been performed by HERA in December 1999 [49]. After solving several safety relevant hardware problems inside the setup a commissioning of the system has started in July 2000. The system is not yet finally commissioned but has already demonstrated that it can improve the rate stability significantly.

[33] another measure would be to scrape away a significant fraction of the affected proton bunch.
[34] which is important to obtain a high specific e-p collision luminosity.

Further Plans and Prospects

The effort to understand and improve the beam related problems of the target operation will continue during the luminosity upgrade shutdown period with the main emphasize on coasting beam and rate stability related topics. This includes the detailed analysis of the data taken during the last years and the further development of target-beam simulations. In addition the theoretical modeling and calculations from the machine physicists are required. The hope is that the comparison and discussion if the result leads to an improved understanding. The further fruitful and constructive cooperation with the HERA machine physicists is here essential for all progress and improvements in the future.

2.1.4 Shutdown Plans: Hardware Upgrades & Repairs

The two main hardware building blocks of the HERA – B target are the target mechanics including stepping motors and controllers and the counters including the required electronics. For both parts major upgrades are foreseen during the shutdown 2000/2001.

Target Mechanics

The actual target mechanics is already since five years in nearly continuous operation. The fact that no spare units are available and that we observed indications of aging and wear out[40] led to the decision to rebuild the mechanics. Several weak points have been located in the old construction. Therefore it was decided to redesign the complete target mechanics.

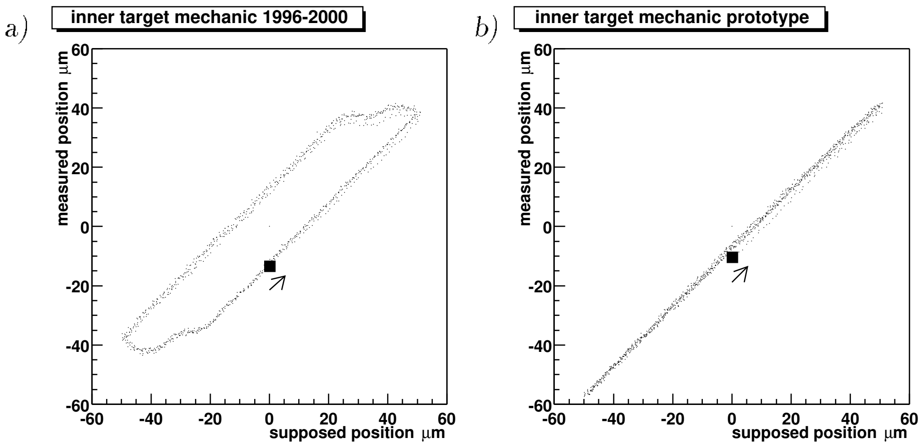

Figure 30: *Measured hysteresis of the actual (a) and the new (b) target mechanics.*

Based on the old design, the experience of the survey and picking up ideas from the VDS manipulator design a very nice solution was found which leads to an improved mechanical accuracy. Fig. 30 shows the measured hysteresis for one axis of the actual setup and of a prototype for the new mechanics. Whereas the old setup shows a significant hysteresis of around 20 μm this problem is completely vanished in the new design. A sketch of the new target mechanics is shown in Fig. 31. The main design criteria was to build something what is rather simple and solid to obtain a precise and robust device. One other key design criteria was the modularity of the system. The most important changes compared to the actual mechanics are:

- A rigid x-y table for the lateral adjustment connected with a large bellow to the VDS vessel.

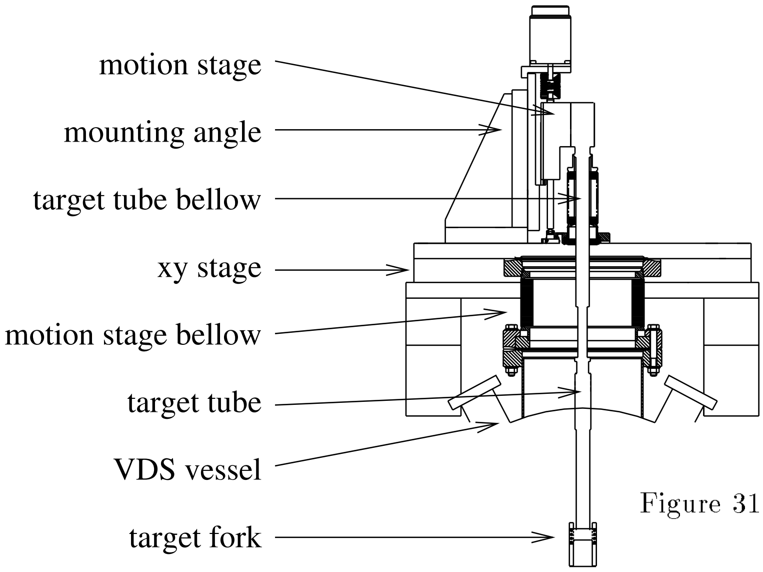

Figure 31: *Scheme of the new target mechanics.*

- Separate small bellows for the transversal movement of the targets mounted on top of the x-y table.
- The target "tube" which goes into vacuum and on which the target forks are mounted is now milled from one block of metal.
- Planar surfaces milled with high precision together with high precision mounting guidance are used for all mounting points at which different parts are screwed together.

Two prototypes have been build in the last year. The old mechanics station on the above side was replaced during the Xmas shutdown 1999 by a prototype mechanics, which has been operated successfully since that time. The second prototype was used for several survey measurements and as starting point for various smaller improvements. In the beginning of September 2000 the revision of the design will be finished followed by the ordering of components and the manufacturing of the new target mechanics. The mechanics is expected to be ready in January 2001 and after some tests it will be installed in May 2001.

The final fork design is actually under consideration. The baseline design foresees a smaller fork width with an opening of 24 mm, this allows a much simpler exchange of single target forks through the round opening for the small bellow on the x-y table[35]. Open issues are e.g. details concerning the cabling of the forks and the mounting of the wires and end-switches. A final design is anticipated after some tests which are scheduled for November 2000.

This rebuild of the target mechanics does not affect the infrastructure. I.e. all parts like cables, end-switches and end-switch box, stepping motor controllers and power amplifier, the target control software etc. can be reused. Some mechanical alignment and intensive survey tests are foreseen but the final alignment has to come from VDS data. The expected costs of around 100 kDM are covered by the University of Dortmund.

Counters & Electronics

The target steering, the HERA – B luminosity determination and the monitoring of beam related rate properties relies mainly on a set of scintillating counters. The actually used hodoscope counters

[35] An optional reuse of the actual target forks is foreseen.

are since five years in continuous operation, there exist no spares and we observed indication of a decreased performance, esp. in the time resolution. This lead to the decision to build one additional set of hodoscope counters, again consisting out of four pairs of scintillating counters. Basic design requests are to obtain a better time resolution (≤ 300 ps) and to cover a larger acceptance (factor four compared to actual counters). The expected costs of around 30 kDM are covered by the University of Dortmund.

For the electronics some maintenance work, an inspection of the modules and a revision of the cabling is foreseen. In addition a few improvements of the setup are under consideration, e.g. to order spares for important components (HV-system), provide additional signals (gated rates and coincidences) and the installation of a multi-hit TDC system.

2.1.5 Shutdown Plans: Software Setup

The considerations on software related developments and improvements have started. For some improvements it is most likely more efficient to perform them during the startup and commissioning phase in the autumn 2001.

TaCoS: A global revision of the target control system (TaCoS) is foreseen. There exists detailed plans, proposals and wish lists. Topics under consideration are e.g. to fix known bugs, a more flexible reconfiguration, the beam finding part, improved online monitoring, the distribution of target info etc.

System Aspects: The structure of the complete setup after the shutdown in the year 2001 is under discussions. The questions here are mainly related to the handling of the database servers and files, the analysis platform and the online monitoring. The anticipated goal thereby is to obtain an even more powerful and reliable system with a simpler setup which reduces the maintenance effort further.

DQM and SCS: A further integration of target diagnostic into the data quality monitoring (DQM) and of control processes into the common slow control system (SCS) is foreseen.

HERA information: The software for the data exchange between the HERA experiments (Netmex) has to be revised. Obsolete info should be removed, new desired data should be added and the programs should be included into the SCS.

2.1.6 Target Setup & Commissioning Plans for the Year 2001

Besides the modifications discussed in the previous section we intend to modify the wire geometry. The proposal is to use as default $50\,\mu$m round Ti wires. The actual run experience with such a wire looks very promising and one expects an improvement in the rate stability. Before taking the final decision there are a few questions related to the impact on coasting beam and the target efficiency which has to be studied in more detail. Whether also other target materials should be installed depends strongly on the HERA – B run plans and physics goals for the run period in the year 2001. In case of a strong wish to have different materials to study e.g. A dependencies we propose to consider following options:

- W: wire $50\,\mu$m
- Al: wire $50...100\,\mu$m or a ribbon with $50\,\mu\text{m} * 500\,\mu$m thickness

- Fe: wire $50\,\mu$m
- C: ribbon with $100\,\mu\text{m} * 1000\,\mu$m thickness

A first reasonable opportunity to exchange target wires might be during the Xmas shutdown 2001.

The improved target environment should be available from the beginning of August 2001, a stable operation of HERA which allows the operation of the detectors and a physics data taking is not expected before September 2001. The general intention is to provide again a stable, reliable and fully operational device which is able to achieve the desired performance. A couple of commissioning steps are required during the startup phase in the year 2001. Special emphasize requires here the operation of the new hardware components (mechanics and counters) and the modified target control system. Here one really has to ensure a very high level of reliability and safety. The commissioning requests have to be included into the general HERA – B run plans for the year 2001 and depend in addition strongly on the progress of the HERA commissioning after the luminosity upgrade shutdown. For the target operation no serious problems are expected, the main concerns are related to the HERA operation and the beam quality (coasting beam, rate stability, backgrounds, side-bunches and uniform bunch contributions).

Basic Functionality: experience shows that its feasible to establish the basic functionality within a few fills even after a long shutdown. One has to check:

- all wires are reaching the beam and produce rate
- the acceptance of the counters and therefore the rate known within 50 %
- first judgment on beam related topics: background, rate stability, bunch variations, coasting beam
- safety features

In case there occurs no unexpected serious problems the target operation after that first step can be handled over to the usual shift crew

First Calibration & Alignment: this requires a working and reasonable calibrated ECAL and an aligned VDS. One should expect at least a period of one month from the first data taking until one achieves a rate calibration better than 10% and a target alignment with a precision below $10\ \mu$m. This accuracy should be sufficient for most commissioning steps of the HERA – B detector. Further improvements depends on the progress of the ECAL and VDS detector. After the first month one should have also a clear picture concerning the calibration and stability of the charge integrators.

Beam Related Studies: all plans and progress on beam related topics like coasting beam and beam tail shaping depends strongly on the HERA performance and their plans. But one should foresee reasonable time slots in the schedule to perform here some measurements.

Long Term High Rate Multi-wire Operation: the final commission makes most likely just sense at a point when HERA – B intends to operate for a longer contiguous time period with these settings. Before that period several tests are necessary to judge already early on the performance and to discuss and develop potential measures to improve it.

2.2 Beam-Pipe

2.2.1 Introduction

Within the HERA – B experiment, the proton beam-pipe is divided in two major sections:

- A thin-walled 12 m long pipe which starts at the exit window of the vertex vessel and extends downstream to the beginning of the muon absorber.
- A 7 - 14 cm diameter stainless steel pipe (5,2 m long) traversing the Muon system.

The second section is a conventional steel pipe, which does not need any optimization with respect to the thickness of the wall. In contrast to this, the first section has to be designed very carefully in order to reduce the interaction of tracks coming from the vertex to a minimum.

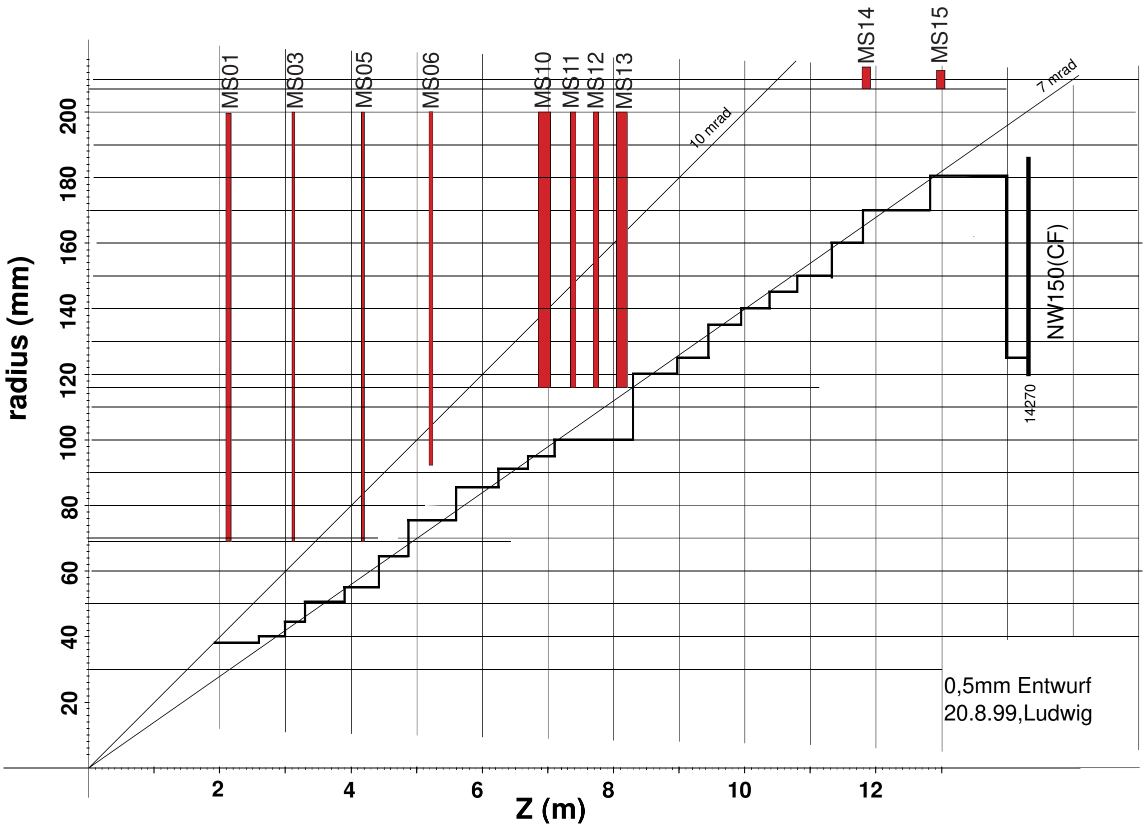

Figure 32: *Sketch of the actual HERA – B proton pipe. The inner tracker chambers are indicated schematically.*

For the time being, this pipe is made of 25 Aluminum cylinders with a wall thickness of 0,5 mm. The inner diameter is increasing from 38 mm at the vertex vessel to 180 mm at the end (within this chapter, this beam-pipe will be called "version A"). The pipe has been designed such that its shape follows a cone with a half-angle of 7 mrad (see Fig. 32). The average length of the cylinders is 47 cm. Due to the fact, that the complete pipe has a constant wall thickness, the required stability has to be obtained by increasing the number of stiffener rings (see Fig. 35) from zero at the beginning to eight for the thickest cylinder. An additional consideration was a clearance of at least 5 mm with respect to the inner tracker chambers.

In order to determine the contribution of the beam-pipe to the occupancy of the detector, the interaction of minimum bias events has been studied with a full GEANT simulation of the complete detector, with and without the beam-pipe. From these two simulations the contribution of the beam-pipe can be calculated. As a figure of merit the fraction of hits in the various detector components being due to tracks generated by interactions in the beam-pipe are plotted in Fig. 33a. The beam-pipe starts at a z-coordinate of about 200 cm. Chambers installed in the dipole magnet of the spectrometer (230 cm < Z < 640 cm) are severely affected by interactions taking place in the beam-pipe.

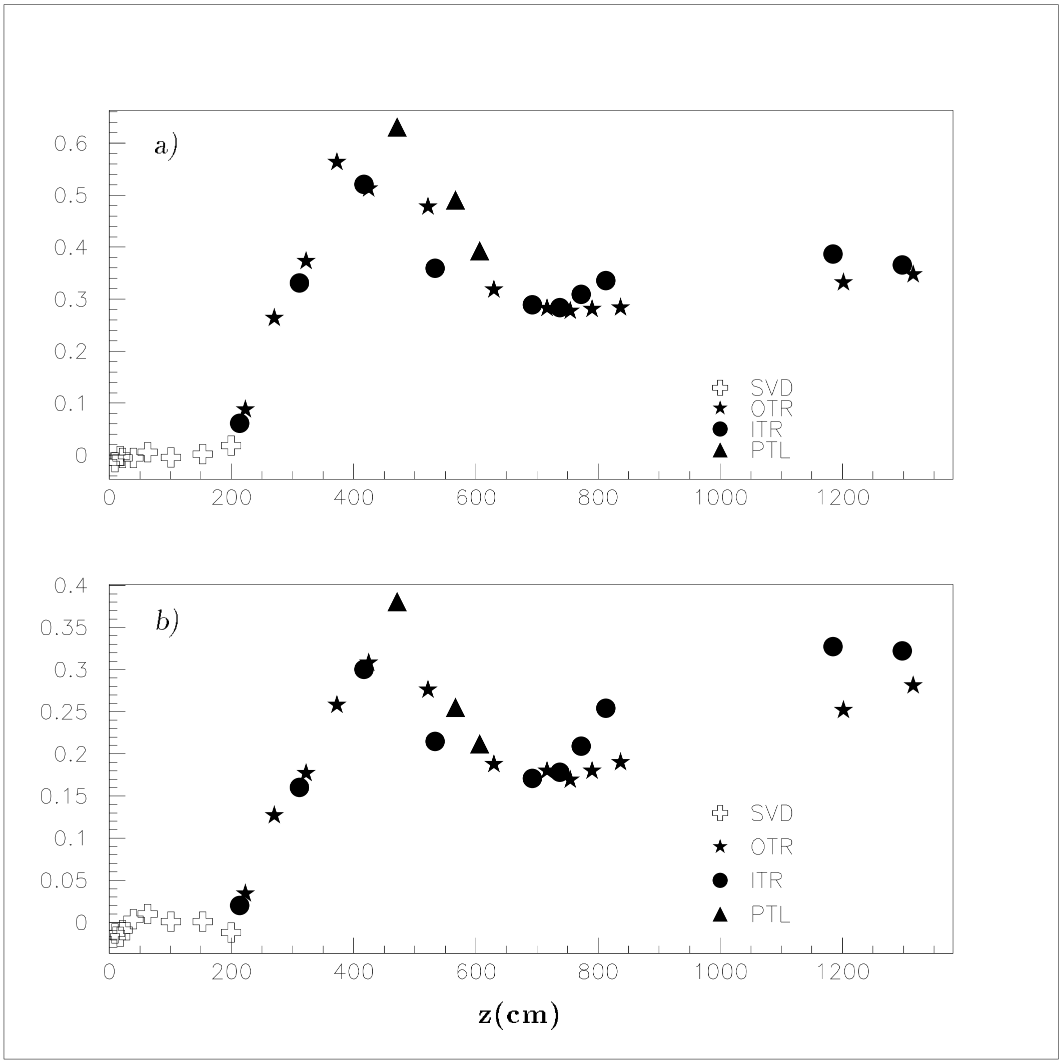

Figure 33: *Fraction of hits due to the beam-pipe plotted vs. the z-coordinate. a) The actually installed version (version A); b) version B.*

2.2.2 Previous Upgrade Plans

Design considerations:

Since three years there are ideas to improve the beam-pipe by reducing its wall thickness. A design proposed in 1997 is described in Table 13. At that time, no experience concerning the installation

Table 13: *Comparison of the different beam-pipe designs.*

z-coordinate (cm)	wall thickness (mm)			stiffener rings per cylinder		
pipe version	A	B	C	A	B	C
193 < z < 715	0,5	0,3	0,3	0 - 2	0 - 3	0 - 3
715 < z < 832	0,5	0,57	0,35	2 - 4	0	2
832 < z < 1342	0,5	0,5	0,4 - 0,53	4 - 8	1	1 - 3

of the inner tracker chambers and with the required clearance with respect to the beam-pipe was available. Therefore the segment of the beam-pipe between magnet and RICH, where four ITR layers (see Fig. 32) have to be installed very close to the pipe, was designed without any stiffener rings. The results of the Monte Carlo simulation are shown in Fig. 33b). A direct comparison of this design (called "version B") with the pipe presently installed (version A) (see Fig. 34) reveals the pros and cons.

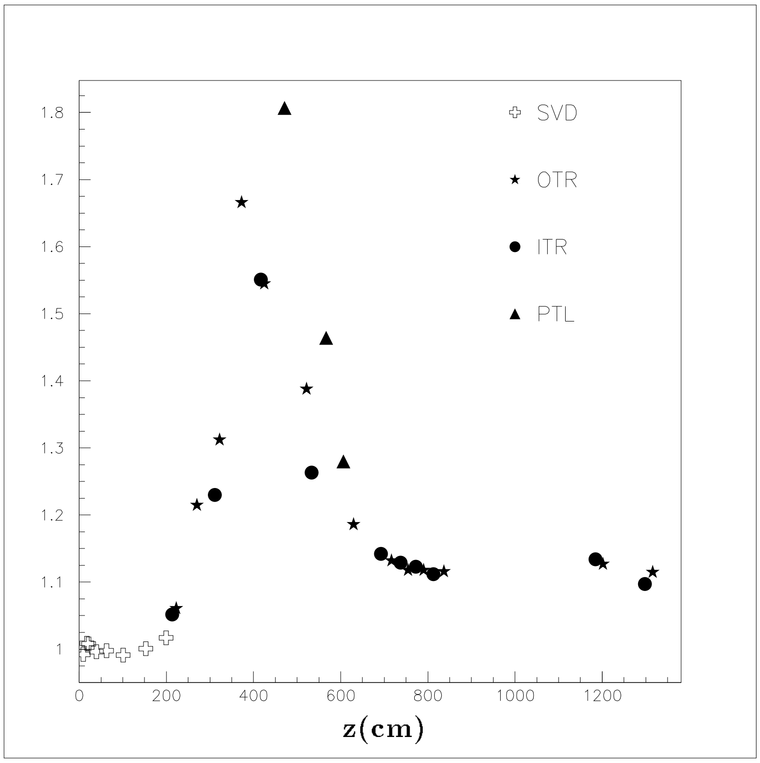

Figure 34: *Ratio of hits of version A and version B plotted vs. the z-coordinate.*

As expected, the largest improvement is obtained for the chambers installed in the magnet. For the rest of the detector only a small reduction in the contribution of the beam-pipe to the occupancy has been achieved. This can be explained by two different reasons:
1) After the magnet the occupancy in the tracking chambers is dominated by background tracks produced in the chambers themselves and their support structure (see Fig. 33a).
2) For pipe version B a substantial reduction in material was achieved only for the first section of the pipe (see Table 13).

Technical realization:

The basic idea was to produce Al cylinders with a wall thickness of 1.3 mm, reduce the thickness down to 0.3 mm by chemical milling and then press-form the resulting pipe in order to obtain the required stability. The press forming is expected to increase the stability of the pipe by about a factor of three. To give you an example: A pipe with flat surface which stands a pressure of 0,9 bar after evacuation should stand a pressure of 2,7 bar after the press folding. However, the factor of three can be obtained only when the pipe shows no deviations from perfect symmetry. Following these ideas, the first test cylinders have been produced. However, the first try to produce a complete pipe failed for two reasons.

a) When applying the technique of chemical milling to a larger amount of pipes, we realized that this process is very unreliable. Some etched cylinders looked very nice, others had a very uneven surface or even holes. However, all of them were treated in exactly the same way in the same chemical bath. The only explanation we found was that the failures must be due to different intrinsic properties of the Al rods themselves. As a consequence, this production technique was given up.

b) A more careful examination of the press formed cylinders with a new, very precise thickness-gauge revealed that they were slightly out of shape. Both flanges at the end of the pipe were distorted and showed some deviations from being a perfect circle. As expected, when pressure testing these pipes, they collapsed at a too small pressure.

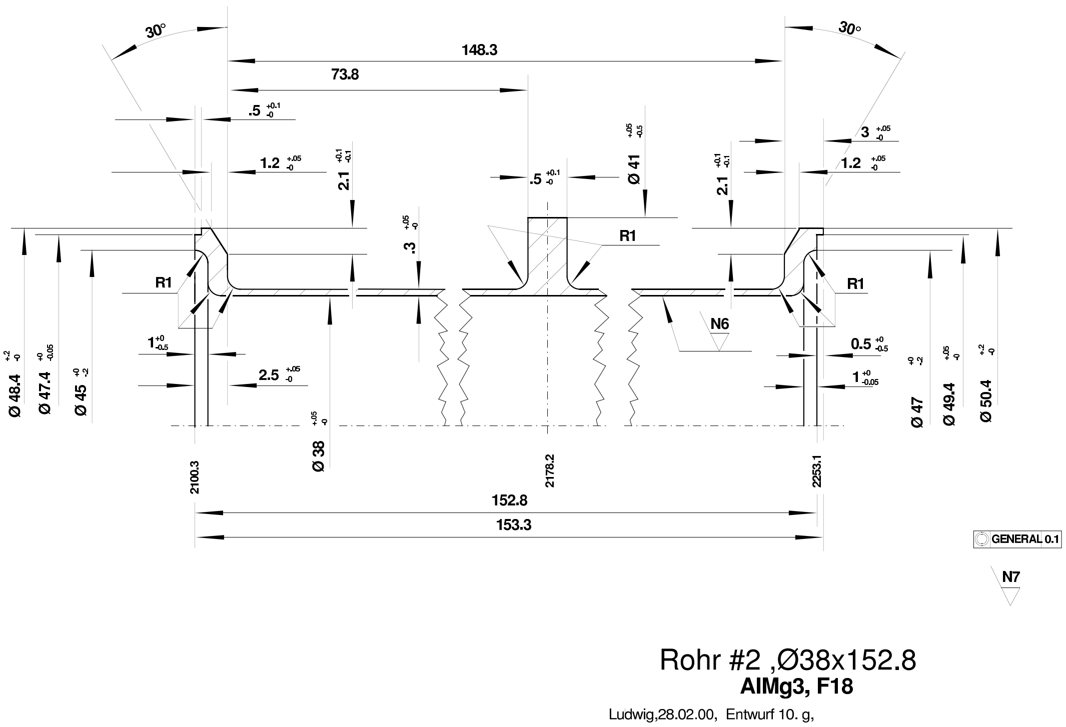

Figure 35: *Technical drawing of one of the cylinders.*

2.2.3 Plans for the Shut-down

Design and stability calculations:

In order to improve the design "version B", it was decided, based on the very positive experience with the installation of the inner tracker chambers, to reduce the wall thickness of the middle section and allow for some stiffener rings. In close collaboration with the DESY design group the stability calculations which fix the amount and cross section of the stiffener rings per cylinder were redone. These are the relevant numbers determining the stability of the pipe when diameter and wall thickness are given. As an example, one of the cylinders is depicted in Fig. 35. Based on our experience, this new version (called "version C") seems to be the optimum which can be achieved. The Monte Carlo calculations are just in preparation. The goal for the shut-down is to solve all remaining problem with the mass production of version C, manufacture all pipes and install the new pipe by the end of the shut-down.

Milling of cylinders:

Since the chemical milling was given up, the question had to be solved how to clamp the cylinder during the milling process. Several techniques were studied. Clamping tools were found which would allow to mill the cylinders in one step down to the final thickness of 0.3 mm with very small tolerances. However, this solution had to be excluded due to its high price. After several experiments a new recipe came up. Very precise steel cylinders will be produced which just fit into the Al pipes when these have been heated up. This trick results in a very precise support for the Al-pipes allowing the milling with very small tolerances (0,01 mm). After the milling both the steel cylinder and the Al-pipe are heated up again and the Al-pipe can be removed. This procedure has been tested successfully with some prototypes. We are just negotiating with different workshops how to ensure the timely milling of all 33 cylinders which have to be available by beginning of next year.

Press forming of cylinders:

The above-mentioned problems during the press forming process could be solved in the following way. In order to avoid the distortions of the welding flanges, some special clamps were designed which enclose the flanges during the press forming process. In addition, a reinforcing crease has been applied to both ends of the cylinder adjacent to the welding joints. Applying these new ideas to two cylinders during the press-forming yielded very nice results. These prototypes didn't show any substantial deformations and they fulfilled our stability requests. After that, the whole procedure was repeated again with several new test cylinders to test the reproducibility. Now we are confident that the time-schedule can be met.

Time schedule:

Milling of all cylinders	15/01/2001
Press-forming	15/02/2001
Welding	30/04/2001
Installation of complete pipe	15/05/2001

2.3 Vertex Detector System

The HERA-B Vertex Detector System (VDS) has the task of providing the track coordinates for the reconstruction of the B meson decay vertices and the impact parameters of the tagging particles. The required vertex resolution amounts to about 5% of the average B decay length (10 mm), and 20 to 30 μm in transverse direction. Even better resolution is desirable for a measurement of the much faster B_s mixing. The VDS information is already used at the second trigger level for background suppression.

The VDS consists of 64 double-sided silicon microstrip detectors which are arranged in eight superlayers (SL) of four quadrants around the proton beam axis, covering an angular range from 10 to 250 mrad (see Fig. 36).

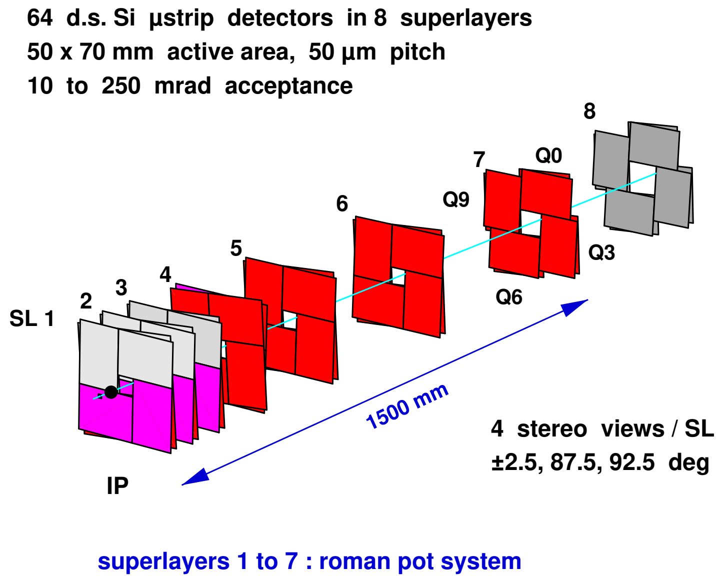

Figure 36: *Isometric view of the arrangement of detector wafers in the VDS. The dark shaded wafers in superlayers 1 to 7 are installed since June 1999; the system is complete since March 2000.*

To minimize mutliple scattering, the first seven SLs are realized as a Roman pot system, that is - together with the target wire stations - contained in a 2.6 m long stainless steel vessel. The eighth SL is mounted 2 m from the targets, immediately behind the 3 mm thick aluminium exit window.

The VDS operation requires an extensive infrastructure, which includes e.g. 16 remotely controllable manipulators for the precise positioning of 20 Roman pots, and adequate cooling for detectors and readout chips which are operated in vacuum. Since the VDS is an integral part of the HERA proton storage ring, three of its auxiliary systems have to perform with the utmost reliability: (i) the moveable RF shield inside the vertex vessel, (ii) the pumping system providing specified pressures for the primary (ring) and secondary (Roman pot) vacuum systems, and (iii) the leak-free water cooling system within the Roman pots; failure of any one of these systems could immediately stop the operation of HERA.

2.3.1 Status

The VDS has been operated routinely with partial instrumentation for several years at interaction rates up to 40 MHz. A brief history of the system is given in Table 14. Reports on the status over recent years have been published elsewhere [50, 51].

Table 14: *A short history of the Vertex Detector System.*

Date	Milestone
Nov 1995	ultra high vacuum vessel for vertex detector system delivered
Mar 1996	vessel with six manipulators and preliminary infrastructure installed
Apr 1996	test installation of 3 detector modules with preliminary mechanics and electronics
Jan 1997	3 detector modules with improved mechanics installed for first J/Ψ search.
May 1998	final infrastructure and 17 modules with final mechanics and Helix2.1 readout installed for system commissioning
May 1999	44 final detector modules with Helix2.2 readout installed for physics running
Dec 1999	vessel completely instrumented with 56 detector modules
Mar 2000	system completed with 8 modules outside the vessel.

Since March 2000, the system is completely installed. The system is also largely commissioned and the data produced are well understood.

As the demands on the VDS have not yet warrented operation at the full radiation load, the modules have so far been positioned at a slightly larger distance to the beam (15 mm) than design (10 mm). In addition, only 3 out of 4 stereo views were implemented for the first three superlayers.

In parallel to the hardware implementation, extensive software [52, 53, 54] has been developed and tuned. It includes packages for raw data processing like cluster finding and sparsification, for track reconstruction and vertexing, for the alignment of the 32 individual pairs of detector wafers, for the monitoring of data quality, and, last but not least, for the general slow control and interlock system. All this code is designed to run on-line and allows the use of the VDS in a stand-alone analysis as well as in conjunction with other subsystems.

2.3.2 Performance

The overall performance of the VDS is as expected. At the moment, the performance is generally evaluated in stand-alone mode.

Signal to Noise

Fig. 37 shows the cluster signal (S) to noise (N) ratios S/N for each chip of a typical double-sided detector module. For the n-side, the values are all well above 25; for the p-side, they vary systematically reflecting the increased and varying capacitive loads for the chips which are due to the (unavoidable) longer and varied traces on the Kapton cable connecting chips and detector.

An extensive study of the width of the S/N distributions has been done. As an example, Fig. 38 shows how different cluster sizes contribute to the overall S/N distribution. The figure also demonstrates how well signal and noise are separated, even on the p-side.

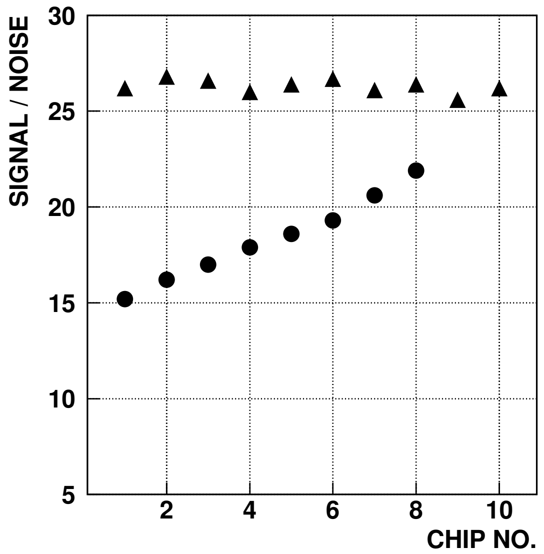

Figure 37: *Chipwise S/N ratios for the p-side (dots) and the n-side (triangles) of a double-sided detector module.*

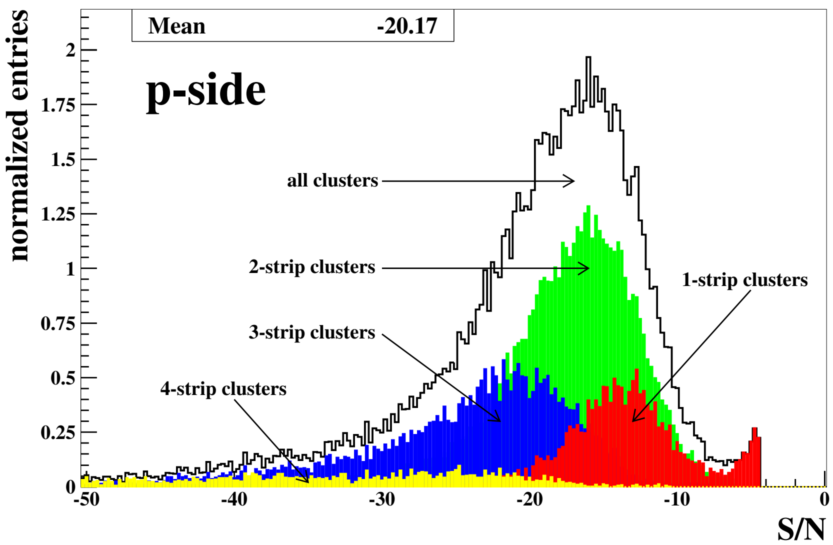

Figure 38: *Distributions of the signal-to-noise ratios (S/N) on the p-side of a silicon detector module; the contributions of various cluster sizes are indicated.*

Hit Efficiency

The hit efficiency is determined by ignoring during track reconstruction both planes of the detector under study and using reconstructed tracks with at least 10 hits in the VDS as well as an associated primary vertex. These tracks are used to predict hits on the two detector sides under study. The predictions have to fall into an area which starts 1000 μm inside the sensitive area. Only track predictions which have no other track crossing within 400 μm are used. If there is no hit within 200 μm of the predicted position an inefficiency is assumed.

The efficiencies obtained are thus detector efficiencies weighted with the track densities in our detector. The large search windows eliminate possible problems due to misalignments.

Table 15 shows the results obtained from run 14577 for superlayers 1 to 8, respectively. More than 80% of all detector planes exhibit efficiencies that are better than 97%. The lower efficiencies of the remaining planes can be traced to isolated bad readout chips. There are in average about 20 such chips, some intermittently, in the system. At the end of the 2000 run period, this number had increased to about 40 chips due to the (avoidable) loss of two planes in superlayer 8.

Table 15: *Efficiencies of the detector planes in superlayers (SL) 1 to 8 as measured in run 14577. The quadrants (Q) of the first three SLs are instrumented with a single- and a double-sided detector and so have only 3 planes (L1, L3, L4).*

SL	Number of detector planes with efficiencies			
	≥99%	≥98%	≥97%	< 97%
1	7	7	7	5 : Q1L3(68%), Q2L3&4(dead), Q3L3(55%), Q4L3(83%)
2	5	7	8	4 : Q1L3(76%), Q2L3,4(93,73%), Q4L3(82%)
3	3	8	10	2 : Q1L3(75%), Q4L3(92%)
4	10	14	15	1 : Q2L1(92%)
5	9	13	14	2 : Q2L2(90%), Q3L2(93%)
6	9	13	15	1 : Q2L3(96%)
7	12	13	14	2 : Q3L1(93%), Q4L1(83%)
8	11	14	14	2 : Q2L3(96%), Q3L3(75%)
sum	66	89	97	19 : Q1,2,3,4: (3,8,4,4), L1,2,3,4: (3,2,12,2)

Tracking Efficiency

The results presented here have been obtained with a tracking package based on cellular automata using space points; a detailed description of the algorithm and the performance studies can be found in [53]. Another VDS tracking package [52] yields similar results using a Kalman filter approach. The tracking efficiency was studied with Monte Carlo (MC) events. In Table 16, results from a study using events with 4 Poisson distributed interactions are given. We do not simulate noise as the observed noise level is significantly below 0.1%.

Table 16: *Results of a tracking efficiency study using events with 4 Poisson distributed interactions generated in a Monte Carlo simulation for three different detector efficiencies.*

Hit eff.	Refset	Allset	Clones	Ghosts	Time
100%	96.5%	85.5%	3.2%	14.3%	33 ms
95%	95.3%	83.6%	3.0%	15.2%	34 ms
90%	93.8%	81.0%	2.5%	16.7%	35 ms

As reference tracks (Refset) we take tracks that hit three superlayers of the VDS and have a momentum above 1 GeV. The set of tracks labeled "Allset" also contains tracks which hit only two superlayers. No momentum cut is applied. These tracks are used in order to study the performance of the code in the case of relaxed track requirements. Obviously, the implementation of - in general - four views per superlayer is providing enough redundancy so that even a low hit efficiency of 90%

does not lead to a significant loss in tracking efficiency.

Primary Vertex Resolution

The primary vertex resolution is studied in MC and in data. Fig. 39 gives the results of a MC study with events where 4 interactions are mixed according to a Poisson distribution.

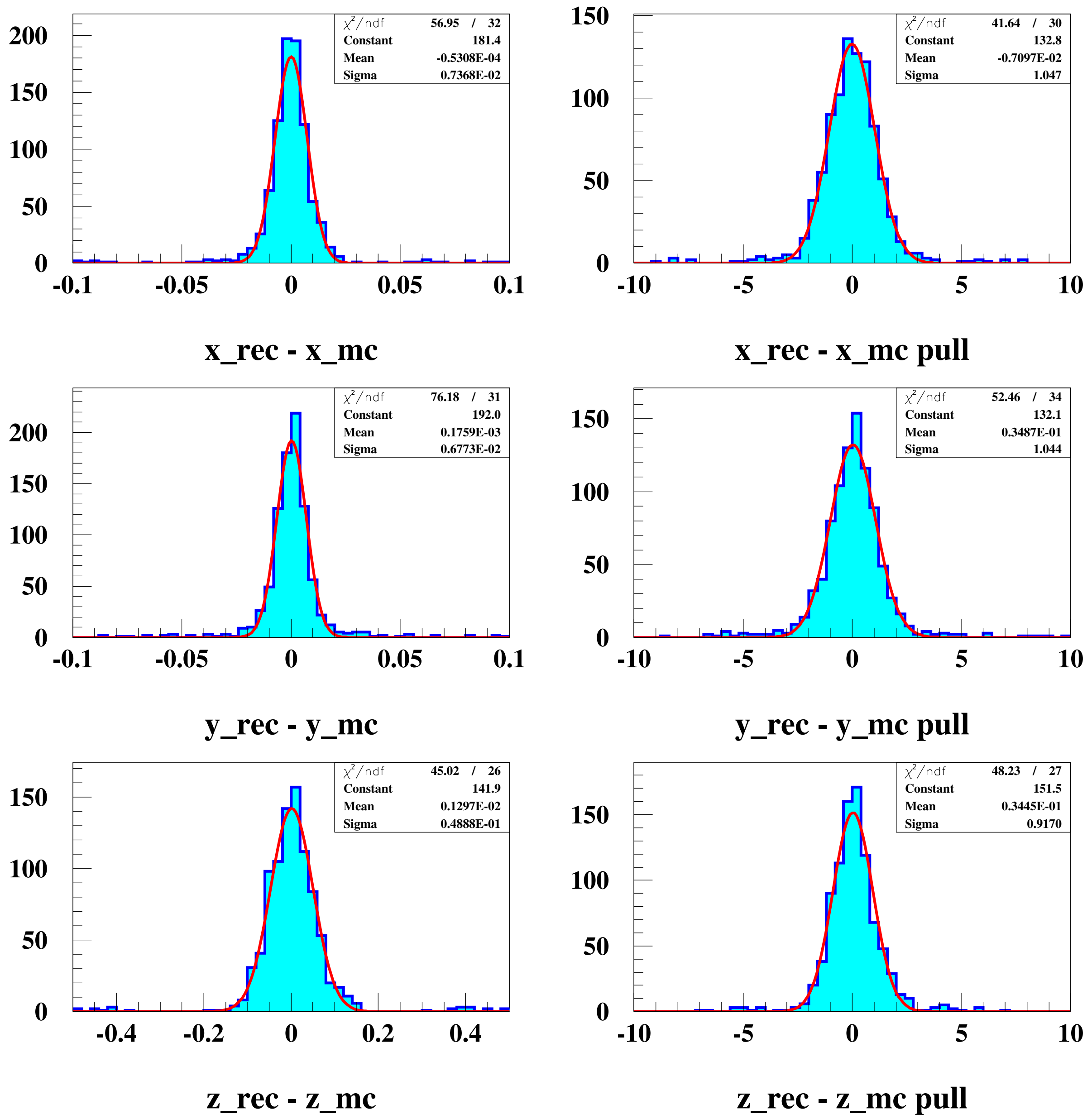

Figure 39: *Resolutions for primary vertices and pull distributions for the two transversal (x, y) and the longitudinal (z) coordinates (units in cm). The pull distributions do not have the width 1 due to the inaccurate momentum estimate in this VDS stand-alone analysis.*

Studies in real data using the known position of the wires confirm the resolutions of about 70 μm transversally and 500 μm longitudinally. These resolutions are obtained with VDS information only. Thus the momentum estimate which is done purely geometrically is crude. This limits the resolution as can also be seen in the pull distributions which do not have a width of unity.

The efficiency of the primary vertex finder is for minimum bias events 94% $\pm$ 1%. This is basically independent of the interaction rate. However, at higher interaction-rates a substantial amount of vertices are split or merged. Table 17 gives an overview about the quality of reconstructed vertices. Fig. 40 shows as example an event taken at 40 MHz interaction rate in which five primary vertices have been reconstructed on four target wires.

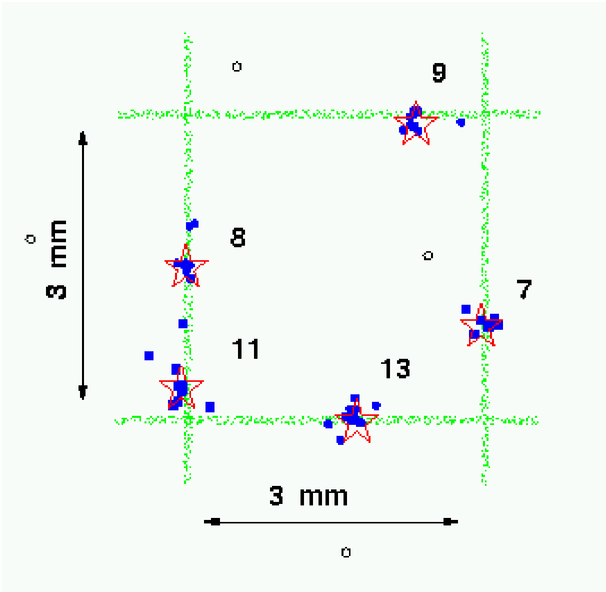

Figure 40: *Impact points of tracks in the target plane and reconstructed vertices for an event with 5 primary vertices. The total number of reconstructed tracks is 65; the numbers of tracks contributing to each vertex as well as the positions of the four target wires are indicated.*

Table 17: *Results of a MC study to determine the significance of reconstructed vertices. Good vertices are vertices that can be attached to a MC vertex. Clone vertices are vertices where the MC vertex was split. Mixed vertices are vertices which can be associated with more than 1 MC vertex: to first order two vertices cannot be resolved and are merged. Ghost vertices are vertices that cannot be associated with a primary MC vertex. The numbers are given for exactly 1 interaction and and for 4 interactions Poisson distributed over 8 wires. All numbers are* $\pm$ *1%.*

#int.	good	clone	mixed	ghost
1	95%	2%	-	3%
<4>	59%	31%	6%	4%

Secondary Vertex resolution

The work to fully exploit the VDS to study secondary vertices is still in progress. We present here results from MC studies where the momentum was smeared by 1%, which is roughly twice the resolution specified in the Design Report. The results do not change significantly if we assume a momentum resolution of 2%, which seems realistic so far as indicated by the present mass resolution of the $J/\Psi \to \mu^+\mu^-$ peak. Table 18 shows spatial resolutions for 2-, 3-, and 4-track vertices of the decay $B_s \to J/\Psi\Phi \to e^+e^-K^+K^-$.

Table 18: *Spatial resolution for the longitudinal (z) and the two transverse (x,y) coordinates of multitrack secondary vertices as determined in a MC study of the decay $B_s \to J/\Psi\Phi \to e^+e^-K^+K^-$.*

#tracks in vertex	mass constraint	σ_z / μm	$\sigma_{x,y}$ / μm
4	no	280 ± 10	21 ± 1
4	yes	280 ± 10	21 ± 1
3	no	300 ± 10	24 ± 1
2	no	375 ± 10	25 ± 1
2	yes	325 ± 10	26 ± 1

For four and two track vertices, a B or J/Ψ mass constraint was either applied or not. According to these results, the VDS meets the specifications of the Design Report.

Having so far no sample of b-hadrons selected from our data, we extracted distributions for selected direct $J/\Psi \to \mu^+\mu^-$ candidates.

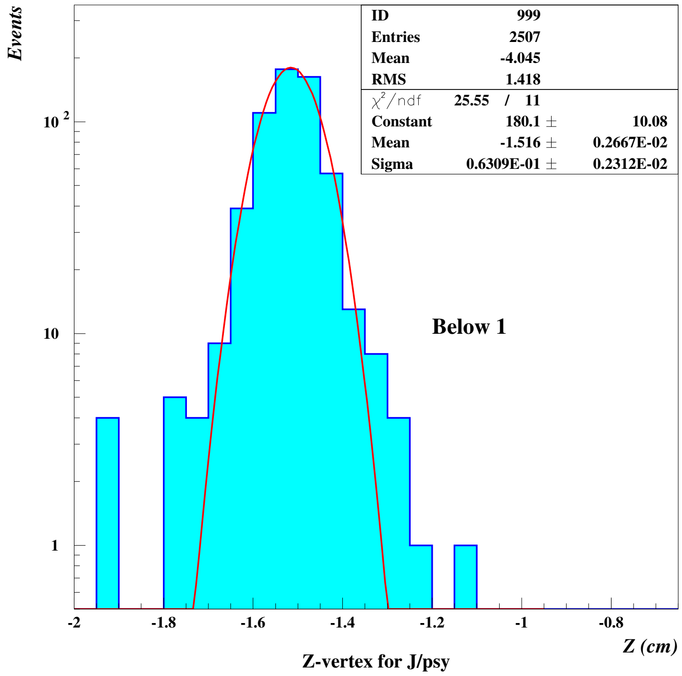

Figure 41: *Longitudinal distribution of $J/\Psi \to \mu^+\mu^-$ candidates from the "below-1" titanium wire*

Fig 41 shows the longitudinal vertex distribution for the wire 'below-1' (Ti); similar results have been obtained for the 'inner-2' carbon wire. The events are selected using a χ^2 per degree of freedom (dof) cut of 10 after a constrained fit to the J/Ψ mass. The widths of the distributions are different for the 0.5 mm thick titanium and 1 mm thick carbon wire - 630 μm and 750 μm, respectively. In both cases, the total width of the distribution shows extra contributions in the order of 510 μm and 610 μm respectively. This is under study. Expected contributions are from misalignments in the detector, incorrect MC description and from combinatoric background. If a χ^2/dof cut of 1 is applied, which reduces the sample by a factor of about 4, the widths of the distributions go down to 600 μm and 670 μm respectively. This indicates that combinatorial background contributes significantly, as contributions to width of about 190 μm and 340 μm are eliminated.

Alignment

The quality of the alignment can be studied much in the same way the efficiency of the modules is studied.

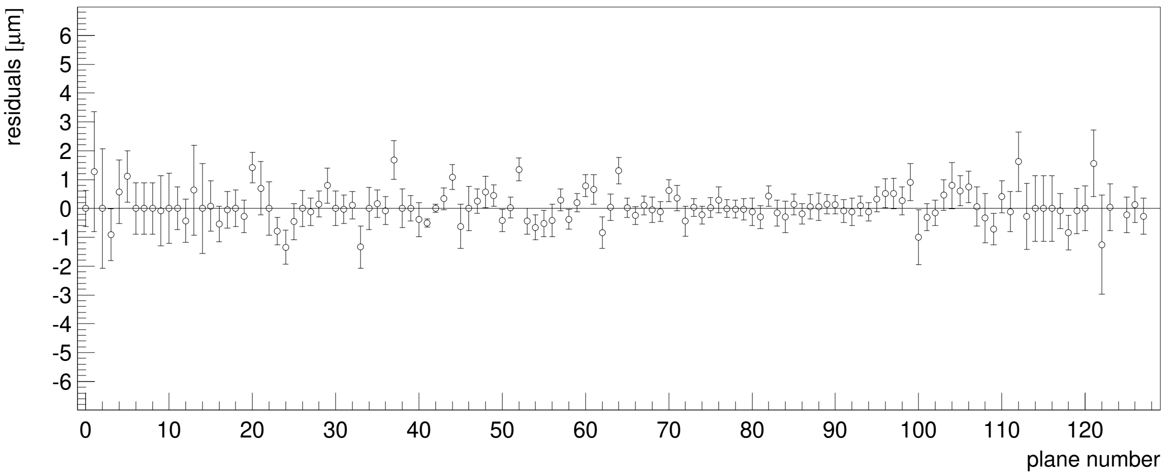

Figure 42: *Residuals of track penetration points for each plane, if the plane under study is not used for tracking.*

Tracks are reconstructed without the use of the plane under study and then the mean of the residuals is a measure of misalignments. Fig. 42 shows that the residuals scatter within ± 2 μm about zero.

2.3.3 Radiation Damage

The innermost edges of the silicon microstrip detectors are expected to experience a fluence of $3 \cdot 10^{14}$ minimum ionizing particles per cm^2 (or 100 kGy) during one year (10^7 s) of nominal operation after which they will be replaced. The results of dedicated irradiation studies [55] with single-sided p on n detector modules indicate acceptable detector performance up to the expected maximum fluence: the irradiated detectors can be biased beyond 500 V, and for detectors with polysilicon bias resistors the increase of the noise is consistent with the increase of the bulk leakage current. Using the full HERA-B readout chain and operating the detector at 8° C, a clear separation of signal and noise was observed even at maximum fluence, and the corresponding S/N value was 14.

In the year 2000, the radiation load at HERA-B was about one order of magnitude lower than during nominal running conditions (see Table 19). Thus, no conclusions on the ultimate radiation tolerance of the installed detector modules are possible. The measured doses, as well as the moderate increase of leakage currents, show no significant deviations from the expectation.

Table 19: *Increase of leakage currents in detectors of superlayers 6 and 8 during the two indicated run periods in 2000. The accumulated number of interactions (#int.) is also shown as a fraction of interactions (#int_n) for one year (10^7 s) of nominal HERA-B running at 40 MHz. Quoted doses have been measured with glass dosimeters directly behind the exit window of the VDS vessel at a radial distance of 35 mm from the beam axis.*

run period	#int.	#int_n	dose(35 mm)	ΔI(SL6, 0°C)	ΔI(SL8, 20°C)
Mar 3 - Jun 06	2.2·10e13	5.5%	110 Gy	6 μA	12 μA
Jun 7 - Aug 28	1.8·10e13	4.5%	96 Gy	3 μA	8 μA

2.3.4 Material Budget

Fig. 43 shows that muons from J/Ψ decays cross, on average, 7% of a radiation length (RL) in the VDS. The distribution in Fig. 43 is rather similar to that shown in the Design Report (see Fig. 114 therein) for the 'thick' quadrant version with 1.2% RL in the detector planes and 1.6% RL in the support arms. The slight shift to somewhat larger values is in part due to the RL in the support arms, which is actually larger ($\approx$2.2%). The tail of the distribution extending beyond 10% RL is mostly due to the four ceramic hybrids carrying the readout chips; the Design Report did not take into account their contributions, which amounts to about 4% RL in an area of 73×42 mm^2.

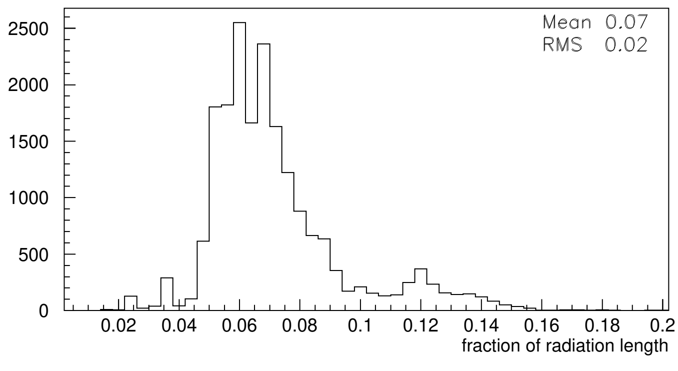

Figure 43: *Distribution of radiation lengths crossed by J/Ψ muons in the present VDS installation.*

2.3.5 Improvements

During the luminosity shutdown the VDS group is planning to implement the improvements listed below.

RF shield

The present RF-shield consists of four 5 μm thick and 12.7 mm wide stainless steel bands which surround - at square cross section - the proton beam axis inside the VDS vessel on a length of 2 m. During injection, the distance of the bands to the beam axis is 20 mm; for nominal running, the bands have to be pushed to 7 mm. Thus there is a safety margin of only 0.65 mm on each side of each band which cannot be visually inspected when the vessel is evacuated. Since a rupture of any band could immediately stop the HERA operation, and since the exchange of a broken band would take almost one week, we have so far avoided moving the bands to radial distances lower than 9 mm.

To safely safely reach the design value of 7 mm, we plan to install bands with a reduced width of 7 mm which have been manufactured for us on special request. With these narrower bands, the tolerances of the RF shielding mechanics are much more relaxed, and the amount of shielding material is reduced by almost 50%. As in the present installation, the bands will be coated with aluminum in order to increase their electrical conductivitiy.

Shielding Caps

In each Roman pot the installed detector modules are covered by a 150 μm thick aluminium cap which serves to protect the modules against RF pick-up and to separate the secondary vacuum in the pot from the primary vacuum of the storage ring. Caps of optimized shapes are produced as single seamless pieces by galvanic deposition of aluminium on (re-usable) stainless steel form pieces. Depending on the module lengths, the cap lengths range from about 90 to 430 mm. For the very long caps it turned out to be impossible to remove the Al-deposit without damage from the steel nucleus. Thus the 430 mm long caps were produced by welding a shorter cap on top of a cylindrical tube. This solution represented a viable backup alternative, at the expense of a non-optimized shape at the transition between cylinder and elliptical cap base.

The problem of removing the Al deposit from the form piece would be trivial if the form piece could be dissolved or melted without affecting the Al coating. Continued test series have shown that tin might be a suitable material for this purpose due to its low melting point and its mechanical properties which allow production of a polished form piece in the institute's workshop at reasonable effort. Coating of two tin form pieces for very long caps is now in progress, and we expect the samples back by the end of September.

Modules and HELIX Readout Chips

In the current installation, all quadrants of superlayers 1,2 and 3 are instrumented with pairs of single- and double-sided silicon detectors. For the next instrumentation only double-sided detectors will be used. In order to accomplish this, the mechanics of the modules for these superlayers has been improved.

All new modules will use the new version 3.1 or 3.1a of the HELIX readout chip which is available since July 2000, and which has successfully passed all tests so far. Compared to the installed version 2.2, both new versions feature (i) an improved control logic including (ii) a modified reset scheme for the pipeline amplifier to avoid drifts of the baseline, (iii) a modified bias current generator to fix the 'wake-up' problem of version 2.2, and (iv) a modified guard-ring structure to minimize crosstalk between comparators and pre-amplifiers. Many of these changes were already present in version 3.0. Version 3.1a has, in addition, a modified current source which no longer exhibits any oscillations, a feature that is most relevant for the Inner Tracker application.

Cooling

While the detectors in the VDS vessel are operated at about 0° C, the operation temperature of detectors in SL 8 - being installed in a box after the exit window - could not be reduced below 20° C so far. We plan to improve the gas cooling such that this temperature can be lowered by at least 5° C.

Flux Monitoring

So far, dosimeters attached to SL8 have been used to monitor the integral radiation load of the detector modules. We plan to build and install a low-mass counter array at the exit window of the VDS vessel which will allow the time-resolved monitoring of interaction and/or background rates.

2.3.6 Module Production and Installation Plan for the Year 2001

It is planned to produce a complete set of new modules by the middle of 2001. The silicon detectors and first samples of the new HELIX-3.1 readout chips ($\approx$400) are available; the mechanical parts are either on hand or have been ordered.

The production of the VDS-modules proceeds in steps. The last step is the attachment of the electronics hybrids and their bonding. All modules will be prepared for this step by the end of October 2000. At that time, all ceramic hybrids will be loaded with passive components, and about one third of them will be already equipped with readout chips. The production of complete modules will thus start in November, and all modules should be finished by June 2001.

During the shutdown we will repair the bad Helix-2.2 modules in SL 8 and replace the modules in the 3 o'clock quadrants of SLs 1 to 3, that is in Roman pot 103, by 3 pairs of double-sided Helix-3.1 modules. Apart from these changes, we will resume the VDS operation in 2001 with the Helix-2.2 detector modules from 2000, which have experienced negligible radiation damage so far (see section 2.3.3). The date for the replacement of these 'old' Helix-2.2 modules has still to be determined; a possible time slot could be the shutdown at the end of 2001.

2.4 Inner Tracking

The inner tracking system covers the area around the beam pipe up to distances of 25 cm. It has to cope with particle rates up to $2 \star 10^4$ mm^{-2}s^{-1}. Its purpose is twofold: It delivers tracking at small radii delivering coordinates for about 40% of all tracks from B-decays. In addition it is expected to provide input for the first level trigger using four trigger stations.
The inner tracking uses MSGC/GEM detectors — in total 184 with 768 anode strips each — organized in 10 tracking stations along the beam line as shown in Fig. 44.

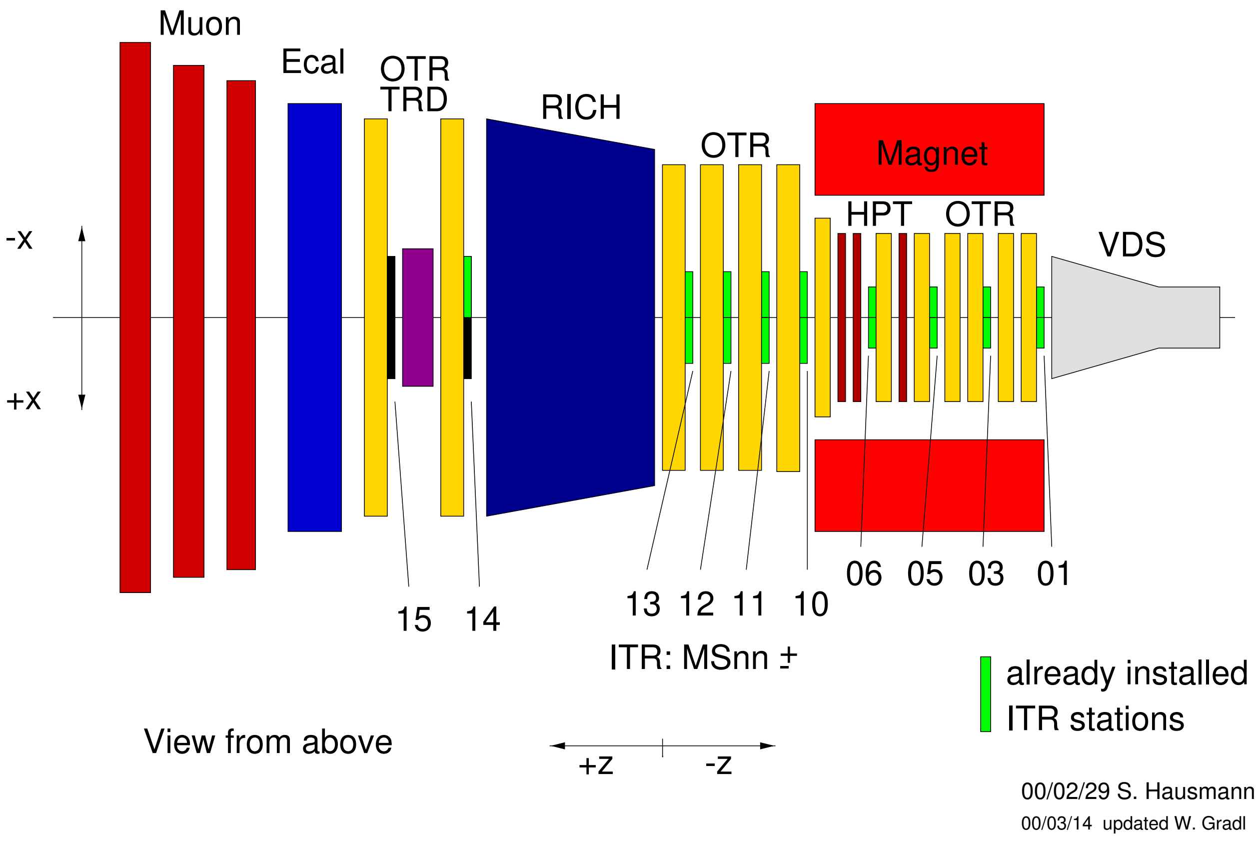

Figure 44: *Geometry of HERA – B tracking. The inner tracking stations which were installed during the run 2000 are indicated.*

2.4.1 Status of Installation and Subsystems

In the course of the year 2000 we have installed and commissioned all stations except the last two trigger stations behind the RICH detector with a total of 138 MSGC/GEM detectors. The detector does not deliver useful trigger information at present because of too high trigger thresholds (see below). This is the reason why the last two stations have not been installed. The detectors are in regular operation and included in data taking.

Detector status:

In general the detectors are working well and show stable operation. In the course of commissioning a certain number of defects have however shown up.

- One detector has developed a GEM short which was irrecoverable and two other detectors have massive damages on the cathode side leading to a complete loss of these detectors. Three more detectors show too large GEM spark rates and can therefore be operated only at reduced GEM voltages and therefore lower efficiency.
- In total we have observed 70 cathode shorts but at most 2 within one detector. Without further intervention a cathode short prevents the operation of 16 neighboring anodes, which are protected by a common HV resistor. These cathode shorts occurred during the initial commissioning phase of the detectors and must be regarded as 'infant mortality' due to faults in the substrates or dirt. This corresponds to a loss of 1.1% of strips.
- About 0.7% of individual anodes are broken or not connected. Most of them are production failures during lithography.
- At present 9 additional detectors cannot be operated because of HV problems like broken HV connections. These are recoverable once we have access and can be avoided in future.

The observed problems are summarized in Table 20. All broken detectors will be replaced resp. repaired during the shutdown. In addition we will cut the individual anodes which produce the cathode shorts. This will reduce the fraction of missing or broken anodes to a total of about 0.8% of isolated strips.

Table 20: *Problems observed during ITR operation.*

Problem	**Consequence**
1 GEM short	1 chamber off
2 severe MSGC defects	2 chambers off
3 GEMs sparking	3 chambers with reduced eff.
70 cathode shorts	efficiency reduced by 1.1 %
7 % interupted anodes	efficiency reduced by 0.3 %
9 HV problems	9 chambers off

The detector readout shows some additional failures which could not be repaired during the run because there was not sufficient access. Possible error sources are failure of interfaces for control signals or readout, broken components on the front end electronics or problems with the low voltage power supplies. All errors have occurred stochastically. In most cases the error rate could be reduced by system improvements. Towards the end of the run 5 detectors could not be read out at all, in addition 4 detectors showed one front end card with two HELIX chips (1/3 of a detector) which delivered no readout.

The readout clock is operated at 10 MHz. We plan to increase the rate to 20 MHz which has been demonstrated to work for all but 2 half stations. Because priority was given to physics data taking the collaboration decided to stay with 10 MHz during the year 2000 run and solve the remaining problems afterwards.

The gas system works very reliably controlling the gas pressure relative to the ambient pressure to better than 20 μbar.

The HV system including slow control works reliably and allows routine automatic ramping of the detectors and continuous control of all currents and voltages including several hardware protection features against discharges. It also counts GEM sparks and includes automatic recovery from them.

Summary: The detectors have shown stable running for several months. The fraction of broken strips as well as the number of cathode shorts is tolerable. Some basic weaknesses of the HV cabling and protection have led to 9 detectors which cannot be operated at present. The origin of these problems is known, they can easily be repaired outside of the pit and the problems can be avoided in future. The fraction of chambers which cannot be operated in the long run is therefore expected to be tolerable.

2.4.2 Detector Operation

All detectors needed consequent training during target operation. The drift and then the GEM voltages were raised slowly during operation over a period of typically one week. This led to a continuous reduction of the number of GEM sparks and automatic shutdowns of detectors due to high currents. All detectors, which are operated with an $Ar : CO_2$ 70:30 gas mixture, were first operated with a cathode voltage of 510 V and a GEM voltage of 420 V. With these conditions (same voltages for all detectors) the detector pulse height and correspondingly the gas gain varies by up to a factor 2.5 between different detectors. This is due to fluctuations of the GEM gain. The gain, however, does not vary over the area of individual detectors. Inspection of a sample of GEMs indicated a slight miss-alignment of the upper and lower copper holes for some GEMs and variations in the Kapton hole diameter. The latter is very sensitive to the parameters of the etching process. In a next step the gas gains were therefore adjusted by raising the GEM voltages individually. The variation of pulse heights for different detectors is now reduced to about 60%.

The GEM spark rate is continuously measured and recorded. It is proportional to the target rate and increases with gas gain. The measured GEM spark rate at a target rate of 10 MHz is about 1/day/detector in average. This is an acceptable value which does not affect the detector performance.

Summary: The detectors are routinely operated and work reliably after training and individual adjustments.

2.4.3 Tracking

The cluster analysis for the inner tracking detectors is done online by the level 2 trigger processors. The average noise per channel is determined for each run and cluster finding is based on a combined cut in signal over noise first for the strip charge and subsequently for the cluster charge of neighboring strips. This sparsification process is controlled by an online monitoring program which also logs relevant information into a database for each run.

The raw cluster charge distributions show a large number of hits with low pulse height which are not connected to particle tracks. For hits associated to tracks, Fig. 45 shows the cluster charge, the signal/noise distribution and the strip multiplicity for a typical detector with average gas gain.

The efficiency of the tracking detectors can be determined only after track reconstruction. This requires external detector information from the vertex detector or the outer tracking system. Tracks which are reconstructed in the vertex detector system and which pass through the active area of the MSGC/GEM detectors of the first tracking station (MS01) have been used to determine the absolute efficiency of these detectors. The result is shown in Fig. 46 for 7 detectors of this station as a function of the GEM voltage. Results for the other stations should be similar since the operating conditions are the same as for station 1. Precise results will be available soon. They rely on the

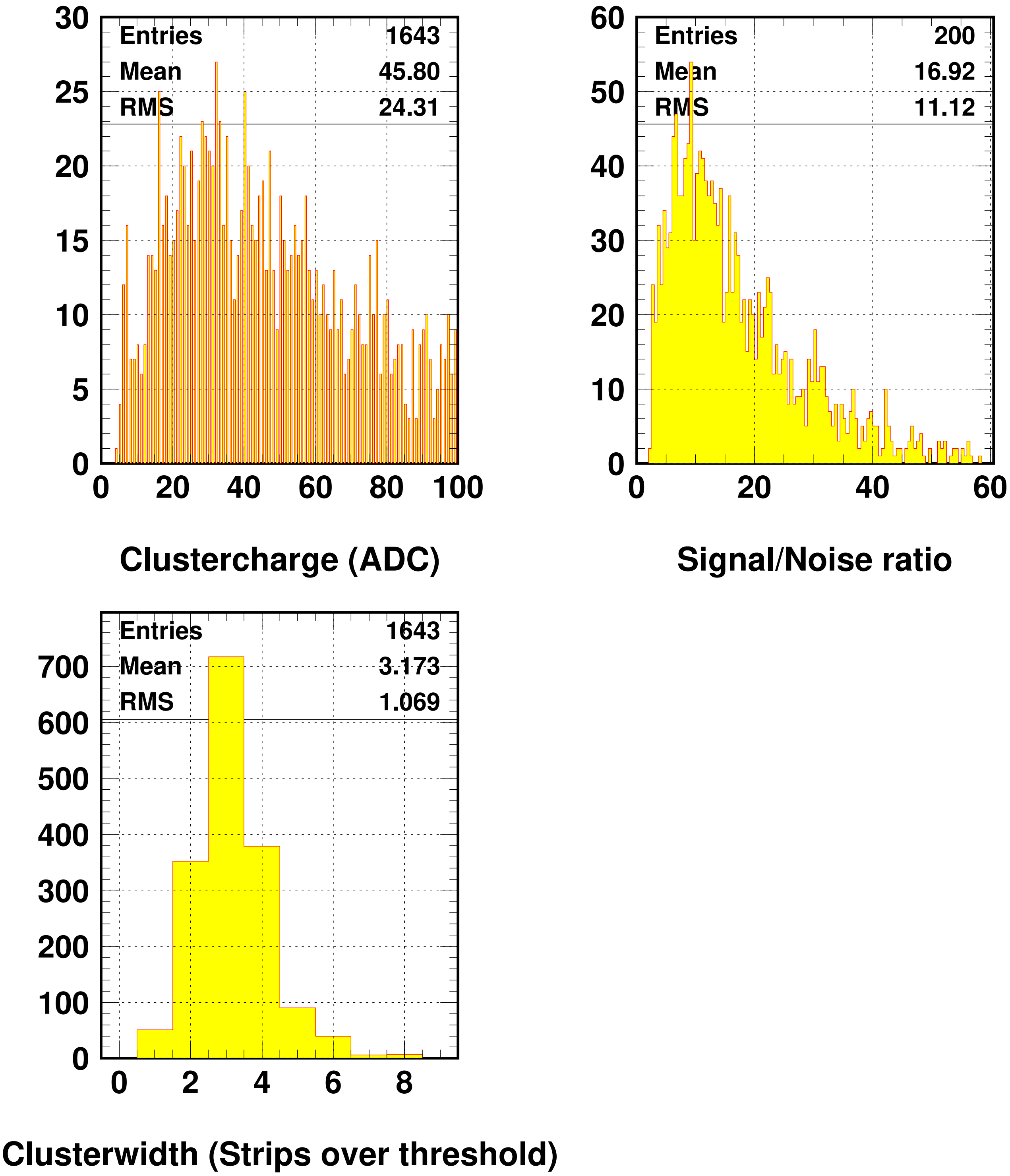

Figure 45: *Distribution of the cluster charge, the signal/noise ratio and the strip multiplicity for hits associated to a track for the detector* $\mathrm{M01}+-4+0\mathrm{K359}$ *which shows average efficiency.*

ongoing improvement of the tracking software including the OTR.

It can be seen that the observed difference in efficiency shrinks from about 25% before the adjustment of the GEM voltages to less than 5% at the final settings (filled symbols). The global

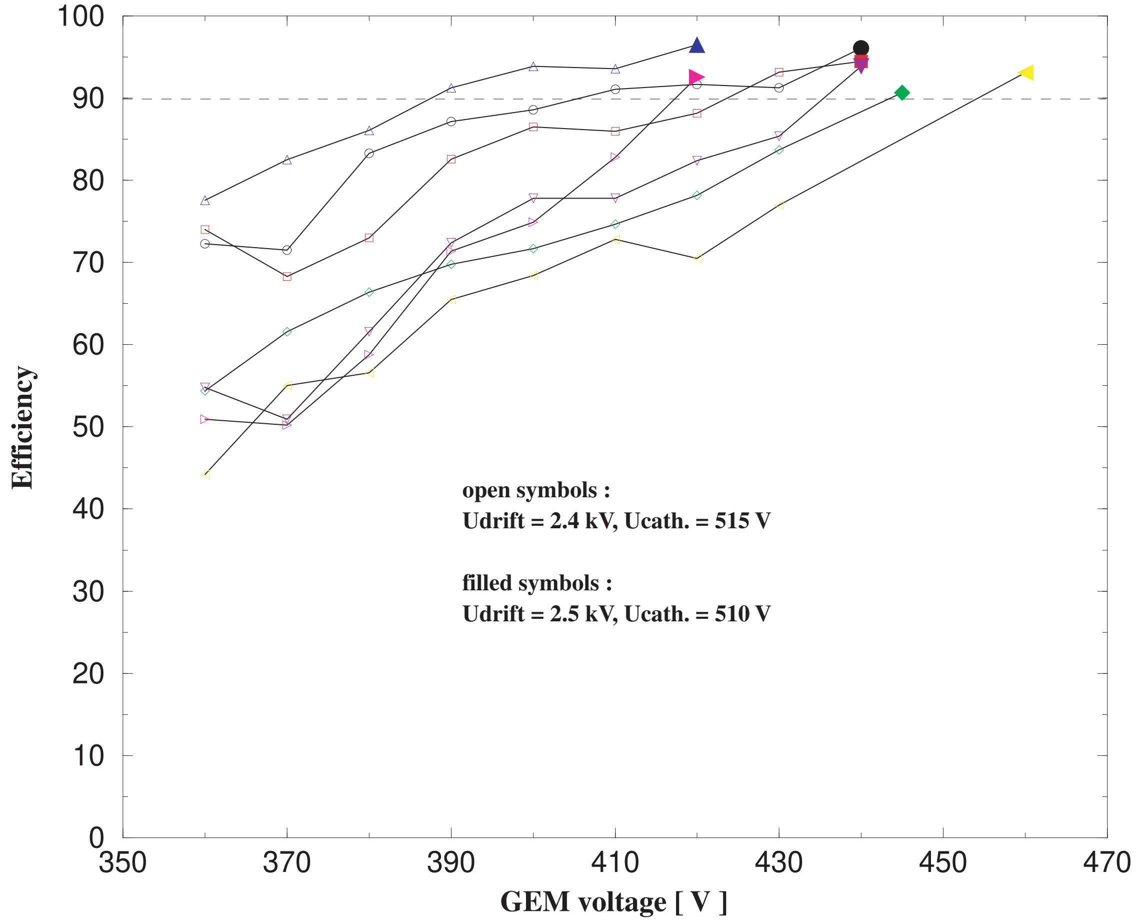

Figure 46: *Efficiency of detectors of station MS01 versus GEM voltage for fixed cathode and drift voltages. The filled symbols show the efficiencies for the current voltage settings after individual gain adjustments.*

efficiency as determined with external tracks saturates between 91% and 97% and does not further increase with cathode or GEM voltage despite the fact that signal/noise increases. We conclude that the detectors have sufficient gas gain for full hit efficiency. The saturation at this level is not fully understood and presently under study.

External tracks are also being used to align the detectors individually with respect to each other and the rest of HERA – B. Detectors within one half station which are mounted on the same support structure are aligned to better than 100 μm. At present, detectors of different stations are aligned to better than 200 μm. A significant improvement of the alignment using the global HERA – B tracking is currently being worked on.

The inner tracking clusters are fed into the offline reconstruction program to find tracks in the inner tracker system alone using stations MS10 to MS13 and common tracks with the outer tracking and the vertex detector. Figure 47 shows a typical event with tracks from outer and inner tracking.
.

The first results look promising, more work is however needed to tune the parameters for track finding and to determine the overall track efficiency for the inner tracking system. We are confident however that the inner tracking system will contribute adequately to the track reconstruction for

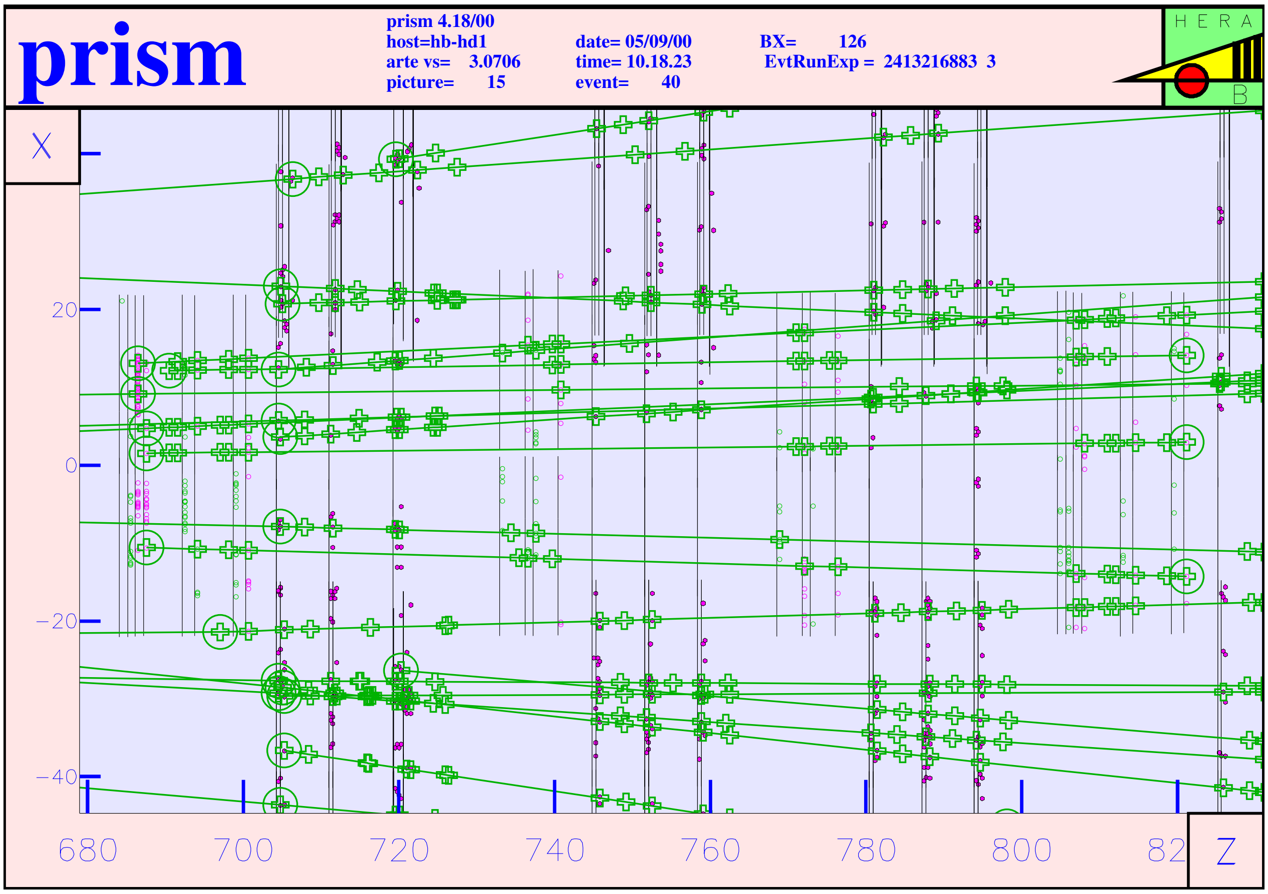

Figure 47: *Data event display showing the tracking area of stations MS10 to MS13 with hits and reconstructed track segments in the inner and part of the outer tracking system.*

the physics data which has been recorded in 2000 once the fine tuning has been finished.

2.4.4 Trigger Signals

First level trigger signals are delivered by 4 trigger stations, two in front of the RICH and two behind. The trigger is derived on the HELIX128 chip by discriminating the analog signal for each strip and a subsequent OR of the trigger signals of 4 neighboring strips. Each chip therefore delivers 32 trigger signals for each bunch crossing. In order to guarantee high efficiency each trigger station is build using double layers of MSGC/GEM detectors with identical strip orientation. The trigger signals of the two layers are ORed on the front end. In total there are 96 detectors used in the trigger of which 48 behind the RICH have not been installed for the run 2000.

The present trigger installation works technically, it does however not give high enough efficiency because the trigger threshold for the discrimination of the strip charges cannot be lowered below a signal corresponding to about 25000 electrons. Below this threshold the trigger outputs of the chips start to oscillate because the output signals of the trigger drivers are coupled back weakly to the analog input of the chips via power lines and printed circuit board. Since this problem could not be solved in time it was decided to concentrate on the tracking performance of the inner tracking system for the year 2000. In the meantime substantial progress has been made. Main improvements come from two sources: 1) The voltage swing of the trigger output drivers was reduced from ± 2 V to ± 0.3 V thus reducing the primary source of the problem. 2) The grounding concept of the detectors and the chips was significantly improved. This has the consequence that new trigger driver electronics is needed. These improvements allow to reduce the trigger threshold to an equivalent of about 7000 electrons, limited by noise. Three double layers of trigger detectors with different combinations of these improvements were operated in HERA – B in August. Systematic test runs show an efficiency of double layers compatible with full efficiency but certainly higher than 90%.

2.4.5 Improvements of the Inner Tracking Detector during Shutdown

Major improvements are planned for the shutdown period.

- All detector stations will be taken out from the experiment to replace resp. repair broken chambers.
- The improved grounding scheme will be applied for all detectors. This includes the replacement of all HV cables on the stations with improved RF filtering.
- The two trigger stations after the RICH will be completed and installed.
- All front end cards for the detectors used in the trigger will be replaced using a new chip version. This is the biggest change which is necessary because the analog pipeline of the present chips is too short by five columns (500 ns).
- The trigger driver front end cards will be replaced by new ones adapted to the low voltage swing of the trigger outputs.
- We intend to test new gas mixtures like $Kr : CO_2$ or $Ne : CO_2$ to increase the signal.
- The available data taken under various conditions will allow to study in detail the reason for the observed saturation of the efficiency at too low values. The software, i. e. cluster finding and tracking will be improved.

These measures are well prepared and planned. Material needed has been ordered and will be available in time.

2.4.6 Summary

The inner tracking system based on MSGC/GEM detectors has overcome many major problems. During the last months there has been considerable progress. The system is quite vulnerable and not very robust in the intense hadronic environment, since the detectors have to be operated near the discharge limit to get acceptable efficiency. The problem of gas aging prevents the use of organic gases which have much better quenching properties.

Nevertheless the detector system was shown to allow routine operation with high reliability and good efficiency over long periods. A substantial improvement is still possible during the shutdown to further eliminate weak points. The system will be able to contribute to the first level trigger after the shutdown improving the overall trigger acceptance of the experiment by about 30%.

We are confident that we will have a reliable inner tracking system with the expected tracking and trigger performance at the restart of the running.

2.5 Outer Tracker

2.5.1 Hardware Status

Compared to the Technical Design Report the Outer Tracker (OTR) has undergone various stages of development. An overview of the final design and the operation parameters can be found e. g. in [56]. In the following we report the current status of the OTR and summarize some activities during the installation and commissioning phase (1999 – 2000) as far as it helps in understanding the still existing problems.

Chamber Assembly and Installation: The installation of the Outer Tracker chambers was carried through in parallel to the module production and the chamber assembly. The mechanical installation as well as the electrical connection of the super-layers was achieved mainly during monthly mini-shutdowns of 3 days length. This was possible since the readout and auxiliary electronics which are attached to the super-layer frames had been assembled and electrically tested before or during the chamber assembly outside the experimental area. By January 2000 all OTR super-layers had been installed.

The time schedule for OTR module production, chamber assembly, and installation did not allow for building a full-size prototype of a large chamber. Certain problems encountered during the assembly of the first chambers required some ad hoc modifications of the module design and of the assembly and installation procedures. The most important addition to the module production procedure, as described in the Module Production Guide [57], was the mechanical reinforcement by means of carbon-fiber (CF) rods. As a consequence, the chambers which were installed first show some deviations from the otherwise uniform OTR design:

MC2–	:	Prototype modules with graphite-coated Pokalon foil.
PC1–	:	Some modules without reinforcement.
PC4–	:	Many modules without reinforcement.
TC1–	:	Most modules without reinforcement.

The chamber TC2– originally contained no reinforced modules at all. This was changed in a major overhaul operation during December 1999 (see below: 'High Voltage Stability').

It is noteworthy that the caps of the two super-layer halves, although rather complicated, fit perfectly and did not cause problems when closing both halves. However, the installation of the modules inside the caps had in some cases problems because of too tight dimensions. For the modules above and below the beam pipe which are mechanically only attached at one end, the mechanical reinforcement was particularly important.

Readout Electronics: The electrical readout of the Outer Tracker [60] consists of the amplifier-shaper-discriminator boards (ASD-8) plugged to the signal feed-through connections on the gas-box, the TDC boards residing in crates mounted at the chamber frames, and the Second Level Buffer (SLB) boards situated in the electronics trailer. Trigger link boards provide the optical connections to the First Level Trigger (FLT) electronics. They are connected by cables to the hit-out connectors of the TDC boards.

Table 21 summarizes the installed components of the readout electronics and the failures observed during the first year of operation.

Table 21: *Components of the readout electronics and the failures observed during the first year of operation.*

Boards	amount	failures
ASD-8	7200	14[a]
LV distribution boards	212	4
TDC	955	3
TDC crates (power supplies)	99	3
SHARC SLB boards	34	1
Triggerlink boards		see below

[a]Additional 138 ASD8 boards delivered no signals for unknown reasons (possibly bad connections)

ASD-8 Threshold and Noise Behavior: Before installation all ASD-8 boards have been tested and classified according to their efficiency and noise behavior [60]: The boards are sorted into 4 categories with different gain, each subdivided in 3 sub-categories with different signal-to-noise distance. For each of the 12 classes a so called "noise reference threshold" U_{ref} was determined. This is the threshold value at which the ASD-8 board starts to show noise in the laboratory ($> 2\,kHz$). It is used as reference value for the ASD-8 operation at the chambers.

During the assembly of the chambers grounding and shielding was improved until the noise occupancy of all channels was smaller than 10^{-2} at a threshold value of $U_{th} = U_{ref} + 200$ mV. The increase of the threshold by ΔU_{th} with respect to the value determined in the laboratory test is attributed to the operation inside a large system (system effects).

After the installation in Hall West the noise behavior of the chamber test was reproduced and no noise degradation was observed. The situation changed for the trigger layers when the trigger link-boards were installed.

TDC System: The TDC readout (955 TDC boards) was in general operated under stable conditions. At high trigger rates (> 1 kHz) approximately 1.5 % of the boards showed readout problems which have been traced to either connection problems of the SHARC cables to the SLB boards or problems of the transmission of the FCS signals. The FCS problems observed initially have been fixed by improving the termination of the backplane of the central FCS crate. The connections of SHARC cables will be systematically tested and improved during the shutdown.

Noise generated by the TDC–TLB connection: The hit outputs of the TDC boards are connected by 17-pair flat cables (length between 1 and 4 m) to the Trigger Link Boards (TLB). The hit outputs are single-line TTL signals. Every signal cable comprises 32 signal lines and 2 ground lines. The cables act as antennas and emit high-frequency electromagnetic noise, most likely generated by the fast TTL drivers on the TDC boards. The noise is transmitted to all signal (ASD8-to-TDC) cables in the neighbourhood of the trigger link cables. The electromagnetic noise travels along the signal cables and triggers oscillations of the corresponding amplifier boards making the operation of the chamber impossible. The effect occurs as soon as cables are connected to the hit-out of the TDC. It does not depend on the termination of the trigger link cables or whether they are connected to a TLB or not. The cable routing as well as the distance to the signal cables play an important role.

The following measures to reduce the emission of electromagnetic noise by the trigger-link cables have been tried with very little or no success:

- different shieldings of the trigger-link cables,
- increase of the number of ground lines (1 ground-line per signal-line),
- conversion of the single-line TTL outputs to differential LVDS signals.

The only measure which showed at least in the laboratory a significant improvement was the installation of commercial noise filters (ferrite rings) around the trigger-link cables directly at the output of the TDC board. In situ the installation of 4 such rings per cable was necessary to allow for an operation of the trigger chambers at least with an increased threshold value.

Figure 48 shows the noise occupancy versus the threshold increase ΔU_{th} for 8 super-layers of the –x side: MC1–, MC2–, PC2–, PC3– (not trigger layers), PC1–, PC4–, TC1–, TC2– (trigger layers). The noise rates are taken without beam. Under beam conditions the thresholds have to be increased by about 100 mV above the point of stable operation suggested by this measurement (for yet unknown reasons this increase has to be much higher for TC2–). The final threshold values ΔU_{th} at which the chambers have been operated are listed in Table 22. Values of ΔU_{th} of 500 mV and larger are cutting into the cell efficiency of the corresponding layers (see also section 2.5.3).

Trigger Link Boards (TLB): The Trigger Linkboards (TLB) have been available only in late fall 1999 and therefore had to be installed in situ. As the boards were missing during assembly time several problems of the entire system were identified very late.

All problems related to the TLB itself could be solved by now. Two problems remain in the transmission to the TFU's of the FLT: Failures of the Autobahn chips and instabilities in the optical transmitter-receiver system, due to sensitivities to the operating temperature and to the duty cycle of the data stream. A repair/upgrade program for the shutdown is described in section 2.5.4.

Detector Operation: Besides the below mentioned HV problems the operation of the Outer Tracker chambers did not cause any problems: The detector is fully integrated into the central Slow Control System (an exception is the gas monitoring), a calibration process running on the SLT farm evaluates the channel status, calculates the t_0, and updates the databases if necessary. The calibration process also provides data quality histograms at the hit level. Higher level monitoring of the reconstruction and the track quality is not yet available and will be developed during the shutdown.

Gas System: The gas system of the OTR produces the desired gas mixture (standard mix is Ar 65% CF_4 30% CO_2 5%) and circulates the counting gas through the detector. It controls the flows and regulates the pressures in all 26 OTR half–super-layers, purifies the gas upon return from the detector, and automatically performs a quantitative analysis of main and trace (O_2, N_2, H_2O) gas components for the common input and the outputs of all half–super-layers.

The system has been supplying all OTR chambers with gas since the beginning of the HERA-B run in January 2000. In February the flow reached the design value of 1 vol/h in all MC chambers and PC2, PC3 chambers; the flow in the large trigger layers is currently limited to 0.8 vol/h; it is planned to remove this restriction during the luminosity shutdown. For most of the running period the detector has been operating with a total flow of $\approx$ 18 m^3/h which corresponds to a totally circulated volume of $\approx$ 80000 m^3 over the year 2000 run period. Fresh gas has been continuously added at rates of 0.5–2%/h by the mixing station. The monthly gas consumption of CF_4 – by far the most expensive gas component at about 70 DM/kg – was about 400 kg/month. Even though the

Table 22: *Operation thresholds of the Super-layers.*

Super-layer	MC1–	MC2–	MC3–	MC4–	MC5–	MC6–	MC8–
ΔU_{th} [mV]	200	200	200	200	200	200	200
Super-layer	MC1+	MC2+	MC3+	MC4+	MC5+	MC6+	MC8+
ΔU_{th} [mV]	200	200	200	200	200	200	200
Super-layer	PC1–	PC2–	PC3–	PC4–	TC1–	TC2–	
ΔU_{th} [mV]	600	500	400	500	600	600	
Super-layer	PC1+	PC2+	PC3+	PC4+	TC1+	TC2+	
ΔU_{th} [mV]	600	500	400	600	500	500	

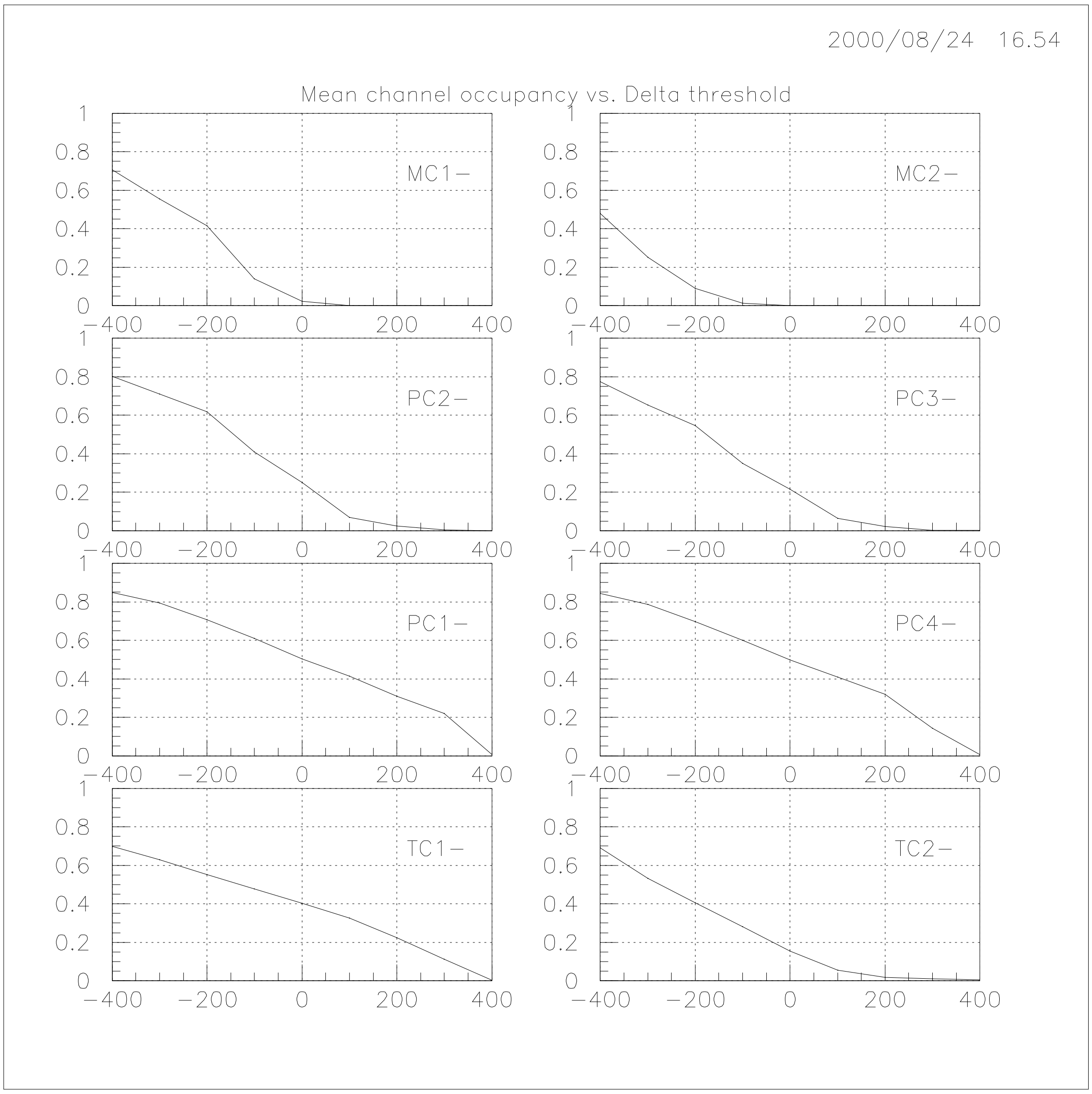

Figure 48: *Noise occupancy versus threshold increase* ΔU_{th} *for 8 super-layers of the* $-x$ *side (5 mm cells).* ΔU_{th}*=0 corresponds to the noise level reached in the laboratory tests. The increased noise level in the trigger layers PC1,4 and TC1,2 is clearly visible.*

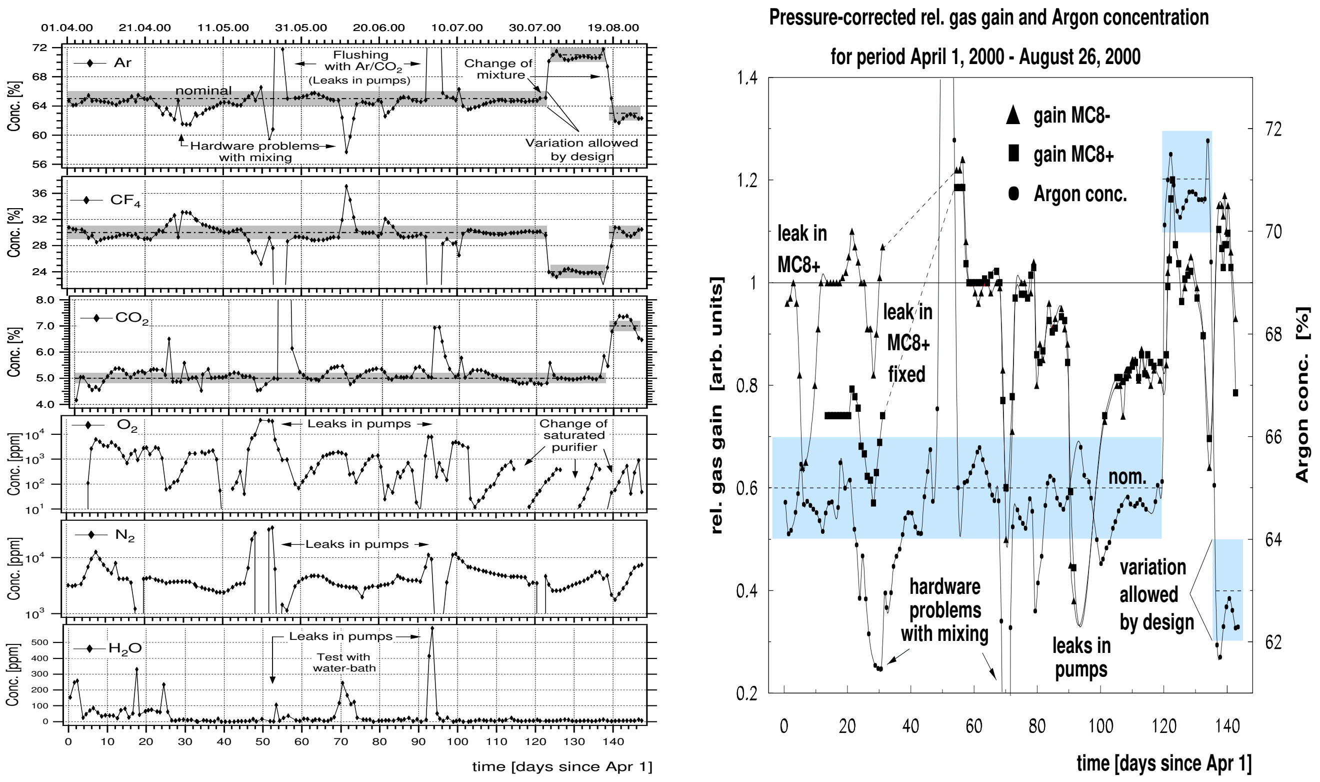

Figure 49: *Left: Concentrations of main and trace components in the OTR counting gas measured at the common input. Right: Gas gain measured in MC8 and Argon concentration.*

total amount of gas ordered for the 1999 run proved to be sufficient also for the run in 2000, serious problems with CF_4 supply were encountered because the main vendor Air Products was repeatedly incapable to deliver CF_4 bundles on time. Operations could only continue because additional CF_4 bottles were purchased from another vendor on short notice and because the fresh gas consumption was lowered to a uncomfortably low level. It is recommended to consider switching to a new supplier in the future and to negotiate appropriate penalties for delivery delays in any new contract with CF_4 suppliers.

The pressure regulation of the chambers worked well keeping them at slight overpressures of 0.3-0.6 mbar relative to ambient air pressure. A system of safety valves successfully prevented all chambers from becoming dangerously over- or underpressurized while preventing air from entering the chambers during pressure alarms.

The purification system for removal of oxygen and water was commissioned by mid-April. During commissioning it was observed that the oxygen purifier capable of regeneration absorbs not only oxygen, but also significant amounts of CO_2 and water. Appropriate CO_2 conditioning procedures after regeneration were successfully established to ensure a stable CO_2 concentration in the counting gas. Due to the water absorption by the oxygen purifier the detector was operated with very dry gas ($c(H_2O) < 20$ ppm) for most of the 2000 run even after the water purifier had been excluded from the system (see Figure 49 (left)). With several leaks fixed in early July one regenerated purifier could keep the oxygen content at levels below 200 ppm for about 10 days giving the gas crew considerably more than the needed minimum of 3 days to regenerate the second oxygen purifier in parallel.

The gas system caused a total OTR downtime of about two weeks in 2000. This time was mostly needed to find leaks that had developed in the system. Leaks occurred in the bellows of 4 of the 14 metal bellows pumps that circulate the gas. The leakage is most likely due to metal shavings and/or dust getting wedged in the outside of the moving bellows and finally causing a rupture. In order to prevent further leaks, 5 pumps were lifted up from the floor of the pump house and an air filter was installed. During the shutdown it is planned to install a leak detection system for the pumps using an oxygen meter and valve system (cost $\approx$ 25 kDM) to pinpoint any future pump leaks very quickly; this should drastically reduce the downtime caused by leak hunts for faulty pumps. Further leaks were caused by fittings that had loosened, most likely due to vibrations on the gas trailer. As a preventive measure the gas crew now regularly tightens all fittings in the underpressure part of the system.

Figure 49 (left) shows that for most of the run period the gas system was able to keep the variation of the main gas concentrations within the range allowed by design: (65$\pm$1)% for Argon, (30$\pm$1)% for CF_4, and (5$\pm$0.2)% for CO_2. A variation of Argon concentration by 1% corresponds to a change in gas gain of $\approx$15% under nominal operating conditions. However, a loose cable in the mixing system caused temporary deviations of several percent from the nominal Argon content, which corresponded to a measured gain drop of about 50% as shown in Figure 49 (right). In addition, unavoidable air pressure changes and correlated variations of the absolute chamber pressure of up to 40 mbar can produce gain changes of up to 25%.

The variations in gas concentrations were reduced by improving the corresponding monitoring and alarm system. However, there are indications that the losses of wires in the OTR are correlated with high gas gain. Consequently, the gas gain must be better regulated in the future. It is planned to build a feedback system based on gain measurements in 5 mm and 10 mm honeycomb monitor chambers that regulates the HV for the OTR (see section 2.5.4).

High Voltage Stability: From the very beginning of OTR operation in July 1999 it was observed that HV groups occasionally failed. The average long term rate of these failures was one HV group per 5 hours up-time of the Outer Tracker, but there were strong fluctuations. Since a HV group combines 16 readout channels, the failure of a single channel causes a loss rate which is a factor 16 higher.

The failure rate was especially high in TC2–, the first assembled and installed large chamber. Here it was suspected that this was caused by mechanical instabilities of the modules, none of which was reinforced with CF rods. The complete overhaul of TC2– in December 1999 comprised the following steps:

1. The gas box was opened in situ, i.e. the chamber was retracted from its beam position but not removed from the detector. Then the modules were removed layer by layer, put into boxes, and transported to the repair area.

2. All modules were reinforced with six 4 m long CF rods each.

3. All reinforced modules were subjected to a rigorous HV test in air. With reference to a flat table, the module was bent with a sagitta of 8 mm, a condition similar to what was observed on modules installed in TC2– during the first assembly. All wires which then showed shorts or excessive dark currents were disabled. Compared to the original test procedure which only checked perfectly flat modules, the number of eliminated wires roughly doubled, raising the fraction from 0.6 to 1.3 %.

4. The repaired and tested modules were reinstalled in the gas box which then was closed and sealed again.

During the 8 months of running time after this repair only 16 of 606 HV groups in TC2− showed problems, compared to 115 groups during the 5 months before the repair. While this is a remarkable improvement, it is not a complete cure of the problem which shows that a full understanding of the OTR HV stability problem is still lacking.

As of mid August 2000 there were 499 defect HV groups in the whole Outer Tracker. Table 23 shows their distribution over the 13 super-layers, together with the corresponding percentages of damage.

Table 23: *Distribution of defect HV groups in the Outer Tracker.*

	$-x$			$+x$			both x		
SL	total	bad	%	total	bad	%	total	bad	%
MC1	78	1	1.3	60	1	1.7	138	2	1.4
MC2	84			66	2	3.0	150	2	1.3
MC3	108	1	0.9	90	8	8.9	198	9	4.5
MC4	114	12	10.5	96	11	11.5	210	23	11.0
MC5	44	1	2.3	41	2	4.9	85	3	3.5
MC6	120	1	0.8	102			222	1	0.5
MC8	126	9	7.1	136			262	9	3.4
PC1	621	30	4.8	496	44	8.9	1117	74	6.6
PC2	415	47	11.3	337	27	8.0	752	74	9.8
PC3	415	29	7.0	337	18	5.3	752	47	6.3
PC4	625	26	4.2	500	47	9.4	1125	73	6.5
TC1	584	53	9.1	498	48	9.6	1082	101	9.3
TC2	606	16	2.6	520	65	12.5	1126	81	7.2
Sum	3940	226	5.7	3279	273	8.3	7219	499	6.9

A statistical analysis of the faulty groups yielded the following results:

- Modules with 5 mm cells are more affected than modules with 10 mm cells. This indicates that mechanical imperfections which are much more critical in 5 mm than in 10 mm cells may contribute to the problem. Modules in the spatially tight region of the overlap caps have failed more often than others. Apart from that the faults do not concentrate in particular module types or module regions. Particularly high loss rates in certain super-layers, e.g. MC4, could not be traced back to any specialties of production, assembly etc.
- The repaired chamber TC2− has a significantly smaller fault rate than all other large chambers with reinforced modules. This indicates that not only the module reinforcement but also the more rigorous module testing are necessary for enhancing the HV stability. Another possibly relevant difference of TC2− and all other large chambers is that about 30 % of its modules are equipped with "old" type HV boards.
- It may be interesting to note that MC2−, the only chamber with graphite coated modules, had no losses despite being operated from the very beginning. Although this observation is not statistically significant, one may speculate that the higher surface resistance of the graphite compared to the gold coating is limiting discharges. In this chamber all modules are equipped with "old" HV boards.

In addition a series of other tests was performed. The results can be summarized as follows:

- The measured Ohmic resistances of the broken HV groups show a broad distribution between 200 kΩ and 20 MΩ, with a sharp peak at 1.1 MΩ. The peak is created by shorted drift cells and accounts for less than 10 % of the faulty HV groups. This indicates that broken wires or otherwise shorted drift cells cannot be the major source of the OTR HV problems.

- HV groups continue to fail even without beam. Due to the limited time of this test the failure rate could not be significantly distinguished from the one observed with beam.

- There are no obvious correlations with environmental conditions (air pressure, chamber temperature) or gas quality (fraction of contaminants).

- Increasing the argon fraction of the gas at the expense of the quenching components (CF_4 and CO_2) significantly raises the fault rate. Tests with decreased argon fraction were terminated by the end of the 2000 run, within the limited statistics there are only indications that the HV fault rate is slightly smaller than with the original gas. This will be investigated in more detail during the shutdown 2000/2001.

- Increasing the resistance in the common supply line of a HV group (serving 16 wires) from 0.1 to 1.1 MΩ prevents the group from failing. During the last months of running, this modification was made to about 20 % of the OTR HV groups and none of them failed afterwards while in the same time 80 failures occurred in the unmodified part of the detector. Simulations using SPICE have shown that with the lower resistance the time between an initial (presumably non-destructive) breakdown of a drift cell and the return of the high voltage to its nominal value is very short (around 1 ms, depending on some assumptions). This possibly is too short for the charged remnants of a discharge to disappear from the affected cell region, thus creating the conditions for repetitive and finally destructive discharges.

All these external observations did not provide sufficient evidence to draw final conclusions about the reason for failing HV groups in the Outer Tracker. There only were strong indications that discharges and mechanical module imperfections are important ingredients.

The inspection of damaged modules from the chamber PC1+ at the beginning of the 2000/2001 shutdown revealed a somewhat unexpected major source of the OTR HV problems: In 39 out of 49 cases the "short" was caused by a burnt-in carbon trace of varying resistance across either of two capacitors on the bottom side of the HV board. In no case any of the 15 top side capacitors caused the problem. This systematic difference probably has to do with the differing mounting techniques used for top and bottom side components, investigations are ongoing. Only two of the 49 faulty HV groups (and of 496 groups in total) are related to shorted drift cells. This count does not include the four cases of obvious mechanical module damage.

We are currently trying to understand the experimental findings from the above list in terms of this new situation. In particular there are no convincing models yet for the different behavior of 5 and 10 mm cells and for the effectiveness of the increased resistance in the common supply line of a HV group.

Dead and Noisy Channels: The number of dead OTR channels in the HERA-B data at any point in time is strongly determined by the organization of the HV distribution. Each of the 160 HV sources on the supply unit in the electronics trailer serves up to 6 cables. Each of these cables serves up to 16 HV groups on the detector, and each HV group supplies 16 wires. As soon as a single wire develops a short, it shuts down its serving HV source. This disables up to $6 \times 16 \times 16 = 1536$ wires, about 1.4 % of the OTR channels. Disconnection of the proper cable to the detector reduces this number to 256 wires or 0.2 % of the OTR. A further reduction to the 16 wires of the failing HV group requires access to the detector which is possible once per month, sometimes more often. Elimination of the failing wire needs extraction of the module from the detector which requires a major shutdown.

Depending on the cable and HV group disconnection status the number of dead channels in the OTR varies between 5 and 15 %. As can be seen from table 23, towards the end of the 2000 run disconnected HV groups accounted for 6.9 % dead channels. Wires which were cut during module testing prior to installation contribute less than 1 %, the same is true for bad HV connections inside the gas boxes. Problems in the readout electronics contribute another 2 % of dead channels (see table 21).

Assuming that in general only one broken wire is responsible for a failing HV group, a module repair by bad wire disconnection reduces the number of dead channels by a factor 16. If all defect OTR modules could be repaired during the 2000/2001 shutdown a base contribution of about 2 % dead channels from single disconnected wires would remain.

During the 2000 run about 5 % of all ASD-8 channels were marked as noisy on the basis of their large occupancy and/or bad TDC spectrum shape. It should be possible to considerably reduce this rate by the noise reduction measures scheduled for the shutdown (see section 2.5.4).

2.5.2 Track Reconstruction Software

Status of Reconstruction with Ranger: The general concept of track reconstruction in the Main Tracker is described in [58]. The first step is to find track segments in the pattern tracker (PC area). Track segments found in the pattern tracker are propagated through the magnet, determining the particle's momentum, an estimate of which is already given by the track deflection relative to the direction to the target. In a subsequent step, these track candidates will have to be matched to the track segments in the silicon vertex detector. The resulting tracks are then continued downstream to the lepton identification devices. As an additional tool, the use of external seeds for track reconstruction is foreseen. External seeds could be track segments in the VDS (downstream propagation) or seeds generated on the basis of information from the ECAL, RICH, MUON detectors (upstream propagation). All described features are implemented in a software package called *ranger* [59] which consists of a set of procedures for pattern recognition in the Main Tracker and track parameter reconstruction (fitting) in the full HERA-B detector. The reconstruction software is fully commissioned on simulated and real data. It is available for online and offline analysis.

Efficiencies are calculated for reference tracks which are a track class defined by both the geometrical acceptance and the physics interest of the experiment. A reference track in the pattern tracker is required to cross at least 18 layers of the tracker. A track candidate is regarded to properly reconstruct a particle if at least 70% of the hits where caused by this particle. The performance of the reconstruction program was studied using samples of simulated golden B decays and unbiased inelastic interactions passed through the full HERA-B detector simulation procedure. To take into account the OTR performance, mask files with the description of not working cells were used. The efficiency to reconstruct a muon from a golden B decay for different performances of the trackers is shown in Fig. 50a. The reconstruction efficiency depends only weakly on the target rate (see Fig. 50b).

The computing time shown in Fig. 50c increases only slightly faster than linear as function of the number of interactions. The different steps of the reconstruction share this time quite unequally: For the combined OTR and ITR reconstruction and for 5 inelastic interactions the tracking in the

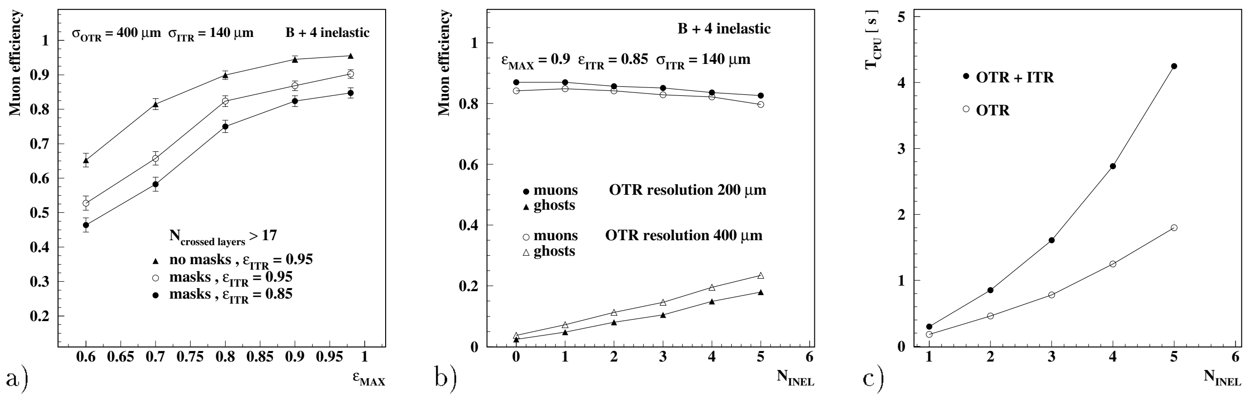

Figure 50: *a) Efficiency of muon reconstruction as function of OTR cell efficiency. b) Efficiency of muon reconstruction as function of the number of superimposed inelastic interactions. c) Computing time of combined pattern and magnet tracker analysis as function of the number of inelastic interactions.*

PC area takes 85% of the time, the magnet propagation 13%, and the propagation in the TC area 2%. Improvements of the first step will be worked on in the future.

A comparison of the computing time for reconstruction of real and simulated events shows that tracking for real data is still a factor of about 1.7 longer. Only part of it can be explained by a higher occupancy for real data (factor 1.4). These differences have to be further studied.

Tracker Alignment: The OTR consists of 978 modules. Each module is divided into up to 4 active areas. Each of these areas is represented within the geometry description as a so called GEDE table. These GEDE volumes are considered as the basic alignment units and treated as rigid bodies. The alignment data structures allow in general for 3 rotations and 3 translations although only 3 of these transformations are assumed to be dominant (du: direction perpendicular to the wire and the z-axis, dz: along the z-axis and $d\alpha$: stereo angle correction).

At present only du and the z-position of a whole layer are taken into account by the alignment procedure. The procedure is based on tracks given by the reconstruction program *ranger*. The Kalman filter algorithm of *ranger* has been proven to be robust enough to do tracking even in a situation with large misalignment (i.e. in the order of several millimeters). Therefore the alignment parameters can be determined by an iterative approach. The largest disadvantage of such a method is the necessary computing time. At present the processing time per event is of the order of half a second and the number of events to be processed for the OTR alignment is about 400k. Therefore one iteration needs about 50 hours CPU time.

Within a super-layer the spread around the nominal position has been found to be approximately 1 mm. Larger deviations are observed for special modules (e.g. above the beam pipe) or between the 5 mm and 10 mm modules which have different mounting plates.

The alignment has been tested mainly for the linear tracking region (PC and TC) and residuals with external tracks show a clear improvement in width. Also the studies on the efficiencies of the OTR (see below, Fig. 52a) give as a by-product an upper limit on the precision of the alignment in the PC region. In the study the rms spread of the cell position averaged over one module is about 100 μm for the 5 mm modules in PC− and about 250 μm for PC+.

For the magnet chambers work is in progress. Unfortunately due to frequent accesses in the magnet area the chamber positions are changing and – contrary to the PC and TC chambers – there exists no mechanism for a precise re-positioning of the super-layers. Therefore different sets of alignment constants are needed for short periods of runs.

The internal module alignment has been studied by analyzing average shifts of the wire positions between two mono-layers within a single module. By considering the difference between residuals in different mono-layers the result is independent of the (inter) module alignment. The observed shifts are in general smaller than about 60 μm and thus confirm the design goal of 100 μm for the relative cell alignment within one module.

Individual module alignment in z position and stereo angle and also a possible online alignment are still open questions. Although none of these is expected to be a problem in principle, detailed work will be necessary. Furthermore any alignment algorithm will benefit if the time consumption of track reconstruction can be reduced.

Tracker Calibration: The Outer Tracker reconstruction uses as input the wire positions, the measured drift distances and the corresponding errors of a set of hits. As the detector measures a TDC value and not a distance, a calibration procedure is required.

Calibration of the TDC Offset: The TDC value that is output from the front-end electronics can be translated into a drift time by subtraction of a channel dependent TDC offset t_0. The TDC is synchronized to the bunch clock. Substantial evidence is found that the t_0 calibration must be performed for every channel separately to reach the required precision.

Different methods have been developed to determine the t_0 from a TDC spectrum only. The systematic uncertainty (among others due to differences in wire length) is estimated to be of the order of 100 μm.

Methods to improve the t_0 calibration are under development. A correction for the signal propagation time in the wire by using the y coordinate information of the reconstructed track is expected to provide a better correspondence between TDC spectra from sectors with a different wire length. The ultimate precision might be obtained by using residuals from track fitting. However, since the number of degrees of freedom is enormous, it is not evident that such a procedure will converge.

Calibration of the Drift Time Space Relation: The drift time obtained after subtraction of the TDC offset is translated into an estimate for the distance-of-closest-approach and a corresponding error. These two relations are called the drift time space relation or rt-relation $r(t)$ and the resolution function $\sigma(t)$.

The relations are determined from reconstruction of real data by requiring that for every 'drift time bin' the distribution of normalized residuals[36] is centered around zero and has unity width.[37] In order to obtain smooth functions, the relations are parameterized in terms of polynomial B-splines. An iterative method has been developed that performs an 'unbinned' calibration in order to fully use the available statistics.

It is assumed that only a small number of rt-relations is required to calibrate the detector. In particular there is only one such relation for all 5 mm cells in the field free region of the detector. In the magnetic field region, the rt-relation significantly depends on the strength of the field. An effort

[36] The normalized residual is the residual divided by the estimated error.

[37] As the residual distributions are rather non-Gaussian, the width is iteratively determined in terms of the root-mean-square within 3 sigma of the average of the distribution.

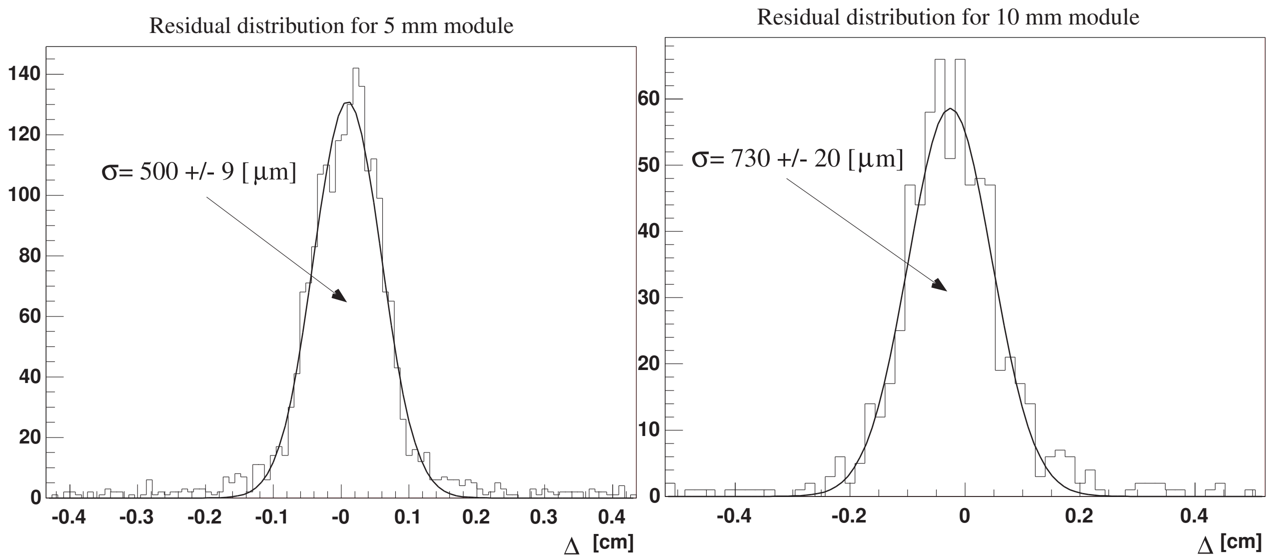

Figure 51: *Residual distribution of a typical 5 mm module (left) and 10 mm module (right) in the PC area.*

Table 24: *Conditions for runs used for the efficiency analysis. The "new" threshold values for the PC super-layers are given in Table 22. In run 14577 the "old" threshold was 100 mV higher for super-layers PC1+, PC2+, PC3−, PC3+, PC4−. The gain is given relative to a nominal gain.*

Nr	Run	date	rate [MHz]	Ar/CF_4/CO_2	Threshold	HV [V]	Gain
1	14577	12.04.00	4.9	65/30/5	old	1700/1900	1.13
2	16990	11.08.00	5.0	70/25/5	new	1650/1850	1.02
3	17255	25.08.00	2.0	63/30/7	"	1715/1915	1.17
4	17254	25.08.00	1.8	"	"	1785/1985	1.46

to calibrate the detector in the magnetic field is under way.

Figure 51 shows the observed residual distribution of two typical modules in the PC area. The current estimate of the average resolution for 5 mm and 10 mm cells is $600 \pm 50\ \mu$m and $700 \pm 50\ \mu$m, respectively.

2.5.3 Detector Performance

Cell and Track Efficiencies: The outer tracker cell efficiencies were estimated for super-layers PC1, PC2, PC3, PC4 which are used for pattern recognition and in case of PC1 and PC4 for triggering. Four runs taken between beginning of April and end of August 2000 (Table 24) have been analyzed and compared.

Taking run 17255 as an example the cell efficiency as a function of the distance from the wire is shown in Fig. 52a for the upper long wire part (sector 1) of a standard module of super-layer PC1−. From the fitted curve the efficiency in the plateau was determined to be 0.93. This region has a radius of about 2 mm around the wire. In the region outside of the plateau which corresponds to the edges of the hexagonal cell, the efficiency drops to zero. The efficiencies of the 128 cells of the

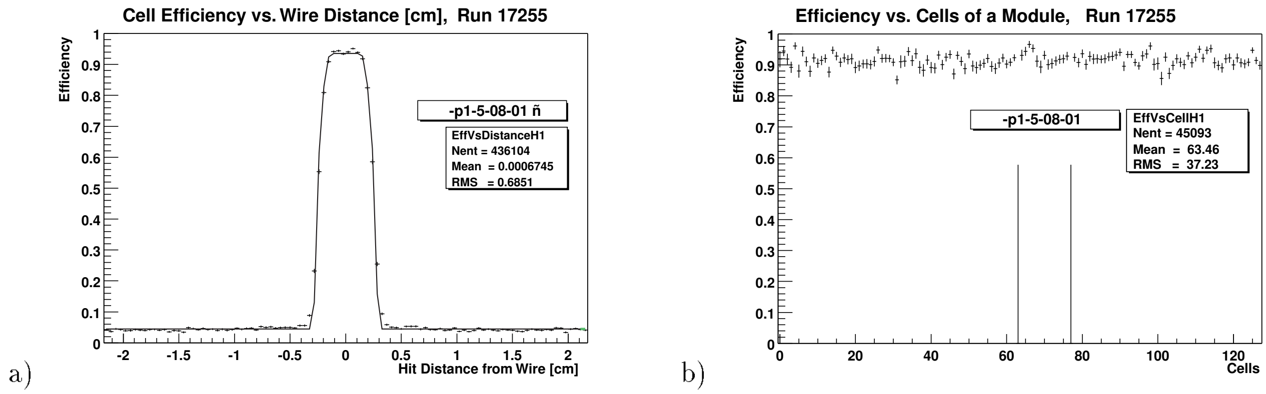

Figure 52: *a) Dependence of the cell efficiency on the distance from the anode wire (5 mm cell) for module 8 in sector 1 in stereo layer 5 of super-layer PC1−. b) Efficiency of the 128 cells of the same module.*

same module sector given in Fig. 52b are rather constant and mainly above 0.90.

The fitted plateau efficiencies of all 5 mm module sectors of super-layer PC4− are plotted in Fig. 53 for the four runs. A clear gain dependence is observed comparing the runs 17255 (gain 1.17) and 17254 (gain 1.46) which were taken on the same day with the same gas mixture and air pressure values. The corresponding results for the 10 mm modules can be found in Fig. 54. A small number of modules with efficiencies below 0.7, mainly caused by low statistics or a large number of disconnected HV groups, have been excluded. The resulting super-layer efficiency is the mean of the distribution which is still influenced by the tail of bad modules. Most of the distributions peak around or well above 0.90.

This analysis was performed for a total of about 1000 module sectors in all eight super-layers halfs PC1− to PC4+. The mean values are distributed in Fig. 55 as a function of the threshold for runs 14577 and 16990. For both, 5 mm and 10 mm modules, there is a clear threshold dependence. A more detailed comparison of both runs is difficult since several parameters as threshold, gas mixture and high voltage were changed.

The runs 17255 and 17254 differ in the high voltage settings only which results in different gains of 1.17 and 1.46, respectively. The values in Fig. 56 show therefore not only the threshold dependence but also a significant gain dependence. The gain values were measured with radiated cells of super-layer MC8 (see also Fig. 49 (right)).

Summarizing the results of the preliminary efficiency analysis, it can be stated that there is a clear dependence on the threshold and the gain. The 5 mm modules of super-layers with the smallest threshold have efficiencies above 0.90. The efficiency for 10 mm modules is with one exception larger than for 5 mm modules. A fair comparison between runs 14577, 16990 and runs 17254, 17255 is not possible since the number of dead HV groups has increased considerably over the running time. More detailed studies will be performed with the existing data to estimate the inefficiencies due to the wire strips within the module. Furthermore, the analysis will be extended to the TC and MC super-layers.

Resolution and Alignment Results: In the previous section the spatial resolutions of OTR hits have been shown (Figure 51). The resulting estimates of the average resolutions are 600 ± 50 μm

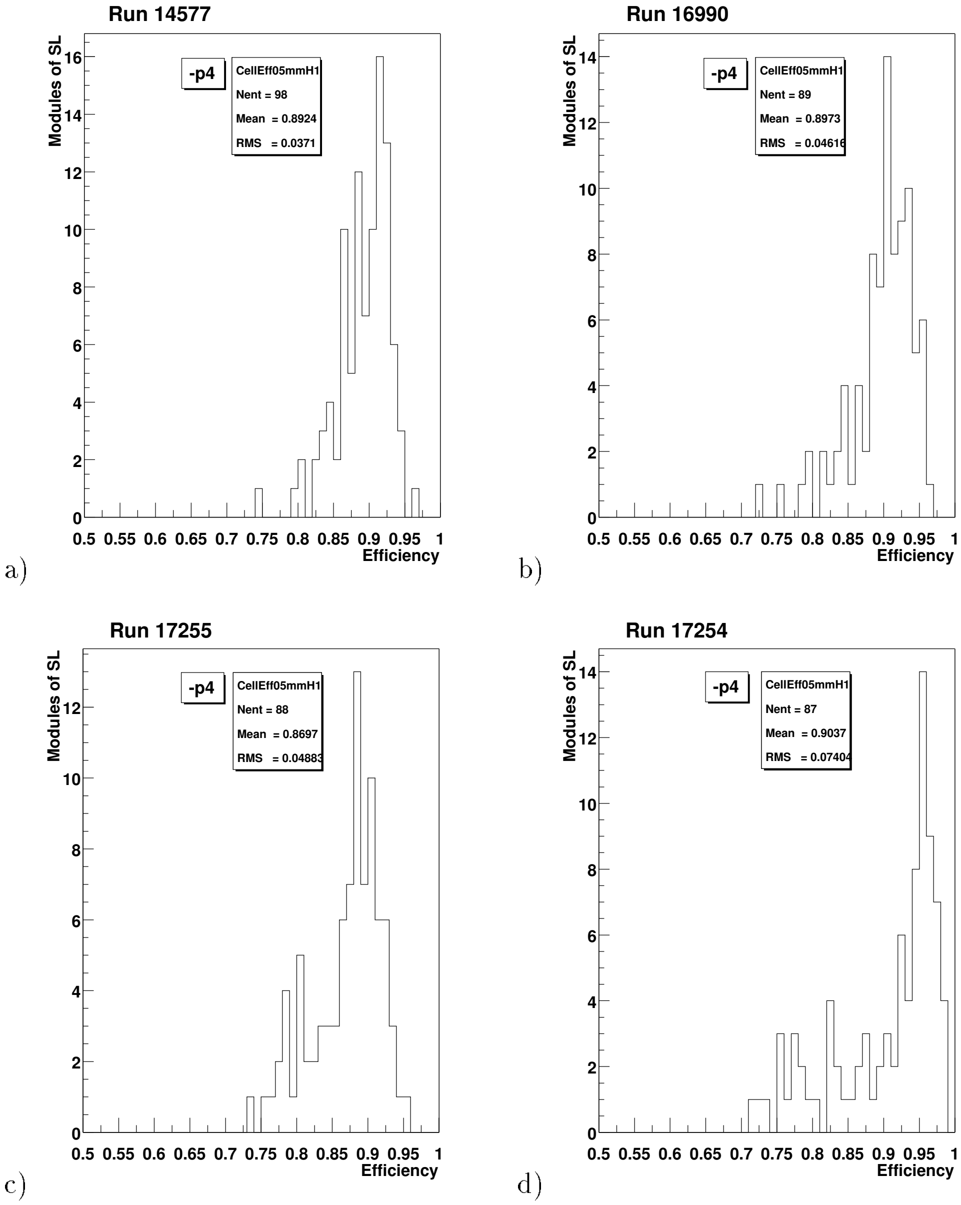

Figure 53: *Efficiency of 5 mm modules of super-layer PC4− for four different runs. a) run 14577, b) run 16990, c) run 17255, d) run 17254.*

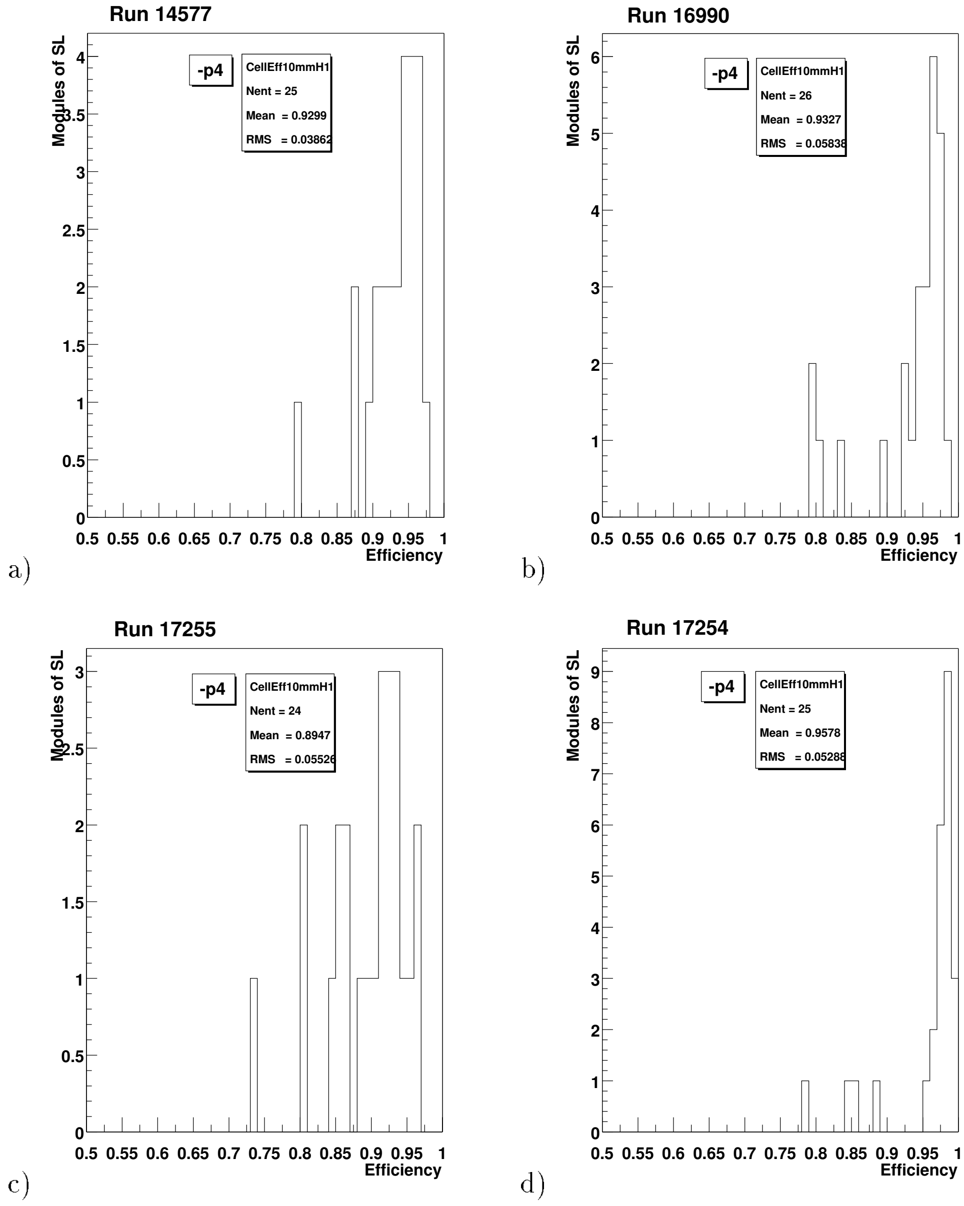

Figure 54: *Efficiency of 10 mm modules of super-layer PC4– for four different runs. a) run 14577, b) run 16990, c) run 17255, d) run 17254.*

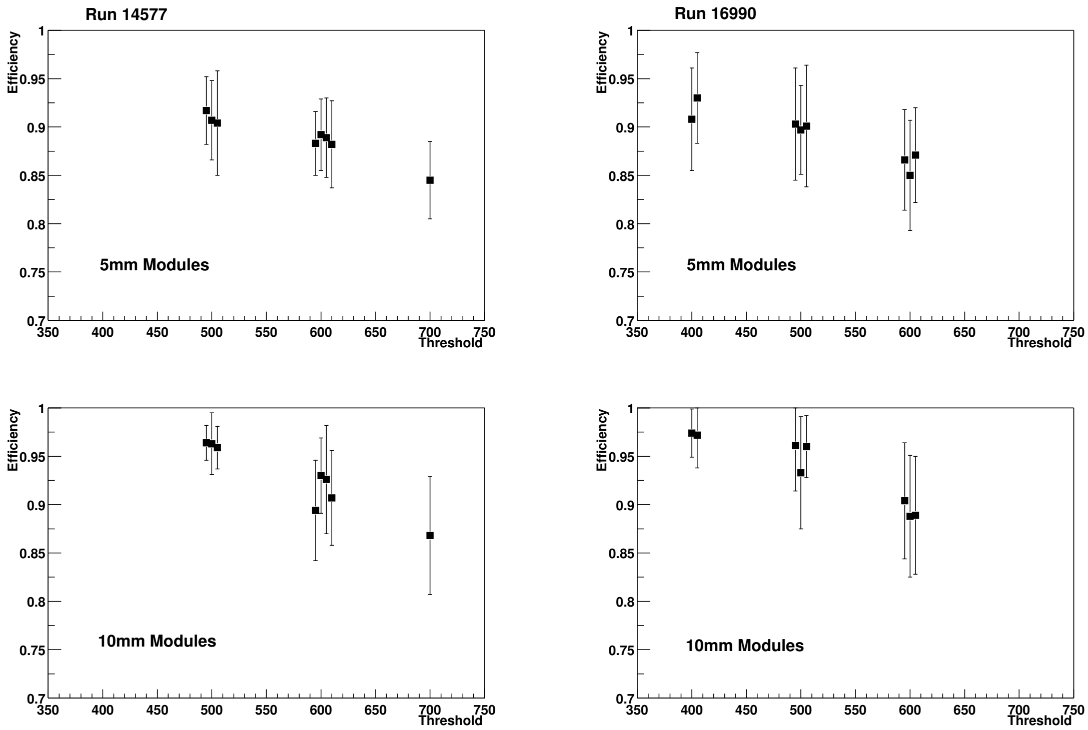

Figure 55: *Average efficiency of the PC super-layer halfs for runs 14577 and 16990 taken under different conditions (see tab. 24). The error bars are the rms values of the distributions.*

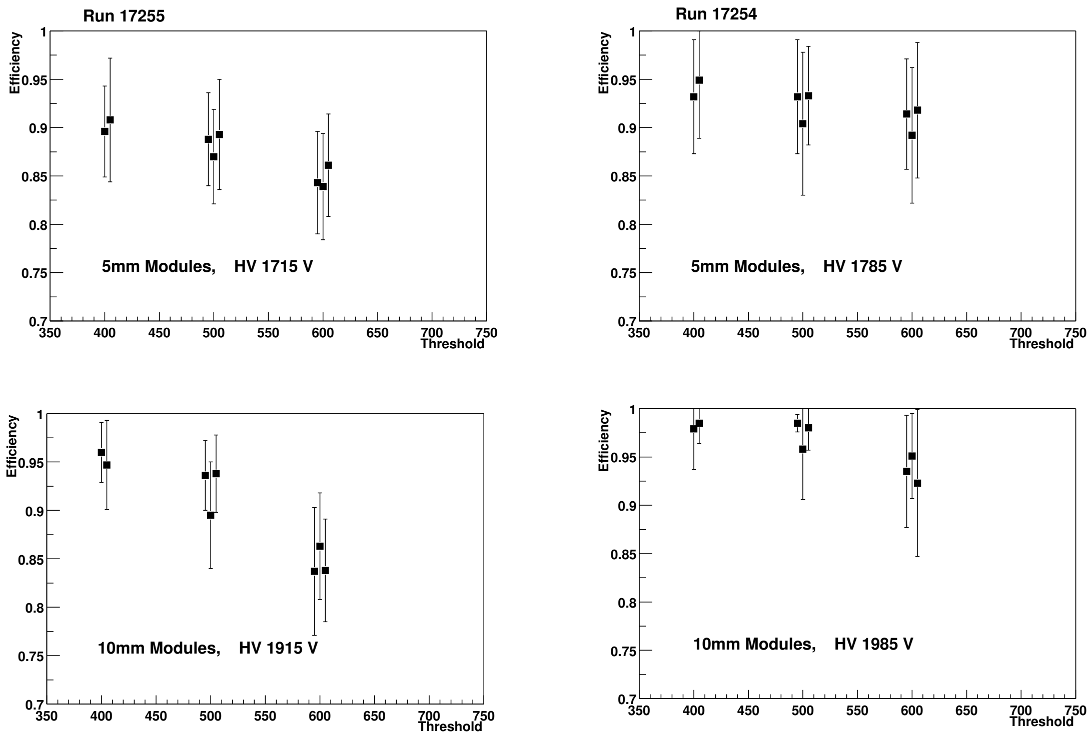

Figure 56: *Average efficiency of the PC super-layer halfs for runs 17255 and 17254 taken under identical conditions, except the high voltage. The corresponding gains are 1.17 and 1.46.*

and $700 \pm 50\,\mu$m for 5 mm and 10 mm cells, respectively. This is much larger than the 200 μm which had been assumed in the design phase of the detector and verified in test measurements.

The procedure to determine the resolution from residuals of reconstructed tracks yields a result which reflects both the intrinsic resolution of the wire chambers and the remaining errors in the calibration and alignment. In order to understand the resolution it is essential to disentangle these effects.

If a charged particle creates more than one hit within a certain module, the correlation between the drift times of those hits can be used to obtain an estimate of the resolution relatively independent of the module alignment. Following this analysis the current estimate of the intrinsic resolution of a 5 mm cell is $350 \pm 50\ \mu$m. This value sets the landmark for the calibration and alignment of the whole detector.

Still, the 350 μm is substantially larger than the 200-300 μm that has been observed in test measurements. This can be explained by the fact that the ASD-8 amplifiers have to be operated at higher thresholds and lower gas gain than used for the test measurements, due to the HV and noise problems (see the discussion in section 2.5.1).

The remaining difference between the observed average resolution of 600 μ, the internal resolution of 350 μ and the alignment errors of 100 to 250 μ can probably be attributed to the degrees of freedom that are not yet considered in the alignment procedure, i.e. dz and stereo angle corrections. Different aproaches to include these into the alignment procedure are under consideration.

Concluding remarks on the OTR Performance Studies: The presented studies on efficiencies, alignment and resoltion are still very preliminary and incomplete. We are well aware that not all quoted results are consistent and that more detailed studies are necessary. For example, the hit resolution obtained from fitted tracks of about 500 to 1000 μm, the internal resolution of 350 μm and the observed alignment errors between about 100 and 250 μm seem to be inconsistent.

Concerning the efficiency studies, the results have to be compared to the expected geometrical acceptance, sorted according to module qualities and interpreted in terms of tracking and triggering efficiencies.

The hope is also that the repair and upgrade programm for the OTR during the shutdown will improve the performance considerably. The run 17254 with the gain increased by 1.46 gives a guide line of what could be expected.

2.5.4 Repairs and Upgrades During the Shutdown

General Plan: The HERA shutdown 2000/2001 will be used to fix problems which have been encountered in the OTR during installation, commissioning, and first running experience. The major observed draw backs are (see section 2.5.1):

- high voltage instabilities of the modules which cause shorts in the HV groups;
- noise induced by the signal cables connecting the TDCs of the trigger layers to the TLBs;
- instabilities of the optical links between TLB and FLT.

Solutions for these problems are considered vital for the operation of the OTR after the shutdown. The actions which will be taken during the shutdown are explained below.

Apart from working on these major problems, some maintenance and upgrade work will be done, both on hardware and software:

- Improvement of the cabling of the TDC system to the SLB boards and the FCS system;
- improvement of gas gain monitoring and installation of an automatic gain steering;
- installation of a leak control system for the gas system;
- improvement of calibration and alignment, implementation of dedicated fast tracking, integration into the online system;
- improvement of reproducibility of the positions of the magnet chambers;
- improvement of tracking, like ghost rate reduction and implementation of external seeds;
- studies of chamber performance, tracking efficiencies.

Module Improvements: The major OTR activity scheduled for the 2000/2001 shutdown is a substantial reduction of the dead channel count by repairing as many modules as possible. This requires the gas boxes of the super-layers to be opened, followed by extraction, repair, test and re-installation of the modules. In addition two working places for module production have been set up and production materials have been provided, just to be prepared to replace strongly damaged modules by new ones.

This is a major logistics and manpower effort. A detailed time schedule and manpower distribution until the end of this year exists. The operation has started with the treatment of the most crucial trigger layers which will last until about February 2001. Dependent on the experience the remaining PC layers will be repaired during spring 2001. It is currently unlikely that MC chambers can be repaired.

The following investigation and repair activities are foreseen:

- All bottom side capacitors on the HV boards (not only the damaged ones) will be exchanged using a clean soldering technique which avoids any adhesive and uncontrolled disposal of soldering fluid. This technique has already been established. For the whole OTR this means the exchange of 14 500 SMD capacitors, for the trigger layers PC1, PC4, TC1, and TC2 only 9 000 are enough.
- All modules without reinforcement will be reinforced with CF rods. This mainly affects the chambers TC1− and PC4−. Minor mechanical damages will be repaired, severely damaged modules have to be rebuilt.
- All repaired modules will be subjected to a rigorous HV test, which identifies short and hot wires, while mechanically exercising the module. All bad wires will be disconnected from the HV board. Experience with TC2− shows that this procedure doubles the bad wire count compared to testing the module in a perfectly flat state. The expected total cut rate is 1.5 %. If the total dark current of a module cannot be substantially reduced by disconnecting a few wires (< 5 by previous experience), the module should be rebuilt.

- After installation of each module layer in the gas box the capacitances at various points of the HV system will be measured. Various error conditions (unplugged HV cables, unplugged ASD-8 boards etc.) are characterized by typical values of the capacitance w.r.t. ground. For each installed layer there will be a final HV test.
- The modifications of the HV circuitry resulting from the investigations described below will be implemented for the whole Outer Tracker.
- Even though the main source of HV trouble in the Outer Tracker has been identified by now, it is still foreseen to thoroughly investigate a small number of damaged modules. However, the priority of these activities has decreased a bit:
  - In order to better understand what causes the breakdown of wires, a few selected modules will be carefully dissected and later be subjected to a materials analysis. Even if the scope of the broken wire problem has shrunk a lot, it is still important to understand the reason for this to happen.
  - For another damaged module the pulse heights along the wire will be measured for all drift cells. These measurements will be repeated for different module deformations. This serves a better understanding of the influence of the unavoidable module deformations on the performance of the Outer Tracker.

With these modifications it should be possible to safely operate the Outer Tracker at a higher gain than in the 2000 run.

Drift Gas Studies: As discussed in section 2.5.1 (High Voltage Stability) there are indications that the HV failures are caused by discharges in a cell. It is therefore important to investigate whether the quenching properties of the drift gas, mainly determined by the CO_2 and CF_4 content, are sufficient. Depending on the observations made on the opened drift cells, in particular if we can identify the location of discharges (e.g. on the strips?) we consider a detailed investigation of the influence of CO_2 and CF_4 on discharges.

As we know from various laboratory tests, the water content in the drift gas is another important parameter. In the closed gas system with active purifiers (operating since April 2000) the drift gas was particularly dry, below about 20 ppm (Fig. 49). At such a low water content anode etching was observed in laboratory tests (note that there the irradiation level was much higher than expected in HERA-B). On the other side, a water content above about 1000 ppm was observed to make the strips conductive. As a compromise between these boundaries the OTR group has earlier decided to run at about 200 to 300 ppm of water. To maintain this level while running the purification system turned out to be difficult. A system for controlled water injection has meanwhile been developed and is currently tested in a limited part of the OTR (superlayers PC2 and PC3).

Review of the HV Protection System: The positive results obtained by adding a protective resistor into the common supply line of HV groups (see section 2.5.1, 'HV Stability') suggest to review the whole HV protection scheme of the OTR. This includes the scheme of current limitation and tripping of the HV supplies as well as the protection resistors in the HV circuitry.

In the circuit successfully tested in the OTR an additional resistor of 1 MΩ was added in the supply line of a HV group. However, this is not optimal since at the highest anticipated currents per HV group the voltage drop would be about 35 V. This would cause too high a dependence of the gain on the interaction rate. Currently different schemes to obtain a constant HV up to a certain threshold current are investigated.

Noise Reduction: In order to increase the single cell efficiency, further measures to decrease the noise must be taken during the shutdown. A possible re-routing of the trigger link cables for PC1+ (ΔU_{th}=600 mV, see table 22) should decrease the noise for this chamber to the level of the other PC superlayers.

Further noise reduction is only possible by eliminating/attenuating the source of the noise on the TDC board: Currently the effect of the fast TTL driver is studied. Possibilities are investigated to remove the drivers from the TDC boards. A replacement of these drivers by differential low voltage drivers (LVDS) is considered and will be tested. However, an implementation of differential cables would require substantial modifications on both the TDC and the TLB side.

If the tests are successful at least some trigger chambers could be improved during the shutdown. A treatment of all trigger layers seems difficult given the time the electronics will be accessible during the shutdown.

Triggerlink Boards: The current quality of the optical link between TLB and TFU is judged to be insufficient to fulfill the requirements by the FLT (see section 2.5.1). Therefore it is planned to rebuild, at least partially, the transmitters on the TLBs. The possible changes are:

1. The offset and modulation currents of the laser diodes on the optical transmitter become remotely programmable.
2. Use nowadays commercially available integrated drivers for the laser diodes.
3. The boards will be tested more rigorously before installation.
4. In order to avoid FLT inefficiencies, signals from broken OTR wires should be turned on permanently in the wire memory of the FLT. A serial interface using FCS strobe signals is foreseen to set bits to 1.
5. The cooling of the boards has to be improved.

Automatic Gas Gain Control: Because of the observed gain dependence of HV failures it was decided to improve the gain monitoring and to develop an automatic gain steering. The monitoring is currently done with special monitor chambers in the gas input and output and in addition by 4 channels dedicated analog readout of Fe-55 spectra in both MC8 super-layer halves. During the shutdown the ‘intra-super-layer monitoring’ will be extended to include a PC and a TC chamber. The input for the automatic gain steering will be provided by a special chamber (‘Karlsruhe type’) in the input flow (outside the HERA radiation).

2.5.5 Outer Tracker Summary

The Outer Tracker sub-detector was ready for data taking by the beginning of this year. After the installation of the last super-layer in January the commissioning of the readout electronics, the slow control and the gas system was successfully completed around April, when routine data taking started. The detector is since then smoothly running. Tracking, alignment and calibration are well advanced and continuously improving. Efficiency and resolution studies have led to a good understanding of the detector properties and of possible improvements.

The major worry during running in 2000 was the progressive HV instability which in the end left almost 7 % of the OTR channels dead. Meanwhile the major source of this trouble has been identified and corrective action has been initiated. There exists a detailed plan of shutdown activities to repair the Outer Tracker modules. The confidence that the planned measures will be successful is based on three observations: First, the HV instability problem has changed its character from fundamental to mostly technological. Second, the treatment of TC2– in December 1999 led to a very low loss rate in this super-layer. And third, there is a highly significant lack of any failures in super-layers equipped with additional protective resistors.

The other major worries are the noise induced into the trigger layers by the TDC-to-TLB connection and transfer instabilities of the optical link to the FLT. These effects cause a decreased efficiency for the tracking and the trigger. Both problems will be worked on as well during the shutdown.

Apart from these problems the Outer Tracker is running well suggesting that the design is in principle sound. The problems encountered can mainly be traced back to the time pressure during the detector development and a missing full-scale prototyping.

2.6 Status of the High-p_T Trigger

2.6.1 Overview

The concept of the high-p_T trigger is as follows: tracking chambers with a pad-type readout are placed within the spectrometer magnet. Pad hits are input to dedicated processors, and high-p_T tracks are selected based on the hit patterns. Such tracks tend to bend little or make larger angles with respect to the beam, and their hit-patterns are distinct from those caused by minimum bias tracks.

The tracking chambers with pad readout come in two types: gas-pixel chambers for the region nearest the beam, and straw-tube chambers with "pickup-pads" for the larger outer region. Both types of chambers required extensive research and development [61, 62]. The gas-pixel chambers use short anode wires oriented parallel to the beam. The pad is formed by four potential wires in the corners and one signal wire in the center. The tracks going from the main vertex to the inner high-p_T chambers are almost parallel to the wires. They pass through about 3.5 cm of gas so that the amount of primary ionization is large; moreover, the drift times for these electrons are almost the same (for the central region of the chamber where gas amplification is maximal) and there are no boundary effects. Thus the signal has a fast rise-time and the fraction of total charge collected during the integration time of the ASD-8 is substantial. The signal wires are connected to the ASD-8 cards (located outside the acceptance) via twisted pair cables having a diameter of only 50 μm/conductor and a length of about 1.4 m.

The straw tube chambers utilize straw tubes against which are positioned printed circuits consisting of a pad pattern. These pads are positioned very close to, or in contact with, the outer surface of the straw tubes; the distance of separation is $\lesssim 300$ μm. A gas avalanche occuring at an anode wire then induces an image charge on the pad directly above the avalanche. The pads connect to traces which bring the signals out to ASD-8 cards located outside the acceptance. No signal is read from the anode wires directly, and the inner surface of the straw tubes (which constitute the cathode) must be resistive instead of conductive (metallized) –as is typically found on straw tubes– in order for a substantial signal to be induced on the pads. The induced signal is $\sim 1/3$ of that collected by the anode wire.

There are a total of 12 chambers for the high-p_T system: six gas-pixel chambers for the inner region and six straw tube chambers for the outer region. Half of the chambers are located on the $+x$ side of the proton beam and half on the $-x$ side. For each side the six chambers are positioned at three different distances from the target: $z \simeq 450$ cm (the PT1 station), 570 cm (PT2 station), and 610 cm (PT3 station). The inner region chambers have a total of 11960 channels and cover the angular ranges $10 < \theta_x < 58$ mrad and $10 < \theta_y < 44$ mrad; the outer region chambers have a total of 6240 channels and cover the ranges $38 < \theta_x < 250$ mrad and $44 < \theta_y < 143$ mrad. The amount of material comprised by these chambers is listed in Table 25; the total amount is 2.6% of a radiation length for all three inner chambers traversed by a particle, and 3.9% for all three outer chambers.

The inner gas pixel chambers were constructed at ITEP, Moscow and were completed in October, 1999. The outer straw tube chambers were constructed at the University of Cincinnati and Princeton University and were completed in June, 2000. All inner chambers and 4 of 6 outer chambers were installed during the 2000 running period. The final chamber configuration is shown in Fig. 57.

Due to their positions within the magnet and the high interaction rate and track multiplicity of HERA – B , the high-p_T chambers are subjected to a substantial amount of ionizing radiation. Such ionization can polymerize impurities in the gas volume, and such polymers can subsequently coat the

Table 25: *Material constituting an inner and outer high-p_T chamber.*

Chamber	Material	Depth (mm)	Rad. lengths (%)
Inner	G10 plates	0.20	0.21
	stainless steel field wires, $\phi = 300\ \mu$m	35	0.20
	Solder		0.12
	Twisted-pair cable, $\phi = 50\ \mu$m		0.07
	Gas	35	0.03
	Miscellaneous		0.25
	Total $\times$ 3 chambers:		**2.6**
Outer	straw tubes	0.060 (wall)	0.084
	tungsten anode wires, $\phi = 20\ \mu$m	$0.020 \times (\pi/4)$	0.004
	carbon fiber support tubes	0.89 (wall)	0.16
	silver thread	0.5	0.093
	honeycomb support panels (G10 faces)	1.0	0.048
	honeycomb circuit panel (G10 faces)	1.0	0.52
	aluminum foil (ground)	0.025	0.029
	kapton insulator	0.025	0.009
	pad circuit (G10 substrate)	0.20	0.103
	pad circuit (Cu traces + pads)	0.025	0.174
	carbon fiber plates	1.6	0.042
	G10 strips	1.6	0.027
	Total $\times$ 3 chambers:		**3.9**

anode wires. To minimize aging effects, we use counting gases with very small or negligible amounts of a quenching hydrocarbon component such as CH_4. The mixture for the gas pixel chambers is $Ar/CF_4/CH_4$ 68/30/2, and the mixture for the straw tube chambers is Ar/CO_2 80/20. The large fraction of CF_4 used in the gas pixel chambers is believed to be beneficial for aging. The mixture for the straw tube chambers has been measured to give minimal or negligible aging at high dose rates [63].

2.6.2 Performance of Inner Chambers during the 2000 Run

All six chambers were operational at a voltage setting at least 50 V above the value corresponding to the beginning of the efficiency plateau. During the last month of data taking, the chambers were operated routinely along with the rest of the HERA – B detector. The number of dead channels is relatively small: out of 11 960 channels, 18 are dead due to missing wires or disconnected cables and 12 have lost one wire (from two in the cell) resulting in an efficiency loss of about 30%. An attempt will be made to repair these channels during the Lumi shutdown. There were 227 channels dead due to bad ASD-8 cards (which we believe can be recovered), and 61 channels dead for unknown reasons. There were 593 noisy channels with an occupancy greater than 20% (the real occupancy in minimum bias events is less than a few percent). The majority of these can be made quiet by increasing the ASD-8 discriminator threshold; this results in a small loss ($\sim$20%) in cell efficiency. There were 73 channels which remained noisy even at high threshold settings. We believe that better shielding may further reduce the number of noisy channels. A typical hit map for PT1 (two chambers, one for $+x$ and one for $-x$) is shown in Fig. 58. The chamber performance achieved during the 2000 run and

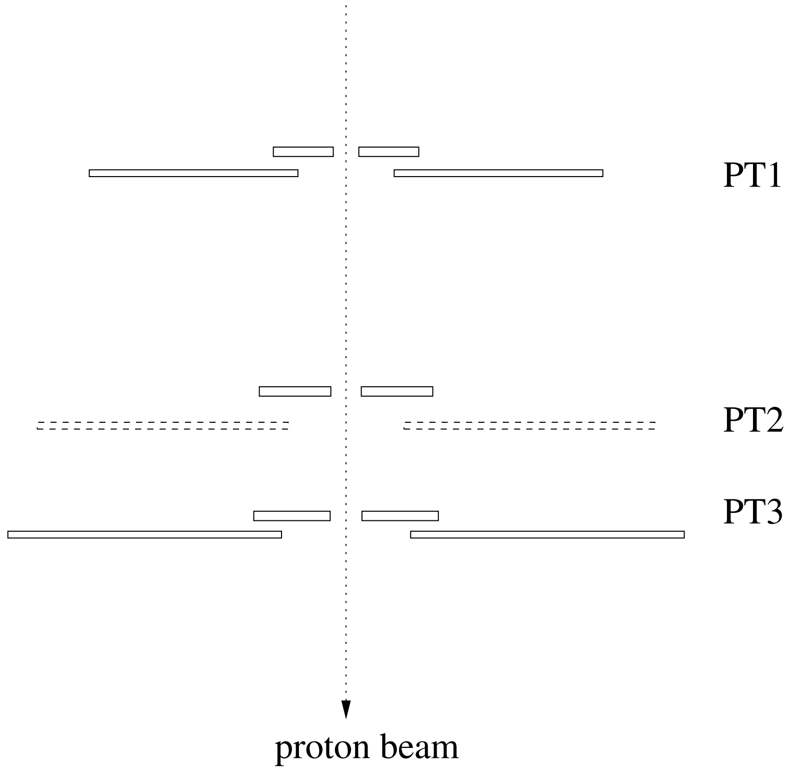

Figure 57: *The configuration of high-p_T chambers for the 2000 run. The outer PT2 chambers (shown dashed) were not installed due to the very limited access to the detector.*

that expected for the 2001 running period are summarized in Table 26.

Table 26: *Inner chamber performance achieved during the 2000 run and that expected for the 2001 running period.*

	Present	**2001**
Number of dead wires	30 (0.25%)	$< 30 (< 0.25\%)$
Number of channels dead for unknown reason	61 (0.5%)	$< 20 (< 0.2\%)$
Number of bad ASD-8 channels	227 (1.9%)	~ 8 ($< 0.1\%$)
Number of very noisy channels	73 (0.6%)	a few
Number of noisy channels requiring higher threshold	520 (4.3%×20%=0.86%)	$< 0.2\%$
Overall inefficiency	4.1%	$\lesssim 1\%$

The single-cell efficiency was determined using tracks defined by matching VDS, ECAL, and RICH segments. In order to reduce the ghost rate, a coincidence was required with two other high-

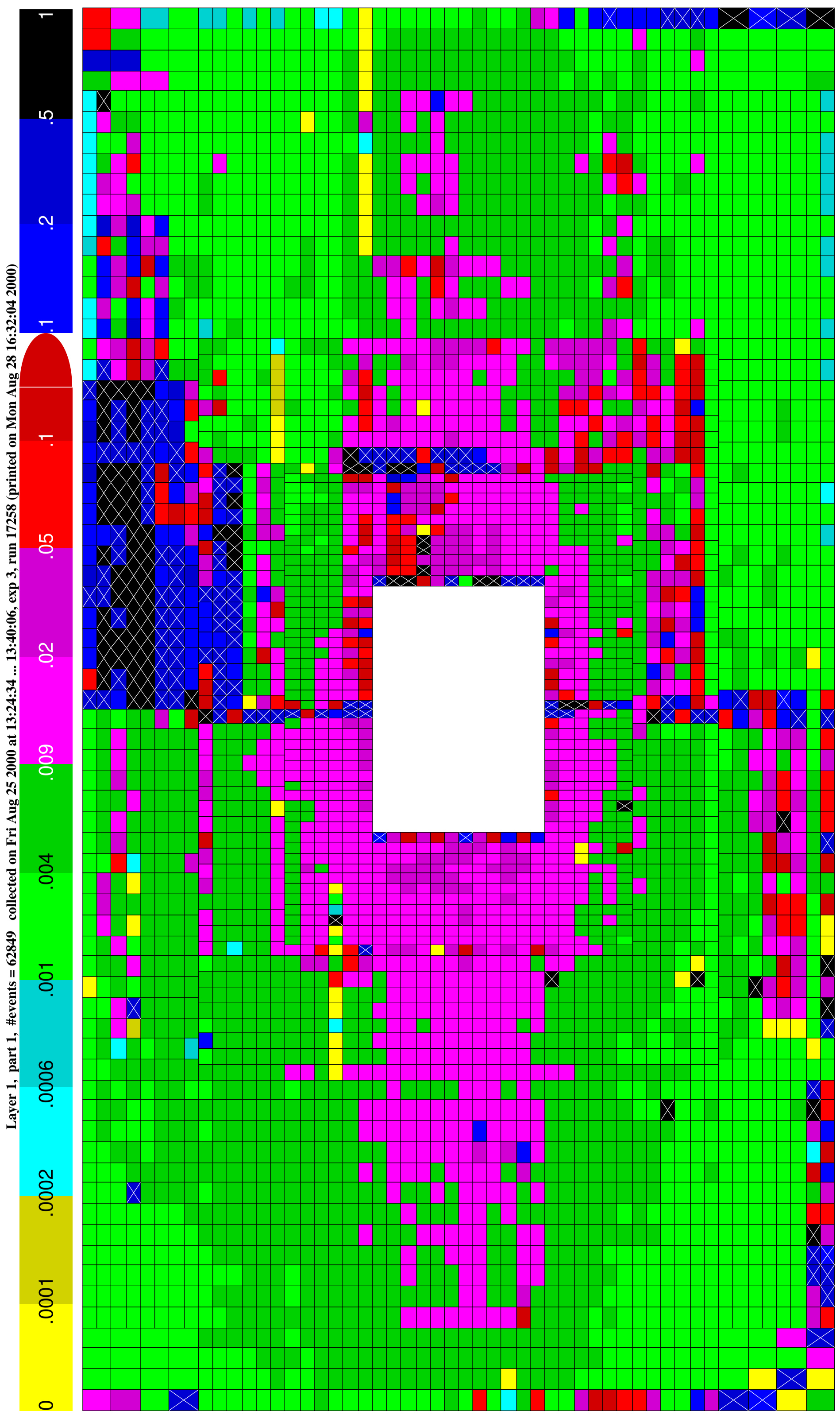

Figure 58: *Hit map of PT1 inner chambers during 2000 run. Cells with crosses were masked out (not used) for pretrigger studies.*

p_T stations (e.g., PT1 and PT3). All known dead and hot channels were excluded. The efficiencies obtained for different chambers and cell sizes are shown in Fig. 59.

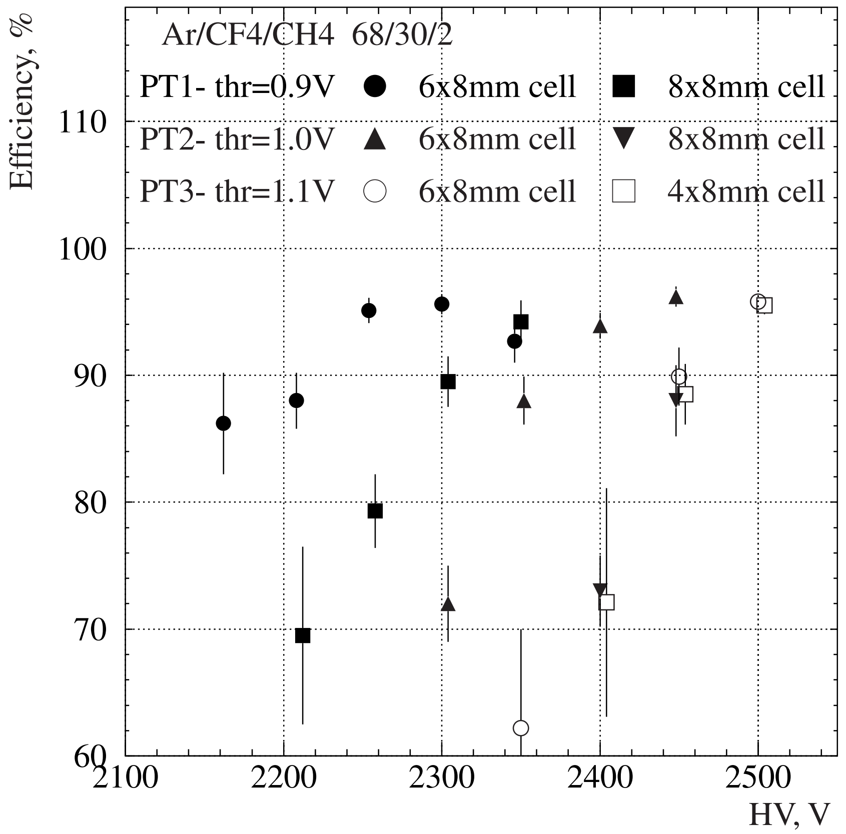

Figure 59: *Efficiencies measured for inner high-p_T chambers during the 2000 run using VDS-ECAL-RICH tracks.*

The PT2 and PT3 chambers have larger cell sizes than PT1 and thus require higher HV settings. The efficiency measured reaches a plateau of about 96% and does not increase further. This could indicate that some fraction of the reference tracks are ghosts or come from the coasting beam; alternatively, there may exist a timing problem or an electronics inefficiency with large signals. The timing of signal readout from the the front-end electronics was achieved using the leading edge of signals arriving after an empty bunch. The timing accuracy obtained was better than 5 ns. Previous tests at the ITEP synchrotron yielded a single-cell efficiency higher than 99% for fluxes up to about 5×10^5 particles/cm^2-s. These measurements, however, were performed without a magnetic field.

The inner chambers have been aligned using VDS-OTR-RICH tracks. The precision achieved is better than 0.2 mm in the y-direction and better than 1.3 mm in the x-direction –with one exception: the PT1+x chamber was erroneously raised by 1.3 mm in y when it should have been lowered. We have not corrected for rotations, which Fig. 60 implies are at the level of $\lesssim$2.5 mrad; this level of chamber rotation has negligible impact upon pretrigger efficiency. The achieved accuracy in y alignment is within our requirements, and we expect to obtain improved precision in x with subsequent iterations of the chamber alignment procedure.

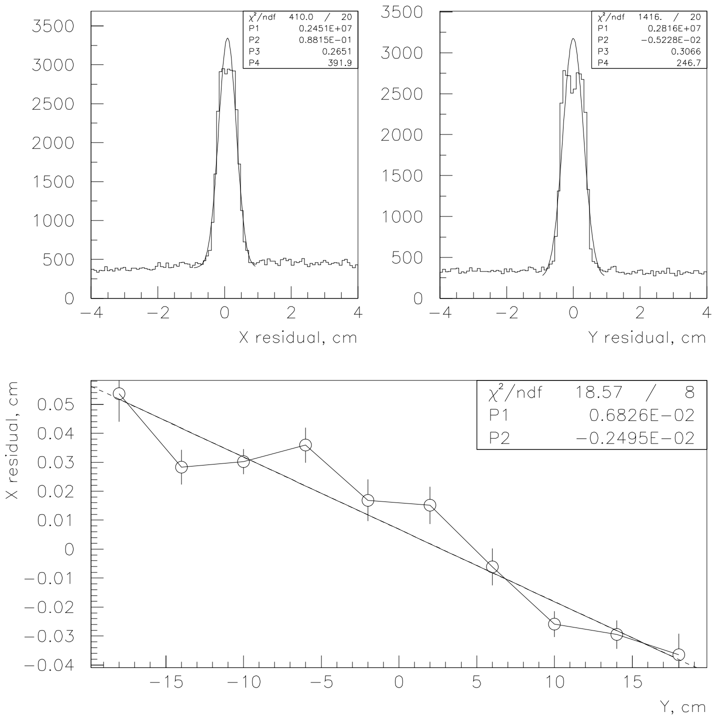

Figure 60: *Alignment achieved for inner high-p_T chambers.*

The pretrigger rate as a function of interaction rate is shown in Fig. 61 (for inner chambers only). All channels with occupancy larger than 20% have been masked out and not considered. The average number of pretriggers is 0.18/BX at an interaction rate of 5 MHz; this is about 60% larger than the Monte Carlo prediction of 0.11/BX. The contributions from the $+x$ and $-x$ sides are equal. The pretrigger rate drops if one makes more stringent cuts on noisy channels. The pretrigger rate is 1.06/BX at an interaction rate of 20 MHz, again somewhat larger than the Monte Carlo prediction of 0.61/BX. The rate of the high-p_T pretriggers in coincidence with the electron (muon) FLT-SLT trigger with $p_t > 1.5\,(1.0)$ GeV/c is 0.82/BX at 2 MHz. This is a factor of two larger than the Monte Carlo prediction. The distribution of pretriggers among cells of the inner PT1 chambers is shown in Fig. 62.

In summary, the inner high-p_T chambers have been commissioned. The overall chamber efficiencies were found to be 92%, which takes into account the single cell efficiency (96%, Fig. 59) and the percentage of bad channels (4%, Table 26). This provides an overall efficiency of $(0.92)^3 = 0.78$ for the high-p_T hadron-lepton trigger and $(0.78)^2 = 0.61$ for the high-p_T trigger with two hadrons. The pretrigger rate is within a factor of two of Monte Carlo predictions and thus we expect to obtain a rejection factor similar to that given in the TDR. However, there still remain several concerns:

- The sources of noise have not been identified and may change in an uncontrollable way. The level of noise may increase.
- In order to minimize the amount of material in the chambers, the anode wires were soldered on the HV side of the chamber at one point only. Unfortunately this has resulted in the loss of 17 wires. It is not known how this process will develop in time, although most of the wires were lost at the beginning of the run and no new problems arose during the last month of running.

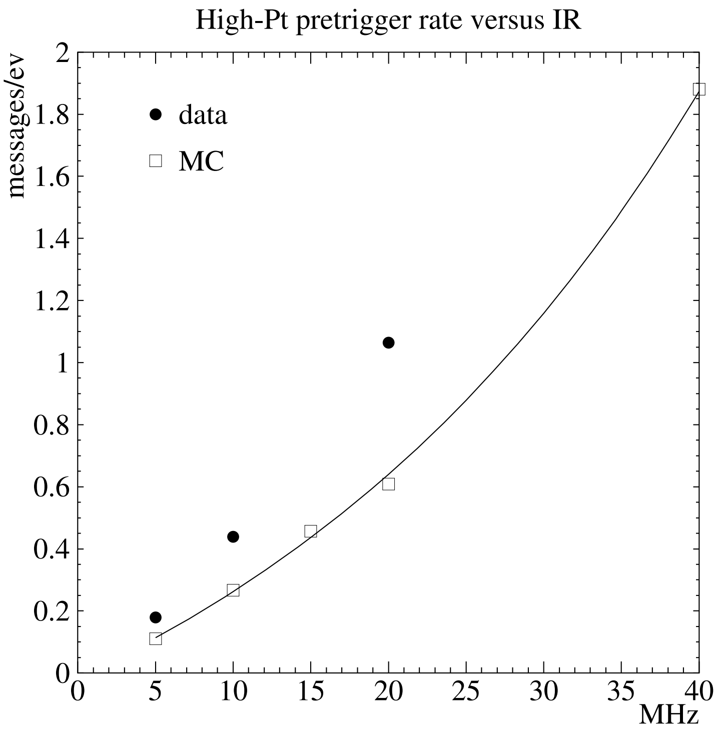

Figure 61: *Pretrigger rate as a function of interaction rate.*

- The expected amount of collected charge is about 0.6 C/(cm-year) at an interaction rate of 20 MHz, but aging of the chambers has been studied in the HERA – B environment for only a small fraction of this amount. We have tested our gas mixture in HERA – B using a muon tube chamber, and no aging was observed at the nominal gas gain of the inner high-p_T chambers. At larger gas gain, however (a factor of five higher), aging occurred very quickly.

Our plans for the Lumi shutdown are as follows:

1. noise studies, tests of ASD BLR;
2. shielding of chambers;
3. repair of wires;
4. modification of the cable support to make them movable together with the chambers;
5. upgrade of the gas quality control system;
6. automatic HV adjustment to compensate changes in the gas gain due to pressure variations;
7. production of spare chambers;
8. production of spare electronic modules (FE and FED);
9. studies of pretrigger and trigger rates, chamber efficiencies, etc. using collected data.

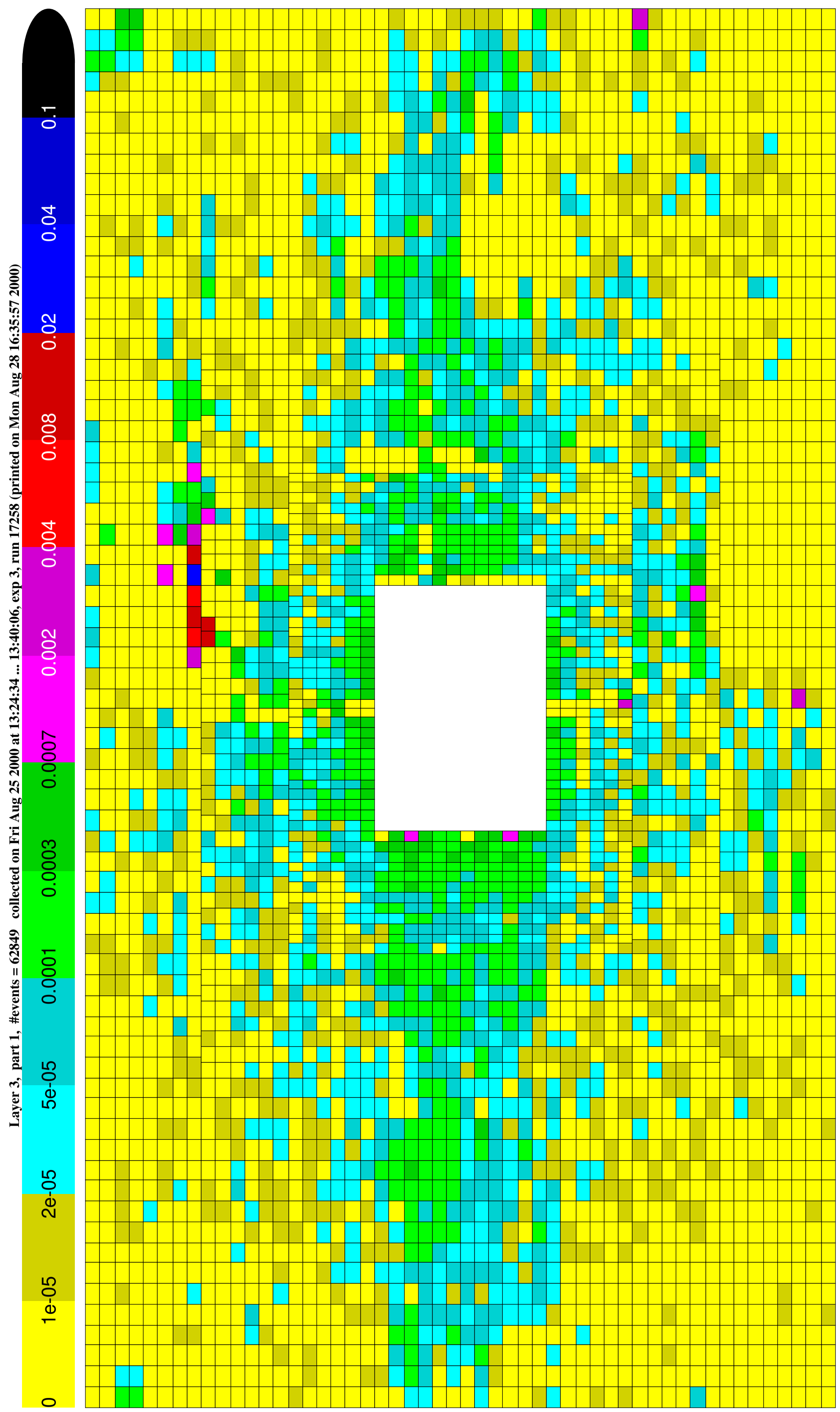

Figure 62: *Distribution of pretriggers among cells of the inner PT1 chambers.*

2.6.3 Status of Outer Chambers during the 2000 Run

During the 2000 running period, four of six outer high-p_T chambers were installed in the experiment and run regularly at nominal high voltage. The very limited access to the detector (one scheduled day per month) precluded installation of the remaining two chambers. The chambers that were installed were partially instrumented with front-end ASD-8 cards and read out. The cards were fully operational and we had no difficulties setting threshold values (via a DAC) for the ASD-8 discriminators. All straw tubes except two out of 1488 were active. We were encouraged by the fact that after all chambers had undergone final adjustments, there were no high voltage problems for the remainder of the run ($\gtrsim$ 4 weeks), which included 1-2 hours running at an interaction rate of 10 MHz. We observed no dark currents or drop in chamber currents over time (for fixed interaction rate), as is symptomatic of radiation damage and wire chamber aging.

Unfortunately we observed a substantial amount of noise and oscillations on the ASD-8 cards. After applying additional shielding to the chambers (consisting of aluminized mylar having thickness of 70 μm) and reconfiguring the grounding scheme of the ASD-8's, the noise was substantially reduced. However, we did not have time to sufficiently study the oscillations and understand their sources. At various times the oscillations disappeared and the readout appeared satisfactory; in one instance during an access we observed clean signals from cosmic rays on a digital oscilloscope. However, the intermittent nature of the oscillations/noise prevented us from measuring chamber efficiencies or inputting meaningful signals to the pretrigger electronics. Fig. 63 shows pad occupancy as a function of threshold setting of the ASD-8 discriminator. The figure displays eight channels of an ASD-8 for a PT3 chamber. The open circles were more typically observed, and illustrate unphysically large occupancy even up to high threshold settings (the occupancy from real particles was at most a few percent). This behavior is characteristic of oscillations in the electronics. The dark squares show the same channels during a different time period when the electronics were quieter. The horizontal scale is in DAC counts; a value of 170 corresponds to about 1.6 V. For this threshold the chambers should be $\gtrsim$99% efficient (based on testbeam data).

Our plans for the Lumi shutdown are as follows:

1. study and understand sources of noise and how to shield from them;
2. study and understand oscillations, improve grounding scheme to prevent them;
3. install last two (PT2) chambers;
4. install all ASD-8 cards and cables;
5. complete installation and cabling of all front-end readout crates;
6. replace fuses in some low voltage distribution boards.

2.6.4 Status of Pretrigger Electronics

After several modifications of the link and pretrigger boards, a solution was found that provides a relatively stable operation of the optical links. Six modified link boards and four modified pretrigger boards were installed in the experiment and worked essentially error-free during periods without target operation when the number of hits was small (i.e., re-initialization was required once every 10 minutes). During data taking, errors in the bunch number transmission occurred occasionally, presumably due to the larger number of hits in the data streams. This may imply that the DC

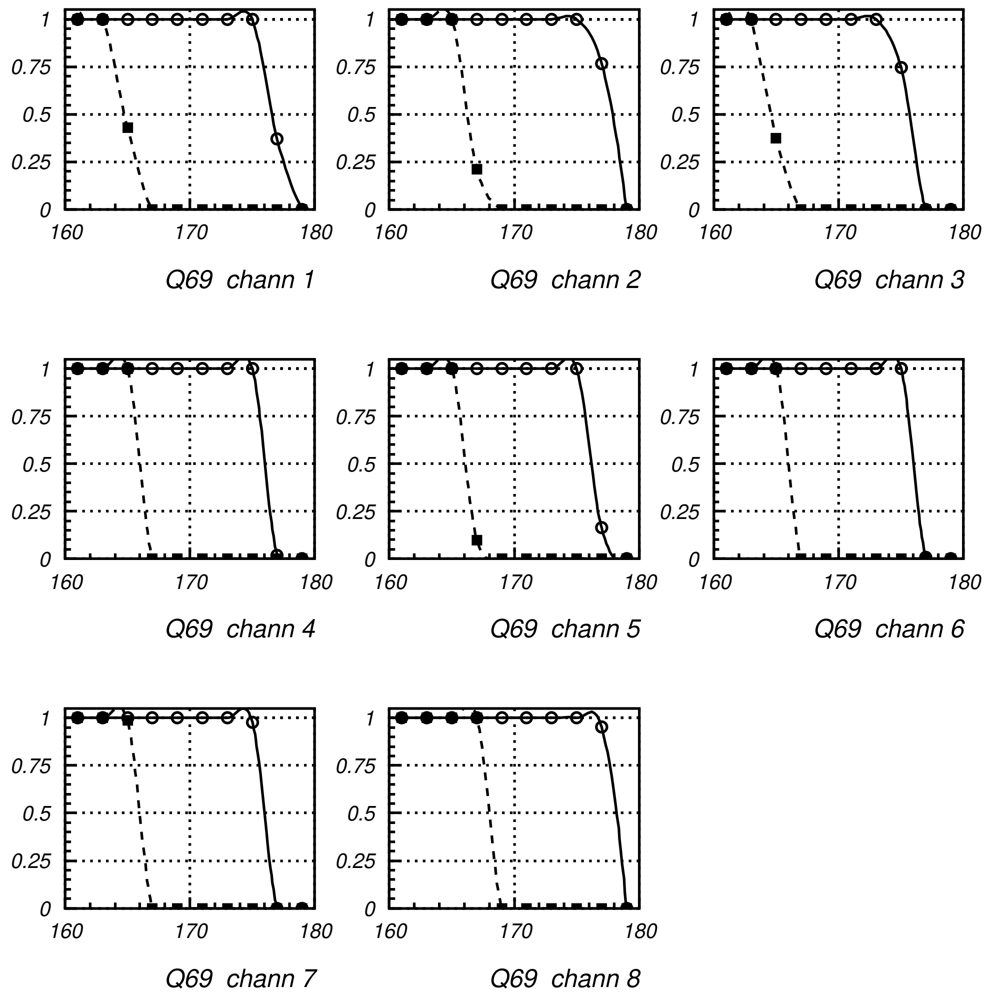

Figure 63: *The measured occupancy of eight ASD-8 channels for an outer PT3 chamber as a function of threshold setting of the ASD-8. The high occupancy represented by open circles indicates oscillations. The data represented by dark squares was obtained during a period when the chambers were quieter. The horizontal scale is in DAC counts; a value of 170 is equivalent to about 1.6 V.*

offset for the optical receivers should be increased at higher interaction rates. This can be achieved by adding DACs to the optical receivers of all pretrigger boards, which we plan to implement. The problem will be studied during the Lumi shutdown.

A slice test using 12 rows of pads in the inner chambers with the FLT in transparent mode has been performed. Data is transferred from the link boards to the pretrigger boards in two cycles per bunch crossing. It was found that the first data transmission cycle gives an incorrect bunch number distribution; this problem is under investigation. In the second transmission cycle there is agreement between the FLT record and the DAQ data 93% of the time. Fig. 64 shows the x distribution in PT1 for tracks causing a pretrigger, as obtained from the FLT record and from the DAQ data.

One serious concern we have is whether the present optical link can provide the required stability over an extended period of time. Thus we are considering whether it worthwhile to develop a new, more reliable optical link for the experiment. For example, one improvement would be to provide

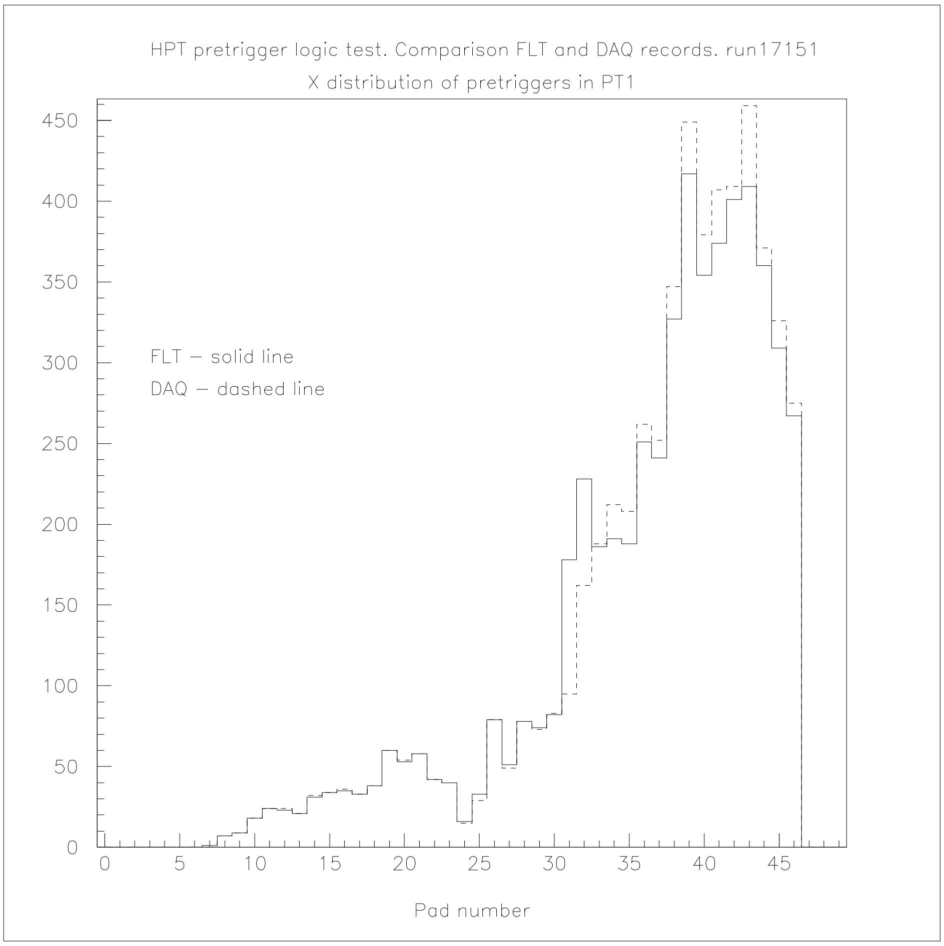

Figure 64: *The x distribution in PT1 of tracks causing a pretrigger.*

DACs for remote adjustment of the receivers. The plans for the pretrigger electronics during the Lumi shutdown are as follows:

1. study the pretrigger electronics using test signals;
2. upgrade of pretrigger electronics;
3. installation and commissioning of the pretrigger electronics;
4. debugging of the pretrigger-FLT chain.

The costs associated with upgrading the pretrigger electronics (item 2 above) are listed in Table 27.

Table 27: *Costs for upgrading the pretrigger electronics during the Lumi shutdown.*

Activity	**Estimated Cost (kDM)**
Modification of 44 pretrigger boards	
(i.e., change to Autobahn handshake)	0
Equipment of 44 pretrigger boards with 12-fold DAC's	3
VME control of 11 Front End Crates	
1 VME board (+ 1 spare)	2
11 Front-end receivers (+ 2 spare)	12
100 m cable + connectors	1
Equipment of 70 link boards (type BCD)	
with 12-fold DAC's (optional)	5
Equipment of 18 link boards (type A)	
with 16-fold DAC's (optional)	2
Additional components (to replace bad ones):	
160 ptical transmitters	0
100 optical receivers	0
50 Autobahn chips	0
Total:	25.0

2.7 The **HERA – B** RICH

The HERA – B Ring Imaging Čerenkov detector (RICH) is used for identifying and tracking charged particles. Čerenkov rings formed on the focal surface of the RICH provide information about the velocity $\beta = v/c$ and the direction of a charged particle passing the radiator. The particle's velocity is related to the Čerenkov angle by the Čerenkov law, $\cos\theta_C = 1/n\beta$ (where n is the refractive index of the radiator). Čerenkov angles are determined by measuring the radii of Čerenkov rings detected with the RICH. The track direction is found from the location of the center of the Čerenkov ring on the focal surface and can be used to improve the tracking capabilities of a spectrometer by directly providing precise direction information which can be used, among other things, to determine the particle's momentum. The measured velocity and momentum p together determine the mass m of the particle. In the small angle approximation the Čerenkov angle relation can be rewritten as:

$$\theta_C^2 = \theta_0^2 - \frac{m^2}{p^2} \tag{8}$$

where $\cos\theta_0 = 1/n$. This relation can be illustrated as in Fig. 65, where the square of the Čerenkov angle is plotted against $1/p^2$. Particles of a given mass belong to linear bands with a slope of $-m^2$.

The HERA-B RICH detector was installed in Spring 1998, and has been in stable operation over the last two years. Following commissioning, the performance of the HERA – B RICH was found to meet design expectations. Event analysis tools which enable both a stand-alone search/measurement of individual rings and analysis of events based on the information from tracking systems have been developed. In what follows we shall report on performance studies and the stand-alone ring search and particle identification capabilities of this device.

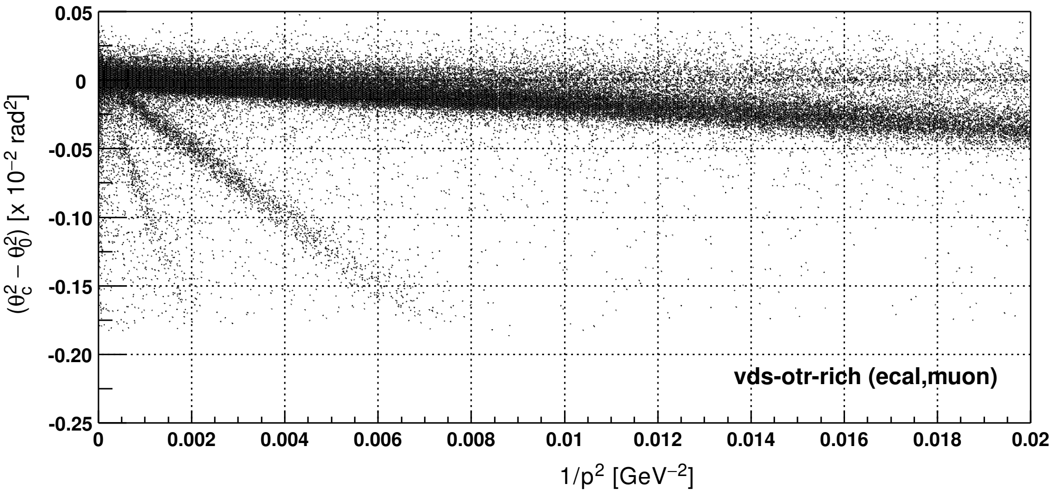

Figure 65: *r2p2 plot: the difference of squares of the measured and the maximal value of Čerenkov angle, $\theta_c^2 - \theta_0^2$, is plotted as a function of $1/p^2$ to find the particle identity through association with a particular band corresponding to a stable charged particle. Bands for electrons, pions, kaons, and protons can be clearly seen.*

2.7.1 Expected Performance

The performance characteristics of a RICH detector for particle identification and tracking are governed in large part by two critical parameters, the angular resolution for individual photons σ_θ, and the mean number of detected Čerenkov photons N_γ. In HERA – B RICH design studies it was determined that an angular resolution of $\sigma = 0.7$ mrad is needed in the central region and that more than 20 photons must be detected on average per $\beta = 1$ track [26].

For reasons of detector occupancy, angular resolution, quantum efficiency and costs, Hamamatsu M16 and M4 PMTs were chosen for the RICH photon detectors. The expected single photon resolution is 0.7 mrad and 1 mrad for the regions occupied by M16 and M4 PMTs, respectively.

The yield of Čerenkov photons depends on Čerenkov angle θ_C and radiator length L according to $N_\gamma = N_0 L \sin^2 \theta_C^2$, where N_0 is a figure-of-merit reflecting the quantum efficiency and optical efficiency of the RICH system. From the data available on quantum efficiency, mirror reflectivities, window and optical system transmissions of the components we have employed in the HERA – B RICH, one calculates the HERA – B RICH ($L = 2.75$ m) merit factor to be $N_0 = 43$/cm, which gives the the mean number of photons expected for particles approaching the velocity of light $N(\beta = 1)_\gamma = 32$ and the limiting Čerenkov angle $\theta(\beta = 1)_0 = 52.3$ mrad.

2.7.2 Measured Single-photon Angular Resolution

The RMS spread in Čerenkov angles for single photons can be estimated taking the mean of the hit residuals σ_θ for each single ring. To reconstruct the rings, a stand-alone RICH pattern recognition algorithm (RISE) is used followed by a ring fit with the center and the radius as free parameters. The values of σ_θ are displayed in Fig. 66. The distribution is a convolution of the contributions of the M16 and the M4 PMTs, but is dominated by the considerably larger number of M16 channels. The measured resolution is consistent with the expectations as noted above. This result is in agreement with an independent check, where we have used the data collected in the absence of magnetic field. In this case straight tracks, defined by a high energy cluster in the calorimeter and the position of the target wire, were used to determine the Čerenkov angle for each individual hit on the photon detector [67]. The resulting resolution is 0.7 mrad for the finer granularity (M16) cells, and 1.0 mrad for the coarser (M4) ones.

2.7.3 Measured Photon Yield

We have sought to understand the photon yield using several approaches [64, 65]. In every instance, the results are consistent with the expected yield estimates. For all rings found by the stand-alone ring-finding algorithm, the number of photons can be determined. From this, the raw photon yield can be calculated [64] and is histogrammed in Fig. 67. This distribution includes all rings found without corrections for acceptance losses such as shadowing due to the beam pipe. The width of the observed distribution is explained by Poisson statistics. The mean value corresponds to a figure of merit $N_0 = 44$/cm. The result of a "hand-scan" analysis [65] of events with isolated rings is shown in Fig. 67. The analysis determined $N_0 = 43 \pm 4$/cm.

From these studies we conclude that the observed photon yield $N_0 = 43 \pm 4$/cm is completely consistent with expectations. The resulting number of detected Čerenkov photons per $\beta = 1$ track is $N_\gamma = 32 \pm 3$, well above the minimum value required for efficient particle identification.

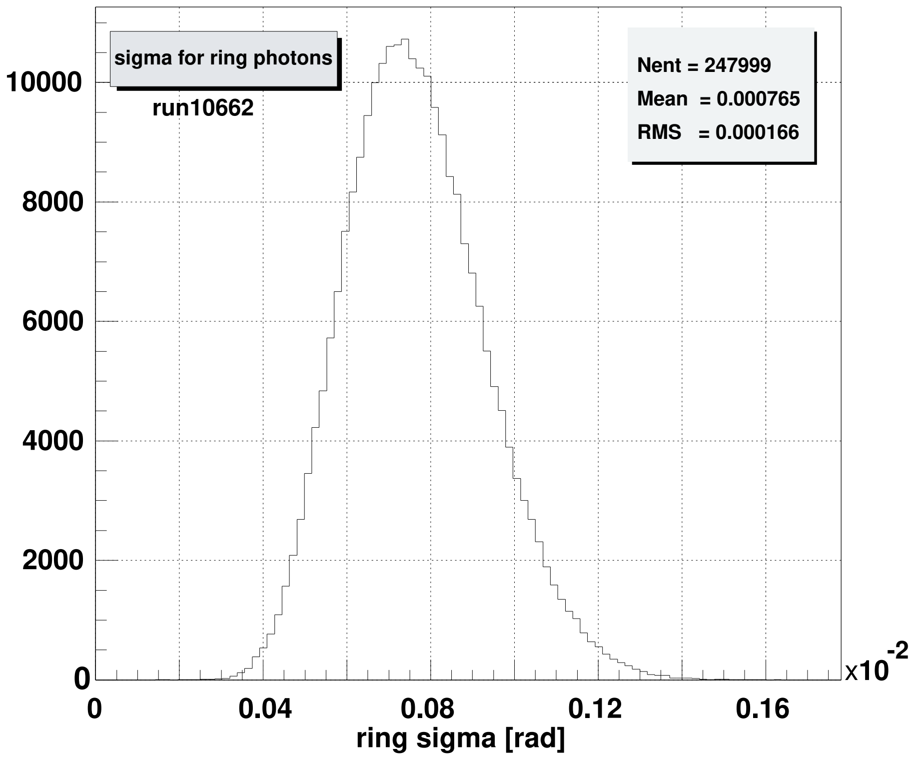

Figure 66: *Single photon resolution*

2.7.4 Stability of Operation

The photon detector has been stably operated since summer 1998. The number of hot channels was reduced to about 25 well identified individual channels, and has remained at that level (Fig. 68) throughout the run. The number of dead channels is, on the other hand, mainly related to missing PMTs which we expect to install during the shut-down. Even now, the detector has only about 2% faulty (dead or noisy) channels. Further, we have observed no changes in the alignment of the optical system.

2.7.5 Tracking Capabilities

Using the RICH in conjunction with other detector sub-systems [70] to measure momentum is an unexpected benefit, in particular for the period when no or little tracking system was available. From the rings found on the photon detector, track directions are deduced and matched in the non-bending plane with the track candidates from the silicon vertex detector. From the deflection in the bending plane the momentum of the particle is then determined.

The high accuracy of the track angle measurement can be checked by comparing the vertex detector track direction with the one measured with the RICH. This is possible in the non-bending plane only, and the result is shown in Fig. 69 as a function of momentum. We also note that this angular resolution is better than the present accuracy of the main tracking system (Fig. 73).

The momentum resolution can be estimated by analyzing the width of the bands of a “r2p2” plot

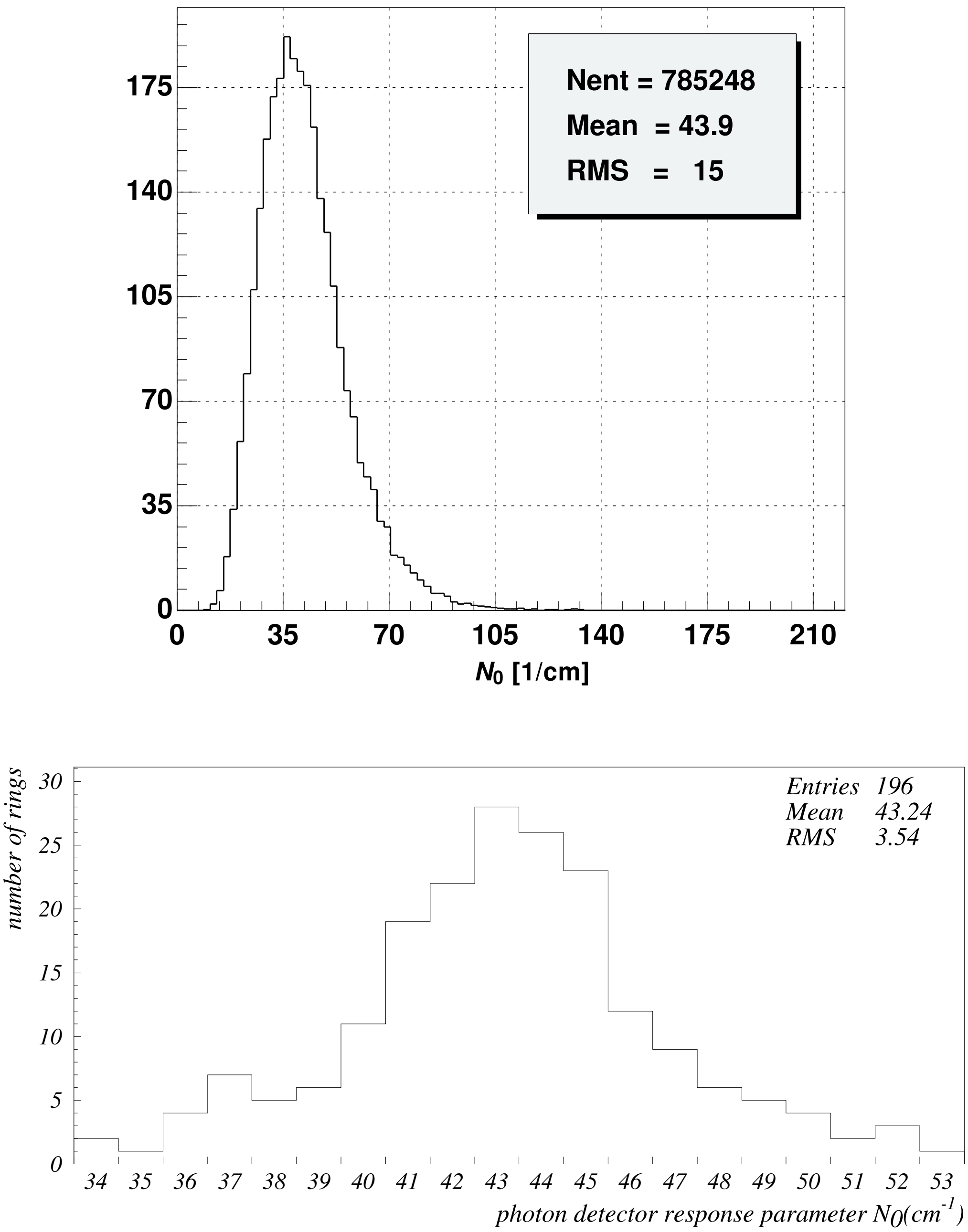

Figure 67: *The figure-of-merit N_0 as found by the stand-alone ring-finding algorithm (top) and by analyzing well isolated tracks in an event scan (bottom).*

(Fig. 65). When momentum is determined only with the vertex detector and RICH [64], we find:

$$\left(\frac{\sigma_p}{p}\right)^2 = \left(1.6 \cdot 10^{-2}\right)^2 + \left(0.15 \cdot 10^{-2}/(\mathrm{GeV/c})\right)^2 p^2 \quad . \tag{9}$$

The resolution is worse than that expected from the measured single-photon yield and angular resolution, taking multiple-coulomb scattering into account. Here the total radiation length was taken from the GEANT detector simulation. Better agreement is achieved, if the constant term is increased by approximately a factor 1.5, which implies a larger multiple-scattering contribution.

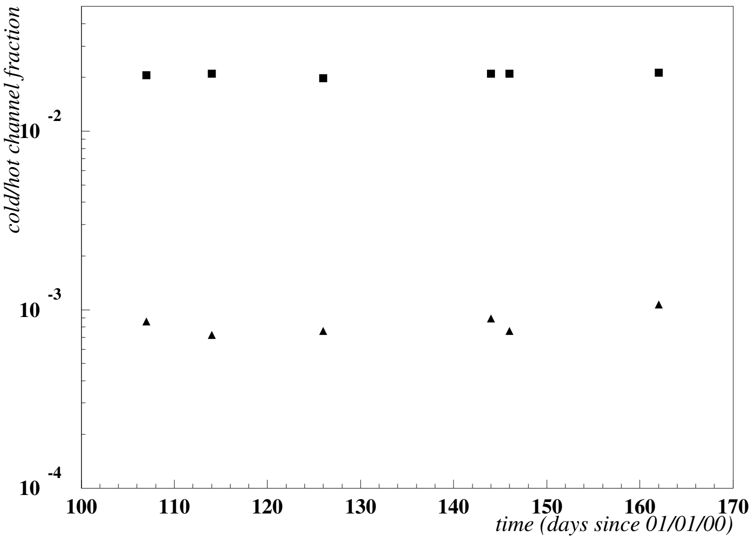

Figure 68: *Variation in time of the fraction of hot (triangles) and cold (squares) channels of the photon detector.*

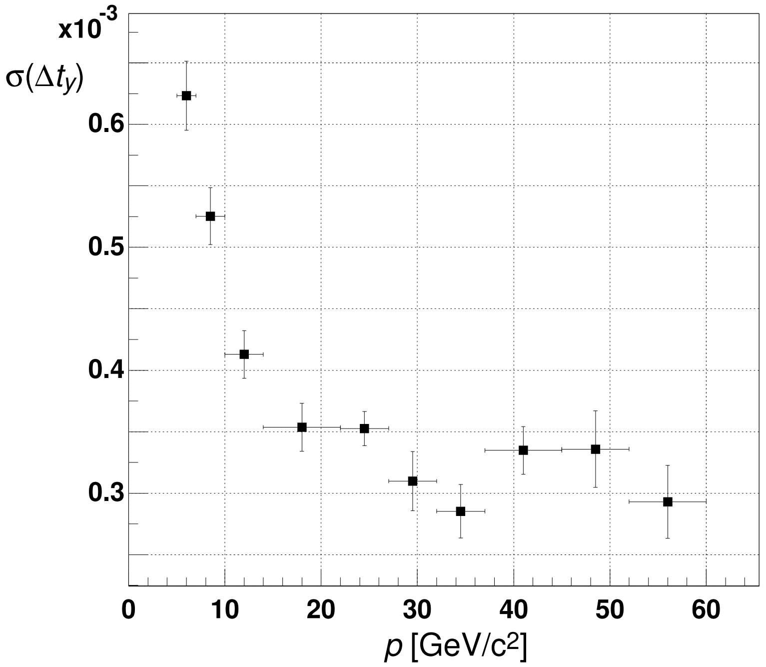

Figure 69: *Resolution in vertical angle difference for pion track matched by the VDS and RICH. To clean the track sample, it was required that the track be associated with the* π*-band of the "r2p2"-plot (Fig. 65).*

The momentum resolution of this rudimentary spectrometer is sufficient to reconstruct particle decays such as K^0_S in the pion-pion invariant mass spectrum (Fig. 70). A clear K^0_S signal is present

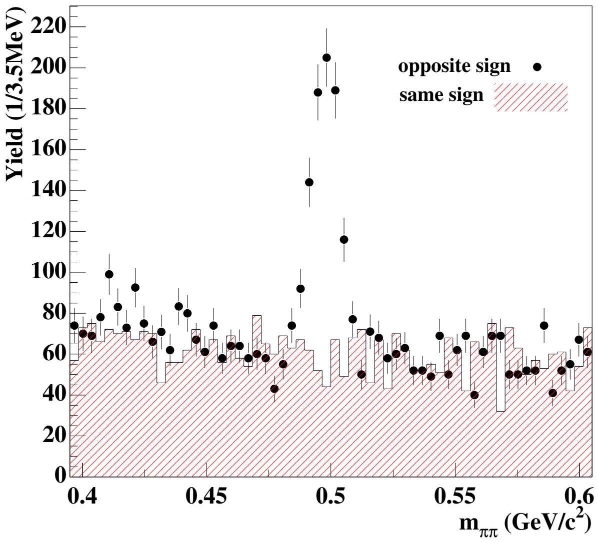

Figure 70: *Invariant mass for pion pairs reconstructed using the VDS and RICH for momentum measurement. Data indicated by points are for opposite sign charges; shaded histogram indicates the corresponding distribution for same-sign charges. Pairs are required to have a vertex downstream of the target wire. Pairs that form a vertex at a target wire show no K^0_S peak.*

for opposite-sign pairs with vertices downstream of the target wires. The RMS width of the peak is 5.7 ± 0.4 MeV/c^2, well centered on the K^0_S mass, which implies an average momentum resolution of $2.0 \pm 0.2\%$. This, in turn, is in reasonable agreement with the momentum resolution quoted above for the tracks making up this peak which have typical momenta in the range from 10 to 15 GeV/c.

The efficiency of the stand-alone ring-finding algorithm depends sensitively on the quality of the detected ring, which is related to the number of photons S attributed to the ring and the background hits B under the ring, estimated using the side bands. We define the significance of the ring detection to be $S/\sqrt{B}$; to keep the number of ghosts at a reasonable level (around 10% in MC simulated 1+4 interactions), a minimal significance of three is required. The efficiency of finding a ring which can be associated with a charged particle track, is shown in Fig. 71; the efficiency reaches values above 90%. The drop at low momenta is caused by the small number of photons in these rings. To determine the efficiency, VDS-OTR matched tracks were used, for which it was checked whether they can be associated with a ring or not. The result was cross-checked using a K^0_S sample reconstructed without the any requirements on RICH information. To further illustrate the capability of the stand-alone ring search, we plot in Fig. 72 invariant mass spectra for two-body final states πp, KK and πp.

2.7.6 Particle Identification Capabilities

The particle identification capabilities of a RICH are exploited by comparing the measured values of the particle momentum p, Čerenkov angle and/or number of detected photons N_γ with the expected values for a given particle hypothesis.

Analysis methods

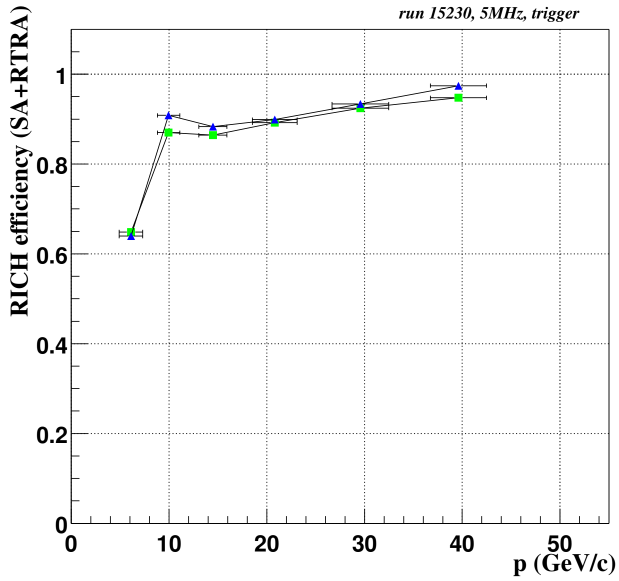

Figure 71: *Efficiency for finding a ring related to a track found in the tracking system, as a function of particle momentum. The efficiency of the stand-alone search (lower curve) increases slightly if for the remaining tracks the track direction is used as a seed for the ring search (upper curve).*

Two analysis methods were employed as particle-identification tools. In the stand-alone ring-finding algorithm (RISE) a ring-fitting procedure (RIFIT) is used to determine the radius and center location of the ring. From the value of the ring radius the Čerenkov angle is deduced. In this case, the particle identification capability can be visualized by plotting the measured values of in θ_c^2 versus $1/p^2$ (Fig. 65). The bands formed by electrons, pions, kaons and protons are clearly visible. The momentum ranges over which a good particle identification—defined as a four-sigma separation of the bands—is possible are given in Table 28.

Table 28: *Momentum range where "2+2 sigma" particle identification with the RIFIT algorithm is possible.*

Band	Momentum Range
$e - \pi$	3.4 – 15 GeV/c
$\pi - K$	12 – 54 GeV/c
$K - p$	23 – 85 GeV/c

A likelihood for each particle hypothesis can be calculated through the deviation of the measured Čerenkov angle from the one expected at a given momentum, relative to the RMS widths of the bands on the r2p2 plot.

The second particle identification method (RIRE/RITER algorithms) relies on the use of the track parameters as supplied by the tracking system to determine the Čerenkov angle for each individual detected Čerenkov photon [26, 71, 72]. For each of the hypotheses the likelihood can then be calculated, based on individual Čerenkov photons.

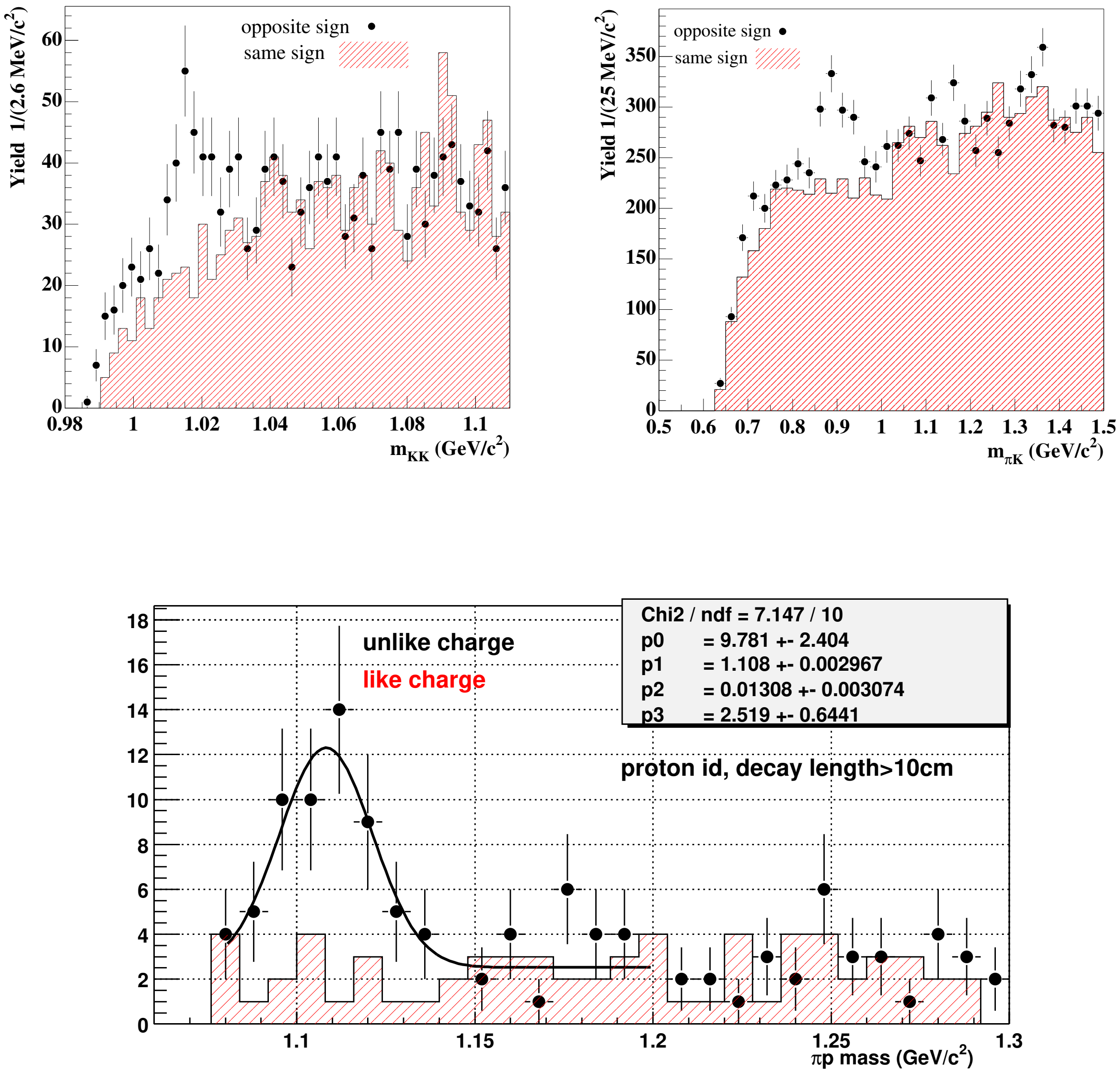

Figure 72: *Invariant mass for kaon pairs (top, left), pion-kaon pairs (top, right), and for pion-proton pairs (bottom) reconstructed using the VDS and RICH for momentum determination.*

This allows also the identification of particles close to or below the Čerenkov threshold, where there are few or no detected photons. Note, that in this case, the measured track direction enters directly into the likelihood calculation, so that it is essential that the tracking system is well aligned and that the direction errors are well understood. The relative alignment of the OTR and RICH was determined from the data, an example of which can be seen in Fig. 73. We note that the error in direction determination (around 1.2 mrad), seen in Fig. 73, is larger than the single-photon resolution (0.7 mrad), and, therefore, degrades the particle-identification performance of the track-based methods.

Identification efficiency

To determine the identification efficiency of the algorithms employed, we have performed an

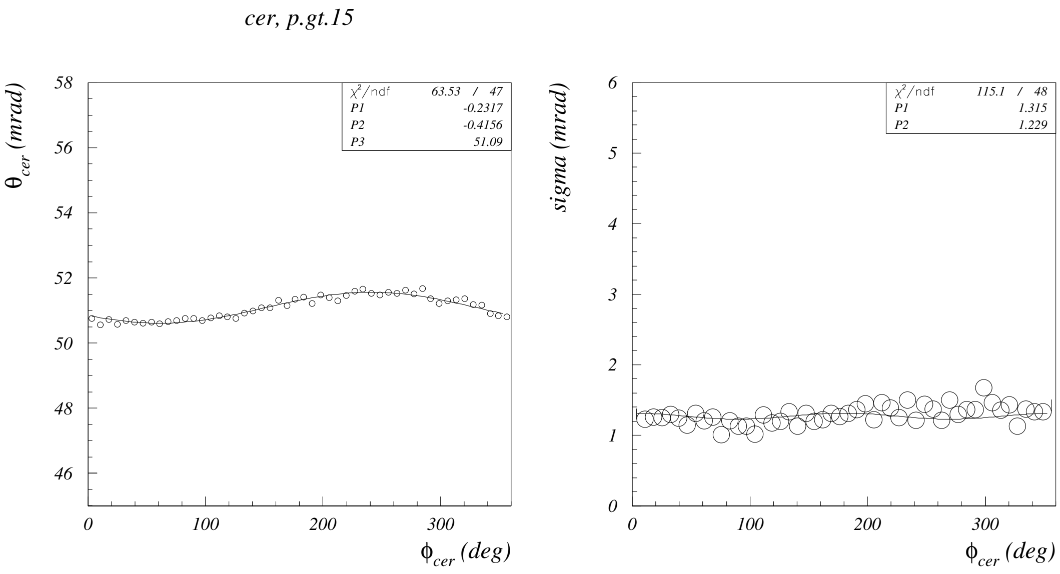

Figure 73: *Relative alignment of the RICH and the OTR: the variation of the mean Čerenkov angle (left) and the error in the track direction as given by the tracking system (right), both as a function of azimuthal angle around track direction. A misalignment of a few tenths of mrad shows up as a sine-modulated mean Čerenkov angle.*

analysis of well defined final states. In particular, particles which originate from reconstructed secondary vertices of K_S^0 (Fig. 74) and Λ (Fig. 78) decays and which have a matched OTR segment, were used in the study. The momentum distribution of pions in the sample, collected from the minimum bias run 14577, is shown in Fig. 76.

In Fig. 75, the efficiency and the misidentification probability of the ring-fitting algorithm (RIFIT) are shown for pions with momenta between 14 and 35 GeV/c as a function of the likelihood cut. The low misidentification rate is explained by the large separation of the kaon band from other bands in the selected momentum region. In Fig. 76, the efficiency is plotted as a function of momentum. The efficiency reaches a value of 0.9 for momenta around 20 GeV/c. As expected, the efficiency follows the variation of the mean number of detected photons.

In Fig. 77, the efficiencies and fake probabilities are shown for the track-based algorithm. The efficiency is high (0.8 - 0.9) in the momentum region close to the threshold, and starts decreasing at higher momenta. This behavior is understood: the efficiency at higher momenta is dominated by the present alignment accuracy of the tracking system. In Fig. 78, yet another proof is given of the identification abilities of the HERA-B RICH near threshold using pions and protons from Λ decays. In this case most pions have momenta slightly above threshold, between 5 and 10 GeV/c, and almost all protons are below threshold.

The performance at high momenta was explored by using the decays $J/\psi \rightarrow \mu^+\mu^-$ in the data recorded with the trigger requiring two muons with high transverse momenta. The resulting efficiency plot is shown in Fig. 80.

To summarize we note that the two analysis methods, if properly combined, look very promising

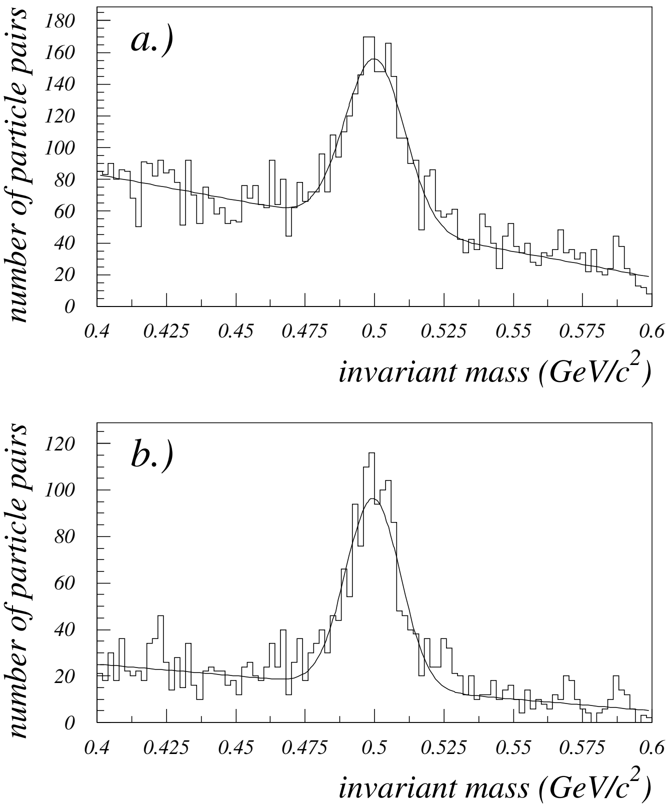

Figure 74: *Two pion invariant mass plot for tracks with detached vertices without and with a requirement that both particles are pions.*

for an efficient particle identification. Due to the excellent angular resolution and the high photon yield of the HERA-B RICH, the ring fit method promises the most accurate determination of the Čerenkov radius. The performance suffers from rings with low significance (small number of photons or high background level), where it becomes more difficult to determine all ring parameters simultaneously. In the track-based algorithm, the ring center and the radius are fixed and, therefore, an efficient identification near the Čerenkov threshold is possible. It is worth noting that the performance of the HERA – B RICH, in particular the identification efficiency at high momenta and at high track densities, will benefit considerably from improvements in the alignment of the tracking system.

We illustrate the performance of a combination of the two identification methods on an example of the analysis of $D^0 \to \pi^+ K^-$ and $D^+ \to \pi^+\pi^+ K^-$ final states, where a clear charm signal can be observed (Fig. 81).

2.7.7 Plans for the Shut-down

Photon detector

In addition to the about 25 faulty PMTs, most of which are expected to be replaced by the

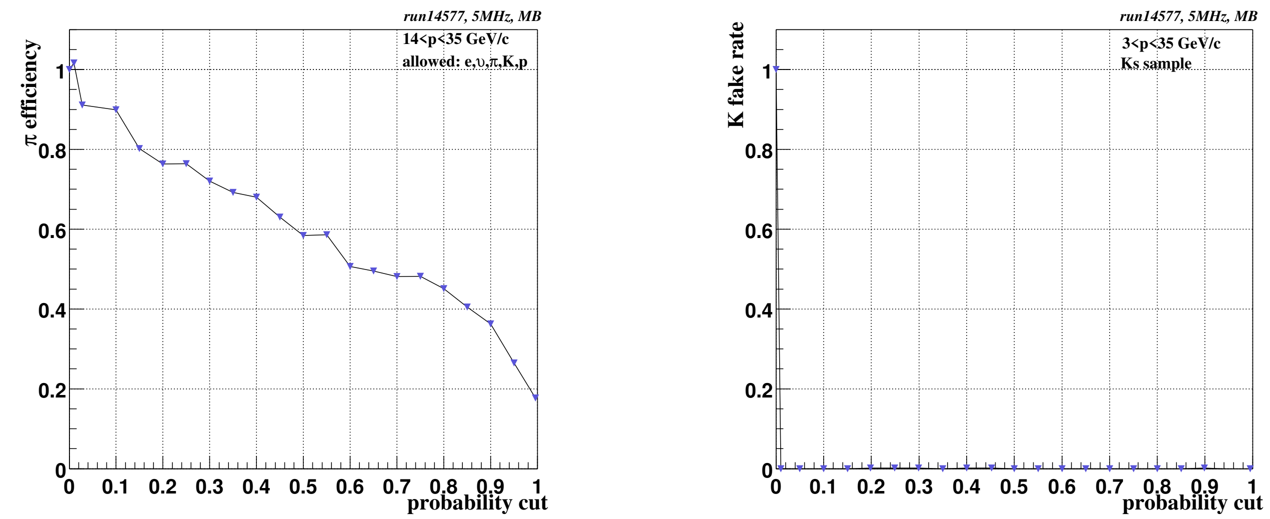

Figure 75: *Stand-alone identification efficiency as determined by using tracks from the K_S^0 decays in minimum bias events: probability that the particle was identified as a pion (left) or misidentified as a kaon (right), for pions with momentum between 14 and 35 GeV/c.*

,

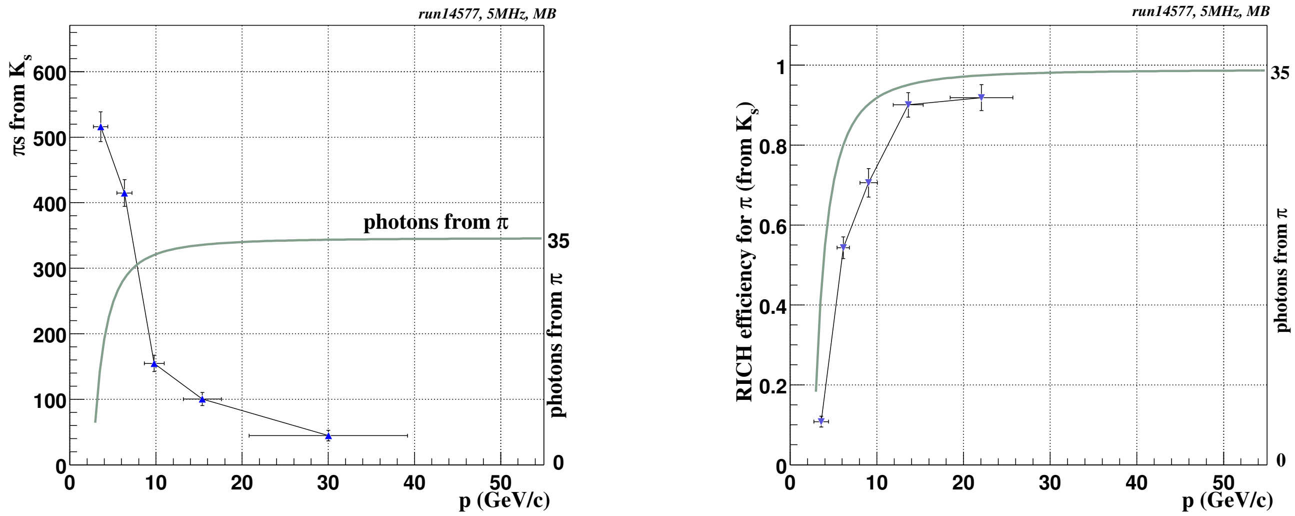

Figure 76: *a) Momentum distribution of pions from reconstructed $K_S^0 \to \pi^+\pi^-$ decays. b) Stand-alone identification efficiency as a function of momentum, as deduced from K_S^0 decays in minimum bias events.*

manufacturer, an additional set of 10 have been ordered. With these, we expect to fill all empty PMT slots on the detector, which will then remove most of the dead channels. We will have a few spare pieces left and do not foresee any danger, however, since our past experience shows that we have a vanishingly small PMT failure rate.

Gas system

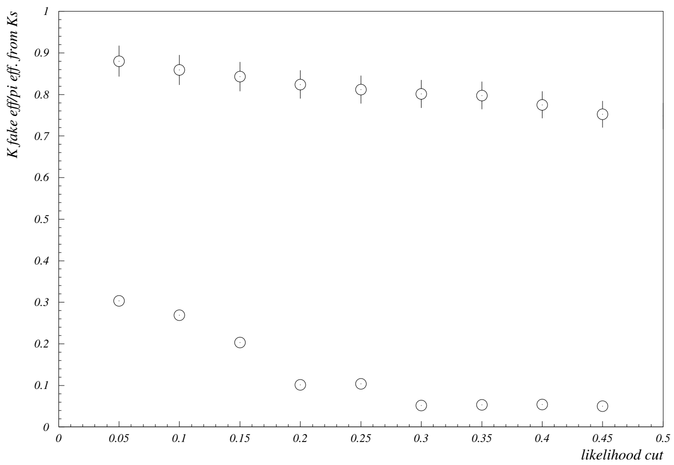

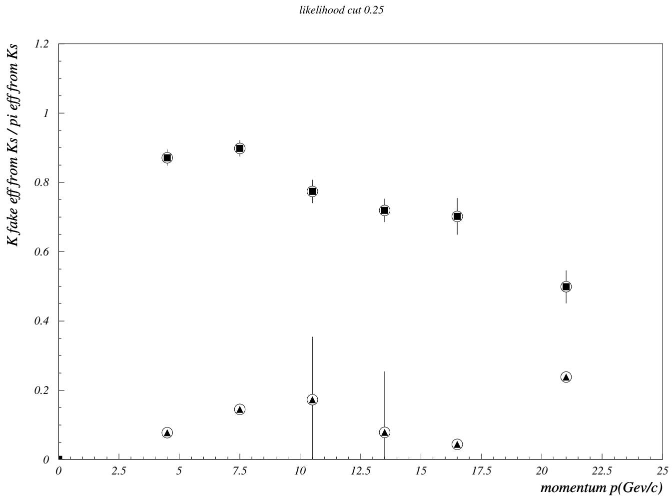

Figure 77: *Track based identification efficiency as deduced from* $K_S^0 \to \pi^+\pi^-$ *decays in minimum bias events. Above: probability that the particle was identified as a pion (open circles with error bars) and kaon (open circles) as a function of the likelihood cut. Below: momentum dependence of the efficiency (full circles) and fake probability (open circles with triangles) at a fixed likelihood cut of 0.25.*

A few upgrades to the RICH gas system have been suggested to improve operations. In fact, almost all expert interaction with the gas system could eventually be eliminated. Most of the operations difficulty with the gas system was due to the lack of C_4F_{10} reserve. However, it is clear that understanding the different flow rates of gas in the various stages of the system would make possible the automatic regulation of the manual valves, including the back-pressure regulator and the throttle valve.

Flow Sensor and Regulation: A measurement of the flow into the vessel is possibly interesting. However, since most flow sensors are force sensors, the mass of the medium changes the response. During changing mixtures, a reasonably priced sensor will give an ambiguous response. For stable mixtures, the relative response can be tuned. The total flow into the vessel can be regulated from

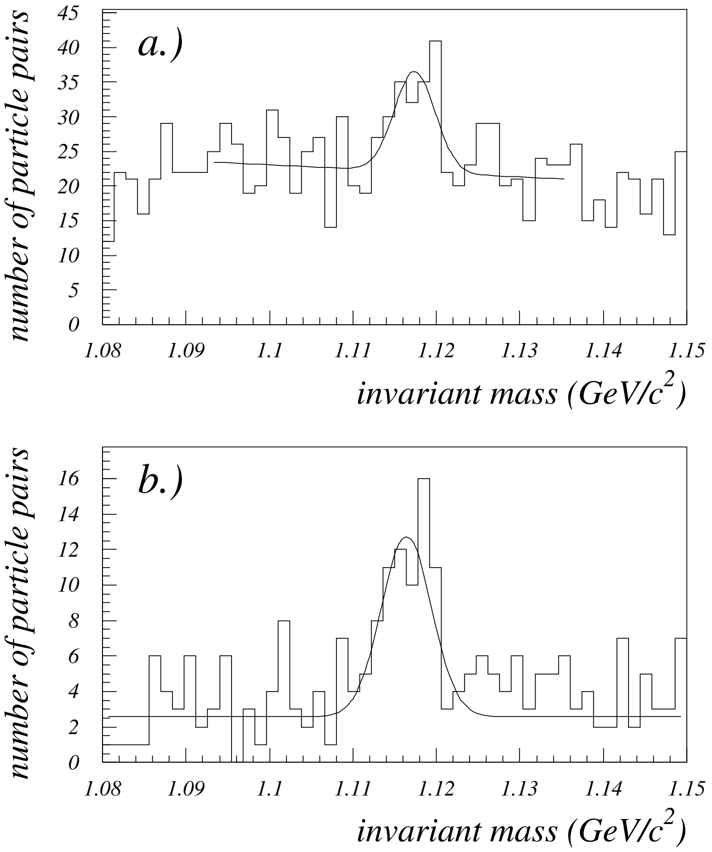

Figure 78: *Pion-proton invariant mass plot for tracks with detached vertices without and with a requirement that the positive particle is a proton and the negative one is a π.*

the process controller with the replacement of the manual throttle valve with an electronic stepping valve (valve body with stepping motor attachment). As input, the process controller will take the compressor speed and possibly check this against the measured flow rate.

Back-pressure Regulation: The total flow into the vessel is the combined flow of gas through the back-pressure regulator and the evaporated C_4F_{10} from the liquid buffer volume. The back pressure regulator may be fitted with a stepping motor and driven by the process controller based on pressure readout. Here we need only an appropriate stepping motor and a replacement of at least one analog manometer.

Distillation: One other possible upgrade would be to replace the heat exchangers in the distillation process. However, the current set up is clearly limited by temperature and not the efficiency of the heat exchangers. This would only be a viable upgrade if it can be shown that a different arrangement of heat exchangers would give the same or better distillation performance while making a better match to the power requirements of the installed cooling compressor.

To conclude we note that several possible upgrades exist. Certainly we should pursue those that can safely remove what little manual intervention is currently needed. Possible improvements to the distillation process should be critically studied.

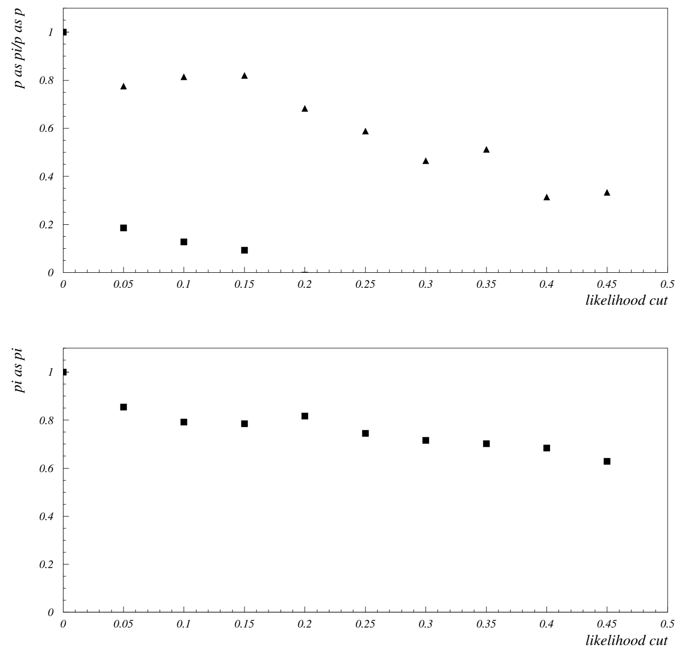

Figure 79: *Track based PID efficiency for the decay products of Λ in minimum bias events: positive particle identified as a proton (above, triangles) and pion (above, squares), and negative particle identified as a pion (below).*

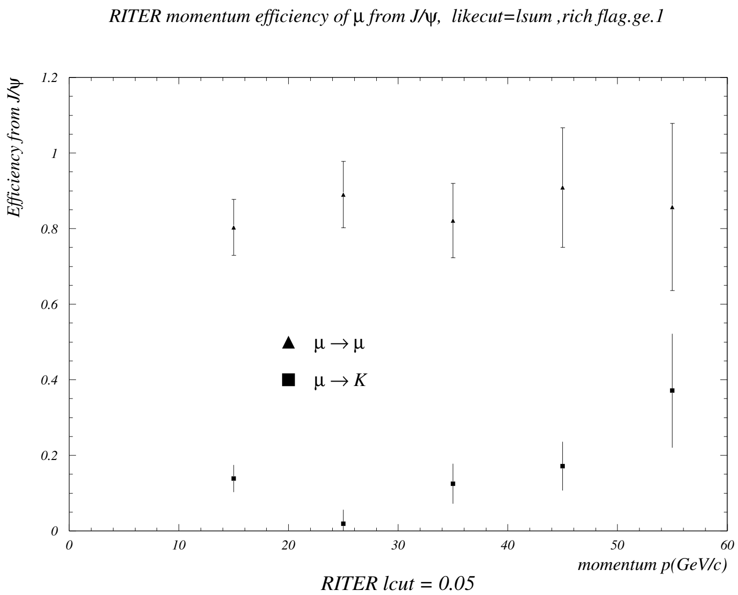

Figure 80: *Track based identification efficiency as deduced from $J/\psi \to \mu^+\mu^-$ decays in triggered data: a very preliminary result on the momentum dependence of the efficiency (triangles) and fake probability (squares) at a fixed likelihood cut of 0.05. Note that the highest momentum bin refers to all tracks above 50 GeV/c.*

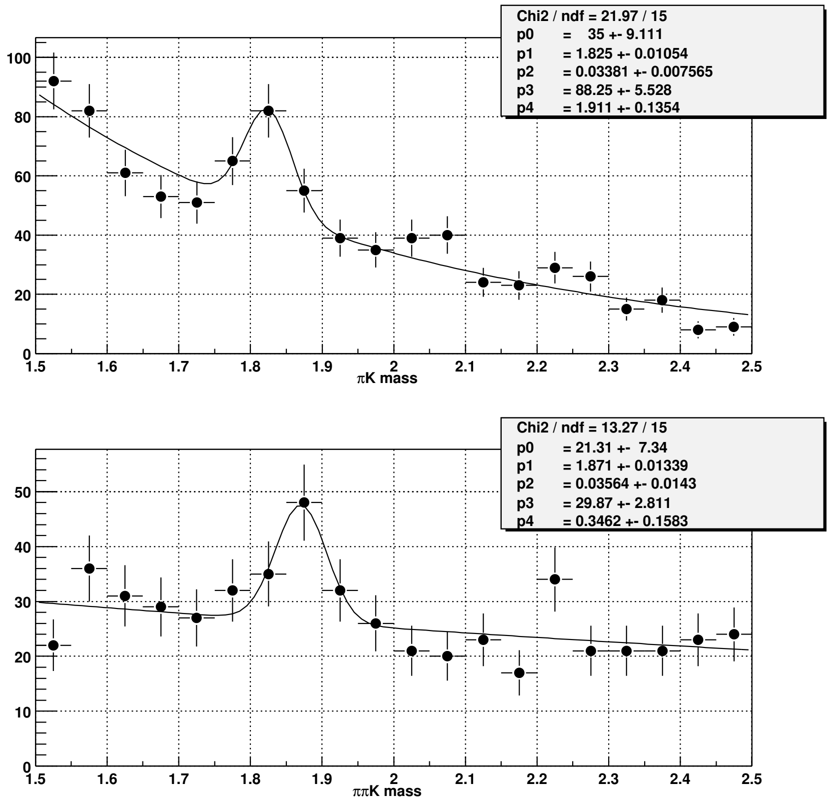

Figure 81: *Invariant mass distribution for π^+K^- (top) and $\pi^+\pi^+K^-$ (bottom). Tracks were required to have matched OTR and VDS segments, and to have a common vertex which should not be part of the primary vertex. The π/K identification was based on the higher likelihood value from both types of identification algorithms.*

2.8 Transition Radiation Detector

The Transition Radiation Detector (TRD) is part of the electron identification system of the HERA – B experiment. The major role of the TRD is the efficient detection of electrons and the rejection of hadrons at the level of less 10% in the inner region of the Electromagnetic Calorimeter where the angular density of secondaries and occupancies is very high.

The TRD has also good pattern recognition and tracking capability due to the multi-hit (15-20 hits/track) detection of each track, so called "continuous tracking". The pattern recognition of the electron track is very straight forward and efficient due to the detection of the TR X-ray energy deposition.

The main concept of the TRD is based on a fine grained structure [73] of the TR radiator (polypropylene fibers) and the sensitive elements (straw proportional tubes), where track position and transition photon measurements are taken. Good electron/hadron separation is possible in the energy interval of 1-2 GeV (threshold of TR) to about 100 GeV when hadrons start to radiate.

The hadron rejection by the TRD is achieved by counting the number of TR-hits, i.e. the hits with energy deposit more than E_{thr} inside the straw drift tubes, which are the main detecting element of the TRD.

For E_{thr} above a few KeV the hits from the hadron track originate mostly from energetic knock-on electrons, while for high momentum electron tracks a large proportion of such hits are produced via the absorption of TR photons in Xe with is the main component of the gas mixture.

The Transition Radiation Detector [74] consists of 2 super-layers with straw planes tilted by ∓ 30 degrees relative to the horizontal axes. Each super-layer contain 16 planes of straws interlayered with the radiator layers.

The radiator consists of polypropylene fibers with a diameter of 20 μm resulting in a total radiator thickness of 1.6 cm per layer. As beam test performed at DESY have shown, the efficiency of a radiator made from fibers is about 20% better than the efficiency of traditionally used transition radiators.

The active detector elements of the TRD are constructed from thin multilayer (Kapton + carbonload Kapton + Al) cylindrical drift tubes. Straws of two different lengths (65 and 135 cm) with a diameter of 6 mm are used. The detector is operated with a gas mixture of $Xe:CF_4:CO_2$ 70:20:10 at a gas gain of 2.5×10^4. This mixture combines the advantages of efficient TR-absorption with short total drift time and stability with respect to discharge [17]. The total drift time for 6 mm straws is 64 ns.

The straw Transition Radiation Detector concept has been developed during the last several years within the framework of the RD-6 program of the ATLAS experiment at LHC [75].

2.8.1 Status

The Transition Radiation Detector was installed in HERA – B during the summer of 1999 and tested during run 99 and run 00. The high voltage system has been implemented in the HERA – B slow control system. For the last two years, a temporary gas system using premixed gases was used.

Signal processing and readout electronics The front-end electronics of the TRD was developed on the basis of the ASDBLR front-end chip [76]. It is an 8 channel bipolar integrated circuit designed for use in straw - based tracking and Transition Radiation Detectors. It's specifications are:

- A shaping time of 8 *ns* at the discriminator level of inputs signal. Selectable ion tail cancelation for two gas options: fast gas mixture (tracking) and Xe-based gas mixture (TRD);
- The baseline restoration breaks the DC path with non linear (diode based) recovery elements. The recovery time is less than 90 ns for a 100 fC signal;
- Stable threshold operation at rates of up to 20 MHz. Low Level Discriminator (tracking) up to 20 fC (10 uA/fC), high Level (PID) Discriminator up to 200 fC (1 uA/fC);

The front-end electronics based on the ASDBLR chip are completely compatible with the HERA-B front end drivers and can provide different type of connections for particle identification and tracking modes.

The TRD connection to HERA – B readout system is via the standard Front End Drivers FED TDChit boards, where the the hit information is used for particle identification and tracking. Testing of the readout chain with a complete ASDBLR front-end, FED TDC with drift time measurement and standard connection to HERA – B DAQ, is now finished.

The current Fast Control System of the TRD is now the final version and connected to FCS HERA – B .

Slow Control of TRD is implemented in the Common HERA – B Slow Control System.

The critical point of the TRD is the production of the Front-End Drivers TDChitboards which is planned for the beginning of 2001.

2.8.2 Detector Performance

During the data taking periods 1999 and 2000 the TRD was tested with the available electronics in the common frame readout of HERA – B . In addition, an aging test was done on an alpha-beam (Karlsruhe).

Results of the aging test:

- No variation in the signal amplitude due to space charge effects up to rates of 4.5×10^5 per one cm of the anode wire, five times above the highest particle density at HERA – B .
- The anode wires have collected an integrated charge up to 2 C/cm, corresponding to three years of HERA – B TRD running. No aging or etching was observed.

The detector performance together with specially developed front-end electronics (base on ASDBLR) has been tested at the HERA – B spectrometer with target rates of up to 30 MHz.

Fig. 82 shows a TRD drift time spectrum measured at HERA – B . Fig. 83 shows the HERA bunch structure measured by the TRD and shows the synchronization of the TRD readout with the common DAQ. The structure of the HERA beam can be clearly seen in comparison with a random signals which was used for the trigger. Fig. 84 shows the stand-alone reconstruction of tracks in

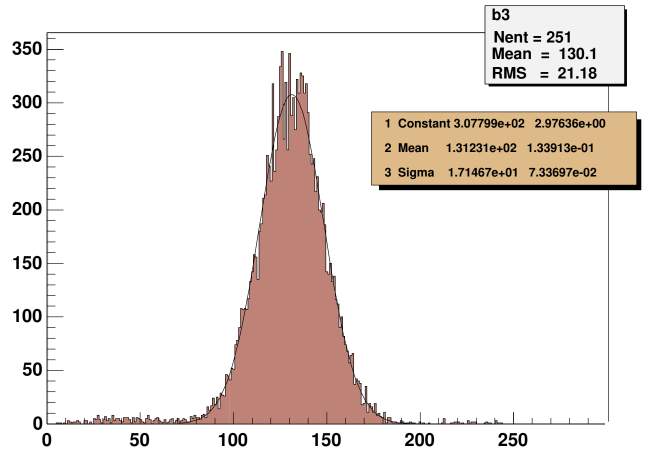

Figure 82: *Drift time spectra for TRD ASDBLR front-end electronics*

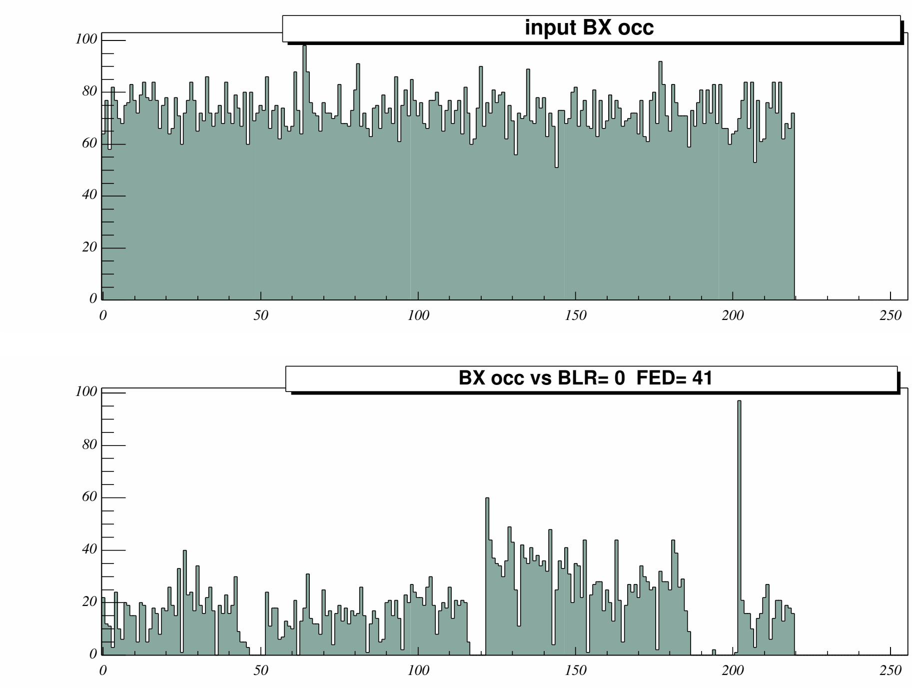

Figure 83: *Bunch structure of HERA as measured by the TRD in a minimum bias run*

TRD by using 5 layers of straws planes. This presents the reconstructed angle of tracks in the area of the TRD and shows the tracking capability of the TRD. Fig. 85 shows the correlations between ECAL reconstructed clusters and reconstructed tracks (planes)in the TRD. The plot shows the distance between the nearest ECAL clusters and planes reconstructed in the TRD. This plot shows the experimental data without alignment.

2.8.3 Shutdown Plans 2000-2001

- As mentioned above the main task of 2000-2001 shutdown is the production and installation of Front End Drivers based on TDChit boards, this will give the possibility of using the full scale

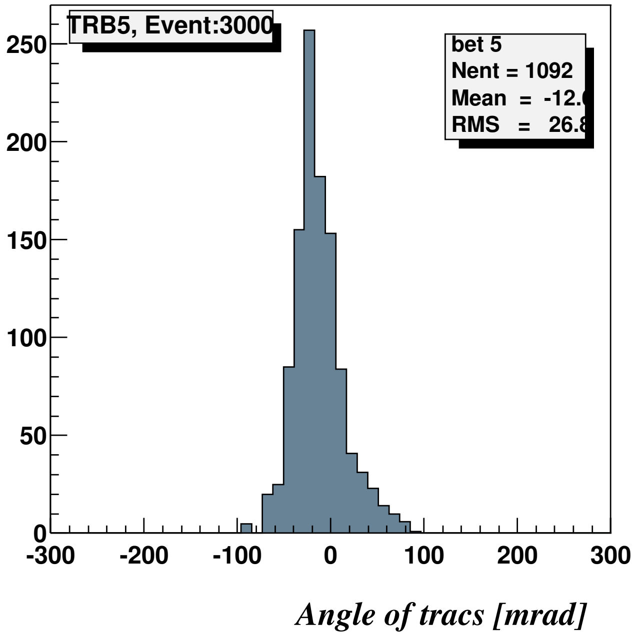

Figure 84: *Standalone reconstructed tracks direction of the TRD (5 layers)*

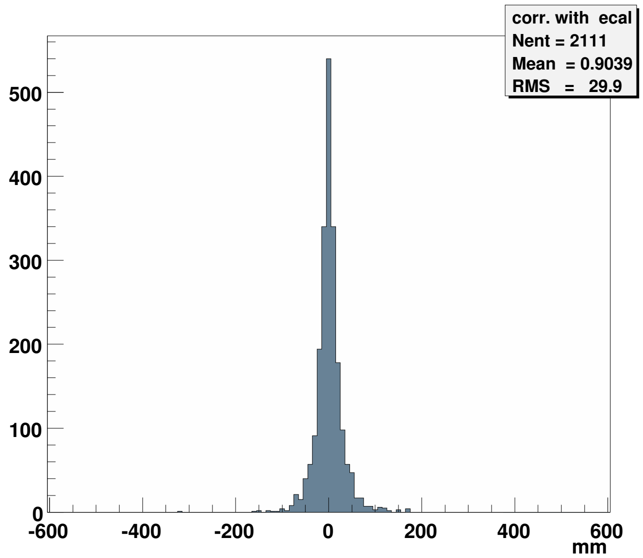

Figure 85: *Distance between clusters of the ECal and reconstructed track planes of the TRD*

TRD for particle identification and tracking in the inner area of HERA – B spectrometer.

- Assembling the closed loop gas system with purification element.
- Improvement of the reconstruction and particle identification software of the TRD.

2.9 Electromagnetic Calorimeter

2.9.1 General Remarks

The HERA – B Electromagnetic Calorimeter had been assembled in autumn 1997, and equipped with photomultipliers/bases, a test LED system and cabled during winter shut-down 1997/1998. At that time the installation of readout electronics also had been started. First data were taken in spring 1998, when HERA – B magnet was switched off. Initial calibration of R/O equipped part had been done assuming an azimuthal symmetry of ECAL occupancy. The first π^0 signal was observed soon and the measured invariant mass of π^0 peak was used for an absolute calibration of the calorimeter. With increasing statistics other particles decaying into γ 's were observed (like η and ω) also. During the year 1998 the installation of the pretrigger electronics started. Analyzing the data taken with ECAL pretrigger in 2-cluster mode with high E_T threshold (to match DAQ bandwidth) allowed to extract clear $J/\Psi \to e^+e^-$ signal [77]. In summer 2000 the installation of readout and pretrigger electronics had been completed and ECAL acceptance reached its designed value.

In the following sections the main problems observed during ECAL operation will be considered. Proposed solutions together with financial issues will be addressed in the upgrade/repair plan section.

2.9.2 Radiation Hardness

Materials chosen for the construction of the modules were tested for radiation damage up to doses corresponding to more than a year of HERA – B operation at full luminosity ($\sim 5Mrad$ at showermax position for those ECAL cells which are closest to the beam). Integrated luminosity collected during previous HERA – B operation now achieved $\sim 40\%$ of designed HERA – B annual dose. No radiation damage of the modules had been observed. As stated in [1], annual replacement of innermost ECAL modules had been foreseen, but for the moment there is no sign of necessity of such an operation. Moreover, in order to measure radiation damage in realistic HERA – B conditions, it seems reasonable to postpone the module replacement until 2001/2002 shut-down (see plans). Estimated light yield of the most damaged modules will not degrade more than $\sim 30\%$ which is acceptable from the point of view of ECAL performance (few percent degradation of energy and spatial resolution). In contrast to this, the active Cockroft-Walton showed significant radiation damage already after 25% of designed annual dose. The problem was traced to the damage of DAC chip MAX515CPA used for HV control. The solution of the problem had been found soon after occurring of the first base failures. It required the redesign and replacement of ECAL CW control boards located under ECAL and minor changes of existing CW bases (just removal of the chip, cabling was not changed). The corresponding upgrade of the innermost ECAL part had been done very quickly, so the problem practically had no influence on ECAL data quality. It was decided to upgrade the remaining part of Inner ECAL to the radiation hard version during the lumi shut-down (see plans). As Middle (and Outer) ECAL are concerned, the expected dose for bases there is small enough to leave the present design without modifications. Other components that are used for C-W base construction, proved to be radiation hard to survive at least one year of HERA – B operation at full luminosity. In order to have enough spare bases for the replacement and further improve radiation hardness, the production of new set of Inner bases (fully SMD based, compatible with old design) is foreseen.

2.9.3 Noise Problem

ECAL readout suffers from significant pick-up noise. The origin of the noise is still not fully understood, most probably there are several noise sources. The level of the noise is correlated with the operation of other power-consuming electronics located nearby to ECAL readout electronics at the electronic hut (like FLT crates). The distribution of the noise over ECAL clearly follows R/O board structure (or coaxial signal cable grouping done by the same scheme). Several measures taken like changing of R/O crates grounding scheme, improving input connector contacts and so on decreased the level of the noise, but further reduction of an order of magnitude is still needed. One should emphasize that the noise is seen by readout ADC's due to the 50-Ohm termination of signal cables from both sides. There is a possibility to redistribute noise and decrease its level at ADC input by increasing the output impedance of PM bases. This solution was tested for different PM types used in HERA – B ECAL as well as AC coupling for bases with preamplifiers. Simultaneously with noise reduction it leads to increasing of the signal amplitude by a factor of 2 that further improves signal-to-noise ratio. The drawback of such a solution are base line shifts caused by signals from previous bunch crossings (at level of 1 % of previous BX signal amplitude). In turn it leads to an average base line shift which is automatically taken into account by ADC pedestal measurements simultaneously with data taking and variations of the base line due to short term "memory" of 40 meter coaxial cables (4 previous BX's). It is equivalent to a pile-up with ~ 0.2 "smoothed" interactions in addition to an average of 4 interactions per BX at HERA – B , which seems to be negligible. Nevertheless a detailed MC study of such an effect is foreseen.

2.9.4 Readout Electronics

During the last period of data taking the remaining part of the Outer ECAL readout and pretrigger boards have been installed. The whole readout and pretrigger system is now completed and the shutdown period will be focused on the improvement of performances of the two systems based on the past experience. Main efforts will concentrate on the noise reduction and improvement of the reliability of data transmission both to pretrigger and to *SHARC* 's.

Analog circuits:

As it was discussed above the planned modification of the bases will cause an increase of the analog signals by a factor of 2. The gain of amplifiers on the readout boards side should accordingly been decreased to keep the optimal PM dynamic range. This implies the modification of few components in the analog cards sitting in the readout boards. Analog cards with nonlinear transfer function (HAMAMATSU region) will be replaced with linear ADC cards that show better signal/noise performance.

Digital part:

Data transmission from Readout boards to *SHARC* boards came out to be a very critical point due mainly to the connector being used. We have already a design of an interface piggy back to be mounted on the existing connector on the readout board. The connection should be more stable since we will use standard flat cable connectors. The mechanics of the interface is such to minimize problems coming out by the added connection.

2.9.5 Slow Control

Presently ECAL slow control consists out of the following parts:

- PM HV control - allows to set, monitor and keep history of individual high voltage channels. Using LED pulses and feedback from DAQ, system is able to adjust HV of individual channels to get desirable PM gain variation. The system includes a hardware protection against overcurrent for groups of bases. The status of HV protection and recovery procedure are software controlled.
- LED control system - to set any desirable pattern of LEDs to be fired by test pulse system and to vary the amplitude of LEDs pulses. At present the last option is not available due to frequent failures of the regulated voltage power supplies. A solution exists and will be implemented during shut-down.
- Test pulse system - to issue LED ignition pulses, FCS external triggers and test trigger pulses to ECAL readout / pretrigger. The First BX signal (prescaled and delayed) is used to initiate the sequence. Prescale factor, individual delays, enable/disable of pulses are software controlled. Being connected to ECAL trigger inhibit system allows also to inhibit pretriggers during particular bunch crossings. The last option is not tested yet.
- Crate control - the part of common HERA – B crate control system. Requires some minor modifications - in particular moving of control software from VME computer sitting in the crate controlled by this software.

In addition there is a set of various tools for different test purposes. Most of them are using direct access to ECAL electronics via VME, alternative to the main data taking path.

Two additional systems are going to be built:

- Low Voltage control system to monitor ECAL LV status directly. There are two options: to built the system based on old VME-based multichannel ADC available at Bologna group, or built a new one based on commercial slow control ADC's.
- Timing Control System (TCS) to monitor the adjustment of FCS and test pulse system timing. Because of many common features of TCS for different subdetectors its design should be done in a centralized way.

2.9.6 Calibration

Up to now the calibration of the calorimeter is based on information provided by ECAL itself [78]. Basic assumption is that the occupancy in minimum bias data is a smooth function of ECAL coordinates. Absolute calibration is done using the measured position of π^0 peak in two-cluster invariant mass spectrum. Having enough statistics the calibration of individual ECAL cells using π^0 method becomes possible. To provide such a statistics, a so-called on-line calibration method [79] is used - information is processed at the 2-nd Level Processing where rates of several kHz are available. Usually statistics of about several tens of millions events is collected in 2-3 hours of HERA – B operation. In this case the precision of the calibration is estimated to be about $2-3\%$. Few months ago an improved version was implemented - now calibration data are collected at the 2-nd Level continuously during any data taking using ECAL, thus avoiding the loss of valuable beam time for special ECAL calibration runs.

A complementary calibration method using E/P information (cluster energy, measured by ECAL is compared with matching track momentum and electron peak is searched) from runs with Outer Tracker was developed recently. It works at the 4-th Level Farm, where OTR reconstructed tracks are available. Results are promising, but require more detailed study, both on Monte-Carlo and real data.

Another method is under development - calibration using MIP signals - which also works at the 4-th Level Farm. This method is expected to be rather fast but is very sensitive to the actual noise level. Therefore is was not used up to now.

2.9.7 Monitoring

The operation of the calorimeter is monitored at several levels [78]. There is a special monitoring node at the 2-nd Level, where the ECAL response to LED pulses + randomly triggered data are analyzed. This level periodically provides an information concerning pedestals and status of individual ECAL channels being used for control, data reconstruction and trigger programming. Information at the 4-th Level is controlled by the global Data Quality control system. The experience of the last year showed that the system is reliable and convenient. Upgrade wish is to replace 2-nd Level monitoring node (hb-cr17) with double-processor computer like 4-LT nodes - it will improve the performance by a factor of 2.

2.9.8 Performance

Data collected during HERA − B operation are still under processing. Results presented in this paper could be considered as an example to illustrate ECAL performance. They are based on the analysis of about 1.2 million of events. The used set-up included about 80% of the Inner and Middle sections of ECAL instrumented with readout electronics. About 10% of ECAL pretrigger boards were installed. Trigger conditions were the following: at least one ECAL cell with a transverse energy E_T greater than 1 GeV in the equipped pretrigger region and at least two clusters on ECAL with $E_T \geq 1.1\ GeV$ and with invariant mass above 2.2 GeV/c^2.

The two-cluster invariant mass distribution is shown in the Fig. 86, where each cluster had E_T above 0.3 GeV. A clear π^0 peak with the width of $\sigma(m)/m \sim 7\%$ is seen.

When events with two clusters with $E_T \geq 0.6\ GeV$ are selected (Fig. 87, additional cuts are: distance between clusters above 4 ECAL cells, E_T of clusters pair is above 2 GeV), a very clear η peak can be seen. In this case the mass resolution is about $\sigma(m)/m \sim 5\%$ which is better than for π^0 as expected.

Fitting the π^0 mass peak allowed to extract information on energy (Fig. 88) and position resolutions. As shown in [80] energy resolution was estimated to be $\sigma(E)/E = (22.5 \pm 0.5)\%/\sqrt{E} \bigoplus (1.7 \pm 0.3)\%$ in the region $12 - 60\ GeV$ what is close to design values. Spatial resolution was estimated to be $\sigma_{x,y} = 0.2\ cm$ and linearity better than 0.5% in $12 - 80\ GeV$ range.

It should be mentioned that the above analysis was done for an ECAL region with relatively low noise level. It provides the confidence that ECAL performance can achieve designed values after the reduction of noise.

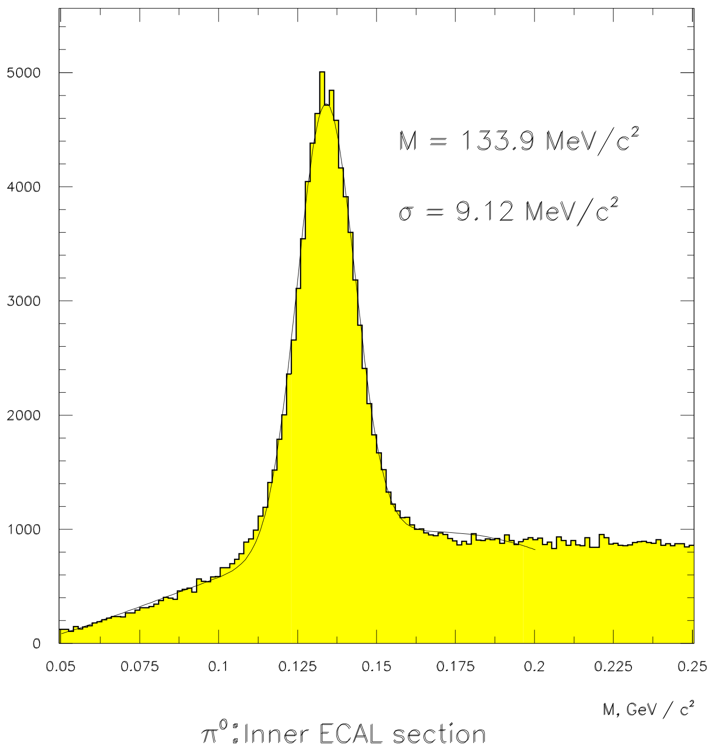

Figure 86: π^0 *signal in two-cluster invariant mass spectrum, Inner ECAL.*

2.9.9 Upgrade/Repair Plans

Innermost ECAL modules:

The module replacement procedure had been described in [1], but had never been tested in reality. Important is to prove such a procedure even if there is no actual need to replace working modules. The plan is to take out one of the innermost modules and temporary replace it with a dummy module (to be made). The irradiated module together with a new module will be tested at DESY test beam with the same set of photomultipliers in order to measure directly the effect of radiation damage. Test includes light yield measurement, transverse and longitudinal scan and energy scan to get energy resolution. After beam tests the module will be installed back to ECAL.

Test beam will be available at the second week of January 2001, requested beam time - 1 week, manpower - 2 people (taken into account in visits plan).

For the module replacement in future (16 Inner modules equipped with HAMAMATSU PMs) we are planning to produce necessary module components during lumi shutdown. Production of spare scintillator tiles had been started at Moscow (should be covered by ITEP financing), KURARAY WLS fibres had been ordered in the beginning of June 2000 (cost is 8.3 kDM, reserved in ECAL financial plan). Reassembly of the modules may require the production of some additional tools,

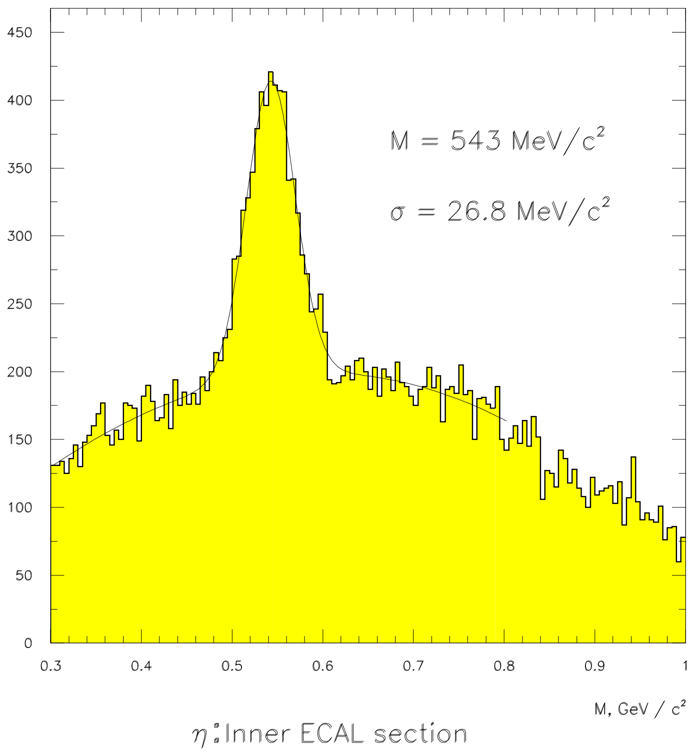

Figure 87: *Inner ECAL, two-cluster invariant mass at η mass region.*

that is mainly foreseen to be done at ITEP, but some reserve at DESY (about 5 kDM) would be necessary for year 2001.

Upgrade of Inner HV system:

As it was observed earlier, the DAC chip MAX515 used for the HV control at Cockroft-Walton bases proved to be not radiation hard. Innermost section of ECAL (HAMAMATSU equipped region) was upgraded last year to a new control scheme with remote voltage control. These scheme had been proven during last months experience. To provide safe and stable operation of ECAL in future, it is necessary to upgrade the rest of Inner ECAL to a new control scheme. 20 control boards and 70 on-module distributor PCB's are produced, components had been ordered and partly arrived. Last delivery (quad DAC chips MAX5250) is expected by December 2000.

Total cost of such a production is 20 kDM, money reserved and partially spent.

Low voltage power supplies, misc.:

The purchase of 3 LV power supplies (type EWS-300-6) had been foreseen. Ordered in June, received in August. Cost - 3 kDM. Front panels and cable support for C-W distributors should be produced and installed. Estimated cost - 2.5 kDM

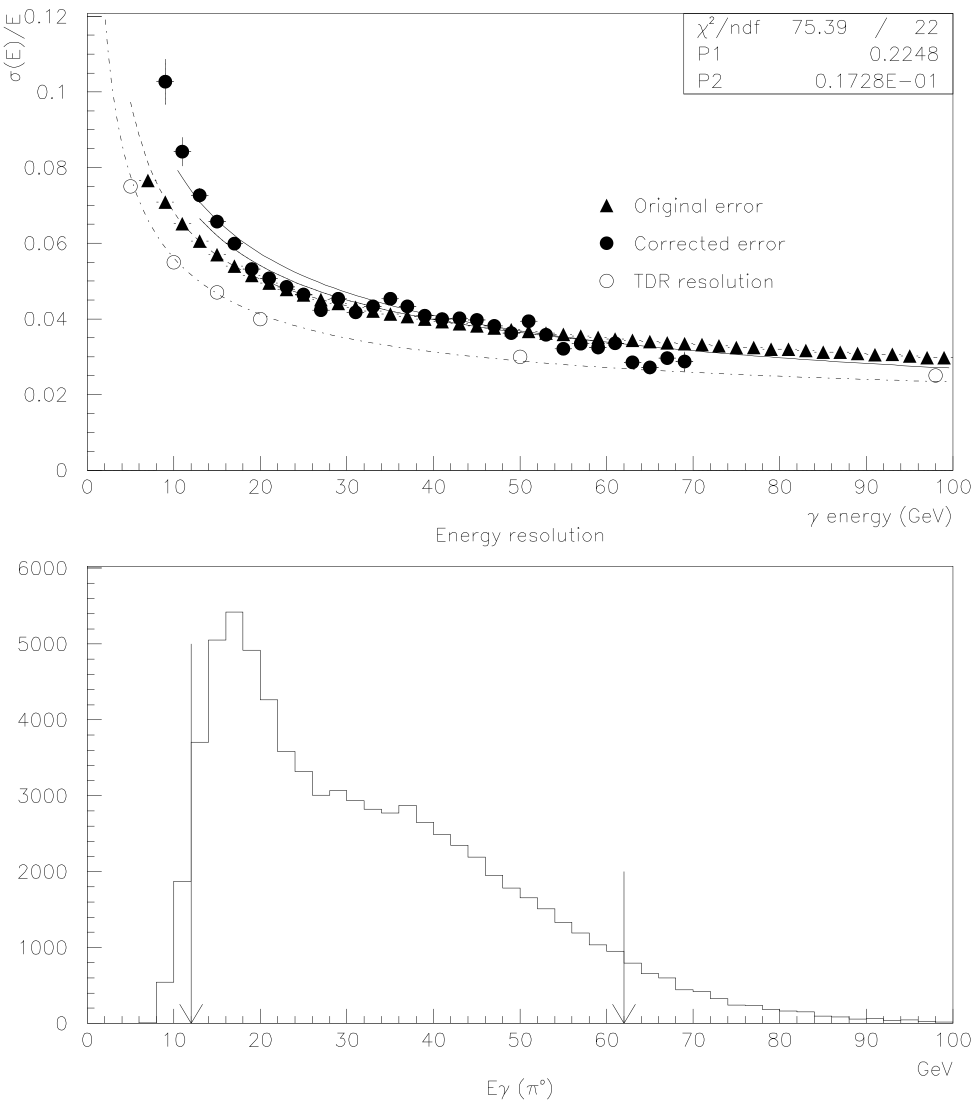

Figure 88: *Inner ECAL energy resolution.*

Replacement/repair of cables:

During last year some control cables were damaged and need to be repaired. In addition some of twisted-pair control cables for the Inner ECAL are of the old type and need to be replaced by standard cables. To improve the reliability of HV control and provide better ground connection between ECAL channels the replacement of Middle/Outer chip-select cables is also foreseen. Overall cost of cables/connectors estimated to be 5 kDM. Will be ordered soon (delivery estimated to be fast).

Modification of CW bases (noise reduction):

At present ECAL suffers from significant noise. In addition to improvement of grounding scheme (isolation between R/O crates and racks, disconnecting extra power grounding), the modification of all CW bases (6000 pieces) is foreseen. For Innner FEU-68 bases AC coupling together with decreasing of output impedance should significantly reduce the noise and increase 2 times signal amplitude. For Middle/Outer FEU-84 simple exchange of 1 resistor per base (50 Ohm to 1 KOhm) should give the same result. Complementary modification of input ADC circuits at the R/O boards will decrease the noise factor of 2 in addition. Unfortunately the final test of proposed changes had not been done (FCS system is not able to acquire consecutive triggers), so the solution is based only on calculations and LED signal measurements.

Cost of components - negligible. Manpower - at the low limit (1 technician for 5 months)

Production of spare Inner CW bases:

In order to improve the reliability of the system it was decided to produce a spare set of inner CW bases (upgraded version, fully compatible with the present one). PCB design is almost finished, ordering of components is in progress. Main problem - very long delivery time (for example chip capacitors could be delivered by SIEMENS only in 15 months !). Cost estimate 65 kDM, manpower also at the low limit.

Table 29: *ECAL request for lumi shut-down.*

Item	Cost	Status
WLS fibres	8.5 kDM	ordered
Tools	5 kDM	reserve
Inner HV upgrade	20 kDM	partially ready
Spare power supplies	3 kDM	received
Front panels etc.	2.5 kDM	not ready
Cable replacement	5 kDM	not ready
New HV bases	65 kDM	ordering started
Total:	109 kDM	

Readout Electronics:

Upgrade of Readout Electronics includes modification of the analog ADC cards (change of amplifiers gain, see section 2.9.3), and improvement of R/O to $SHARC$ connection reliability.

FCS system:

One of the crucial point as far stability of operation is concerned is the necessity to monitor the stability of the gate delivered by the FCS system. For this aim we are going to build a slow control system based on standard VME TDC's. This system could come out to be of general interest also for other subsystems. We will discuss it with the collaboration.

High and Low Voltage monitor system:

One of the item not implemented in the actual slow control was the monitor of the status of the ECAL High- and Low- voltage system. We have already a design for this based on standard ADC

VME modules. We will implement it during the shutdown period.

Pretrigger rate monitor:

One of the most important figure of the stability of the pretrigger operation is the measurement of the rate of candidates delivered to the FLT. We are going to improve the already used system (based on obsolete VME scaler) with a new one based on commercially available VME scalers.

Energy Inhibit card:

It is already available a new version of the card that should represent the final version of this item . The card is under test but unfortunately we were not able to test it on beam. During the shutdown period we will work in order to have it available and properly working for the start of the run in the year 2001.

Funding and manpower:

The Bologna group is issuing a request to INFN to provide the money needed for the development and installation (with the associated manpower) of the last 5 of above mentioned items.

2.10 Muon System

2.10.1 Status of Muon System Hardware

The Muon system hardware is essentially complete.

All 342 tube chambers, 132 pad chambers, and 16 pixel chambers are installed and running in HERA – B. In addition, two spare pixel chambers exist, of the type used in super-layers 1, 2, and 3. Chamber operation has been smooth and reliable.

The chambers are supplied high voltage from a CAEN HV mainframe. The output channels of the unit are split to provide 522 separate HV cables to the detector. The high voltage is computer controlled using standard HERA – B software. Voltage ramp-up and ramp-down are performed automatically within the HERA – B DAQ framework. And, as done for several other systems in HERA – B, a beam-dump inhibit signal is generated when the HV is on.

The gas system has been in continuous operation since April. Gas pressures and flows are continuously monitored and alarms are produced when any of the parameters is outside the normal operating range. A few *accidental* tests of the monitor and alarm system were made while doing minor work on the system. Serious gas problems will trip a HV interlock, shutting down the chamber HV.

All readout electronics are installed and operating. The readout system consists of the front end readout (ASD-8 based cards mounted directly on the chambers), front end drivers (the first level buffer, located in special crates near the detector), and trigger link boards (located in the front end driver crates). In addition, the pad readout has pre-amplifiers to drive the signal from the pad through ~ 3 m of cable to the ASD card located at the end of the chamber, and pixel mapping boards to re-organize the trigger signals for the pixel chambers to the format required by the pretrigger and FLT. The Muon system has $15,232$ instrumented tube wires, $8,308$ instrumented cathode pads, and $5,304$ instrumented pixels, for a total of $28,844$ instrumented channels of which $11,020$ are used by the pretrigger, and $13,704$ are used by the FLT.

The trigger links are covered in the pretrigger and FLT sections.

The front end readout is based on the ASD-8 chip [81]. Uniquely in HERA – B, the Muon electronics is designed to provide separate threshold settings for each ASD-8 channel [82]. In principle, this allows for the optimization of each channel for maximum efficiency. Each threshold level is generated by digital-to-analog converter (DAC).

To control $28,844$ DAC channels, we use 72 embedded controllers to which we communicate via 8 RS485 serial links from a VME CPU. The controllers serve a dual purpose by locally monitoring the voltages, currents, and temperatures in the readout system. Both functions have worked out well. Though not used to the fullest extent possible, thresholds are adjusted individually to suppress non-functioning channels, and to quiet isolated noisy channels.

The front end drivers (FED's) are similar in design to those of the outer tracker, high-p_{T}, and RICH detectors. The front end drivers receive timing signals from the fast control system, and detector signals from the front end readout. Detector signals are assigned to the bunch crossing in which they are received, and buffered for up to 128 bunch crossings while awaiting a first level trigger decision. The signals are also routed via trigger links to the pretrigger and first level trigger system.

2.10.2 Performance and Running Experience

The muon detector has been in continuous operation since April 2000 when the recirculating gas system began operation. Detector operation is controlled by the shift crew.

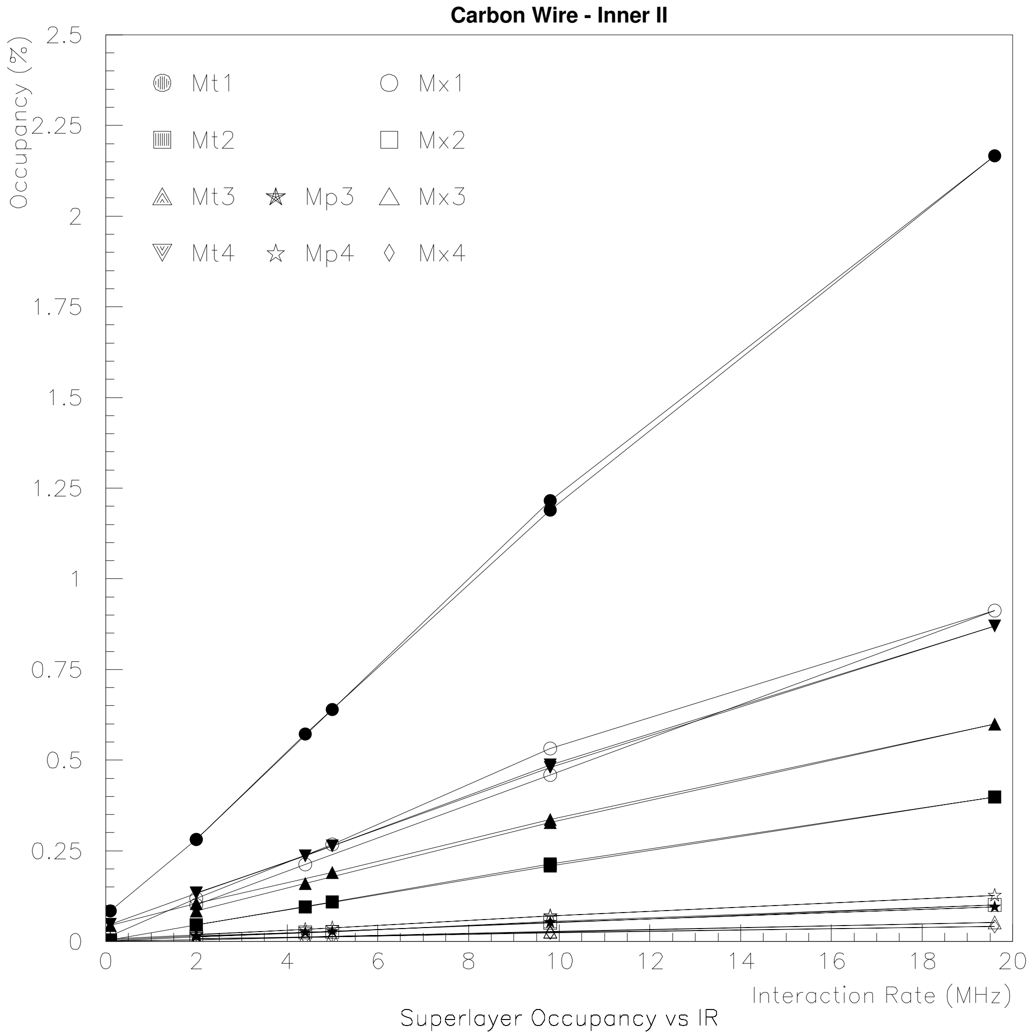

Figure 89: *Occupancies as a function of target rate for different parts of the Muon system.*

We made a number of checks of system performance. The occupancies and track rates are seen to scale linearly with target rate (Fig. 89). The small deviations from linearity are expected since we are using the target rate settings rather than the measured target rates.

The occupancy distributions are displayed in the compact set of plots in Figs. 90 and 91. Some observations on the occupancy distributions:

- There is evidence for backscattering into MU4, but, since augmenting the shielding behind MU4 in fall 1999, the amount doesn't pose any problems for detector operation or Physics.
- The highest occupancies are in MU1, as expected, and don't exceed 10% at 40 MHz target rate.

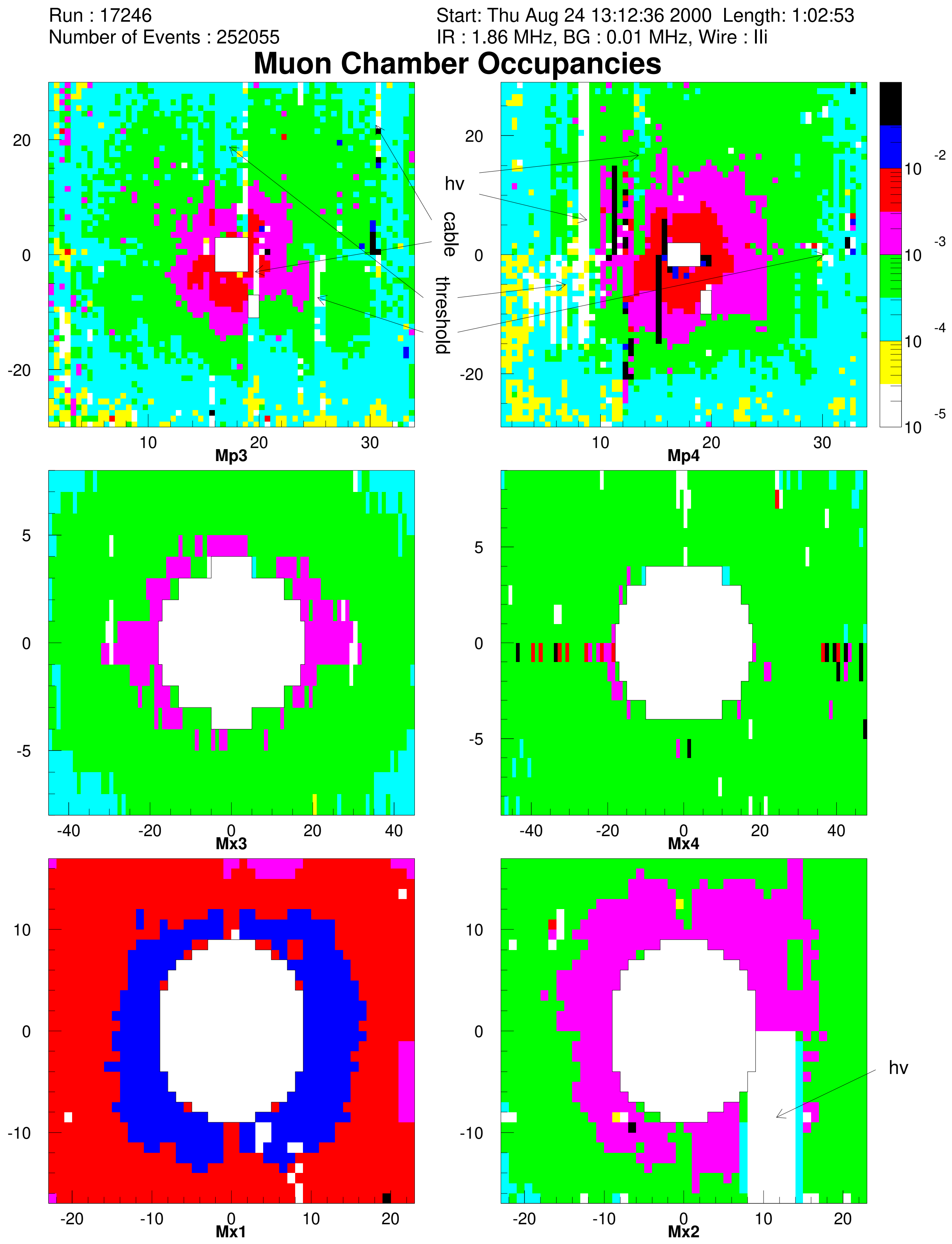

Figure 90: *Occupancies in the pad and pixel channels. The term "cable" refers to a suspected problem with a signal cable. "Threshold" refers to a high threshold value set to suppress noise and resulting in decreased readout efficiency. The term "hv" refers to a problem in applying the high voltage bias.*

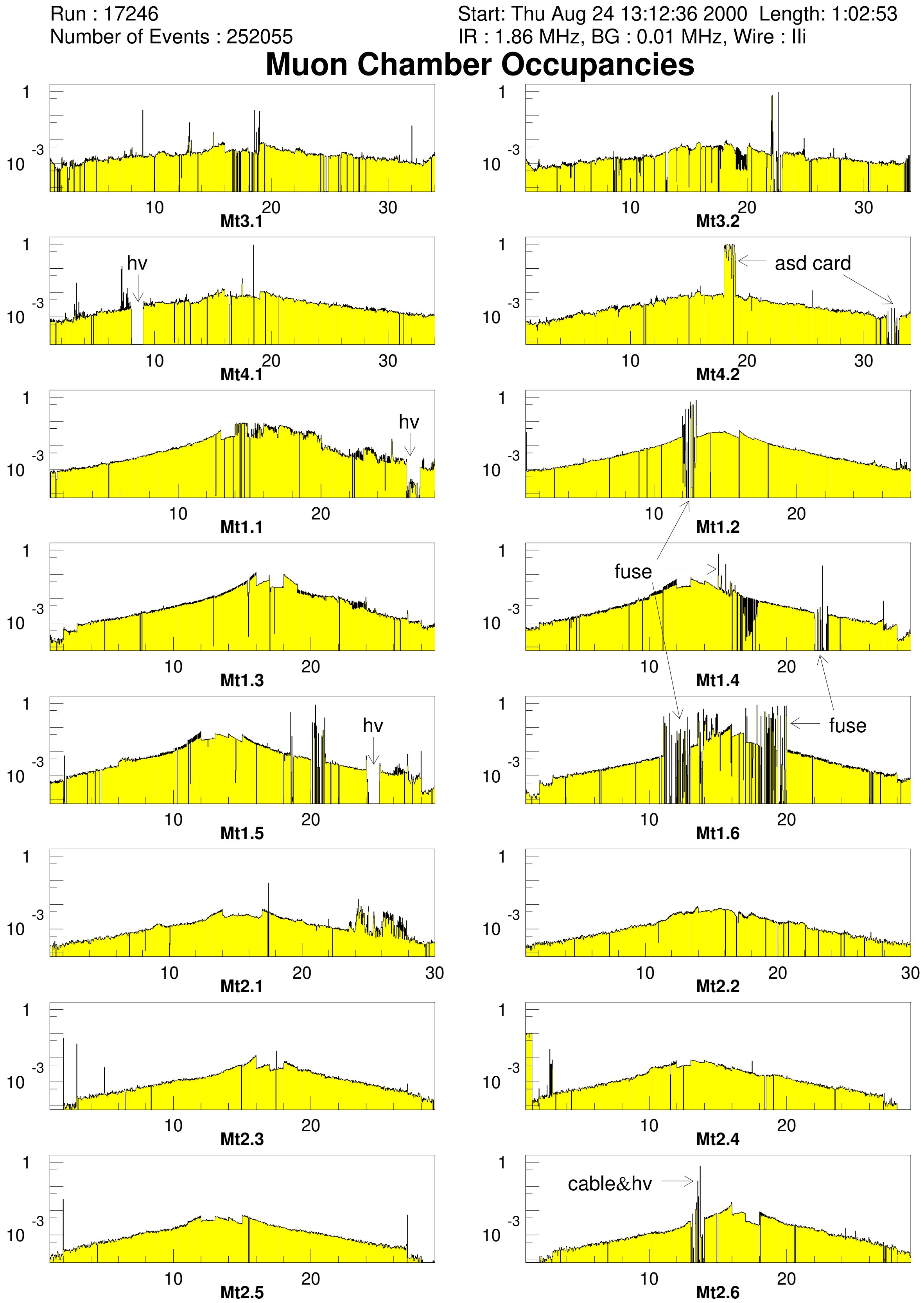

Figure 91: *Occupancies in the tube channels. The term "asd card" indicates that the thresholds could not be set on the asd card. "Fuse" means that a power fuse blew on a power distribution card which supplies the indicated chamber. The other terms are explained in the previous figure caption.*

Again, this isn't expected to pose any problems.

- The occupancy distributions are smooth, except for known chamber or readout problems, and across boundaries between chambers of different sizes.

The cause for each region of bad channels is indicated on the occupancy distribution plots of Figures 90 and 91. The types of problems, explained in the figure captions, will be repaired during the 2000-2001 shutdown.

The ultimate measure of system performance is the tracking efficiency, especially for high momentum muons. Unfortunately, a source of high momentum muons is not readily available, so we use the plentiful muons from π and K decays. These are less desirable because their momentum spectrum peaks near the threshold energy for muons. These low energy muons will suffer more from scattering effects, resulting in an underestimate of the efficiency.

Table 30: *Efficiencies measured for the Muon detector. Efficiencies for Monte Carlo data incorporating only geometric effects are shown for comparison to data, where available. "Single" means the single layer efficiency of a double layer chamber, and "double" means the double layer efficiency – pads are double layer only, and pixels are single layer only. Due to the tracking algorithm used, it was not possible to determine the double layer efficiency of the MU3 and MU4* 0° *wires. The efficiencies listed in the "all regions" include all regions of a layer and hence take into account the effect of non-working channels.*

region	MC data		real data good regions		real data all regions	
	single	double	single	double	single	double
MU1 0°	93.5%	99.8%	85.3%	96.6%		89.4%
MU1 +20°	92.2%	99.5%	85.4%	97.8%		95.0%
MU1 20°	92.1%	99.6%	84.8%	97.5%		76.2%
MU2 0°	91.5%	99.6%	82.5%	97.4%		97.3%
MU2 +20°	91.1%	99.3%	82.2%	98.3%		97.9%
MU2 −20°	91.1%	99.0%	84.2%	98.3%		95.5%
MU3 0°	89.6%		84.4%		83.2%	
MU4 0°	89.3%		84.0%		83.9%	
MU3 pads						75%
MU4 pads						68%
MU1 pixels			85%			
MU2 pixels			85%			
MU3 pixels			91%			
MU4 pixels			85%			

The efficiency measurements are displayed in Table 30. The tube chamber efficiencies are determined by modifying the stand-alone track finding code such that hits in a particular sub-layer are not required, then taking the ratio of tracks with hits in that sub-layer to the total number of tracks found (the tracks must extrapolate into or through the layer in question). Each tube sub-layer is composed of a double layer of tubes offset by half a cell, so we quote the efficiency for a single layer of tubes and the double layer, where a hit can be registered in either or both layers. The efficiencies in the tube chambers are lower in the data than in the Monte Carlo, especially the single layer efficiencies. This Monte Carlo incorporates only geometric effects (size of cell and aluminum walls in the chambers) and thus the difference with data is due to the intrinsic efficiency of the detector.

The calculation of the pad efficiency is a bit more difficult because the stand-alone tracking algorithm can't be used – the tracking algorithm starts from pad coincidences. A special algorithm was developed to determine the pad efficiency. Using hits in the $0°$ tube chambers, a MU1 hit is paired with all MU2 hits within an acceptance angle, designed to enhance the sample with good tracks with $p > 10\,\mathrm{GeV/c}$. The line formed by these hits is extrapolated to MU3 and MU4, and the residuals to nearby hits determined. If a MU3 (MU4) hit residual is less than 10 cm, then the smallest residual in MU4 (MU3) is histogrammed. A second histogram is made for the case that a pad hit is coincident with the wire hit. The resulting histograms have signal to background ranging from $10 : 1$ to $1 : 1$, so background subtraction is done using sidebands. Finally, the pad efficiency is calculated as the ratio of the wire + pad signal to the wire signal.

The pad efficiency numbers should be treated with some care. Although the statistical errors are a couple of percent, variations between runs with similar conditions are about 20%. These systematic variations are not understood; it is suggested that they may arise from the process of determining the background subtracted signal from the residual histograms. This question is currently under study. The cause of the low pad efficiency is discussed further below.

A preliminary calculation of the pixel efficiency is shown for completeness. These numbers are a first try at determining the pixel efficiency and the algorithm is still being tuned. The basic idea is to make use of the fact that small angle muons tend to have rather high momenta, so the tracks point back to the target. The calculation starts by forming clusters from hits in the pixel detectors. Then, starting from two super-layers, pairs of clusters that point back to the target are chosen. A cluster on a third super-layer is required to lie within 5 cm of the line to the target. The residuals of clusters in the remaining layer are histogrammed, and the number of entries in the signal peak is determined – background subtraction is important mostly for MU1. Finally, the efficiency is determined from the ratio of the signal entries to all the candidate lines with clusters in the other layers.

It is not understood why the measured pixel efficiencies are more than a few per cent lower than 100%. Additional data analysis is planned in which the inner tracker information will be used to confirm muon tracks. Also, a program is planned to measure the efficiencies of the pixel chambers in a test beam or with cosmic rays.

We made efficiency measurements in the test beam to benchmark the tube and pad chamber performance. Figure 92 shows the test beam results for the tube chamber efficiency using three different gas mixtures. Last year we operated the muon chambers with the $Ar/CF_4/CO_2$ gas mixture at a voltage of 2400 V.

In Fig. 93 we display measurements of the pad efficiency (circles) along with the tube efficiency for the corresponding conditions. Note that the pad readout efficiency lags the tube efficiency by about 150 V. This measurement lead to a decision in June to raise the operating voltage to 2450 V and eventually 2500 V. The immediate effect was a dramatic rise in the pad efficiencies and the first observation of a J/ψ mass peak in real time.

At the end of the year 2000 run, the preamp voltages were set to about 3.8 volts. Unfortunately, even at 2500 volt chamber bias, the operating point is just at the knee of the plateau curve. The result was that even for chambers with good values of ASD threshold (0.9 volts or below), the best readout efficiency was in the range 85% to 90%. In the subsequent section on Shutdown plans, we discuss ways to improve the efficiency.

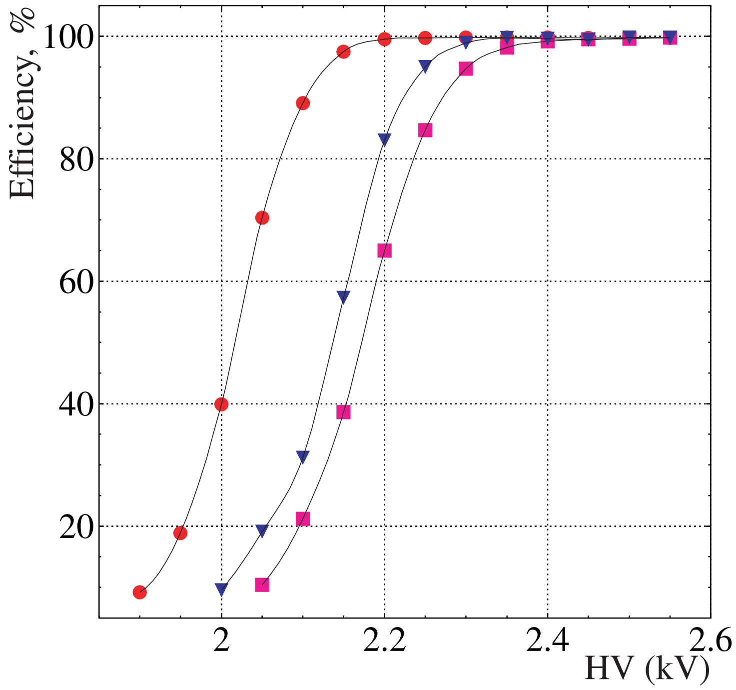

Figure 92: *Efficiency of a tube chamber double layer as a function of high voltage from test beam measurements. All measurements are taken with an ASD threshold of* 0.9 V *and a* 96 nsec *time window. The curves are for the gas mixtures Ar/CF$_4$/CH$_4$ (74:20:6) (circles), Ar/CF$_4$/CO$_2$ (65:30:5) (triangles), and Ar/CF$_4$/CH$_4$ (67:30:3) (squares).*

2.10.3 Chamber Aging Studies

Irradiation with a ^{106}Ru source showed that tube chambers filled with Ar/CF$_4$/CH$_4$ (67:30:3) and Ar/CF$_4$/CO$_2$ (65:30:5) mixtures are able to tolerate doses up to 2 C/cm per year without visible aging effects. Since it is not clear how to extrapolate aging results from small to large areas of irradiation, we have carried out the aging tests with large area tube chambers in the high-rate hadronic HERA – B environment.

We placed test chambers between the ECAL and the first muon absorber, where the particle flux is extremely high. The chambers were subdivided to allow groups of anode wires to be operated at different gas gains. Our results showed that aging in the case of the gas mixture Ar/CF$_4$/CH$_4$(67:30:3)+ 500 ppm H$_2$O depends on the gas amplification factor and area of irradiation. Electron microscopic analysis of irradiated anode wires operated at a gas gain of $\sim 10^5$ revealed deposits containing carbon and fluorine as the only detectable elements (hydrogen is not detectable). At the same time, irradiated wires operated at smaller gas gains of $\sim 2 \times 10^4$ showed no aging effects up to an accumulated charge of 0.8 C/cm.

Using the gas mixture Ar/CF$_4$/CO$_2$(65:30:5) + 1000 ppm H$_2$O no aging effects were observed up to a total charge of 0.8 C/cm when operated at gas gains up to $\sim 2 \times 10^5$. This is the gas mixture that we currently use.

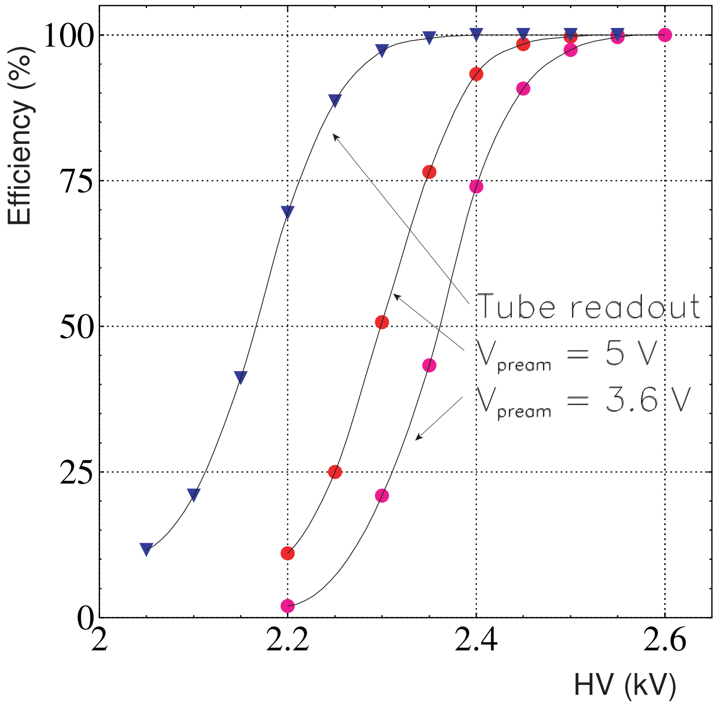

Figure 93: *Efficiency of the tube (triangles) and pad (circles) readout of a pad chamber as a function of high voltage from test beam measurements. The pad measurements are for a single layer, with a tube hit required in triggering. Data are shown with preamplifier bias of* 3.6 V *and* 5.0 V*. The ASD threshold is* 0.9 V *and the timing gate width is 400 ns.*

2.10.4 Shutdown Plans

The main goals during the shutdown are to improve the efficiency of the pad system, to repair chambers and readout electronics and to be ready for data taking in 2001.

One factor affecting the pad efficiency is illustrated in Figure 94 which shows the average ASD threshold for the half of each pad chamber closest to the beam (see [83]). Some chambers did not have an internal grounding modification (due to the tight time schedule for installation). These chambers are identified as “no pad ground” in the figure and were responsible for the bulk of the pad channels with high thresholds and hence low efficiency. During the 2000-2001 shutdown, these chambers will be modified.

Pad chambers with good threshold values, when operated at 2500 volts in the 2000 run, achieved efficiencies of about 85-90%. With the modification just mentioned, repair of some chambers and some other modifications under consideration (see below), the pad system as a whole should be able to operate with efficiencies of $\sim 90\%$ for the 2001 run.

One of the pad plateau curves shown in Figure 93 is for a pad preamp bias voltage of 5 volts. (In the 2000 run, a bias of 3.5 volts was used.) The higher electronic gain with 5 volts bias results in a plateau curve shifted to lower HV values and hence higher efficiency at a given HV value. It is currently not possible to operate the pad preamps beyond a bias of about 4 volts because the noise rate becomes too large. We are investigating ways to further reduce the noise. Preliminary

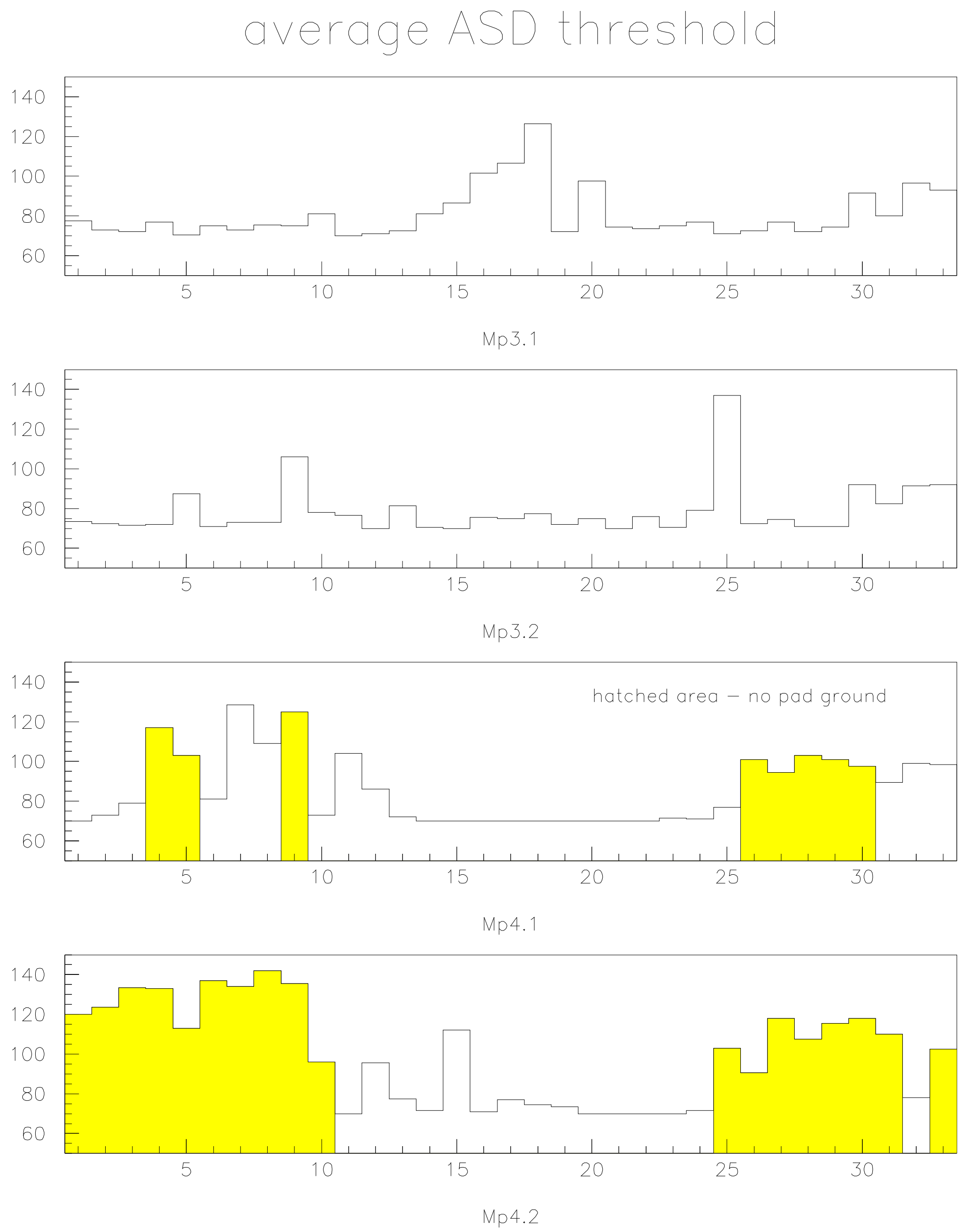

Figure 94: *Average per half chamber nearest the beam of ASD threshold in millivolts. Some chambers did not have an internal grounding modification (due to the tight time schedule for installation). These chambers are identified as "no pad ground" in the figure and were responsible for the bulk of the pad channels with high thresholds and hence low efficiency. During the 2000-2001 shutdown, these chambers will be modified.*

measurements with a single pad layer have identified some promising modifications which include

- installation of additional filter capacitors on the preamp power bus, and
- replacement of cable termination resistors on the ASD card with capacitors to better match the cable impedance.

Tests with full chambers will be necessary to assess the effectiveness of these modifications. Furthermore, it is not realistic to assume that all pad chambers could be removed, modified, and reinstalled before the tunnel closure in the summer of 2001.

Further improvement in efficiency is possible with chamber bias at 2550 volts. However, this is near to the minimum voltage for streamer formation of about 2600 volts. Safe maximum interaction rate would have to be determined for operation at 2550 volts.

A modification that could be implemented on a longer time scale is to replace the existing ASD readout cards with a modified design. The idea is to increase the shaping time of the amplifier used before the discriminator stage. The ASD-8 chip has a shaping time of about 6 ns, but the rise time of the pad pulse is about 25 ns. Thus, the ASD-8 responds to only a small fraction of the pad signal. An amplifier stage with a longer shaping time could operate at higher charge thresholds and lower noise compared to the ASD-8. Furthermore, the larger signal available at the input to the comparator would result in high efficiency.

To implement the replacement of ASD cards for the pad channels would require design of a new circuit, prototype testing, large scale production and installation in the West Hall. It is unlikely to replace all ASD cards before the tunnel closure in 2001 because all top pad chambers have to be dismounted be access the lower ones. The muon group will prepare a cost and time estimate.

The other items to work on are much more routine. We will repair some detectable gas leaks in pad chambers and make repairs to some chambers and components that are not easily accessible. Additionally, we have been asked to complete the removal of some foam material that fails to meet safety standards.

Some power distribution boxes on the MU1 frame are in inaccessible locations are will be moved. Also, we will consider using resettable fuses to reduce the recovery time time after a fuse trips. A few chambers with broken anode wires or other HV problems such as cables will be repaired.

The gas leaks that we want to repair are detectable, but not serious enough to interfere with the 2000 run. The necessary manpower is already arranged and a work schedule is being developed. The most serious problem is that the majority of the chambers that need to be removed are on the platform that will sit between the tram bridge and the West Hall crane shaft. We will probably have to arrange to access these chambers during weekends when crews are not at work.

Some aspects of the gas system need to be completed. Gas quality monitors will be installed. These are small drift tubes with readout to monitor the gas gain and purity. A gas purification system will be installed that is a small copy of the outer tracker system. The slow control software will be upgraded to allow for automatic adjustment of chamber HV bias to compensate for changes in atmospheric pressure.

Finally, we note that pixel chamber MX2 needs repair of one HV section and correction of a cable mapping problem for two cables. As mentioned earlier, work must be done to understand the efficiency of the pixel chambers.

3 The Trigger System: Status and Prospects

3.1 The First Level Trigger

3.1.1 Introduction

Trigger Scheme Since HERA − B had been designed to investigate CP violation in the B meson system using the decay $B^0 \rightarrow J/\psi\, K^0_S$, the trigger strategy of HERA − B aims to find J/ψ's using the First Level Trigger (FLT). The design specifications of the FLT are a suppression by a factor 200 at an efficiency of about 50 % [84].

The J/ψ candidate is selected by requiring two opposite charge electrons or muons having the appropriate mass of the J/ψ. First, muon and electron/positron candidates are identified by pretrigger systems. Afterwards the FLT determines the track parameters and by measuring their respective momentum and charge. Subsequently the di-lepton invariant mass is calculated.

In total there are three pretrigger systems working in parallel and independently. The MUON pretrigger uses hit information from the cathode pad chambers of the last two superlayers of the muon system. The pretrigger of the electromagnetic calorimeter (ECAL) uses the energy of group of cells, called "cluster energy". The third pretrigger type is not used to trigger on J/ψ's, but instead it is directed at finding hadrons with large transverse momentum. The High-p_T-pretrigger uses three layers of pad chambers located inside the magnet, it is considered as the first upgrade of HERA − B and only a preliminary commissioning was undertaken.

After track seeding by the pretriggers, the FLT traces the track opposite to its flight direction. The tracking procedure is region of interest (RoI) based, i.e. only a small part of a detector layer is probed by each search iteration (Fig. 95). The location and size of the RoI are determined by the previous tracking steps. So called Track Finding Units (TFUs) are the central part of the FLT. They decode messages, check for detector hits, extrapolate tracks and send the updated messages off to the following TFUs. With this method a very high data volume is processed at very high rates, see Fig. 96. It needs to be pointed out that the FLT tracking requires a hit in every trigger tracking layer; an electron, for example, has to be detected by 12 layers of four OTR superlayers.

Once tracks are reconstructed, their kinematical parameters and the invariant mass of track pairs are determined by the Track Parameter Unit (TPU) and the Trigger Decision Unit (TDU) respectively. The trigger decision is derived and is distributed by the Fast Control System (FCS), which initiates the transfer of the buffered data from the detector front end electronics to the higher level triggers. For several reviews and descriptions of the system see references [85, 86, 87, 88, 89].

Table 31: *Overview of the electronics boards for HERA − B 's hardware trigger.*

	Optical Links	Data Link	Logic Boards	Interface Boards
ECAL	n/a	n/a	128	9
MUON	600	40	40	20
hi-p_T	1100	80	40	8
FLT	3400	200	80	n/a

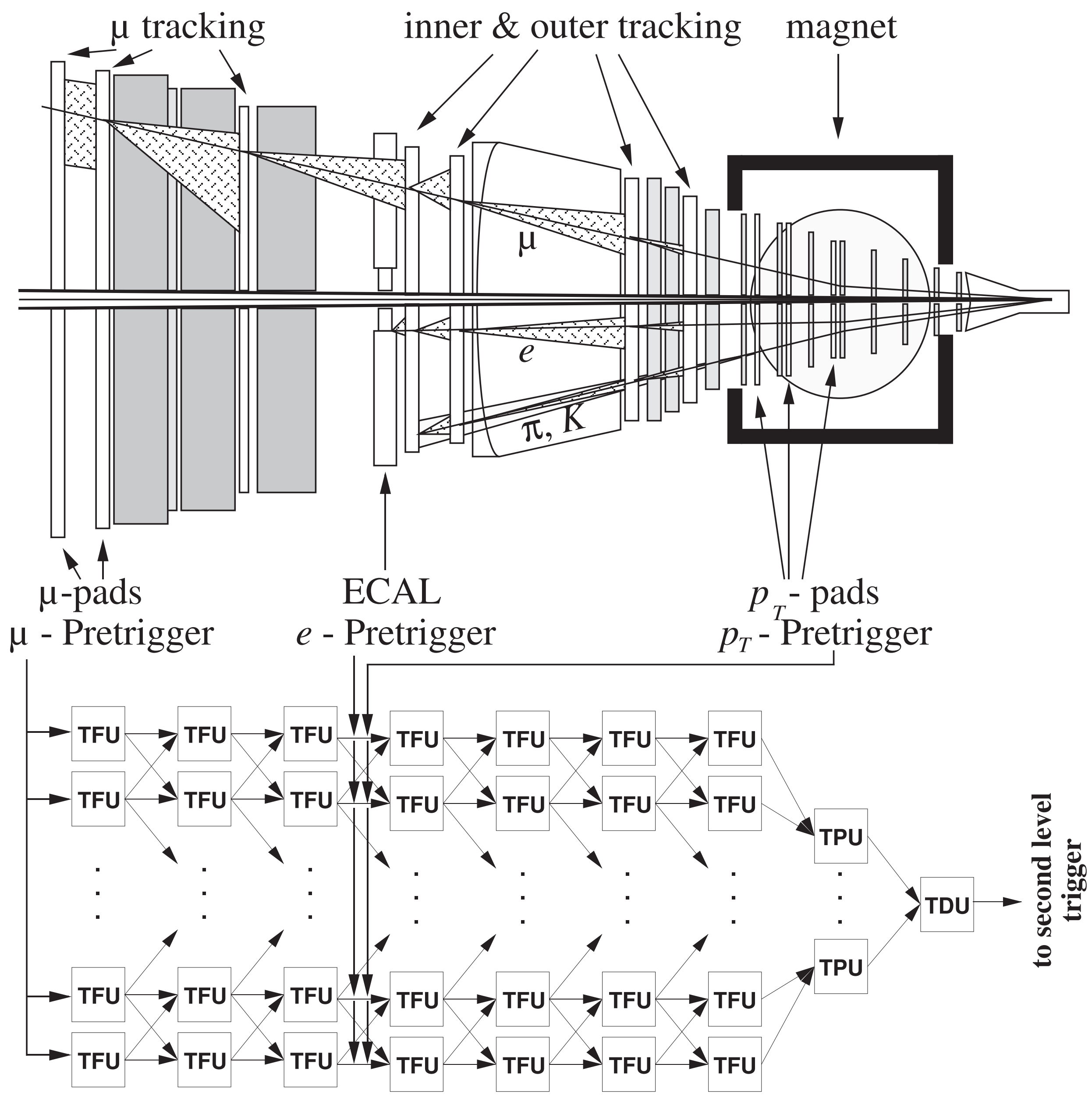

Figure 95: *The HERA – B detector and First Level Trigger. The interaction region is to the right.*

Prelude to this report The main accomplishments of the year 1999 were that the production of a sizable amount of hardware, see Table 31, was organized and successfully finished. In addition, the FLT group at DESY finally reached a size appropriate for the task at hand: the commissioning of the system. Several basic tests had been accomplished in 1999, for example it was shown that TFUs can be connected to tracking chambers and find hits as specified. A small network of TFUs had been installed it was shown that messages can be passed successfully [85].

What had to follow was an even more dearing and daunting task, the commissioning of the entire

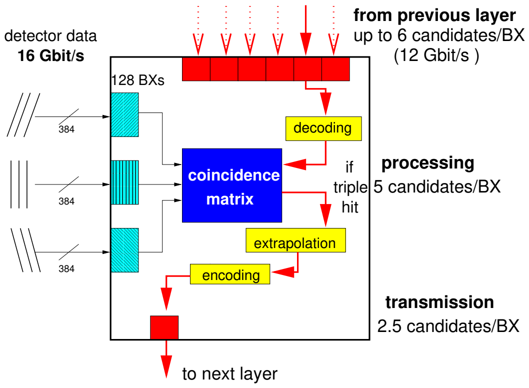

Figure 96: *The FLT Track Finding Unit.*

network. The control software had to reach a state that it would operate reliably and in conjunction with the HERA – B data acquisition software. In addition, a lot of time would need to be devoted to develop software tools that would allow to monitor and control a network of boards, and that would allow to debug the system if need would arise. Also, the MUON and ECAL pretrigger systems had to be integrated into the FLT operation. The trigger simulation needed to be advanced further. All those tasks were completed prior to the end of the 2000 run period.

Moreover a substantial amount of work of the FLT group went into the installation of the FLT Link Boards (FLT_LB)[38]and the debugging of the respective FLT data link to the OTR and MUON systems. The ECAL pretrigger simulation was developed and improved to understand the performance of the ECAL pretrigger. The following sections describe the main problems encountered and the current understanding of the system. Due to the fact that data taking only concluded very recently, the analysis of the extensive amount of data is ongoing. Consequently we would like to point out that more of the FLT behavior should be understood soon. The FLT section is followed by separate parts for the individual pretrigger systems.

3.1.2 Operation

ECAL pretrigger operation This subcomponent worked in stable conditions since the beginning of the year. Therefore initially, the FLT was used in the so called *transparent* mode: incoming messages were forwarded without any kind of data processing. The pretrigger messages were forwarded to the SLT after the TDU selected events based on the number of ECAL pretrigger candidates. This set-up required the basic functionality of six different electronics components:

- PECL [39] to LVDS [40] multiplexers
- LVDS to LVDS repeaters
- TFU LVDS message boards [90]
- TFU boards [92]
- TDU/TPU LVDS message boards [90]

[38] Also referred to as TLB – trigger link boards.
[39] Positive Emitted Coupled Logic.
[40] Low Voltage Differential Signal.

- TDU board

Fig. 97 shows the connection scheme: the PECL signals coming from the pretrigger were transformed in LVDS via PECL to LVDS multiplexers (2 inputs, 1 output). The LVDS signal was repeated by repeater fan-out so that the ECAL pretrigger output could be sent simultaneously to the different TC2 TFUs for the trigger tests and to the TDU for the "normal J/ψ production" mode.

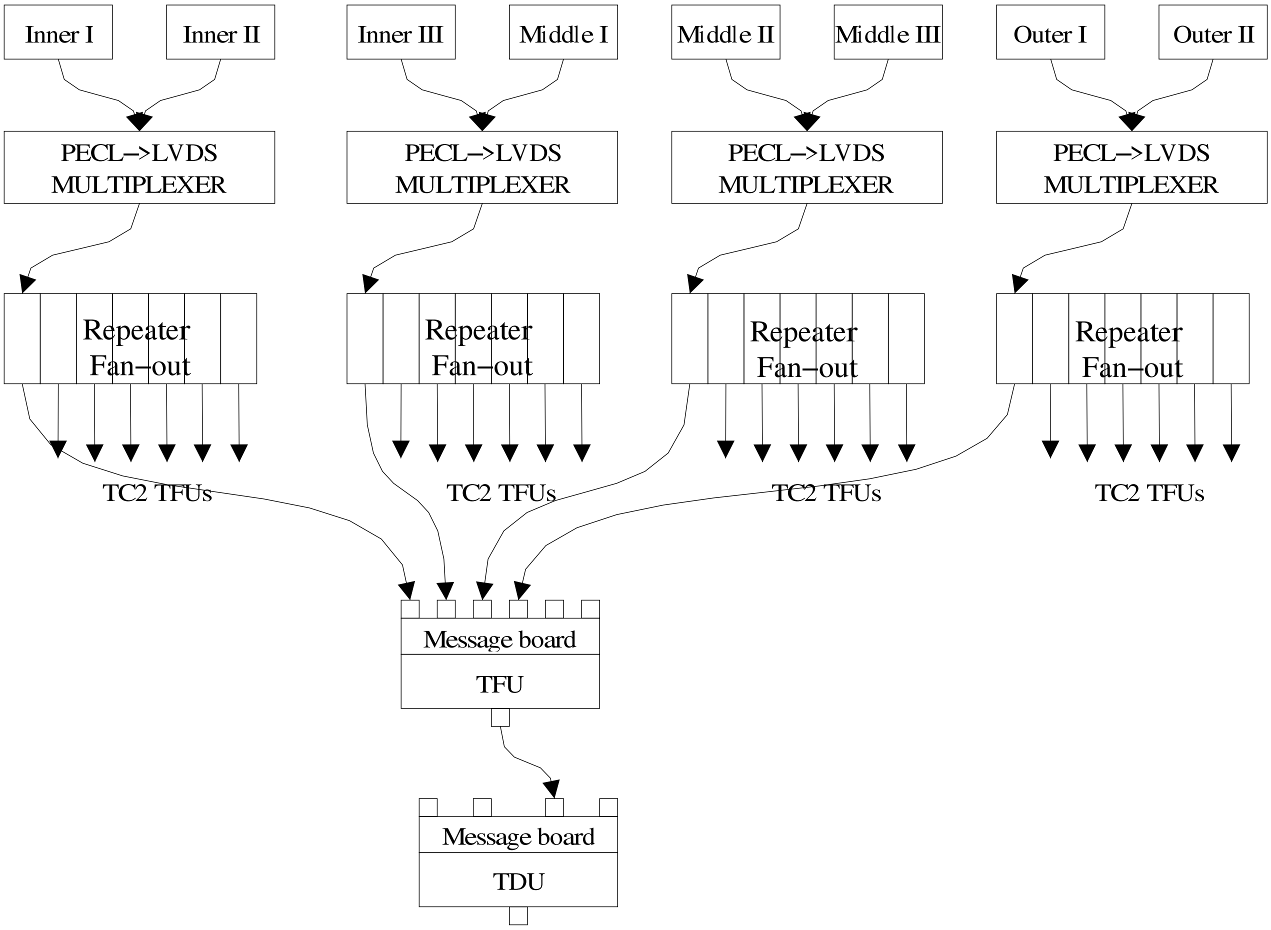

Figure 97: *ECAL pretrigger connection scheme.*

In the "normal J/ψ production" mode one transparent TFU was used to multiplex the messages coming from the four ECAL pretrigger crates. In this way only one TDU receiver was needed to collect all the ECAL pretrigger messages. The TDU was used to select events with two or more particles with the same identifier such that only this part of the pretrigger message was needed to be transferred properly, even if in principle the entire record could have been delivered [41].

The "normal J/ψ production" mode was used for several months that we could study the behavior of the electronics components. The following problems appeared:

1. It was discovered that when switching off the crates containing the multiplexers, the drivers of the pretrigger boards (ECAL, MUON and High-p_T) could be damaged due to an over-current

[41] Some information related to (X,Y) position were corrupted by the transparent TFU. Some studies were done to understand this unexpected behavior but no explanation is currently available.

passing through the cables. To solve this problem an interlock was introduced in order that all the pretrigger crates are also switched off if the multiplexer crate is.

2. The output of the multiplexer sometimes appeared corrupted. This problem was at first fixed by a hardware reset button which was added for this purpose. Later on modifications of the board firmware were applied and the behavior of these boards became stable.

3. The status of the repeaters is undefined when they are switched on. Even if most of the time they still transmit the data correctly, sometimes data are corrupted. This problem will probably be solved during the next shutdown introducing a software reset on the repeaters.

Bit error measurements were performed to study the behavior of the multiplexer-repeater chain. The procedure is the following: each pretrigger board sends a certain number of messages to one TFU via the multiplexer and the repeaters. The message is read from the message board and is compared with the incoming message. The bit differences are counted. For each pretrigger crate the measured bit error rate is less than $5 \cdot 10^{-7}$, which is acceptable with respect to the detector inefficiencies. The bit error measurements were constantly repeated during the run period and have shown a stable behavior of the chain. It is planned to introduce during the shutdown a quick connection test at boot time to check the connection status online.

The cabling between the pretrigger crates and the TFUs in TC2 was also done. In total 12 TFUs were connected to the pretrigger. Similar bit error measurements were performed for each TFU which confirmed the results described above.

MUON pretrigger operation The MUON pretrigger was also operated for a couple of months in stable conditions. With the experience acquired with the ECAL pretrigger, its connection was almost straightforward. Ten PECL to LVDS multiplexers, two transparent TFUs and several repeaters were necessary to forward the MUON pretrigger messages. The connection scheme is shown in Fig. 98. The repeaters were used, because the distance between the multiplexer and the TFUs was greater than two meters. This configuration was used for the "normal J/ψ production" mode as in the case of the ECAL. The X,Y information was needed by the SLT code, the transparent TFU was also used and tested to forward it [42].

A connection test between the MUON pretrigger and the concerned TFUs was performed many times during the run period. Also in this case the resulting bit error rate is less than $5 \cdot 10^{-7}$.

To switch between pretrigger mode and tracking with the TFU network, it was necessary to plug the output of the two TFUs covering the MU4 superlayer to the corresponding TFUs of the MU3 superlayer (see dashed lines in figure 98) so that in this case the TFUs used to forward the pretrigger messages to the TDU were the same TFUs used for the FLT tracking tests.

The TFU network The TFU network is obviously the most difficult part to operate. It consists of 55 TFUs (44 for OTR plus 11 for MUON), as many TFU message boards and a very large number of repeaters. The number of inter-TFU connections is about 140 and the number of optical links plugged to the front of the TFUs is about 1000. The final cabling was completed and tested around February 2000 even if small adjustments of the optical link cabling were done until the end of the run. Many efforts were spent to test the network. Three basic checks are described in the following:

[42] In case of the MUON pretrigger the information never appeared to be corrupted.

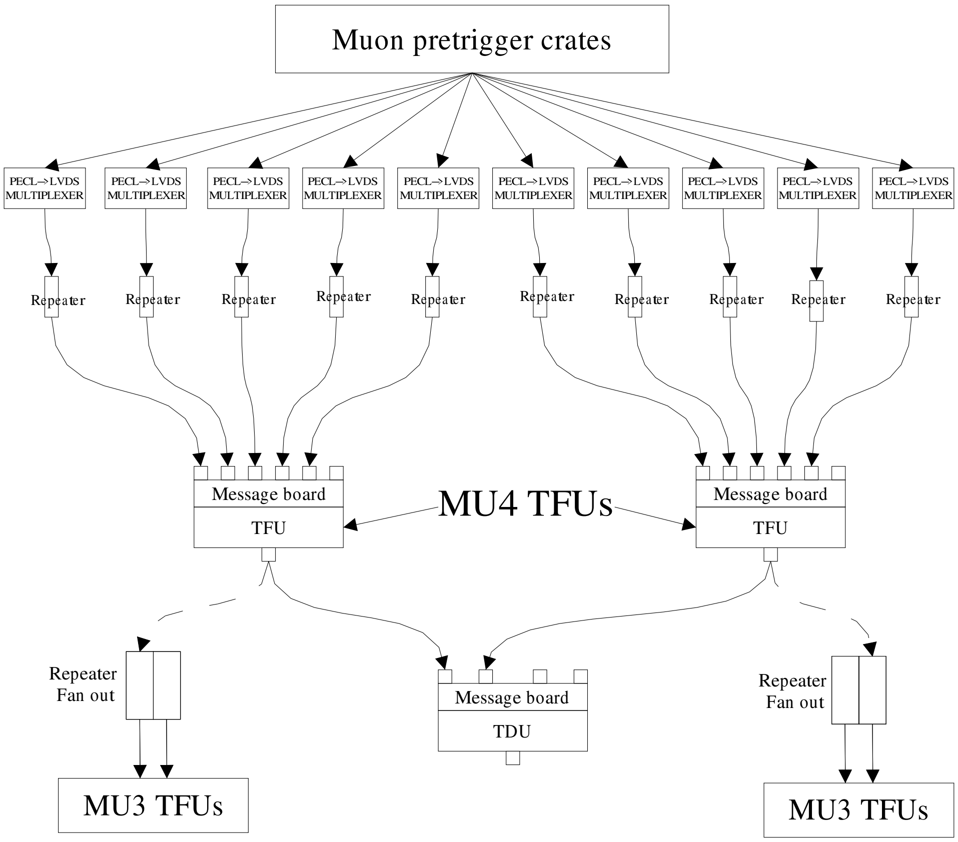

Figure 98: *MUON pretrigger connection scheme.*

Table 32: *Tracking OTR efficiencies measured with the test vector. Report to Fig. 99 to know the correspondence between FLT and OTR sectors.*

FLT Sector	Efficiency	FLT Sector	Efficiency
00	(96.9 ± 0.9) %	06	(97.8 ± 0.7) %
01	(95.2 ± 1.0) %	07	(99.8 ± 0.2) %
02	(98.0 ± 0.6) %	08	(85.8 ± 1.6) %
03	(95.8 ± 0.9) %	09	(88.2 ± 1.5) %
04	(95.6 ± 0.9) %	10	(99.0 ± 0.4) %
05	(96.2 ± 0.9) %	11	(98.6 ± 0.5) %

Inter-TFU connection test

It consists of exchanging messages between all the TFUs which are supposed to be connected to each other. The source TFU sends one or more random messages to the destination TFU. Then a comparison between received and original messages is done. This test is performed every time the system is initialized from the DAQ for a new run and it is considered to be part of the initialization procedure. The number of messages exchanged during the test is 80 per connection ($\sim$ 11000 in total). The time needed is about three minutes. This test showed that the repeater worked not always in stable way. Sometimes the repeater has to be switched off and on to recover the correct data transmission. A similar behavior was observed in the pretrigger connection test and probably will be solved by introducing the software reset of the repeaters.

Test vector
The aim was to test the processing of tracks in the hardware chain. For each OTR/FLT sector a fake track was generated and the related hits were used to fill the wire memories of the concerned TFUs. The pretrigger message was also generated and loaded into the concerned TFU of the first superlayer. Then a cycle by cycle processing was performed and the content of each pipe of each TFU was compared with what is foreseen by the simulation. For each sector of the OTR, the test showed an almost perfect agreement with the simulation[43]. This means that tracks lost in the hardware were also lost in the simulation. The tracking efficiencies estimated with this test are reported in Table 32. All the inefficiencies come from intrinsic features of the algorithm used to follow the tracks and no limitation is coming from unexpected behavior of the hardware.

Multimessaging test
The goal of this test was to check the message transmission between the TFUs of the network when the message rate is large. The test was performed using the TFUs connected to the $-$Y region of the OTR (Fig. 100). All TFUs were prepared to be transparent so that they were simply forwarding all the messages they were receiving. A large amount of messages (about 600 million) was transmitted continuously from each TFU in TC2 to the TFUs in TC1 at a rate of 85.5 kHz. Since each TFU in TC1, PC4 and PC1 was receiving messages from exactly three TFUs of the previous superlayer, the number of messages was triplicated in each superlayer and therefore, the TFUs in PC1 were receiving messages at a rate of 2.3 MHz. However the entire content of the messages could not be checked at this high rate. Only the messages in the PC1 TFUs were compared to the input messages in TC2 at random. No bit errors were found after checking 225000 messages leading to a message error rate less than $4 \cdot 10^{-6}$ or a bit error rate less than $5 \cdot 10^{-8}$, and no message was lost.

Optical link performance test It consists in testing the transmission of detector data (MUON and OTR) from the FEDs to the TFUs. A central component of the data transmission scheme is the Trigger Linkboard (TLB). The TLBs were introduced in order to rearrange the detector cells. This rearrangement is necessary because the detectors representation in the TFUs is different than the one of the HERA – B description. A second purpose of the TLB is to make the desynchronized data processing through the TFUs possible, by adding a BX number to the hit pattern.
The full transmission chain is organized as follows. The hit output of the FEDs is transferred via 34 pin ribbon cables[44] to the TLBs. Every input connector is assigned to a MACH chip which converts the 32 input bits to a 24 bits word. This assignment is programmable and depends on the planed rearrangement of cells (mapping of OTR and MUON detectors [91]). In one 96 ns clock cycle two different 24 bits words are fed into one Autobahn chip, that serves three MACHs in parallel (3×32 input bits are mapped to 2×24 output bits). The data are serialized and sent by optical link to the TFUs.
As a first hint to test the quality of data transmission through the optical link, the error counter on the TFU was used. If two of the detector data incoming BX numbers are not consecutive (only 3 of 8 bits are compared), the counter is incremented. From its contents a bit error rate of $10^{-6} - 10^{-5}$ for 4% of optical links was derived, all the others showed a bit error rate less than 10^{-7}. This result could be confirmed using a test mode of the TLBs and comparing the wire memory data with the expected pattern. Unfortunately the conditions were not very stable. Because of dying Autobahn chips, optical transmitters, receivers and fibers, the full system had to be controlled regularly and the corresponding hardware had to be exchanged. There is still some place for improvements in this

[43] The simulation does not reproduce exactly all intermediate steps in the messaging processing even if the output messages are correct.
[44] Two lines are used as ground lines.

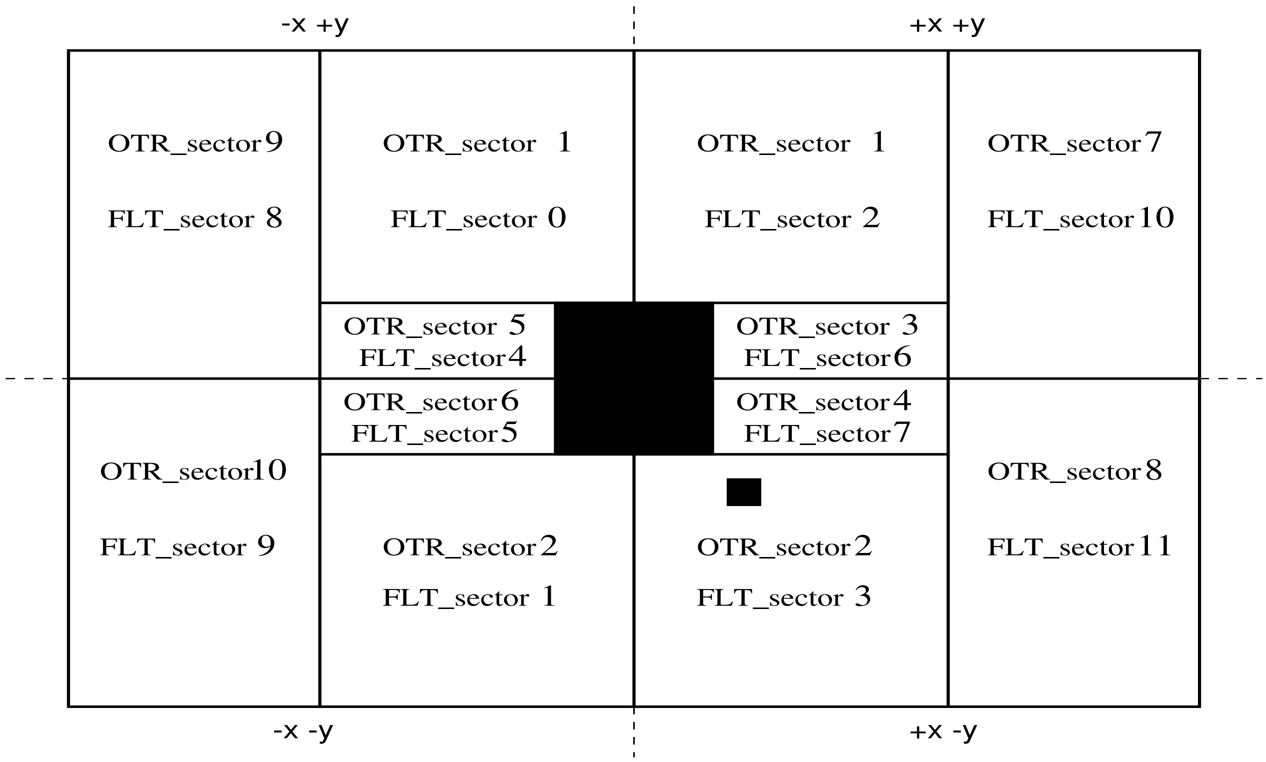

Figure 99: *FLT numbering conventions with respect to the OTR sectors.*

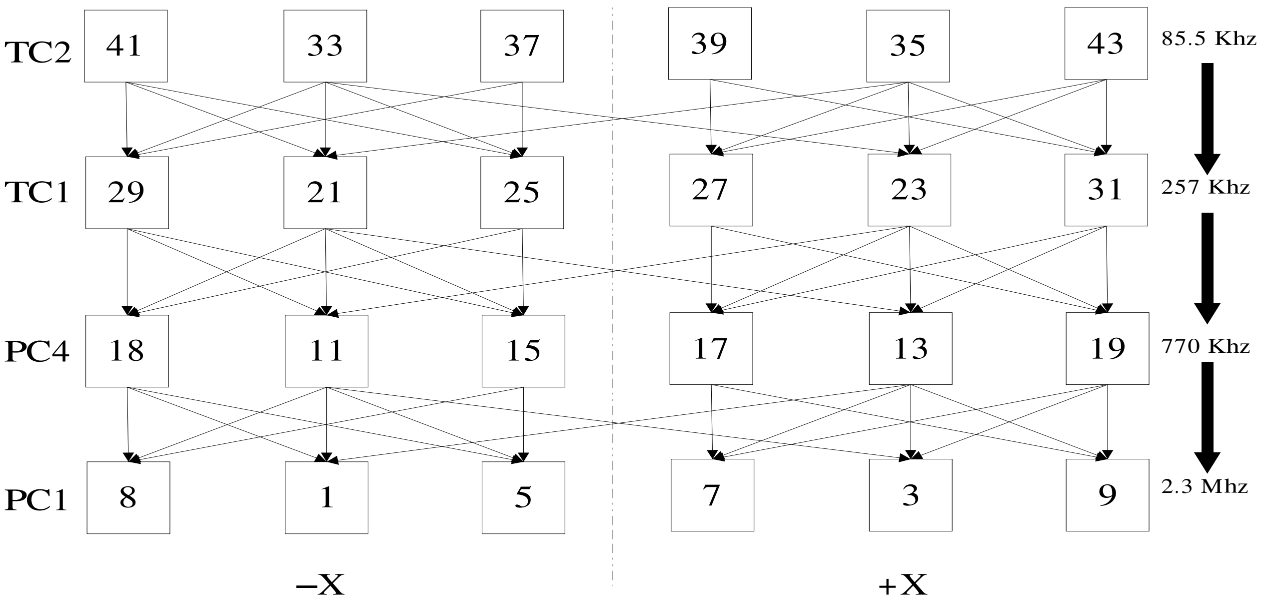

Figure 100: *Scheme of the TFU interconnections used in the multimessaging hardware test. The TFUs covering the -Y part of the OTR superlayers were used (the numbers inside the TFU drawings refer to the logical TFU numbers).*

field.

The second step was to test whether the rearrangement of detector cells is done by the TLBs as supposed. To perform this in a statistical way, the detector occupancy corresponding to the area covered by each TFU is transferred by software and compared to the wire memory occupancy of the corresponding TFU. Then a test value is calculated for each bit in order to decide if the TLB operation is done in a right way or not. Since a comparison of a characteristic pattern is more convincing then one of a steady pattern, the thresholds of the ASD8 were lowered by some 100mV. In this way it is possible to find out all kinds of mapping problems like wrong programmed TLBs, mixed up optical fibers, broken pins and mixed up or not well plugged ribbon cables. After several iterations of comparing occupancies to solve problems, currently about 1.5% of all wire memory bits are still wrongly mapped, and the attempt to set all these bits failed in 90% of the cases because of a software problem in the programming of the TLB chips. These 1.5% concern the OTR links, the MUON ones showed no error. This problem is clearly identified and investigations to solve it already started.

Fig. 101 shows an example of this comparison procedure for a full wire memory content of one stereo angle handled by one TFU (8 links of 48 channels). The "test value" shows that some channels of link 7 do not reproduce in the TFU wire memory the OTR occupancy.

A comparison between detector data and wire memory contents was also performed on an event-by-event base. Due to a not working test mode of the TLBs this was only done for a few links. As a result the probability that a real detector hit is not seen in the corresponding wire memory is 10^{-4}. On the other hand there are some events with an additional entry in the wire memory but no corresponding hit in the detector, with a probability of 10^{-3}. This test has to be further developed to be applied to all links.

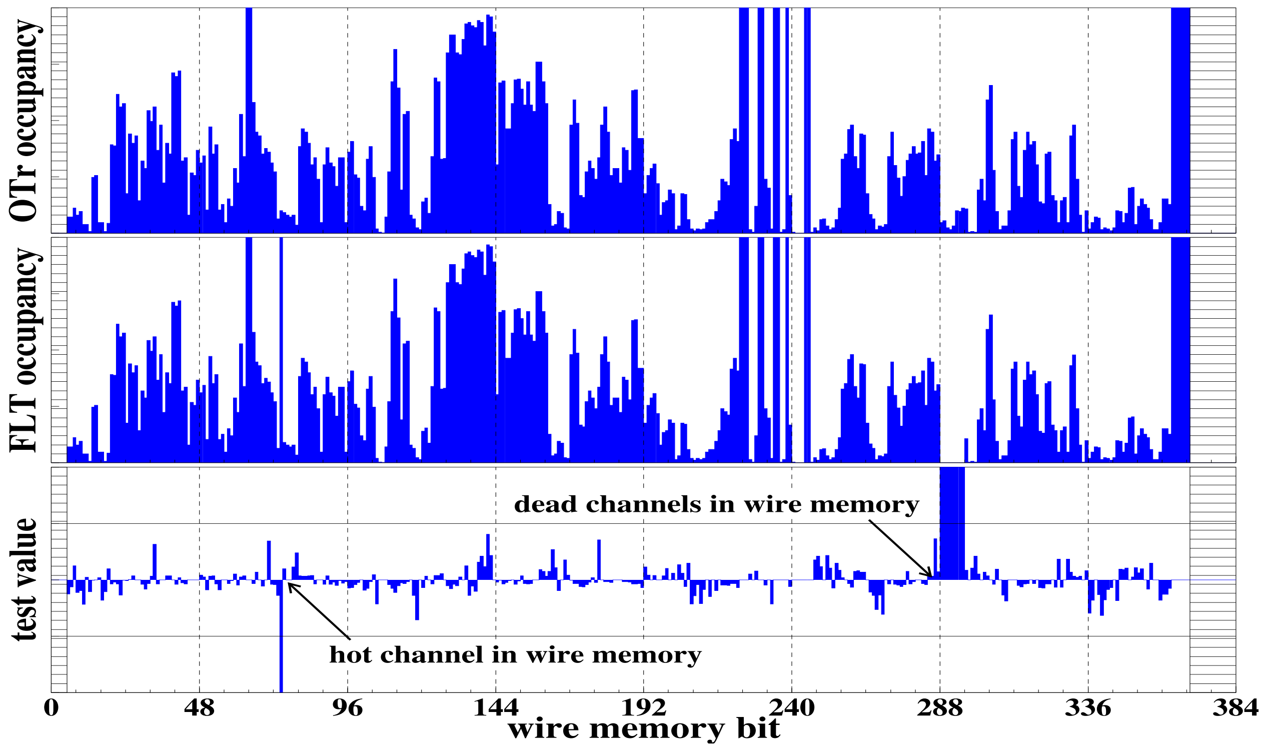

Figure 101: *Statistical comparison between the detector occupancy (here OTR) and the corresponding FLT wire memory. The "test value" gives the performance of the data transmission of the TLB within a 2σ statistical error.*

Track Parameter Unit (TPU) Three TPUs [93],[94] were used during the run period. A test vector was performed to study these boards using simulated tracks coming from J/ψ decaying into $\mu^+\mu^-$. The corresponding message was sent to the message board and a cycle by cycle processing was performed. A comparison of the content of each pipe between hardware and simulation showed a perfect agreement. The operation of the double track rejection feature [45] that is the possibility to reject similar tracks looking at the value of Px/Pz and Py/Pz and at the identifier (electron or muon) was also tested. Fig. 102 shows this effect and an example of cut on the transverse momentum ($P_T > 0.5GeV/c$) is also shown.

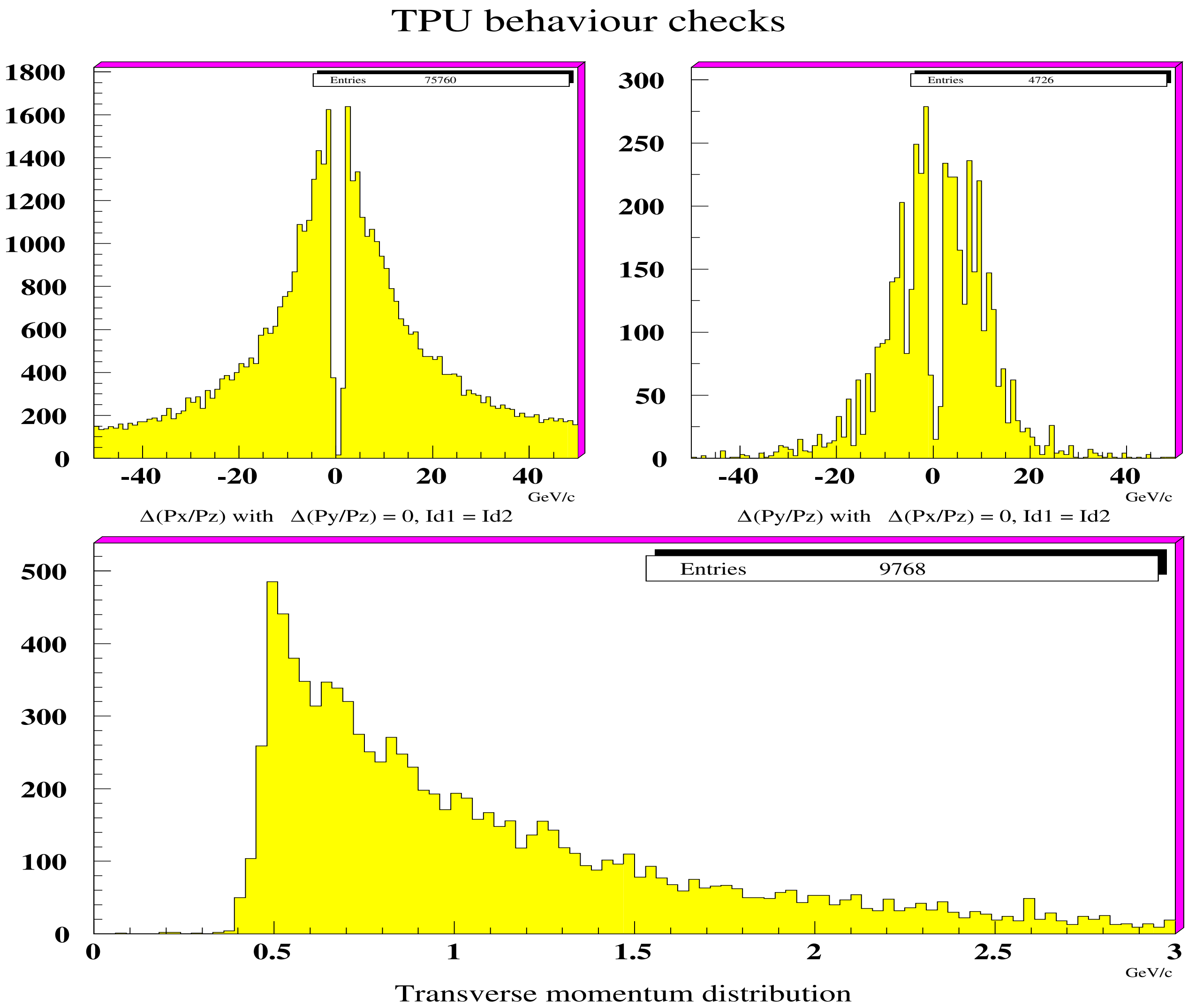

Figure 102: *The upper part of the plot shows the effect of the TPU track rejection: tracks with the same Px, Py and Id are suppressed. The lower plot shows the effects of a transverse momentum cut ($P_T > 0.5GeV/c$). Due to the approximations done in the P_T calculations performed in the TPU the cut is not sharp.*

Trigger Decision Unit (TDU) The TDU can be used in two different modes: the *count trigger mode* in which only the identifier of the particle is used to generate a trigger decision and in *pair*

[45] Also called the "clone track" rejection.

trigger mode where the final decision is based on the properties of track pairs (invariant mass, energy asymmetry, charge difference, etc.). Since August 1999 the TDU was used in count trigger mode, and only in the last month of running the pair trigger mode was tested. The rate reduction depended on the run conditions and it was fluctuating by a factor five to ten. In Fig. 103 the distribution of the track multiplicity for a run taken at a target rate of 5 MHz without the pair trigger is shown.

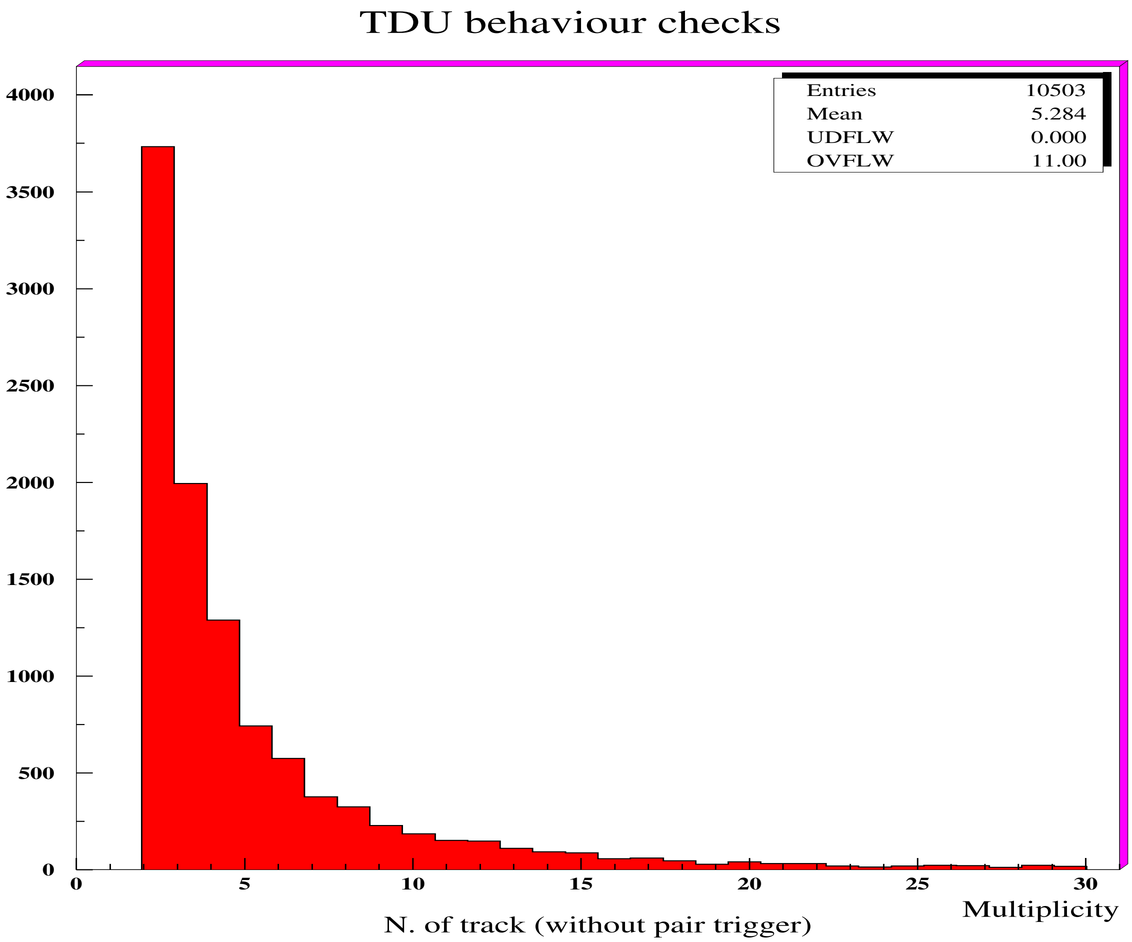

Figure 103: *Number of track distribution*

Fig. 104 shows the experimental latency for muon and electron tracks without Bremsstrahlung recovery, which is the time needed by the pretriggers and the FLT to process an event. Note that the latencies for all tracks of an event are entering these plots. The tails are actually dominated by events with very large multiplicities. To avoid dead time, the latency of the track which generates the first trigger has to be smaller than the time the primary data can be kept in pipelines (12.3 μs for the 128 BX deep FED buffers). Fig. 105 shows the different contributions to the latency. They are also given in Eq. 10 and Eq. 11. For more details about the FLT latency, see also [95].

$$\Delta t_{\mu-tracks} = (\Delta t_{\mu\mathrm{pre}} + \Delta t_{MUONFLT} + \Delta t_{\mathrm{OTRFLT}} + \Delta t_{\mathrm{TPU}} + \Delta t_{\mathrm{TDU}} + \Delta t_{\mathrm{FCS}}) \tag{10}$$

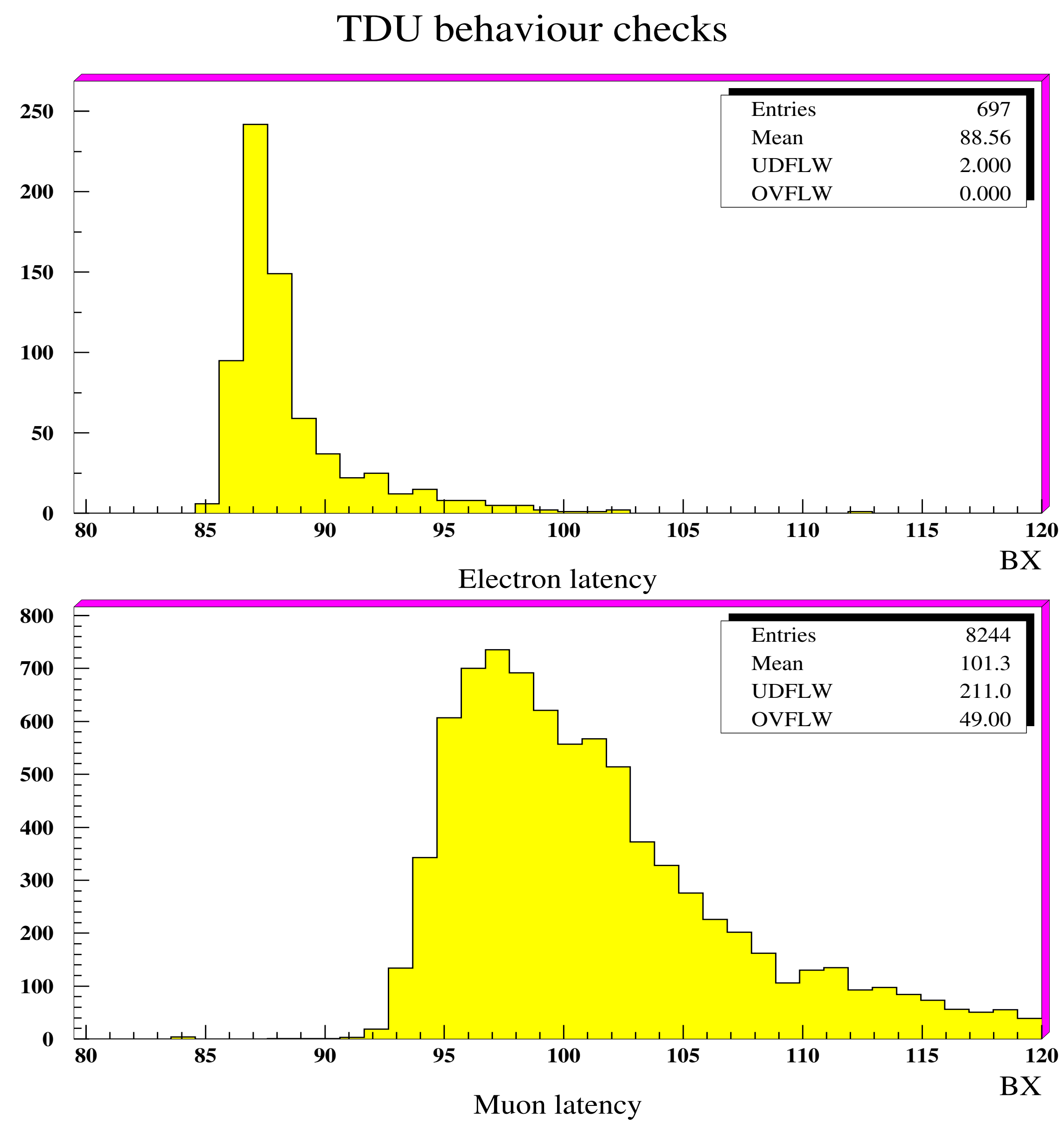

Figure 104: *Latency distributions for electron and muon tracks.*

$$\Delta t_{e-tracks} = (\Delta t_{\rm epre} + \Delta t_{\rm OTRFLT} + \Delta t_{\rm TPU} + \Delta t_{\rm TDU} + \Delta t_{\rm FCS}) \qquad (11)$$

It is important to notice that only the latency of the first trigger occurence is critical, if it is greater than (12.3 $\mu s - \Delta t_{\rm FCS}$), because only then it will be lost since the FCS discards it. The upper plot of Fig. 106 shows where the FCS cut is: in the case of a muon track the trigger is not accepted if its latency is greater than 103 BX ($\simeq 10\ \mu s$).

To have an estimate of the percentage of lost triggers the following arguments can be used: one can assume that the latency distribution of the second trigger is similar to that of the first one[46].

[46] It will be a little bit delayed so the estimation is pessimistic.

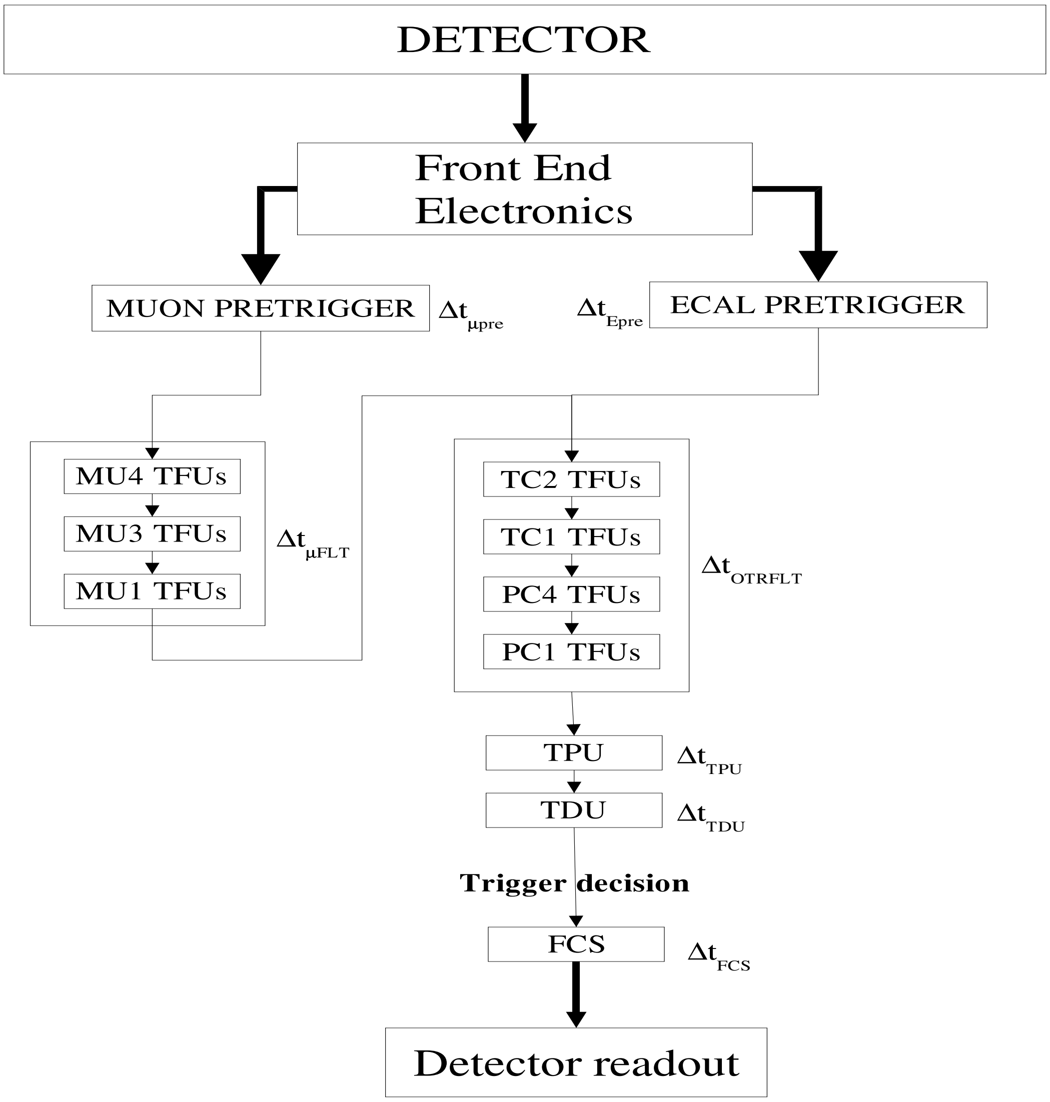

Figure 105: *Contribution to the latency given by different parts of electronics*

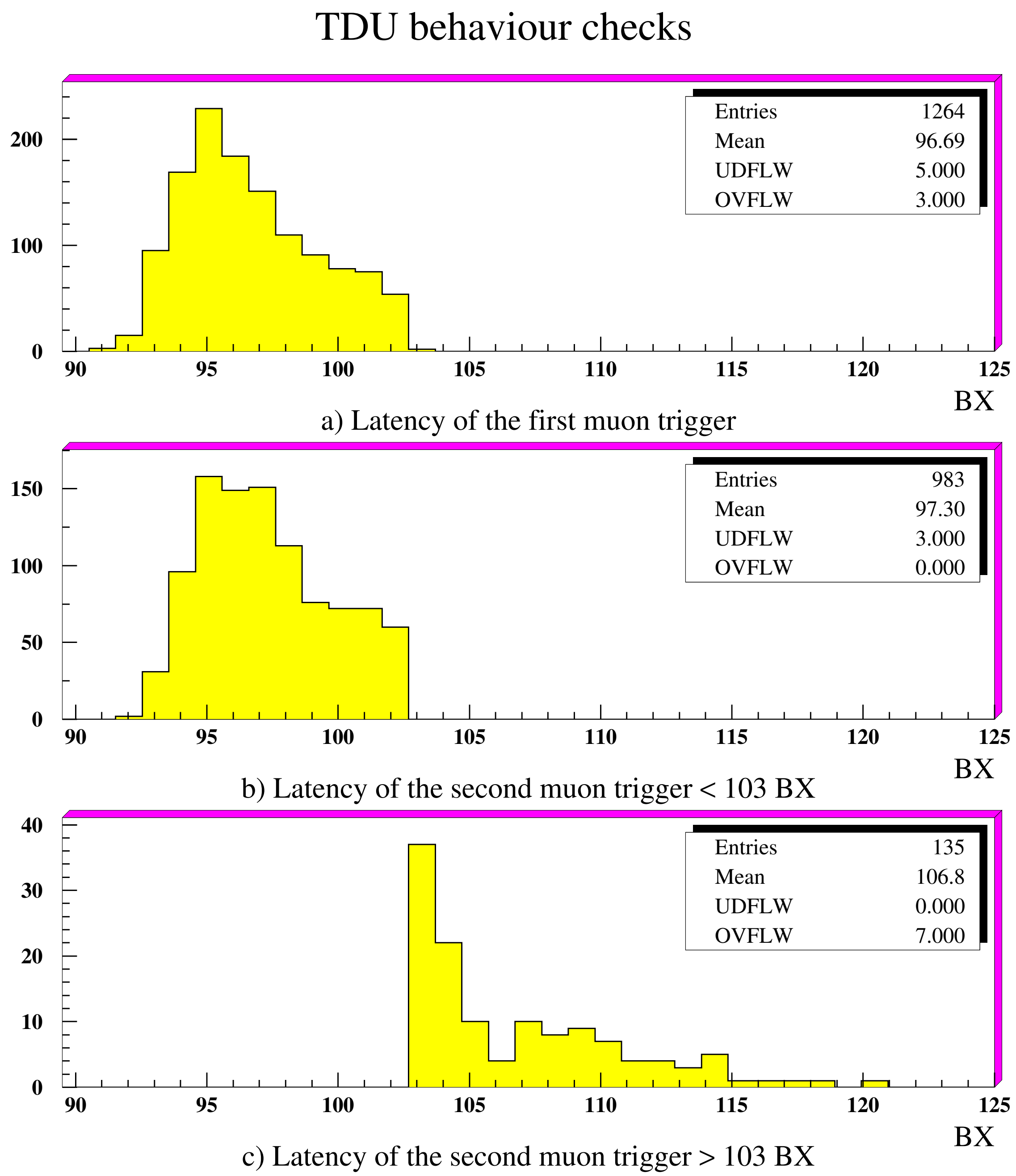

Figure 106: *Estimation of the lost MUON triggers due to the latency. a) Latency of the first trigger for muon tracks. The cut at 103 BX applied by the FCS is clearly visible. b,c) Latency of the second trigger for muon tracks (events with a latency* $<$ 103 *BX and* $>$ 103 *BX).*

By definition, the information of the second trigger is stored, because there is always the first trigger which arrives earlier. Sometimes the second trigger arrives so late ($\geq 12\mu s$) that the TDU record for that BX is already sent to the readout boards and the informations are lost. Looking at the tail shape of the electron latency we will assume that this contribution is negligible. So the ratio between the number of second triggers which arrive after and before 10 μs can be considered as a good estimate of the lost triggers. In Fig. 106 the latency of the second trigger before and after $10\mu s$ is shown. From there the percentage of lost MUON triggers is estimated to be about 12 %. One

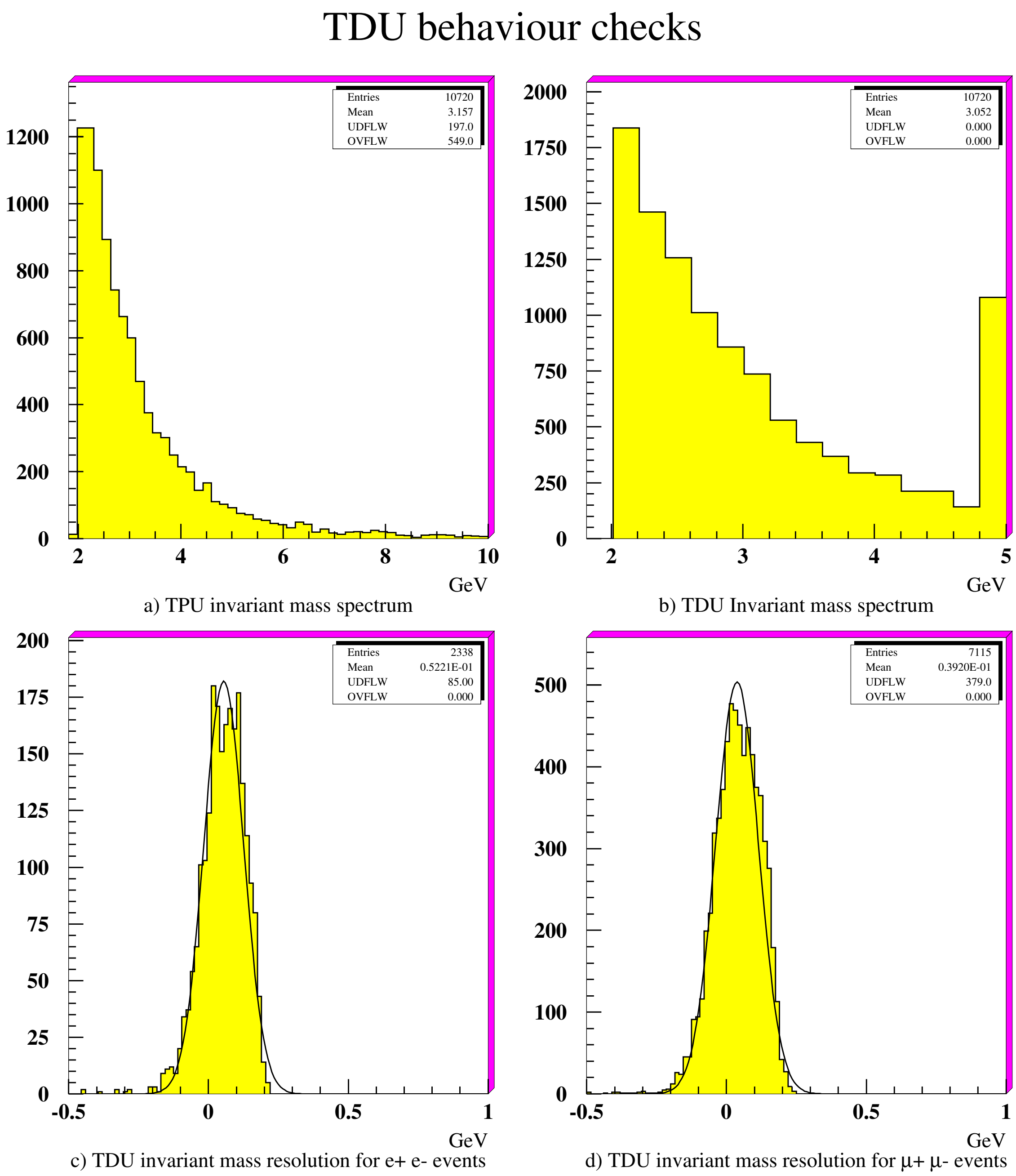

Figure 107: *Invariant mass calculation from an FLT triggered run.* **a)** *Done using the TPU parameters (Px, Py, Pz).* **b)** *Done by the TDU hardware (notice the overflows).* **c)** *TDU mass resolution (compared to TPU) for e^+, e^- events.* **d)** *TDU mass resolution (compared to TPU) for μ^+, μ^- events.*

possibility to reduce this number should be to exclude the MU4 superlayer from the trigger but the effect of this on the performance of the FLT has still to be studied.

Finally in Fig. 107 the behavior of the TDU for the invariant mass calculation is shown. The peak at 5 GeV/c is due to the TPU masses greater that 5 GeV/c which become overflows in the

TDU. The resolution and the shift on the resolutions are a consequence of the binning used in the LUTs. It is important to remember that the values of Px and Py calculated in the TPU are already approximated so that the real resolutions on the invariant mass are worse. These plots demonstrate that the invariant mass calculation performed by the TDU is correct and again that the hardware behaves as expected.

3.1.3 Performance

In this section we present preliminary results on the evaluation of the FLT efficiency. First we show some technical data to demonstrate the functionality of the system. Then we come up with efficiency measurements on muon and electron tracks comparing the tracks found by the FLT to reference tracks. Since the definition of a muon track always involves the muon detector and hence it is difficult to establish an unbiased reference signal we utilize runs with observed J/ψ signals to establish muon efficiencies. This technique is not applicable to the electron case due to Bremsstrahlung which leads to a wide J/ψ signal and a poor track definition.

First checks The information of the FLT track recorded by the data acquisition is composed of one impact point (x, y) at the TC2 superlayer and the direction of the track. One can use this information to extrapolate to any superlayer.

A simple way to evaluate the quality of the FLT tracks is to plot the difference between the x-position of the hits in the detectors (OTR or MUON) and the position of the FLT track impact point in each superlayer. These plots are called "hit-track residuals". There should be always hits close to the track in the layers used for triggering. Fig. 108 shows the hit-track residuals for the PC1, PC4, TC1 and TC2 chambers of the OTR, the dashed lines corresponding to mixed events (using the hits of the previous event). The data used to do these plots were triggered by requiring one track (muon or electron) from the FLT. An enhancement of hits close to the track in all the three stereo views of all the superlayers can be seen. The width of these distributions is smaller in TC2 and PC1. This is due to the fact that the track is constraint in these superlayers since the interaction point is given in TC2 and the last update of the slope is done in PC1. The background level is due to hits uncorrelated to the tracks - either since the track is a ghost or the hit is spurious. Note, that for each event the distances from all hits in the entire superlayer to all tracks are plotted in Fig. 108. This includes layers which are not used in the FLT. The number of entries in the histograms is different in each plot since the number of layers/projection is different in the three projections/superlayer.

Looking into the hit-track residuals of the detectors that the FLT does not use, as for example PC2 and PC3 (shown in Fig. 109), one can also see an enhancement close to the track. These plots prove that the FLT finds real tracks.

The extrapolation of the track can also be done with the MUON detector. Due to the multiple scattering a worse resolution is expected. Fig. 110 shows the hit-track residuals for the three stereo views in MU1 and for the single view in MU3 and MU4.

Preliminary FLT efficiency The FLT is meant to do tracking at the hardware level. Having that in mind, a simple way of evaluating its efficiency is to check if the tracks built by using other detectors than OTR are found by the FLT algorithm. Therefore, this method includes inefficiencies not only of the FLT algorithm but also of the OTR cells and the pretrigger.

A series of dedicated efficiency runs were taken from the start of the FLT commissioning. In

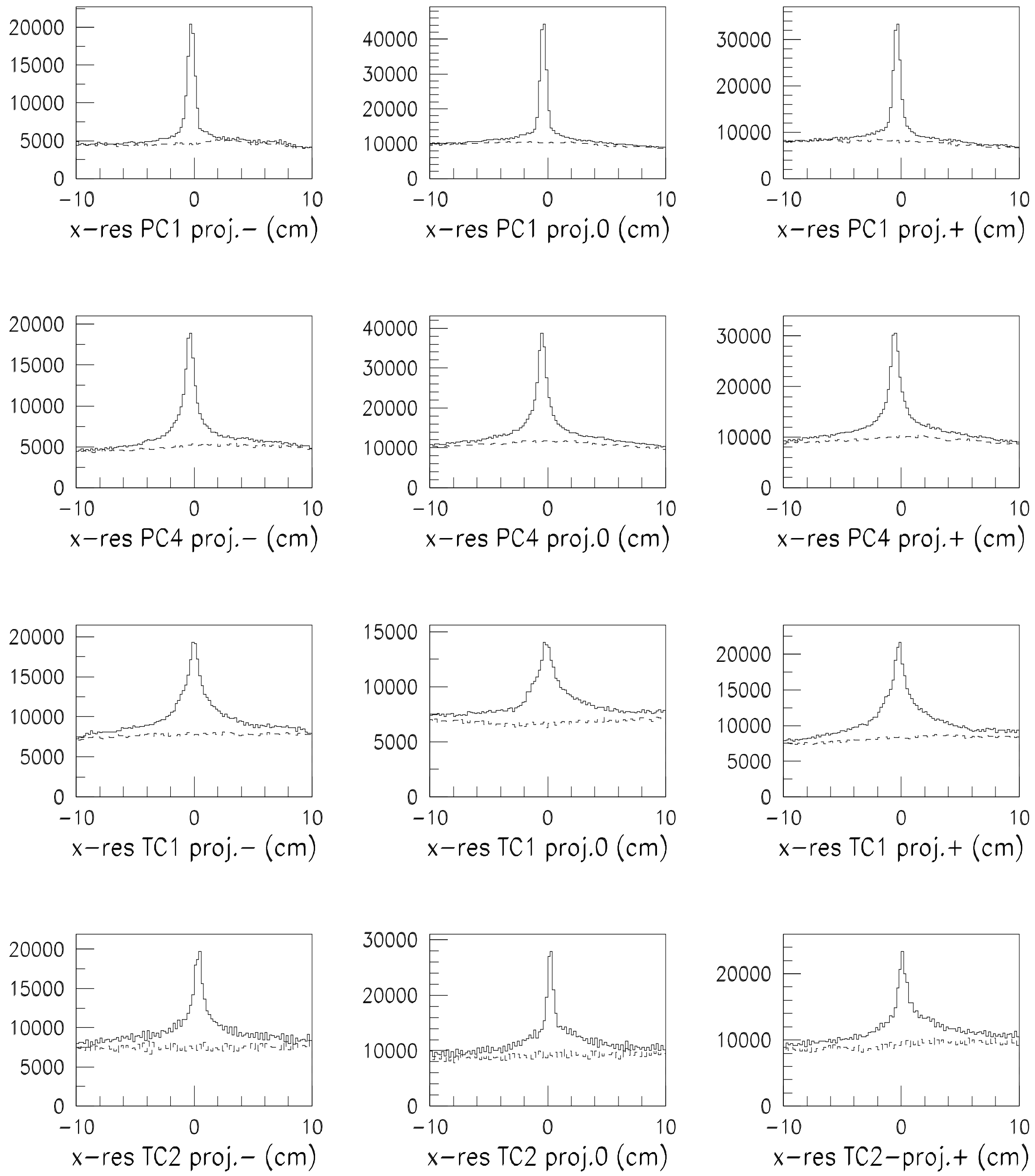

Figure 108: *Hit-track residuals in PC1, PC4, TC1 and TC2.*

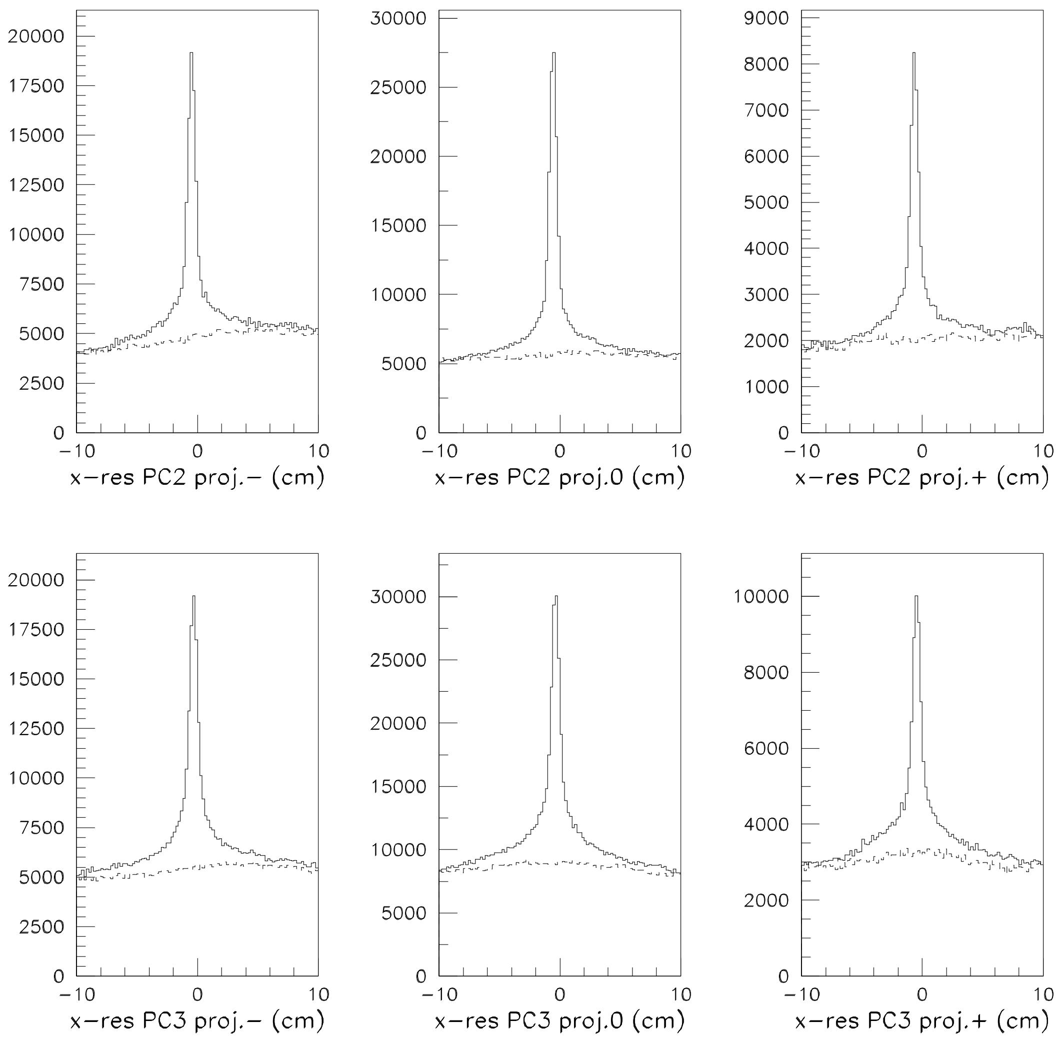

Figure 109: *Hit-track residuals in PC2 and PC3.*

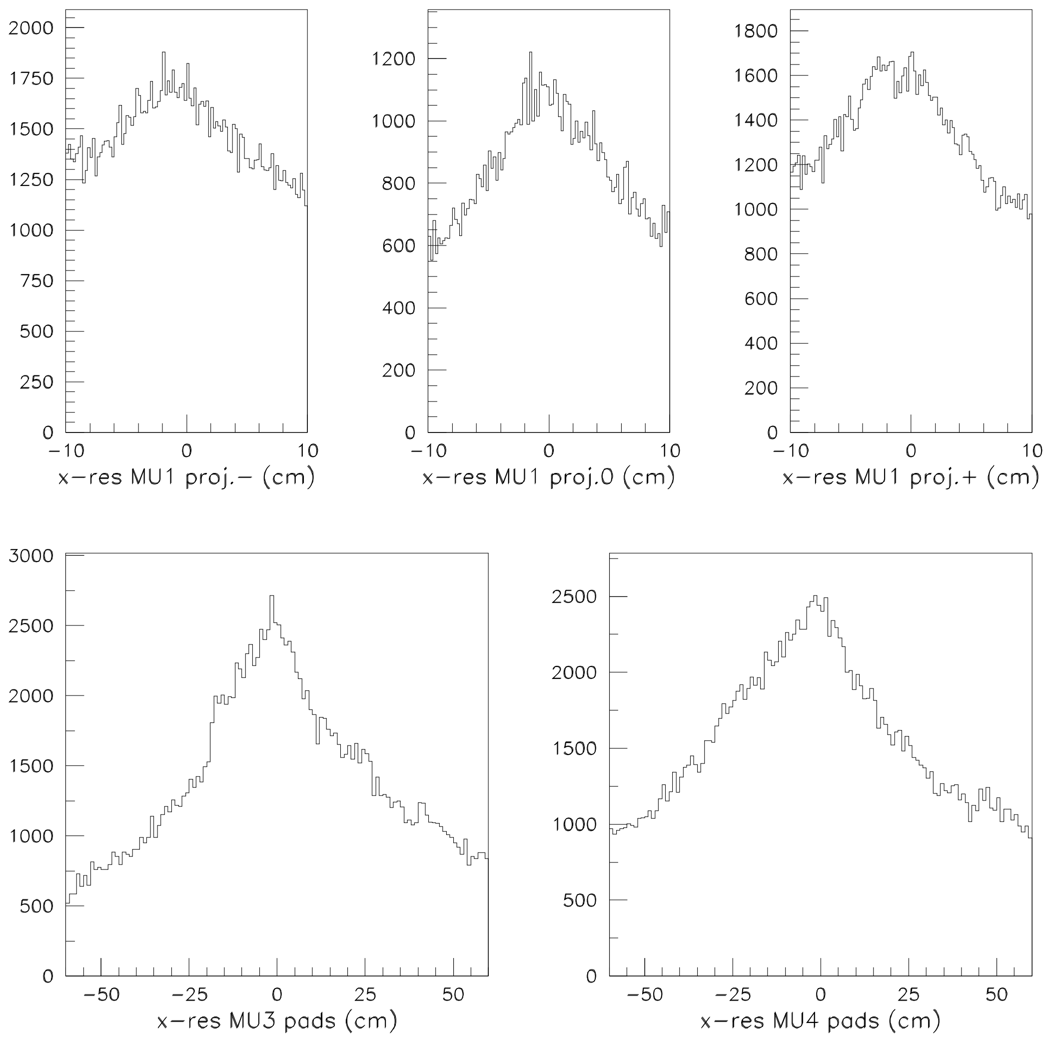

Figure 110: *Hit-track residuals in MU1, MU3 and MU4.*

these efficiency runs the FLT was not triggering but the SLT was requiring an ECAL cluster with a transverse energy E_T above 1 GeV and the FLT information was recorded. E_T is defined as:

$$E_T = \frac{\sqrt{x^2+y^2}}{z}\,E\,. \tag{12}$$

The FLT efficiency is measured by an offline analysis. A set of reconstructed "reference" tracks is selected and their track parameters are compared to those of the recorded FLT tracks. The quality of the matching between the reference tracks and the FLT tracks is defined in terms of a pseudo-χ^2 of the four track parameters: x and y coordinates in TC2 and the slopes $t_x = p_x/p_z$ and $t_y = p_y/p_z$. The efficiency is extracted from the pseudo-χ^2 probability distribution.

Electron track efficiency

Electrons are found by the FLT algorithm after having the ECAL pretrigger message seeds been successfully propagated through the FLT network. ECAL pretrigger seeds are generated upon the occurrence of an ECAL cluster with $E_T > 1$ GeV.

The analysis is performed by using the electrons in the 23k events of run 16919, taken on the 8th of August 2000 at a 4 MHz interaction rate. The reference tracks for electrons are defined as offline reconstructed ECAL clusters with $E_T > 1.2$ GeV matching a ring in the RICH and being within the acceptance of the OTR superlayers used by the FLT. Since the ghost track rate is still too high, the reference tracks are also required to match reconstructed tracks in the vertex detector.

Fig. 111 shows the differences of the track parameters of the FLT tracks and the track parameters of the reference tracks. The track parameter resolutions are determined from a Gaussian fit to these plots. The preliminary results are:

$\sigma_{t_x} = 0.00132$ rad, $\sigma_{t_y} = 0.00128$ rad, $\sigma_{x_{\mathrm{TC2}}} = 1.07$ cm, $\sigma_{y_{\mathrm{TC2}}} = 0.96$ cm.

A pseudo-χ^2 is calculated by taking the best match of a reference track to one of the FLT tracks recorded in the event. If no FLT track was recorded, the pseudo-χ^2 is set to infinity. The left plot in Fig. 112 shows the pseudo-χ^2 distribution while the right plot shows the pseudo-χ^2 probability. A clear separation between matched (all bins but the first) and non-matched tracks (first bin) can be observed in the pseudo-χ^2 probability plot. A preliminary result for the electron efficiency is determined to be:

$$\eta_e = 70 \pm 2\,\%. \tag{13}$$

By requiring the reference tracks to have ECAL clusters with different E_T values, compatible efficiencies are obtained. This result includes possible ECAL pretrigger inefficiencies, OTR cell inefficiencies, errors in optical or electrical transmission, etc. Moreover, the efficiency is not uniform over the FLT volume. The (−x,+y) quadrant has the highest efficiency whereas the (+x,−y) quadrant is significantly less efficient. The reasons are still not understood but it might be due to a non-uniform performance of OTR or ECAL. Since the electron pretrigger efficiency is 95% the pure FLT tracking efficiency is 74% .

Muon track efficiency

The reference tracks for the muons are muon reconstructed tracks that have an OTR segment close to it. This means that t_x differs less than 10 mrad, x less than 10 cm and y less than 30 cm.

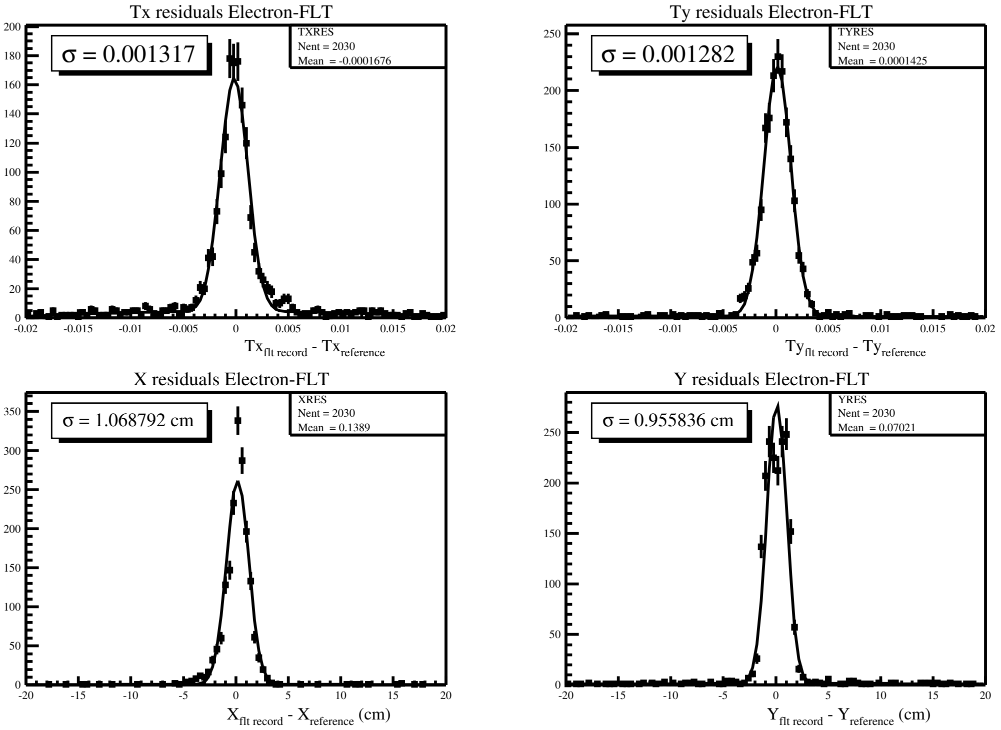

Figure 111: *Residuals of the FLT tracks minus reference tracks for the four track parameters: x and y coordinates in TC2 and the slopes t_x and t_y.*

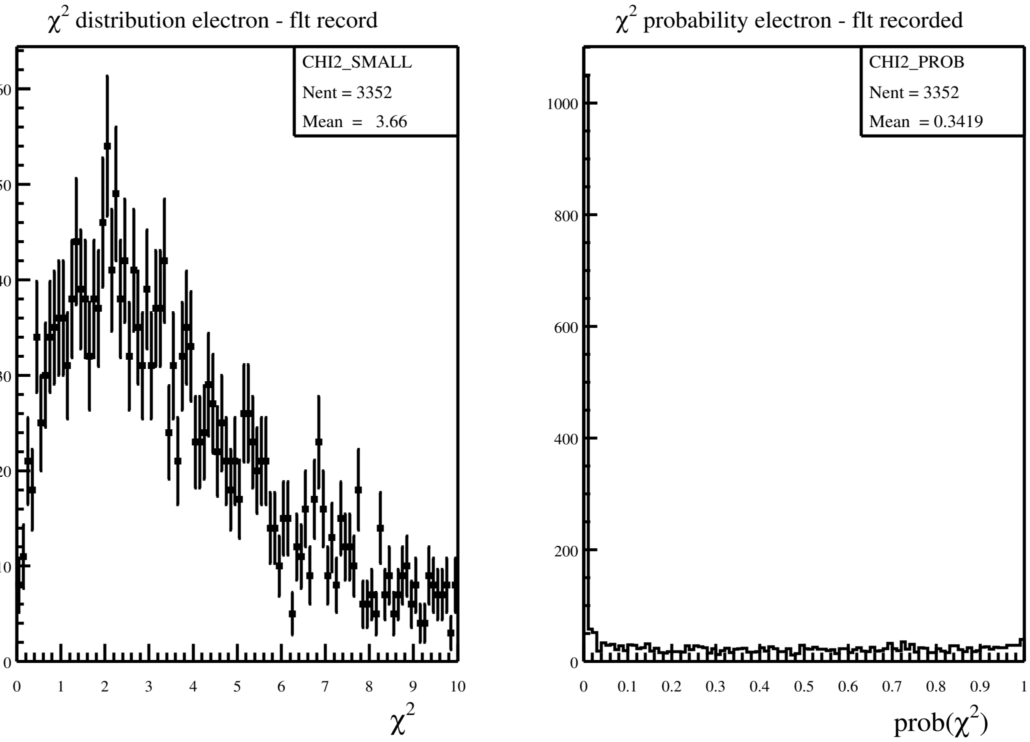

Figure 112: *pseudo-χ^2 and pseudo-χ^2 probability of the match between reference tracks and FLT tracks.*

If there is more than one possibility, the closest match to the OTR track is taken. The reason to use the OTR is that the reconstructed muon with only the MUON detector has very inaccurate parameters due to the multiple scattering. By using the OTR and taking the MUON detector as particle identification, the residual distributions look much better.

This analysis is still ongoing and the result is still not completely understood. A preliminary result will be available soon.

Simulation of the FLT algorithm The simulation of the FLT algorithm is implemented in a bit-wise way identical to the real system. In fact, this simulation has been used in the test vector mentioned in section 3.1.2 to verify the hardware. However, no latency or message overflow conditions are simulated. With a sample of taken event data one can simulate the FLT online performance.

Electron efficiency measurement using the simulation

The data that have been used in the simulation are the same as before. By using a method similar to the one described in section 3.1.3 but taking the simulated tracks matched to the reference tracks instead of the FLT recorded messages, the FLT efficiency can be measured, thus providing a cross-check. By applying this method the electron FLT efficiency is found to be: $\eta_e(\text{simulation}) = 69 \pm 2\%$. Here only the trigger and not the detector has been simulated instead the recorded detector data have been used as input to the trigger simulation.

1.5% of the flt-input hits had a faulty data transmission or were wrongly mapped. This effect enetrs with the 12 power since 3 layers in each superlayer from TC2 to PC are required to establish a track. The simulation is based on the assumption that all hot channels are always on which is to optimistic. Both effects together result into an expectation of 85% lower efficiency in reality as compared to the MC. Hence the above result becomes 0.59 which is 20% lower then the result obtained online. This effect has not been understood. We work on an improved model for the links and try to resolve the inconsistency by further analysis.

The simulation can be used to trace down at which OTR superlayer the messages were lost. Table 33 shows how many of the ECAL pretrigger simulated messages successfully reach the PC1 superlayer, matching to the reference tracks. More work needs to be done in order to understand the inefficiency. Possible reasons are malfunctioning links, message pileup in the TFUs, intrinsic inefficiencies of the FLT algorithm or bit errors. Further investigations will follow.
So far, this analysis has only been applied to the electrons, it is planned to use it also for the muons.

Table 33: *FLT simulated message losses at the individual OTR superlayers. Simulated messages are matched to reference tracks.*

Number of valid FLT simulated messages out of					
ECAL pretrigger	TC2	TC1	PC4	PC1	Efficiency
3352	3020	2926	2790	2304	69 %

Monte Carlo expectation

The simulation has also been used on Monte Carlo (MC) generated events in order to extract an expected efficiency. A full GEANT simulation has been used. By running it on $J/\psi \rightarrow \mu^+\mu^-$ MC events, an efficiency of 51% per muon track and of 22% per J/ψ have been extracted. This Monte Carlo does include a realistic OTR model. The MUON detector model implements the chamber geometry as designed but no chamber inefficiencies are simulated. The large inefficiency originated from the pads, used by the MUON pretrigger, are also not taken into account.

As described in section 3.1.2, 12% of the messages are lost due to time overflow (too late arrival). J/ψ events are not expected to be more busy in terms of FLT messages then ordinary events. Hence the average message latency should be applicable. The observed large message counts in pair triggered events are attributed to high multiplicity background events and should not influence the triggering of J/ψ events. However, no study to verify possible correlations between the presence of real straight tracks and the message traffic has been done.

The 1.5% of missing hits in the OTR due to wrong mapped bits in the TDC to TFU connection result in a lower muon track efficiency since 12 layers (3 in each superlayer from TC2 to PC1) are required to establish a FLT track. The MUON links are assumed to be 100% efficient. This effect is not taken into account in the current FLT simulation. On the other hand the assumption that all hot channels are always on which is used in the OTR simulation is to optimistic. Both effects together result into an expectation of 85% lower efficiency in reality as compared to the MC. Furthermore the muon efficiencies as implemented in the MC are too optimistic. As explained in the muon section they are lower by 0.88 per track.

Applying the data link imperfections, the muon inefficiency and latency losses to the MC numbers, the single track muon efficiency estimate is 33% and the efficiency per J/ψ is 10% . In comparison to the TDR values of ≈ 1 to find a J/ψ inside the detector geometry with both tracks reaching the last MUON station, we are missing a factor 10 which is due to the latency (1.3), the data links (1.6), the muon chamber efficiency (1.6), the OTR cell efficiency (1.3) and the FLT tracking efficiency (1.04). The missing factor 2.2 is attributed to non-understood chamber geometries and is subject to further study. Note, that the pad efficiency is not included in the numbers quoted here.

Extracting the efficiency for tracking of muons in the OTR only we find 68% in the MC which turn into 57% after application of the link inefficiencies. Although the same OTR stations as for the electrons are used for the muons in the OTR the algorithm differs slightly since the RoIs are much larger in the muon case and the muon detector has different alignment parameters than the ECAL used to start an electron search.

FLT efficiency on selected J/ψ data events

Events selected from runs triggered by the SLT can be used to estimate the J/ψ efficiency of the FLT. These events are selected to be in the J/ψ mass region having tracks in the muon system, the OTR and the VDS with $P_T > 1.3\,\mathrm{GeV/c}$. In Fig. 113 the J/ψ mass of these events is shown. Running the FLT simulation on these events a J/ψ efficiency of 12% is found. This number is determined by running the SLT algorithm on the FLT found events and then fitting the J/ψ again. The SLT efficiency on these already triggered events is estimated to be 93% based on re-running the SLT without the FLT. The FLT geometrical coverage on both leptons from the J/ψ is 89% relative to the SLT since the FLT requires tracking in PC1 while the SLT algorithm can skip this layer and is hence less affected by the absence of the ITR. The size of the effect was estimated based on the SLT track information from the selected events. Correcting by the SLT re-run efficiency the FLT efficiency is found to be 14% . Of course, it contains all chamber efficiencies but none of the "online" corrections are applied. Using the link efficiency and latency cut values from above we estimate an online efficiency of 9% . This has to be compared to the 10% estimated from the MC.

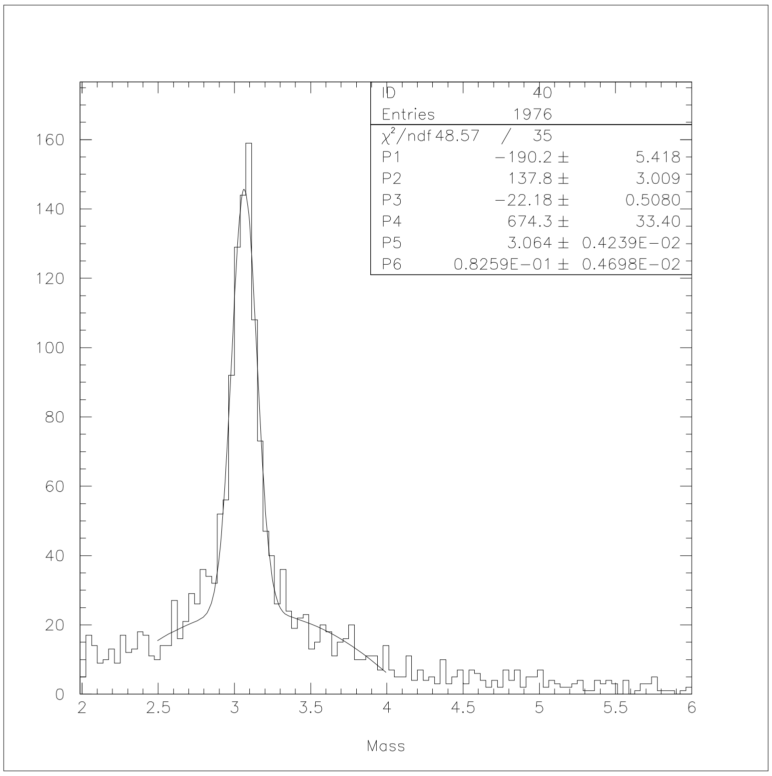

Figure 113: *Mass plot of the hard selected SLT muon J/ψ.*

The largest difference to the MC running is due to a much lower efficiency to find both tracks in the MU1 layer. This is not yet understood but might be attributed to either a low tube chamber efficiency in the stereo views which are not used by the SLT algorithm or by some intrinsic geometrical features of the chambers which are not described by the MC. The global alignment is taken into account since it has been determined using the muon tracks from the same event sample. A further explanation might be that some of the tracks are not real muons and are discarded by the FLT which requires more hits in the muon system than the SLT. Since approximately half of the events in the selected sample are not J/ψ decays this can explain part of the effect. Further analysis is required to single out the cause of this discrepancy.

The data can also be used to estimate a muon tracking efficiency by comparing the recorded SLT tracks to the simulated FLT tracks. We find an efficiency of 31% which becomes 23% after applying corrections for the data links and the latency losses. This has to be compared to the MC expectation of 33%. Note that this number is not compatible with the assumption that the two J/ψ tracks are independent since the 9% event efficiency is not compatible with the squaring the track efficiency $0.23^2 = 0.053$. Either there are some correlations (which eg. are present in the geometry) or there is something wrong with the with the track matching which is used to extract the track efficiencies.

Using intermediate simulation results the efficiency for finding a muon track inside the OTR can be obtained. We find a number of 70% . This number should apply equally to muons and electrons and can hence be used to estimate electron efficiency. Again this number has to be multiplied by the data link efficiency, then the online track efficiency should be 58% .

First look at FLT triggered runs In the last few weeks of the HERA operation some runs triggered by the FLT were taken.

FLT track efficiency from single track running

Some runs were taken where the FLT was requiring one muon track with $P_t > 1$ GeV/c, while the SLT was emulating the muon pad coincidences (the muon pretrigger), requiring at least two tracks in the MUON detector and doing afterwards all the SLT tracking algorithm (see SLT section) independently of the FLT track. A factor 1.5 higher J/ψ production rate using the FLT in a one track mode was observed compared to using the pretriggers only together with the SLT. The SLT algorithm was unchanged. Due to pre-scaling in the pretrigger only mode and differences in the dead time the ratio of the J/ψ production rates in the two modes is 36%.

In order to convert this production ratio into a FLT track efficiency we have to take into account that the SLT tracking efficiency is 1.04 higher if the FLT was triggering because the FLT selected events with tracks having a sufficient number of hits in the detector. Since the FLT was only requiring one out of two possible muon tracks, the single track efficiency is $\eta_{track} = 1 - \sqrt{1 - 0.36/1.04} = 0.19$. Unfortunately the same exercise for the electron channel was not done due to the absence of an observable J/ψ signal in the last weeks of HERA running.

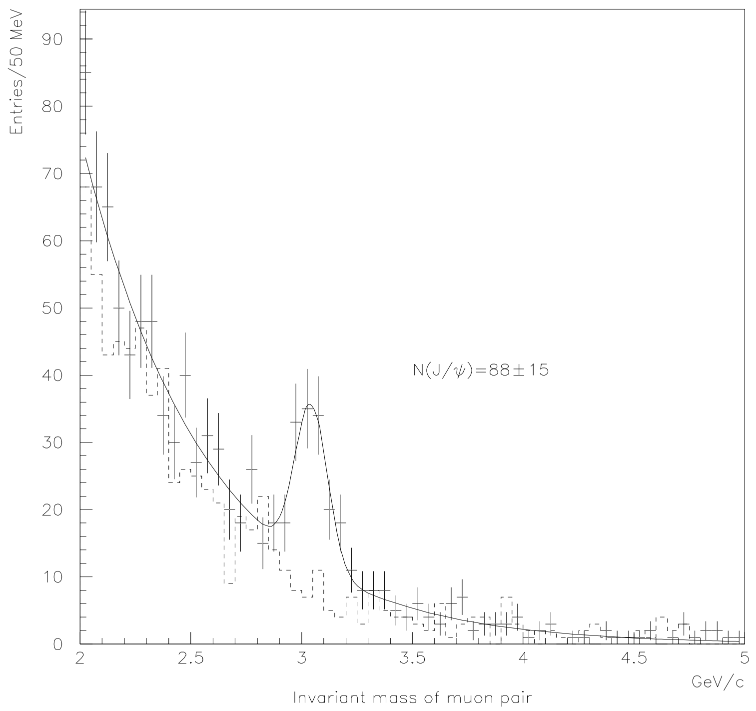

Figure 114: *Mass plot of the two muon tracks found by the SLT in the FLT single track triggered runs.*

Fig. 114 shows the mass of the two muon tracks with opposite charge found by the SLT in these runs. The dashed line corresponds to the events where the two tracks have the same charge. The peak of the J/ψ can be clearly observed.

These runs will be used in the future to analyze the pair trigger information of the FLT.

FLT track efficiency from pair triggering

Some runs were also taken by using the TDU in pair trigger mode. In these runs a large number of tracks is found per event, in addition many track combinations are present in the high mass area. The mass spectra for a run of 6.5 hours is presented in Fig. 115. No J/ψ signal can be observed. We would expect about 300 J/ψ events during this running with an 100% efficient FLT. An upper limit of the J/ψ efficiency of the FLT can be estimated to be 10%.

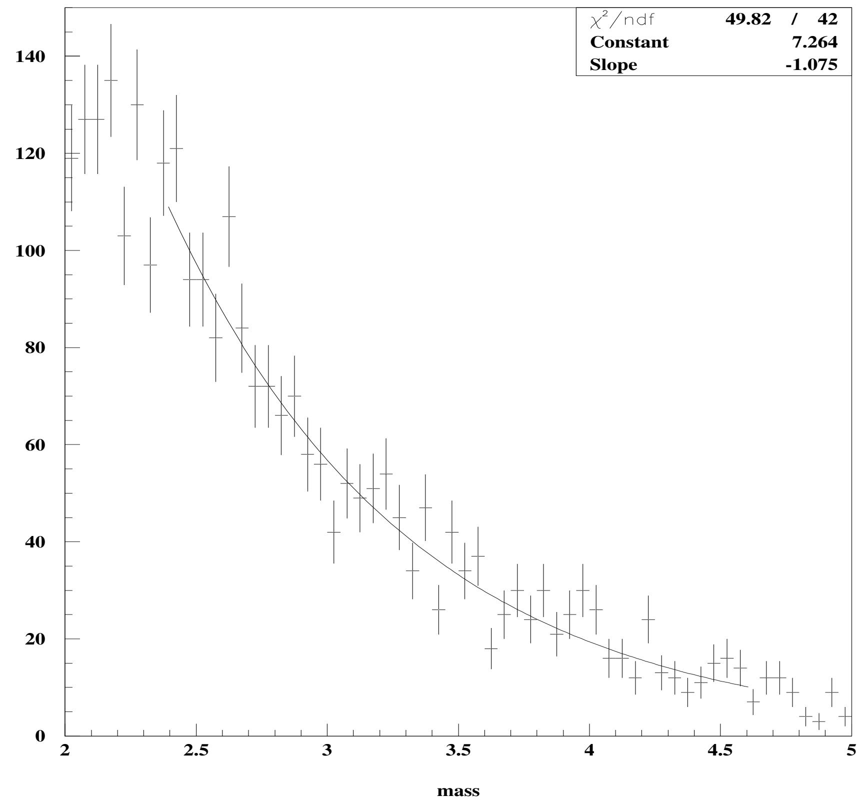

Figure 115: *Two muon invariant mass plot for pair triggered events.*

FLT efficiency summary

Table 34 summarizes all the efficiency measurements. Since the electron J/ψ efficiency is dominated by Bremsstrahlung effects and we are mainly interested in FLT features we do not list it here. As discussed above there is a discrepancy between the MC and the observed efficiencies. It has to be pointed out that for the FLT track efficiency from single track running we need to match the SLT tracks to the found FLT one in order to make progress. We also need to state a J/ψ event efficiency. This analysis is in an early state and more work is required to extract a result.

The difference in the muon track efficiency between the MC and the real data is not understood but is suspected to come from problems in the muon system as explained above. The single track efficiency for the electrons as measured from the online tracking is higher than the one extracted from the simulation on the same data. The simulation is consistent with the efficiency for finding a muon in the OTR only wich is 57% as determined from MC. The inconsistency between the simulation and the online tracking is not understood but should be resolved by introducing a proper model for the link and latency behaviour into the FLT simulation. By now we can only treat this 20% relative difference as systematic uncertainty in our measurements which can be hopefully resolved by further analysis.

Table 34: *Summary of the different FLT tracking efficiency estimates. All numbers are for tracks or J/ψ events which are in the FLT fiducial volume. Note that the muon pretrigger and pad efficiencies are not included here.*

method	muons		electrons	
	track	J/ψ	track	J/ψ
reference tracks (FLT record)	-	-	0.74	-
reference tracks (simulation)	-	-	0.59	-
MC	0.33	0.10	-	-
selected J/ψ	0.23	0.09	-	-
single track J/ψ	0.19	-	-	-
pair trigger	-	< 0.10	-	-

FLT run summary A collection of runs were taken between April 2000 and the HERA shutdown. These runs helped understanding the FLT operation and allowed the progression from one OTR sector to the complete OTR and MUON detectors used for triggering. They will also be used to study in more detail the system. Table 35 summarizes the different run conditions, most of them were taken with an interaction rate of 5 MHz.

3.1.4 Conclusions

The FLT has been designed under the assumption of very efficient tracking detectors whose positions are known very precisely. These requirements were not fulfilled. Our intermediate term plans deal with finding feasible ways to adapt the FLT algorithm to the existing detector:

- During the last run period the only way to deal with cases where both cells contributing to a FLT hit were dead was setting the hit always to one. This spoils the ghost suppression and is a likely culprit for the large message multiplicity. We found a way to allow one out of the 3 hits required in the coincidence matrix to be missing (this involves "only" a modification of the firmware on the TFU boards and is not yet tested). This can surely be a solution in the low occupancy or small RoI areas of the tracking and help improving the efficiency without compromising the ghost rate. This design change has to be studied using MC and the recorded data to evaluate their performance.
- Secondly, we try to improve our understanding of the actual detector geometry. We saw for example a significant improvement for muon FLT candidates when adjusting the MU1 alignment using SLT tracks. Implementing a better model of the detector geometry into the LUT coding should recover some of the efficiency losses (up to 30% of events). Furthermore a correct alignment will allow us to shrink the RoI sizes and hence reduce the ghost rate and message multiplicity.

We consider the FLT data links (optical links) a problematic segment of the technical implementation of the FLT and pretriggers. However we managed to eventually reach a state of acceptable

Table 35: *Summary of the different FLT running operations.*

Running condition	comments
ECAL, Muon pretrigger only	shows the pretrigger setup (missing,noisy boards)
FLT sector 1 (OTR)	tracking through 1 sector of the 4 OTR superlayers
FLT -X-Y quadrant (OTR)	extension from 1 sector to 1 quadrant of the 4 OTR superlayers
FLT all (OTR)	extension to all 5mm OTR sectors for the 4 superlayers
MUON	all 3 MUON superlayers
MUON and OTR	muon tracking through all the 7 superlayers included 10mm OTR sectors
FLT all and TPU	integration of the TPU in the system, remove clone tracks
FLT all and TDU	test the pair mode
Efficiency runs (OTR, MUON, OTR and MUON)	only SLT as trigger to calculate FLT efficiencies
FLT all, rate scan	runs at different target rates (5-10-15-20 MHz)
TPU and TDU study	use different LUTs and cut parameters to test their algorithms
FLT as trigger	count mode one or two tracks and pair mode of the TDU used to trigger, decision sent to the SLT

and stable operation. Therefore we conclude that there are no fundamental, but only "technical" problems which we assume can be fixed. We do not foresee a general replacement of all links. We will undergo a redesign of the sender circuitry in order to understand whether we can improve its stability and find an automated configuration technique (rather then on board potentiometers). We plan to only replace boards which show problems.

High occupancy events lead to large number of messages in the trigger system. These might temporarily clog the messaging system by filling many of the message FIFOs. The system needs some time to process all the events. Therefore "hot" events influence the latency of the following events. This effect is called *message congestion* and leads to excessively large system latency and loss of efficiency[47]. We only had our first experience with this situation, however we can make qualitative arguments how certain modification would influence the situation. So far the ECAL pretrigger has been operated without bremsstrahlung recovery mode. If it is enabled the latency for electron and

[47] On TFU and TPU level old messages are deleted, unfortunately the TFU rejection rate is not recorded.

positron candidates is expected to increase by 0.9 to 1.4 μs [95]. In order to reject high multiplicity events early in the processing, the ECAL Energy Inhibit (EEI) card was designed. It sums up the total energy of the inner ECAL and once operational it will inhibit the generation of pretriggers for events that have been flagged. By now this board has not been commissioned but it will be instrumental to reduce message congestion, especially for runs around the design interaction rate of HERA – B . Other inhibit schemes, for example using scintillating counters or information of certain detector components, can also be implemented, since all pretrigger systems have an *inhibit input* implemented. However such schemes have to be thought up and all electronic will have to be designed. In order to reduce the latency for muon candidates we are looking into removing MU4 from FLT tracking (MU4 data will, of course, still be used by the MUON pretrigger). Further improvement can be made by changing the protocol between the TDU and the Fast Control System. A general re-design of the Fast Control System Mother in order to speed it up should be considered. We could also gain some time by removing the PECL message system in the pretriggers and directly sending messages at LVDS signal levels instead.

We can make no statement on the long term stability of the electronics. This concerns in particular the optical data link to the FLT and the MUON and High$_T$ pretriggers. The optical link uses the Motorola Autobahn Spanceiver that suffers from excessive heat generation and is no longer manufactured. However there has only been a modest failure rate of these chips, which has leveled of during the run period. The cooling of the Autobahn chips has been improved for on the TFUs (24 chips per board) during the last few months and should also be improved for all other boards (typically 8 chips per board).

Neither the ITR nor the MUON pixel part have been included in the FLT yet. Both use some distinct electronic boards. The Inner Tracker trigger link boards have been tested extensively (see section 2.4.4) and are expected to work after only little commissioning. The MUON Pixel Mapping Boards have already been used by the MUON pretrigger group and the FLT_LB's used for the pixel chambers have only a slight modification compared to the version used for both the MUON tubes and the OTR. Consequently the commissioning of the respective systems is expected to run smoothly. The potential physics pay off for the experiment is substantial. When adding the inner detectors to the trigger the number of signal events is expected to double!

Our immediate attention is directed at our analysis effort. Substantial amount of data spanning a large parameter space has been taken towards the end of the HERA running period. The analysis of these FLT commissioning runs should allow us to get a much better understanding of the trigger performance. It is likely to resolve a number of currently existing inconsistencies. However it needs to be pointed out that the required thorough investigation will take time.

3.2 The ECAL Pretrigger system

The main purpose of the electromagnetic calorimeter pretrigger is to provide electron/positron candidates for the First Level Trigger[26].

The selection of candidates is performed by a cluster finding algorithm that selects the 3x3 matrices of cells (nonets) having a local maximum of energy deposit and satisfying certain programmable threshold conditions.

For the J/ψ trigger runs, the e^+/e^- candidates were selected using the following relations:

$$E_5 > E_{TH}/2 \tag{14}$$

$$E_{cand} = \sum_{i=1}^{9} E_i > E_{TH} \tag{15}$$

$$E_{TH} = K_{TRIG}\left(\frac{1}{\sqrt{x^2+y^2}} + \frac{1}{\sqrt{x^2+|y^3|}}\right) \tag{16}$$

In these equations E_5 represents the energy deposited in the central cell of the nonet, E_{cand} the energy of the lepton, x and y are the horizontal and the vertical distances (in cm) from the beam axis and K_{TRIG} is a constant term (typically $K_{TRIG} = 550\,GeV\ cm$). The threshold depends on the position of the cluster in the ECAL. In addition, for example for photon studies, the thresholds can also be defined requiring a given transverse deposited energy in ECAL as:

$$E_{TH} = E_T\left(\frac{\sqrt{x^2+y^2+z^2}}{\sqrt{x^2+y^2}}\right) \tag{17}$$

where E_T represents the cut-off transverse energy (typically $E_T = 1\ GeV$) and z is the ECAL distance (in cm) from the interaction region.

If a candidate satisfies these conditions, the pretrigger calculates the following quantities and passes the encoded information to the FLT:

- the position of the electromagnetic cluster (with a center of gravity algorithm corrected for the $S-shape$ effect).
- the address of the Region of Interest (RoI) in the tracking system.
- a flag which indicates if the electromagnetic cluster transverse energy is above a second threshold greater than the previous one (to trigger on high E_T photon candidates).
- the energy lost by the lepton for bremsstrahlung (BR) photon radiation.

This last original feature provides a safety margin for the pretrigger efficiency of the calorimeter. An electron can emit a BR photon after, before and inside the magnet. In the first case the photon and the electrons travel together and hit the calorimeter nearly in the same region allowing an automatic energy recover. In the second case, the photon follows a straight line from the vertex region to ECAL and the impact position can be determined (and the energy can be determined) knowing the electron/positron cluster position and energy. However, if the bremsstrahlung photon is emitted while traversing the magnet region, there is no way to determine with ECAL alone were the impact point is.

The total number of pretrigger boards needed to cover the whole calorimeter is 128. The corresponding numbers to the different ECAL sections together with the total number of channels handled by a single board is reported in Table 36.

Table 36: *Number of Pretrigger boards per ECAL section.*

ECAL section	N. of Pretrigger boards	region of cells per board	Primary channels	Boundary channels
Inner	42	10×5	50	34
Middle	48	8×6	48	32
Outer	38	8×6	48	32

In the global design of the pretrigger system the three different ECAL regions are treated independently; Monte Carlo simulations have shown that this worsens the overall electron pretrigger efficiency for the $B^0 \longrightarrow J/\psi K_S^0$ channel by $\approx 2\%$, but it greatly simplifies the electronics. Each pretrigger board can process signals coming from a 10x5 or 8x6 region of cells (covered by 2 read-out boards) plus the 34 or 32 border cells that are needed to have complete nonets. A system of passive distributors along the connection from the front end to the pretrigger boards provide the correct routing for all channels. In this way, there is no loss of efficiency due to pretrigger cards border effects.

3.2.1 Technical Description

At each BX, the electron pretrigger board (EPR) receives an 8 bit word for each input channel (primary or border one) from the read-out. Seven bits represents the calibrated and compressed energy value of the cell, while the 8^{th} bit is a flag containing the information whether the energy of the readout calorimeter cell fulfills the condition (14).

In Fig. 116 a block diagram of the HERA – B ECAL pretrigger card is shown. The board is a 9U VME standard card.The data coming from the read-out through the Input Interface (IIF) are processed in the following main blocks[97, 98, 99]:

- *Local Maxima Finder Unit (LMFU)*: It applies the cluster finding algorithm and it evaluate the coordinates of the local energy maxima.
- *Process Controller (PC)*: It performs a pipelining of the candidates found by the LMFU and by the Bremsstrahlung Request Interface (see below) allowing to process up to 3 candidates per board per BX.
- *Event Buffer and Multiplexer (EBM)*: It allows to extract the 7 bit energy values of the central cell and of the eight neighboring cells of the cluster.
- *Data Processing Unit (DPU/LUT)*: It is the data processor that performs all the computations (like total energy, center of gravity, etc.) needed to form the electron pretrigger message to be sent to the FLT. The structure of this unit is based on LUTs, providing a high flexibility for the pretrigger algorithm choice and its possible updating.
- *Bremsstrahlung Request Interface (BRI)*: It checks the presence of possible bremsstrahlung clusters in the same or nearby EPR boards. The clusters found are sent to the DPU for processing.

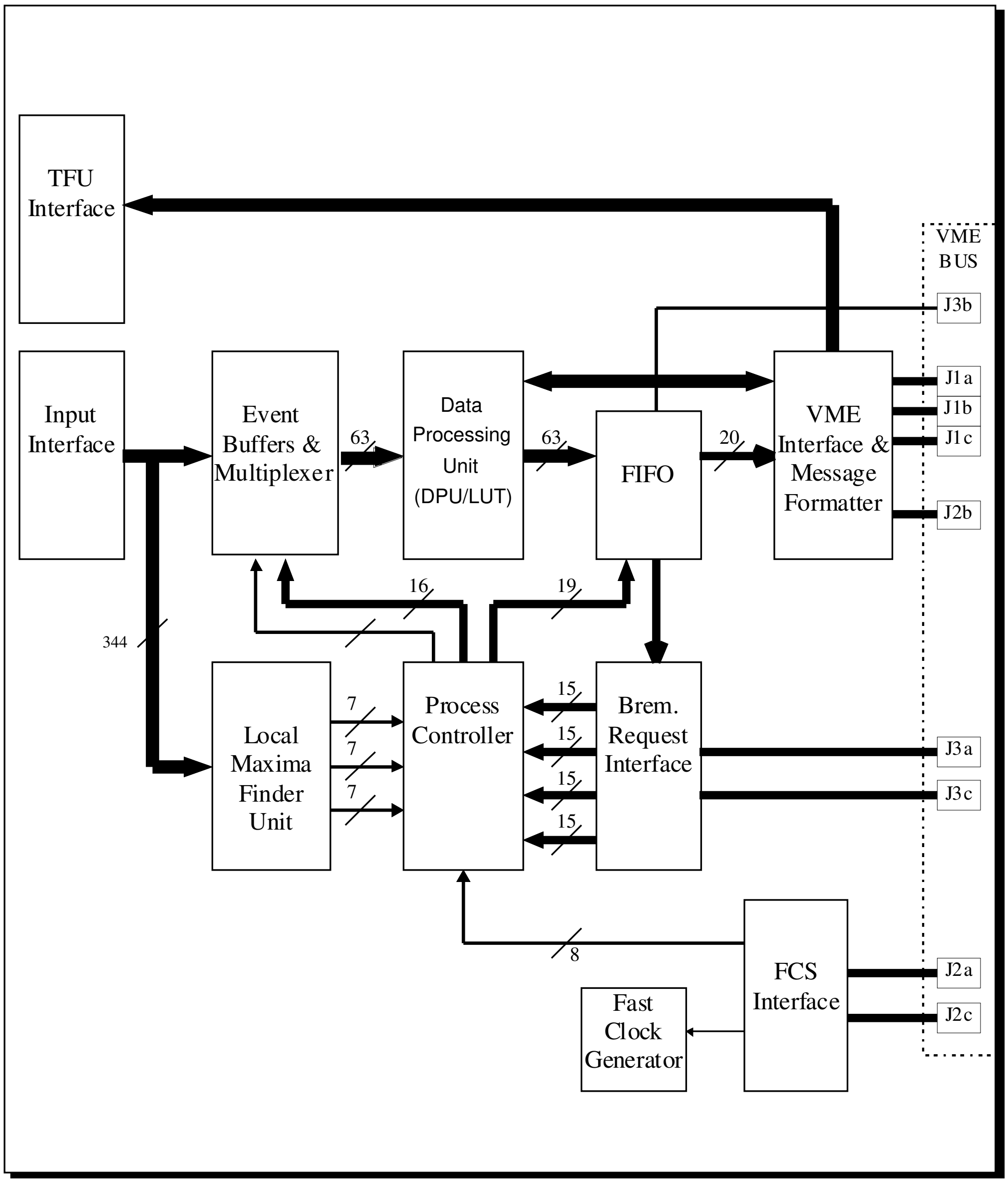

Figure 116: *The* HERA – B *ECAL pretrigger card block diagram.*

- *VME interface and Message Formatter (MF)*: An 80 bit message is formed here containing all the quantities determined by the DPU and needed by the FLT TFUs. The messages are subsequently sent to the *TFU Interface (TFUI)* that transmits them at a clock frequency of 40 MHz.

- *FCS Interface (FCSI)*: It is the interface to the HERA clock providing a global timing signal. A 7 bit BX number is delivered to this interface that is used for data addressing and labeling.

The total latency of the pretrigger system has been evaluated by a detailed simulation to be about $1.5\,\mu s$ without the bremsstrahlung recovery algorithm and about $3.5\,\mu s$ with it[96].

3.2.2 Present Status and Performances

Since the beginning of year 1999, a part of the ECAL pretrigger system ran continuously providing the main trigger for the HERA – B experiment and allowing the detection of the first J/ψ signals[103]. The inner and middle section of ECAL are instrumented since the beginning of year 2000 and the system has been fully equipped during the very last part of the data taking. Actually all the 128 boards of the system are installed and 5 spare boards are available.

During this long period the system operated reliably under different conditions. The EPR performance was checked both during data takings with online tools and offline with specific analyses of recorded data. In Fig. 117 the effect of the cut applied at the pretrigger level is shown.

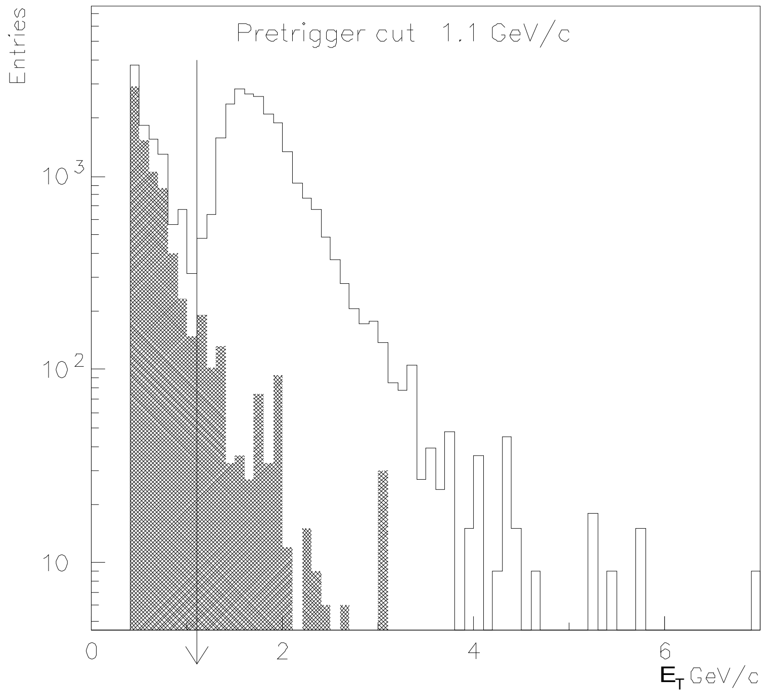

Figure 117: *Transverse energy (E_T) spectrum for triggered (open histogram) and non-triggered events (hatched histogram) for boards sitting at the same distance from the beam pipe.*

The hatched histogram represents the transverse energy (E_T) distribution for clusters reconstructed in an ECAL board where the pretrigger system was not activated. The open histogram shows the E_T from a board where the pretrigger was selecting clusters with a threshold $E_T \geq 1.1\,GeV$. The two boards were placed at the same distance from the proton beam pipe. The two distributions, corresponding to the same number of acquired events, show clearly the cut of the pretrigger system. In Fig. 118 the measured variation of the output rate of the ECAL pretrigger system as a function of the target rate and of the transverse energy cut applied is shown.

From a fit on these measurements we can get the following formula useful for a rough (15% level) evaluation of ECAL pretrigger rate as a function of E_T and the target interaction rate:

$$r(kHz) = I(MHz) \cdot \exp\left(7.2 - 3.2 \cdot E_T(GeV)\right) \tag{18}$$

where r is the ECAL pretrigger rate in kHz, I is the target interaction rate in MHz and E_T is the energy threshold in GeV as defined in (17). As a consequence, for instance, asking for the presence

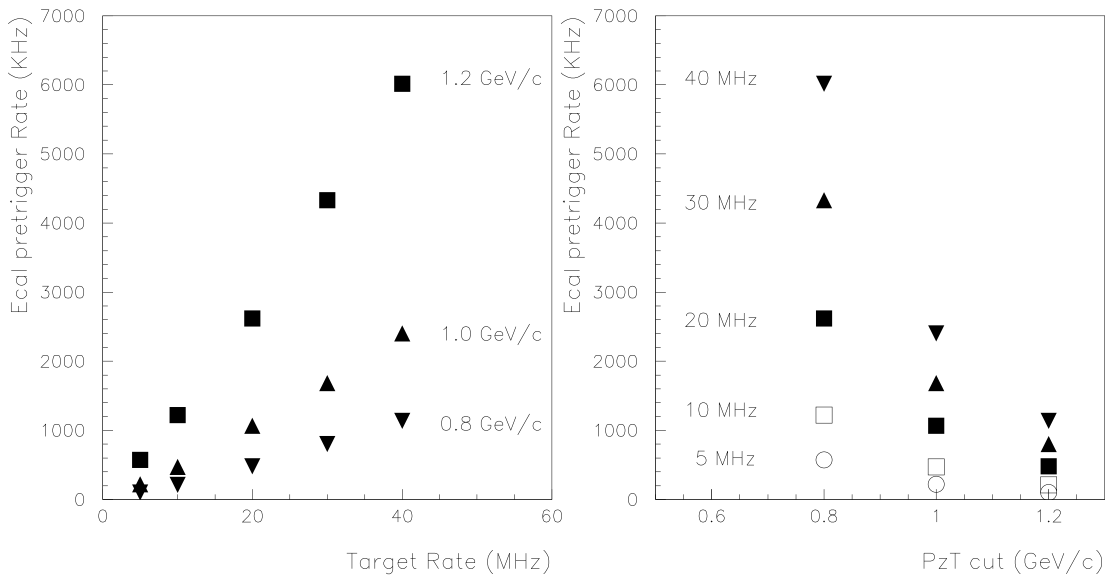

Figure 118: *Output rates from the ECAL pretrigger system as a function of the transverse energy cut applied for different target rates.The trigger were provided by the Inner and Middle sections of the calorimeter.*

of at least one cluster in the ECAL pretrigger system with $E_T \geq 1\ GeV$ we get a reduction factor of ~ 20 at 5 MHz of interaction rate.

In order to have the full control of the pretrigger functionality, performance, and debugging many software tools have been developed. Two bit level simulations of the EPR, one asynchronous and the other sequential, allow to study the latency and the efficiency for specific physics issues. A versatile program to build the read-out and pretrigger LUTs allowed an easy change and update of all threshold settings each time it was needed. The calibration constants are loaded from a DB and all the data used for the LUT production are recorded, in order to keep a history of the EPR setting used for each run.

The trigger performances during data taking were monitored continuously by a dedicated program[102]. This program has been conceived to work on three different levels of detail:

- general: For each ECAL section, many quantities like occupancies, transverse energy, rate and bunch crossing (BX) distributions are checked.
- single board: For each board the above mentioned quantities can be checked.
- single channel: For each channel the total energy and the transverse energy distribution is monitored.

Other general monitors[100, 101] and data quality check programs, integrated into the general DAQ system or stand alone, complete the debugging tools.

One of the main problems that affected the pretrigger performance for some time is the presence of hot channels that provides candidates above the trigger threshold continuously. This is now solved by the online monitors that signal the presence of hot channels followed by a procedure to mask them.

During year 2000 run dedicated data taking was performed in order to check two crucial points: the latency of the system and its efficiency.

Concerning the first point, the latency of the pretrigger without the bremsstrahlung recovery request has been found to be below 2μs. A detailed description of the results is reported in subsection 3.1.2.

For the efficiency studies, dedicated data sets were taken with the EPR trigger and a suitably adapted SLT code. Only events satisfying the EPR conditions (more than one cluster with $E_T >$ 1 GeV) at the pretrigger level OR in the online SLP reconstruction were recorded. In the offline analysis the clusters found from the pretrigger were compared with the clusters reconstructed offline applying the same threshold.

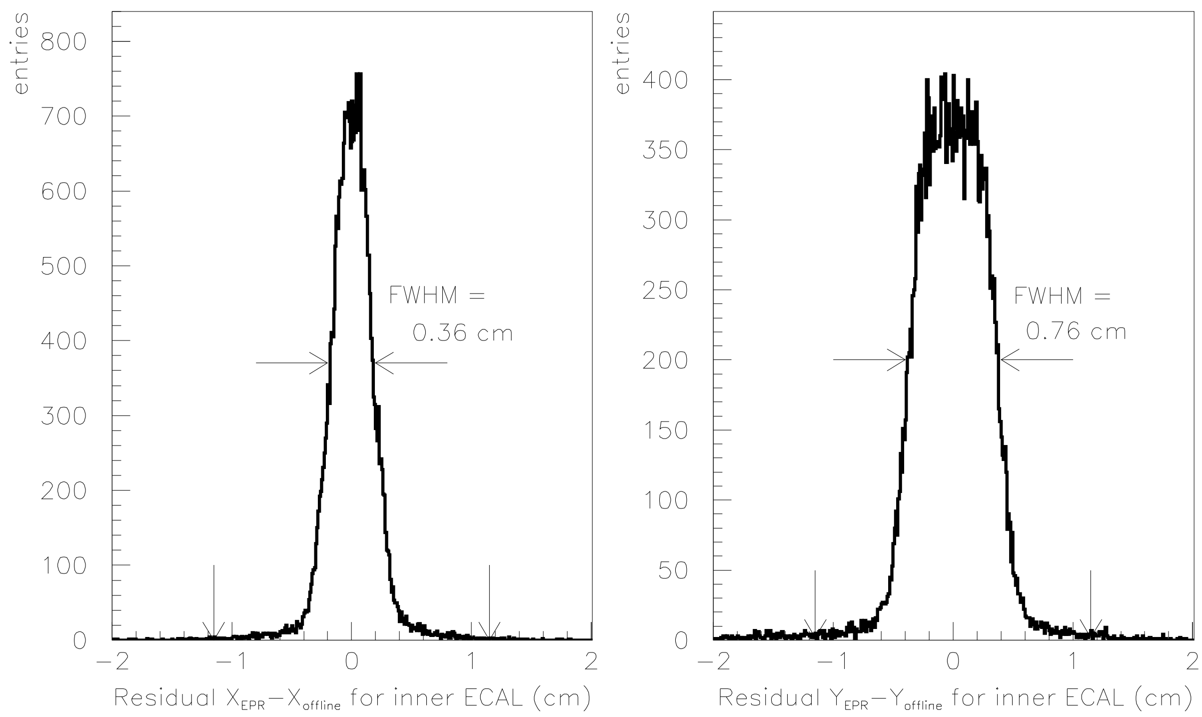

Figure 119: *Residuals between the X (left) and Y (right) coordinates of clusters as measured by the pretrigger (EPR) and by the offline reconstruction for Inner ECAL signals. The widths observed are mainly due to the compression (and worsening) of the position measurement needed for encoding the FLT message. Lower arrows define the inner ECAL cell size window.*

In Fig. 119 the residuals between the pretrigger cluster coordinates (X_{PTR}, Y_{PTR}) and the corresponding quantities closest offline reconstructed cluster for the Inner ECAL section are compared. A good match is clearly seen: more than 99.5 % of the coordinate pairs for X and 98 % for Y are within half of a cell size. The widths of the residuals are almost entirely due to the approximations needed for encoding the information for the FLT message. Similar distributions are obtained for the Middle and Outer sections. The ECAL pretrigger efficiency has been then obtained by comparing the number of clusters reconstructed in both way. The results are summarized in Table 37.

Table 37: *ECAL pretrigger efficiency.*

ECAL section	N. of Pretrigger Channels	Average efficiency (%)	Bit error (%)	Masked channels (%)
Inner	2100	97.2	1.6	4
Middle	2128	94.8	1.6	5
Outer	1728	91.7	2.8	8

The average efficiency for the different ECAL sections is well above 90% and it is mainly affected by the different cluster finding algorithms used by pretrigger and offline reconstruction.

Another important parameter that could affect the FLT performance are the bit errors present in the cluster energy determination. In fact the energy value is used by the FLT in order to determine the position of the Region of Interest (RoI) in the OTR chambers. In Fig. 120 the energy correlation between pretrigger and offline energies is shown. The few events sitting above the line are due to bit errors in the pretrigger energy determination.

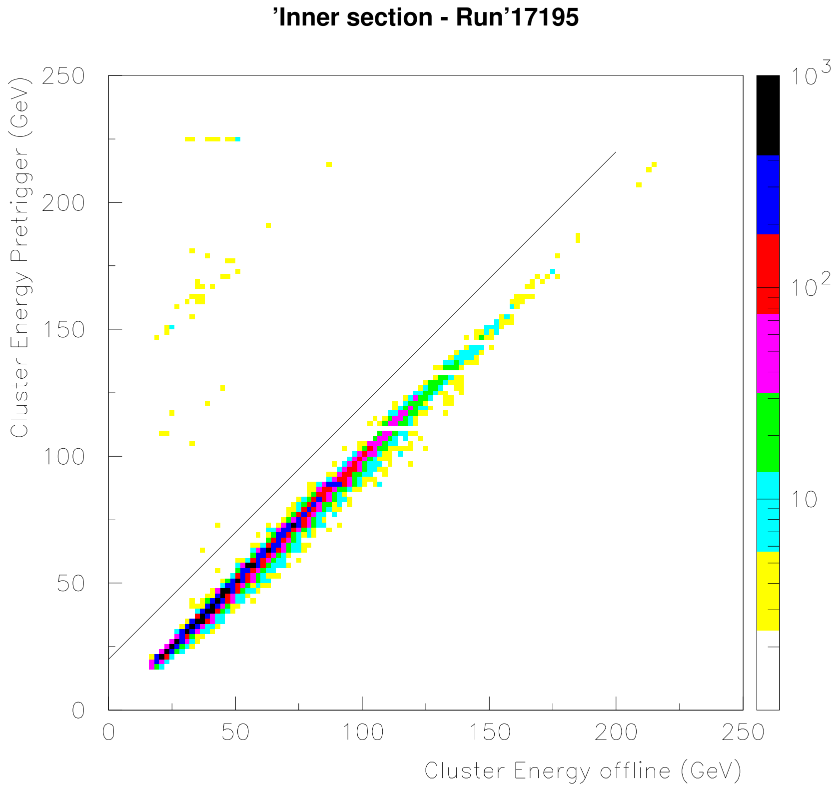

Figure 120: *Correspondence between the the pretrigger and the reconstructed energy of the clusters.*

In the 4^{th} column of Table 37 the corresponding fraction is reported, where the maximum value is below 3% and can be reduced masking neighboring cells in the cluster construction. In the 5^{th} column of Table 37 we report the percentage of channels that have been masked on the pretrigger board. The causes for the masking and their relative percentage are explained in the next section.The higher value of masked channel in the outer ECAL are due to a less precise calibration in that region (the last to be activated in the data taking). For sake of clarity it has to be noticed that the percentages of bit errors reported in the 4^{th} column of Table 37 represent the ones remaining after the masking procedure.They are in principle eliminable as will be explained in the next section.

3.2.3 Future Plans

The pretrigger performance is affected not only by the problems inside the system, but also from the ones coming from the different components of the ECAL as photomultipliers, high voltage system, readout boards, and cable connections. The pretrigger system worked smoothly once the feature to mask noisy channels via software has been implemented. The main problems and loss rates are given in the list:

- Hot channels ($\simeq 1.5\%$). Due to:
    1. pretrigger board input channel (can be fixed)
- Cold channels ($\simeq 1\%$). Due to:
    1. bad low/high voltage distribution (can be fixed)
    2. bad transmitter on the readout board (can be fixed)
    3. broken connecting cable (can *not* be fixed)
    4. bad receiver on the pretrigger board (can be fixed)
- Bit errors ($\simeq 5.0\%$)[48]. Due to:
    1. bad transmission from the readout board (can be fixed)
    2. bad connecting cable (can *not* be fixed)
    3. bad working pretrigger board (can be fixed)

Most of the problem sources can be cured except the ones stemming from bad readout to pretrigger connections (twisted pair cable) due to the large number of cables whose routing is quite complex. A minor contribution (about one per cent) from this source is expected to be fixed by a carefully check before the installation.

The remaining part can be cured during the shutdown period testing dynamically the data flow from the readout to the pretrigger. A procedure has been implemented to pulse the readout system with fixed signals, read the respective pretrigger messages and then compare them with the expected ones. In this way it is possible to test the complete ECAL data chain from photomultipiers to pretrigger boards. The procedure has already been used to test the system. All the pretrigger channels can be checked with statistical significance in less than one hour.

By means of this procedure, the whole system can be fully debugged fixing the problems that in some extent are spoiling the performances of the system.
The commissioning of the ECAL pretrigger system is therefore concluded excluding the feature of the bremsstrahlung recovery that has not been tested till now although almost completed and foreseen for the next upgrade of the pretrigger logic.

[48]This percentage includes the percentages quoted in the 4^{th} column of Table 37

3.3 The Muon Pretrigger System

3.3.1 Requirements and Coincidence Algorithm

The muon pretrigger processes the digitized data of the pad readout of superlayers MU3 and MU4, provided by the front end driver (FED) readout buffer system, to calculate seeds for track finding in the first level trigger (FLT). The superlayers are designed as pad chambers in the outer region and as pixel chambers in the inner region near the proton beam pipe, where higher occupancies are expected, see section 2.10. In the outer region the chambers are divided in a $+y$ and $-y$ part, each consisting of 66 columns with 30 pads per column in MU3 and 29 pads per column in MU4. Pseudo pads, made up of four combined pixel cells, are used for calculating seeds in the pixel system of superlayers MU3 and MU4. There are 16 columns of pseudo pads consisting of 16 pseudo pads in MU3 and 18 pseudo pads in MU4. A data rate of 10.6 GByte/s has to be processed in parallel.

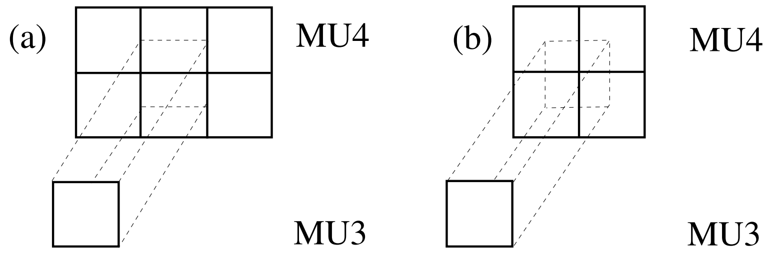

Figure 121: *Track seeds are defined by coincidences. In the pad system (a) there is an 1 : 6 and in the pixel system (b) there is an 1 : 4 coincidence scheme.*

Track seeds are defined by coincidences as shown in Fig. 121. In the pad system three neighboring pads in x, accounting for the deflection in the magnetic field, and two neighboring pads in y are combined in a logical "OR". A coincidence is defined as a logical "AND" between a pad from MU3 with the "OR" of six pads in MU4. In the inner region the momenta of muons are larger which leads to smaller effects of multiple scattering and smaller deflection in the magnetic field. In this region four pseudo pads are used to form a coincidence with a logic "AND" with one pseudo pad in MU3, shown in Fig. 121. In the following we will concentrate on the pad system. The difference to the pixel system is described later.
The total time available for the FLT to provide a trigger decision is 12.288 μs. Included in this time is the time used by the pretrigger to deliver a seed to the FLT. To achieve best performance the time for the pretrigger calculations must be shorter than 1 μs. For an overview of the system latency see also reference [95].

3.3.2 System Overview and Latency

The data of MU3 and MU4 is processed by the muon pretrigger synchronously to the BX clock. Correspondingly, the design concept of the muon pretrigger is based on a pipelined architecture. The muon pretrigger is realized as a modular system, composed of about 100 large 9U VME boards. An overview of the system is given in Fig. 122. The pretrigger link boards (PLB), located in the FED crates, receive the pad data and timing information including a BX identifier from the fast control system (FCS). A PLB consists of eight channels, each handling the data of one pad column. Because of the pin limitation of the FPGA [104], which performs the coincidence finding algorithm on the pretrigger coincidence unit (PCU), the data of one column is transmitted in two cycles,

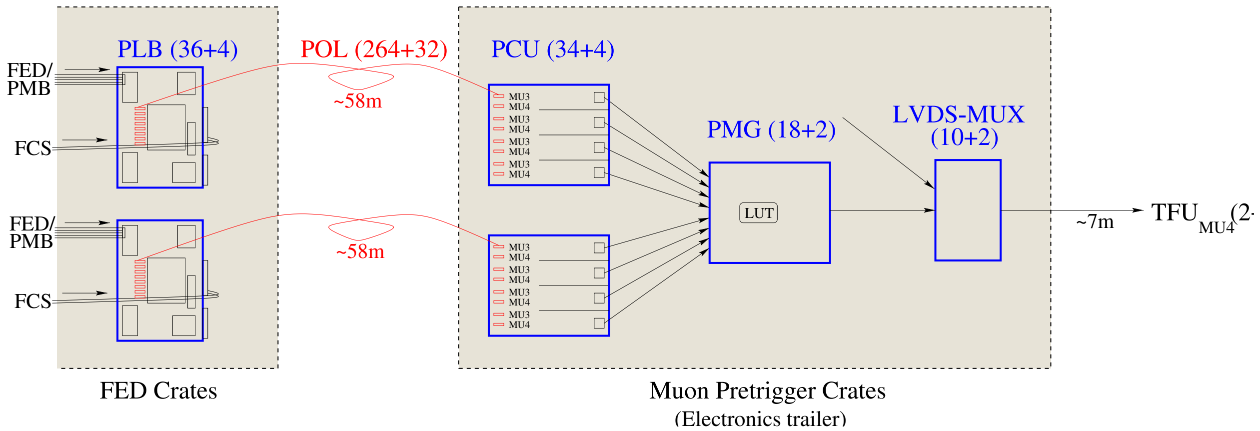

Figure 122: *Overview of the muon pretrigger system. The numbers in brackets present the numbers of the components used for the total system, namely pad system + pixel system.*

marked with the BX number and a cycle number. The frequency on the PLB is more than twice the BX clock frequency. Special chips [105] serialize the data and transmit them via pretrigger optical links (POL) [106] over a distance of 58 m, to the PCU, located in the electronic trailer outside the experimental area. The data rate of the links is 100 MByte/s. All transmission lines, consisting of transmitting chip, POL and receiving chip [105], work asynchronously to each other, having their own clock and control device each. In total 40 PLBs and 296 POLs are used.

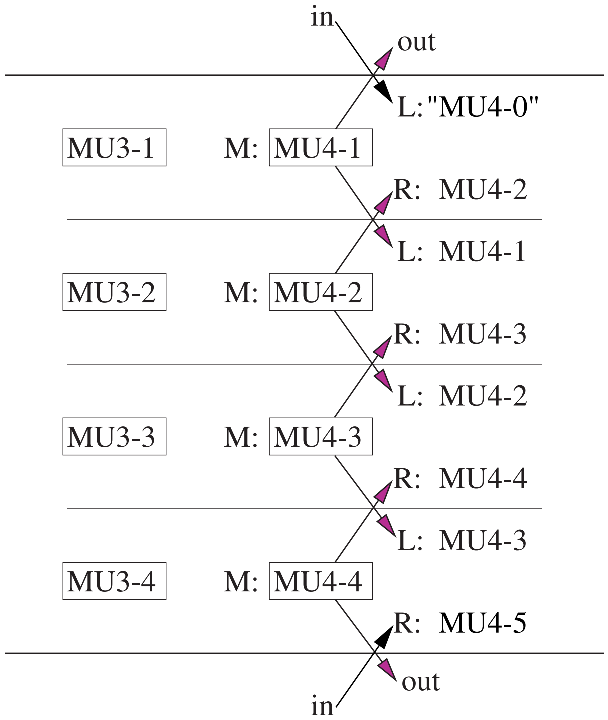

Figure 123: *Distribution of MU4 data on the pretrigger coincidence unit. The data of one MU4 column is distributed to the data of three MU3 columns. The data of two MU4 columns are transmitted to and received from neighboring PCUs.*

The PCU is composed of four identical channels, performing the coincidence finding algorithm for one column of MU3. Due to the coincidence scheme shown in Fig. 121 (a), six columns of MU4 are required on a PCU board, as shown in Fig. 123. Every PCU has got eight serial inputs for optical links, split into four links for MU3 data and four links for MU4 data. The data of two MU4 columns is transmitted from one PCU to the neighboring PCUs via SCSI cables. The coincidence scheme demands that the data from one MU4 column has to be distributed to the data of three MU3 columns. Synchronizing the data from different receiver chips, storing it under the address of the BX number in dual ported RAMs, implements an additional test feature. The dual ported RAMs can be read out by VME, interfering with processing but offering the possibility to check the data transmitted by the POL.

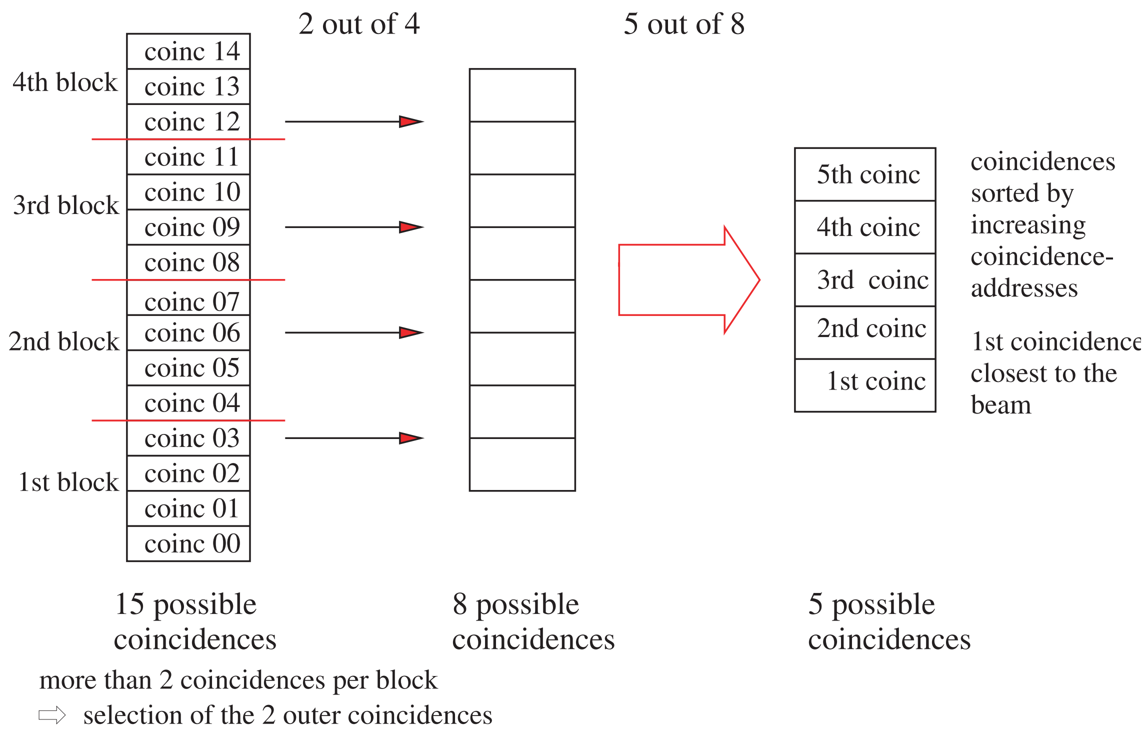

Figure 124: *Selection scheme for the pad system. The 15 possible coincidences per cycle are divided into 4 blocks. Out of these at most 4 times 2 coincidences are selected. The next pipeline step selects at most 5 out of 8 possible coincidences.*

The following pipeline steps of the coincidence finding algorithm are embedded in one FPGA per MU3 channel. The data read out of the dual ported RAMs is written in the input register of the FPGA. It is possible to mask out every single bit independently to give highest flexibility in masking hot pads, which could lead to wrong coincidences. The next pipeline step performs the "OR" and "AND" connections according to the coincidence scheme. Transmitting the data of one column in two cycles leads to 15 possible coincidences per cycle. These possible coincidences are divided into four blocks, as shown in Fig. 124. If there are more than two coincidences per block the outer most two coincidences are selected resulting in four "2 out of 4"selection. The next pipeline step selects those five out of eight possible coincidences, which are nearest to the beam pipe. The selection in both pipeline steps is done using look up tables (LUT). Monte Carlo studies and measurements [107] showed that there is almost no loss of information induced by the selections, because of the very low probability of more than two coincidences in one column per cycle. The remaining maximal 5 coincidences are written to so-called zero suppression FIFOs. If there is no coincidence found, the write access to the FIFOs is suppressed.

The difference between the pixel and the pad system is described in the following. One column of MU3 data and two columns of MU4 data is used performing the coincidence algorithm in the pixel system. The PCU hardware is the same as in the pad system. The only difference is the programming of the FPGA which performs the calculations of the algorithm.
In contrast to the pad system there is no "OR" connection of the MU4 pseudo pads. Furthermore there are only eight possible coincidences per cycle, decreasing the complexity of the pipelined architecture. The first selection step is abandoned. Five out of eight possible coincidences are selected using a LUT. They are stored in the zero suppression FIFOs.

After performing the coincidence algorithm the concept of synchronous data processing is abandoned and replaced by a concept of data driven messages. The contents of the zero suppression FIFOs is stored in a serialization FIFO and also in a test FIFO, which is readable via VME. A flag is set to indicate that valid data is present in the serialization FIFO to be read out by the pretrigger message generator (PMG). The formats of the PCU messages for the pad and the pixel system are listed in Table 38. The pattern indicates which MU4 pads/pseudo pads have lead to the coincidence. The coincidence address in combination with the cycle number gives the MU3 pad position of the coincidence.

Table 38: *PCU message format pad and pixel system*

pad system	
Bit	Information
0	cycle number
8...1	BX number
11...9	pattern
15...12	coincidence address
pixel system	
Bit	Information
0	cycle number
8...1	BX number
11...9	coincidence address
15...12	pattern

One PMG is able to read out the information of two PCUs, corresponding to eight PCU channels. In case that more than one serialization FIFO contains valid data, the serialization FIFOs are read out sequentially, resulting in an additional serialization step. The PCU message serves as an input to a LUT, generating the message for the track finding units (TFU) of the FLT. The TFU track search uses the pretrigger message to determine its first RoI. In total 38 PCUs and 20 PMGs are used, installed in seven VME crates.
The LVDS multiplexer (LVDS-MUX) receives the messages of the PMG. It performs a logic level transformation to match the TFU's input interface specifications and multiplexes the messages of two PMGs to one input of the TFU. In total 12 LVDS-MUX are required. The pretrigger message is made up of 80 bits.

As described before, the concept of parallel data processing leads to a message driven design after calculating the coincidences. The latency for the part of the system that is realized as a pipeline is fixed. The latency for the data driven part is strongly related to the number of messages found on the PCU, therefore the latency of this part is given for one message generated. Additional messages add latency, because of additional serialization steps on the PCUs, PMGs and the LVDS-MUX. The muon pretrigger latency is listed in Table 39.

Table 39: *Muon pretrigger latency*

component	$t_n - t_{n-1}$	comment
PLB	300 ns	
54 m optical fiber	260 ns	±10 ns
PCU	700 ns	±50 ns
PMG	300 ns	
LVDS-MUX	230 ns	
total	1.79 μs	±60 ns

3.3.3 Efficiency Measurements

In order to measure the muon pretrigger efficiency track seeds for the FLT were given by messages produced by the pretrigger hardware, but it was not included in the trigger chain. The messages generated by the pretrigger were recorded together with the hit data of the muon drift chambers. To determine the pretrigger efficiency, messages produced by a pretrigger simulation were compared to the messages generated by the pretrigger hardware. The simulation of the muon pretrigger uses the pad hit data of superlayers MU3 and MU4 and performs identical calculations as the pretrigger hardware. The number of matched messages found by the simulation, for which a corresponding message from the pretrigger hardware was found, was determined (N_{match} in Fig. 125). Then the pretrigger efficiency was calculated for each pad as the ratio of matched messages to the total number of simulated messages ($N_{simulation}$). Fig. 125 shows the distribution of the efficiency values obtained.

The measurement showed that more than 50% of the pretrigger channels had an efficiency above 99%. The efficiency of approximately 28% of the channels was between 95% and 99% and of approximately 7% of the channels between 80% and 95%. Low efficiency values in the remaining channels are caused by hardware problems somewhere in the data readout chain.

3.3.4 Software and Monitoring

The online software programs initialize, control and monitor the muon pretrigger hardware. The software consists of two processes on each VME CPU in every muon pretrigger VME crate, called 'mpre_srv' and 'mpre_slave', one central coordinating process 'MPRE_BOSS', a monitoring process 'mpre_monitor', an error logger 'mpre_errlog' and an expert user interface 'mpre_con'. All these processes are booted by the common HERA – B DAQ environment. For an overview of the system, its communication and its interfaces refer to Fig. 126.

The 'mpre_srv' and 'mpre_slave' are accessing and controlling the hardware in the VME crates. In this scheme 'mpre_srv' receives commands via RPM[49] and executes fast hardware accesses, while commands that would block the communication from outside processes to 'mpre_srv' are passed to 'mpre_slave' via shared memory. The 'mpre_slave' process also provides permanent control of

[49] "Really Powerful Messaging", custom made HERA – B messaging software.

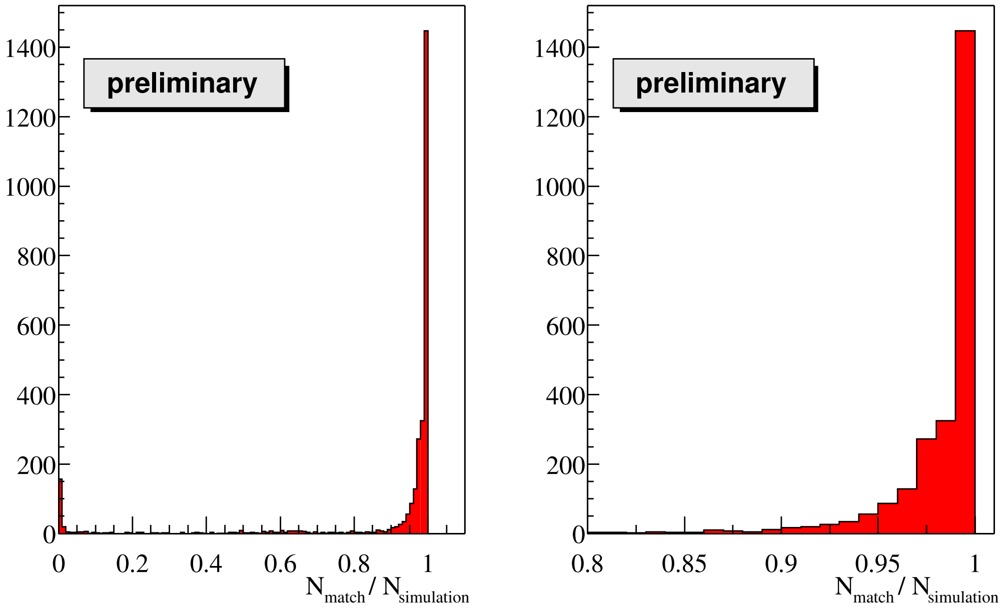

Figure 125: *Distribution of efficiency values for single pads. The right histogram is a magnification of the left one. Only pads with* $\mathrm{N}_{simulation} \geq 10$ *were taken into account.*

the hardware status. Processes in different VME crates operate independently from those in other crates.

The central process 'MPRE_BOSS', obeying the HERA – B central run control state transitions passed by the state machine control (SMC) protocol, is controlling and coordinating the 'mpre_srv' processes. It provides the only interface to systems outside the muon pretrigger, such as the data monitoring process (dmon) 'mu_mpre', DAQ and FLT. A set of test messages and defined time outs ensures that the system communication is always available.

The 'mpre_monitor' process is monitoring the performance of the muon pretrigger. It receives information retrieved directly from the pretrigger hardware. This data represents a small sample of the complete pretrigger data stream which is chosen statistically. It converts these data to RHP[50] histograms and scans the data for hot channels. So automatic control and masking of hot channels is provided.

An error logger 'mpre_errlog' receives error and information messages and stores them. In addition it forwards severe error messages to the common HERA – B error logging facility.

In case expert access to the system is required, an expert user interface called 'mpre_con' is available.

A setup database contains information about the hardware system setup and HERA – B status as well as initialization information. The standard database environment is being used. Changes of the system status are written to the database, providing continuous logging of the system status.

[50] "Remote Histogramming Package", another HERA – B software package.

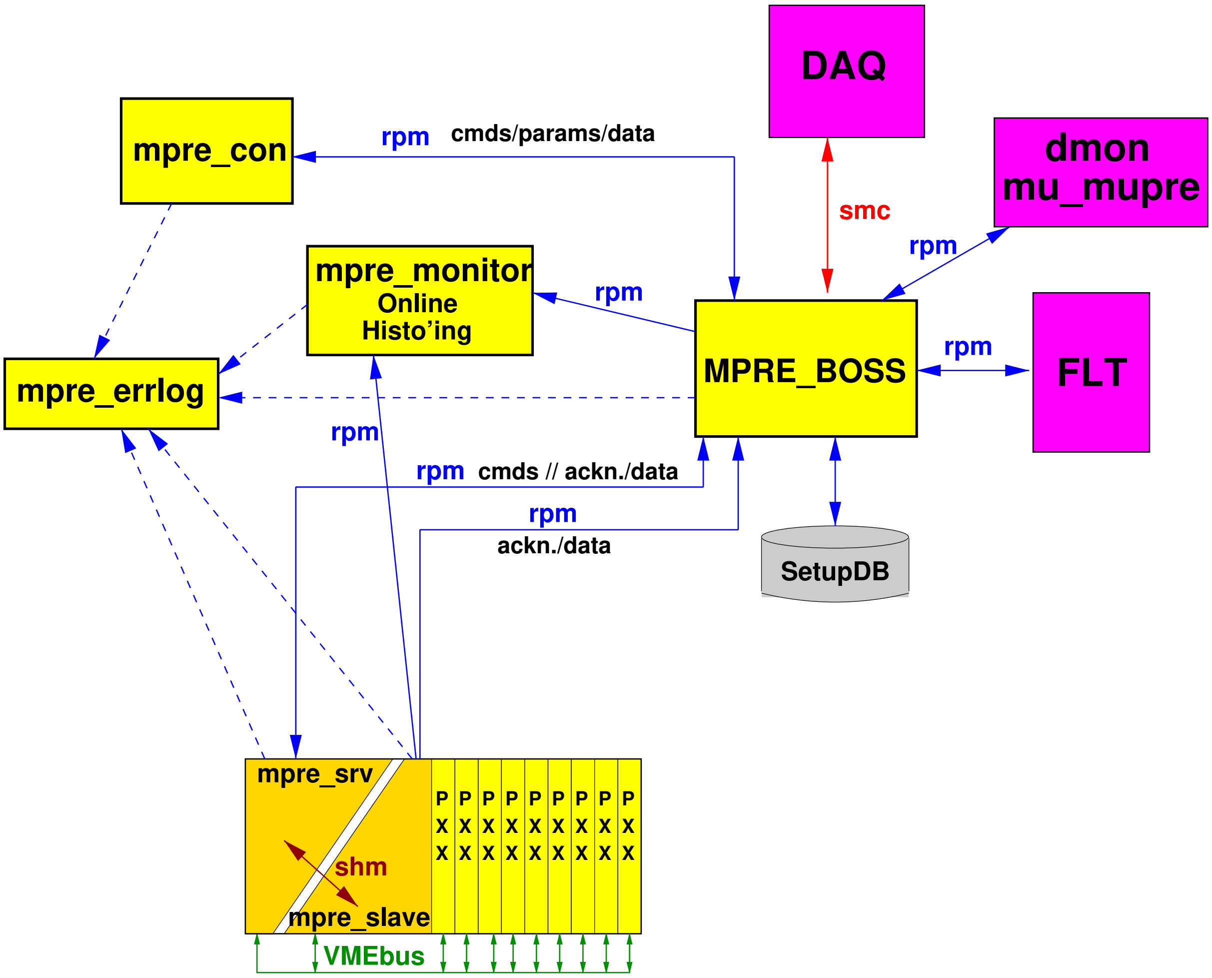

Figure 126: *Overview of the online and monitoring network.*

3.3.5 Future Improvements

During the shutdown the whole muon pretrigger system will be further improved. Especially the monitoring capabilities of the online software will be enlarged. On the hardware side a sufficient number of spare modules for an envisaged lifetime of the HERA – B experiment of several years will be produced. In addition, hardware studies of the optical links will be continued in order to increase their reliability.

3.4 High-P$_T$ Pretrigger

3.4.1 Introduction

The aim of the High-P$_T$ pretrigger is to select the high-P$_T$ track candidates in the event and to send the kinematic information on them as inputs for the FLT parallel to the MUON and ECAL pretriggers. Two types of triggers have been proposed: the so called "hadron–lepton and "hadron–hadron" triggers, here "hadron" stands for *any* track.

In the first case the typical FLT requirements for 40 MHz running are $p_T(\text{hadron}) > 1.8$, $p_T(\mu/e) > 1.0/1.4$ GeV/c. This trigger plays a key role in the B_s mixing measurement. It gives the high quality lepton tag for the B_s flavor while the high-P$_T$ hadron is usually produced by the B_s meson itself (e.g. in $D_s^{(*)}\pi$, $D_s^{(*)}3\pi$ modes). In addition to the B_s mixing studies the hadron–lepton trigger also provides the possibility to collect large samples of B, B_s, Λ_b decays which can be used to attack the CP-violation problem ($B^0 \to a_1\pi$, $B^0 \to D^{(*)+}D^{(*)-}$ decays) and to study other fields in the b quark physics.

The hadron–hadron FLT requirements for IR = 40MHz are $P_T^{1,2} > 1.5$ GeV/c, Mass(12) > 4.5 GeV/c^2, $\frac{|E_1-E_2|}{E_1+E_2} < 0.5$. The main purpose of this trigger is to study the two body $B_{(s)}, \Lambda_b$ decays. In particular it allows to collect large samples of $B^0 \to K^+\pi^-$, $\bar{B}^0 \to K^-\pi^+$ decays. The asymmetry between the two branching ratios provides the information on the angle γ in the unitarity triangle.

One should note that the value IR = 40 MHz was optimized for the J/ψ trigger. If the IR will be lower one can gain extra statistics using lower pretrigger cuts.

3.4.2 Pretrigger Logic

The High-P$_T$ track candidate is triggered as a coincidence of 3 fired pads in 3 High-P$_T$ superlayers, which lie near a straight line coming from the target. The High-P$_T$ superlayers are positioned at z=470, 560 and 610 cm. The cell size varies from 4x8 to 8x8 mm^2 in the inner chambers of the first superlayer, and further from 15x30 to 30x60 mm^2 in the outer chambers. The cell structure in the second superlayer is the projective copy of that of in the first superlayer with the scale factor determined by the ratio of the z coordinates. The third superlayer is shifted from the projectivity by half a cell. This makes the chamber geometry between the chamber zones with different cell sizes and at the chamber borders very complex.

The typical High-P$_T$ coincidence logic is 1-3-2 which means the coincidence of the fired cell in the first superlayer with one of 3 cells (+1, 0, -1) in the second, and the coincidence of this cell in the second superlayer with one of 2 cells (-1/2, +1/2) in the third (see Fig. 127). Contrary to the MUON pretrigger logic no overlap along Y direction is provided, i.e. the corresponding logic along Y is always 1-1-1. This means that in terms of the information flow no cross talk is needed between different groups of projective horizontal rows. The pretrigger electronics can serve one row completely isolated from the others.

In case of low rates for the 1-3-2 logic (e.g. due to a low interaction rate) there is the possibility to switch to the 1-5-2 logic. This means lower effective P$_T$ cut. The read out and pretrigger logic system are described in detail in references [108] and [109].

The performance of pretrigger logic is extraction O(10^7) events out of a few 10^{12} possibilities at a 40 MHz interaction rate.

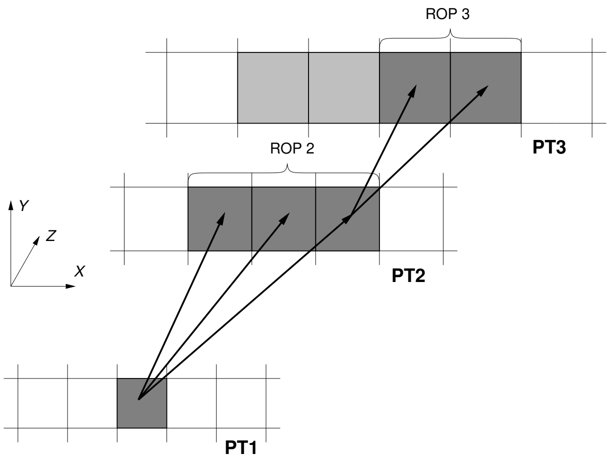

Figure 127: *Triple coincidence between hits in 3 superlayers for the 1-3-2 logic.*

3.4.3 Electronics Overview

The High-P_T pretrigger electronics comprises

- the High-P_T Link Boards which transmit the data from the Front End Driver Boards (FEDs) to the High-P_T pretrigger boards via optical links;
- the High-P_T Pretrigger Boards which "sparcify" the data: they select the groups of hits which produce coincidences and send them to the High-P_T Message Generators;
- the High-P_T Message Generators which analyze the patterns of coincidences and produce the output messages for the TFUs according to the LUTs.

There is a total of 12 chambers: six gas-pixel chambers for the *inner region* and six straw tube chambers for the *outer region*. Half of the chambers are located on the $+x$ side of the proton beam and half on the $-x$ side. The inner region chambers have a total of 11856 channels and cover the angular ranges $10 < \theta_x < 58$ mrad and $10 < \theta_y < 44$ mrad; the outer region chambers have a total of 6240 channels and cover the ranges $38 < \theta_x < 250$ mrad and $44 < \theta_y < 143$ mrad.

3.4.4 The Link Board

There are 4 Front End Driver Daughter Boards (half of the crate) for one quadrant of the inner region in one High-P_T superlayer. Each board serves up to 256 pads.

The Link Board has been designed as a piggy-back card which is screwed directly onto the FED daughter board. It accepts all 256 hits. This information is stored in the registers and then multiplexed to Autobahn transmitters.

The Pretrigger Board accepts the hits from two horizontal rows in all 3 superlayers. During the first half of the bunch crossing period of 96 nsec it process the first row, during the second half - the second row. Thus it should be connected to 6 Link Boards: for $+x$ and $-x$ sides of 3 superlayers. The chamber geometry (the number of cells per row) is different in different regions. Therefore 2 types (5 options) of Link Boards are provided, they serve either 8 or 6 $+x/-x$ halves of rows. In addition for some Link Boards there is a dedicated Link Interconnect which passes the data from one Link Board to another and only then to the Pretrigger Board.

Status All FEDs and the Link Boards have been produced and shipped to DESY. All boards for the inner High-P_T and part of the boards for the outer are installed in the crates under the magnet. FEDs can be read out via the SHARC links in a standard way used in other subdetectors. Parallel to it the information from the Link Boards goes to the Pretrigger Boards placed in the trailer via optical links.

3.4.5 The Pretrigger Board

A pretrigger board filters the raw data and reduces the output data rate to an acceptable level. A pretrigger board serves complete rows of pads of three chamber layers. The maximum number of pads per row is 96, every 48 nsec in total 278 bits of data together with a time stamp are sent to pretrigger board via 12 links. It receives data from six half-layers of chambers and tests them for coincidences. Data which match to the pretrigger algorithm are stored for necessary time, data items are being extracted from stored data and transmitted in a special format to the message generator.

On each of 12 link channels of a pretrigger board bunch crossing number bits are also transmitted and these are the only predictable information can be used to monitor reliability of the data transfer. If a comparison fault is detected, an error flag is set and the event is suppressed.

The pretrigger boards fulfill some specific procedures which are necessary for initialization, configuration, running, monitoring/diagnostic and self-testing.

3.4.6 The Message Generator

The message generator acquires data sets from a group of pretrigger boards, transforms them into a number of messages and distributes messages among FLT processors. Calculation of track parameters provided by means Look-up table.

3.4.7 Status

All boards are produced and were tested. Different tests have been performed in the West Hall, they showed that logic and transmission between boards and FLT TFUs is reliable. During in situ tests an instability of data transmission via optical links was observed. However after intensive study a solution was found that provides a relatively stable operation of the optical links. Six modified link boards and four modified pretrigger boards were installed in the experiment and worked essentially error-free during periods without target operation when the number of hits was small (i.e., re-initialization was required once every 10 minutes). During data taking, errors in the bunch number transmission occurred occasionally, presumably due to the larger number of hits in the data streams. This may imply that the DC offset for the optical receivers should be increased at higher interaction rates. This can be achieved by adding DACs to the optical receivers of all pretrigger boards, which are planned to implement. The problem will be studied during the luminosity shutdown.

A slice test using 12 rows of pads in the inner chambers with the FLT in transparent mode has been performed. Data was transferred from the link boards to the pretrigger boards in two cycles per bunch crossing. It was found that the first data transmission cycle gives an incorrect bunch number distribution; this problem is under investigation. In the second transmission cycle there is agreement between the FLT record and the DAQ data 93% of the time. See also section 2.6.4 for some results obtained in conjunction with the detector.

3.4.8 Plan for Luminosity Shutdown

1. study the pretrigger electronics using signals or noise in the chamber electronics - try again to adjust the pretrigger boards; - install modified pretrigger boards(12 links) and test them
2. upgrade of pretrigger electronics - modification of 44 pretrigger boards, equipment of 44 pretrigger boards with DACs; - VME control of 11 FEDs; - equipment of 70 link boards with DACs;
3. installation and commissioning of the pretrigger electronics
4. debugging of the pretrigger-FLT chain

3.5 Second Level Trigger

3.5.1 Introduction

The Second Level Trigger has been designed to reduce the event rate by two orders of magnitude from an FLT output rate of 50 kHz and to provide high efficiencies on the interesting physics triggers. The algorithm is based exclusively on data from within Regions-of-Interest (RoI) pointed to by the previous trigger step. During second level processing, event data resides in the distributed Second Level Buffer (SLB) system. The SLT processing is performed on a large computer farm, where events are handled in parallel by the farm nodes. Detector data from within RoIs is fetched on demand over the low-latency switching network which provides full connectivity between the SLB boards and the processing nodes. Processing is continued through multiple steps until the track candidate either is found no longer valid and therefore dropped or has passed all requirements. For each step, additional data is pulled from the SLB system. Surviving track candidates form the basis of the event level decision. In case of an accept, the full event data is finally collected in the trigger node for event assembly and further non-RoI based (third level) processing.

3.5.2 SLT hardware

The switching network has been implemented from the same type of SHARC cluster board used for the SLB. This board carries six SHARC processors which can communicate via a global memory bus. With each processor having six link ports, the cluster board has a total of 36 parallel links and thus constitutes a flexible network building block. The 140 SHARC boards, which comprises the SLB, are grouped into blocks of 12 boards each, as shown in Fig. 129. Each SLB board receives messages via a SHARC link from one additional cluster board, as shown in the left of the figure. Outgoing messages are routed through the board on the right. Similarly, the processing nodes are grouped into blocks, with one cluster board for incoming messages and one for outgoing messages. As illustrated in Fig. 130, the switching network is completed by connecting the outputs of each of the SLB blocks to the inputs of each of the processor blocks, and vice versa. Limitations in the network performance come from the maximum sustainable transaction rate of the SHARCs devoted to switching, the 40 Mbyte/sec maximum link bandwidth, and the 160 Mbyte/sec bandwidth on the cluster board bus. The maximum transaction rate is determined by the CPU time needed to route a message from input to output port. For our RPS messaging software [110], we measure 5 μsec per transaction implying a maximum transaction rate per SHARC of 250 kHz.

The SLT trigger farm comprises a total of 240 Pentium II based Personal Computers. With 100 PCs running at 300 MHz and the remaining 140 running at 450 MHz, the total performance amounts to 93 Gcycles/sec. Each computer is equipped with 64 Mbytes of RAM, a standard 1.44 Mbyte floppy drive, a cheap graphics card, and a Fast Ethernet adapter. To reduce cost and the number of movable parts, the nodes have been kept disk-less. Interfacing to the switch is provided by a custom-build SHARC-link/PCI-bus interface [110], which has one input and one output channel. Its main ingredients are a pair of SHARC link emulators, two 16 kbyte FIFOs and a PCI controller. The card provides in principle a 40 Mbytes/sec throughput in either direction[51] and a message latency of about 1 μsec. For remote monitor and control, a slow control card has been developed. The card, which is based on the CAN field bus industrial standard, allows nodes to be switched on/off and measurement of temperatures and voltages. In case of overheating, nodes are switched off automatically.

[51]The PCI bus of the PCs in the SLT farm are limiting the throughput to less than 10 Mbytes/sec

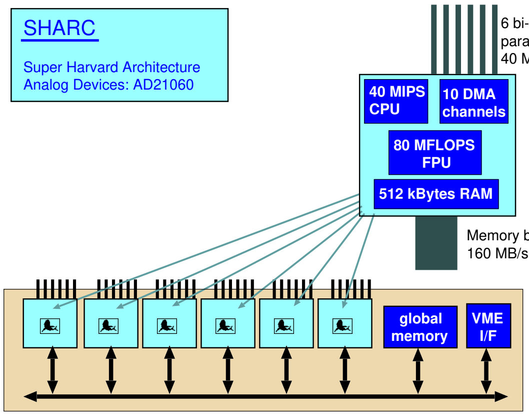

Figure 128: *The SHARC cluster board carries six ADSP21060 processors sharing a global bus.*

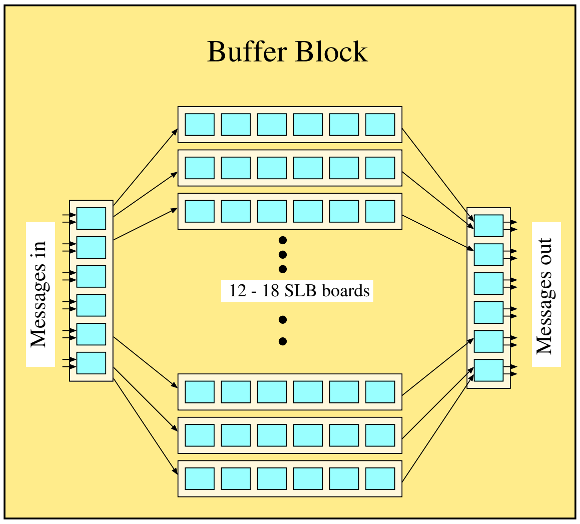

Figure 129: *The SLBs are grouped into blocks for connection to the switch. Each block is serviced by one additional SHARC cluster board for incoming messages and one for outgoing messages.*

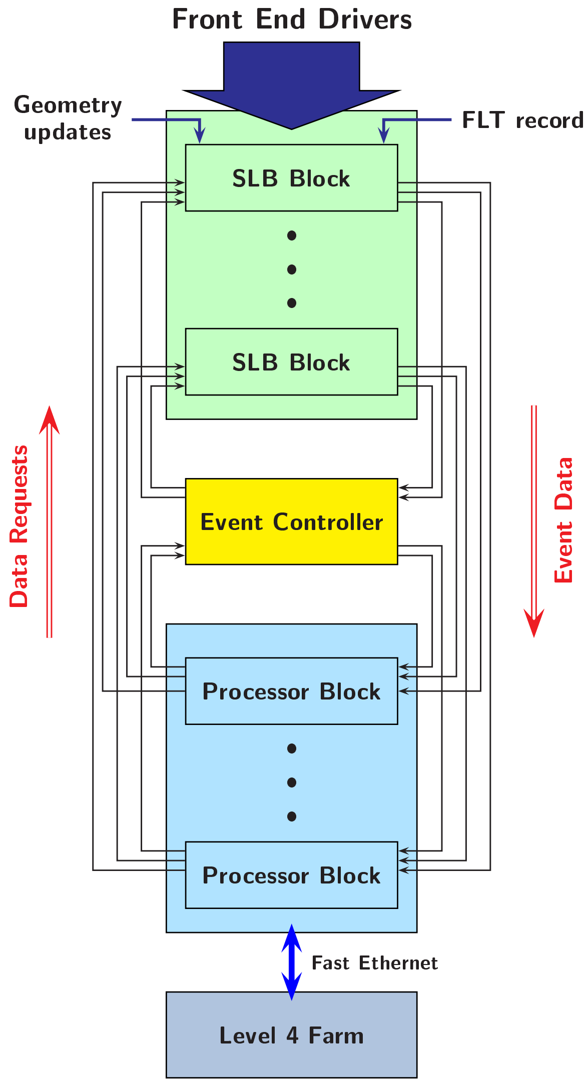

Figure 130: *The topology of the* HERA – B *higher level triggering and data acquisition system. The SLBs are organized in blocks as shown in Fig. 129; these blocks are interconnected to blocks of second and third level processor nodes.*

The farm is running under the Linux operating system. A much reduced system has been prepared on a single standard floppy disk, which is used as boot medium. After booting, the nodes acquire their IP addresses via the BOOTP protocol, so that boot floppies can be kept identical. The typical SLT processing time (3 msec) is shorter that the default Linux time slice (10 msec), and since Linux has no support of pre-empting, it is essential to keep the nodes as clean as possible, so that the trigger process does not have to compete for resources. A special-purpose driver for communication over the SHARC/PCI interface has been developed. The driver is optimized to service a single application and thus does not have all the features of a general purpose Unix driver. To avoid the overhead of copying data between kernel and user space, data is transferred directly between the interface and user space. Communication happens asynchronously. The SLT software uses the same RPS messaging interface used in the SHARC world. Messages from the SHARC links are received via a polling protocol. The complete SLT and TLT code is linked into one executable. Whereas the executable is distributed to the farm nodes via NFS, a system has been developed to broadcast calibration constants via the SHARC switch.

3.5.3 SLT Algorithm

The major emphasis of the SLT is a complete reconstruction of track candidates defined by the FLT. Firstly, ghost tracks are rejected in the trigger chambers behind the magnet by performing pattern recognition and track fit in this area. This improves on the FLT tracking by inclusion of the two additional super-layers, PC2 and PC3, and by the about one order of magnitude improved spatial resolution obtained from the OTR drift time measurement. Assuming that surviving track candidates originate from the target area, they are then propagated backwards through the magnetic field to the silicon detector where a hit pattern from a matching track segment is searched for. This step aims to suppress remaining ghost tracks and electrons from photon conversions as well as tracks not originating from the target area such as muons from pion or kaon decays. Surviving track candidates are used for the global event decision. First of all, the tracks should originate from the same primary interaction. For the hypothesis of a leptonic J/ψ decay, the two trigger tracks should form a common vertex, with an invariant mass consistent with that of the J/ψ. The resulting event sample can be enhanced in B-meson decays by requiring that the decay vertex be displaced relative to the target wire. For the selection of other types of B-decays, impact parameter cuts are used to ascertain that the trigger tracks were produced away from the target wire in a way consistent with the finite B-meson lifetime.

The code elements of the SLT algorithm are presented in sequence in the following. Each code element defines the RoI for the following step. The RoI is generally defined as a 3σ road around the track candidate.

SLICER: Based on data from the x-view tracking chambers behind the magnet, this step performs a fast removal of ghost tracks. A histogramming method is applied to check that hits in the six super-layers form a pattern compatible with that of a straight track hypothesis. Sub-RoIs are constructed by dividing each end of the FLT RoI into n_s slices in x, and connecting these in all possible ways. It is requested that at least one of the $n_s \times n_s$ sub-RoIs contain at least one hit in each super-layer and a total of at least 12 hits. Based on Monte Carlo studies, it has been concluded that setting $n_S = 8$ provides a good compromise between execution time and rejection power.

REFIT-X: The track refit algorithm derives from a Kalman-filter formalism, and is similar to the one used for the FLT. Working backwards from the calorimeter surface, all x-view hits within the RoI are in turn assigned to the track candidate(s). In case of multiple hits in a given chamber, multiple track candidates result. For each hit assignment, the track candidate parameters and the χ^2 are updated. After each super-layer, candidates are filtered by a χ^2 requirement, and by requiring that there be at most two adjacent layers with “missing” hits. Only the best five candidates are kept, where the track quality is defined as $Q = N_{\text{holes}} + 0.05 \cdot \chi^2$, with N_{holes} indicating the number of “missing” hits.

REFIT-Y: After the x-coordinate of the track is known from REFIT-X the stereo-view hits give information about the y-coordinate. Using this information, REFIT-Y performs a track fit in a way similar to that of REFIT-X.

L2MAGNET: The fast traversal of the magnetic field relies on a parameterization of the effective field integrals as a function of the track slopes, t_x and t_y, in front of the magnet. The field integrals are stored as lookup tables, and interpolations between the discrete (t_x, t_y) points are performed. To use this scheme for the backwards traversal, an iterative method is applied. The RoI size in front of the magnet is influenced by the measurement precision behind the magnet and by the size of an effective target box, which includes all active target wires and allows for the finite B-meson decay length. In case a hit in the first magnet chamber super-layer can be successfully assigned to the track, the RoI is adjusted accordingly. Notice, that this module performs no rejection.

L2SILI: Also the tracking in the silicon detector relies on a Kalman-filter method. In this case the x- and y-view hits are treated synchronously in a single propagation of the track candidate through the detector. Multiple scattering is accounted for both in the detector itself and in the beam pipe material. During the traversal, track candidates are filtered by a χ^2 requirement, and by requirements on the number of missing hits. The final tracks are required to have at least three hits distributed over at least two super-planes per view.

L2VERTEX: Based on a χ^2 cut, it is determined whether the two trigger tracks form a common vertex. If this is not the case, impact parameters are determined for both tracks with respect to the target wire. These parameters form the basis of the global event decision.

Another important part of the SLT code is the MAP/PAM complex. MAP provides the mapping from physics coordinates to channel numbers, and forms the basis for the formulation of data requests to the SLB. Data packets returned from the SLB are received through PAM, which converts channel numbers back into physical coordinates. The clustering of VDS hits is performed using the same procedure as in the off-line reconstruction.

3.5.4 The Use of SLT in 1998–2000

All HERA – B operation so far has relied heavily on the SLT, which has proven to be a flexible and powerful instrument able to cope with the evolution of the rest of the experiment. Due to the late appearance of the FLT, much data-taking has relied on an "emulation" of the FLT functionality in the SLT. From the start-up in 1998, events with high $p_{\rm t}$ electron candidates were selected by the ECAL pretrigger, and the SLT processing then consisted of a full reconstruction of the ECAL data followed by a search for high mass electron pair candidates. Soon, the VDS reconstruction (L2SILI) was included, so that ECAL clusters could be matched to track segments in the VDS. In the presence of the magnetic field, the RoI position was predicted using the known $p_{\rm t}$ kick in the magnet and the ECAL cluster energy as the momentum estimate of the track. After having recorded sufficient data with the OTR in place, mapping and alignment constants were available in the late spring 2000, so that commissioning of the SLICER/REFIT algorithms could take place. The ITR has so far not been used by the SLT, because the detector was not ready until late in the run, both hardware-wise and in terms of software interface of the detector and calibration data to the SLT. Later, $J/\psi \to \mu^+\mu^-$ decays were made accessible through the incorporation of the muon pretrigger. The "emulation" of the FLT functionality in this case was based on pad chamber coincidences from the muon pretrigger, followed by a RoI-based hit-search in the two most upstream tube chamber stations of the MUON system (X-View only). For each pair of muon pretriggers, all four charge combinations, (++), (+−), (−+), and (−−), were searched for. This is opposed to the situation for electron pretriggers, where only the opposite charge combinations (considering only pairs of "outwards"-bending tracks in the magnetic field) were searched for.
Since a large fraction of trigger runs acquired at HERA – B so far have been taken in "FLT-emulation" mode, it is worth at this point to summarize the main achievements reached with the Second Level:
• The first important SLT achievement was the online observation of a J/ψ signal as shown on Fig. 131.

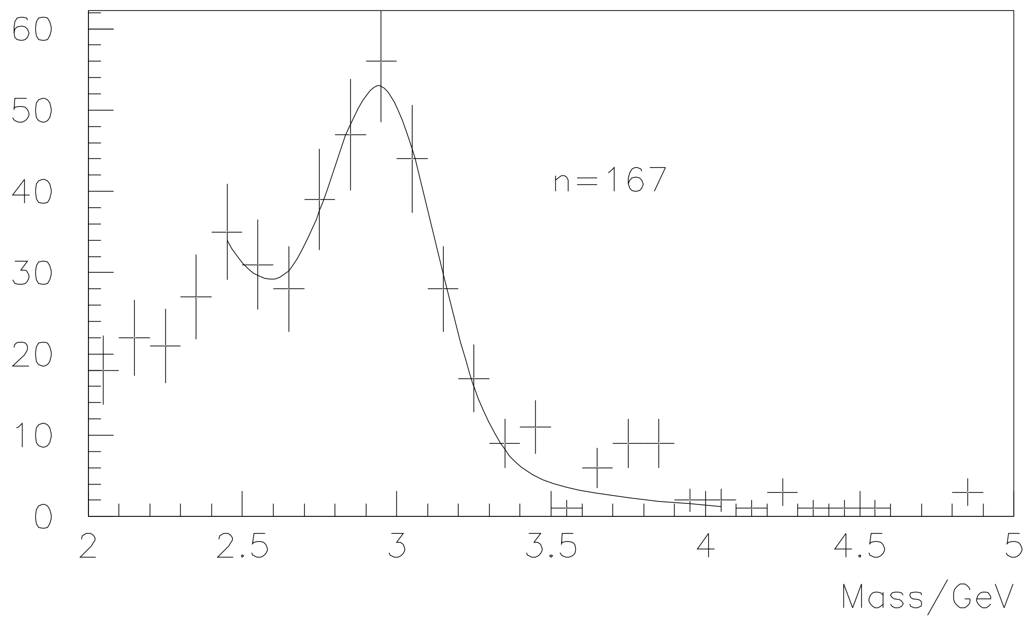

Figure 131: *A $J/\psi \to e^+e^-$ signal extracted from the SLT monitoring. A Bremsstrahlung requirement was applied on one of the electron candidates in order to enhance the signal over background ratio. The observed online rates were of $\sim$ (200 J/ψ/hour).*

This observation represented a first proof of functionality of the HERA – B SLT hardware scheme. A $J/\psi \to e^+e^-$ rate of (200 events)/hour was observed online.

• The second main achievement was a stable running of the full SLT chain in both the electron and muon channels. Although the system has been operated at relatively low interaction rates compared to design values, a substantial amount of prompt-J/ψ data has been produced in absence of the FLT. The corresponding data-analysis is presented in the physics section of this report.

After the introduction of the OTR algorithms in the SLT, the efficiency on the J/ψ signal has decreased, mainly related to the OTR detector condition, which was itself in a commissioning phase. The SLICER/REFIT cuts had to be tuned accordingly (as described in the following section) for the remaining part of the trigger production runs. Nevertheless, the observed J/ψ rates were compatible within a factor 2 with Monte-Carlo expectations, throughout most of the run period. Unstable detector efficiencies (not fully taken into account in the simulation) could easily explain this missing factor. Only during the last weeks of data taking, the J/ψ production rates have decreased dramatically[52], both in the electron and muon channels. This efficiency drop coincided in time with changing conditions of the OTR gas and High-Voltages, but the problem has not yet been disentangled and is still under investigation.

One should keep in mind that the SLT-performance is highly dependent on the nature of its seeding. Therefore we will not extend here the discussion on SLT efficiencies, background-rejection and latencies achieved without FLT seeding, but rather refer the reader to the following section where

[52] A decrease of a factor ~ 4 in the electron channel and at least of a factor 2 in the muon channel have been observed

the full HERA – B trigger-chain is considered.
An overview of the main trigger samples involving the SLT during the year-2000 run period is given in Table 40.

Table 40: *Produced Trigger data at HERA – B during the year-2000 run period. The pretrigger labels are "E" for ECAL and "μ" for MUON, the SLT labels are "V" for Vertex detector tracking and "O" for Outer tracker tracking, the labels "1" or "2" stand for the number of required tracks.*

Type	Start	Trigger			Events	$J/\psi \to \mu^+\mu^-$	$J/\psi \to e^+e^-$
		Pre	FLT	SLT	$\cdot 10^{-6}$	Events	Events
Di-lepton	29 Apr	E	-	V,2	12	-	30,000
Di-lepton	15 Jun	E	-	OV,2	1	-	
Di-lepton	28 Jun	Eμ	-	OV,2	3.7	3,000	
Di-lepton	18 Aug	Eμ	1	OV,2	1.0	$\simeq$100	-
Single lepton	24 Aug	Eμ	1	OV,1	3.1	$\simeq$100	-
Di-lepton	19 Aug	Eμ	2	OV,2	1.0	-	-

The interaction rates were 2 MHz for Single lepton runs and 5 MHz for Di-lepton runs. The quoted number of $J/\psi \to e^+e^-$ events is the estimated number of events without Bremsstrahlung requirement in the reconstruction [53]. The full trigger-chain including the FLT was operated only at the end of the run period. The analysis of this data is still on-going, which explains the very approximate (or missing) J/ψ yields in the last 3 rows of Table 40.

3.5.5 The SLT Performance in August 2000

In this section, we attempt to present some elements of the SLT performance by the end of the run period in August 2000. The data-taking included several different running modes, some of them based on the FLT. The SLT performance clearly depends critically on the quality of its input data including that of the RoIs defined by the FLT. At the moment of writing, the FLT performance is still a subject of intense study, and so necessarily any conclusion on the SLT will be of a very preliminary nature.

From an SLT point of view, the experimental situation included the following elements:

- Inner and middle ECAL;
- Full OTR (no drift time information used in SLT). No ITR. Magnet chambers not used;
- MUON chambers x-view and pads (pixel chambers not used);
- The VDS (not in final position);

Considering the unstable OTR chamber efficiencies, the SLICER and REFIT algorithms were modified, essentially by making less stringent cuts in the hit-counting. The main modification consists in allowing a completely empty super-layer (no hits required) within a Region of Interest. All results presented below are based on this "looser" SLT version. Another special feature of the current

[53] The double Bremsstrahlung requirement has a ~10% efficiency, therefore the estimated number of produced J/ψ events in the electron channel is ~10 times larger than the observed one.

SLT-algorithm is the enhanced hit search-window ($\pm 2.5cm$) in the OTR, in order to decrease the dependence of the SLT-performance on possible detector misalignment. On Fig. 132, the residuals between FLT input RoI's (electron channel) and the SLICER hits are shown in each OTR super-layer.

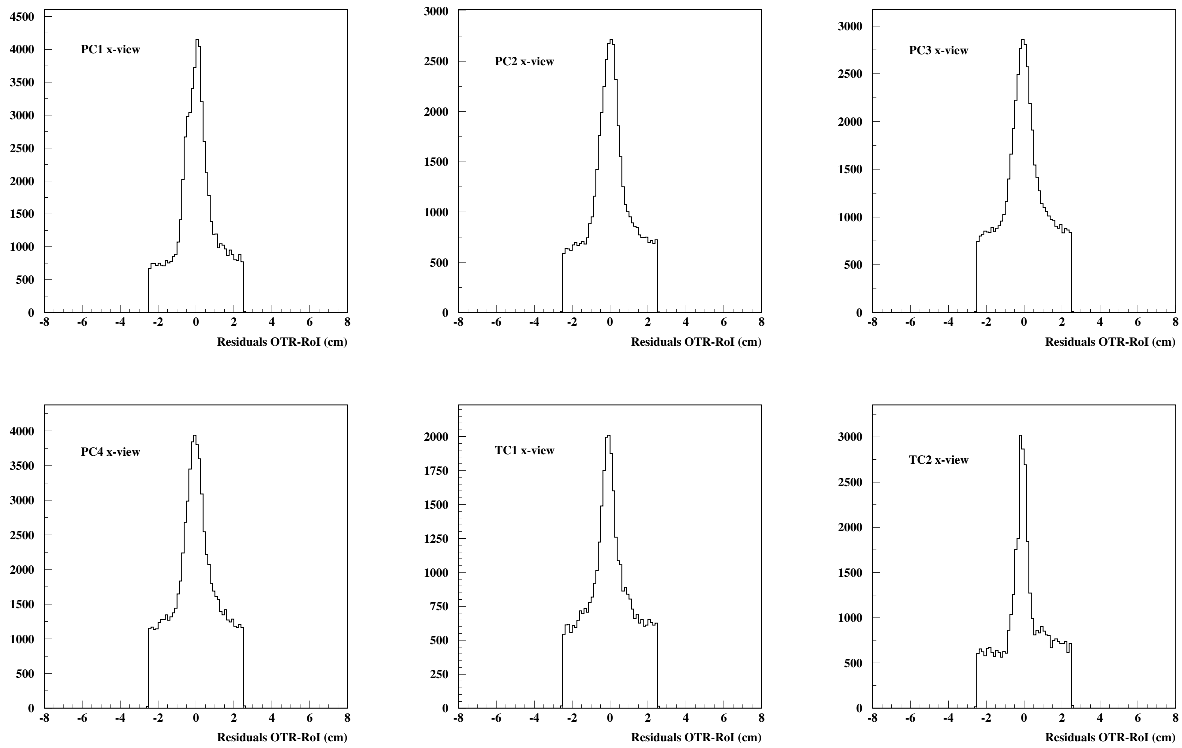

Figure 132: *Residuals between the FLT RoI and the X-View hits in the OTR seen by SLICER. The widths are of ~1cm. The search windows in the SLT have been enlarged to ±2.5cm to account for possible chamber misalignment.*

The average residual-width is of ~1cm, including both 5mm and 10mm chambers, and the distributions are centered at 0 with an accuracy of a few millimeters. These values are currently sufficient, given the enlarged hit-search windows in the SLT. Nevertheless, a systematic sector-dependent study should be performed in order to improve the understanding of the detector alignment, which will eventually allow us to reduce the size of the search windows in the SLT and hence further improve the background-rejection of the trigger.

Efficiency

The SLT efficiency on events with a leptonic J/ψ decay has been investigated by a Monte Carlo study. The August 2000 experimental situation was modeled. In an attempt to factorize out the influence of the OTR efficiency, the study was repeated with two different OTR performances: i) realistic, as of August 2000, and ii) ideal, i.e. 100% efficiency. The results are presented in Table 41.

It should be emphasized that the quoted numbers are per event (two tracks). A lepton pair is considered accepted if it satisfies the trigger condition at a given SLT-step and if the two RoIs are

Table 41: *Monte Carlo estimates of the SLT triggering efficiencies for events with leptonic J/ψ decays.*

	Realistic OTR		Ideal OTR	
Algorithm	e^+e^-	$\mu^+\mu^-$	e^+e^-	$\mu^+\mu^-$
SLICER	0.99	0.99	1.00	1.00
REFIT-X	0.92	0.91	0.94	0.96
REFIT-Y	0.93	0.97	0.97	0.99
L2SILI	0.88	0.89	0.92	0.94
L2VERTEX	0.97	0.98	0.97	0.98
Overall SLT	0.72	0.76	0.81	0.88

matching with the Monte-Carlo truth information. In general, the results are better in the muon channel, which is to be expected since the muon channel has a cleaner signature. Going through the various steps, even for the ideal OTR, we observe a small drop of efficiency in SLICER/REFIT of 5% (9%) for muons (electrons). These drops are most likely related to geometrical effects in the tracking algorithms. The efficiency drop in L2SILI (6% for muons and 8% for electrons) are larger than expectations from design. Imperfect matching of the FLT RoIs between the REFIT output and the vertex detector could be the cause of this inefficiency and will be investigated during the shut-down.

Background Rejection and Timing Estimates

Investigations of the background rejection and of the execution time of the SLT code has been carried out on various real data sets. An example of such a study is presented in Table 42.

Table 42: *Observed rejection rate and execution time for SLT. The last row is the total latency taking into account the rejection.*

Algo	*Red*	Red_{Des}	$\frac{Time}{Ev}$ *(ms)*	$\frac{Time_{Des}}{Ev}$ *(ms)*
Mess			.38	
MAP_x			2.6	
PAM_x			3.7	
SLI	1.58	4.	1.9	1.
REF_x	3.40	7.	4.2	3.
MAP_y			3.1	
PAM_y			1.4	
REF_y	13.7	13.	3.0	3.
MAP_{SILI}			.18	
PAM_{SILI}			33.	
SILI	105.	130. (+vertex)	47.	7.
TOT	105.	130.	19.	3.

In this particular example, HERA – B was run with a 5 MHz interaction rate, data was triggered by the FLT pair trigger, and the SLT required two tracks. Furthermore, only events with less that 20 FLT tracks have been considered. Opening up for more FLT tracks leads to a lower reduction and

thus to a higher execution time. It is observed, that the FLT tends to pass a large number of tracks on to the SLT. Many such tracks differ by only one or a few hits. Such tracks could be merged at the SLT level before running the algorithms. In the current situation, both the execution time and the bandwidth over the switch suffers from the fact that the "same" FLT track is treated multiple times. By following such a strategy and by a general optimization of the code, we believe the execution time could be brought down considerably. Dedicating something like 180 nodes for the SLT processing (the rest for event-assembly and third level processing), the execution time per event should be less than 3 msec to cope with an input rate of 50 kHz. To summarize the current SLT timing performance, a total latency of 19ms has been measured, corresponding to 10KHz input capability with 180 processing nodes. We are therefore a factor $\sim$5 away from design [111]. Improvements can certainly be made on the hit-requesting part which has not been optimized at all and carries about half of the latency. The timing of the algorithm itself (mainly L2SILI) will also be optimized. Furthermore, RoI sizes will be reduced and FLT clones will be merged. Finally, the currently loose SLICER/REFIT cuts will be strengthened back to design values as soon as OTR efficiencies will improve. For all these reasons, we are confident to be able to reach timing performances close to design values.
The overall rejection number looks fine: two orders of magnitude. But we should keep in mind that these measurements have been carried out at low interaction rates. Moreover and similarly to the SLT-timing performances, the SLT-rejections highly depend on the quality of the FLT input seeding. It is therefore too early to draw any solid conclusion on the achieved background rejection power of the SLT. The analysis is carried on off-line based on various FLT-triggered data samples.

Vertex Resolution

Fig. 133 shows the z position of reconstructed vertices. The target wire was at $z = -4.8$ cm. A vertex resolution of about 1.2 mm can be observed. The figure also shows the effect of a detached vertex cut (cut at half the mean B-decay-path) in L2VERTEX: the percentage of events surviving after the cut is decreasing from 9% to 2.5% when the L2VERTEX tracks are additionally required to match with better defined off-line reconstructed VDS track segments. This is an indicator of the the SLT ghost-rate and shows that there is room for improvement in the SLT track-quality.

Future Improvements

The first goal for the near future is to understand all aspects of the SLT-performances in the data samples acquired in the year-2000 run, mainly those involving the FLT. The Monte-Carlo simulation should also be made more realistic according to changing run conditions.
In terms of future improvements, clearly the "standard SLT algorithm" has to be finalized for the upcoming runs: the main missing items are:
• add drift time information in REFIT to improve track-resolutions.
• finalize the magnet tracking (including the first magnet chamber super-layer) in order to improve the matching quality between OTR and VDS tracks.
• finalize the L2VERTEX package and introduce it as an active trigger element.
• integrate the Inner Tracker System as a SLT detector component
Furthermore, several SLT items will be subject to fine-tuning during the shut-down, like the optimization of the RoI sizes and cuts in SLICER and REFIT, the improvement of the multiple scattering treatment in L2SILI and the decrease of the timing at various levels of the SLT-algorithm.

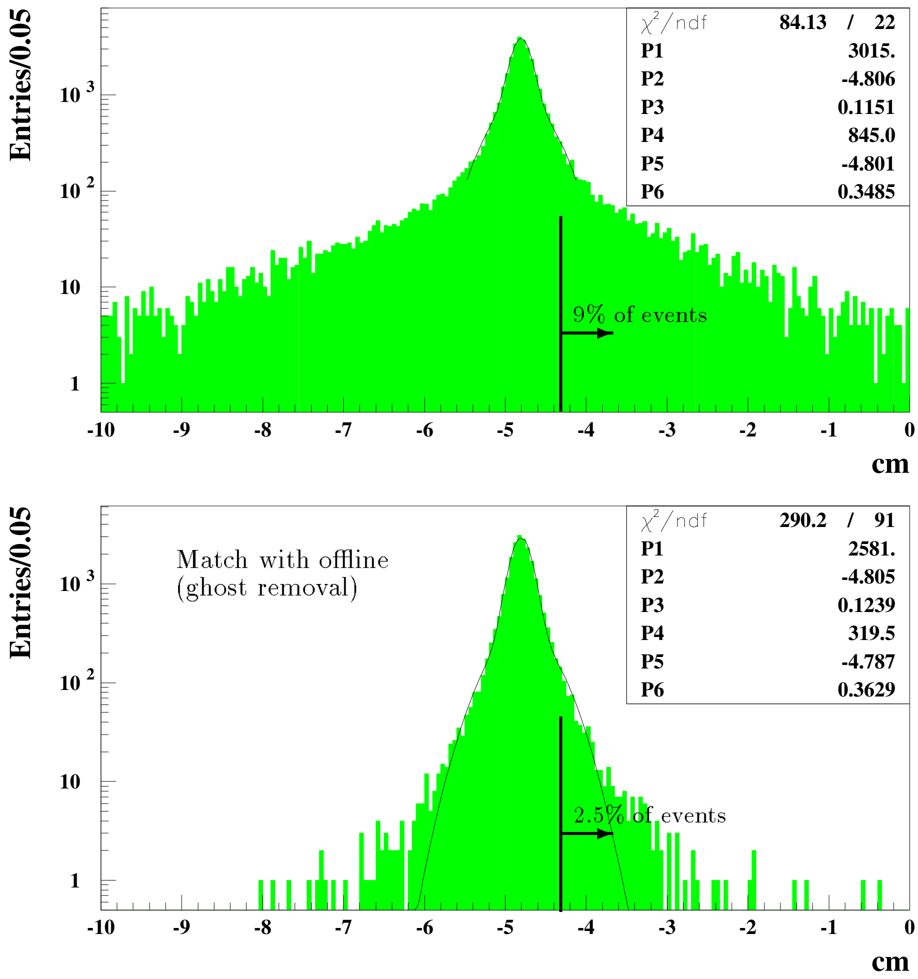

Figure 133: *The z position of reconstructed vertices. At top, all vertices. At bottom, only vertices where L2SILI tracks have been confirmed by the off-line reconstruction code "CATS".*

3.6 Third Level Trigger

3.6.1 Changes since the Technical Design Report

Both tasks and technical realization of the Third Level Trigger have seen major changes since the HERA – B Technical Design Report [1]. The implementation of the SLT as a farm of commodity processors and the transition to an event-based processing at the SLT moved functionality from the TLT to the SLT. The TLT takes now advantage of the same hardware as the SLT. TLT algorithms will be executed after the SLT step and the event building by the same processor of the SLT/TLT PC farm. The basic characteristics of the TLT is its rapid local access to the entire data of an event, implying that the processing is not limited to the particles in the RoIs. The TLT is to reduce the rate for certain event classes from about 500 to 50 Hz. The processing time at disposal is 100 ms per event, which means that typically 50 of the 240 SLT/TLT PCs will execute the TLT step at a time.

The TLT is now considered as a system which is to supply additional suppression for event classes where the information available at the SLT might not suffice to bring down the event rate without impairing the efficiency for signal events. In particular for the J/ψ trigger, an additional TLT step should not be necessary. The good-quality vertex formed by the two trigger leptons is a strong handle to reject background events. In addition, one can check at the SLT whether the measured momenta of the trigger particles sum up to a vector pointing from the vertex to the nearby target wire. The main focus of the TLT will be on event classes with fewer kinematical constraints, notably without a vertex formed by two trigger particles. Such events occur when the trigger particles come from different B hadrons or from different stages of the decay chain of one B. Copious events of interest are those in which both B mesons decay semileptonically or a count trigger selects for example the combination of one high-p_T lepton and one high-p_T hadron.

3.6.2 System Status

So far, suitable TLT algorithms have been studied with the aid of Monte Carlo simulations. It was investigated in how far the reconstruction of additional tracks in the VDS can be exploited for TLT applications. For this purpose, a track reconstruction for the VDS has been developed which is fast enough to allow for track finding and application of trigger algorithms within the time slot of 100 ms. The track reconstruction is able to operate both on the SLT/TLT PC farm and within the offline analysis framework ARTE. The incorporation into the SLT framework was exercised in 1999 when the TLT reconstructed tracks in an online test. The robustness of the pattern recognition algorithm has been demonstrated by its use within the data quality assessment, which runs routinely on the online reconstruction farm. The TLT track reconstruction was operated for extended time periods and provided early estimates of the VDS performance. Events with a number of tracks with impact parameters above a threshold were classified as selected by the TLT software. The analysis of these data is pending.

3.6.3 Monte Carlo Studies for a TLT using the VDS

The time slot available for the TLT is long enough to allow for local pattern recognition in subdetectors. In contrast to the information from the particle identification devices (RICH, ECAL, TRD), tracks found in the VDS can be assigned directly to the interaction which caused the trigger at the first and second level. The VDS was therefore the first system investigated for TLT purposes while other approaches have not been studied yet in detail.

The reconstruction of additional SVD tracks can contribute to trigger decisions in various ways.

- The **reconstruction of the primary vertex** provides a mean to refine the impact parameter cuts applied by the SLT to the trigger particles. Instead of the distance of closest approach between track and target wire, the DCA between track and primary vertex could be used.
- The **reconstruction of secondary vertices** points to events with extended lifetime.
- The **reconstruction of tracks with non-vanishing impact parameters** outside of the RoIs indicates the presence of the decay chain of a B hadron.

The TLT has to cope, however, with the problem that the momentum of the found VDS tracks is not known. The missing momentum information prohibits to estimate the influence of multiple scattering in the determination of track parameters precisely. It prevents the proper calculation of the error of derived quantities, like impact parameters.

The options listed above and the impact of the missing momentum were studied using Monte Carlo simulations [112]. The TLT algorithm were tuned to accept double-semileptonic B events and to reject high-p_T inelastic events. The inelastic events were required to have two well-measured VDS tracks with a p_T greater than 1 GeV, which were assumed to be mis-identified as leptons.

The result of these studies proves that the usage of a suitable approximation for the track momentum and the material passed by a particle allows to estimate the track parameters at the target with sufficient accuracy. The impact parameter resolution was found to deteriorate from $(23 \oplus 31/p_T)\,\mu$m (p_T in GeV) to $(31 \oplus 31/p_T)\,\mu$m when the momentum approximation was used instead of the Monte Carlo momentum.

The TLT studies indicate that the gain in signal efficiency, which can be obtained from the firm knowledge of the primary vertex, is negligible. The reconstruction of secondary vertices has been attempted for the decay

$$B^0 \to D^{*-}(\to \bar{D}^0\pi_s^-)\, l^+\nu_l,$$

where a vertex of the trigger lepton l^+ and the slow pion π_s^- or a charged track from the $\bar{D}^0$ was searched for. Difficulties in the recognition of real vertex candidates result in a lower efficiency for signal events (at the same suppression of background processes) than cuts that the SLT can impose on the impact parameter of the trigger lepton.

The search for additional tracks with non-vanishing impact parameters was found to be the most promising option. A track trigger algorithm combines the impact parameters and their errors into a discriminator function (see [112] for details) which is used to distinguish between signal and background events. The gain in signal efficiency can reach up to 30 % depending on the required suppression and the actual values of impact parameter cuts at the SLT (Fig. 134).

3.6.4 Plans for the Luminosity Shutdown

According to the simulations, a TLT based on VDS tracks can help to record signal events at higher efficiency. During the shutdown, the data recorded in the year 2000 run will be analyzed. These data provide a way to tune and to develop TLT algorithms using background event samples which were directly obtained from the experiment. This measure will help to make TLT applications more realistic. It is well conceivable to implement emerging trigger algorithms (which are e.g. targeting at *charm*) in the TLT as long as the timing constraints are obeyed.

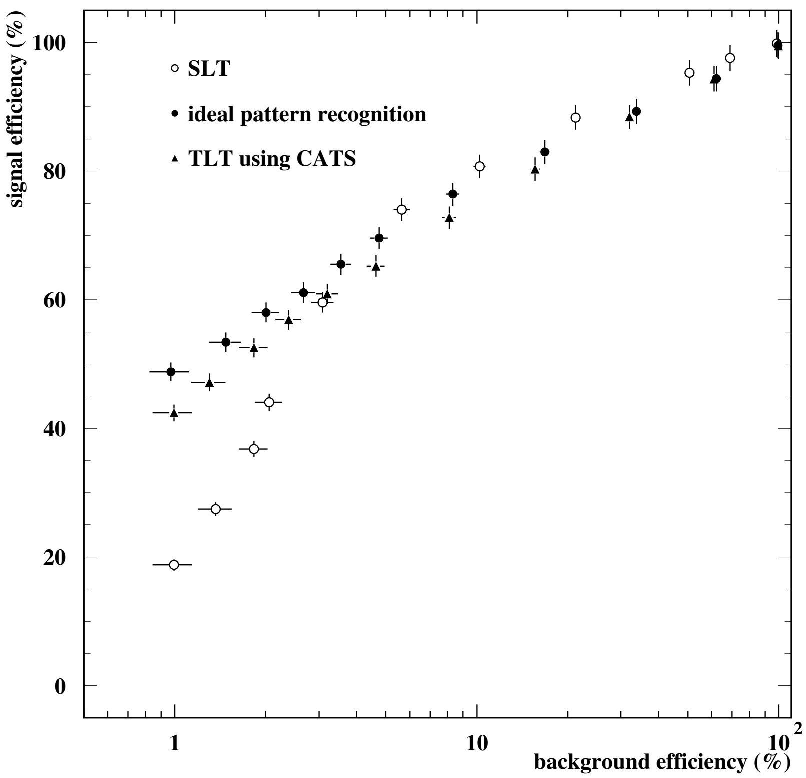

Figure 134: *Monte Carlo simulations of the conceivable impact of TLT algorithms. The efficiency for signal events (double-semileptonic B decays) versus the efficiency for background processes (high-p_T inelastic tracks mis-identified as leptons) is shown. The black symbols represent the track trigger algorithm, where the assignment of SVD hits to tracks was taken from the simulation (dots) or provided by the CATS program (triangles). The open dots denote the signal efficiency obtained by the SLT alone. The SLT was assumed to cut on the quantity $d_1^2 + d_2^2$, where the d_i are the impact parameters of the two trigger particles found in the RoIs.*

From the technical point of view, it seems advisable to switch from the presently used TLT pattern recognition to CATS, which is the leading algorithm for offline VDS reconstruction. CATS has a better track finding efficiency than the TLT tracking (about 97 % vs. 85 %) and is already very fast. In its present state, the CATS processing time for triggered events at 5 MHz interaction rate is roughly 200 ms. The speed of the algorithm can be increased for example by restricting the reconstruction to those tracks, which originate from the target wire identified by the SLT. Moreover, the usage of CATS will make the transfer of the experience, which is gained in the event reconstruction, to the TLT much easier. This is even more pronounced since the search for detached vertices is performed using CATS and a new software package for primary and secondary vertex finding. The successful transition to CATS requires some modifications to the program in order to interface it with the SLT framework.

3.7 Farm

3.7.1 Introduction

HERA – B has entered a new regime with respect to data rates and volumes which are comparable to numbers expected in the LHC-era. The DAQ and trigger system [116, 117] exploits four levels to select a rate of less than 1 Hz of interesting physics events from the initial rate. The designed background suppression is $O(10^6)$.

To allow for immediate data analysis and to avoid time-consuming re-processing of data, events will be reconstructed online before being archived to tape. Archiving is planned at a rate of 20 Hz which leads to a data volume of 20 TB/year assuming 100 kB/event and 10^7 s/year. Since trigger efficiency and background suppression depend heavily on the quality of calibration and alignment of the detector components, online monitoring and updating of the constants database is implemented. During event reconstruction, quantities which are needed for calibration and alignment are derived and sent to a central destination. By making use of the data coming from the reconstruction, constants are updated. New constants are distributed to the reconstruction processes and to the trigger system.

HERA – B 's large data volume of 20 TB/year and processing times for event reconstruction of several seconds require a clear strategy for data handling. The paradigm is to bring the application to the data rather than performing offline event reconstruction from archive. Processing must be performed in the data path as far as possible. Moreover, fully reconstructed events can immediately be handed over to the user.

A standard (Unix-like) environment in the online system, allows to use HEP offline software developments directly, e.g. event reconstruction programs on the farm. Hence, the separation between online and offline software can be given up, which allows for efficient work and easy implementations.

3.7.2 Concept

The main tasks of the 4LT system are:

- Full online event reconstruction,
- event classification,
- final event selection (4LT trigger step),
- data logging and archiving,
- data quality monitoring (DQM),
- preparation of data for calibration and alignment (CnA),
- event data re-processing in shutdown periods.

The system must guarantee event data transfer. Therefore a push architecture, exploiting a safe message passing protocol based on TCP/IP, is used for the event data stream, whereas monitoring information is collected from the nodes by a pull architecture.

To process events at a rate of 50 Hz with processing times of 4 s on a modern CPU (Intel Pentium-III/500 MHz), 200 farm nodes are needed. The network must be capable of routing 5 MB/s to the farm nodes and 2 MB/s from the farm to archive.

3.7.3 Implementation

Concept and architecture of the 4LT farm allow to use commodity hardware for costs reasons, e.g. off-the-shelf components. See also [121]. The processing power can be provided by modern PC-CPUs. The moderate bandwidth requirements can be met by standard network components, e.g. Fast-Ethernet.

Hardware

Processing nodes: As farm nodes Intel-CPUs were chosen which are housed in dual-CPU PCs. The PCs are equipped with Pentium-III/500 MHz processors, 256 MB SDRAM, and 13.1 GB (E)IDE-disks. Each node buffers $O(10)$ events in its local memory.

Network: The network is built of 24-port CISCO-switches (see Fig. 135). The farm nodes are grouped into eight so-called mini-farms. The data link to mass storage media is realized by means of GigaBit-Ethernet. Event data is stored intermediately on large disks before being copied to tape.

Services: Three PCs are used to provide NFS-service for executables, collect and display slow control data by way of an http-server, and allow for local event data logging. The logging node houses large SCSI-disks which can keep event data for several hours of standard running at 2 MB/s. In addition, a local tape drive (DLT7000) is planned to run independently of DESY's central archiving facilities.

Software

Operating system: The farm-PCs run Linux which has become a standard software platform in HERA – B as well as in HEP in general. On each farm node a multi-process environment is available. Tasks are implemented as separate processes which communicate by means of Unix IPC-tools such as message queues, shared memory, and semaphores.

System software: Event data transfer is based on the Internet protocol TCP/IP. For the collection/gathering of information for data quality monitoring as well as for calibration and alignment, a UDP-based in-house development is used. Tape access is done via OSM.

Slow control: Monitoring of the main parameters of the farm nodes is included into the HERA – B slow control framework. A web page was set up which allows to visualize the availability of farm nodes as well as crucial numbers such as the loads of the PCs and their temperatures. In addition, an automatic procedure is available which notifies the shift crew and on-call experts in case of problems.

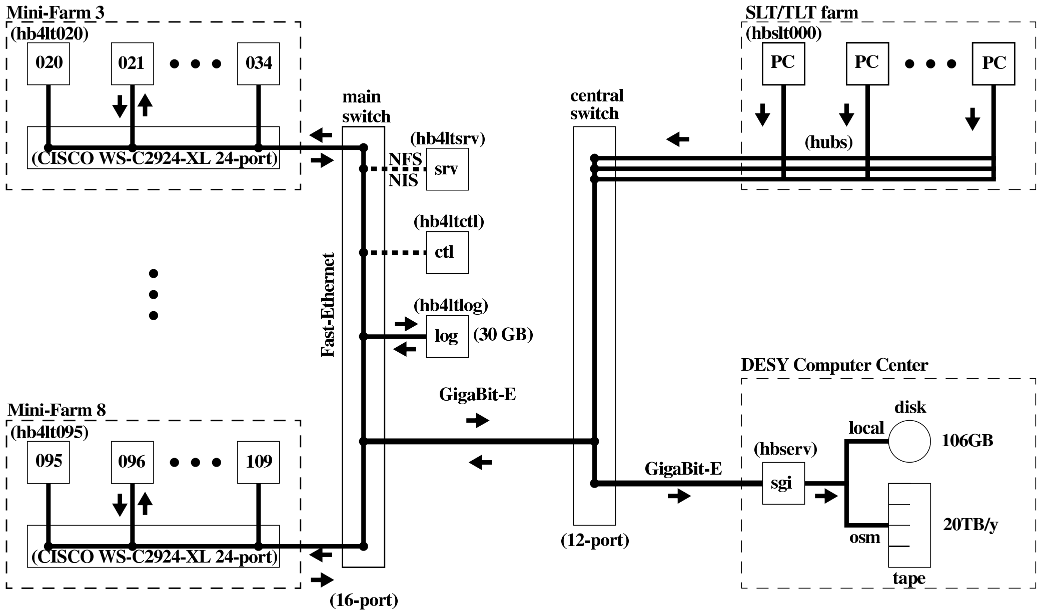

Figure 135: *4LT farm network.*

Application software: HERA – B 's main development platform has become Linux (S.u.S.E.). Most of the computing from Monte Carlo generation to analysis work is done on PCs. Application software such as event reconstruction and analysis packages are housed in the frame program *Arte* which handles I/O and memory management. The frame program can be directly used on the 4LT farm without modifications. In the online case I/O of events is done from/to shared memory rather than files (see Fig. 136).

3.7.4 Status in 2000

The 4LT farm hardware was completed beginning of 2000. The usage of commodity off-the-shelf components as processing nodes and for the network allowed to easily meet the time, costs, and manpower estimates. The price per node was DM 1500. The application of Linux as a software platform for online and offline turned out to be advantageous. It is possible to use the typically offline developed HEP application software without any modifications.

To date 186 CPUs in 93 dual-processor PCs are used regularly to perform full online event reconstruction. From the data path point of view the designed event and data rates could be clearly exceeded. It could be shown that event data can be transferred at 10 MB/s into 4LT which corresponds to an event rate of 100 Hz at a raw data event size 100 kB. Event data logging from 4LT to the central logging facility could be performed at rates up to 12 MB/s.

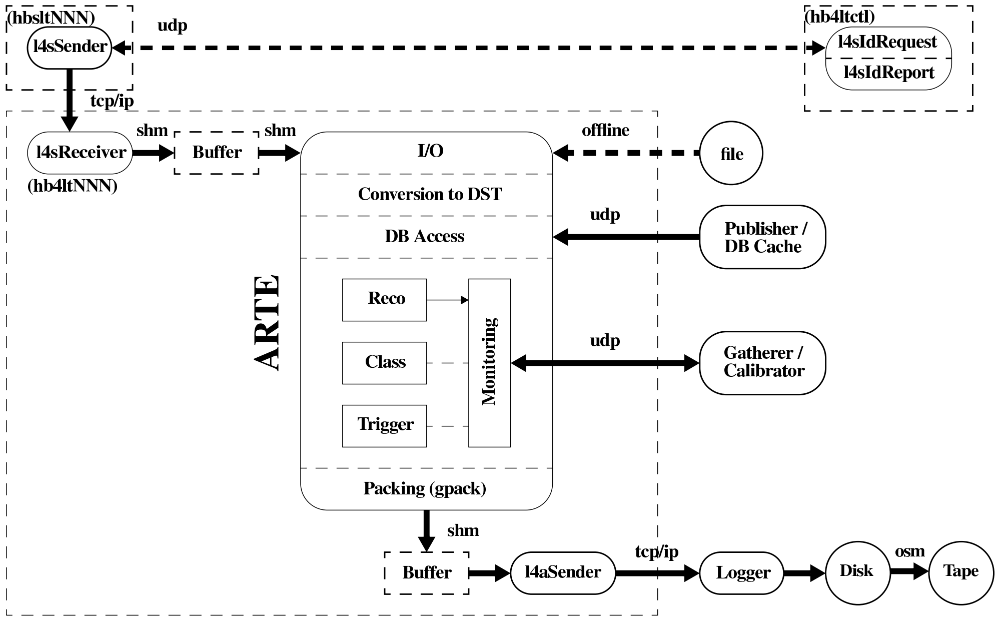

Figure 136: *Processes per 4LT node.*

When running with full online event reconstruction, the rates are limited by the processing time of the reconstruction program. It takes currently 4 s/event at 5 MHz interaction rate.

The reconstruction software also includes event classification according to physics characteristics. In addition, a sophisticated data quality monitoring system (DQM) was introduced which allows to obtain immediate feedback on details of the event data while running. This very useful feature would not be possible without online event reconstruction.

Together with the DAQ group a system was set up to exploit the 4LT farm for event data reprocessing. It works similarly to the usual online processing scheme and makes use of most of the online processes, in particular the logging and archiving facilities. Only the data source is different. Instead of passing raw event data from the DAQ system (via the SLT farm) to the 4LT farm nodes, a process retrieves data files from tape and distributes event by event to the 4LT farm nodes.

3.7.5 Data Handling

Data handling in HERA – B is one of the most crucial items. The distinct physics program in conjunction with the small $b\bar{b}$ ratio compared to the inelastic cross section leads to a vast number of events and therefore huge data volumes. Given the experiences of this year's running the anticipated yearly data volume is 30 TB which corresponds in $200 \cdot 10^6$ events with an average event size of 150 kB. Only a few percent of these events contain valuable physics but require detailed analysis strategies to be found. To carry out physics analyses, usually only small numbers of events have to be selected from the data sets. Moreover, the analysis of the golden decay channel as well as other interesting CP-violating decay channels requires access to all events accumulated over years.

Event files with raw data information ($\approx 100 - 130\,$kB/event) plus reconstruction output ($\approx 20 - 50\,$kB/event) are called Data Summary Tapes (DST). Event files without raw data information are called MINI-files. HERA – B 's concept of data sets and its access foresees to store only MINI-files with a subset of information per event and only parts ($1 - 10\,\%$) of DST-files with full information on disk. Per year a disk capacity of 1 TB must be added.

Event classification The scheme described above calls for well-elaborated online event classification within the reconstruction program. Events are flagged due to their contents with respect to physics classes. The frame was set up and used. The current implementation incorporates mainly searches for specific decay channels containing particles such as K_s^0, K^*, Φ, D, D_s, etc., detached vertices, and of course $J/\Psi \to l^+l^-$. Events which are flagged due to this classification criteria are being written to disk as selected files.

Tools A procedure to automatically copy archived files from tape to disk on request, which includes fully efficient usage of the disk space by automatically deleting old files, was commissioned (*staging*).

Event data access by means of index-files and run catalogs, which contain the location and in particular the classification flags of all events, was developed.

3.7.6 Perspectives

It is planned to extend the 4LT farm to the design number of 200 CPUs. This can easily be achieved by substituting older single-CPU machines which will then be re-used for DAQ or database purposes. Main emphasis must be put on improving the timing of reconstruction software which should be feasible. Therefore the installation of many more farm nodes is not foreseen. Moreover, upgrading of the 4LT farm would require substantial extensions of the infrastructure, e.g. housing, cooling, and networking. Once these problems are solved, the modular structure of the 4LT farm and the usage of standard off-the-shelf components allows a cheap and quick update. Net costs per CPU of DM 1500 are realistic.

The reprocessing scheme was used in run breaks successfully, e.g. during injection, and will carry out reprocessing of event data taken in 2000. The limited amount of data of 8 TB taken in 2000 compared to the design value of 30 TB/year, can be re-processed even a few times. Assuming a realistic bandwidth of 4 MB/s from tape to disk, already the read-in of this year's data volume from archive takes one month. Such attempts will certainly fail in the following years when the anticipated volume of 30 TB/year is stored and the run-free time becomes less.

Data access and disk space in HERA – B will remain a crucial issue.

During shutdown main emphasis should be put on

- maintaining reconstruction software,
- improving the reconstruction software also with respect to timing,
- elaborating event classification to allow for a safe online selection of event classes,

- developments of the online calibration and alignment scheme.

Prerequisites for a successful physics program hence a feasible analysis strategy in the future are that

- MINI-files are small enough to be stored on disk ($\approx$ 20% of the DST-data),
- standard physics analysis can be fully based on MINI-files,
- online classification leads to a small selection of events,
- re-processing of selected data sets is well planned and organized,
- at last, users act disciplined.

Figure 137: *The completed 4LT Farm.*

3.8 Data Acquisition System

3.8.1 Introduction

The HERA – B data acquisition system is made of all trigger levels (SLT, TLT and 4LT) and the logging protocol plus the interconnections (Hardware and Software) between them. The DAQ report centers in the FLT-SLT interconnection and the global run control software including the calibration and alignment protocol.

The technology applied to each level had been selected to accomplish the requirements of the trigger protocols, see Fig. 138. The DAQ system is built from 4 components:

- Fast Control System designed by the Electronic Department at DESY to synchronize the subdetector Front End pipelines readout and interfaces to the DAQ.
- ADSP21060 SHARC Processors (40 MHz): Digital Signal Processors (DSP) from Analog Devices which are used for data buffering for the SLT and data switching.
- A farm of Pentium PC's for SLT/TLT. A SHARC-link to PCI-bus interface holds the communication between the SHARC switch and the PC's.
- A farm of Dual Pentium III PC's (500 MHz), for the 4LT. The data transfer between SLT and 4LT nodes is done by Fast Ethernet.

There are independent reports on FLT, SLT, TLT and 4LT/Logging.

3.8.2 The SHARC Cluster Board

The SHARC board is a 6U VME card designed by MSC in Stutensee (Germany) in collaboration with HERA – B . Each board holds 6 ADSP-21060(SHARC) chips by Analog Devices.

The ADSP-21060 chip has a 512 kBytes of on-chip memory to hold event data and software code. The 6 ADSPs share a global memory bus for inboard communication, with a maximum bandwidth of 240 MBytes/s in 48 bit word mode. Each SHARC chip on the board drives 6 parallel transceiver link ports for off-board communication, capable to transmit 40 MBytes/s per link. The SHARC links are used to connect SHARCs in the *switch* architecture. The ADSPs have 10 independent DMA controllers, 6 of the for SHARC link data transfer and 4 for the global memory bus communication.

3.8.3 Second Level Trigger Switch and Data Buffering

The SLT 3.5 requires a low-latency, high bandwidth switching network to route data requests from the trigger processors to the buffer nodes. The switch will also carry the supervisor and buffer manager traffic as well as event data into the Second Level Trigger farm for event building.

The 140 SHARC cluster boards which comprise the Second Level Buffer (SLB) system are grouped into 10 *buffer* blocks of 14 boards, each as it is shown in Fig.139. Each SLB receives messages from the SHARC board on the right. Outgoing messages are routed through the board on the right.

Similarly the 240 SLT nodes are grouped into 12 *processor* blocks, with one SHARC board for incoming messages and one for outgoing messages. The switch is completed connecting the outputs

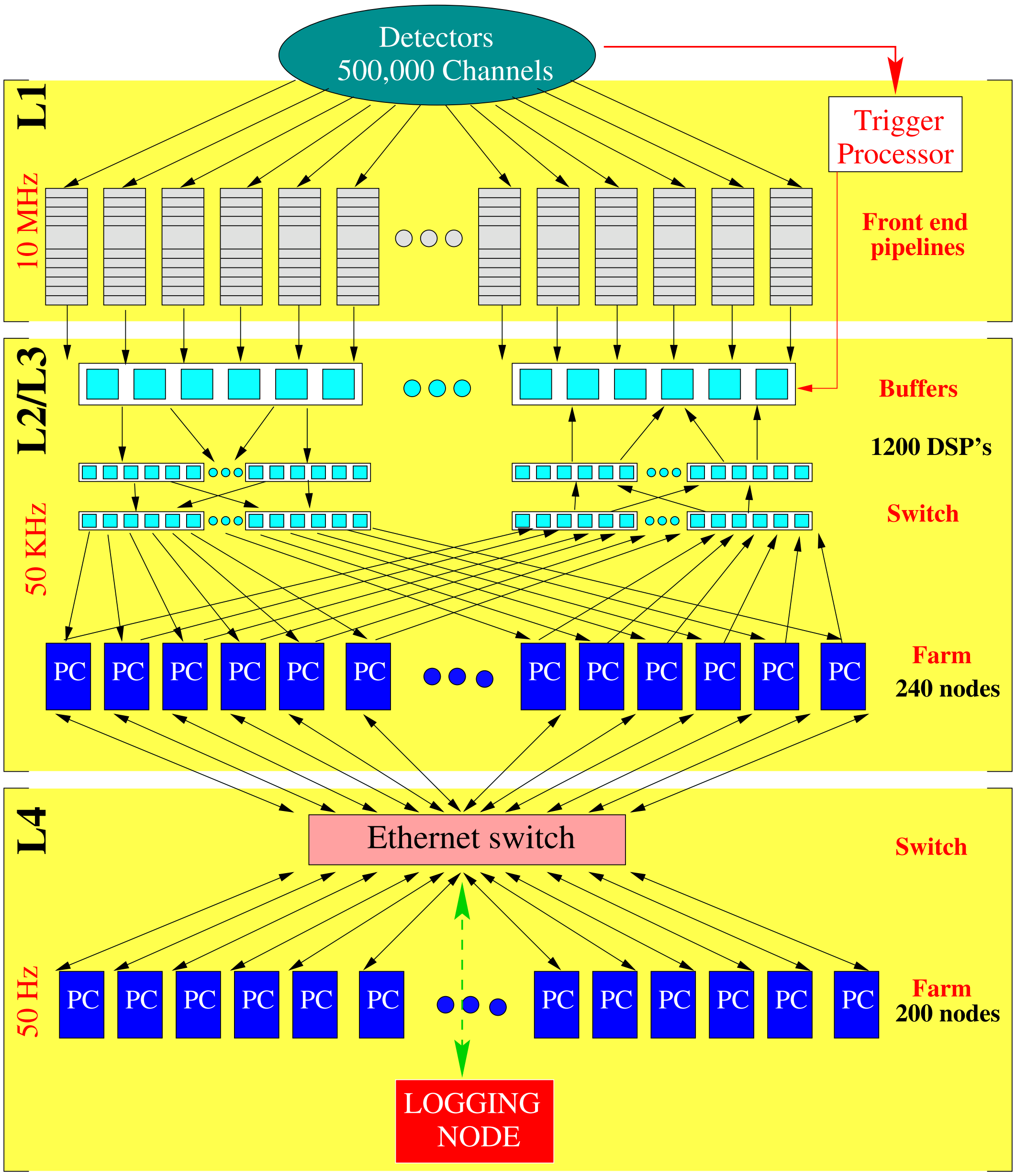

Figure 138: *HERA − B Data Acquisition system scheme and correspondence to the HERA − B trigger levels.*

of each of the SLB blocks to each input of the processor blocks and vice versa. An additional SHARC cluster board, the event controller, is added to the system as master buffer manager and to interface the Fast Control System to the SLT nodes.

3.8.4 Logging

The Fourth Level Trigger (4LT) can be characterized as offline-like with respect to real-time requirements. The total rate from the SLT/TLT to the 4LT farm has been estimated to be larger than 10 MB/s with an average event size of 150 kBytes. SLT/TLT accepted events are routed to the 4LT farm nodes by a switching network, see Fig. 138, with dynamic association of SLT/TLT nodes (sources) to 4LT nodes (destination). Reconstructed events are routed to a logging machine (e.g.

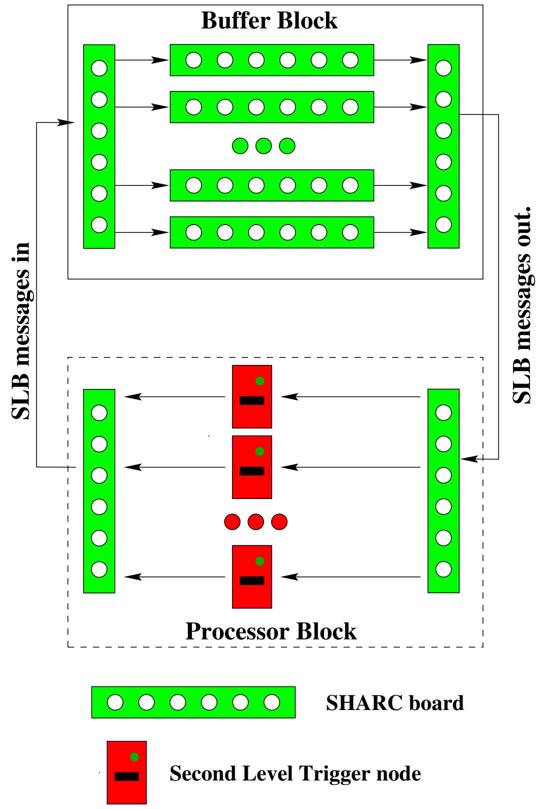

Figure 139: *Scheme of the switch architecture with one Buffer Block and one Processor Block.*

IRIX) through a Giga-Bit line. The logging machine buffers the acquired events in a 106 GByte disk before data is stored on tape.

3.8.5 Status and Performance

The DAQ system was completed during the 2000 run. The system was built up following the needs of the different subdetectors. This method ended up in a non-optimal topology that can be summarized as follows:

- 12 switch Processor blocks, each one holding connections for 20 SLT nodes.
- 10 switch Buffer blocks. Three of them were connected to the vertex detector SLB boards and the remaining 7 were connected to OTR, ITR, ECAL, MUON, RICH, HIPT and TRD SLB boards.
- 2 SHARC boards were devoted for the EVC and interface to the Fast Control System.

Due to the low trigger rate, this topology was never limiting the performance of the acquisition but it gave the possibility of understanding the limitation and capabilities of the system.

3.8.6 Event Building

SLT/RoI protocol

Switch performance The maximum transaction rate in the switch is a function of the data transaction capabilities of the hardware and the software protocol overhead for the message routing. The SHARC hardware is able to transmit/receive up to 40 MBytes/s in a single link and 160 MBytes/s on the external bus.

The SLT protocol is made of two level of message sizes. The SLT request data for a Region of Interest (RoI) for the trigger decision and build the complete events with positive decisions. The RoI protocol is mainly limited by the transaction rate (1/overhead) since the message size is small. The Event Building is limited by the total switch bandwidth, since it is optimized to the largest possible message size.

The limitations of the switch performance was measured using a test bench. A series of simple topologies with controlled data flux were investigated. The transaction performance was investigated in two different cases [126]:

- Routing from SHARC link to SHARC board bus and vice versa: Overhead = 5.6 μs. That is 31.5 MBytes/s for a typical message size (0.8 kBytes). The maximum rate and bandwidth as a function of the message size is shown in Fig. 140. These values are computed for short cables, 80 MHz clock. The value for long cables at 40 MHz is estimated to be 17.5 MBytes/s for a typical message size (0.8 kBytes).

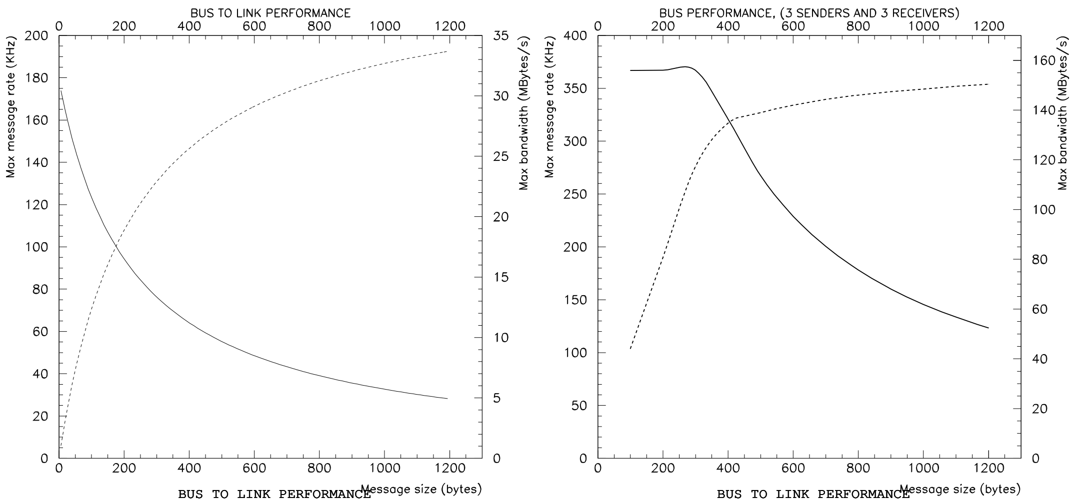

Figure 140: *Left: Maximum message rate (solid line) and bandwidth (dashed line) in a BUS to LINK message routing as a function of message size. Right: Maximum message rate (solid line) and bandwidth (dashed line) in a BUS to BUS message routing as a function of message size.*

- Routing through the SHARC board bus. The bus is shared normally by several sender-receiver pairs. The value to be quoted in this case is the occupancy of the external bus, (i.e. fraction of the time the bus is occupied transmitting data).

The switch performance has been measure in the real environment.

- The maximum switch throughput was measured building the complete detector at the highest speed. For 450 kBytes detector size a maximum of 2.2 kHz was observed, 1.0 GBytes/s. The limitation came from one of the switch blocks (vertex detector) that was moving up to 120 MBytes/s for messages of approximately 600 Bytes. This number is slightly smaller than the one quoted in the test-bench studies ($\approx$ 140 MBytes/s) where less message collisions are expected. The maximum message rate can be as well estimated to be $\approx$ 320 kHz from the Test bench results ($\approx$ 320 kHz) and the measured inefficiencies at the real setup (120/140) due to message collisions on the switch board.

- The Bus to Link performance was measured in an special readout configuration where the transaction was limited by a single link connection. In this case a maximum of 32 MBytes/s was obtained for 800 Bytes message length.

SLB code performance The second level buffer code is responsible of receiving and storing the detector data during the second level trigger decision, it has to serve data to both the Region of Interest and event building protocol and it has to maintain the buffer chain to receive data from the Front End Electronics. The performance of the code is basic to define the limits of the Second Level Trigger. The fraction of buffer updates had been fixed to 5% of the total event rate, i.e. buffer chain is updated in groups of 20. The response time of the event building protocol has been measured to be 66 μs (i.e. 15 kHz) for 800 Bytes and 30 μs (i.e. 30 kHz) for 140 Bytes (Typical Region of Interest in the OTR). Approximately 20 μs is taken by the message receive and transmit overhead, which gives a maximum theoretical limit of 50 kHz.

The maximum speed allowed by the SLT depends on the average number of requests per event that is handled by a single SHARC. To reach the expected value of 50 kHz, an average of 0.6 request per event is allowed. The right distribution of hot detector regions in the Second Level Buffer is critical to achieve the design values.

Event Controller performance The Event Controller is the core of the Second Level Trigger traffic over the switch. It is in charge of receiving the trigger from the Fast Control System and associate a free Second Level Trigger Node to the corresponding buffer index where data is stored. It is at the same time the responsible of freeing Second Level Buffers when they are freed by the nodes (Master Buffer Manager). The Event Controller is implemented as a multiprocessor task where tasks are distributed between several SHARC chips in a board using the multiprocessing capabilities of the SHARC board. The actual implementation of the event controller is able to handle up to 70 kHz input rate from the Fast Control System.

3.8.7 Prospects

The DAQ system has been tested over the 1999 and 2000 HERA – B runs. The system was able to maintain 22 kHz input rate to the Second Level Trigger. The rejection factors and FLT/SLT implementation were not at the nominal values, see FLT and SLT contributions to this report, so the question about the real performance of the HERA – B Data Acquisition System is still open. The results from the test bench and the message transaction over the switch give the possibility of extrapolating the performance under various scenarios.

Switch improvement and performance estimate The 2000 switch configuration was made of 12 Processor blocks and 10 Buffer blocks, with 120 link connections between them, with a non optimized topology. The better distribution of the buffer connection could improve the performance of the switch. Assuming a perfect distribution of the load the performance is just function of the number of Processor and Buffer blocks [54] Two possible scenarios are presented in table 43 where the number of additional SHARC boards and cost estimate are presented, we assume that the number of Processor blocks is the same that the Buffer blocks. Due to the large uncertainty both in the performance of the trigger and the validity of the DAQ estimates, the rational decision will be to implement the largest switch possible, limited by the availability of space and financial support.

Table 43: *Expected performance for two different switch topology scenarios and the comparison with the actual configuration. The RUN 2000 configuration numbers include the inefficiencies from the non-uniform buffer connection to the switch. The cost estimate does not include the possibility of additional spare SHARC boards.*

Configuration	Bandwidth (GBytes/s)	Message rate (MHz)	Add. SHARC boards	Cost estimate (1000 DM)
RUN 2000	1.0	2.6	—	—
12+12 blocks	1.4	3.8	4	≈ 20
15+15 blocks	1.8	4.8	16	≈ 80

Another concern is the low performance of the Second Level Buffer code. Three kind of action has to be taken:

- Distribute the load of the system for the Region of Interest protocol in the Second Level Trigger. The measured values on the Second Level Buffers for a request of one OTR Front End Driver is 30 KHz, i.e. each OTR/ITR Second Level Buffer cannot receive more than 30/50 requests per event. A rational distribution of the OTR and ITR Front End Drivers on the second level trigger could improve the performance. Specific SHARC boards can be devoted for those regions where the trigger RoI's are too large.
- Improve the performance of the Second Level Buffer code. The Test Bench results show that we should concentrate in the receive/answer protocol overhead, since the data copy seems to be fast enough. The possibility of rewriting part of the code in assembler and/or simplifying the error checks are under consideration.
- Investigate the influence of the switch code in the performance of the Second Level Buffer code.

[54]The inter-block connection is not a limiting factor, for 12+10 blocks, the maximum bandwidth is 3.9 GBytes/s for short cables and 2.1 GBytes/s for long cables. These values are well above the expected 1.2 GBytes/s for the 10 Buffer blocks.

3.9 Online Calibration and Alignment (CnA)

In HERA – B all trigger levels and the online reconstruction depend on and have to access the most recent calibration and alignment (CnA) data. Procedures to monitor, determine and distribute such data, before the events are routed to the mass storage media for archival, have been developed and commissioned.

3.9.1 Description and Implementation

Updated CnA constants are produced online in the reconstruction farm and in dedicated second level nodes. In order to obtain quickly the required statistics from the online reconstruction farm, a gathering system has been implemented to collect and merge from the nodes the necessary information to produce updated constants. In the second level, the dedicated CnA nodes get calibration triggers at a sufficient rate.

The set of CnA constants used during data-taking at any time is identified by the so-called *CnA key*. This key is written in the event header. It allows an event to be associated with all the calibration and alignment data used in its trigger process and online reconstruction.

The format of the CnA constants as stored in the database servers might be different to the format required by the trigger processes. To centralize the formatting of the constants and save CPU processing time in the trigger processes, the so-called *CnA formatters* have been introduced in the system.

A pushed architecture has been designed for a low latency distribution of the CNA data to the Second level trigger processors. The updated CNA constants are multicasted using the fast and reliable SHARC links. On the other hand, the larger processing time of the online reconstruction nodes (secs), allows a slower distribution using a pull architecture. The reconstruction nodes fetch the updated CNA data from fast Database memory caches via fast Ethernet.

Fig. 3.9.1 illustrates the online distribution of CnA data to the trigger and online reconstruction processes. The distribution is initiated by the storage of new constants into active database servers which propagate the updates to the key server.The update is sent in turn to the *CnA manager*, the process in charge of the synchronization of the distribution. The CnA manager requests the Event Controller to pause the run and the involved formatters to build and distribute the updated constants to the trigger processes. Once the distribution is concluded successfully the Event Controller is contacted again to resume the run. The online reconstruction processes retrieve the new constants from fast memory database caches when events with the new key arrive to the farm.

3.9.2 Status and Performance

During the 2000 run both the loading of the CnA constants at booting time in the trigger and reconstruction processes and the online distribution of updated constants were done routinely. The attained performance of the loading of the constants in the second level processes through the SHARC switch was 1GB/sec. With the introduction of fast memory database caches, the performance of the loading of the constants in the online reconstruction farm was found to be sufficient, of the order of 15MB/sec. Still some work has to be invested to improve the reliability of the loading.

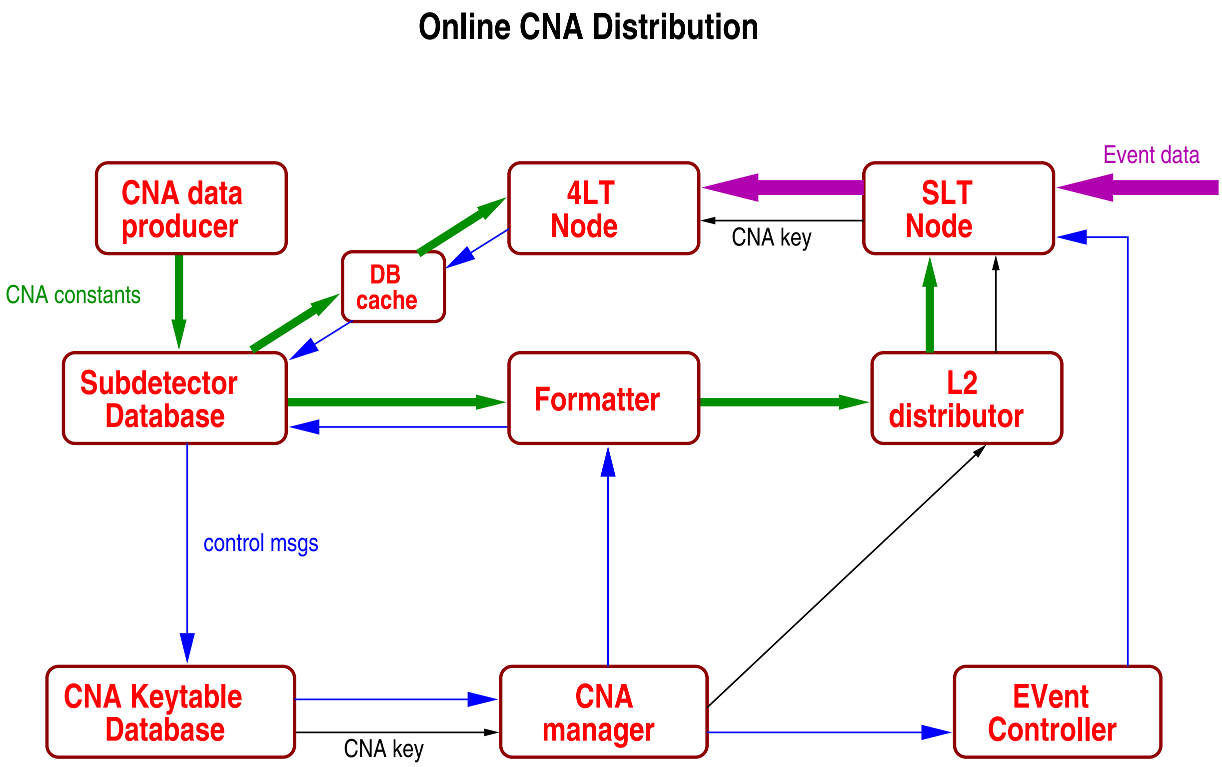

Figure 141: *Online distribution of CnA constants.*

4 Achievements of the Physics Run 2000

4.1 Introduction

The year 2000 running was optimized for detector and trigger commissioning. Still, some time was devoted to dedicated physics running. In April, four HERA fills were used for a systematic study of normal inelastic interactions using different target wire materials. In the course of trigger optimization, a lot of data were taken with di-lepton triggers for collection of J/ψ decays, first only with the electron pretrigger, later also with a muon pretrigger. Towards the end of the running period, a sizeable amount of data was collected using a single high-p_T lepton trigger.

4.2 Minimum Bias Triggers

Normal inelastic interactions constitute the bulk of all interactions seen in HERA – B and form the background from which the heavy flavor decays have to be disentangled. A detailed analysis of the characteristics of these interactions thus not only presents the simplest physics case, but also has to be seen as an integral step of the commissioning of the experiment. For the minimum bias running, the interaction rate was set to a nominal value of 5 MHz and data were recorded with a random trigger that uniformly sampled all HERA bunches. Although at a mean interaction rate of 0.5 events per bunch crossing (BX) most of the events were empty, there was also a sizeable fraction of overlap events, on one hand because of poissonian fluctuations in the number of proton nucleon collisions, on the other hand because of bunch-to-bunch variations in the beam currents and/or emittances. The data are therefore also important to develop accurate luminosity monitoring methods for HERA – B.

4.2.1 Luminosity Monitoring

In order to determine absolute cross sections, the integrated luminosity of the experiment has to be accurately measured. Using random triggers which by definition sample the total inelastic proton-nucleon cross section, the integrated luminosity, L, can be determined from the total interaction count, N, using the known size of the total cross section, σ,

$$L = \frac{N}{\sigma} \quad .$$

Interaction counts can be performed in two complementary ways. One either exploits an observable quantity which is proportional to the number of interactions that have occurred, or one determines the fraction of empty events to extract the poisson probability for an interaction in one bunch crossing.

Candidate quantities that are sensitive to the number of interactions are hits in the scintillator counters of the target system, energy deposit in the ECAL, hits in the RICH detector, or number of tracks or vertices in the VDS. In all cases a calibration is required which determines the average signal from a single interaction. This has been done for the target scintillators and the ECAL energy sum using rate scans. In the limit of vanishing target rate, single interactions completely dominate the signal in non-empty events. Details of such methods are described in [127, 128]. They are robust and independent of any assumption about fluctuations in the target rate.

The alternative approach based on counting empty events has the advantage that, except for the probability of observing a non-empty event, nothing about the average signature has to be known. These acceptances can be easily obtained from data, if independent systems (e.g. different sub-detectors) are combined. The method, however, requires that the fluctuations in the number of interactions per bunch crossing obeys poisson statistics. For conditions with bunch-to-bunch fluctuations (in current and/or emittance), a BX-dependent analysis is mandatory. Although that may look like an unnecessary complication for the analysis of random-triggered minimum bias events, it has to be emphasized that this has anyhow to be done for triggered events since the trigger efficiency for individual bunches is expected to depend strongly on the individual bunch interaction rates.

Finally, as will be shown in the following, combining both methods allows to verify the poisson ansatz from the data themselves, and even to extract small corrections for individual bunches by parameterizing deviations from the poissonian behavior as rms-fluctuations of the mean.

For a system of two independent detectors one obtains the following set of master equations for the probability $p_{1,2}$ to observe an empty event in system 1 or 2, respectively, or p_0 to have an empty event simultaneously in both:

$$\begin{aligned} p_1 &= (1-q_1)\exp\left(-a_1\mu + \frac{1}{2}a_1^2\sigma^2\right) \\ p_2 &= (1-q_2)\exp\left(-a_2\mu + \frac{1}{2}a_2^2\sigma^2\right) \\ p_0 &= (1-q_1)(1-q_2)\exp\left(-a_0\mu + \frac{1}{2}a_0^2\sigma^2\right) \quad , \\ & \text{with} \quad a_0 = a_1 + a_2 - a_1 a_2 \quad . \end{aligned}$$

Here, μ is the mean number of interactions per BX, $q_{1,2}$ are the probabilities to record an event due to backgrounds or electronic noise, and $a_{1,2} < 1$ are the efficiencies to record a real event. The quadratic correction term in the exponentials is obtained by convoluting the simple poissonian expressions $\propto \exp(-a_i\mu)$ with a gaussian distribution for μ of width σ, thus using the rms-scattering of μ around its central value as a simple model for non-poissonian fluctuations.

In total there are therefore six unknowns for three measurements. Of those the parameters μ and σ have to be assumed to be BX-dependent, the others are global quantities. The need to do the analysis separately for each bunch thereby turns into an asset, since it allows to extract the global parameters together with the local ones from a global fit. It turns out, however, that blindly fitting both μ and σ for each bunch tends to be numerically unstable if there are bunches which contribute only with a very small rate. To stabilize the procedure, one can classify the bunches on the basis of an inclusive quantity which is proportional to the number of interactions per BX, like for example $\langle \mathrm{tr/bx} \rangle$, the average number of tracks per BX seen in the silicon vertex detector. One has $\langle \mathrm{tr/bx} \rangle = \alpha\mu$, with α the number of tracks per interaction within the acceptance. With the relation

$$\ln\frac{p_0}{p_1 p_2} = a_1 a_2 \mu + \frac{1}{2}\sigma^2 a_1 a_2 (a_1 a_2 - 2a_1 - 2a_2 + 2)$$

one thus obtains in case of negligible rate fluctuations:

$$\frac{1}{\langle \mathrm{tr/bx} \rangle}\ln\frac{p_0}{p_1 p_2} = \frac{a_1 a_2}{\alpha} \quad . \tag{19}$$

For bunches with sizeable rate fluctuations, the ratio is changed (normally lowered, since the acceptances $a_{1,2}$ are typically large). Plotting the ratio as function of the BX number thus allows to spot bunches which suffer from rate fluctuations. If the fluctuations are proportional to μ, then a plot of the ratio versus $\langle \mathrm{tr/bx} \rangle$ shows a slope.

In case that rate fluctuations have to be taken into account, this method is used to identify bunches which have a significantly lowered ratio (eq. (19)) and exclude them from a global fit that is performed under the assumption of negligible rate fluctuations. The fit yields the global parameters a_1, a_2, q_1 and q_2 together with the mean number of interactions per BX, μ, for all bunches under consideration. The parameter α is then extracted from eq. (19) and can be used to count the interactions in the bunches that were excluded from the poisson fit. As a cross check of the procedure, the ratio of $\langle \mathrm{tr/bx} \rangle / \mu$ has, within errors, to be the same for all bunches.

The first system used for the determination of the integrated luminosity of the minimum bias data was the combination of ECAL and RICH, requiring at least 1.5 GeV energy deposit in the inner part of the ECAL and at least 20 hits in the RICH. The second independent system was formed by the vertex detector and the outer tracker, using the event selection criteria as described in section 4.2.2. The total number of events accepted and analyzed is given by

$$N_{\mathrm{ev}} \;=\; a_2 \sum_{\mathrm{BX}} N_{\mathrm{BX}} \;\; \mu_{\mathrm{BX}} \;=\; \frac{a_2}{\alpha} \sum_{\mathrm{BX}} N_{\mathrm{BX}} \langle \mathrm{tr/bx} \rangle$$

where a_2 is the acceptance of the VDS-OTR system.

The procedure is illustrated in Fig. 142 which shows in a dramatic way that any precision cross section measurement will require a luminosity monitoring at the level of individual bunches. It is reassuring to observe that, despite of large variations in the luminosity of the individual bunches, the inferred number of tracks per interaction is the same for all.

4.2.2 Single Particle Inclusive Distributions

Single particle inclusive distributions were studied for normal inelastic proton-nucleus collisions recorded by the random trigger. To discard empty events or backgrounds caused by coasting beam interactions, good events were required to have a well defined timing in the outer tracker with a mean drift time between $150 < t_d < 175$ ADC-counts and a rms variation $\mathrm{rms}(t_d) < 50$ counts. In addition, the event had to have a primary vertex candidate, made of at least two pairs of tracks with a transverse distance below 1 mm at $z = z(\mathrm{target})$. The tracks had to have at least 6 hits in the vertex detector and pass within 1 cm distance of the average target position.

Tracks from a match between vertex detector (VDS) and outer tracker (OTR) were accepted for the analysis if they had at least 6 VDS hits and at least 20 hits in the OTR. To avoid "clones" (multiply reconstructed tracks), each segment from either the VDS or the OTR was accepted only once. If a segment was associated to more than one track, the candidate with the larger total number of hits was chosen. In case of a tie, the one with the smaller χ^2 in the track fit was taken.

Finally, in order to stay clear from acceptance boundaries, tracks were required to have a momentum $p \geq 2$ GeV, a transverse momentum $p_T \geq 0.1$ GeV and $|x_F| \leq 0.2$. In the center-of-mass system the phase space thus is restricted to the central region. Inclusive distributions, normalized to the number of proton-nucleus interactions, were studied as function of transverse momentum,

$$\frac{1}{N_{\mathrm{ev}}} \frac{\mathrm{d}n}{p_T \mathrm{d}p_T} \qquad \text{with} \qquad p_T = \sqrt{p_x^2 + p_y^2} \quad ,$$

pseudo-rapidity, related to the polar angle θ with respect to the z-axis,

$$\frac{1}{N_{\mathrm{ev}}} \frac{\mathrm{d}n}{\mathrm{d}\eta} \qquad \text{with} \qquad \eta = -\ln\left(\tan\frac{\theta}{2}\right) \quad ,$$

and the Feynman scaling variable x_F,

$$\frac{1}{N_{\mathrm{ev}}} \frac{\mathrm{d}n}{\mathrm{d}x_F} \qquad \text{with} \qquad x_F = \frac{2p_z^{\mathrm{cm}}}{\sqrt{s}}$$

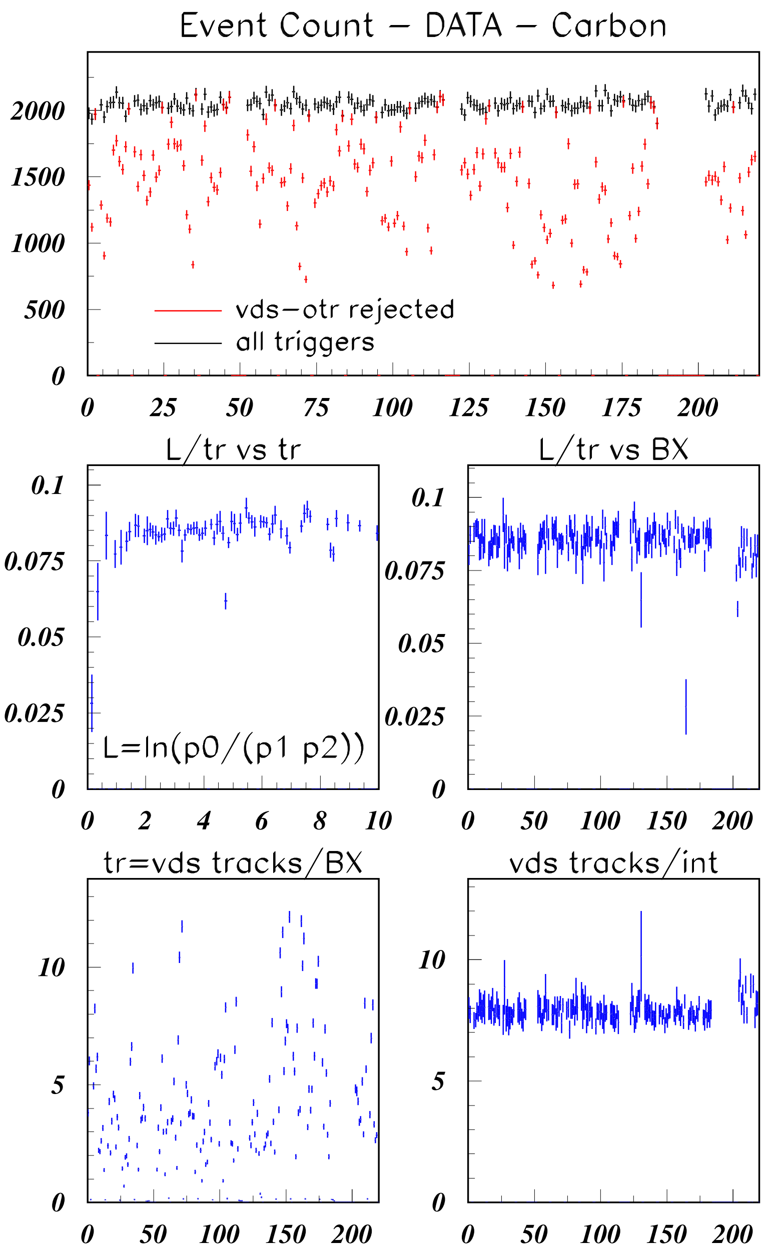

Figure 142: *Luminosity determination for data taken with a carbon wire target. The first plot shows the distribution of the number of random triggers as a function of the bunch number. By definition, the distribution should be flat (excluding non-filled bunches). Also shown is the number of events rejected by the event selection criteria. For some bunches, the rejection rate is close to* 100%. *As a check for rate fluctuations the two plots in the middle show the ratio* $\frac{1}{\langle \mathrm{tr/bx}\rangle}\ln\frac{p_0}{p_1p_2}$ *as function of* $\langle$tr/bx$\rangle$ *and the BX number. Some entries are seen to be subject to rate fluctuations, but in general the ratio is quite stable. The last row finally shows* $\langle$tr/bx$\rangle$ *(left) and the inferred number of tracks per interaction (right hand side) as function of BX.*

which, taking the pion mass to calculate the energy, can be expressed as

$$x_F = \frac{1}{m_\mathrm{p}}\left(p_z - E_\pi\sqrt{1-\frac{2m_\mathrm{p}}{E_b}}\right) \quad .$$

Here, m_p denotes the proton mass and E_b the energy of the incident proton. The spectra were determined separately for positive and negative particles and as function of the nuclear mass number, A, of the target material. The results were compared to Monte Carlo simulations, both on reconstruction level and on Monte Carlo truth level. In order to have well defined multiplicities and particle compositions, the Monte Carlo truth was defined such that all particles with a lifetime below 1 ns are forced to decay at the primary vertex while all other particles are considered to be absolutely stable. Like the data, also the Monte Carlo truth was restricted to the central region $|x_F| < 0.2$.

The available data sets are listed in Tab. 44. The interaction counts were determined by the method described in the previous section. A 5% systematic uncertainty has to be added to the statistical errors given in the table. The large error for the aluminum target reflects the fact that those data are affected by sizeable rate fluctuations.

Table 44: *Summary of the statistics for real data and Monte Carlo data for the different target materials. The Monte Carlo events have been passed through the full detector simulation. Monte Carlo truth is not listed, as there the statistical uncertainties are negligible. A 5% systematic uncertainty has to be added to the statistical error of the event counts.*

Target	A	Wire	Run	triggers used	interactions	MC
Ti	48	Inner 1	14551	200,000	44,247 ± 464	21,489
C	12	Inner 2	14577	450,000	127,280 ± 414	39,997
Al	27	Upper 2	14606	150,000	21,928 ± 2069	13,679
W	184	Lower 2	14639	300,000	28,520 ± 367	22,553

The track density as function of pseudo-rapidity η and azimuthal angle ϕ is shown in Fig. 143 for minimum bias data taken with a carbon target. Experimental results (upper plots) for positive

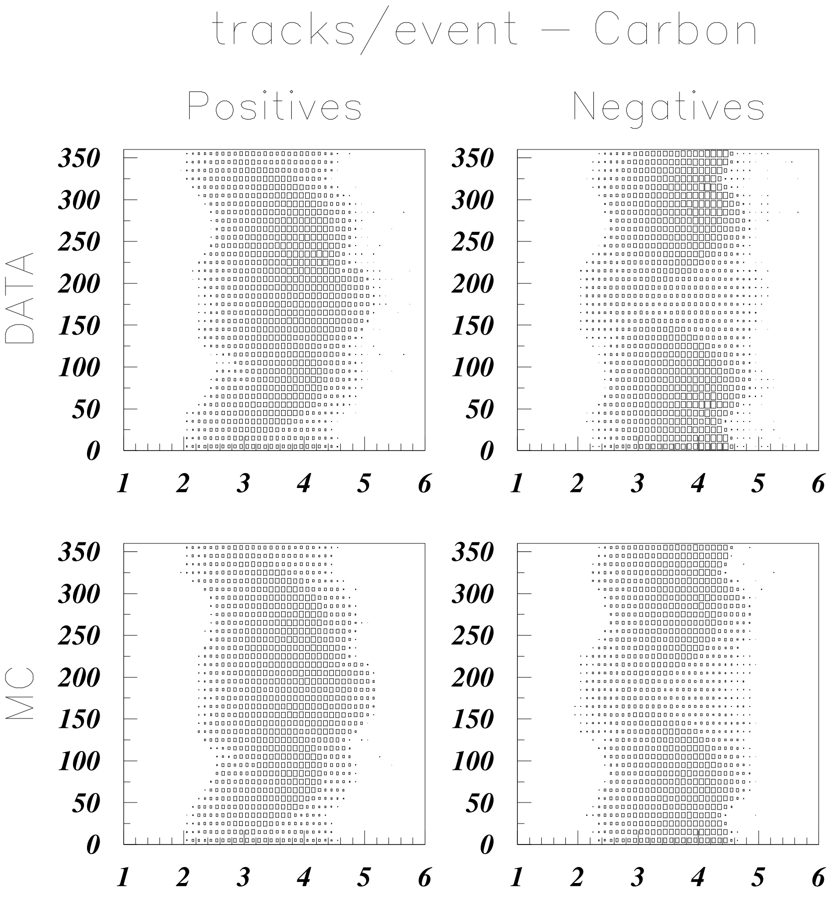

Figure 143: *Track density as function of pseudo-rapidity and azimuthal angle in normal inelastic interactions recorded with a carbon target. The charge dependent low efficiency regions at $\phi = 0°$ and $\phi = 180°$ are due to the Inner Tracker not yet being used in the analysis.*

and negative particles (left and right column, respectively) are compared to reconstructed Monte Carlo events (lower plots). Data and Monte Carlo are in good agreement. Also well simulated are the extended regions of low tracking efficiency around $\phi = 0°$ for positive particles and $\phi = 180°$ for negative particles, caused by the fact that the Inner Tracker was not yet used in analysis, since positive particles emitted at $\phi = 0°$ and negative particles emitted at $\phi = 180°$ are bent towards the Inner Tracker by the magnetic field. The plots show that the current tracking system covers a range from $2.5 < \eta < 4.5$. With the rapidity of the center-of-mass system $y_{\rm cm} \approx 3.8$ it follows that in the center-of-mass system the current coverage for the backwards hemisphere is twice that of the forward hemisphere. Studying the angular coverage for the other target materials, one finds very similar results. The height of the rapidity plateau, however, grows with the nuclear mass number of the target material. This A dependence of the charged particle multiplicity will be discussed in section 4.2.4.

The invariant cross section per event as function of transverse momentum is shown in Fig. 144, again for proton-carbon interactions. The statistics is sufficient to measure the cross section up

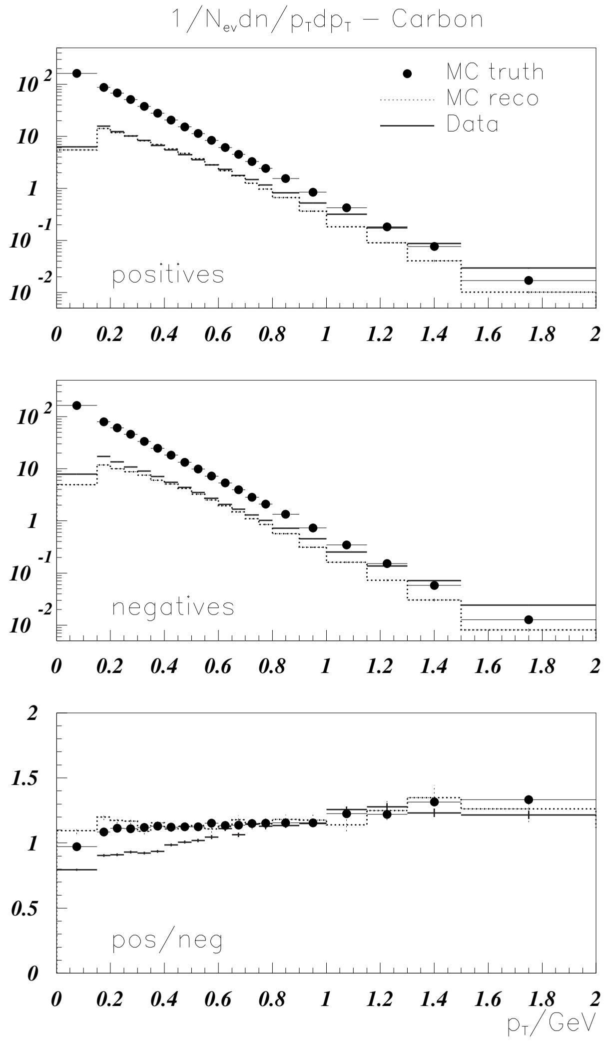

Figure 144: *Transverse momentum spectra for normal inelastic interactions in proton-carbon scattering. The data for positives and negatives are compared to Monte Carlo predictions after reconstruction and on the generator level ("truth"). Also shown is the ratio of positives over negatives.*

to transverse momenta of 2 GeV/c. The agreement between data and Monte Carlo prediction after reconstruction is quite satisfactory, except maybe for the large p_T region, where the measured spectra are slightly harder compared to the Monte Carlo expectations. The bulk of the relatively large correction between reconstruction level and generator level is understood to come from the relatively narrow rapidity range covered by the detector. For the charge ratio, most of these acceptances cancel, and for $p_T > 0.5\,\mathrm{GeV/c}$ one finds good agreement between data, simulation and Monte Carlo truth. The deficit of low-p_T positive particles in the data is currently not understood.

4.2.3 Strangeness Production

Another aspect of normal inelastic proton-nucleus collision is the study of strangeness production. The HERA – B tracking system can be employed to look for V^0-decays of K^0_S and Λ particles. The result from a simple combinatorial analysis for all target materials is shown in Fig. 145. For the K^0_S signal, two oppositely charged tracks were required, which form a vertex with a transverse distance to the primary vertex smaller than 0.035 cm, and which is located at least 5 cm downstream of the primary vertex. Both tracks were assigned the pion mass for the invariant mass calculation. Candidates for Λ hyperons were selected on the basis of opposite-charge track pairs which form a vertex with transverse distance to the primary vertex smaller than 0.02 cm, situated at least 10 cm downstream of the primary vertex. To form the invariant mass, both combinations to assign the pion mass to one track and the proton mass to the other were taken together, i.e. there is no discrimination between Λ and $\overline{\Lambda}$. Comparison with Monte Carlo simulations shows that the widths of the mass peaks, measured to be 8 MeV for the K^0_S meson and 3.4 MeV for the Λ hyperon, agree well with the expectations. There is, however, some discrepancy in the production rates. Leaving out the numbers for aluminum, which due to instabilities in the interaction rate have significantly higher systematic uncertainties, one finds the following K^0_S multiplicities per 1000 events:

Target	data	Monte Carlo	MC/data
C ($A = 12$)	3.8 ± 0.4	19.8 ± 1.3	5.2 ± 0.6
Ti ($A = 48$)	4.8 ± 0.7	15.7 ± 1.7	3.3 ± 0.6
W ($A = 184$)	5.7 ± 1.2	9.0 ± 1.5	1.6 ± 0.4

In view of the fact that after full detector simulation the single particle inclusive distributions are described pretty well, typically within 20%, the large discrepancies between data and Monte Carlo expectations, in particular in the A dependences, are puzzling. The most likely explanation is that on one hand the single track reconstruction efficiency is overestimated in the simulation, although hardly as much as 30%, and that the nuclear dependence of strangeness production is not correctly modeled in the simulation.

More quantitatively, the simulations were performed assuming a single hit efficiency of 80% for all active cells of the outer tracker. Under these conditions the ratio between Monte Carlo truth level and reconstruction level at central rapidities, $\eta \simeq 3.8$, is 1.5. Thus from the Monte Carlo simulation a single track efficiency of $\varepsilon = 0.66$ is expected. From the observation that reconstructed Monte Carlo data and real data agree at the 20% level, one concludes that the single track reconstruction efficiency for real data is given by $\alpha\varepsilon$, where $\alpha = N_\mathrm{data}/N_\mathrm{MC}$ is the (unknown) ratio between the true multiplicities in real data and in Monte Carlo data. The parameter α can be estimated from the ratio of K^0_S yields in Monte Carlo simulations and real data. Assuming that in first approximation the efficiencies for the pions from the K^0_S decay are uncorrelated, one finds $N_\mathrm{MC} = N^\mathrm{t}_\mathrm{MC}\varepsilon^2$, and $N_\mathrm{data} = N^\mathrm{t}_\mathrm{data}(\alpha\varepsilon)^2$. Here, $N^\mathrm{t}_{\ldots}$ denotes the true K^0_S multiplicities in real data and Monte Carlo simulations, respectively. One obtains $R = N_\mathrm{MC}/N_\mathrm{data} = (N^\mathrm{t}_\mathrm{MC}/N^\mathrm{t}_\mathrm{data})/\alpha^2$, and, if the K^0_S multiplicities scale with the charged particle multiplicities, one finally gets $R = 1/\alpha^3$. The multiplicities quoted above can thus be interpreted by an A dependent multiplicity ratio α, which varies from $\alpha \simeq 0.58$ for carbon to $\alpha \simeq 0.85$ for tungsten. On the other hand, since the single track finding efficiency, which should be independent of the target material, is proportional to α, it seems that the most likely explanation for the low K^0_S yields in the data is a slightly lower track finding efficiency, compared to

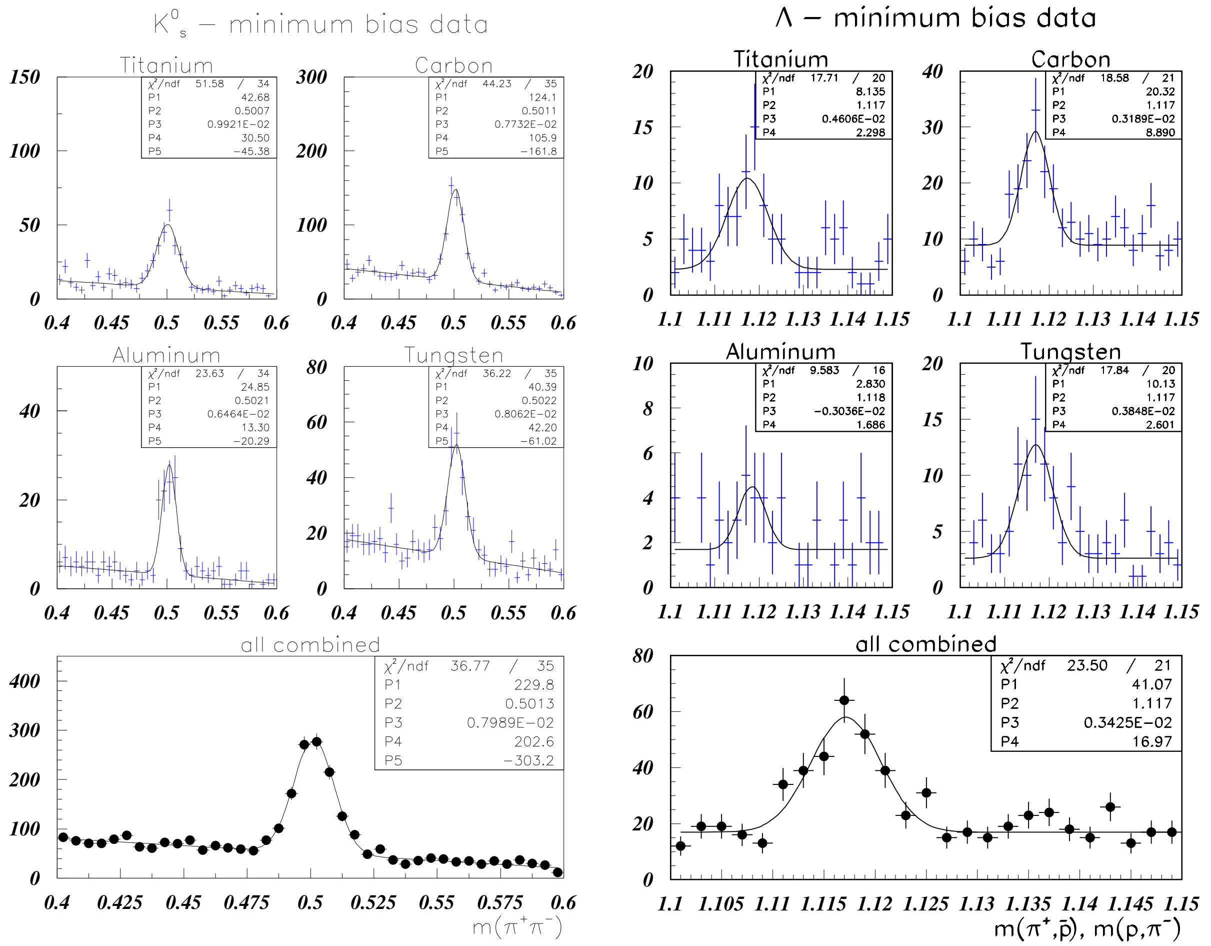

Figure 145: *V^0 production in minimum bias data as function of the target material. Signals from K^0_S and Λ-particles are seen in all data sets.*

that extracted from the simulation, together with a wrong A dependence in the physics generator.

4.2.4 Multiplicities

When studying nuclear dependencies, one of the simplest quantities to look at are multiplicities of produced particles. In the analyses described above, the charged particle multiplicity per event as observed in the vertex detector was a by-product of the determination of the integrated luminosity. Although not yet corrected for detector effects, it at least gives some indication of the A dependence of this observable. A more in-depth analysis will be soon available [129].

Another interesting quantity is the number of K^0_S mesons per 1000 events, which is obtained from the study described in the previous section. Again, no correction for efficiencies was applied. The results for carbon (A=12), titanium (A=48) and tungsten (A=184) are shown in Fig. 146. The data with the aluminum target, which suffered from significant rate fluctuations and thus ended up with large uncertainties in the event counts, are omitted. The errors are statistical only. For the charged particle multiplicities they are smaller than the size of the symbols.

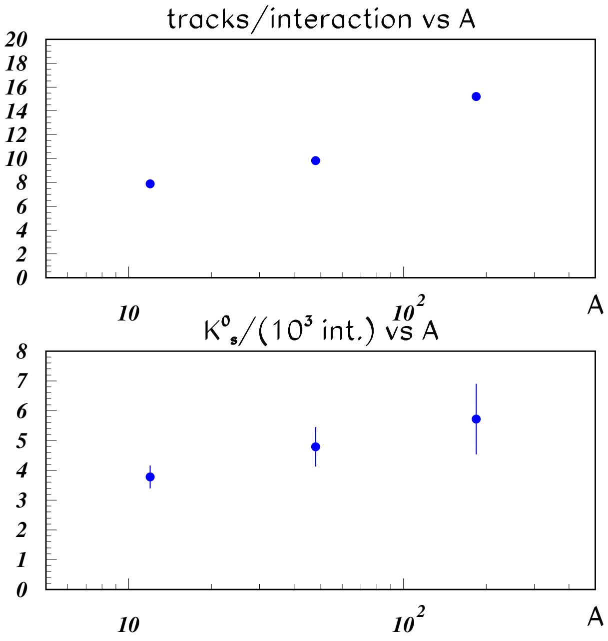

Figure 146: *A dependence of the charged particle multiplicities as recorded with the vertex detector and of the number of* K^0_S *mesons produced in* 1000 *minimum bias events. No efficiency corrections are applied.*

4.2.5 Particle Fractions

Using the particle identifications capabilities of the RICH detector, particle fractions can be determined by matching a Cherenkov ring to the track direction from the main tracking system. After a careful check of the relative alignment between RICH and tracking system, and after correction for residual offsets, the combined information of ring radius and track momentum was translated into a likelihood for the different particle hypotheses. For this analysis only pion, kaon and proton likelihoods were considered, normalized such that they sum up to unity. From these normalized likelihoods $\mathcal{L}_\pi$, $\mathcal{L}_\mathrm{K}$ and $\mathcal{L}_\mathrm{p}$, the particle fractions f_π, f_K and f_p were determined in each momentum bin, by maximizing the likelihood function

$$\mathcal{L}_E = \prod_{i=1}^{N_\mathrm{tot}} \left(f_\pi \mathcal{L}_{\pi,i} + f_\mathrm{K} \mathcal{L}_{\mathrm{K},i} + f_\mathrm{p} \mathcal{L}_{\mathrm{p},i} \right) \quad ,$$

subject to the constraint

$$f_\pi + f_\mathrm{K} + f_\mathrm{p} = 1 \quad .$$

Here, N_tot is the total number of tracks in a given bin. The result is shown in Fig. 147. The full symbols represent the pion (circles), kaon (squares) and proton (triangles) fractions found for the minimum bias data obtained with the carbon target, the open symbols represent the same for a Monte Carlo calculation including full detector simulation, and using the same analysis chain. The agreement between data and Monte Carlo expectation is very satisfactory. Only for momenta below 20 GeV/c, some discrepancies in the proton fractions are seen which could point towards residual problems in the particle identification scheme.

In order to minimize bin-to-bin migrations, the binning for Fig. 147 was chosen to match at least twice the error of the track momentum. In case of low statistics, which applied to the bins at high momenta, the bin size was increased further to assure a sufficient number of entries per bin.

An estimate for the size of the detector effects in the measurement of particle fractions can be gained from the comparison between Monte Carlo truth and reconstructed Monte Carlo data, shown in Fig. 148. The relative size of the corrections are in general below 10%. The correction procedure to be applied to the momentum spectra or the inclusive distributions for other kinematic variables, like pseudo-rapidity or x_F, will be based on a detailed analyses of the migration matrix [130] between the true and the measured particle fractions.

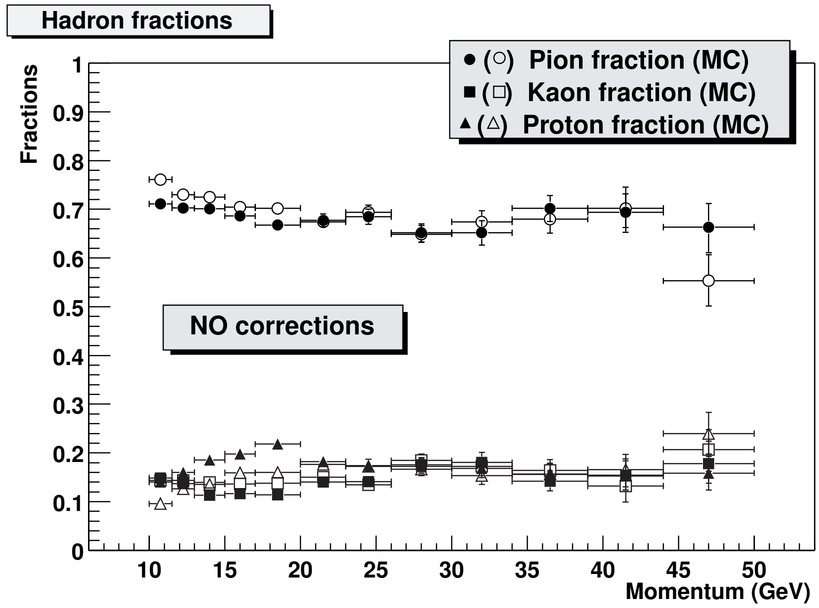

Figure 147: *Comparison between real data and reconstructed Monte Carlo data for pion, kaon and proton fractions in minimum bias events.*

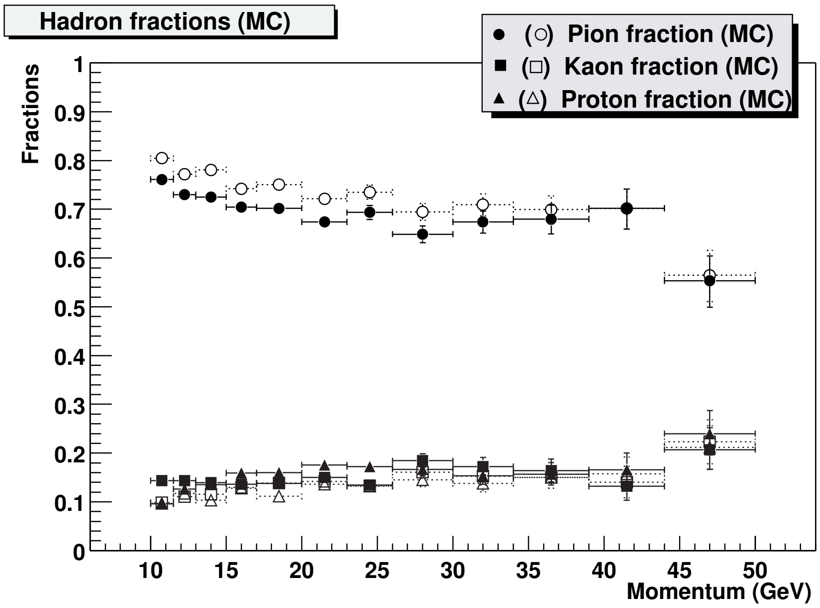

Figure 148: *Comparison between Monte Carlo truth (open symbols) and reconstructed Monte Carlo data (full symbols) for pion, kaon and proton fractions in minimum bias events.*

4.3 Double Lepton Triggers

Di-lepton triggered data were taken with the electron and the muon pretriggers. Although the latter yield a J/ψ signal which is much cleaner than the one from the electron data, the muon pretrigger became fully operational so much later, that currently the signal from the electron data is still better understood.

4.3.1 Electron Triggers

The preliminary analysis presented here is based on a subsample of 2 million events out of a total sample of 16 million events. The analysis of the complete data set is ongoing. The data were taken with the carbon wire at an interaction rate of 5 MHz. From a total of 4.4 million events, a subsample of about 2 million was used in the analysis. The pretrigger threshold for both clusters was set to $E_T = 1.2$ GeV. After the complete ECAL reconstruction on the second level trigger processor farm, events were recorded if clusters at a relaxed threshold $E_T = 1$ GeV were found, and both clusters were associated with VDS tracks, where only out-bending pairs with an invariant mass above 2 GeV/c^2 were accepted. For the offline analysis the cuts were tightened further, requiring $E_T > 1.35$ GeV, at least 10 hits in the VDS segments associated with the ECAL clusters which in the non-bending plane had to be within 2.5 cm of the extrapolation from the VDS track segments. In the preliminary analysis, the outer tracker information was not yet used because of the lack of high quality calibration and alignment constants.[55] The track momentum was therefore computed from the VDS-ECAL combination alone, and was required to be above 5 GeV/c. To enrich the fraction of electrons or positrons, the ratio $E/|p|$ of the tracks had to be within 30% around unity, with E the cluster energy from the ECAL and p the momentum estimate, derived from the track direction in the vertex detector and the impact point of the track in the ECAL. The cut was adjusted to the width of the E/p distributions shown in Fig. 149, which reflects a not yet final calibration of the ECAL and uncertainties in the momentum reconstruction.

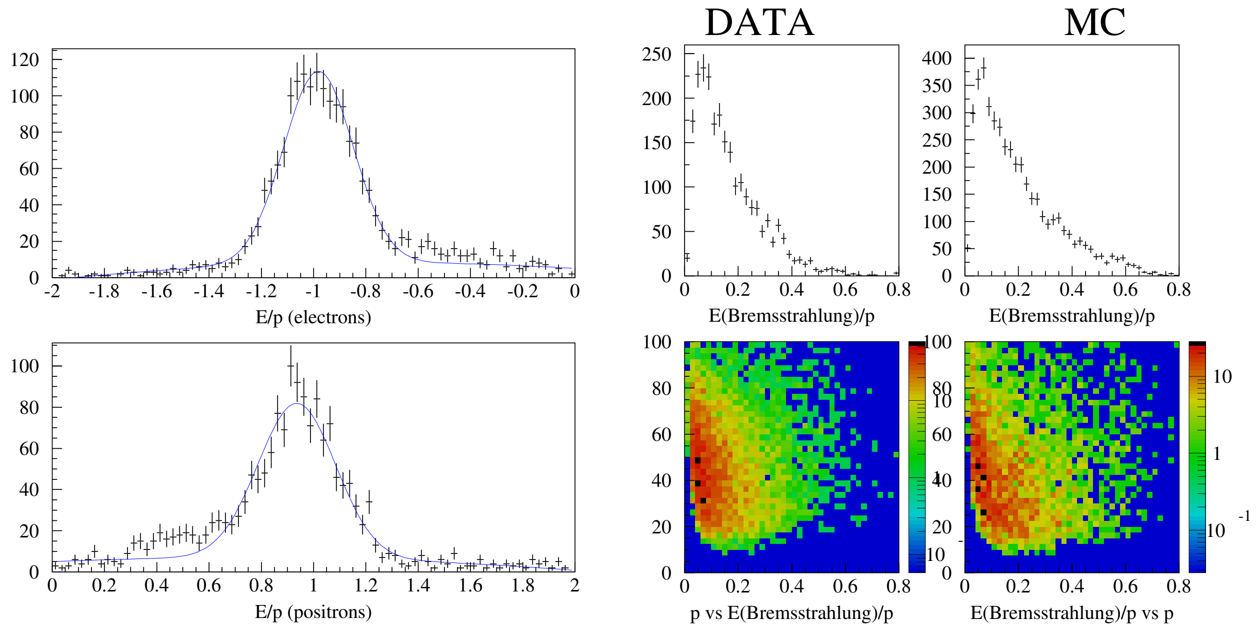

Figure 149: *Electron identification. The left hand plot shows the distribution of the ratio E/p for electron and positron candidates. On the right hand side, the bremsstrahlung spectra, scaled to the momenta of the electrons or positrons, are displayed for data and Monte Carlo simulation.*

To finally eliminate almost the entire background, each electron candidate was required to have a bremsstrahlung cluster from radiation in front of the magnet. This double bremsstrahlung requirement lead to a very efficient cleanup of the data sample. To check the systematics of this method, the bremsstrahlung spectrum normalized to the track momentum is shown for data and Monte Carlo simulation in the right hand plots of Fig. 149. The characteristics of the bremsstrahlung is

[55] The OTR information is used in the currently ongoing refined analysis.

well reproduced. The Monte Carlo simulation is based on 75 k events with a directly produced J/ψ meson, overlayed with an average number of 0.5 normal inelastic interactions, varied according to a poissonian. Efficiencies of the vertex detector as well as a dead/hot channel map of the ECAL are taken into account.

The resulting signal is shown on the left hand side of Fig. 150. It contains a total of 326 ± 44 signal events, where the error is purely statistical. In the plots on the right hand side, the properties of the reconstructed J/ψ mesons are compared to Monte Carlo expectations. One sees that the observed angular distributions and momentum spectra are generally well reproduced by the Monte Carlo simulations. When extrapolated to an analysis using the full detector working at design, the simulation predicts a much more pronounced J/ψ peak which is narrower by more than a factor of two.

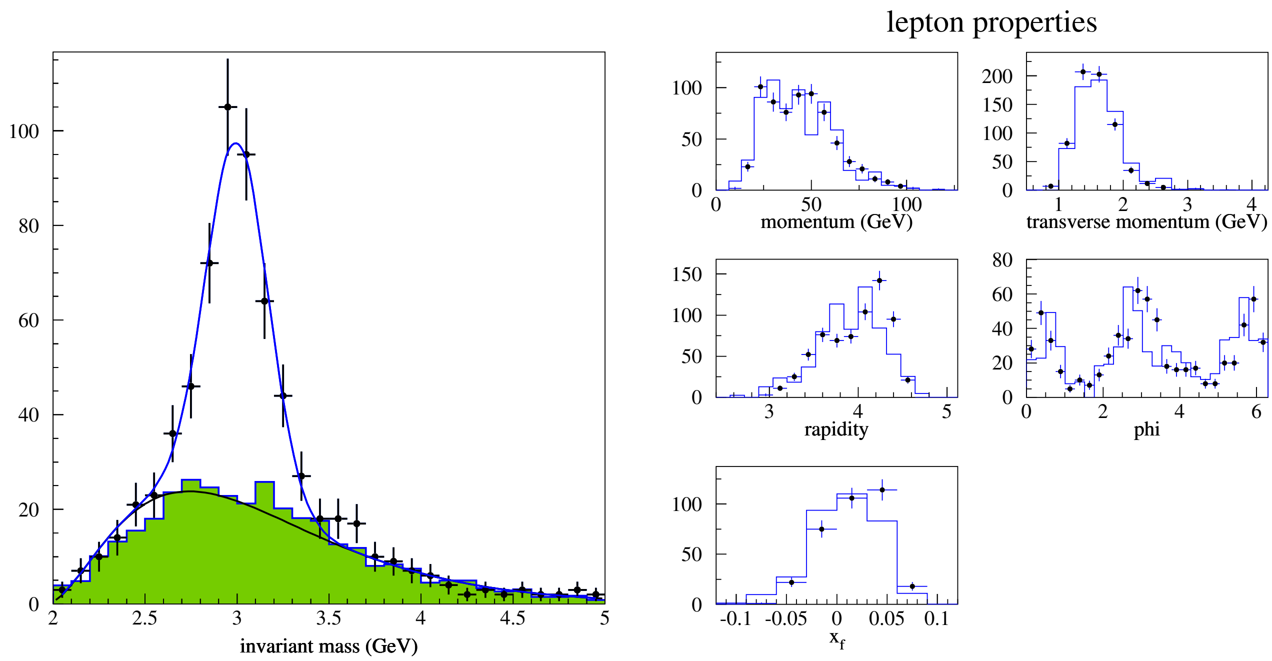

Figure 150: *The left hand plot shows the* J/ψ *signal seen in the electron triggered data (together with event mixing background and fits to the spectra). The right hand side presents a comparison between data and Monte Carlo for the angular distributions and momentum spectra of the* J/ψ *mesons.*

In order to convert the signal into a cross section, the trigger efficiency, integrated luminosity and dead time has to be evaluated. The trigger efficiency was determined by a separate simulation. Together with the reconstruction and analysis cuts it leads to a value of 0.08% for the total J/ψ efficiency. Integrated luminosity and dead-time for the data were logged together with the target rates and DAQ monitoring. From these inputs the cross section for J/ψ production is estimated to be $\sigma(\mathrm{J}/\psi) = 270$ nb/nucleon. The statistical error for this number is 13% from the data and 23% from the Monte Carlo simulation. The dominant systematic errors are 15% for the integrated luminosity, 35% for the simulation of dead and noisy regions in the ECAL and 10% for the efficiency of the second level trigger. The final cross section from the analysis of electron data is $\sigma(\mathrm{J}/\psi) = 270 \pm 128$ nb/nucleon. The result is compared to other published measurements in Fig. 151.

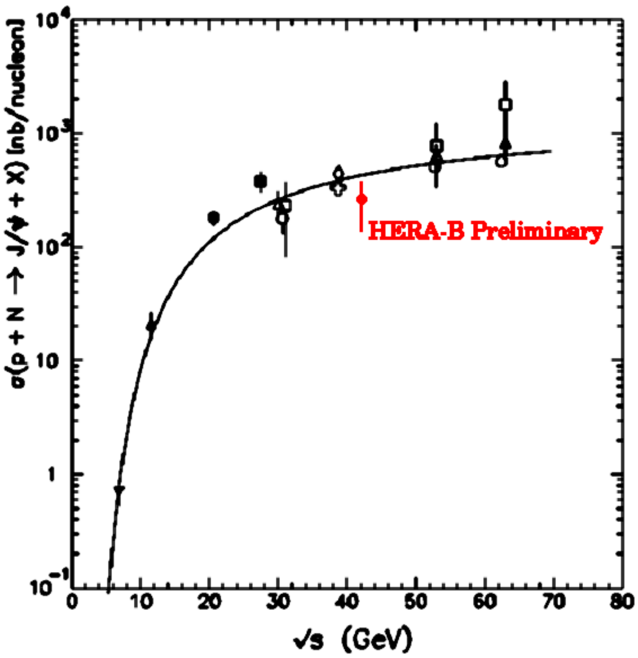

Figure 151: *Comparison of the HERA – B measurement for the J/ψ production cross section with other published results.*

4.3.2 Muon Triggers

The muon pretrigger became fully operational in June 2000. Since then it ran concurrently with the electron trigger. A di-lepton trigger was applied for most of the time and about 3.7 million events were collected, of which about 15% were due to muon triggers. The data were taken in single wire operation, either using a carbon or a titanium wire, and the interaction rate was 5 MHz. The muon pretrigger required the presence of two track candidates in the MU3 and MU4 pad chambers of the detector. These two candidates were used to seed the second level trigger selection, where two fully reconstructible tracks were required. The SLT was based on the SLICER/REFIT algorithms and exploited the information coming from the outer tracker chambers. Finally, the reconstructed track candidates were matched with two segments in the VDS (applying the L2SILI algorithm).

In the following, a preliminary analysis of about 75% of the events is presented. The offline reconstruction was mainly based on the SLT information. The SLT track momentum was used, while in order to improve the precision of the reconstructed track directions a full VDS reconstruction was applied and a match between the two SLT tracks and the two VDS segments was required.

The obtained $\mu^+\mu^-$ invariant mass distribution is shown in Fig. 152. On the left side the points are corresponding to opposite-charge di-muons, while the dashed histogram is obtained from same-charge pairs. A clear peak containing $\simeq 2800$ signal events is evident. The position, $M_{\mu^+\mu^-} = 3.07\,\mathrm{GeV/c^2}$, is close to the nominal J/ψ mass value. The width of the peak, $\sigma = 75\,\mathrm{MeV/c^2}$, is about a factor 2 larger than the one expected for a fully commissioned detector and reconstruction chain, due to the fact that the detector alignment is still not finalized and that the reconstruction packages are not optimized.

The selected data sample was also used to tune the vertex packages. The final goal is to detect displaced vertices in order to determine the $\mathrm{b\overline{b}}$ cross section. The left part of Fig. 153 shows the distribution of the z coordinates of reconstructed primary vertices for the di-muon events. Two clear peaks, corresponding to interactions in the carbon wire (at $z \simeq -4.8\,\mathrm{cm}$) and in the titanium wire (at $z \simeq -1.5\,\mathrm{cm}$), are evident. In order to select a clear J/ψ sample the di-muon candidates were

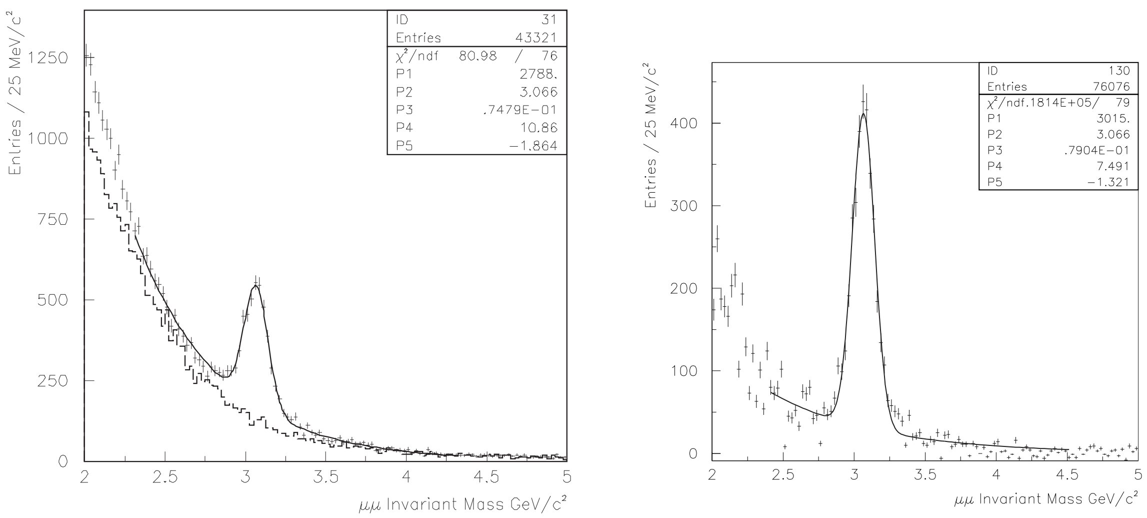

Figure 152: *Left side: Invariant mass spectrum of muon pairs. The points correspond to opposite-charge pairs, the dashed line to same-charge pairs. Right side: Invariant mass distribution obtained from the subtraction of the two distributions.*

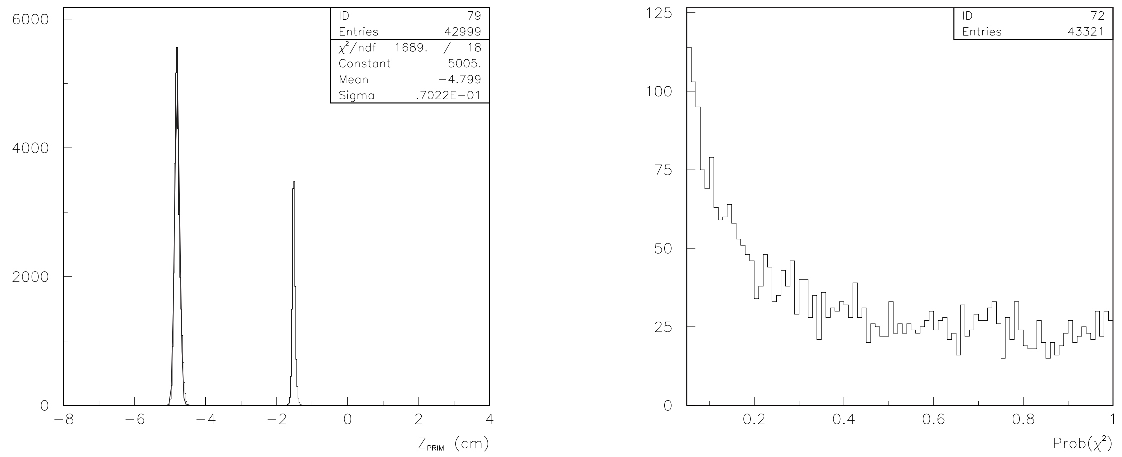

Figure 153: *Left side: Primary vertex distribution of the di-muon events. Right side:* χ^2 *probability distribution for di-muon events obtained from a vertex fit with mass constraint.*

run through a vertex fit, requiring at the same time a J/ψ mass constraint. The distribution of the corresponding χ^2 probabilities, $P(\chi^2)$, is shown in the right part of Fig. 153. Applying a cut on the fit probability, $P(\chi^2) > 0.05$, a sample of $\simeq 3200$ events was selected.

In the upper part of Fig. 154 the J/ψ decay path length, projected on the beam direction ($\Delta z = z(\mathrm{J}/\psi) - z(\mathrm{primary})$), is shown. The peak centered at zero with a rms width of $\simeq 630\,\mu$m is corresponding to direct J/ψ mesons, produced at the primary vertex. The J/ψ mesons stemming from $\mathrm{b\overline{b}}$ pairs should have positive Δz. The expected rate is one detached J/ψ meson per $\simeq 2000$

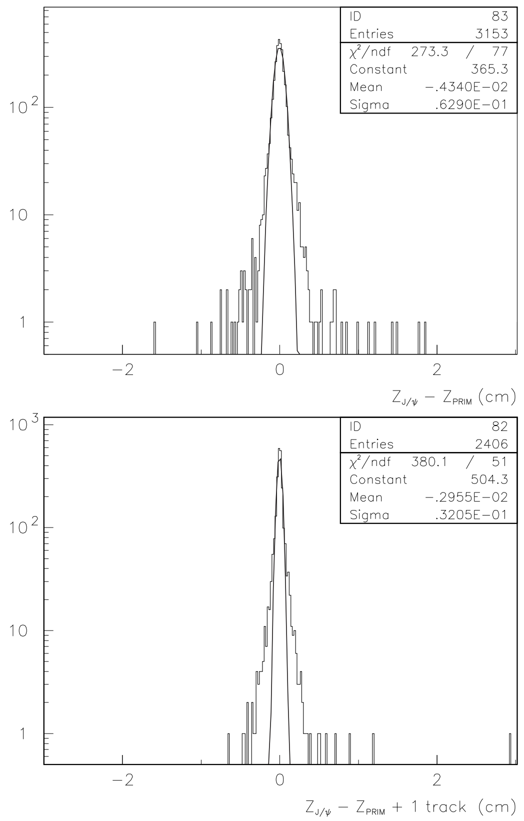

Figure 154: *Upper part: z distance between primary vertex and $\mu^+\mu^-$ vertex. The number of events in the window* $[0.5 \ldots 2]$ cm *is* 18*, the number of events in the window* $[-2 \ldots -0.5]$ cm *is* 15*. Lower part: The same distribution, but requiring that at least one extra track is compatible with originating at the dimuon vertex.*

direct J/ψ mesons for $\sigma_{b\bar{b}} \simeq 12$ nb per nucleon. One can try to detect the presence of such events by comparing the number of events in downstream and upstream windows in z. In the lower part of Fig. 154 the same distribution is shown, requiring that at least one extra track is originating at the J/ψ vertex. As one can see, the total number of events in the plot is reduced, but the displaced vertex distribution is cleaned up.

Despite the low statistics, this result is encouraging and shows the capabilities to reconstruct detached vertices. More work is needed in order to optimize the software tools as well as the alignment of the detector. It is also evident that, in order to measure the b$\overline{\text{b}}$ cross section, it is necessary to use the full J/ψ sample collected with the electron trigger.

4.4 Single High-p_T Lepton Triggers

In addition to trigger commissioning by selecting a data sample where the trigger bias applies only to one of the leptons from a J/ψ decay, the objective of taking data using single high-p_T lepton triggers was to explore the potential of HERA − B to do charm physics on the basis of a heavy flavor enriched data sample, which may even offer an alternative and independent way to measure the beauty production cross section. At a p_T-threshold of 1 GeV/c, data were taken with a single muon trigger either selected by the second level trigger, or by the combined system of first level and second level trigger. At a higher p_T-threshold of 1.5 GeV/c, data were recorded with either a muon or an electron trigger.

A first look at the single muon triggered events showed, that for the same selection cuts as for the analysis of the minimum bias events, there was a 40% increase in the rate of reconstructed K^0_S mesons. Invariant mass peaks from K^0_S and Λ production are shown in Fig. 155. As in the case of the minimum bias analysis, Λ and $\overline{\Lambda}$ hyperons are not distinguished. The number of events in the peaks is 4416 ± 102 for the K^0_S meson and 499 ± 37 for the Λ hyperon. The mass resolutions are 6.4 MeV/c^2 and 2.3 MeV/c^2, respectively.

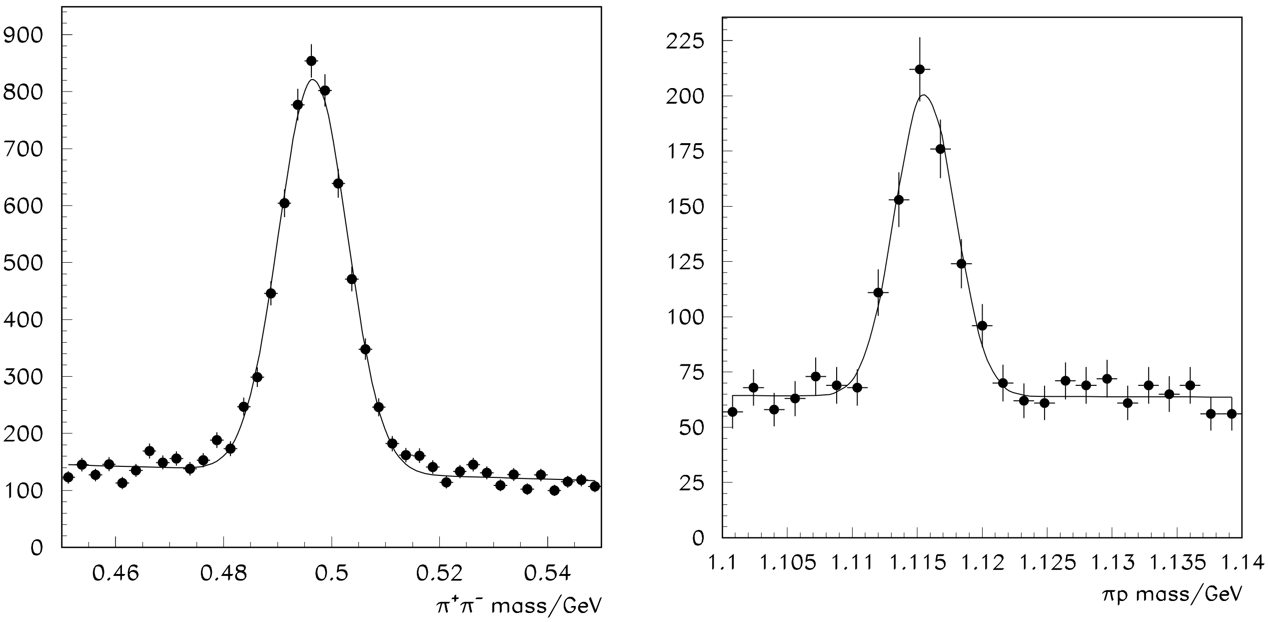

Figure 155: K^0_S *and* Λ *signals seen in events recorded with the single high-*p_T *muon trigger.*

Selecting tracks with hits in the muon system and plotting the mass spectrum of opposite-charge muon pairs, one finds a J/ψ signal on an exponentially falling background. The results are shown in Fig. 156. In the lower plot, the J/ψ mass region is shown in some detail. The signal is clearly visible, amounting to 73 ± 16 events above background.

The fact that the single lepton trigger indeed enriches charm events is demonstrated by an analysis looking for open charm from D^0 and $D^\pm$ decays. In order to select the processes $D^0 \rightarrow \pi^+ K^-$ and $D^\pm \rightarrow K^\mp \pi^\pm \pi^\pm$, a secondary vertex signature was required. In addition, the vector sum of the momenta attached to the secondary vertex was required to point back to the primary vertex. For the mass assignment, the tracks had to be in the respective bands of the so-called $r^2 - p^2$-plot of the RICH particle identification. All mass plots are to be understood to include also the charge conjugated case. The results are shown in Fig. 157. As a cross check, it was verified that the signal is not seen in the Cabibbo suppressed channels. In the ≈2 million events with a hard trigger (single high-p_T particle or high-mass lepton pair required), analyzed so far, a signal is found in all data sets. Although significant signals are observed both for neutral and charged D mesons, one finds a significant mass shift for the D^0 while the $D^\pm$ appears to be unbiased. The reason is currently not understood. A possible explanation could be a bias in the momentum measurement for high-momentum particles, which would affect more the two-body decay of the D^0 than the three-body decay of the $D^\pm$.

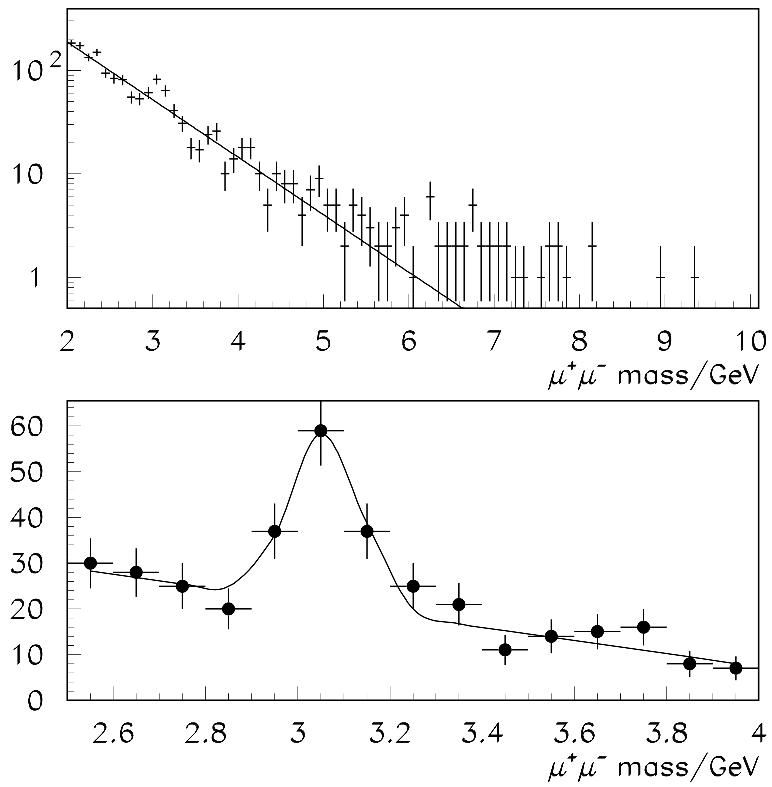

Figure 156: *Invariant $\mu^+\mu^-$ mass spectrum from events with a single high-p_T muon trigger. The upper plot shows the entire spectrum above $2\,\mathrm{GeV}/c^2$, the lower one selects the J/ψ mass region.*

4.5 Summary

The year 2000 physics running was an important step in the commissioning of the detector, the reconstruction and the physics analysis. The minimum bias data were essential for understanding the tracking system and lead to first results on inclusive particle spectra, strangeness production, particle fractions and multiplicities in normal inelastic proton-nucleus collisions for target materials in the range A=12 (carbon) to A=184 (tungsten). In addition, the data were used to develop various methods for luminosity monitoring in HERA – B. Double lepton triggers were used for the commissioning of first and second level triggers, and for a measurement of the J/ψ production cross section. Finally, the single high-p_T lepton trigger was used to collect a heavy flavor enriched data sample which is less biased than the data taken with the double lepton trigger. It will be used to fully develop the tracking, vertexing and particle identification potential of HERA – B by doing heavy flavor physics in the charm and maybe also the bottom sector. First preliminary results have been obtained. The analysis is ongoing.

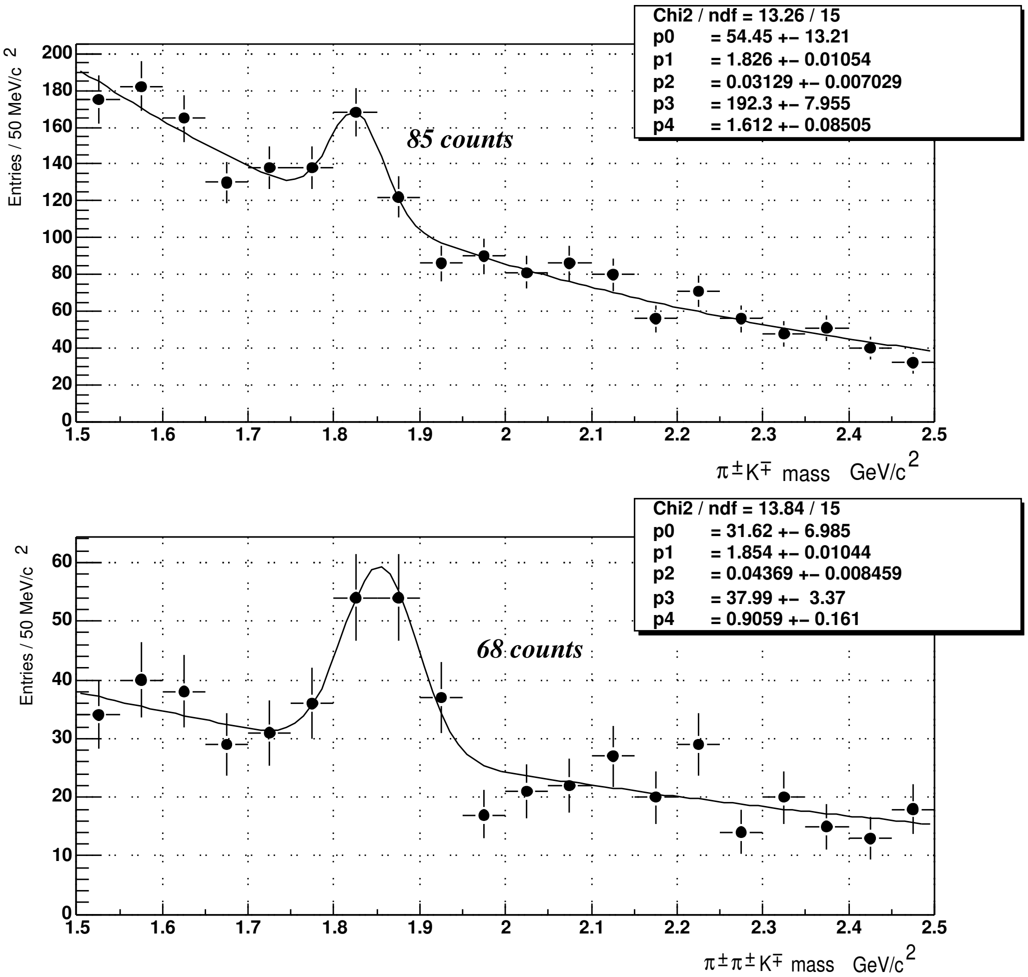

Figure 157: *Invariant mass spectra for* $\pi^+\mathrm{K}^-$ + *c.c. (upper plot) and* $\mathrm{K}^-\pi^+\pi^+$ + *c.c. systems (lower plot).*

5 HERA-B Physics Beyond the Shutdown

The following sections comprise a compilation of contributions each of which evaluates the HERA – B potential to contribute to a particular physics topic. The document and supporting work was, for the most part, done during the technically demanding year 2000 commissioning run, and manpower was therefore severely constrained. Furthermore, in view of the short time available to assemble the report, it was difficult, if not impossible, to shape the individual sections into a coherent whole in terms of assumptions being made, level of detail, and the form in which results are presented. Furthermore, while some of the contributions, in particular those dealing with the measurement of $\sin(2\beta)$, B_s^0 mixing, and the measurement of the FCNC decay $B^0 \to K^{*0}\mu^+\mu^-$ are based on full Monte Carlo detector simulations, most others lack in-depth simulations.

Nevertheless, an attempt has been made, to structure the report in a logical way which is most appropriate for folding in detector performances. The sections are organized in terms of the required trigger capabilities, rather than physics topics. Given uncertainties in the areas of trigger performance, rate capability, reconstruction efficiency, and $b\overline{b}$ cross section, it is impossible to make accurate predictions of the physics potential for the future running of HERA – B. Therefore, in the following sections, we assume the full design trigger capacity as a baseline, from which one can easily down-scale to any arbitrary trigger performance. In addition, the physics potential is discussed for the design interaction rate of 40 MHz, as well as a more conservative rate of 20 MHz, which is nonetheless still an extrapolation from the 5 MHz rate used for most data-taking during the year 2000 run. Also, a rather conservative scenario with 80% track reconstruction efficiency per track is discussed when critical for the physics topic under investigation.

Some of the physics topics have been looked at for the first time, sometimes with the result that HERA – B can not make a significant contribution even at design performance. Such negative results are listed as well for future reference.

The interesting topics in the field of charm physics require a relaxation of trigger thresholds (invariant masses, transverse momenta etc.) and therefore greater demands are placed on the second and higher trigger levels. The feasibility is yet to be evaluated. Most likely a charm physics program can not be carried out in parallel with a B physics program in a transparent way.

For most of the B physics measurements considered here, our most serious potential competition comes from the Tevatron RUN II program, depending on how quickly the Tevatron and the collider experiments reach design performance. Since we are unable to judge this, we offer two evaluations. The first, in Table 45, compares HERA – B's physics reach to existing measurements and extrapolations of existing experiments. The second, in Table 46 assumes that the TEV II experiments quickly reach design performance. Most likely, the situation by mid-2002 will be somewhere in between the scenarios.

In both tables, we indicate competitiveness for a baseline scenario which assumes a 20 MHz interaction rate, a single-track reconstruction efficiency of 80%, full trigger functionality and a $b\overline{b}$ cross section of 12 nb. We also indicate what would happen if the rate of accepted $b\overline{b}$ events falls below the baseline by a factor of 10. Once again, reality will most likely lie between these limits.

From Table 45, it can be seen that, even for relatively modest assumptions on the performance of HERA – B, much of the field of heavy flavor physics is open to us. Even with optimistic assumptions on the capabilities of competing experiments, Table 46 shows that HERA – B can produce competitive or at least interesting and significant results in some areas of heavy flavor physics, but only if the baseline scenario is reached.

For completeness, we note that HERA – B can make significant contributions in the areas of heavy quarkonium production and spectroscopy, and of the physics of soft and hard proton-nucleus interactions even in the most pessimistic scenario.

Table 45: *Summary of requirements and performances of HERA – B for the main physics topics, measured against the presently available experimental results and extrapolations of existing experiments (excluding the TEV II experiments). Needed triggers are indicated by a cross. A double-cross indicates that the trigger must be operated at reduced thresholds (invariant masses, transverse momenta etc.). The assessment of competitiveness is made for a baseline scenario which assumes an interaction rate of* 20 MHz, *a conservative single-track reconstruction efficiency of* 80%, *and the full trigger functionality. A second scenario is included which assumes that the reconstructed* $b\overline{b}$ *rate is 10% of the baseline. The* $b\overline{b}$ *production cross section is assumed to be* 12 nb *per nucleon for the baseline scenario (more precisely, a* $b\overline{b}$ *production rate of* 18 Hz *is assumed), a value which is at the lower end of the range allowed by existing measurements. This cross section could be larger by up to a factor* 5.

	Trigger Requirements				Competition	Potential (% of baseline)	
Topic	μ	e	hpt	FLT		100%	10%
B physics							
$\sigma_{b\overline{b}}$	×	×	–	×	-	***	***
$\sin(2\beta)$	×	×	–	×	e^+e^-,TEV I	*	–
$CP(B_s^0 \to J/\psi\Phi)$	×	×	–	×	LEP,SLC,TEV I	*	–
b lifetimes	×	×	–	×	LEP,SLC,TEV I	***	**
$\Delta\Gamma_s$	×	×	–	×	LEP,SLC,TEV I	***	*
$B_s^0 \to \mu^+\mu^-$	×	–	–	×	CLEO,TEV I	***	**
$B^0 \to K^{*0}\mu^+\mu^-$	×	–	–	×	e^+e^-,TEV I	***	**
$B^0 - \overline{B^0}$ Mixing	×	×	–	×	e^+e^-,TEV I	*	–
$B_s^0 - \overline{B_s^0}$ Mixing	×	×	×	×	LEP,SLC,TEV I	***	–
α, γ	×	×	×	×	e^+e^-	*** (?)	–
rare B → hadrons	×	×	×	×	e^+e^-,TEV I	*** (?)	–
Charm physics							
$D^0 - \overline{D^0}$ Mixing	×	–	–	××	e^+e^-	**	*
$D^0 \to \mu^+\mu^-$	×	–	–	××	E771,e^+e^-	***	**
$D^0 \to e\mu$	×	(×)	–	××	E789,e^+e^-	***	**
QCD physics							
Drell-Yan	×	×	–	×	E866	***	**
Quarkonia	×	×	–	×	E866	***	**
soft pN	–	–	–	–	-	***	***
hard pN	–	×	(×)	(×)	-	***	***

*** Possible to perform the first or best measurement.
** Sensitivity worse than extrapolated values of competition but still interesting.
* Sensitivity comparable to existing measurements attainable.

Table 46: *Assessment of the HERA – B physics potential as in Tab. 45, however measured against the full design performance of present and future competition, including the TEV II program.*

Topic	Trigger Requirements μ	e	hpt	FLT	Competition	Potential (% of baseline) 100%	10%
B physics							
$\sigma_{b\overline{b}}$	×	×	–	×	-	***	***
sin(2β)	×	×	–	×	e^+e^-,TEV II	*	–
CP($B_s^0 \to J/\psi\Phi$)	×	×	–	×	TEVII	*	–
b lifetimes	×	×	–	×	TEVII	**	*
$\Delta\Gamma_s$	×	×	–	×	TEVII	**	–
$B_s^0 \to \mu^+\mu^-$	×	–	–	×	TEVII	**	–
$B^0 \to K^{*0}\mu^+\mu^-$	×	–	–	×	e^+e^-,TEV II	***	–
$B^0 - \overline{B^0}$ Mixing	×	×	–	×	e^+e^-,TEV II	*	–
$B_s^0 - \overline{B_s^0}$ Mixing	×	×	×	×	TEVII	**	–
α, γ	×	×	×	×	e^+e^-,TEV II	** (?)	–
rare B→hadrons	×	×	×	×	e^+e^-,TEV II	** (?)	–
Charm physics							
$D^0 - \overline{D^0}$ Mixing	×	–	–	××	e^+e^-	**	*
$D^0 \to \mu^+\mu^-$	×	–	–	××	E771,e^+e^-	***	**
$D^0 \to e\mu$	×	(×)	–	××	E789,e^+e^-	***	**
QCD physics							
Drell-Yan	×	×	–	×	E866	***	**
Quarkonia	×	×	–	×	E866	***	**
soft pN	–	–	–	–	-	***	***
hard pN	–	×	(×)	(×)	-	***	***

*** Possible to perform the first or best measurement.
** Sensitivity worse than extrapolated values of competition but still interesting.
* Sensitivity comparable to existing measurements attainable.

5.1 Physics of Proton-Nucleus Interactions

The physics of inelastic proton-proton and proton-nucleus interactions at center of mass energies around 40 GeV has been a topic of intense investigations at the CERN-ISR and in the FNAL fixed target program at the Tevatron, the latter just being terminated. Although the physics topics, connected with multi-particle dynamics of soft interactions, the interpretation of hard scattering events in the framework of perturbative QCD, and the study of nuclear effects in soft and hard reactions, are by no means primary goals of the HERA – B experiment, it is clear that large data samples of soft and hard proton-nucleus interactions will be (some already have been) collected by this experiment. Huge statistics in combination with large phase space coverage of high granularity tracking and calorimetry, combined with excellent particle identification capabilities, put HERA – B into a position to significantly expand the research program of the predecessor experiments. The collaboration clearly owes the high energy physics community a proper exploitation of this additional physics potential. This section will highlight some of the relevant physics topics and give rough indications of the possibilities of HERA – B.

5.1.1 Normal Inelastic Proton-Nucleus Interactions

HERA – B has already collected millions of normal inelastic events, so called minimum bias events, albeit with a not fully commissioned detector with somewhat reduced inner acceptance limits around polar angles of $\theta_{min} \approx 15$ mrad, instead of the design value $\theta_{min} \approx 10$ mrad. In the future, with the inner tracker operational[56] and the vertex detector moved into design position, higher quality data will be collected with practically unlimited statistics for target mass numbers $A = 12, 27, 63.5, 183.8$ and large phase space coverage of tracking, calorimetry and particle identification. Two types of triggers are available (and have been successfully tested in spring 2000):

- Zero Bias Trigger: Events are selected randomly in coincidence with a bunch crossing. Such events are constantly taken at a small rate for monitoring purposes and are also collected in intermediate target scans for luminosity calibration. The analysis becomes much easier, however, if data samples are taken at small interaction rates of typically 5 MHz (in order to avoid multiple interactions in one bunch crossing) and for individual target wires. One million triggers can be taken in a ≈ 10 hour run, however, due to the low interaction rate, only part of the triggers (roughly one half for 5 MHz trigger rate) will contain a normal inelastic interaction. The data taking is entirely limited by the event logging bandwidth.

- Minimum Bias Trigger: Events are selected by the second level processor farm by requiring minimal signals above noise thresholds in the detector. Tests in spring 2000 were based on the logical OR of energy clusters in the calorimeter and hits in the RICH detector and have been shown to select practically all inelastic events with particles inside the geometrical acceptance by comparison to the zero bias trigger sample. More sophisticated triggers can be employed in the future if necessary. This trigger scheme allows to reduce the interaction rate to a very small value, like 1 MHz, so that multiple interactions are practically negligible. Therefore, each triggered event contains exactly one interaction, while the data taking speed is the same as for the zero bias trigger since the limiting factor is still the data logging bandwidth.

Relevant physics topics are related to the multi-particle dynamics, and the transition from soft to hard scattering, always in connection with nuclear effects, expressed by nuclear mass number

[56] The trigger functionality of the inner tracker is not required in this context.

dependencies. An important topic in itself is the tuning of physics generators for proton-nucleus interactions which are the basis of background simulations for any of the physics processes of primary interest at HERA – B.

The physics handles for resolving the dynamics of proton-nucleus scattering can be roughly divided into three categories:

1. Inclusive single particle spectra.
2. Two (and more) particle correlations in phase space, both of short range and of long range character.
3. Charged multiplicity distributions, multiplicity distributions in transverse momentum and/or rapidity bins and forward/backward multiplicity correlations.

In the following, some comments are made on the available information and the extent to which HERA – B can further contribute to the field.

Inclusive Single Particle Spectra

The most complete measurement of inclusive charged particle spectra for the special case of proton-proton interactions at HERA – B cms energies has been performed by the SFM experiment at the CERN-ISR and can be found in [131]. The measurements cover almost the full phase space and extend into the region of large transverse momentum where hard parton-parton scattering starts to dominate. The spectra were measured separately for positive and negative particles, but no particle identification was available[57].

Averaging over the azimuthal angle ϕ (with respect to the event axis), the single particle kinematics can be described by two independent variables, the transverse momentum, p_T, and a longitudinal variable measured in the proton-nucleus center of mass system, the two popular choices for which are the rapidity

$$y = \frac{1}{2}\ln\left(\frac{E+p_L}{E-p_L}\right) = \ln\left(\frac{E+p_L}{m_T}\right)$$

and the Feynman-x variable

$$x_F = \frac{p_L}{p_{L,\max}} \approx \frac{2p_L}{\sqrt{s}} = \frac{2m_T}{\sqrt{s}}\sinh y \quad ,$$

where

$$\begin{aligned} m_T &= \sqrt{m^2+p_T^2} \\ E &= m_T\cosh y \\ p_L &= m_T\sinh y \end{aligned}$$

are the transverse mass of the particle (of mass m), the particle energy in the cms, and the longitudinal particle momentum in the cms, respectively. The center of mass energy is related to the proton beam energy E_b via

$$\sqrt{s} \approx \sqrt{2m_{\mathrm{p}}E_b} \quad ,$$

[57] The experiment was equipped with threshold cherenkov counters covering selected small phase space regions. These were used for particle identification in special trigger regions for high-p_T physics and charm physics.

with m_p being the proton mass. For the HERA beam energy of $E_b = 920\,\mathrm{GeV}$ one finds $\sqrt{s} = 41.6\,\mathrm{GeV}$. The rapidity y_lab in the lab system (rest system of the target) is connected to the cms rapidity y via a constant shift,

$$y_\mathrm{lab} = y + \ln\left(\frac{\sqrt{s}}{m_\mathrm{p}}\right) \quad ,$$

hence differential rapidities $\mathrm{d}y$ are Lorentz invariant. Because of the large forward boost in the lab system, particle masses can often be neglected with respect to the longitudinal momenta, in which case the rapidity y_lab can be approximated by the pseudo-rapidity

$$\eta = -\ln\tan(\theta/2) \quad ,$$

a quantity directly connected to the polar angle θ as measured by the detector.

The dynamics of single particle production is quantified by the Lorentz invariant differential cross section

$$E\frac{\mathrm{d}^3\sigma}{\mathrm{d}p^3} = 2\frac{\mathrm{d}^3\sigma}{\mathrm{d}\phi\,\mathrm{d}y\,\mathrm{d}p_T^2} = \frac{1}{p_T}\frac{\mathrm{d}^3\sigma}{\mathrm{d}\phi\,\mathrm{d}y\,\mathrm{d}p_T} \quad ,$$

or, if averaged over the azimuthal angle ϕ (which the cross section does not depend on),

$$E\frac{\mathrm{d}^3\sigma}{\mathrm{d}p^3} = \left\langle E\frac{\mathrm{d}^3\sigma}{\mathrm{d}p^3}\right\rangle_\phi = \frac{1}{\pi}\frac{\mathrm{d}^2\sigma}{\mathrm{d}y\,\mathrm{d}p_T^2} = \frac{1}{2\pi}\frac{1}{p_T}\frac{\mathrm{d}^2\sigma}{\mathrm{d}y\,\mathrm{d}p_T} \quad .$$

The parameterization of the inclusive cross section from reference [131] was used to estimate the number of particles per phase space bin in case of HERA – B, assuming a total of one million inelastic interactions taken with a titanium target. The total inelastic cross section for proton-proton interactions,

$$\sigma_\mathrm{pp}|_{\sqrt{s}=41.6\,\mathrm{GeV}} \approx 30\,\mathrm{mb}$$

was scaled to the total inelastic cross section for proton-nucleus interactions using the approximate parameterization [26]

$$\sigma(A) \approx \sigma_\mathrm{pp} \cdot A^{2/3} \cdot (1.3 + 0.15\log_{10} A)$$

for the dependence on the nuclear mass number A of the target (valid for $A > 6$). Similarly the inclusive cross section can be parameterized to scale like A^α, where the exponent α is a function of p_T. At $p_T < 1.5\,\mathrm{GeV/c}$, the exponent α is smaller than one due to re-absorption of hadrons produced within the nucleus. At $p_T > 1.5\,\mathrm{GeV/c}$, the exponent α becomes slightly larger than one due to multiple parton scattering inside the nucleus (the so-called Cronin effect [132, 133]). Data for a wide range of target materials and transverse momenta or transverse energies are available from the FNAL fixed target program [134, 136, 137, 138, 139, 140]. A simple dependence

$$\alpha(p_T) \approx 1.2 \cdot \left[1 - 0.533\exp\left(-0.74\frac{p_T}{\mathrm{GeV/c}}\right)\right]$$

was extracted from the measurements in reference [137]. The number of tracks ΔN in any given phase space interval for a total of N_inel inelastic events are then estimated by

$$\Delta N = 2\pi N_\mathrm{inel}\int\mathrm{d}y\int\mathrm{d}p_T\,p_T\left(E\frac{\mathrm{d}^3\sigma}{\mathrm{d}p^3}\right)\Bigg|_{y,p_T}\frac{A^{\alpha(p_T)}}{\sigma(A)} \quad .$$

The resulting x_F and y distributions are presented in Figs. 158, 159 in intervals of transverse momentum. The distributions are separated for positive and negative particles. Note that both the charge ratios and the forward/backward symmetry of the distributions will be somewhat altered compared to the simple scaling from proton-proton distributions (especially in the backwards hemisphere) due to the fact that the target is a nucleus containing both protons and neutrons, but no data are available to take these effects properly into account. Also, the particle composition of the spectra is not well known for small and medium transverse momenta, except in limited regions of polar angles [135, 136]. The figures should hence be regarded as a rough guideline as to what kind

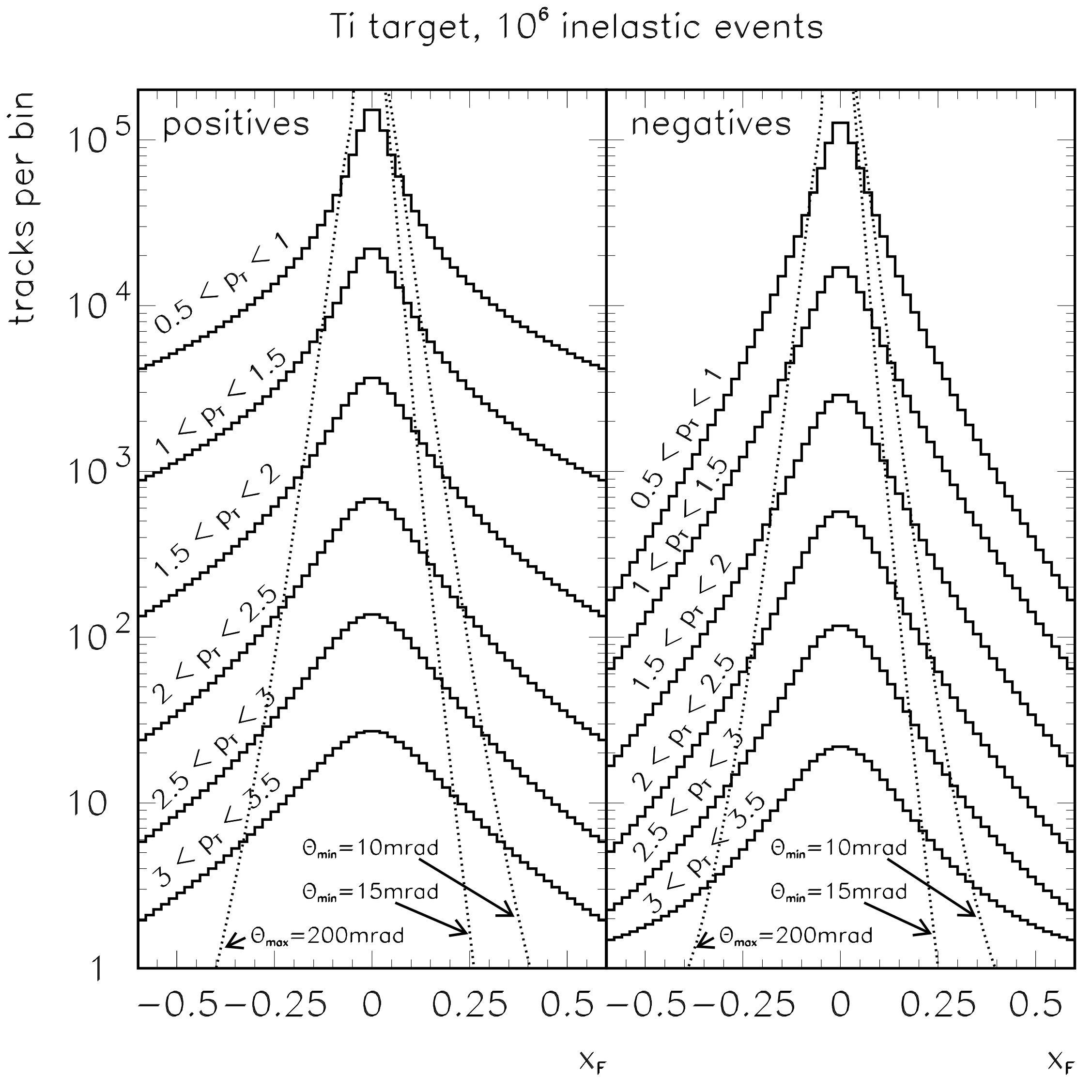

Figure 158: *Expected Feynman-x distributions for transverse momentum bins assuming* 10^6 *inelastic events on a titanium target. The distributions are plotted for positive and negative particles separately. Also shown are lines of constant polar angle in the* HERA – B *system.*

of statistics can be achieved.

Also shown in Figs. 158, 159 are lines of constant polar angles θ, indicating the typical outer acceptance of the HERA – B spectrometer around $\theta_{\max} = 200\,\mathrm{mrad}$, the design inner acceptance limit at $\theta_{\min} = 10\,\mathrm{mrad}$ and a more conservative inner acceptance limit for incomplete inner tracking

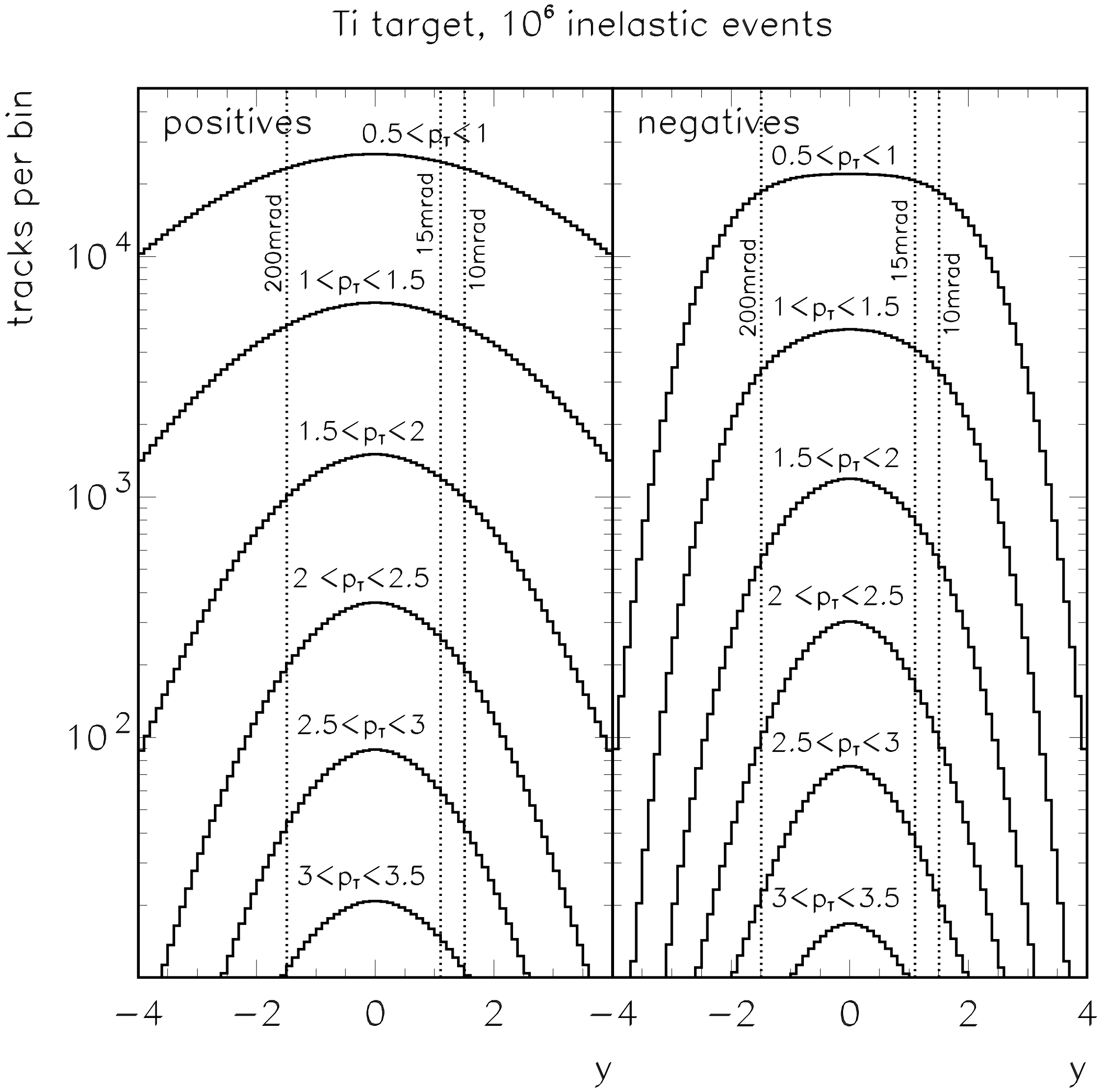

Figure 159: *Expected cms-rapidity distributions for transverse momentum bins assuming* 10^6 *inelastic events on a titanium target. The distributions are plotted for positive and negative particles separately. Also shown are lines of constant polar angle in the* HERA – B *system.*

at $\theta_{\min} = 15\,\mathrm{mrad}$. For massless particles these limits correspond to 91% (resp. 79%) of the full solid angle in the cms. As can be seen, the spectrometer covers a wide range of the longitudinal phase space both in the forward and in the backward cms hemisphere. HERA – B will therefore allow very detailed measurements of identified inclusive particle spectra and their nuclear dependencies in the central production region and also to extend these measurements far into the hard scattering regime $p_T > 2\,\mathrm{GeV/c}$, where single hard parton-parton scattering is the dominating mechanism. Due to the limited outer acceptance and absence of very forward detectors, HERA – B will, however, not contribute to the analysis of the extreme forward/backward regions and leading particle effects.

Particle Correlations

An important tool for the study of details of the particle production mechanisms in inelastic hadron hadron collisions is the analysis of particle correlations in their kinematical variables (transverse momentum, rapidity, azimuthal angle), and their quantum numbers (charge, strangeness, baryon-number). The observations can be used to disentangle cluster models for hadronic production which are characterized by their predicted short range and long range correlations. This topic has received great attention in the analysis of non diffractive proton-proton and light ion collisions at the CERN-ISR, e.g. through the analysis of two particle [156, 157], three particle [158], and many particle [159] correlations. HERA − B offers the opportunity to extend these measurements for short and medium correlation ranges in rapidity to the case of proton-nucleus collisions and to analyze for the first time strangeness and baryon number correlations which have not been accessible at the ISR experiments due to insufficient particle identification capabilities.

Correlations between very forward/backward particles have also been investigated at the ISR by means of special forward detectors, even including particle identification [160, 161]. This kinematical regime is not accessible for HERA − B because of the limitations in forward and backward acceptance as visible in Fig. 159.

Multi-Particle Dynamics

A large variety of methods have been employed to understand the multi-particle dynamics in hadronic interactions at HERA − B energies. Most information is available for proton-proton interactions at the ISR. Given the enormous statistics estimated above, HERA − B can extend these measurements for the case of proton-nucleus interactions. In addition, production mechanisms can be differentiated between pions, strange particles and baryons using the particle identification capabilities. Some important observables are listed for illustration.

- The charged multiplicity distribution and its moments for the full phase space [141, 142] or individual rapidity bins [143] can be exploited to analyze the correlation between particles due to the production mechanism.

- The average transverse momentum in the central rapidity range has been observed to increase with the central multiplicity in proton-proton [144] and in proton-anti-proton collisions as well as light ion collisions [145] and in proton-nucleus collisions [137]. Besides constraining the model space, these measurements are particularly interesting when interpreted in the framework of thermo-dynamical models [146, 147], in which the average p_T is a measure of the temperature and the central multiplicity is a measure of the entropy of the hadronic source, the size of which can be obtained from Bose-Einstein correlations [148, 149, 150, 144]. Correlations between these thermo-dynamical quantities are important for the understanding of phase transitions to a quark-gluon plasma.

- Significant non-statistical event by event fluctuations in the average transverse momentum have been observed in proton-proton and light ion collisions [151] and for proton-nucleus interactions [137]. In thermo-dynamical models, these observations measure temperature fluctuations in hadronic collisions, caused by a combination of dynamical effects in the interaction and statistical fluctuations due to the finite number of particles in the final state [152, 153].

5.1.2 High p_T Physics and QCD Tests

Already the minimum bias data samples discussed in section 5.1.1 extend well into the region of hard parton scattering which starts to dominate the steeply falling cross section for soft interactions at $p_T \approx 2\,\mathrm{GeV/c}$ [135, 154, 155], and thus allow the analysis of the transition from soft to hard scattering, an important physics topic in itself. In this section the region of very hard scattering, triggered by single high p_T particles or alternatively by high p_T high mass particle pairs, will be discussed. The interactions are describable by the scattering of asymptotically free partons (quarks, gluons and tightly bound di-quarks) which can be rigorously computed in the framework of perturbative QCD.

Again, such measurements are not new and have received much attention by the ISR experiments and by the fixed target program at FNAL. High p_T single particle production has also advanced to an important physics topics for the case of photon-proton scattering at HERA. As will be shown below, HERA – B will nevertheless have the possibility to extend the level of detail of these measurements in a way that a new quality of QCD tests seems reachable. This is due to a combination of the extremely high statistics, the large phase space coverage and, most importantly, the fact that pion, kaon, proton and anti-proton identification is available in the full phase space. Nuclear effects, on the other hand, don't play the important role as in minimum bias events although they are still visible as a small nuclear enhancement of the inclusive cross sections per nucleon with increasing nuclear mass number A (the so-called Cronin effect [132, 133]). This can be interpreted by multiple parton scattering in the nuclear environment. HERA – B will be able to extend these measurements. One point of interest is the study of resonance production and decay inside nuclear matter. The underlying physics is discussed in some detail in section 5.2.2. Nuclear effects will therefore not be further discussed here.

Theoretical Framework

A schematic (simplified) representation of the hard proton-nucleon scattering is shown in Fig. 160 for the example of single high p_T hadron production. Two quasi-free partons (quarks or gluons), carrying momentum fractions according to their Bjorken-x values x_1, x_2, distributed according to appropriate structure functions G, undergo a hard parton-parton scattering, describable by a perturbative QCD matrix element, leading to a differential cross section $\mathrm{d}\sigma/\mathrm{d}\hat{t}$. Two high p_T partons emerge back-to-back in azimuthal angle and hadronize into two jets of large transverse momenta. The remnants of the incoming nucleons don't participate in the hard scattering and hadronize into two spectator jets of small p_T in forward/backward directions. Such four-jet topologies have been clearly confirmed at the ISR [162]. The fractional momentum densities of hadrons in the final state jets are described by appropriate fragmentation functions D. In the special case of a single high p_T particle trigger, realizable at HERA – B on the basis of the ECAL pretrigger or the high-p_T pretrigger, one of the high p_T jets, called the towards jet (or trigger jet) contains a leading hadron (the trigger particle) which carries a large fraction ($\approx 50\%$ to almost 100% depending on p_T) of the total jet momentum. The recoiling parton hadronizes in an unbiased fashion into the recoiling jet, called the away jet. Similarly, double high p_T triggers can be used to select special events in which both the towards and the away jets contain a leading particle. Such configurations give direct access to the parton-parton kinematics since the fragmentation effects become very small and are easily correctable [163].

The case of direct photon production can also be visualized by Fig. 160 if the complete towards jet is simply replaced by a single photon of large transverse momentum. In this case, the incoming partons are always one quark and one gluon (neglecting the small contribution of antiquarks in the nucleons).

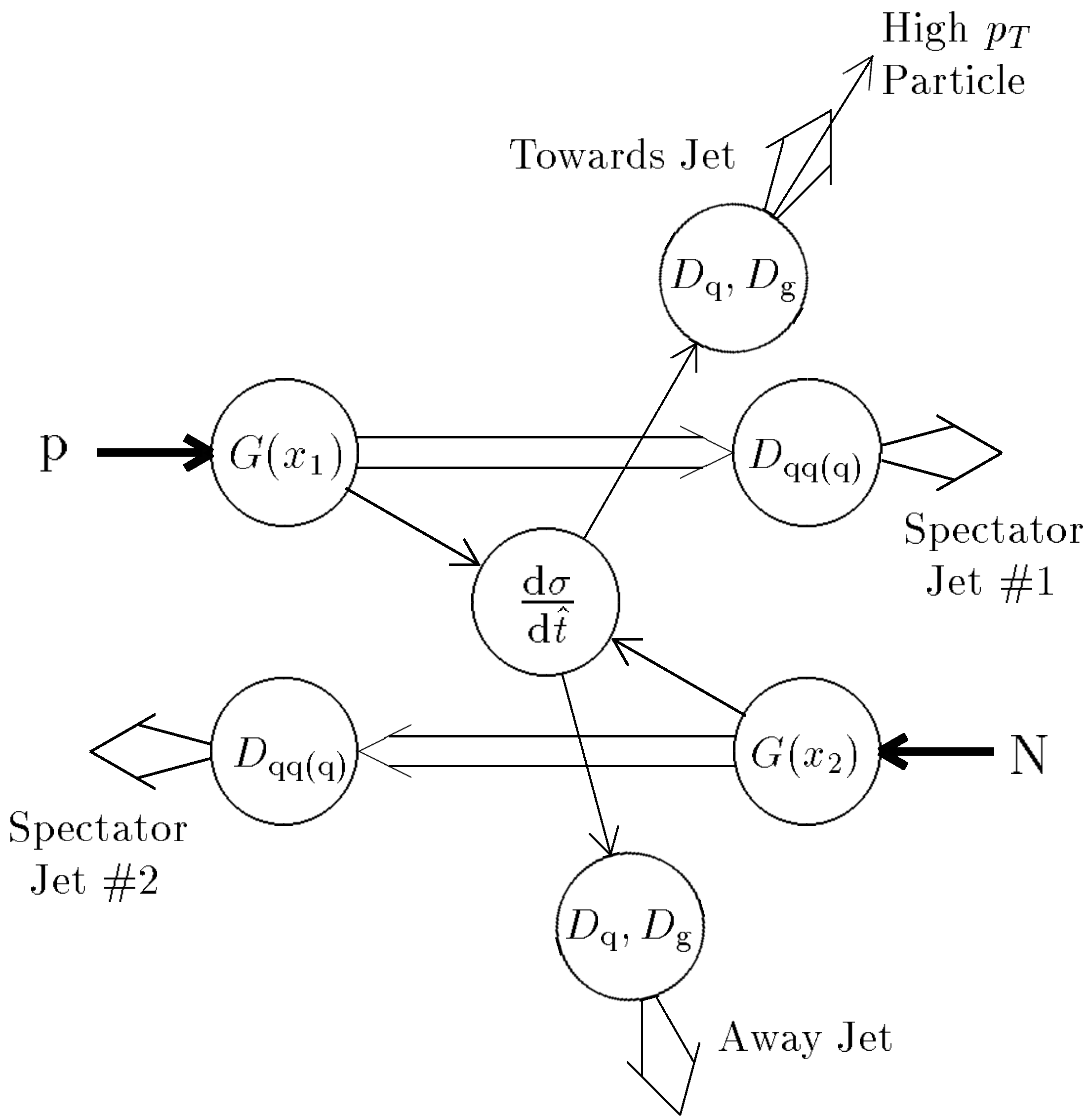

Figure 160: *Schematic representation of parton-parton scattering in hard proton-nucleon (*pN*) interactions. The structure functions of the colliding nucleons, the short distance parton scattering cross section and the fragmentation functions of the scattered high p_T partons and the two spectator systems are indicated by circles. In the case of direct photon production, the figure still holds with the towards parton and towards jet replaced by a single high p_T photon.*

Neglecting the antiquarks in the incoming nucleons, high p_T hadron production is mediated by the parton-parton scattering processes

$$\begin{aligned} \mathrm{q}_1 + \mathrm{q}_2 &\rightarrow \mathrm{q}_1 + \mathrm{q}_2 \\ \mathrm{q} + \mathrm{g} &\rightarrow \mathrm{q} + \mathrm{g} \\ \mathrm{g} + \mathrm{g} &\rightarrow \mathrm{g} + \mathrm{g} \\ \mathrm{g} + \mathrm{g} &\rightarrow \mathrm{q} + \overline{\mathrm{q}} \quad , \end{aligned}$$

where the individual subprocesses can be strongly enriched by the requirement of identified high

p_T hadrons of appropriate valence quark content in the final state. For the case of single direct photon production the only leading subprocess which does not involve antiquarks from the incoming nucleons is

$$\mathrm{q} + \mathrm{g} \;\rightarrow\; \mathrm{q} + \gamma \quad .$$

Therefore, direct photon production is not only a clean testing ground for perturbative QCD [164] but is also a powerful tool for the measurement of the gluon structure function at large values of Bjorken-x [165].

The kinematics of the scattering process can be described by the following variables:

$x_{1,2}$	Bjorken-x of incoming partons
$\vec{k}_{T\,1,2}$	transverse momenta of incoming partons
$\theta^\star$	scattering angle in the parton-parton cms
$z_{1,2}$	fractional momenta of leading hadrons in towards and away jet
$\vec{q}_{T\,1,2}$	transverse momenta of leading hadrons in towards and away jet

Neglecting the transverse momenta $k_{T\,1,2}$, the squared parton-parton cms energy $\hat{s}$ is connected to the squared proton-nucleon cms energy via

$$\hat{s} \;=\; x_1\, x_2\, s \quad .$$

The kinematics can also be expressed in terms of the rapidities $\hat{y}_{1,2}$ of the towards and away parton and their (identical) transverse momenta $\hat{p}_T$ in the lab system, i.e. quantities which are directly accessible from measurement,

$$\begin{aligned}
\hat{y}_1 + \hat{y}_2 &= \ln\left(\frac{x_1}{x_2}\right) \\
\hat{y}_1 - \hat{y}_2 &= 2\,\ln\tan\left(\frac{\theta^\star}{2}\right) \\
\hat{p}_T &= \frac{\sqrt{\hat{s}}}{2}\,\sin\theta^\star \quad .
\end{aligned}$$

The parton kinematics can be inferred from measured quantities using the reverse transformations

$$\begin{aligned}
x_{1,2} &= \frac{\hat{p}_T}{\sqrt{s}}\left(e^{\pm\hat{y}_1} + e^{\pm\hat{y}_2}\right) \;=\; \sqrt{\frac{\hat{s}}{s}}\,\exp\left(\pm\frac{\hat{y}_1+\hat{y}_2}{2}\right) \\
\sqrt{\hat{s}} &= \frac{2\hat{p}_T}{\sin\theta^\star} \;=\; 2\hat{p}_T\cosh\left(\frac{\hat{y}_1-\hat{y}_2}{2}\right) \\
\tan\left(\frac{\theta^\star}{2}\right) &= \exp\left(\frac{\hat{y}_1-\hat{y}_2}{2}\right) \quad .
\end{aligned}$$

The parton-parton scattering amplitudes contain mixtures of $\hat{s}$, $\hat{t}$, and $\hat{u}$ channel diagrams where $\hat{s}$, $\hat{t}$, and $\hat{u}$ denote the Mandelstam variables on the parton level,

$$\begin{aligned}
\hat{t} &= -\hat{s}\,\sin^2\left(\frac{\theta^\star}{2}\right) \;=\; -\hat{p}_T^2\,\left(1 + \exp\left(\hat{y}_2 - \hat{y}_1\right)\right) \\
\hat{u} &= -\hat{s}\,\cos^2\left(\frac{\theta^\star}{2}\right) \;=\; -\hat{p}_T^2\,\left(1 + \exp\left(\hat{y}_1 - \hat{y}_2\right)\right) \\
\hat{s} &= -\hat{t} - \hat{u} \quad ,
\end{aligned}$$

so that the momentum transfer squared, Q^2, which the structure functions, fragmentation functions and coupling constants depend on logarithmically, can only be defined in an effective way, the most popular choice [166] being

$$Q^2 \;=\; \frac{2\,\hat{s}\,\hat{t}\,\hat{u}}{\hat{s}^2\,+\,\hat{t}^2\,+\,\hat{u}^2} \quad .$$

The inclusive invariant cross section can be expressed by a convolution of the structure functions, the hard scattering cross section, and the inclusive fragmentation functions (as indicated in Fig. 160). For example, in the case of inclusive single high p_T hadron production, the differential cross section reads

$$\begin{aligned} \mathrm{d}\sigma^{\mathrm{AB}\to\mathrm{CX}} \;=\; & \sum_{\mathrm{ab}\to\mathrm{cd}} \frac{\mathrm{d}x_\mathrm{a}}{x_\mathrm{a}}\,\frac{\mathrm{d}x_\mathrm{b}}{x_\mathrm{b}}\,\mathrm{d}^2k_{T\,\mathrm{a}}\,\mathrm{d}^2k_{T\,\mathrm{b}}\,\mathrm{d}\hat{t}\,\frac{\mathrm{d}z_\mathrm{C}}{z_\mathrm{C}}\,\mathrm{d}^2q_{T\,\mathrm{C}} \\ & G_{\mathrm{A}\to\mathrm{a}}(x_\mathrm{a},\vec{k}_{T\,\mathrm{a}},Q^2)\,G_{\mathrm{B}\to\mathrm{b}}(x_\mathrm{b},\vec{k}_{T\,\mathrm{b}},Q^2)\,\frac{\mathrm{d}\sigma^{\mathrm{ab}\to\mathrm{cd}}}{\mathrm{d}\hat{t}}\,D_{\mathrm{c}\to\mathrm{C}}(z_\mathrm{C},\vec{q}_{T\,\mathrm{C}},Q^2) \quad . \end{aligned}$$

The central hard parton scattering process can be described in the framework of perturbative QCD. Calculations are available on leading order [167, 168, 169] and (at least partly) on next-to-leading order [170, 171, 172]. It is now a well established fact that these QCD prediction have severe shortcomings in explaining high p_T cross sections without the ad hoc assumption of very large primordial transverse momenta k_T of the partons emerging from the incoming hadrons and undergoing the hard scattering, much larger than the expectation of $\approx$250 MeV/c from the Fermi motion of partons within the nucleon, the latter indeed manifested by the transverse momentum spectra of hadrons from soft inelastic interactions. The average values of k_T have been found to be of order 1 GeV/c from single high p_T charged hadron production at the ISR [173, 174], from high p_T single and double π^0 and direct photon production at FNAL [175] and from the di-photon data of WA70 [176] at CERN. The large value of k_T has been successfully explained by the SFM experiment at the ISR on the basis of a parton shower model [177], combined with the leading order QCD amplitudes. Similarly, the WA70 direct di-photon data have been explained by re-summation of soft-gluon emission [178]. Despite these partial successes, the understanding of hard scattering processes in hadronic interaction remains an active field of theoretical research.

Single-Particle Inclusive Cross Sections

In this section, only channels based on ECAL pretrigger signals are discussed. The possibilities of HERA – B will be significantly enhanced as soon as also the high-p_T pretrigger system can be used to select events with a single high p_T charged hadron or a high mass pair of charged high p_T hadrons which are produced almost back to back in azimuthal angle.

The simplest high p_T trigger is based on a single high E_T cluster in the electro-magnetic calorimeter, leading to a pretrigger signal, possibly cleaned on the higher trigger levels to enrich single high p_T photons.[58] The main sources for such events are:

- High p_T π^0 production via hard quark-quark, quark-gluon and gluon-gluon scattering with one of the scattered high p_T partons producing a leading π^0 in an early stage of fragmentation.

- Direct photon production via a hard quark-gluon scattering $\mathrm{qg} \to \mathrm{q}\gamma$.

[58] Preliminary data samples have already been recorded in short periods during the year 2000 running and are currently being analyzed.

The second process is suppressed for not too large transverse momenta because of the electromagnetic coupling in the scattering process. At very large transverse momenta, the direct photon process is, however, dominating because π^0 production is then strongly disfavored by the steeply falling fragmentation function.

In order to estimate the rates to be expected at HERA – B, recent high precision cross section measurements [175] of the FNAL experiment E706 were used. The experiment measured direct photon and π^0 production in proton-beryllium interactions at a proton beam energy of 800 GeV for the central rapidity range $-1.0 < y < 0.5$ and for transverse momenta ranging from 3 GeV/c up to ≈ 10 GeV/c. The invariant cross sections per nucleon can be described analytically by the empirical parameterization

$$\begin{aligned}\left(E\,\frac{\mathrm{d}^3\sigma}{\mathrm{d}p^3}\right)_{\pi^\circ;\mathrm{E706}} &= \exp\left(14.87 - 3.16p_T\right) + \exp\left(9.09 - 1.94p_T\right)\\ \left(E\,\frac{\mathrm{d}^3\sigma}{\mathrm{d}p^3}\right)_{\gamma;\mathrm{E706}} &= \exp\left(10.32 - 2.60p_T\right) + \exp\left(4.31 - 1.43p_T\right) \quad ,\end{aligned}$$

where p_T is measured in GeV/c and the invariant cross section is measured in nb/(GeV/c)^2. Note the flat p_T dependence, especially for the direct photon spectrum, compared to normal inelastic events which lead to inclusive cross sections falling like $\exp(-6\,p_T)$. These analytical expressions can be converted into a π^0 or γ differential production rate $\mathrm{d}\dot{N}_{\pi^\circ,\gamma}/\mathrm{d}p_T$ for HERA – B , computed for the central rapidity range $-1 < y < 1$ of width $\Delta y = 2$ and normalized to the total target rate $\dot{N}_{\mathrm{targ}}$,

$$\frac{1}{\dot{N}_{\mathrm{targ}}}\,\frac{\mathrm{d}\dot{N}_{\pi^\circ,\gamma}}{\mathrm{d}p_T} = 2\pi\,p_T\,\Delta y\,\frac{C(A)}{\sigma(A)}\left(E\,\frac{\mathrm{d}^3\sigma}{\mathrm{d}p^3}\right)_{\pi^\circ,\gamma;\mathrm{E706}}$$

where $\sigma(A)$ is the total inelastic cross section (see section 5.1.1) and where

$$C(A) = 9\cdot\left(\frac{A}{9}\right)^{\alpha_{\pi^\circ,\gamma}}$$

with

$$\alpha_{\pi^\circ} = 1.08 \qquad\qquad \alpha_\gamma = 1.04$$

extrapolates the E706 cross section to any target mass number A using the measured Cronin effect in this p_T range. The (small) corrections for the higher beam energy at HERA – B and the applied simple linear scaling of the average E706 cross section at central rapidity to the full $\Delta y = 2$ range are neglected since they tend to cancel.

The result of this calculation is displayed in Fig. 161a. As can be seen, already for small target rates of 1 MHz, high p_T π^0 mesons and direct photons are produced at very large rates, even when counted for small p_T bins of 200 MeV/c width. In order to understand the implications for the HERA – B trigger, the π^0 rate has been converted into a photon rate from the $\pi^0 \to \gamma\gamma$ decay using the convolution

$$\frac{\mathrm{d}\dot{N}_{\pi^\circ\to\gamma}}{\mathrm{d}p_T} \approx 2\int_{p_T}^{\infty}\mathrm{d}q_T\int_0^1\mathrm{d}x\,\frac{\mathrm{d}\dot{N}_{\pi^\circ}}{\mathrm{d}q_T}\,\delta\left(p_T - xq_T\right) = \int_{p_T}^{\infty}\mathrm{d}q_T\,\frac{2}{q_T}\,\frac{\mathrm{d}\dot{N}_{\pi^\circ}}{\mathrm{d}q_T} \quad .$$

The resulting total rate of photons (direct or from π^0 decays) is plotted in Fig. 162a for p_T bins of 200 MeV/c width and normalized to the target rate. The corresponding trigger rate (normalized to the target rate) is shown in Fig. 162b as function of the p_T cut applied in the ECAL pretrigger. As can be seen, a p_T cut at 4 GeV/c produces a trigger rate of about 10 Hz per MHz of target rate.

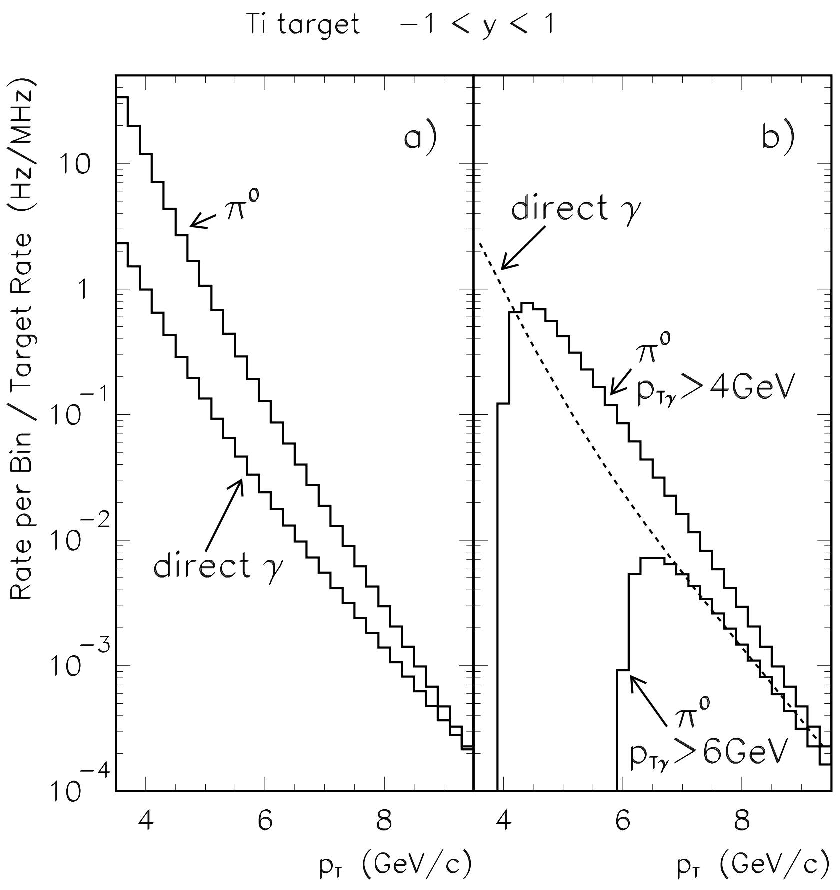

Figure 161: *Expected high p_T production rates (in* Hz*) per target rate (in* MHz*) for π^0 mesons and direct photons in the central rapidity range $-1 < y < +1$ for individual p_T bins of size* 0.2 GeV/c. *a) Total production rate. b) Accepted π^0 rate for single photon trigger cuts at $p_{T\gamma} > 4$* GeV/c *and $p_{T\gamma} > 6$* GeV/c *(with the total direct photon rate shown for comparison).*

Therefore, the full data logging bandwidth can be exploited at small target rates of a few MHz, so that enormous data samples (of the order of 1 million events) can be taken during short dedicated high p_T trigger runs, exactly like in the case of the minimum bias trigger. Again, due to the small target rates, multiple interactions are rare, a fact which facilitates the analysis of the underlying event. At a larger trigger threshold of 6 GeV/c, the trigger rate drops to about 0.1 Hz per MHz of target rate, so that the high p_T trigger can be added as a low rate background trigger during the mainstream heavy flavor data taking program at larger target rates. Again, huge data samples at highest p_T will be collected in a few weeks of running.

The effect of the trigger cuts on the π^0 sample can be judged from Fig. 161b, which displays the fraction of the π^0 mesons of Fig. 161a leading to a single photon above trigger threshold. As can be seen, the π^0 sample still dominates the direct photon sample by roughly a factor of two for a p_T threshold at 4 GeV/c, while the two samples are comparable for a threshold at 6 GeV/c.

In principle, HERA − B can easily incorporate double high p_T triggers for special studies of the parton-parton kinematics and measurements of structure functions. However, since the single high p_T statistics will be very large, the design of a special trigger is probably not necessary since each

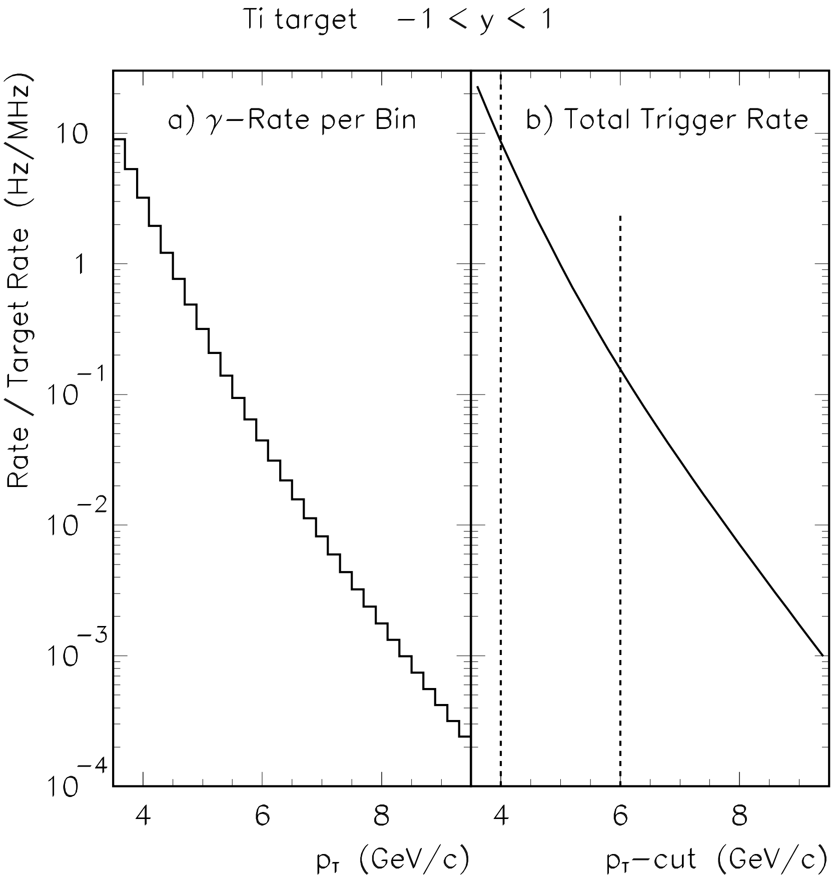

Figure 162: *Expected high p_T production rates (in Hz) per target rate (in* MHz*) for photons, either from π^0 decays or directly produced, in the central rapidity range $-1 < y < +1$. a) Rate for individual p_T bins of* 0.2 GeV/c *width. b) Total rate as function of the p_T threshold of the ECAL pretrigger.*

high p_T event contains a recoil jet at large transverse momentum which produces a second high p_T particle in a substantial number of cases (typically in about 10% of the events [179]). Double high p_T samples of sufficient statistics can therefore be obtained offline from the complete sample.

In addition to the directly triggered single particle high p_T sample, HERA – B will collect a large sample of Drell-Yan pairs at large transverse momenta through the standard high mass dilepton trigger. As shown in reference [180], the treatment of this process is analogous to the treatment of direct photon production, with the direct photon replaced by a virtual photon with virtuality given by the dilepton pair mass. This process offers a sensitive QCD test, combined with a measurement of the gluon structure function at large Bjorken-x. At the same time, the experimental uncertainties connected to the direct photon selection are removed, as well as theoretical uncertainties in the cross section calculation. Moreover, the sensitivity to the parton k_T is largely eliminated.

Particle Fractions at High p_T

The cross section measurement itself tests the QCD prediction on the basis of the sum of all partonic contributions. Important additional tests are possible, if the different types of high p_T hadrons are separated. It is well known, at least for certain kinematical regions, that the valence quark content of the high p_T hadron strongly enriches the type of parton from which it is originating [181, 182, 183]. The following tagging types exist:

$$
\begin{array}{rrcl}
\pi^+ & (\mathrm{u\overline{d}}) & \longrightarrow & \text{up quark} \\
\pi^- & (\mathrm{d\overline{u}}) & \longrightarrow & \text{down quark} \\
\mathrm{K}^+ & (\mathrm{u\overline{s}}) & \longrightarrow & \text{up quark} \\
\mathrm{K}^- & (\mathrm{s\overline{u}}) & \longrightarrow & \text{gluon} \\
\mathrm{p} & (\mathrm{uud}) & \longrightarrow & \text{di-quark} \\
\bar{\mathrm{p}} & (\mathrm{\overline{u}\overline{u}\overline{d}}) & \longrightarrow & \text{gluon}
\end{array}
$$

One of the simplest and most direct observables to disentangle the parton level contributions is hence the ratio of inclusive cross sections for identified high p_T hadrons as function of p_T and y. Examples for such measurements in part of the phase space can be found in [184, 185, 186].

Baryon Production at High p_T

The particle ratios measured at the ISR and at FNAL revealed the possible existence of a tightly bound di-quark inside the proton, contributing strongly to the high p_T baryon production [185, 186]. Although being reproducible by QCD models when including di-quark form factors [187, 188], the di-quark scattering hypothesis has never been generally accepted. More insight can only be gained by the analysis of the complete event structure, especially the quantum number correlations within the high p_T jets and between the high p_T jets and the spectator jets, as well as the high p_T baryon resonance production. All existing results [183, 189] confirm the di-quark hypothesis but suffer either from missing particle identification or small phase space coverage. HERA – B is in an excellent situation to solve this puzzle.

Resonances as Leading Fragments in Jets

Important information about the hadronization mechanisms can be gained by measuring the fraction of resonances at large p_T. This answers the question to which extent the leading fragments in a jet are directly produced from the fragmenting parton (see e.g. reference [190]). Again, HERA – B can make significant contributions because of its particle identification capabilities in the full phase space.

Overall Event Structure

The overall event structure, especially charge and flavor correlations within jets and between the jets, allows the study of fragmentation phenomena and color flow in the hard scattering events [191, 192]. HERA – B will be able to extend the existing knowledge in the field of flavor correlations using particle identification.

Measurement of Parton Level Dynamics and Structure Functions

In reference [163] a new method was developed to get direct access to the parton-parton kinematics. The analysis was based on a clean double high p_T sample, albeit with very limited phase space coverage and only one of the two high p_T particles identified. It was shown that fragmentation effects are small and can be reliably corrected for so that the momenta of the incoming partons as well as the hard scattering angle can be reconstructed on an event by event basis. Using the HERA – B particle identification, it is possible to enrich different parton-parton scattering processes by flavor tagging (see above). By dividing cross sections for different kinematical situations with identical momenta of incoming partons but different scattering angle, a direct measurement of the parton-parton scattering amplitudes is possible since the structure functions cancel out (apart from small scale breaking effects). In [163] this method was applied to a sample enriched in quark-gluon scattering. The measured angular distribution confirmed to a surprisingly high precision the shape of the leading order QCD scattering amplitude. At HERA – B such highly non-trivial tests of QCD amplitudes for identified parton-parton scattering can be for the first time extended to other parton-parton subprocesses, thus offering very deep and qualitatively new tests of QCD.

In analogy, the ratio of cross sections for two kinematical situations with the same scattering angle but different Bjorken-x values can be used to extract the products of structure functions. Together with the measurements of the direct photon cross section this will offer a sensitive test of structure function parameterizations at large Bjorken-x. Such an analysis has not been attempted before.

5.2 Physics of High Mass Lepton Pair Triggers

5.2.1 Drell-Yan Pair Production

The direct production of e^+e^- and $\mu^+\mu^-$ pairs in hadron-hadron collisions is generally well understood; nevertheless, due to its purely hadronic initial state, it needs more non-perturbative input than, for example, deep inelastic scattering, and some interesting experimental questions are still open, where HERA – B could contribute.

HERA – B investigates p-nucleus interactions at a proton beam energy of 920 GeV with a large acceptance universal spectrometer of exceptionally high rate capability, using a lepton pair trigger at the first level. This makes HERA – B a powerful tool to study Drell-Yan physics. In particular, HERA – B has the following advantages:

- The overall acceptance after cuts on lepton momenta (($p > 5\,\mathrm{GeV/c}$, $p_T > 0.5\,\mathrm{GeV/c}$) is about 50%. It has been determined by Monte Carlo simulations for the di-lepton mass regions around the J/ψ and the Υ mass as function of Feynman-x, x_F, and transverse momentum, P_T, of the lepton pair [193, 194]. The acceptance is almost symmetric around $x_F = 0$, and ranges from $x_F \approx -0.4$ to $x_F \approx +0.3$, and it is almost independent of P_T. The polar angle, θ, of the di-lepton flight axis (measured in the di-lepton centre of mass system) can be measured in a very wide range. The acceptance is flat for $-0.6 < \cos\theta < +0.6$, and drops by a factor of 6 when approaching $\cos\theta \approx \pm 0.9$.
- The good mass resolution ($20\,\mathrm{MeV/c^2}$ at the J/ψ and $120\,\mathrm{MeV/c^2}$ at the Υ mass [195]), caused by thin targets and high granularity tracking, improves the measurement of differential cross sections.
- In HERA – B we will investigate e^+e^- and $\mu^+\mu^-$ production in the same run. This will give an additional handle for the understanding of normalization and background (assuming, of course, lepton universality), an increasingly important issue for large statistics experiments.
- Despite the large statistics potential (see below) of the experiment, it is based on *thin* nuclear targets, avoiding contaminations from secondary pion reactions, and allowing the extraction of clean A-dependencies.

It should also be mentioned, that Drell-Yan data can be recorded with an incomplete detector, for instance with a reduced inner tracking acceptance. They are comparatively easy to reconstruct and to analyze. The understanding of the Drell-Yan process is also an important ingredient for the treatment of backgrounds to the quarkonia signals.

From the physics point of view, there are several important topics, where HERA – B may contribute:

- Measurement of the decay angular distribution which has the general form

$$\frac{\mathrm{d}\sigma}{\mathrm{d}\Omega} \sim 1 + \lambda\ \cos^2(\theta) + \mu\ \sin(2\theta)\ \cos(\phi) + \frac{\nu}{2}\ \sin(2\theta)\ \cos(2\phi)\ , \tag{20}$$

  where θ and ϕ are given in the rest frame of the lepton pair with respect to the proton beam axis [196], and where λ, μ, ν are parameters which are probes of the spin and Lorentz structure of the underlying parton dynamics. In analogy to the Callan-Gross relation one expects $\lambda = 1 - 2\nu$ [197]. This prediction is still not tested for proton projectiles, while it is violated in the case of pion beams at large transverse momentum of the di-leptons [198, 199] (see also [1]).

- The high P_T region, for $P_T^2 > Q^2/4$, is rather similar to direct photon production, and can be described by higher order processes $\mathrm{q} + \mathrm{g} \rightarrow \gamma^* + \mathrm{q}$, $\mathrm{q} + \overline{\mathrm{q}} \rightarrow \gamma^* + \mathrm{g}$, the first process being dominating [180]. This allows to constrain the gluon distribution, especially at large Bjorken-x (compare also section 5.1.2).

- Data for the nuclear mass number dependence in a wide x_F and P_T range will give important input for investigations of the quark gluon plasma at CERN and RHIC.

From the cross sections for Drell-Yan $\mu^+\mu^-$ pairs with $Q^2 > 16\,\mathrm{GeV}^2$, $\sigma_{\mu\mu} \approx 0.2$ nb/nucleon[59], and inelastic interactions, $\sigma_{\mathrm{inel}} \approx 12\,\mathrm{mb}$/nucleon (for Ti), one finds a production rate of 0.6 (0.3) $\mu^+\mu^-$ pairs/s for a target rate of 40 MHz (20 MHz) (and the same rate for $\mathrm{e}^+\mathrm{e}^-$ pairs). The expected statistics in each channel for 1 year (10^7 s) running time, assuming 50% acceptance and 80% triggering and tracking efficiency per track, then amounts to 2.1 (1.1) million events. This requires that the first level trigger, which normally cuts around the J/ψ mass, is operated without an upper mass cut, and runs at full design efficiency.

To our knowledge, there are few competing experiments, the most recent being E866 (NUSEA) at FNAL. Being focused mainly on the topic of isospin violation in the nuclear sea quark distributions, it extended its acceptance region to nearly the complete forward hemisphere, allowing to contribute substantially to the above mentioned topics. So far, already from a sample of 300 k $\mu^+\mu^-$ pairs from 800 GeV p-Cu interactions, a new preliminary estimate of λ has been derived [201].

In summary, provided that the first level trigger works at least at 10% of the design efficiencies, HERA – B can be regarded as a second generation Drell Yan experiment. It will allow for the first time a high statistics analysis in almost the full phase space, both in the forward and backward hemisphere, and for a large variety of target materials, making possible qualitatively new tests of the production dynamics which are likely to shed light on yet unsolved theoretical puzzles connected to QCD. On the practical side, the experiment will yield data for a more precise determination of the gluon structure function of the nucleon at large Bjorken-x, thus complementing similar measurements based on high-p_T direct photon production at HERA – B.

5.2.2 Heavy Quarkonium Production

Heavy quarkonium is one of the best systems to study QCD. Where lighter bound states suffer from the theoretical uncertainties associated with the non-perturbative regime and large relativistic corrections, the large charm or bottom quark mass ensure that production of heavy quarkonium can at least partly be calculated perturbatively.

The production of heavy quarkonia has received a lot of attention both from theory and experiment in recent years. Since suppression of J/ψ production was proposed as a signal for the occurrence of de-confined matter [202], large experimental efforts have been devoted to establish this in heavy ion collisions. Whether or not the anomalous suppression measured by NA50 can be solely attributed to the formation of a Quark-Gluon-Plasma, is subject to lively debate. Suppression mechanisms in ordinary proton-nucleus interactions represent important input for resolving this issue.

An accurate interpretation of such suppression requires a good understanding of charmonium production. Originally, heavy quarkonium production was described by the color singlet model (CSM) [203, 204]. However, next-to-leading order predictions for J/ψ production based upon this

[59] See [200] for a compilation of Drell-Yan data.

model disagree with measured cross sections at Tevatron energies by almost two orders of magnitude [205]. This discrepancy is resolved with the introduction of the color octet mechanism (COM), based on non relativistic QCD (NRQCD) [206]. Here a $Q\overline{Q}$ pair can neutralize its color by radiating soft gluons before forming quarkonium. It introduces many universal non-perturbative parameters that need to be extracted from data.

Whereas COM calculations fit the Tevatron data, they do not successfully describe data on J/ψ photo-production [207, 208]. Furthermore, COM predictions for angular distributions of J/ψ decay seem incompatible with data. Considerable theoretical effort is still invested to provide a complete and accurate description of heavy quarkonium production. Precise measurements on quarkonium production will be essential in appreciating the validity of existing and future models.

Cross Sections and Spectroscopy

A set of measurements that will severely constrain the parameters of the COM (NRQCD matrix elements) is the determination of the hadronic production cross section of the various heavy quarkonium states. Theoretical predictions for the lighter states such as J/ψ are hampered by the large ($\approx 50\%$) contribution from radiatively decaying χ_{cJ} and ψ', and consequently involves a large number of matrix elements. Therefore, the cross section determination of excited and non-resonant quarkonium states will further constrain these matrix elements that to date are known to an accuracy of no better than 50%.

It has been shown [209], that the decay $\chi_{c1,2} \to J/\psi\gamma$ can be resolved despite high combinatorial background. The large statistics expected for the J/ψ sample (see Tab. 48 at the end of this section) will most likely make the study of at least some of the other charmonium states (h_c, χ_{c0}, D-wave) possible too.

The lowest mass triplet state (χ_{c0}=$^3P_0$, $J^{PC} = 0^{++}$) has never been observed inclusively due to a relatively low branching fraction for $\chi_{c0} \to J/\psi\gamma$ of 0.66%. A much improved total width has recently been measured by the E835 Collaboration [210] giving a significantly smaller value. It is likely that the $\chi_{c0} \to J/\psi\gamma$ branching fraction will double from its current reference value. Furthermore, it has always been difficult to reconcile the χ_{c0} radiative width with the larger χ_{c1} and χ_{c2} radiative width which should not differ dramatically from simple phase space scaling. A high statistics study might just find the χ_{c0} inclusively.

A statistically significant observation of the state $h_c(3522)$=$^1P_1$, $J^{PC} = 1^{+-}$, resonantly produced in $p\overline{p}$ annihilation, has been reported by the experiment E760 [211] but needs further confirmation. A high statistics study of the decay $h_c(3522) \to J/\psi\pi^0 \to \mu^+\mu^-\pi^0$ should provide highly significant signals at HERA – B. The experiment E705, for instance, reported a 2.5σ "bump" in the $J/\psi\pi^0$ mass spectrum already on the basis of less than 40,000 reconstructed $J/\psi \to \mu^+\mu^-$ decays in 300 GeV $\pi^\pm$-Li and p-Li interactions [212]. The outstanding potential of HERA – B has already been pointed out in reference [213].

There are four $L = 2$ states, $^1D_2$,$^3D_{1,2,3}$, which are totally inaccessible to e^+e^- colliders, with the exception of the $\psi''(3770)$ state. The $\psi''(3770)$ state is believed to be a $^3D_1$ state because it must have a $L = 0$ component, the 3^3S_1 state reliably predicted near 4100 MeV, in order to explain how it is produced in the e^+e^- annihilation. The ψ'' and the $^3D_3$ states are above the open charm threshold while the other two can be expected to have masses below 3880 MeV. However, the decay $^3D_3 \to (D\overline{D})_{L=3}$ should be dynamically suppressed due to the large relative orbital momentum of the D mesons, so that the $^3D_2$ state is expected to be most prominent. The production cross section for this state is believed to be of the same order of magnitude as ψ' state and its branching fractions to $J/\psi\pi\pi$ to be only about a factor of three smaller.

The ground state ($\eta_c(2980) = {}^1S_0$, $J^{PC} = 0^{-+}$) is well established but has never been seen in inclusive hadro-production. There is no clean, triggerable decay channel. Possibilities are offered by the decay $\eta_c \to \phi\phi$, which has a branching fraction of 0.8%, with both ϕ mesons decaying into charged kaons (branching fraction ≈50% for each ϕ). Such a decay is attractive given the RICH particle identification capabilities, the distinctive kinematic signature and the strong $\phi\phi$ decay plane correlation. Other final states include $\pi^+\pi^-\pi^+\pi^-$, $K^+K^-\pi^+\pi^-$, $K^+K^-K^+K^-$, all of which have branching ratios of about 2%. Currently, however, no effective trigger for these decay modes exists.

Similarly, HERA – B will be able to explore the bottomonium system (see Tab. 48 at the end of this section). Apart from the Υ states, χ_b states can be reconstructed through their radiative decays to Υ mesons, for which the standard di-lepton trigger is as effective as for J/ψ mesons.

Concerning the determination of quarkonium masses and of branching fractions, the scope of HERA – B is believed to be rather limited compared to resonant spectroscopy in e^+e^- (or even $p\overline{p}$) collisions or two-photon-fusion. One lacks the constraints of momentum conservation and must sift through the simultaneous non charmonium background interactions as well as more combinatorial simultaneous "spectator" particles.

The possibility for observing a hadro-molecular state, essentially a meson-baryon bound state configuration, exists. The Λp system has weaker attraction (by half) than the np system and is not bound. The $J/\psi p$ system has an almost doubled reduced mass and may exist. Again, the RICH particle identification is advantageous in this context. Such a study would use reconstructed low mass J/ψ mesons (decays from a bound state) in $J/\psi p$ (or $J/\psi\overline{p}$) mass fits. In the same way, $J/\psi K^{\pm}$ mass plots may be searched for bound states.

Quarkonia Spin Alignment

One particularly sensitive probe for understanding the production mechanisms of heavy quarkonium is a measurement of the angular distributions for the leptonic decays. Generally, such distributions are parameterized as

$$\frac{d\sigma}{d\cos\theta} \propto 1 + \lambda\cos^2\theta \tag{21}$$

where θ is the angle between the positively charged lepton and the beam axis in the quarkonium rest frame. Negative (positive) values for λ indicate predominantly longitudinally (transversely) polarized quarkonium states.

One of the implications of the color-octet mechanism for heavy quarkonium production is the prediction that they are largely produced in a transversely polarized state. Even when taking into account the large feed-down from χ_c states, the prediction of the color-octet model at leading twist is at significant variance with available experimental data.

In Tab. 47 the predictions for the different productions models at fixed target energies are summarized and confronted with existing experimental data.

Table 47: *Predicted and measured values of polarization parameter λ for J/ψ and Υ decays.*

	CEM	CSM	COM	E573($\overline{p}+W$), $x_F > 0$	E866 ($p + Cu$), $x_F > 0.25$
J/ψ	0	0.25 . . . 0.50	0.31 . . . 0.63	-0.115 ± 0.061	see Fig. 163
Υ	0		0.24 . . . 0.30	–	–

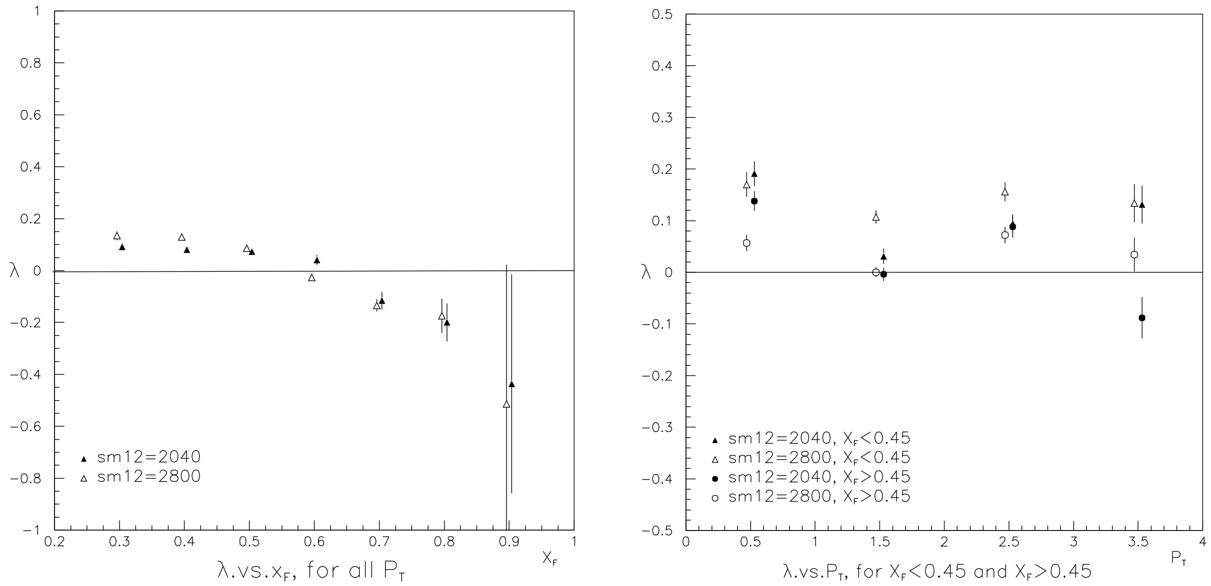

Figure 163: *x_F and p_T dependence of the angular distribution parameter λ as measured by E866.*

The x_F and p_T dependencies of λ, as measured by E866 (Fig. 163), suggest that gluon fusion, which dominates at low x_F, and quark-antiquark annihilation lead to production of J/ψ mesons in different helicity states. Integrated, they result in no net polarization, in clear disagreement with COM predictions. The p_T dependences suggest that gluon fragmentation, possibly a dominant source of quarkonium production at high p_T, predicted to lead to transversely polarized quarkonium states, does not significantly contribute in the fixed target regime.

Nuclear effects such as final state interactions may also affect the polarization, smearing out or suppressing the original state. So far measurements of the A dependence of λ have not been performed.

Insight into the significance of χ_c feed-down for J/ψ polarization can be provided by similar measurements for ψ' decays, where such feed-down is absent.

Whereas higher twist effects are likely to be significant in the case of J/ψ production, they are expected to be small for Υ production due to the large mass of the b quark. Therefore the Υ system provides an excellent laboratory of testing different production mechanisms. In particular it allows to test the factorization approach, which the COM relies on.

Nuclear Dependence

Since the first indications that a signal of anomalous suppression in the production of J/ψ mesons was observed in central Pb-Pb collisions [214], competing interpretations of this effect have been widely debated. The natural explanation of the formation of a quark-gluon-plasma (QGP) is confronted with suppression patterns in proton-nucleus interactions, where no de-confined state is expected to have formed.

Nuclear dependencies of particle production are parameterized as:

$$\sigma_{pA} = \sigma_{pN} A^{\alpha} \tag{22}$$

where A is the atomic number of the nuclear target in the proton-nucleus collision. The exponent α describes the magnitude of nuclear suppression and can take on values between 0.7 (maximally suppressed production) and 1 (no suppression). The dependences of α on kinematic variables such as p_T or x_F indicate suppression effects beyond a constant absorption.

A variety of models have emerged to explain kinematics-dependent nuclear suppression (see [215] for an overview). Most of them are modifications or refinements of one of the following approaches:

- **Nuclear absorption**
  Before hadronization, the unbound $Q\overline{Q}$ pair can interact with the surrounding nuclear material and can thus be absorbed or dissociated into open charm. Since the absorption probability increases with increasing length of the path after which the formation of the quarkonium state takes place, the suppression will be larger at large x_F. In this framework, ψ' mesons would experience larger suppression than J/ψ mesons, since the size and the formation time of ψ' mesons are larger.

- **Comover absorption**
  A bound quarkonium state may interact with secondary co-moving hadrons surrounding it and can thus be dissociated before decay. The kinematic dependences are similar to nuclear absorption. HERA − B is able to reconstruct a large fraction of charged particles. A measured relative depletion of the particle density in phase space regions close to the quarkonium is one possible signature for such a mechanism.

- **Nuclear shadowing**
  Deep-inelastic scattering measurements on nuclear targets have shown a dependence of parton distributions on the atomic number. However, the observed suppression is much larger than expected from shadowing alone. At HERA − B, where the Bjorken-x values for the target partons, x_2, are larger than 0.02 for quarkonium production, the contribution of shadowing will not exceed a few percent.

- **Multiple scattering and energy loss**
  In any stage of quarkonium production, interactions with the surrounding hadronic matter can cause a suppression. A parton involved in the creation of the $Q\overline{Q}$ pair can loose energy (typically 1 GeV/fm) due to soft multiple scattering before the interaction. This increases the effective fractional momentum, x_1, of the parton from the incoming proton that is needed to create quarkonia, depending on the amount of nuclear matter encountered. A colored $Q\overline{Q}$ pair may experience similar energy losses before hadronization, causing a x_F shift of the produced quarkonia towards smaller values. A measurement of the nuclear dependence of Drell-Yan production provides a clean way to factorize out initial state interactions such as parton energy loss or shadowing, since final state interactions are absent in this case.

Recently the E866 collaboration has presented the most precise measurement so far on nuclear dependence of both J/ψ and ψ' production (see Fig. 164). A general increase of α with p_T is observed and can be understood in the framework of soft multiple scattering of the incident partons or final state quarkonia. Such effects broaden the p_T distribution, as confirmed by an increase of $< p_T^2 >$ with the atomic number of the target nucleus. The suppression exponents for J/ψ and ψ' production also follow a similar pattern at high values of x_F, but deviate significantly around $x_F = 0$. At small x_F, the quarkonium states are hadronized essentially within the nucleus. Final state absorption mechanisms affect the larger ψ' meson to a greater extent than the more tightly bound J/ψ meson. The depletion at high x_F can be explained by effects such as initial state energy loss.

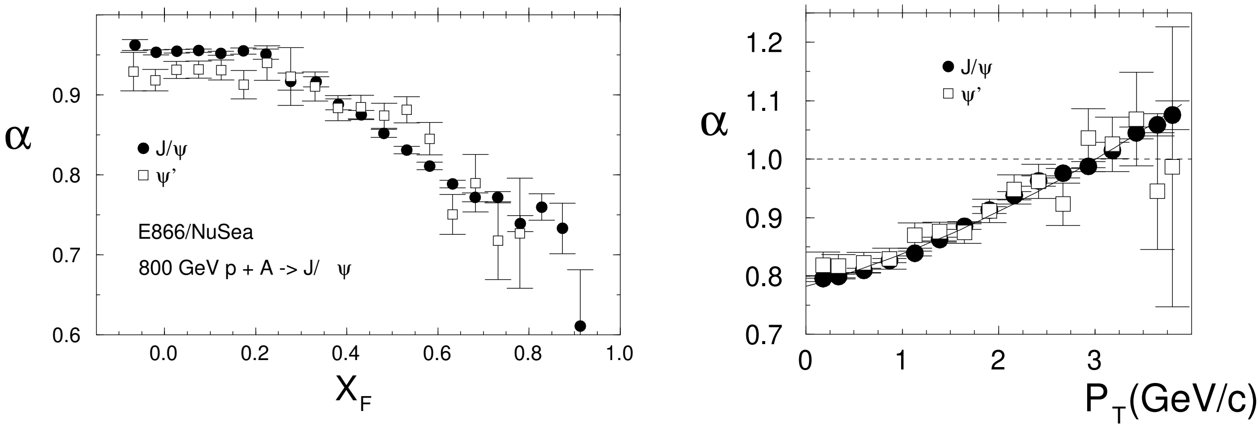

Figure 164: *Kinematic dependence of nuclear suppression for* J/ψ *and* ψ' *production (from [216]).*

Contrary to previous experiments such as E866, HERA – B will be able to reconstruct a large fraction of the associated particles in an event. This will enable measurements of suppression dependence on total transverse energy of an event, similar to measurements in heavy ion experiments. It provides a direct way of comparing the suppression in the fixed target regime to the one attributed to Quark-Gluon-Plasma formation.

In the kinetic regime of HERA – B, extending to x_F values as small as -0.4, no measurements are available so far. This region is especially interesting, since here, for large nuclei, the quarkonia will mainly form inside the nuclei. Extrapolations of different models in this regime give very different predictions. If absorption mechanisms were dominating, the continuation of α to negative x_F would be essentially flat, whereas mechanisms such as final state dissociation favor an increased suppression.

The HERA – B Potential

With its high interaction rate and dedicated di-lepton mass trigger, HERA – B will supersede any existing sample of directly produced heavy quarkonia by an order of magnitude, provided that the first level di-lepton trigger is fully operational. The number of recorded direct J/ψ mesons will be limited only by the bandwidth alloted for these events. Bottomonium and higher mass Drell-Yan pairs can probably be accepted at full production rate. The expected yield for these therefore depends on the assumed performance scenario.

In Tab. 48 the expected number of events recorded in a running year (10^7 s) is compared to existing data samples from other experiments.

The projected statistics in Tab. 48 is optimistic in the sense that full trigger efficiency is assumed, however, even assuming a more realistic medium term goal to commission the di-lepton trigger to a level of 10% of the design efficiency, HERA – B will be competitive from the statistical point of view. Perhaps more importantly, the large angular coverage of the HERA – B spectrometer will open up an acceptance for negative x_F, so far unchartered by any fixed target experiment, so that even smaller trigger efficiencies are interesting. Until now, the variety of models describing nuclear suppression can only be confronted with the data of E866, limited to mainly positive x_F. HERA – B will be able to decisively test their validity in this new kinematical region.

With the size of heavy quarkonium samples, HERA – B has the chance to measure nuclear suppression with an unprecedented precision. Simultaneous operation of different target materials in

Table 48: *Comparison of estimated* HERA – B *potential to Fermilab fixed target experiments and the RHIC experiment PHENIX. Values of other experiments are mainly taken from [216]. For the yield of direct* J/ψ *and* ψ' *mesons a bandwidth of* 5 *events per second is assumed.*

	E772	E866	PHENIX (10^7 s)	HERA – B in 10^7 s 40 MHz 100% eff.	40 MHz 80% eff.	20 MHz 100% eff.	20 MHz 80% eff.
J/ψ	–	2.8 M	1.3 M	50 M	50 M	50 M	50 M
ψ'	12 k	90 k	23 k	500 k	500 k	500 k	$\leq$ 500 k
$\Upsilon(1S)$	17 k	–	0.7 k	100 k	50 k	50 k	25 k
$\Upsilon(2S)$	5 k	–		30 k	15 k	15 k	7 k
$\Upsilon(3S)$	3 k	–		15 k	7 k	7 k	4 k
Drell-Yan	?	130 k	?	2 M	1 M	1 M	0.5 M
$\sqrt{s}$(GeV)	40	40	200	41.6			
x_F	0 to 0.6	−0.1 to 0.9	−0.3 to 0.3	−0.4 to 0.3			
p_T(GeV/c)	0 to 2.5	0 to 4	0 to 10	0 to 5			

HERA – B will significantly reduce systematic errors.

Conclusions

With its unique trigger chain, if operating at least to a level of 10% of the design efficiency, HERA – B will acquire a large sample of heavy quarkonium decays. It enables precise measurements even of non-resonant quarkonium states. Several open questions in the field of quarkonium hadro-production can be addressed.

The validity of the NRQCD color octet mechanism, in particular the universality of the COM matrix elements can be tested through the measurement of production cross sections and spin alignment. Furthermore, HERA – B can measure nuclear suppression in the up to now unchartered negative x_F region with high precision. Such measurements will be most valuable in deciding to what extent the anomalous J/ψ suppression in heavy ion collisions can be attributed to the formation of a Quark-Gluon-Plasma.

5.2.3 Beauty Production Cross Section in Proton Nucleus Interactions

Recent experimental results and developments in theory are beginning to form a coherent picture of heavy flavor production dynamics in fixed target experiments and at colliders [217]. The data are described by NLO perturbative QCD predictions as well as by non-perturbative approaches involving fragmentation effects and the intrinsic momenta of the interacting parton within the parent hadrons. Studies of b hadron production by pions and protons at fixed target energies have been pursued by several experiments at Fermilab and CERN. Data and theory are coming to qualitative agreement but more measurements are necessary to reduce the still large experimental uncertainties. A measurement of the $\mathrm{b\overline{b}}$ production cross section at HERA – B is of course also essential for more precise assessment of the future physics capabilities of the experiment. In this section, a brief overview is given on the current theoretical and experimental situation, along with the discussion of the implications of the developed experimental techniques for the measurement of $b\bar{b}$ production for the HERA – B potential.

Fixed Target $\mathrm{b\overline{b}}$ Hadro-Production

Heavy quark hadro-production can be described with an acceptable accuracy by perturbative QCD. Complete calculations are nowadays available at next-to-leading order (NLO) [218]. These predictions are still affected by rather large theoretical uncertainties. Nevertheless, because of the relatively large b quark mass, the measurements of the beauty hadro-production cross sections and other production characteristics provide a good tests of perturbative QCD or at least an important new ingredient for future theoretical developments.

Currently, theoretical research mostly focuses upon improvements in special kinematic regions where large logarithms in the coefficients of perturbative expansions may arise and spoil the convergence. At very high energies, $\sqrt{s}$, one expects large correction terms, of order $\sigma_{\mathrm{Born}} \times \alpha_s[\log(s/m_{\mathrm{Q}}^2)]^n$, to arise at all orders in perturbation theory.[60] This problem, related to the breakdown of perturbative QCD at small values of Bjorken-x in deep inelastic scattering, is relevant, for example, for bottom production at the Tevatron and at the LHC. At small energies, on the other hand, approaching the threshold region for the production of heavy flavor pairs, terms of order $\sigma_{\mathrm{Born}} \times \alpha_s[\log^2(1-4m_{\mathrm{Q}}^2/s)]^n$ become large. These terms are relevant for the production of top quarks at the Tevatron, for the production of $\mathrm{b\overline{b}}$ at HERA – B, and for the production of charm quarks at relatively small center of mass energies.

Heavy flavor production has been studied extensively in fixed target experiments with both pion and proton beams. The typical center of mass energy is in the range of $10 - 40\,\mathrm{GeV}$, where the bottom cross section is rather small. Therefore, most of the available data concern charmed hadron production. The total cross sections, single-inclusive distributions, and correlations between the quark and antiquark have been measured in both hadro- and photo-production. In these cases, the theoretical tools from perturbative QCD are at their very limit of applicability, because the charm quark mass is very close to typical hadronic scales, and effects of non-perturbative origin are likely to be important. Although modern fixed target experiments have considerably improved the situation, many open problems remain in this field. All experimental results are in qualitative agreement with perturbative QCD calculations, thus supporting the "hard" nature of the heavy quark production phenomena. However, several quantitative deviations from pure QCD are being observed. The models describing non-perturbative phenomena, such as fragmentation effects and the influence of intrinsic transverse momenta of the partons within the parent hadrons, are still being intensively developed and are widely discussed in the literature.

Fig. 165 (left plot) shows the $\mathrm{c\overline{c}}$ and $\mathrm{b\overline{b}}$ cross sections, computed using QCD at NLO, as functions of the beam energy, for π^-N collisions. The same quantities are shown in Fig. 165 (right plot) for a proton beam. The cross sections are calculated using standard parameterizations of parton distributions for the nucleon and the pion. The default values assumed for the charm and bottom masses are $m_{\mathrm{c}} = 1.5\,\mathrm{GeV/c^2}$ and $m_{\mathrm{b}} = 4.75\,\mathrm{GeV/c^2}$, respectively, and the default choices for the renormalization scale μ_R and the factorization scale μ_F are

$$\begin{array}{lll} \text{charm:} & \mu_F = 2m_{\mathrm{c}} & \mu_R = m_{\mathrm{c}} \\ \text{bottom:} & \mu_F = \mu_R = 2m_{\mathrm{b}} & . \end{array}$$

As one can see, the experimental results on total charm cross sections are in reasonable agreement with theoretical expectations if the large theoretical uncertainties are taken into account. The hadro-production data is clearly compatible with a value of $1.5\,\mathrm{GeV/c^2}$ for the charm quark mass. In the case of the bottom production the spread of the experimental results is almost as large as that of the theoretical predictions. In spite of very large errors, the two measurements from fixed target

[60] The quantity σ_{Born} represents the tree level QCD prediction for the observable in question.

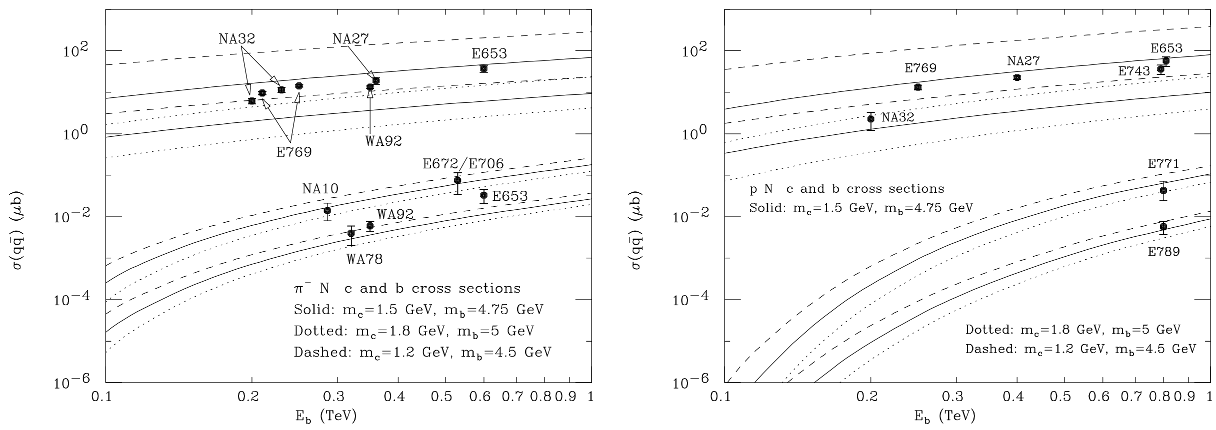

Figure 165: *Cross sections for* b *and* c *production in* π^-N *collisions (left) and* pN *collisions (right). The plots show the comparison between theoretical predictions (see text) and experimental results.*

pN interactions [12, 11] differ at a level of $2.5\,\sigma$. For a more consistent experimental estimate of the production cross section more measurements are required.

Experimental Methods

The experimental technique to measure the $\mathrm{b\overline{b}}$ production cross section can be subdivided into two basic classes. The first class includes methods based on the reconstruction of the exclusive decay modes of B hadrons. Due to the low production cross section in fixed target experiments, such methods have only been used in collider experiments at much larger energies. The second class are inclusive methods, utilizing some general, though quite prominent, signatures of B hadron decays. Two measurements performed by the Fermilab fixed target experiments are discussed here in order to evaluate the applicability of similar techniques for the data collected by HERA – B during the run of the year 2000 and to judge the future prospects.

In the E789 experiment the production of b quarks was measured via inclusive $\mathrm{b} \to \mathrm{J}/\psi X \to \mu^+\mu^- X$ decays [12]. The E789 spectrometer detected pairs of muons produced in 800 GeV/c proton-gold interactions with an effective interaction rate of 50 MHz. To provide sufficient vertexing resolution to distinguish the decays of b hadrons from the copious prompt J/ψ backgrounds, an array of 16 silicon micro-strip detectors (SMD) was used. The primary proton beam was incident along the z axis upon a rectangular gold target, $5\,\mathrm{cm} \times 0.2\,\mathrm{mm} \times 3\,\mathrm{mm}$ in size (in x, y and z). The wire shape of the target and its orientation allowed good localization of y and z coordinates of the primary interaction vertex. The SMDs consisted of $5\,\mathrm{cm} \times 5\,\mathrm{mm} \times 300\,\mu\mathrm{m}$ single sided detectors with $50\,\mu$m strip pitch, situated 37 cm to 94 cm downstream of the target. The angular coverage of the instrumented strips, $20\,\mathrm{mrad} < |\theta_y| < 60\,\mathrm{mrad}$, matched the acceptance of the magnetic spectrometer. The resolution in the $\mathrm{b} \to \mathrm{J}/\psi X$ decay distance, provided by the SMD, was approximately $700\,\mu$m.

The total di-muon data sample collected by E789 corresponds to an observed signal of about 71 000 prompt $\mathrm{J}/\psi \to \mu^+\mu^-$ decays. To select downstream $\mathrm{b} \to \mathrm{J}/\psi \to \mu^+\mu^-$ decays, cuts on the z position of the muon pair vertex and on the impact parameter of each muon track were applied. The impact parameters were defined as the vertical distances (the target wire was oriented horizontally) between the muon tracks and the target center. The impact parameter requirements ensured that neither the μ^+ nor the μ^- track pointed to the target. The $\mu^+\mu^-$ invariant mass spectra for downstream vertices ($z > 0$) and upstream vertices ($z < 0$) were analyzed separately. The spectra with $z < 0$ allowed to evaluate the tails of the vertex resolution function for the prompt J/ψ decays from the data. The J/ψ peak was clearly seen in the mass spectra for $z > 0$, even when large secondary vertex separations were required. In contrast, the J/ψ signal in the spectra for $z < 0$ rapidly died out as the detachment cuts were tightened. The net excess of J/ψ events for downstream vertices was attributed to $b \to J/\psi$ decays. The spectrometer acceptance and analysis efficiency had to rely on detailed Monte Carlo simulations. The integrated b quark production cross section, obtained by a model dependent extrapolation to the full phase space in x_F and p_T, was estimated to be $5.7 \pm 1.5 \pm 1.3$ nb/nucleon.

Another method to measure the $b\overline{b}$ production cross section was used by the E771 experiment which collected events in which both B hadrons decay semi-muonically [11]. The E771 target consisted of twelve 2 mm Si foils spaced by 4 mm. The energy of the incident proton beam was 800 GeV. The silicon micro-vertex detector consisted of 12 layers, positioned downstream of the target for the measurement of primary and secondary vertices. The total di-muon triggered data sample collected by E771 corresponded to an observed signal of about 11 000 prompt $J/\psi \to \mu^+\mu^-$ decays. The continuum muon pairs have been used to search for double $B \to \mu X$ decay events. A set of cuts was imposed in order to isolate a sample of candidates for double semi-muonic b decays and minimize other di-muon backgrounds. Amongst these are the requirements that both muons have a large (4 or 5) number of hits in silicon planes, that both muons have momenta larger than 15 GeV/c, that the di-muon mass is between 2.0 GeV/c^2 and 2.9 GeV/c^2 or greater than 3.3 GeV/c^2, that the transverse momenta of the muons are larger than 1.5 GeV/c and 1.0 GeV/c, respectively, and that the impact parameters of the muons in the x (bend plane) and y projections are larger than $10\,\sigma$ and $3\,\sigma$, respectively. One same sign and five opposite sign di-muon events survived the reconstruction and these cuts. The same sign muon event is consistent with being due to mixing of a neutral B meson. After subtraction of a total estimated background from all sources of 1.21 ± 0.33 events, a cross section of $\sigma(\mathrm{pN} \to b\overline{b}) = 42^{+31}_{-21}$ nb/nucleon was obtained assuming a linear dependence on the nuclear mass number.

During the run of the year 2000, HERA – B has collected a considerable sample of data using di-lepton triggers. The trigger accepted muon and electron pairs. The total accumulated sample contains about 3000 reconstructed $J/\psi \to \mu^+\mu^-$ decays. The magnitude of the $J/\psi \to e^+e^-$ signal (and the signal to background ratio) depends on the $e^\pm$ identification requirements which can be properly tuned according to the particular physics task. Soft requirements result in approximately 40 000 $J/\psi \to e^+e^-$ decays. More strict requirements (two bremstrahlung photons from the e^+e^- final state) leave about 4000 $J/\psi \to e^+e^-$ decays, but the signal becomes very clean. It is possible to use these data samples for the $b\overline{b}$ cross section measurement using both inclusive methods described above.

The vertexing resolution (or tracking accuracy nearby the target) achieved by HERA – B in the run of the year 2000 is close to design specifications and exceeds the capabilities of E771 and E789. For the b production measurement using $B \to J/\psi X$ decays the total available statistics corresponds to about 40 000 $J/\psi \to e^+e^-$ decays, which is comparable to the data sample, used by E789. The method based on double semi-leptonic B decays can be applied to the full di-muon statistics but has to be restricted to the di-electron data with tight identification requirements (necessary to eliminate combinatorial background). Therefore, the total statistics for the double semi-leptonic method appears to be comparable to that of E771. The combination of the two methods should allow to perform a statistically meaningful measurement on the basis of the data already collected.

In conclusion, although the statistics of the year 2000 running is still marginal for a measurement of the $b\overline{b}$ production cross section, HERA – B will clearly be able to perform a high precision measurement as soon as the FLT commissioning improves the collection rates for J/ψ decays and/or semi-leptonic B decays by at least an order of magnitude.

5.2.4 CP Violation in $B^0 \to J/\psi\ K^0_S$ Decays

The observation of CP violation in the golden decay channel $B^0 \to J/\psi\ K^0_S$ is a primary goal of the HERA – B experiment. Experimentally the CP asymmetry

$$A(t) = \frac{\Gamma(B^0 \to J/\psi\ K^0_S) - \Gamma(\bar{B}^0 \to J/\psi\ K^0_S)}{\Gamma(B^0 \to J/\psi\ K^0_S) + \Gamma(\bar{B}^0 \to J/\psi\ K^0_S)} \tag{23}$$

is related to a constant of nature, the angle β of the unitarity triangle,

$$A(t) = -\sin(2\beta)\,\sin(x_d t) \quad , \tag{24}$$

with $x_d = 0.73 \pm 0.03$ [27] being the neutral B meson mixing parameter and t is the decay time in units of lifetime.

Eq. (24) leads to a time integrated asymmetry of

$$A_{\rm int} = -\sin(2\beta)\,\frac{x_d}{1+x_d^2} \quad . \tag{25}$$

The HERA – B detector has been designed to reconstruct the final states $\mu^+\mu^-\ \pi^+\pi^-$ and $e^+e^-\ \pi^+\pi^-$ of the golden decay mode. At the time of the Technical Design Report (TDR) [1] many idealistic assumptions had to be made to estimate the reconstruction efficiencies for these decay modes. Since then software packages became available for track reconstruction and trigger simulation. Several studies have been performed using these programs [2, 3, 4]. The numbers presented here are based on the most recent ones [5], with fully commissioned triggers as a baseline assumption.

Tab. 49 lists the current estimates of the reconstruction efficiencies for the muon and the electron channel in comparison to the TDR. The efficiencies are smaller now due to various effects. The actual mechanical constraints in the fabrication of the Outer Tracker and the compensation coil of the electron beam pipe lead to holes in the acceptance and to an increase in multiple scattering. The lifetime cut was increased in ref. [5] to improve background suppression. This reduces the efficiency by 18% but has practically no impact on the measurement error of $\sin(2\beta)$ since the CP asymmetry only builds up during the mean lifetime of the B meson and can hence anyway not be measured at very small decay times. The geometrical acceptance for pions from K^0_S decays is smaller due to fewer Inner and Outer Tracker super-layers in the magnet.

For the measurement of CP violation the flavor of the B meson at the production time has to be determined (tagged). Several tagging methods have been developed by other experiments and their applicability in HERA – B has been studied repeatedly [4, 7, 8].

Most methods try to infer the charge of the second b quark produced in the proton collision by exploiting the correlation to the charge of the lepton for semi-leptonic B decays (lepton tag), the charge of kaons from the decay chain $b \to c \to s$ (kaon tag) or the sum of the momentum weighted charges of all tracks from the decay chain (charge tag).

Every method has a certain efficiency ϵ for finding a tag and a probability χ of correctly measuring the b quark charge. Hence the measured asymmetry is smaller by the dilution factor $D = 2\chi - 1$ and the error on $\sin(2\beta)$ scales with the tagging power $P = D\sqrt{\epsilon}$. All studies yield similar results of $P \simeq 0.3$.

Table 49: *Reconstruction efficiencies for the golden decay mode in comparison to the TDR. The* K^0_S *reconstruction in ref. [5] is too small due to a bug in the Monte Carlo simulation which was found recently [6]. The number listed here is the corrected one.*

	$B^0 \to J/\psi\ K^0_S \to \mu^+\mu^-\ \pi^+\pi^-$		$B^0 \to J/\psi\ K^0_S \to e^+e^-\ \pi^+\pi^-$	
	TDR	ref. [5]	TDR	ref. [5]
L1 trigger efficiency	62%	55%	45%	35%
lepton tracking in PC	89%	87%	89%	87%
J/ψ vertex+mass	99%	91%	99%	92%
pion tracks (geometry, reconstr.)	63%	50%	63%	55%
K^0_S vertex+mass	97%	93%	97%	93%
B^0 vertex+mass	94%	88%	73%	56%
main vertex	-	92%	-	87%
vertex detector tracking	-	90%	-	90%
lepton particle ID	94%	94%	85%	85%
decay kinematics	80%	-	80%	-
lifetime cut	69%	57%	69%	71%
total	16%	8%	8.3%	3.8%

In case the B meson originates from the decay chain $B^{**+} \to B^0\,\pi^+$ the charge of the pion may be used as a tag. The same charge correlation exists if the pion is the first particle in the fragmentation chain of the b quark.

This "same side tagging" method has successfully been used by CDF [9] and was a powerful tag in their analysis of the golden decay mode [10]. So far this method was not exploited by HERA – B. Hence it is conceivable that the achievable tagging power can be increased.

The expected statistical measurement error on $\sin(2\beta)$ is given by

$$\Delta \sin(2\beta) = \frac{1}{P}\sqrt{\frac{K(t_0)}{N(t_0)}}\sqrt{1+R} \qquad (26)$$

with $N(t_0)$ being the total number of reconstructed golden events with a lifetime $t > t_0$. $K(t_0) = 1.6$ for $t_0 = 0.55$ is a statistical scale factor resulting from the fit of the measured asymmetry using eq. (24) for a given number of events. R is the ratio of background to signal events.

Tab. 50 lists the expected statistical error on $\sin(2\beta)$ for one and four years of running (10^7 s per year) for different scenarios: for the nominal detector at design interaction rate (40 MHz), for a 20% reduced single track reconstruction efficiency and for half the interaction rate. The assumed $b\bar{b}$ production cross section is 12 nb/nucleon. Note that this number is at the lower end of the expectations from measurements [12, 11] ranging from 8 nb/nucleon to about 60 nb/nucleon when scaled to 920 GeV/c proton beam energy.

In the worst case the achievable error on $\sin(2\beta)$ is 0.14 for four years of nominal running of HERA – B. In comparison BaBar, Belle and CDF plan to achieve an error around 0.11 for one year [13, 14, 15]. Even though the situation is less favorable for HERA – B our result will still be valuable. The value of $\sin(2\beta)$ is a fundamental number of the SM and several measurements obtained with different experimental techniques are obligatory, especially if the current central values of CDF on one hand ($\sin(2\beta) = 0.79 \pm 0.44$ [10]) and preliminary results from BaBar ($\sin(2\beta) = 0.12 \pm 0.35$ [16]) and Belle ($\sin(2\beta) = 0.45 \pm 0.45$ [17]) on the other hand sustain with increased statistics. An

Table 50: *The CP reach of HERA – B for different detector scenarios. For the case of a 20% reduced tracking efficiency the* B *meson reconstruction efficiency is reduced by* 0.8^4 *and the tagging efficiencies for the lepton and the kaon tags are scaled by* 80%*.*

	nominal detector	20% reduced trk eff.	half inter. rate
$b\overline{b}$/year	3.7×10^8	3.7×10^8	1.8×10^8
$B^0 + \overline{B^0}$	2.96×10^8	2.96×10^8	1.5×10^8
golden decays	148000	148000	74000
produced $\mu^+\mu^-\ \pi^+\pi^-$ evts	6130	6130	3060
produced $e^+e^-\ \pi^+\pi^-$ evts	6130	6130	3060
reconstr. $\mu^+\mu^-\ \pi^+\pi^-$ evts	490	200	245
reconstr. $e^+e^-\ \pi^+\pi^-$ evts	233	95	116
backgr. fraction in $\mu^+\mu^-$ channel	0	0	0
backgr. fraction in e^+e^- channel	0.1	0.1	0.1
tagging power	0.3	0.28	0.3
error on $\sin(2\beta)$ after 1 year	0.16	0.27	0.23
error on $\sin(2\beta)$ after 4 years	0.08	0.14	0.12

additional measurement even with somewhat lower precision could become very important to clarify the situation.

It has to be realized, of course, that the above projections assume a first level trigger running at design performance, a situation which has been by far missed in the year 2000 commissioning. Should the trigger performance stay much below design, like at a level of 10% of the design efficiency, HERA – B would still be able to show the feasibility of the CP violation measurement using forward spectrometers at hadronic machines but would clearly not be able to contribute in a quantitative way.

5.2.5 CP Violation in $B^0_s \to J/\psi\,\Phi$ Decays

The counterpart to the golden decay mode of B^0_d mesons for the B^0_s meson is the decay to $J/\psi\,\Phi$. The experimentally easily reconstructible final states are in this case $\mu^+\mu^-\ K^+K^-$ and $e^+e^-\ K^+K^-$. For both B mesons it is mainly one decay amplitude which contributes and additional diagrams with different weak phases are expected to be small [219].

There are, however, several important differences between the two cases:

- the oscillation frequency for B^0_s is $x_s > 20$ since the CKM matrix elements of the box diagrams which are relevant for the mixing are much larger. Hence the time integrated asymmetry (eq. (25)) is tiny and a time resolved measurement is mandatory. This requires a good vertex resolution.
- the final state of $J/\psi\,\Phi$ is an admixture of CP-even and CP-odd states since both decay products are vector mesons. For the measurement of the decay distribution an angular analysis is needed.
- the mixing angle for neutral B^0_s is predicted to be small within the Standard Model (~ 0.03) [220]. Hence the observation of sizable CP violation effects would indicate physics beyond the SM.
- the lifetime difference between the CP eigenstates is expected to be much larger than for the B^0_d mesons since the branching fractions for common decay modes of B^0_s and $\overline{B^0_s}$ are not Cabibbo

suppressed [221]. Details are discussed in section 5.2.7.

The decay amplitude depends on the flavor of the B_s^0 meson, the decay width Γ_s, the decay width difference of the CP eigenstates $\Delta\Gamma_s$, the oscillation frequency x_s, the CP violating week phase Φ_s and the decay amplitudes for the different linear polarization states. With a large data sample and a good vertex resolution all parameters can be extracted with this decay mode.

Experimentally the "angular integrated" CP asymmetry is easier to measure

$$A_{\mathrm{ang\_int}}(t) = \frac{D_p}{F_+(t) \; + \; (1-D_p)F_-(t)} \sin(x_s t) \sin\Phi_s \quad , \tag{27}$$

with $D_p = 0.9 \ldots 0.5$ [222] being the "dilution" from the admixture of the different CP eigenstates, and with the functions

$$F_\pm(t) = \frac{1}{2}\left[(1 \pm \cos\Phi_s)\exp\left(+\frac{\Delta\Gamma_s\, t}{2\Gamma_s}\right) \; + \; (1 \mp \cos\Phi_s)\exp\left(-\frac{\Delta\Gamma_s\, t}{2\Gamma_s}\right)\right] \tag{28}$$

causing a slow modulation of the oscillation amplitude. The decay time t is measured in units of life times.

For finite decay time resolution σ_t the CP asymmetry will be washed out by a factor

$$D_s = \exp\left(-0.5 \cdot (x_s\, \sigma_t \Gamma_s)^2\right) \quad , \tag{29}$$

with

$$(\sigma_t)^2 = \left(\frac{m_B}{\langle p\rangle}\sigma_L\right)^2 + \left(\frac{\sigma_p}{p}\, t\right)^2 . \tag{30}$$

Here, σ_L is the decay length resolution and σ_p is the B momentum resolution. For HERA – B we expect from simulations $\sigma_p/p = 0.25\%$ for the $\mu^+\mu^-$ K^+K^- channel and $\sigma_p/p = 1.4\%$ for the e^+e^- K^+K^- channel [223]. The decay length resolution is about $450\,\mu$m for a topological vertex fit and improves to about $350\,\mu$m for a fit using mass constraints. With $m_B/\langle p\rangle = 1/(22\,c)$ one gets for the resolution of the constrained vertex fit $\sigma_t\Gamma_s = 3.5\%$ which is dominated by the decay length resolution. For $x_s = 25$ this yields $D_s = 0.68$.

To estimate the error on a measurement of $\sin\Phi_s$ eq. (26) is modified to

$$\Delta\sin\Phi_s = \frac{1}{P \cdot D_s \cdot D_p}\sqrt{\frac{K(t_0)}{N(t_0)}}\sqrt{1+R} \tag{31}$$

The reconstruction efficiency can be inferred from the one for $B^0 \to J/\psi\, K_S^0$ and the relative efficiency of reconstructing Φ decays (33% [223]) as compared to K_S^0 decays (46%, Tab. 49). Note that at least one kaon is required to be identified with the RICH detector in this analysis and both kaons point to a common vertex. The background fractions are thus expected to be small and are assumed to be similar to the ones for the golden decay mode.

Due to the fast oscillation of the CP asymmetry, the scaling factor $K(t_0)$ is close to 2 and independent of t_0. The precision of the measurement is therefore diminished by a decay time cut $t > t_0$.

Tab. 51 lists for $x_s = 25$ and $D_p = 0.7$ the expected measurement precision after 4 years of running for the three scenarios also assumed in Tab. 50. Obviously, the observation of a small CP asymmetry with the HERA – B experiment is very unlikely and, even for an unexpectedly large weak

Table 51: *CP reach for a measurement of* $\sin\Phi_s$. *The numbers are calculated for* $x_s = 25$.

	nominal detector	20% reduced trk eff.	half inter. rate
$b\bar{b}$/year	3.7×10^8	3.7×10^8	1.8×10^8
$B_s^0 + \overline{B_s^0}$	7.4×10^7	7.4×10^7	3.7×10^7
$J/\psi\,\Phi$	67000	67000	33500
prod. $\mu^+\mu^-$ K^+K^- evts	1970	1970	980
prod. e^+e^- K^+K^- evts	1970	1970	980
reconstr. $\mu^+\mu^-$ K^+K^- evts	117	48	58
reconstr. e^+e^- K^+K^- evts	56	22	30
backgr. frac. in $\mu^+\mu^-$ channel	0	0	0
backgr. frac. in e^+e^- channel	0.1	0.1	0.1
tagging power	0.3	0.28	0.3
error on $\sin\Phi_s$ after 1 year	0.8	1.3	1.1
error on $\sin\Phi_s$ after 4 years	0.4	0.65	0.55

phase Φ_s, the reconstruction efficiency has to be improved in order to establish clear evidence for CP violation.

Alternatively, an angular analysis can be performed. The interference terms between CP-even and CP-odd final states are proportional to [222]

$$e^{-\Gamma_s t}\left(1 - e^{-\Delta\Gamma_s t}\right)\sin\Phi_s \quad . \tag{32}$$

and can in principle be used to measure $\sin\Phi_s$. Note that these terms have the same sign for B_s^0 and $\overline{B_s^0}$ mesons and there is no oscillation involved. Consequently this analysis can be performed with an *untagged* event sample. However for $\Delta\Gamma_s \simeq 0.2\,\Gamma_s$ the factor $e^{-\Gamma_s t}\,(1 - e^{-\Delta\Gamma_s t})$ is very small. With the statistics of HERA – B this technique is therefore not likely to improve the sensitivity.

In conclusion, even in the most optimistic scenario, HERA – B will probably not be able to contribute to the test of CP violation in $B_s^0 \to J/\psi\,\Phi$ decays in any significant way.

5.2.6 Exclusive Lifetimes of Beauty Hadrons

The precise determination of a number of exclusive B hadron lifetimes and of their ratios would be very useful in validating some of the most popular techniques currently used in the theory of B decays, like the heavy quark mass expansion, or the theory of inclusive decays based on the operator product expansion [225].

Today, several of these ratios, notably the ratios of the Λ_b baryon lifetime and the B meson lifetimes deviate significantly from their predicted values [225]. Hence the interest on new and improved measurements.

At HERA – B, several lifetime determinations become available. Particularly simple are those based on decays to J/ψ channels. Tab. 52 summarizes the present knowledge for reconstruction efficiencies for the most interesting decays. The numbers are partly taken or inferred from various simulations, performed for other physics studies, and are partly simply guessed. The reconstruction efficiencies for the decays $K^{*0} \to K^+\pi^-$ and $\Phi \to K^+K^-$ should be similar but were taken from different analyses with different cleaning cuts (especially concerning the particle identification). The

Table 52: *Summary of efficiencies and expected statistics for the lifetime measurements using the most important exclusive decays with a* J/ψ *meson in the final state. The numbers are based on one year (two years) of running at an interaction rate of* 40 MHz *(*20 MHz*).*

	$B^+ \to J/\psi K^+ \to \ell^+\ell^- K^+$	$B^0 \to J/\psi K^{*0} \to \ell^+\ell^- K^+\pi^-$	$B_s^0 \to J/\psi\Phi \to \ell^+\ell^- K^+K^-$	$\Lambda_b \to J/\psi\Lambda \to \ell^+\ell^- p\pi^-$
$b\overline{b}$	3.7×10^8	3.7×10^8	3.7×10^8	3.7×10^8
b hadrons	3.0×10^8	3.0×10^8	7.4×10^7	7.4×10^7
exclusive decays	32400	33600	4000	2800
trigger eff. $(\mu^+\mu^-)$	55%	55%	55%	55%
(e^+e^-)	35%	35%	35%	35%
J/ψ reconstruction	64%	64%	64%	64%
associated tracks	80%	54%	33%	40%
b had. reco. $(\mu^+\mu^-)$	88%	88%	88%	88%
(e^+e^-)	56%	56%	56%	56%
main vertex reco.	90%	90%	90%	90%
5 σ vertex cut	85%	85%	85%	81%
observed decays	4300	3020	220	180
σ_τ [ps]	0.024	0.028	0.10	0.09

differences between these two efficiencies are indicative of the accuracy to which the numbers in the table are known. The event numbers in Tab. 52 are obtained using the default $b\overline{b}$ production cross section of 12 nb per nucleon, and one year of running at 40 MHz interaction rate, or equivalently two years at 20 MHz. The obtainable precisions are summarized in Tab. 53. They are comparable to the current world-average errors from the PDG [226] which are also shown for comparison.

Table 53: *Precisions expected for exclusive lifetimes measurements after one year of* HERA – B *running at interaction rates of* 40 MHz*, or equivalently two years of running at* 20 MHz*, together with current world-average errors.*

Channel	HERA – B	World average error
$B^+ \to J/\psi K^+$	0.024 ps	0.04 ps
$B^0 \to J/\psi K^{*0}$	0.028 ps	0.04 ps
$B_s^0 \to J/\psi\Phi$	0.10 ps	0.06 ps
$\Lambda_b \to J/\psi\Lambda$	0.09 ps	0.05 ps

The numbers in Tab. 53 take into account the expected z resolution of the decay vertex position. The decay length resolution averages to about 500 μm, which combined with an average $\gamma\beta$ factor for B hadrons around 22, gives a decay length significance

$$\frac{\sigma_z}{\gamma\beta c\tau} \sim 0.05 \quad , \tag{33}$$

which is significantly better than that of, for instance, CDF. More detailed analyses have been performed, in particular on the $B_s^0 \to J/\psi\Phi$ channel (that are discussed in sections 5.2.5 and 5.2.7), and they give results consistent with the above numbers.

At the e^+e^- B factories, only the lifetimes of the B^0 and the B^+ mesons can be measured. The precision is not better than that expected for HERA – B. All exclusive lifetimes listed in Tab. 53 are of course accessible at the Tevatron experiments during RUN II. While the current world averages are dominated by the LEP/SLC experiments, the collider experiments will become the strongest competitors in this field with largely increased statistics and improved vertex detectors. Detailed projections from the collider experiments are not available, but scaling from the results of the Tevatron RUN I, the obtainable precisions are expected to be comparable or slightly better than those of HERA – B. Nevertheless, the exclusive lifetime measurement remains a valid and important physics topic for HERA – B, assuming, however, that the J/ψ trigger chain comes reasonably close to its design performance.

5.2.7 Measurement of $\Delta\Gamma_s$ from $B_s^0 \to J/\psi\Phi$ Decays

Theory predicts sizable differences between the lifetimes of the two B_s^0 mass eigenstates [227, 228], recent predictions from lattice HQET theory (in the quenched approximation), matched to next-to-leading order perturbative QCD, being [229, 230]

$$\frac{\Delta\Gamma_s}{\Gamma_s} = 0.050 \pm 0.025 \quad . \tag{34}$$

Here, $\Delta\Gamma_s \equiv \Gamma_L - \Gamma_H$ is the difference between the total widths of the light and the heavy B_s^0 mass eigenstates. There is a theoretically well established relationship between the lifetime difference and the mass difference, $\Delta m_s \equiv M_H - M_L$ which, apart from a QCD correction factor, is given by [228]

$$\frac{\Delta\Gamma_s}{\Delta m_s} = \frac{3\pi}{2}\frac{m_b^2}{m_t^2\, h(m_t^2/M_W^2)}\left(1 - \frac{8m_c^2}{3m_b^2}\right) \quad . \tag{35}$$

Here, $h(m_t^2/M_W^2)$ is a smooth function with values close to one. Note that the prediction does not depend on any element of the CKM matrix. The numerical value is known with poor precision, which should improve in the next few years [228],

$$\frac{\Delta\Gamma_s}{\Delta m_s} = (4.3 \pm 2.0) \times 10^{-3} \quad . \tag{36}$$

Therefore, by measuring the lifetime difference one could indirectly get a new handle on the mass difference, which, when combined with Δm_d, measures $|V_{ts}/V_{td}|$ and provides the length of one of the sides of the unitarity triangle. It should be noted that the previous equation implies that larger values of Δm_s which are more difficult to measure correspond to similarly larger values of $\Delta\Gamma_s$ which are less difficult to measure.

Experimentally, no direct measurement of $\Delta\Gamma_s$ is available up to now. From different lifetime measurements, a limit of $\Delta\Gamma_s/\Gamma_s < 0.66$ (90% C.L.) can be extracted [27].

There are several techniques for measuring $\Delta\Gamma_s$:

- One can measure CP specific lifetimes. For instance, the decay $B_s^0 \to D_s^+ D_s^-$ results in a CP-even final state and, therefore, measures (approximately) $1/\Gamma_L$. Since the average lifetime is well known (and, furthermore, it can be assumed to be equal to the average B_d lifetime) the difference can be obtained.
- One can use flavor specific channels and try to measure two lifetime components in the proper decay time distribution. Possible decay channels are $B_s^0 \to D_s^- \pi^+(\pi^+\pi^-)$, $B_s^0 \to D_s^- \ell^+ \nu_\ell$, etc..

- Approximate CP eigenstates can also be used, in a method similar to the first proposed above. Among those, the most readily accessible in HERA – B is produced in the decay $B_s^0 \to J/\psi\Phi$, which goes to a CP-even final state when the relative angular momentum among the two particles in the final state is 0 (or, more generally, even) and goes to a CP-odd final state when it is 1 (or odd). The $L = 0$ component is supposed to be dominant. This can be checked by studying the angular distribution of the final state. This particular channel has been studied in detail and it will be discussed in some detail in the following.

The branching ratio for $B_s^0 \to J/\psi\Phi$ is around one per mill, which implies that about 4000 events could be produced in one year of running at an interaction rate of 40 MHz, or equivalent in two years of running at 20 MHz, if adding the two channels $J/\psi \to e^+e^-$ and $J/\psi \to \mu^+\mu^-$. The reconstruction has been studied in great detail but is still suffering from not understood inefficiencies of the reconstruction chain which is currently optimized for the year 2000 detector scenario. Some of the numbers of the simulation are included in Tab. 52. In total, assuming realistic numbers for the performance of the improved detector and software, one expects to reconstruct about 220 decays (after applying a decay length cut at a $5\,\sigma$ level), from which the lifetime can be obtained with a precision of 0.10 ps. The lifetime difference is then obtained from

$$\frac{\Delta\Gamma_s}{\Gamma_s} = 2\left(1 - \frac{\tau_L}{\overline{\tau}}\right) \quad , \tag{37}$$

with

$$\delta\left(\frac{\Delta\Gamma_s}{\Gamma_s}\right) \approx 2\left[\left(\frac{\delta\tau_L}{\tau_L}\right)^2 + \left(\frac{\delta\overline{\tau}}{\overline{\tau}}\right)^2\right]^{1/2} \quad . \tag{38}$$

Here, $\overline{\tau}$ is the average B_s^0 lifetime which can be taken to be approximately equal to the very well measured average B_d lifetime. A 0.10 ps determination of τ_L from $B_s^0 \to J/\psi\Phi$ would translate into determination of $\Delta\Gamma_s/\Gamma_s$ with an error of 0.14. Even after several years of running and with improved performance of the reconstruction performance this precision is probably marginal for a direct measurement, especially if one takes into account that, if the assumption of a pure CP-even final state is not appropriate and an angular analysis is necessary, the precision will be further deteriorated by dilution factors.

The by far largest available sample of $B_s^0 \to J/\psi\Phi$ decays, consisting of 58 ± 12 events with a signal to background ration of about 1, has been collected with the CDF detector [231]. Our expected event sample is much larger and, because of the superior particle identification, the background will be smaller.

This measurement cannot be attempted at the B factories, because they do not produce B_s^0 mesons. In the upcoming Tevatron RUN II, however, CDF will increase the statistics by one to two orders of magnitude which should hence result in a much more precise measurement of $\Delta\Gamma_s/\Gamma_s$. Preliminary estimates of CDF are based on extrapolations from the Tevatron RUN I and give projected errors of 0.065 on $\Delta\Gamma_s/\Gamma_s$ for an integrated luminosity of $2\,\mathrm{fb}^{-1}$, corresponding to roughly two years of running [232]. Therefore, the competitiveness of HERA – B looks rather weak in this measurement.

5.2.8 Rare Decays $B^0 \to \ell^+\ell^-(X_s)$

Rare B decays include decays containing two types of transitions on the quark level: $b \to u$ transitions which are Cabibbo-suppressed and $b \to s, d$ transitions which are flavor changing neutral currents (FCNC) and thus forbidden at tree level in the Standard Model (SM) [233]. Rare B decays are an important testing ground of the SM because they allow to probe the detailed structure of the SM beyond tree level. Furthermore they offer an important strategy in the search for new physics since they probe the indirect effects of new particles and interactions in higher order processes [22].

This section concentrates on two exclusive rare decay channels of the B meson. The purely leptonic decays $\mathrm{B}^0_{\mathrm{d,s}} \to \mu^+\mu^-$, having a very clean experimental signature[61] but an extremely small branching fraction, are out of reach to be measured directly in HERA – B. Any sign of these decays would clearly signal new physics. The decay $\mathrm{B}^0 \to \mathrm{K}^{*0}\mu^+\mu^-$, however, is approximately as rare as the golden decay $\mathrm{B}^0 \to \mathrm{J}/\psi\, \mathrm{K}^0_{\mathrm{S}}$, and has a clean experimental signature. Its detection is of great theoretical interest since it would allow to directly test the SM at the loop level.

Theoretical overview

At quark level transitions of b quarks are commonly described in a model-independent way by an effective low-energy Hamiltonian obtained from the operator product expansion (OPE) by integrating out virtual contributions of heavy particles (e.g. top quark, W boson). For the $\mathrm{b} \to \mathrm{q}\,(\mathrm{q} = \mathrm{d, s})$ transitions considered in this chapter the effective Hamiltonian reads

$$\mathcal{H}_{\mathrm{eff}}(\mathrm{b} \to \mathrm{q}) = -4\,\frac{G_{\mathrm{F}}}{\sqrt{2}} V_{\mathrm{tb}} V^*_{\mathrm{tq}} \sum_{i=1}^{10} C_i(\mu) O_i(\mu) \quad . \tag{39}$$

Here G_{F} is the Fermi coupling constant and $V_{\mathrm{tb}}V^*_{\mathrm{tq}}$ are the CKM matrix elements with $\mathrm{q} = \mathrm{d, s}$.[62] The Wilson coefficients $C_i(\mu)$ parameterize the short distance contributions to the decay. They can be calculated in perturbative QCD at the electroweak scale and evolved to the scale $\mu \sim \mathcal{O}(m_{\mathrm{b}})$ by means of the renormalization group equations (RGE). The $O_i(\mu)$ are local renormalized operators with different color and Dirac structures. The relevant operators for the decays treated in this chapter will be given below. Note that the scale μ is chosen such that it separates the short distance contributions (i.e. scales higher than μ) contained in $C_i(\mu)$ from the long distance contributions (i.e. scales lower than μ) present in $O_i(\mu)$ [234].

The decays $\mathrm{B}^0_{\mathrm{d,s}} \to \mu^+\mu^-$

The purely muonic decays $\mathrm{B}^0_{\mathrm{q}} \to \mu^+\mu^-$ $(\mathrm{q} = \mathrm{d, s})$ are governed by two operators (39),

$$O_{9\mathrm{V}} = (\bar{\mathrm{q}}\mathrm{b})_{\mathrm{V-A}}(\bar{\mu}\mu)_{\mathrm{V}} \quad , \qquad O_{10\mathrm{A}} = (\bar{\mathrm{q}}\mathrm{b})_{\mathrm{V-A}}(\bar{\mu}\mu)_{\mathrm{V-A}} \quad ,$$

with V and A denoting vector and axial currents, respectively. In the SM these transitions are dominated by electroweak penguin diagrams with Z^0 exchange and box diagrams with $\mathrm{W}^{\pm}$ exchange. The SM branching fractions are given by [233] (refer to [235] for a review of the NLO QCD corrections):

$$B(\mathrm{B}^0_{\mathrm{d}} \to \mu^+\mu^-) = (1.0 \pm 0.5) \times 10^{-10} \left[\frac{F_{\mathrm{B}^0_{\mathrm{d}}}}{200\,\mathrm{MeV}}\right]^2 \left[\frac{\overline{m}_{\mathrm{t}}(m_{\mathrm{t}})}{167\,\mathrm{GeV}}\right]^{3.12} \left[\frac{|V_{\mathrm{td}}|}{0.0074}\right]^2 \left[\frac{\tau_{\mathrm{B}^0_{\mathrm{d}}}}{1.56\,\mathrm{ps}}\right] \tag{40}$$

and

$$B(\mathrm{B}^0_{\mathrm{s}} \to \mu^+\mu^-) = (3.7 \pm 1.0) \times 10^{-9} \left[\frac{F_{\mathrm{B}^0_{\mathrm{s}}}}{230\,\mathrm{MeV}}\right]^2 \left[\frac{\overline{m}_{\mathrm{t}}(m_{\mathrm{t}})}{167\,\mathrm{GeV}}\right]^{3.12} \left[\frac{|V_{\mathrm{ts}}|}{0.040}\right]^2 \left[\frac{\tau_{\mathrm{B}^0_{\mathrm{s}}}}{1.54\,\mathrm{ps}}\right] \quad . \tag{41}$$

[61] Decays with lepton pairs in the final state are often referred to as "self-triggering" decays.

[62] Due to the dominance of top quark exchange the most important contributions are from V_{tb} and V_{tq}.

The factors $F_{\mathrm{B}_\mathrm{q}^0}$ denote the leptonic decay constants of the B meson (which can be calculated e.g. in lattice QCD), $\overline{m}_\mathrm{t}(m_\mathrm{t})$ is the "running" top quark mass at the scale of the top mass, and $\tau_{\mathrm{B}_\mathrm{q}^0}$ are the lifetimes of the B mesons. The main theoretical uncertainties in the branching fractions result from the decay constants which have errors of $\mathcal{O}(10-20\%)$ [234, 233]. Given a reliable calculation or a measurement of the decay constants $F_{\mathrm{B}_\mathrm{q}^0}$, it should be possible to measure the ratio $|V_\mathrm{td}|/|V_\mathrm{ts}|$ from the ratio of the branching fractions (40) and (41) [234]. Obviously, the SM branching fractions (40) and (41) are too small to be observed, even when assuming the nominal expected number of 7×10^7 B_s^0 mesons produced per year in the fully operational HERA – B experiment.

Due to the dominance of the top quark exchange in the decay amplitudes these decays are sensitive probes for new physics [233]. Several scenarios of physics beyond the SM predict an enhancement in the branching fraction, e.g. multi-Higgs-doublet models, left-right symmetric models and supersymmetric models (for an overview refer to [236]). Expectations for various Technicolor models can be found in [237]. A typical value for the enhancement of the branching fraction due to new physics is approx. a factor of 10. Such an enhancement has been recently shown in a two-Higgs-doublet model, a very modest extension of the SM [238].

The latest experimental limits for these decays have been published by the CDF collaboration in 1998 [239, 27]. Limits on the branching fraction in the channel $\mathrm{B}_\mathrm{d}^0\to\mu^+\mu^-$ have been published by CLEO (for a review cf. [25]). Taking into account the improvement in luminosity gained in the Tevatron RUN II – the total integrated luminosity is expected to be $2\,\mathrm{fb}^{-1}$ – and the detector upgrades of CDF and DØ better limits are expected in the future [24]. A compilation of the current limits and the expectations can be found in Table 54.

Table 54: $\mathrm{B}_\mathrm{d}^0\to\mu^+\mu^-$ *and* $\mathrm{B}_\mathrm{s}^0\to\mu^+\mu^-$*: Experimental limits for the branching fraction at* 90% CL *and expectations for Tevatron RUN II (taken from [239] and [25]).*

Decay	Branching fract. (CDF)	Branching fract. (CLEO)	expected for Tevatron II
$\mathrm{B}_\mathrm{d}^0\to\mu^+\mu^-$	$<6.8\times10^{-7}$	$<5.9\times10^{-6}$	3×10^{-8}
$\mathrm{B}_\mathrm{s}^0\to\mu^+\mu^-$	$<2.0\times10^{-6}$	–	1×10^{-7}

The sensitivity for $\mathrm{B}_\mathrm{d}^0\to\mu^+\mu^-$ in BABAR[63] has been studied for an integrated luminosity of $30\,\mathrm{fb}^{-1}$ (cf. [22] and references therein). The 90% CL upper limit on the branching fraction is expected in the order of $B(\mathrm{B}_\mathrm{d}^0\to\mu^+\mu^-)<5.0\times10^{-7}$. Even using the full data sample of $300\,\mathrm{fb}^{-1}$ BABAR will not be competitive with the Fermilab collider experiments, so the main interest will be to improve constraints for new physics [22].

The sensitivity of HERA – B to detect the decay $\mathrm{B}_\mathrm{s}^0\to\mu^+\mu^-$ is roughly estimated in Tab. 55, assuming an interaction rate of 20 MHz and a conservative single track reconstruction efficiency of 80%. The geometrical acceptance has been estimated from Monte Carlo simulations, the pretrigger and trigger efficiencies are guessed from the expectations derived for the first level J/ψ trigger and folding in the current experience with the SLT. In order to be able to derive an upper limit, additional cuts have to be applied to suppress possible backgrounds. Obvious possibilities are cuts on the (transverse) momenta of the muons, cuts on the decay length of the B_s^0 mesons[64], and cuts on the di-muon invariant mass[65], which are expected to have a very large efficiency for the signal. If necessary, a lepton tag from the associated b hadron can be required which would, however, reduce the signal sensitivity by almost an order of magnitude. Since no detailed simulations have been performed, an

[63] B_s^0 mesons cannot be produced in an $\mathrm{e}^+\mathrm{e}^-$ B factory.

[64] The vertex resolution was found to be $350\,\mu\mathrm{m}$ in the simulation.

[65] The mass resolution was found to be $210\,\mathrm{MeV/c^2}$ in the simulation.

unknown efficiency ϵ_{bkg}, representing the reduction of the signal due to the background eliminating cuts, has been introduced in Tab. 55.

Table 55: *Estimate of HERA – B sensitivity to detect the* $\mathrm{B_s^0} \to \mu^+\mu^-$ *decay for* 4 *years of running at a (reduced) interaction rate of* 20 MHz *and an assumed conservative single track reconstruction efficiency of* 80%. *The (unknown) efficiency of all cuts needed in order to suppress possible background is denoted by* ϵ_{bkg}.

$\mathrm{b\bar{b}}$ per year	1.8×10^8
$\mathrm{B_s^0} + \overline{\mathrm{B_s^0}}$ per year	3.7×10^7
geometrical acceptance	64%
muon pretrigger	95%
FLT	70%
SLT	85%
reconstruction efficiency	64%
background cleaning cuts	ϵ_{bkg}
total efficiency	$0.23 \times \epsilon_{bkg}$
90% CL sensitivity for $\mathrm{Br}(\mathrm{B_s^0} \to \mu^+\mu^-)$ (after 4 years)	$0.7 \times 10^{-7}/\epsilon_{bkg}$

The overall product of acceptance and efficiency for the detection of the decay $\mathrm{B_s^0} \to \mu^+\mu^-$ can thus be expected to be $23\% \times \epsilon_{bkg}$. This implies a 90% CL sensitivity of $0.7 \times 10^{-7}/\epsilon_{bkg}$ of HERA – B to detect a signal after a four year running period. If ϵ_{bkg} can be kept larger than 10% and the di-muon trigger is performing at least with the performance assumed in Tab. 55, this result is not only better than current limits but also interesting, if not competitive in view of the expected sensitivity of the Tevatron RUN II.

The decay $\mathrm{B^0} \to \mathrm{K^{*0}}\mu^+\mu^-$

From the theoretical point of view, a measurement of the fully inclusive non-resonant FCNC decay $\mathrm{B^0} \to \mu^+\mu^-\mathrm{X}$ represents an ideal testing ground for the standard model due to the absence of uncertainties from the hadronic final state. The exclusive decay channel $\mathrm{B^0} \to \mathrm{K^{*0}}\mu^+\mu^- \to \mathrm{K^+}\pi^-\mu^+\mu^-$, chosen to characterize the HERA – B potential in searching for FCNC decays, is theoretically more difficult to treat, but has a very clean experimental signature, giving powerful handles for background suppression, and still has a large branching fraction, only about a factor three smaller than that of the inclusive decay.

The decay is governed by three operators (39):

$$O_{7\gamma} = \frac{e}{8\pi^2} m_{\mathrm{b}} \bar{s}_\alpha \sigma^{\mu\nu}(1+\gamma_5) b_\alpha F_{\mu\nu}, \qquad O_{9\mathrm{V}} = (\bar{q}b)_{\mathrm{V-A}}(\bar{\mu}\mu)_{\mathrm{V}}, \qquad O_{10\mathrm{A}} = (\bar{q}b)_{\mathrm{V-A}}(\bar{\mu}\mu)_{\mathrm{V-A}},$$

$F^{\mu\nu}$ being the electro-magnetic field strength tensor and thus $O_{7\gamma}$ being the magnetic penguin [234]. The corresponding Wilson coefficients are commonly re-defined as follows:

- $C_{7\gamma}^{(0)\mathrm{eff}}$ absorbs the large effects of short distance QCD induced by two-loop diagrams that mix the operators $(O_1 \ldots O_6)$ with the operators (O_7, O_8) [22].
- $C_{9\mathrm{V}}^{\mathrm{eff}}$ contains physics at the weak scale and from the RGE evolution between M_{W} and m_{b} as well as contributions from $(O_1 \ldots O_6)$ including loops with light quark flavors [22]. Note that con-

trary to the inclusive decay, $C_{9V}^{\rm eff}$ does not contain contributions from virtual and bremsstrahlung corrections [233]. These are absorbed in the hadronic matrix element described below.

- C_{10A} does not depend on the renormalization scale but rather only on the top quark mass [234].

The hadronic matrix elements

$$\langle\, \mathrm{K}^{*0}(p',\epsilon) \,|\, \bar{s}\gamma_\mu(1-\gamma_5)b \,|\, \mathrm{B}^0_\mathrm{d}(p)\,\rangle, \qquad \langle\, \mathrm{K}^{*0}(p',\epsilon) \,|\, \bar{s}\sigma_{\mu\nu}q^\nu\frac{1}{2}(1+\gamma_5)b \,|\, \mathrm{B}^0_\mathrm{d}(p)\,\rangle$$

denoting with p, p' the four-momenta of the B^0_d and K^{*0} and with ϵ the K^{*0} polarization, are commonly parameterized in terms of form factors.

An important observable in this decay is the di-muon invariant mass spectrum or equivalently the differential decay rate as a function of $\tilde{s} = \frac{q^2}{M_\mathrm{B}^2}$ with q^2 being the squared invariant mass of the di-muon system and M_B being the B meson mass. These observables contain perturbative and non-perturbative contributions from intermediate $\mathrm{c\bar{c}}$ pairs in the process $\mathrm{B}^0 \to \mathrm{K}^{*0}\,\mathrm{c\bar{c}} \to \mathrm{K}^{*0}\,\mu^+\mu^-$, namely a continuum of $\mathrm{c\bar{c}}$ states and effects of the $\mathrm{c\bar{c}}$ resonances J/ψ and ψ'. The SM prediction for the differential decay rate is shown in Fig. 166 (for details refer to [243]).

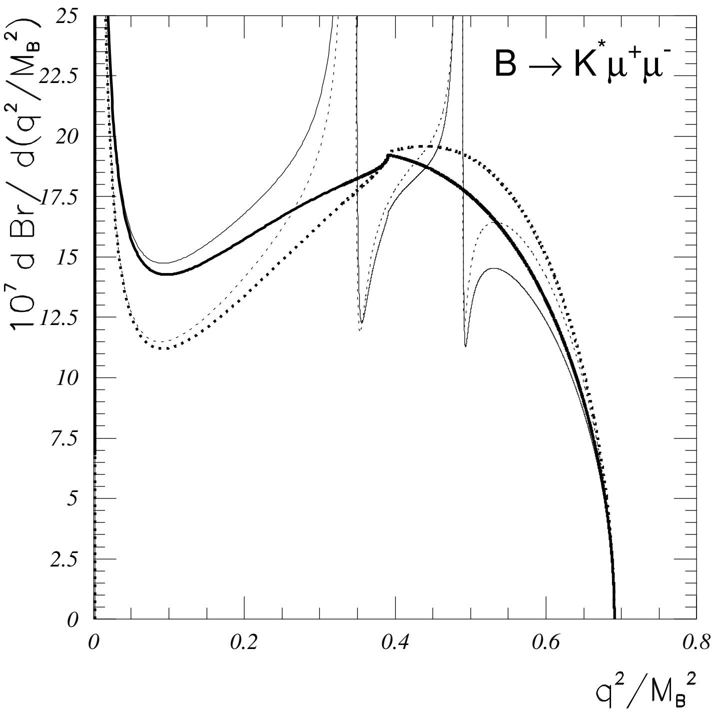

Figure 166: *Differential decay rate as a function of* $\frac{q^2}{M_\mathrm{B}^2}$ *for the decay* $\mathrm{B}^0 \to \mathrm{K}^{*0}\mu^+\mu^-$ *in the SM [243]. Solid and dotted lines refer to different models for calculation of the form factors. Thick lines: non-resonant parts, thin lines: total contribution.*

Another important observable is the lepton forward-backward asymmetry defined as

$$A_\mathrm{FB}(\hat{s}) = \frac{\int_0^1 \mathrm{d}\cos\theta\, \frac{\mathrm{d}^2\mathrm{Br}}{\mathrm{d}\cos\theta\,\mathrm{d}\hat{s}} - \int_{-1}^0 \mathrm{d}\cos\theta\, \frac{\mathrm{d}^2\mathrm{Br}}{\mathrm{d}\cos\theta\,\mathrm{d}\hat{s}}}{\int_0^1 \mathrm{d}\cos\theta\, \frac{\mathrm{d}^2\mathrm{Br}}{\mathrm{d}\cos\theta\,\mathrm{d}\hat{s}} + \int_{-1}^0 \mathrm{d}\cos\theta\, \frac{\mathrm{d}^2\mathrm{Br}}{\mathrm{d}\cos\theta\,\mathrm{d}\hat{s}}}\quad , \tag{42}$$

where θ is the angle between the momentum of the B_d^0 and the μ^+ in the di-muon center-of-mass frame (cf. Fig. 167). The FB asymmetry probes the parity structure of the electroweak interaction: for small $\hat{s}$ the parity-conserving γ exchange is the dominant process, so that A_{FB} is small, whereas for large $\hat{s}$ the asymmetry grows due to the effects of the W and Z exchange [243]. Moreover, the FB asymmetry is sensitive to the relative signs of the Wilson coefficients $C_{7\gamma}^{(0)\mathrm{eff}}$ and C_{9V}^{eff}. Since the SM prediction of the asymmetry is nearly independent of the model involved, deviations from the SM expectation, e.g. $A_{FB} < 0$ for small $\hat{s}$ or a shift in the zero-crossing of the asymmetry function, would be a clear signal for new physics [233].

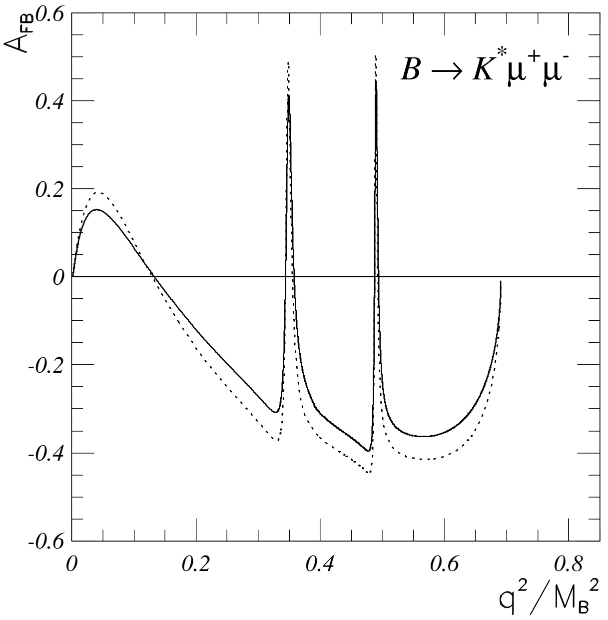

Figure 167: *SM forward-backward asymmetries in the* $B^0 \to K^{*0}\mu^+\mu^-$ *transition as a function of* $\tilde{s} = \frac{q^2}{M_B^2}$ *in various models [243].*

The form factors have been calculated/estimated in various models. Constraints from lattice QCD are discussed in [240]. In [241] a QCD relativistic potential model has been used, whereas in [242] a light-cone sum rule approach including radiative corrections has been chosen. Calculations in a lattice constrained dispersion quark model can be found in [243], and QCD power corrections have been calculated using the heavy quark expansion (HQE) technique and a Fermi motion model for the b quark in the B meson [244].

In stating the branching fraction for $B^0 \to K^{*0}\mu^+\mu^-$ the resonant part of the spectrum is often cut away. A compilation of the non-resonant branching fraction in various models can be found in Table 56 (taken from [243]).

The influence of new physics on branching fractions, form factors and FB asymmetry has been discussed for many extensions of the SM. In [246] the decay is treated in a two-Higgs-doublet model using QCD sum rules, whereas in [247] effects of a fourth generation of fermions are taken into account. The influence of anomalous couplings of the third quark generation are discussed in [248]. A discussion of the sensitivity of the triple gauge boson (WWZ) couplings for new physics can be found in [249]. Correlations between CP violation and FB asymmetries in various supersymmetric models (SUSY) have been worked out in [250]. In [251] the effects of neutral Higgs bosons in SUSY

Table 56: *Non-resonant branching fractions of the decay* $\mathrm{B}^0 \to \mathrm{K}^{*0}\mu^+\mu^-$ *in various models [243]*
.

Model	Branching fraction
quark model (QM) [243] $\times \lvert V_{ts}/0.038\rvert^2$	1.15×10^{-6}
lattice constrained QM [243] $\times \lvert V_{ts}/0.041\rvert^2$	1.10×10^{-6}
Ali [245]	$(1.5 \pm 0.6) \times 10^{-6}$

theories are described. The decay can also be analyzed in a model-independent way using the 10 local operators in (39) [252] or taking into account also two non-local operators [253].

Recent experimental limits for the decay $\mathrm{B}^0 \to \mathrm{K}^{*0}\mu^+\mu^-$ are given in Table 57. Note that they are only a factor of 4 away from the SM prediction.

Table 57: *Experimental limit on* $\mathrm{B}^0 \to \mathrm{K}^{*0}\mu^+\mu^-$ *at* 90% CL*. The DØ experiment has only examined the inclusive decay* $\mathrm{B}^0 \to \mathrm{X_s}\mu^+\mu^-$*.*

Experiment	Decay	Branching fraction
CDF [254]	$\mathrm{B}^0 \to \mathrm{K}^{*0}\mu^+\mu^-$	$< 4.0 \times 10^{-6}$
DØ [255]	$\mathrm{B}^0 \to \mathrm{X_s}\mu^+\mu^-$	$< 3.2 \times 10^{-4}$
CLEO [256]	$\mathrm{B}^0 \to \mathrm{K}^{*0}\mu^+\mu^-$	$< 9.5 \times 10^{-6}$

The decay $\mathrm{B}^0 \to \mathrm{K}^{*0}\mu^+\mu^-$ has been studied extensively by the BABAR collaboration (cf. [22] and references therein) as well as by the LHC experiments [233]. The BABAR collaboration, expects a final statistics of a handful of signal events. The CDF collaboration quotes a higher sensitivity, down to a branching fraction of 2×10^{-7} (corresponding to roughly 10 events) with the expected integrated luminosity of $2\,\mathrm{fb}^{-1}$ for Tevatron RUN II [24] and should therefore be able to detect the decay. To gain enough statistics to measure the mass spectrum and the FB asymmetry, however, an integrated luminosity of $\mathcal{O}(10\ \mathrm{fb}^{-1})$ would be needed [25]. Any potential of HERA – B to measure this FCNC process is therefore important in order to increase the world statistics necessary for sensitive tests of the standard model.

The HERA – B potential has been estimated on the basis of preliminary Monte Carlo studies, aimed primarily at the determination of detection efficiencies and acceptances, rather than an in depth analysis of possible background sources. The results are summarized in Tab. 58, assuming a (reduced) total interaction rate of 20 MHz and a conservative reconstruction efficiency of 80% per track. Some plausible cuts on (transverse) momenta and a strong cut on the decay distance (at 5 mm) were applied in order to suppress backgrounds. The trigger efficiency is denoted by ϵ_{trig}. At design performance it is expected to be of the order 50% to 60%, when restricted to the di-muon invariant mass range above the lower trigger threshold. The efficiency for the non-resonant decay $\mathrm{B}^0 \to \mathrm{K}^{*0}\mu^+\mu^- \to \mathrm{K}^+\pi^-\mu^+\mu^-$ is smaller (compare Fig. 166) since a substantial fraction of decays leads to small invariant masses of the di-muon system. Also, the mass region of resonant J/ψ and ψ' production have to be excluded from the analysis. The potential of HERA – B therefore depends entirely on the lower invariant mass cut for di-muon events at which the trigger bandwidth saturates. This value is not precisely known from simulations and will have to be determined experimentally.

Combining all factors, the total efficiency for detection and reconstruction of the FCNC decay $\mathrm{B}^0 \to \mathrm{K}^{*0}\mu^+\mu^- \to \mathrm{K}^+\pi^-\mu^+\mu^-$ is about $13\% \times \epsilon_{trig}$, corresponding to about $20 \times \epsilon_{trig}$ observed events per year. HERA – B therefore has a chance to contribute in a significant way to the world

Table 58: *Estimate of* HERA – B *sensitivity for the non-resonant FCNC decay* $B^0 \to K^{*0}\mu^+\mu^- \to K^+\pi^-$ *for one year of running at a (reduced) interaction rate of* 20 MHz *and an assumed conservative single track reconstruction efficiency of* 80%. *The total trigger efficiency is denoted by* ϵ_{trig}.

Production per Year:	
$b\overline{b}$ per year	1.8×10^8
$B^0 + \overline{B^0}$ per year	1.5×10^8
$B^0 \to K^{*0}\mu^+\mu^- \to K^+\pi^-\mu^+\mu^-$	150
Acquisition and Reconstruction:	
geometrical acceptance $\mu^+\mu^-$	79%
reconstruction efficiency $\mu^+\mu^-$	64%
geometrical acceptance $K^{*0} \to K^+\pi^-$	84%
reconstruction efficiency $K^{*0} \to K^+\pi^-$	64%
trigger chain	ϵ_{trig}
Background Cleaning:	
p, p_T cuts	80%
decay vertex cut ($\Delta z > 5$ mm)	62%
total efficiency	$0.13 \times \epsilon_{trig}$
$B^0 \to K^{*0}\mu^+\mu^- \to K^+\pi^-\mu^+\mu^-$ per year	$20 \times \epsilon_{trig}$

statistics expected for the next years, provided that the di-muon trigger is running close to design performance and that the trigger threshold can be lowered to a value far below the J/ψ mass.

5.3 Physics of Triggers Based on High p_T Leptons

5.3.1 $B^0 - \overline{B^0}$ Mixing

The current status of the measurement of Δm_d is as follows: While the PDG world average value (dominated by the LEP experiments) is $\Delta m_d = 0.464 \pm 0.018\,\hbar/\text{ps}$, CDF has determined the mixing parameter by looking for like sign leptons in the final state with two muons, and published the value $\Delta m_d = 0.503 \pm 0.064 \pm 0.071\,\hbar/\text{ps}$ [257]. In the following we will roughly estimate the reach of HERA – B for the same final state, i.e. for events where the B^0 meson decays semi-leptonically, $B^0 \to \mu X$, and the associated b quark decays in a similar way, $b \to \mu X$.

Assuming a 20 MHz interaction rate and a 12 nb $b\overline{b}$ production cross section, we expect a B^0 production rate of 19 Hz. With a semi-leptonic branching ratio of 0.1 and a trigger efficiency of 0.1 [258], we expect 1.9×10^5 recorded events per year. This number is further reduced by a factor of about 0.7 because of additional impact parameter cuts necessary to reduce the background from direct charm semi-leptonic decays, and by a reduction factor 0.64, accounting for a conservatively assumed track reconstruction efficiency of 80%. This leads to ≈ 85 k reconstructed events.

To estimate our precision in the determination of Δm_d we will re-scale the CDF value. While CDF used 6 k events in their analysis, and had an error of $\sigma(\Delta m_d)_{stat} = 0.064\,\hbar/\text{ps}$, we would expect a statistical error of roughly $\sigma(\Delta m_d)_{stat} = 0.02\,\hbar/\text{ps}$. If we assume that the systematic error will scale with the increase in statistics as well, we would be able to provide a single measurement with an accuracy comparable to the current world average error quoted above.

Another possible final state that gives access to Δm_d is $B^0 \to J/\psi K^{*0}$, and its charge-conjugate $\overline{B^0} \to J/\psi \overline{K^{*0}}$. About 2500 of these decays can be recorded in a typical HERA – B year spent at 20 MHz interaction rate, assuming full tracking and trigger capabilities. The flavor of the neutral meson at decay is readily measured using the charge of the (identified) kaon in the K^* decay ($K^{*0} \to K^+\pi^-$, $\overline{K^{*0}} \to K^-\pi^+$). The flavor at production is obtained through a combination of lepton and kaon tagging.

The sensitivity to the mixing parameter $x_d \equiv \Delta m_d/\Gamma_d$ is given by the approximate formula [259]

$$S = \sqrt{\frac{N}{2}} f_s P \exp\left(-\frac{1}{2}\left[\frac{x_d \sigma_t}{\tau_{B_d}}\right]^2\right) \quad , \tag{43}$$

where N is the number of events, f_s the fraction of signal events (around 0.9 for HERA – B), P is the tagging power, assumed to be around 0.5, and σ_t is the proper time resolution for the measurement of the B^0 decay, around 0.05 ps in HERA – B . In total, this results in $S \approx 10$, which would imply $\sigma(\Delta m_d) \approx 0.04\,\hbar/\text{ps}$, that would be one of the best single measurements available of Δm_d to date.

The most serious competition comes from the e^+e^- B factories. The BABAR collaboration quotes a potential of measuring Δm_d at the percent level, assuming an integrated luminosity of $30\,\text{fb}^{-1}$, collected after one year of data-taking at nominal luminosity [22]. HERA – B will probably not be able to compete with this precision.

5.3.2 $D^0 - \overline{D^0}$ Mixing

The mixing of the neutral charm meson D^0 to its anti-particle $\overline{D^0}$ is expected to be small in the Standard Model [260]. The mixing is parameterized by the lifetime and mass differences of the two mass eigenstates. The choice of decay channels to search for mixing depends on the HERA – B trigger system. We discuss in the following two decay channels, semi-leptonic and hadronic, which can be studied by HERA – B, once they are fully operational. The preliminary di-leptonic trigger (mostly based on the second level system) has been operated in the 2000 run, with a mass cut of $2.5\,\mathrm{GeV/c^2}$ for the electrons and no explicit mass cut for the muons, and the single lepton trigger has been tested with a p_T threshold of $1.5\,\mathrm{GeV/c}$. In the following, we not only assume the full trigger capabilities of HERA – B, but also that the p_T and mass thresholds, at least for the muon triggers, can be relaxed. Given the present level of commissioning, these requirements can only be hoped to be met in the medium or long term future.

Semi-Leptonic Charm Decays

The mixing parameter for the semi-leptonic technique is defined as,

$$r_\mathrm{mix} = \frac{\Gamma(\mathrm{D^0} \to \overline{\mathrm{D^0}} \to \mathrm{K^+}\,\ell^-\,\overline{\nu_\ell})}{\Gamma(\mathrm{D^0} \to \mathrm{K^-}\,\ell^+\,\nu_\ell)} \quad . \tag{44}$$

Assuming that the mass eigenstates are also CP eigenstates, the time-integrated mixing rate is given by [261, 262],

$$r_\mathrm{mix} = \frac{1}{2}(x^2 + y^2) \quad , \tag{45}$$

where $x = \Delta m/\overline{\Gamma}$ and $y = \Delta\Gamma/(2\overline{\Gamma})$. Here, $\overline{\Gamma}$ is the average decay width of the two mass eigenstates.

For the ease of reconstruction, we focus on low multiplicity semi-leptonic $\mathrm{D^0}$ decay channels: $\mathrm{D^0} \to \mathrm{K^-}e^+\nu_e$ (BR=3.7%) and $\mathrm{D^0} \to \mathrm{K^-}\mu^+\nu_\mu$ (BR=3.2%). The second lepton needed for the di-lepton HERA – B trigger comes from the semi-leptonic decay of the companion charmed particle. The initial flavor of the decaying D meson can be deduced if it is originating from the strong decay $\mathrm{D^{*+}} \to \pi^+\mathrm{D^0}$, with the charge of the pion tagging the initial charm flavor of the D meson.

The best limit on r_mix using the semi-leptonic method ($r_\mathrm{mix} < 5 \times 10^{-3}$ at 90% confidence level) comes from the experiment E791 [263], which finished data taking in 1992. This experiment utilized a 500 GeV negative pion beam with fixed nuclear targets. Like HERA – B, the E791 spectrometer has open-geometry and fine-grained detectors. Both E791 and HERA – B have a silicon vertex detector, downstream drift chambers, Cherenkov particle identification and electron and muon detectors.

In order to determine the trigger efficiency for double semi-leptonic charm events with the HERA – B detector, we have generated a sample of 100 k $c\overline{c}$ events containing a $\mathrm{D^{*+}}$ meson and a companion charmed particle. The $\mathrm{D^{*+}}$ mesons were forced to decay via the chain

$$\mathrm{D^{*+}} \to \pi^+\mathrm{D^0} \to \pi^+\,\mathrm{K^-}\ell^+\nu_\ell \quad ,$$

while the companion charmed particle had to decay semi-leptonically. We assumed that the trigger will require two high-p_T leptons of arbitrary charge and flavor with invariant mass greater than $2\,\mathrm{GeV/c^2}$. The p_T dependence of the trigger efficiency is presented in Fig. 168. As one can see, for the value of p_T cut of 1 GeV/c, the trigger efficiency for the Monte Carlo sample is $(1.2 \pm 0.1) \times 10^{-3}$.

The analysis of the semi leptonic channels is complicated by the fact that the events cannot be completely reconstructed because the momentum of the neutrino is not measured. There are two methods to handle the problem. The first method was employed by the E791 experiment [263], and will in the following be called the Q method. It requires a precisely reconstructed $\mathrm{K}\ell$ vertex. The method exploits the fact that the $\mathrm{D^0}$ momentum is parallel to the vector connecting the primary and secondary vertices, and that the invariant mass of the kaon, lepton and neutrino is equal to the accepted $\mathrm{D^0}$ mass. From these two conditions, a quadratic equation in the neutrino energy is

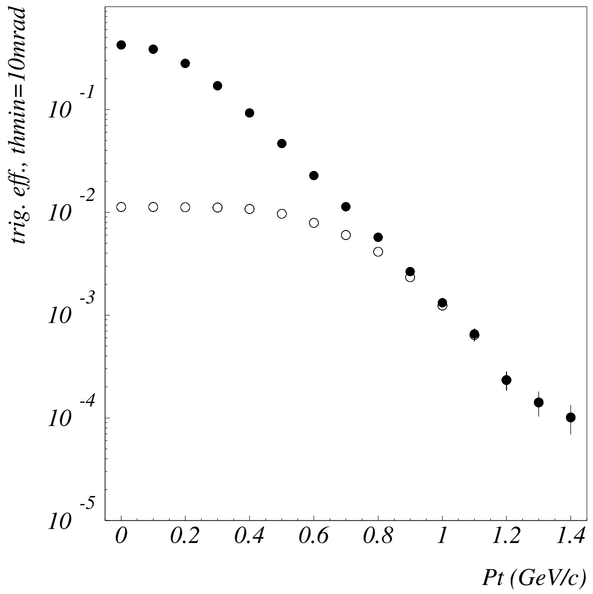

Figure 168: *Dependence of the trigger acceptance (full circles) on the p_T cut for both leptons in the case the trigger covers all tracks with angles* $> 10\,\mathrm{mrad}$. *Open circles denote the trigger acceptance with the additional requirement that the invariant mass of two leptons is larger than* $2\,\mathrm{GeV/c^2}$.

obtained. Due to sizable errors in the reconstruction of the $\mathrm{K}\ell$ secondary vertex, stemming from the rather short flight path of the D^0, only 23% of the generated events have non-negative discriminants. Those events are used in further analysis. The ambiguity in the choice of the sign in the quadratic equation is solved by using the correlation between the momenta of the π^+ and D^0 which, from the Monte Carlo data we find to be $p(\mathrm{D}^0) = p(\mathrm{K}\ell\nu) \approx 13.2 \times p(\pi^+)$. The sign which gives better agreement with this correlation formula is chosen. Monte Carlo simulations show that this algorithm leads to a correct choice of sign in 84% of the events, while for the remaining 16% the effect of the wrong sign choice is almost negligible. Having determined the neutrino momentum, the Q value $Q = M(\pi\mathrm{K}\ell\nu) - M(\pi\mathrm{K}\ell)$ is computed. The Q distribution peaks at $M(\mathrm{D}^{*+}) - M(\mathrm{D}^0) = 5.8\,\mathrm{MeV}$ for $\mathrm{D}^{*+} \to \pi^+\mathrm{D}^0 \to \pi^+\mathrm{K}^-\ell^+\nu_\ell$ decays, while for background the distribution of Q is expected to be smooth and without peaks. As already noted, the method suffers from poor efficiency due to a poor resolution in the D^0 direction.

The second method uses the so-called pseudo-mass technique. The D^{*+} mass is approximated by the quantity $M(\mathrm{K}\ell\pi) - M(\mathrm{K}\ell) + M(\mathrm{D}^0)$. This distribution of this variable peaks at $M(\mathrm{D}^{*+})$ for real D^{*+} decays, while the distribution is expected to be smooth for the background. To estimate the efficiency of the selection cuts, we have generated a sample of 13400 events with $\mathrm{D}^{*+} \to \pi^+\mathrm{K}^-\ell^+\nu_\ell$ decays. The companion charmed particle was forced to decay semi-leptonically. Both leptons in the event were generated with transverse momentum larger than $1\,\mathrm{GeV/c}$. Events were processed with the standard HERA − B reconstruction and analysis packages. Backgrounds were strongly suppressed by requiring the pion to have a transverse momentum $p_T < 0.33\,\mathrm{GeV/c}$. The secondary vertex formed by the K^- meson and the lepton ℓ^+ was determined by finding the point of smallest distance between the tracks. This distance was required to be smaller than 0.5 mm. The primary vertex was determined from the trajectory of the pion in combination with the target wire constraint. The resulting mass shift distributions are presented in Fig. 169. The background distribution for wrong sign combinations was obtained by combining K^- mesons and ℓ^+ leptons from D^0 decays with a random π^- meson from the rest of the event. The efficiency for accepting the signal decay was found to be 67%. An additional cleaning cut on the decay length at 2 mm, corresponding to approximately three times the rms resolution of the decay length measurement, is estimated to have an efficiency of 47%. Our preliminary estimate for the combined efficiency for double semi-leptonic decays from $c\bar{c}$ events, including the trigger, the reconstruction and the decay length cut, is $(3.9 \pm 0.4) \times 10^{-4}$.

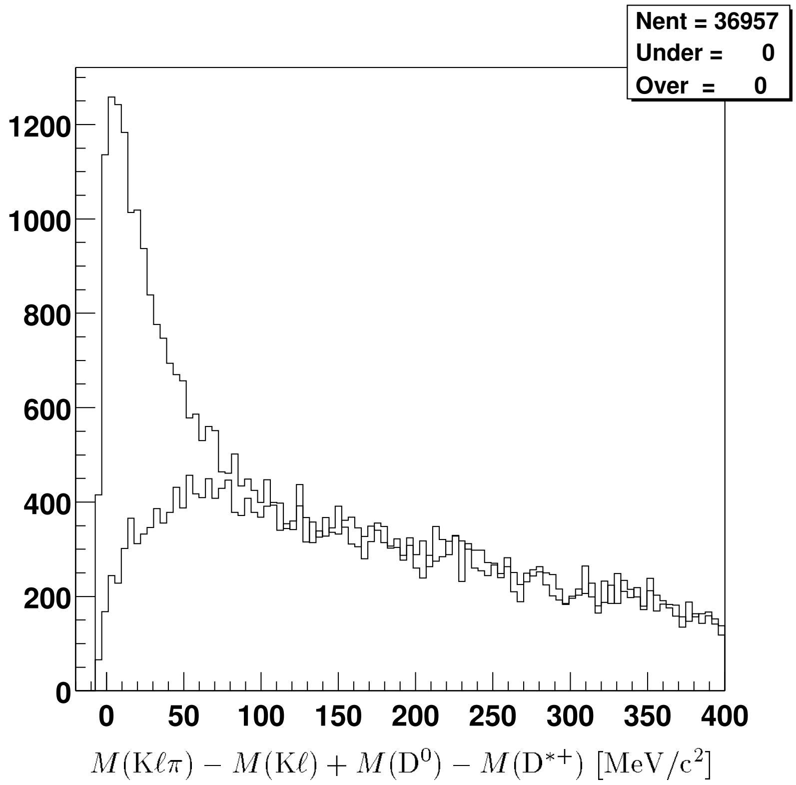

Figure 169: *Distribution of the mass difference* $M(\mathrm{K}\ell\pi) - M(\mathrm{K}\ell) + M(\mathrm{D}^0) - M(\mathrm{D}^{*+})$ *for* $c\bar{c}$ *events with a* $\mathrm{D}^{*+} \to \pi^+\mathrm{D}^0 \to \pi^+\mathrm{K}^-\ell^+\nu_\ell$ *decay and an associated semi-leptonic charm decay. The distribution peaking at low mass differences is obtained from combinations with the correct pion charge. The smooth background distribution is obtained from wrong charge combinations.*

To estimate our reach in r_{mix} we first note that our right and wrong sign distributions in Fig. 169 lead to very similar S/B ratios as those obtained by the E791 experiment using the Q distribution for right and wrong sign combinations. It is therefore reasonable to assume that our capabilities will scale with the square root of the number of reconstructed right sign events. If one assumes the maximum HERA – B interaction rate of 40 MHz, we expect that 10^{11} events containing a $\mathrm{D}^{*+} \to \pi^+\mathrm{D}^0$ decay will be produced per year. Taking into account the probability for a double semi-leptonic decay ($\approx 10^{-2}$) and trigger and reconstruction efficiencies, about 390 k events will be reconstructed per year. This has to be confronted with 2500 events of this type collected by E791. We conclude that our 90% CL reach in the measurement of r_{mix} will be about

$$\sqrt{\frac{2500}{390000}} \times 5 \times 10^{-3} \approx 4 \times 10^{-4} \quad . \tag{46}$$

A compilation of the expected sensitivities for various flavor combinations of trigger leptons and for less optimistic assumptions about the tracking acceptance of the HERA – B detector is given in Tab. 59. The loss of sensitivity for smaller interaction rates and conservative assumptions on track reconstruction efficiency can be obtained from Tab. 60.

Table 59: *Expected sensitivities for various flavor combinations of trigger leptons and for two assumptions about the inner tracking acceptance of the HERA – B detector after one year of running. The interaction rate was assumed to be* 40 MHz, *and full track reconstruction efficiency was assumed.*

trigger type	sensitivity for trigger acc. > 10 mrad	sensitivity for trigger acc. > 15 mrad
$e-e$, $e-\mu$, $\mu-\mu$	4.0×10^{-4}	4.4×10^{-4}
$e-\mu$, $\mu-\mu$	4.6×10^{-4}	5.1×10^{-4}
$\mu-\mu$	8.0×10^{-4}	8.7×10^{-4}

Table 60: *Expected sensitivities for one year of operation for various running conditions of the HERA – B detector. The full tracking acceptance of the HERA – B detector was assumed, and all three flavor combinations of trigger leptons were combined.*

rate	full track reco. eff.	80% track reco. eff.
40 MHz	4.0×10^{-4}	5.7×10^{-4}
20 MHz	5.7×10^{-4}	8.0×10^{-4}

If the effective p_{T} cut on the di-lepton trigger can be relaxed to 0.5 GeV/c, the annual yield of usable semi-leptonic events will be enhanced by a factor of about 8 (see Fig. 168). If this is possible, the sensitivity for mixing for HERA – B can reach about 1.5×10^{-4}. This sensitivity would well exceed the current best limit of about 10^{-3} from CLEO [264] based on hadronic decays of D^0 mesons, and is competitive with the BABAR sensitivity [22] of 2.2×10^{-4}. At this level of sensitivity, many models for new physics can be excluded.

To indicate the performance of the HERA – B spectrometer in the kinematic region of low mass muon pairs, we plotted in Fig. 170 the invariant mass of di-muons obtained by the di-muon trigger of HERA – B. The di-muon mass was determined at the trigger level without using the full tracking information. The spectrum peaks at about 2 GeV/c^2, reflecting a p_{T} cut of 0.7 GeV/c imposed on each muon. The spectrum is strikingly similar to that obtained by E771 with comparable p_{T} cuts [267]. The enhancement at about 1 GeV/c^2 seen in the HERA – B di-muon mass spectrum is consistent with the ρ/ω signal observed by E771. This provides evidence for sensitivity for low mass di-muons arising from double semi-leptonic charm decays in HERA – B.

Hadronic Charm Decays

The search for a mixing signal in hadronic D^0 decays is complicated by the presence of wrong-sign decays not coming from mixing, the so-called doubly Cabibbo-suppressed (DCS) decays. The two contributions can be disentangled by fitting the decay time distribution of wrong-sign decays to an expression which takes the interference between the two sources into account [265],

$$\frac{\mathrm{d}N(t)}{\mathrm{d}t} = N_0\, e^{-\Gamma t} \left[r_{\mathrm{DSC}} + \sqrt{r_{\mathrm{DSC}}}\, y'\, \Gamma t + \frac{1}{4}(x^2 + y^2)\, (\Gamma t)^2 \right] \tag{47}$$

where $y' = y\cos(\delta \pm \phi) - x\sin(\delta \pm \phi)$ and $x' = x\cos(\delta \pm \phi) + y\sin(\delta \pm \phi)$. The factor r_{DSC} is the DCS rate, measured to be about 5×10^{-3}, and δ is a possible strong phase between the DCS and the Cabibbo favored decays. The angle ϕ is the standard model CP-violating phase which appears with two different signs for D^0 and $\overline{\mathrm{D}^0}$) decays, respectively.

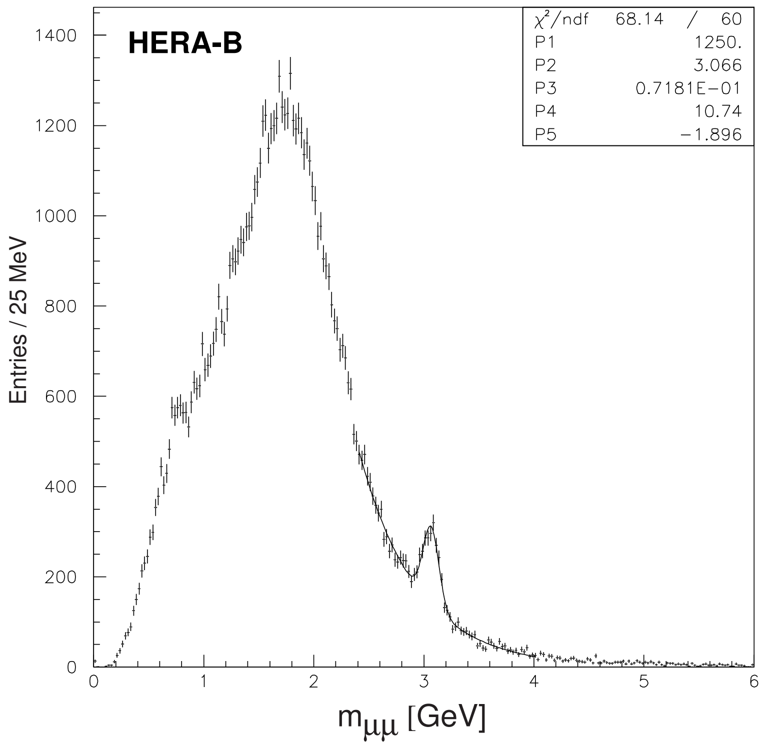

Figure 170: *Invariant mass of di-muons, as observed at the first trigger level at HERA – B.*

To estimate the sensitivity of the hadronic approach, we show in Fig. 171 the fractional deviation of the decay time distribution of wrong sign $D^0 \to K^+\pi^-$ decays from a pure exponential, for several values of x, y, and $\phi + \delta$.

The value of y was fixed at 0.01, 0.02, and 0.03 in the top, middle, and bottom plots, respectively. These values for y are motivated by the recent measurements of FOCUS [266] and CLEO [264]. The three sets of curves are for $\cos(\delta + \phi) = 1$ (upper), $\cos(\delta + \phi) = 0$ (middle), and $\cos(\delta + \phi) = -1$ (lower). For each set of curves, the solid line is for $x = 0$, and the dashed line is for $x = 0.01$. The sensitivity for this search depends on the sample size. For illustration, the statistical errors for 10 000 and 1000 reconstructed $D^0 \to K^+\pi^-$ events are plotted along the x-axis, assuming a bin size of one D^0 lifetime.

As one can see, except for a small region in which the strong interaction phase interferes destructively with the CP violating phase, i.e. $\cos(\delta + \phi) = 0$, y is clearly discernible in HERA – B at the level of 10^{-2}, even with a statistics of 1000 reconstructed $D^0 \to K^+\pi^-$ events. This corresponds to a $r_{\rm mix}$ sensitivity of 5×10^{-5} in the semi-leptonic method, though the semi-leptonic method is independent of the phase angles. The sensitivity on x will depend on the details of the analysis and background sources. One can see from Fig. 171 that, under favorable conditions, x of order 10^{-2} is observable.

This analysis assumes that the trigger which has to include the presence of high-p_T hadrons (high-p_T pretrigger, see section 5.4) in combination with a lepton from the associated semi-leptonic charm decay, has an efficiency of at least 1% on the $D^0 \to K^+\pi^-$ decays without saturating the bandwidth used for the B triggers, and that the background is comparable to that observed at CLEO. These requirements will not be easy to meet but the potential discovery sensitivity justifies further investigations.

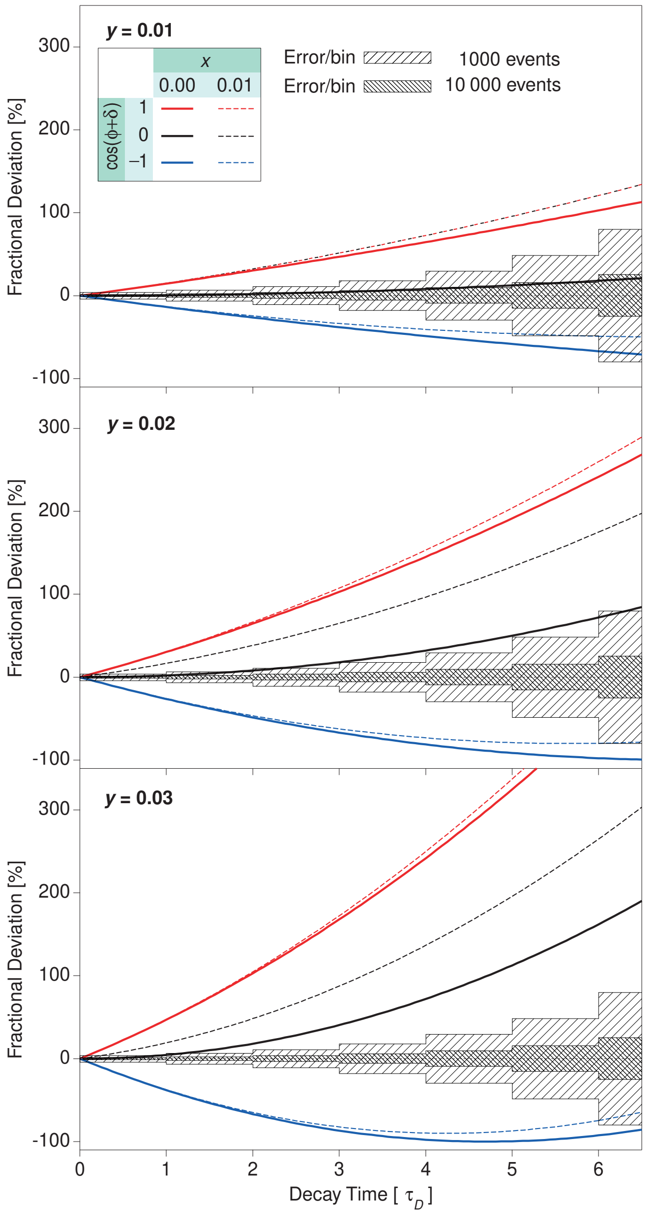

Figure 171: *Fractional deviation of the wrong sign decay time distribution from a pure exponential. See text for details.*

5.3.3 Measurement of $\Delta\Gamma_s$ from Semi-Leptonic Decays

The most promising method to measure the difference in the decay widths of the light and heavy B_s^0 mesons seems to be the lifetime measurement in the channel $B_s^0 \to J/\psi\phi$, discussed in section 5.2.7. An alternative way might be to analyze the decay time distribution of semi-leptonic decays $B_s^0 \to D_s^- \ell^+ \nu_\ell$ and $\overline{B_s^0} \to D_s^+ \ell^- \overline{\nu_\ell}$. The distribution is a sum of two exponential distributions, both convoluted with the same gaussian to account for the resolution in proper time. The contributions to the resolution in proper time (vertex resolution, B_s momentum resolution) were studied in detail when the channel was considered for B_s mixing measurements [268, 269], and it was found that the expected value for the combined error amounts to 0.12 ps.

A simple simulation study was carried out to determine the accuracy in fitting a sum of two exponential distributions with the same number of events, where two parameters, the normalization and the width difference were left to vary freely. Running at an interaction rate of 20 MHz, 450 events of the type $B_s^0 \to D_s^- \ell^+ \overline{\nu_\ell}$ (or charge conjugated) are expected to be recorded and reconstructed per year if the lepton triggers are operating at design performance. In our very much simplified analysis with no background superimposed we find that the resolution in the width difference measurement amounts to about $0.3\,\Gamma$. This precision is good enough to contribute in a significant way to a combined measurement at HERA – B.

5.3.4 Charm Physics

In principle, HERA – B can be regarded as a hadronic charm factory. Assuming an interaction rate of 20 MHz, the annual yield of charm particles at HERA – B is about 3×10^{11}, several orders of magnitude larger than for electron-positron beauty factories. Being optimized for B physics, sufficiently efficient triggering on inclusive charm decays still represents a considerable challenge, especially if trigger cuts have to be relaxed without saturating the bandwidth and impairing the main stream physics program.

The general signature for charm decays are muons of sufficiently high transverse momenta. For special decays, some of which with low multiplicity, purely leptonic final states discussed below, the trigger signature becomes much cleaner, and transverse momentum cuts can in principle even be combined with di-lepton invariant mass cuts, in order to select specific (rare) decays. Even in this case, detailed trigger simulations are, however, missing, so that all estimates are to be taken with appropriate care.

The decays of charm particles can be used to study the details of the standard model, and search for new physics. In the following, we describe several high-impact charm physics topics that HERA – B can pursue. One of the primary topics in charm physics, the search for D^0 - $\overline{D^0}$ mixing, has already been discussed in section 5.3.2 and will not be covered here.

Flavor Changing Neutral Currents

Flavor changing neutral current (FCNC) decays in the charm sector are highly suppressed in the standard model because the GIM cancelation is more perfect for charm decay, where loops receive their contributions from down-type quarks which are much better mass-degenerate than up-type quarks [270]. For example, the classic charm changing neutral current (CCNC) decay $D^0 \to \mu^+\mu^-$, has a theoretical short-distance branching ratio of about 10^{-19} [271]. Even though long-distance effects can enhance the branching ratio by several orders of magnitude, the Standard Model prediction is more than ten orders of magnitude below the current experimental limit, 4×10^{-6} [226]. This opens a large window for new physics. For example, heavy SUSY particles can contribute to the short-distance box diagram, boosting the branching ratio to about $10^{-10\pm 2}$ [272]. The error in the exponent reflects the uncertainty in the scalar quark masses and their couplings. The di-muon decay $D^0 \to \mu^+\mu^-$ is especially clean both theoretically and experimentally. Three-body or high multiplicity CCNC decays have in general higher branching ratios, but are more difficult to trigger in HERA – B. The results are also more difficult to interpret in terms of new physics. We will therefore focus on the decay $D^0 \to \mu^+\mu^-$ in the following discussion.

The current best limit on $D^0 \to \mu^+\mu^-$ comes from E771 [267] which was a fixed target experiment at Fermilab with a detector very similar to HERA – B. The sensitivity of HERA – B on the decay $D^0 \to \mu^+\mu^-$ depends on the efficiency of the di-muon trigger. A transverse momentum threshold of

1 GeV/c, applied in the FLT for both muons, would allow HERA – B to reach a sensitivity of 10^{-7}, a significant improvement over the existing limit. If the di-muon trigger can be operated at a p_{T} threshold of 0.5 GeV/c (for each muon), HERA – B can reach a sensitivity of 10^{-8}, at which level some of the SUSY models would be tested.

Lepton Flavor Violating Decays

Lepton numbers are experimentally known to be individually conserved to high precision. For example, the current limit on the branching ratio of the decay $\mathrm{K}_{\mathrm{L}}^{0} \to \mathrm{e}^{\pm}\mu^{\mp}$ is 3.3×10^{-11} [226]. Lepton flavor violating (LFV) decays are forbidden in the standard model. However, it is still interesting to search for LFV decays in the charm sector. LFV decays can occur if there is a breaking of the horizontal symmetry among the three generations of quarks and leptons [273]. There are models in which the masses of the gauge bosons responsible for LFV processes are different for the up-type and down-type quarks. Hence the stringent limit from the decay $\mathrm{K}_{\mathrm{L}}^{0} \to \mathrm{e}^{\pm}\mu^{\mp}$ does not necessarily apply to charm LFV decays.

The present limit on the branching ratio of the decay $\mathrm{D}^{0} \to \mathrm{e}^{\pm}\mu^{\mp}$ is about 10^{-5} [226]. The sensitivity on LFV decays in HERA – B depends once again on the trigger efficiency. Since the LFV final states involve leptons of different flavors, HERA – B has to develop a high-p_{T} single lepton or μ-e di-lepton trigger with low invariant mass or p_{T} thresholds. As a rough estimate, the expected sensitivity for the branching ratio of the decay $\mathrm{D}^{0} \to \mathrm{e}^{\pm}\mu^{\mp}$ will be comparable to that of the decay $\mathrm{D}^{0} \to \mu^{+}\mu^{-}$, or about 10^{-7} for a p_T cut at 1 GeV/c, and 10^{-8} for a p_T cut at 0.5 GeV/c. This would improve the current limits by several orders of magnitude.

Three-body or higher multiplicity LFV decays, such as $\mathrm{D}^{+} \to \mathrm{e}^{-}\mu^{+}\mu^{+}$, are also interesting, but are even harder to trigger on.

5.4 Physics of Triggers Using High p_T Hadrons

The physics program of the high-p_T pretrigger is based on fully-hadronic decays of B mesons. Such decays probe a wide variety of physics including the angles α, β, and γ of the CKM unitarity triangle, and the mass and decay width differences Δm_s and $\Delta\Gamma_s$ between the two B_s^0 and $\overline{B_s^0}$ mass eigenstates. These measurements can all be used to test unitarity of the CKM matrix, as manifested by the closure of the unitarity triangle; if β is determined by the di-lepton trigger or at BELLE or BaBar, then measuring two of these quantities over-constrains the unitarity triangle.

Extracting these quantities from measurements of CP observables introduces theoretical uncertainty. These uncertainties generally arise from gluonic penguin diagrams, electroweak penguin diagrams, and final-state interactions. However, there has been much theoretical activity in recent years studying and constraining such effects, and measuring fully hadronic B decays is a main objective of "second-generation" B experiments such as LHCb and BTeV. We believe that HERA – B can make an earlier – and significant – contribution in this area once the high-p_T pretrigger and the FLT are fully operational.

5.4.1 High p_T Hadron Production and QCD

The physics of single and double high p_T production has been discussed in detail in section 5.1.2. The ECAL pretrigger offers an elegant possibility to trigger on high p_T direct photons and neutral pions, while charged high p_T hadrons have to be selected from the unbiased decay of the away jet. The high-p_T pretrigger offers the possibility to directly trigger on charged hadrons, either as single high p_T particles or as high mass pairs of high p_T hadrons, produced roughly back-to-back in azimuth. This will further enlarge the variety of hard scattering physics and QCD tests accessible at HERA – B. For details refer to section 5.1.2.

5.4.2 B_s^0–$\overline{B_s^0}$ Mixing

The measurement of the B_s^0 oscillation frequency, Δm_s, provides important constraints on parameters described by the unitarity triangle. Present lower limits on Δm_s are set by LEP experiments, SLD and CDF, all using semi-leptonic B_s^0 decays. Because of the missing neutrino, the proper time resolution for B_s^0 decays in these experiments is not sufficient to discern the very rapid oscillations that are expected. To improve the Δm_s reach, one needs fully reconstructed B_s^0 decays. Among the most promising decay modes are $B_s^0 \to D_s^- \pi^+$ and $B_s^0 \to D_s^- \pi^+ \pi^+ \pi^-$. These final states have relatively large branching ratios and low multiplicities. The CDF group realized the importance of these decays and is constructing a special all-hadronic trigger for RUN II in order to accept them. These decays can also be detected at HERA – B.

B_s^0 decays to $D_s^- \pi^+$ and $D_s^- \pi^+ \pi^+ \pi^-$ can be accepted by a hadron-lepton trigger [1]. The requirements we consider at the first-level of the HERA – B trigger are a high p_T charged track ($p_T > 1.5$ GeV/c) and a high p_T lepton ($p_T > 1.0$ GeV/c for muons and $p_T > 1.4$ GeV/c for electrons). The high p_T lepton is produced in the semi-leptonic decay of the second B hadron present in the event. The charge of the lepton track provides a high quality tag.

The high-p_T pretrigger efficiency was estimated using a full Monte Carlo simulation (ignoring possible dead channels and assuming 99% chamber efficiency, to be compared with 96-97% which has been achieved so far for the inner high-p_T chambers). The muon and electron pretrigger efficiencies should be close to 100% if dead channels are ignored. The FLT was assumed to be fully efficient since a reliable estimate for its future performance is not yet available. The SLT tracking efficiency was assumed to be 90% which is close to the already achieved value of about 85%.

The background rejection by the lepton requirement was estimated using data collected with di-muon and di-electron triggers. The triggers required two muon (electron) pretriggers followed by the SLT (Slicer/Refit algorithms). The obtained suppression for muons (electrons) of 1.5×10^4 (10^3) was multiplied by the experimentally observed SLT efficiency for two tracks in order to obtain the suppression factor for the ideal, fully efficient detector. The SLT efficiency was determined by dividing the number of observed J/ψ mesons by the expected number. The rejection factor for two muons (electrons) was found to be equal to 660 (62) which corresponds to a suppression factor of 26 (8) for a single muon (electron) requirement in case of uncorrelated tracks. Correlations between tracks will be taken into account later. According to the simulations the FLT suppression factor is about 3 times smaller than that from the SLT, i.e. the FLT suppression factor is about 9 (3). These suppression factors were obtained at 5 MHz interaction rate. Pretriggers usually selected bunch crossings with at least one interaction, and no hardware inhibits to suppress events with multiple interactions were applied. Therefore we believe that the suppression factors will be similar at 20 MHz and that only the pretrigger rate will change. The FLT rejection factor was estimated with a cut on the lepton $p_T > 0.7$ (1.2) GeV/c. The same suppression factors are assumed for the tighter cuts, $p_T > 1.0$ (1.4) GeV/c, used for the purpose of this study.

The number of muon pretrigger candidates was observed to be one in 4.5 events at an interaction rate of 5 MHz. From this, taking the missing acceptance and the higher p_T-cut into account, we estimate one muon pretrigger message in two events for an interaction rate of 20 MHz. For the electron pretrigger, a suppression factor of 150 was observed at 10 MHz when requiring one cluster in the calorimeter with $E_T > 1.4$ GeV/c. From this we estimate a suppression factor of 75 for the electron pretrigger at an interaction rate of 20 MHz.

The background suppression by the requirement of a pion with $p_T > 1.5$ GeV/c was estimated using an old Monte Carlo simulation of the pretrigger-FLT chain used for the study of the decay $B^0 \to \pi^+\pi^-$ for an interaction rate of 40 MHz. The actual versions of the Monte Carlo code, though more detailed, could not be used since its predictions are not sufficiently understood at the moment and some de-bugging seems necessary. The suppression factor due to the requirement of a single high-p_T pion was taken to be the square root of the suppression factor found for the requirement of two pions. This automatically takes into account the correlation between the two pions. The trigger rate was re-scaled linearly from an interaction rate of 40 MHz to an interaction rate of 20 MHz which should be conservative. The resulting background suppression factor was found to be 15 at an interaction rate of 20 MHz.

The total background suppression is therefore equal to the product of the suppression factor due to the requirement of a high-p_T pion, the lepton pretrigger reduction factors and the FLT suppression factors for the lepton tracks. The result was finally corrected for the different p_T cuts for the leptons in this study as compared to the real data. In this way, we find a total reduction factor of 290 for muon triggers ($15 \times 2.2 \times 26/3$) and 3000 for electron triggers ($15 \times 75 \times 8/3$). This corresponds to an input rate of 35 kHz for the SLT. This can be further reduced by better shielding of the muon pretrigger chambers or by cuts on the lepton-hadron invariant mass and energy asymmetry $(E_\ell - E_\pi)/(E_\ell + E_\pi)$.

The suppression factors expected by the SLT algorithms are summarized in Tab. 61.

At the third trigger level, the presence of the second B meson in the event can be used to further suppress the background. One can look for additional leptons, a secondary vertex and/or tracks which do not match the primary vertex. This should decrease the background considerably.

Table 61: *Suppression factors of the SLT algorithms when applied for the sample triggered by the lepton-hadron trigger.*

Requirement	Rate Suppression
Slicer/Refit	3×3
Distance between lepton and pion	1.5
Impact parameter of pion	1.5
Lepton identification	5

We plan to reconstruct B_s^0 mesons in 9 decay modes, most of which were reconstructed by LEP experiments. We expect that the excellent vertex resolution and kaon identification at HERA – B will allow sufficient suppression of combinatorial background also in high multiplicity modes.

Efficiencies for the signal detection and reconstruction are shown in Tab. 62. The reconstruction efficiency of each track was assumed to be 96.5%. This number is based on the performance studies of the tracking algorithms for 1+4 interactions. In addition, each track has a probability of about 17% to interact in front of the RICH detector. Using the currently available reconstruction algorithms this leads to a very low efficiency for multi-prong final states. The number of events containing $D_s^-\pi^+$ $(\pi^+\pi^-)$ decays is estimated to be $\simeq 61$ ($\simeq 23$) for one standard year (10^7 s) of operation at 20 MHz.

The efficiency can be improved considerably if one starts reconstruction in the vertex detector and does not require that the track passes the full tracking system. Moreover, if the track direction is determined in the vertex detector, its momentum can be obtained from kinematical constraints. Such a procedure does not deteriorate the proper time resolution significantly. The numbers of events reconstructed with this method are shown in Tab. 62.

The tagging power was re-calculated, starting from the standard HERA – B value of $P = 0.5$, but taking into account that the cascade decays $b \to c \to \ell$ are selected by tighter p_T cuts. For this study, the tagging power is estimated to be $P = 0.6$. The use of secondary kaons and leptons from the decay of the D mesons produced in the semi-leptonic B decay can further improve the tagging power.

Two main background sources were studied, inelastic events where the tagging lepton is fake and both reconstructed D_s^- and B_s^0 mesons are fake, and $c\bar{c}$ events where the tagging lepton is real while the reconstructed D_s^- meson is either real or fake and the reconstructed B_s^0 meson is fake. The estimated suppression factors for these backgrounds are listed in Tab. 63. The signal-to-background ratio (S/B) is about 20 and we hope to improve it further by more optimized cuts on the B_s^0 and D_s^- vertices, by removing tracks from reconstructed strange particle decays, and by using information about the second beauty hadron in the event. The efficiency of the B_s^0 and D_s^- vertex cuts is at the moment slightly smaller than the one given in the Tab. 62. However, the vertex reconstruction studies have just started and we expect some improvement. The background from $b\bar{b}$ events is still under study.

For events with kinematically reconstructed momentum of one of the tracks, the background is expected to be higher and is currently being studied. However, since the S/B ratio is large enough, we do not expect this to become a problem.

For the remainder of this section we fix the assumed S/B ratio at a value of 10.

The B_s^0 and D_s^- vertex resolution was estimated with a full Monte Carlo simulation of the vertex detector and the standard pattern-recognition and vertexing algorithms, but using the Monte Carlo

Table 62: *Expected fraction of signal events per inelastic (minimum bias) event.*

	$B_s^0 \to D_s^- \pi^+$	$B_s^0 \to D_s^- \pi^+\pi^+\pi^-$
Physics:		
$\sigma_{bb}/\sigma_{inel.}$	10^{-6}	10^{-6}
$b\overline{b} \to B_s^0$ (or $\overline{B_s^0}$)	0.16	0.16
$B_s^0 \to D_s^- \pi^+ (\pi^+\pi^-)$	3.0×10^{-3}	8.0×10^{-3}
$D_s^+ \to \phi\pi^+ \to K^+K^-\pi^+$	0.018	0.018
$K^+\overline{K^{*0}} \to K^+K^-\pi^+$	0.022	0.022
$(K^+K^-\pi^+)_{nonres.}$	0.009	—
$K^+\pi^-\pi^+$	0.010	—
$\pi^+\pi^+\pi^-$	0.010	—
$K^{*+}\overline{K^{*0}} \to K_S^0\pi^+K^-\pi^+$	0.009	—
$\phi\pi^+\pi^+\pi^- \to K^+K^-\pi^+\pi^+\pi^-$	0.006	—
Total D_s^+ branching fraction	0.084	0.040
Trigger:		
Geometry, $p_T(\mu) > 1.0$ or $p_T(e) > 1.4$ GeV/c	0.095	0.095
Pretrigger, p_T(had) > 1.5 GeV/c	0.70	0.38
μ Pretrigger	1.0	1.0
e Pretrigger	1.0	1.0
FLT	1.0	1.0
SLT Slicer/Refit	0.9	0.9
Lepton ID	0.95	0.95
Geometrical acceptance	0.68	0.51
Track reconstruction (0.965×0.83 per track)	0.41	0.30
Main vertex	0.94	0.94
B_s^0 and D_s^- vertices	0.81	0.81
$VX(B_s^0) > 3.0$ mm	0.66	0.66
$VX(D_s^-) > 4.5$ mm	0.95	0.95
Summary	3.0×10^{-13}	1.1×10^{-13}
$B_s^0 \to D_s^- \pi^+ (\pi^+\pi^-)$:		
#events/year	61	23
#events/year, 1 track reconstr. in VDS only	37	21
$B_s^0 \to D_s^{*-} \pi^+ (\pi^+\pi^-)$:		
#events/year	56	22
#events/year, 1 track reconstr. in VDS only	34	20
Total number of events	188	86

momentum in the re-fit. For the decay chains $B_s^0 \to D_s^-\pi^+ (\pi^+\pi^-)$, $D_s^- \to \phi\pi^- \to K^+K^-\pi^-$, the resolution, σ_z, of the B_s^0 vertex position was found to be 356 μm for the $D_s^-\pi^+$ mode and 338 μm for the $D_s^-\pi^+\pi^+\pi^-$ mode. The corresponding resolution of the D_s^- vertex position was found to be 777 μm. These values are in good agreement with earlier estimates based on an idealized reconstruction of the vertex track.

The uncertainty in the B_s^0 proper time determination is dominated by the vertex resolution. To estimate the accuracy of the decay length measurement, the B_s^0 vertex resolution for the $D_s^-\pi^+$ and $D_s^-\pi^+\pi^+\pi^-$ decay modes ($\sigma_z = 356\,\mu$m and $\sigma_z = 338\,\mu$m) were added in quadrature to the

Table 63: *Expected suppression factors for backgrounds from inelastic events where both reconstructed* D_s^- *and* B_s^0 *mesons are fake and from* $c\bar{c}$ *events where the reconstructed* D_s^- *meson is either real or fake and the reconstructed* B_s^0 *meson is fake.*

	inelastic	$c\bar{c}$
$\sigma_{cc}/\sigma_{inel.}$	–	10^3
$p_T(\mu) > 1.0\,\mathrm{GeV/c}$ (mis–ID 0.65%)		
$p_T(\mathrm{e}) > 1.4\,\mathrm{GeV/c}$ (mis–ID 1.9%)	1050	200
e ID with TRD	2	1
$p_T(\mathrm{had}) > 1.5\,\mathrm{GeV/c}$	24	16
$VX(B_s^0) > 3.0\,\mathrm{mm}$, $VX(D_s^-) > 4.5\,\mathrm{mm}$	6×10^5	9×10^4
Impact param.(B_s^0)	10	10
χ^2 (Lepton, Main VX) > 10	4	1
Mass cuts	20	20
Track reconstruction	2.5	2.5
Second b hadron in event	> 1	> 1
Summary	$> 6.0 \times 10^{13}$	$> 1.5 \times 10^{14}$
S/B for completely reconstr. B_s^0 decay	> 25	> 64

primary vertex resolution of $150\,\mu$m.[66] The resulting accuracy in the proper time determination was estimated to be $\sigma_t = 0.060\,\mathrm{ps}$ and $\sigma_t = 0.057\,\mathrm{ps}$ for the $D_s^-\pi^+$ and the $D_s^-\pi^+\pi^+\pi^-$ decay modes, respectively.

We have also studied the reconstruction of the $B_s^0 \to D_s^{*-}\pi^+(\pi^+\pi^-)$ decay modes with the subsequent decay $D_s^{*-} \to D_s^-\gamma$. The energy of the photon is small and the fact that the photon is omitted in the reconstruction of the decay should not degrade the proper time resolution significantly. With the approximation $\vec{p}_{D_s^*} \simeq 1.07 \times \vec{p}_{D_s}$, the B_s^0 momentum resolution is found to be $\delta p_{B_s}/p_{B_s} = 2.6 \times 10^{-2}$ and the proper time resolution is $\sigma_t = 0.072\,\mathrm{ps}$ (0.069 ps) in this case.

We expect to collect 56 (22) reconstructed $B_s^0 \to D_s^{*-}\pi^+(\pi^+\pi^-)$ decays in a standard year of running at an interaction rate of 20 MHz, assuming full trigger capabilities. The B_s^0 invariant mass distribution for the D_s^{*-} modes with a missing photon is estimated to be five times wider than that for the fully reconstructed D_s^- modes (see Fig. 172) and the background is expected to be correspondingly larger, but still we expect a large signal-to-background ratio. In addition we expect to collect 34 (20) $B_s^0 \to D_s^{*-}\pi^+(\pi^+\pi^-)$ decays with kinematically determined momentum of one of the tracks reconstructed in the VDS only.

The sensitivity for HERA − B to measure Δm_s, or equivalently $x_s = \Delta m_s/\Gamma_s$ was estimated using the following formula [259]:

$$n_\sigma = \sqrt{\frac{N_{B_s}}{2}}\,\frac{1}{\sqrt{1+B/S}}\,P\,\exp\left(-\frac{1}{2}\,(\mathrm{x_s}\,\sigma_t/\tau_{B_s})^2\right) \qquad (48)$$

Here, n_σ is the "significance", i.e. the number of standard deviations of the measurement of B_s^0 oscillations, N_{B_s} is the number of signal events, S/B is the signal-to-background ratio and P is the tagging power.

Fig. 173 shows the expected significance of our measurement of B_s^0 oscillations, using both the

[66]This resolution assumes a simple constraint from a target wire of thickness $500\,\mu$m. If the primary vertex is reconstructed, the resolution is better. Note that thinner target wires might be installed for the future running.

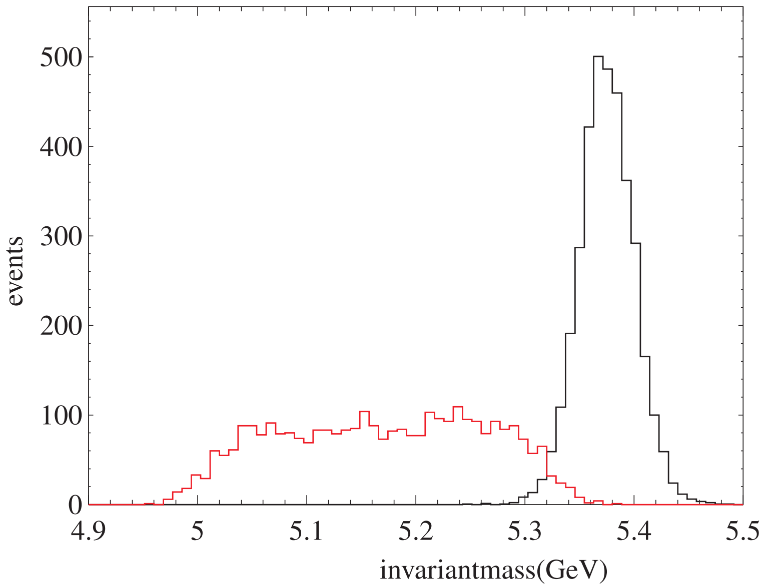

Figure 172: *Invariant mass distributions for the* $\mathrm{D_s^-}\pi^+(\pi^+\pi^-)$ *decay modes (narrow peak) and for the* $\mathrm{D_s^{*-}}\pi^+(\pi^+\pi^-)$ *decay modes, the latter reconstructed with a missing photon (wide peak).*

$\mathrm{D_s^{(*)-}}\pi^+$ and the $\mathrm{D_s^{(*)-}}\pi^+\pi^+\pi^-$ decay modes modes, as a function of the oscillation parameter $x_\mathrm{s} = \Delta m_\mathrm{s}/\Gamma_\mathrm{s}$. Using the fully reconstructed $\mathrm{B_s^0} \to \mathrm{D_s^{(*)-}}\pi^+(\pi^+\pi^-)$ decays, x_s values up to 24 can be measured at a $3\,\sigma$ level within one year of operation at 20 MHz interaction rate. We expect that we will find handles against the larger backgrounds in the partially reconstructed decays. This will allow HERA – B to cover the complete range allowed by the Standard Model.

In order to judge how changes of the HERA – B performance affect these estimates, it is useful to consider the logarithm of equation (48),

$$\ln\left(N_{\mathrm{B_s}} P^2\right) = \left(\frac{\sigma_t}{\tau_{\mathrm{B_s}}}\right)^2 x_\mathrm{s}^2 + \ln n_\sigma^2 + \ln\left(2\left(1 + B/S\right)\right) \quad , \tag{49}$$

The left hand side representing the (lorarithm of the) effective statistics, while the right hand side contains resolutions, backgrounds and the quantity, x_s, to be extracted. Note the quadratic dependence on the oscillation parameter x_s.

Fig. 174 shows the potential of HERA – B to measure x_s with a $3\,\sigma$ significance within one year of running at an interaction rate of 20 MHz. The difference between the x_s–reach parabola and the horizontal line, showing the statistical power of the tagged $\mathrm{B_s^0}$ mesons, gives the safety margin for a $3\,\sigma$ measurement. Potential gains or losses can be evaluated using the following scaling formula:

$$N_{\mathrm{B_s}} P^2 \;=\; 99 \left(\frac{P}{0.6}\right)^2 \left(\frac{f_\mathrm{reco}\left(\epsilon_\mathrm{track}\right)}{f_\mathrm{reco}\left(96.5\%\right)}\right) \left(\frac{\epsilon_\mathrm{trig.}}{\epsilon_\mathrm{TDR}}\right)^2 \left(\frac{\mathrm{IA-rate}}{20\,\mathrm{MHz}}\right) \left(\frac{t}{10^7\mathrm{s}}\right) \left(\frac{\sigma_\mathrm{bb}/\sigma_\mathrm{inel.}}{10^{-6}}\right)$$

A change in the vertex resolution enters in a twofold way. First, it changes the slope of the parabola and, second, it changes the efficiency of the vertex cuts:

$$\Delta \ln\left(N_{\mathrm{B_s}} P^2\right) = \ln\left(\frac{\epsilon\left(\sigma_{VX}\right)}{\epsilon\left(350\mu\mathrm{m}\right)}\right) \tag{50}$$

Tabs. 64, 65, 66 show the impact of the assumptions on track reconstruction efficiency, vertex

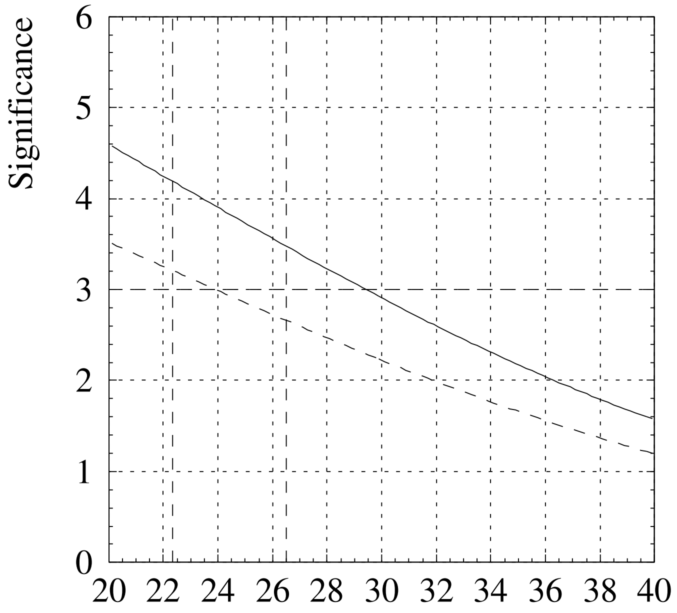

Figure 173: *Significance of B_s^0 oscillation measurements as function of x_s, expected to be achieved after one year of operation at an interaction rate of* 20 MHz, *using the* $D_s^{(*)-}\pi^+(\pi^+\pi^-)$ *decay modes (dashed line). The solid line shows the expected significance, if a kinematical reconstruction for the momentum of one of the tracks is also used. The present experimental lower limit and the upper limit from Standard Model fits are also indicated by vertical dashed lines.*

resolution and the signal-to-background ratio on the measurement. Changes in the tagging power, trigger efficiency, interaction rate and running time are straightforward to calculate.

Table 64: *Shift of* $\ln(N_{B_s}P^2)$ *as function of the reconstruction efficiency* ϵ_{track} *of tracks within the geometrical acceptance (passing at least* 18 *layers of the tracking system). Using Monte Carlo simulations, the track reconstruction efficiency was estimated to be* 96.5% *for* $1+4$ *interactions and a fully efficient tracker. With detector inefficiencies as observed in the run* 2000 *this value is reduced to about* 90%. *Efficiencies studies using the run* 2000 *data and only the outer tracker gave values around* 80%, *albeit with large uncertainties.*

ϵ_{track}	96.5%	92.5%	90.0%	87.5%	85.0%	82.5%	80.0%
$\Delta(\ln N_{B_s}P^2)$	0	−0.23	−0.38	−0.53	−0.68	−0.84	−1.00

Table 65: *Dependence of the fraction of reconstructed B_s^0 mesons per interaction on the efficiency of the B_s^0 vertex cut as function of the vertex resolution. Since there is only a weak dependence, the resolution for the D_s^- meson is not listed separately.*

σ_{VX} [μm]	200	250	300	350	400	450
$\Delta(\ln N_{B_s}P^2)$	0.14	0.09	0.05	0.00	−0.05	−0.10

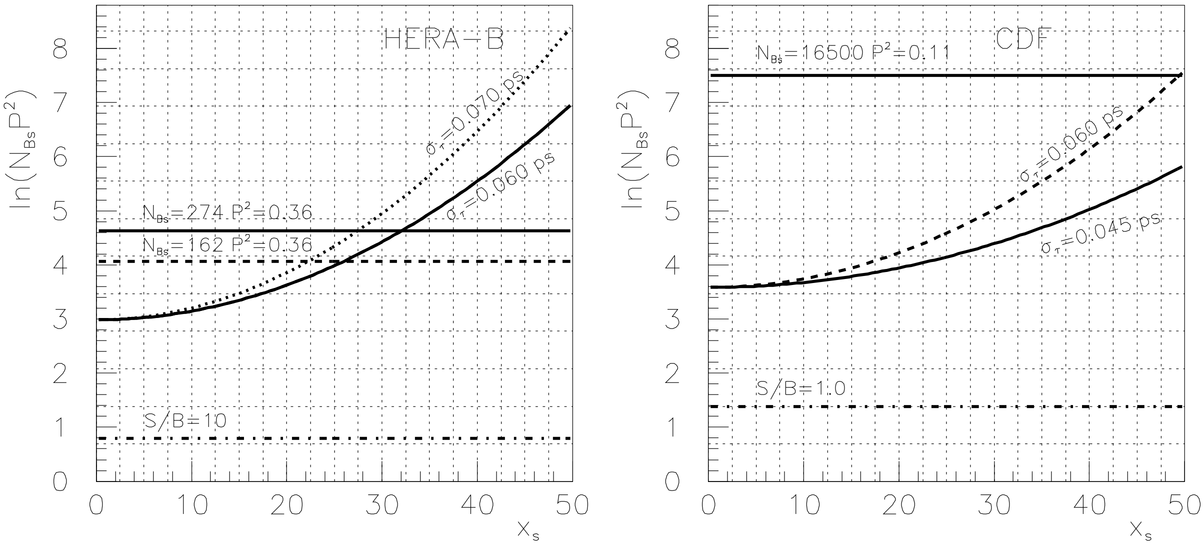

Figure 174: *Logarithm of the product of the number of reconstructed* B_s^0 *mesons,* N_{B_s}*, times the square of the tagging power* P*, plotted versus the mixing parameter* x_s*. The parabolic functions show how many tagged and reconstructed* B_s^0 *mesons are needed for a* $3\,\sigma$ *measurement of* x_s*. The dash-dotted horizontal line shows the (constant) contribution of the background to these parabolas. The solid horizontal line shows the expected statistical power for one year of running. The dashed line indicates the statistical power for the case that only fully reconstructed tracks are used for the analysis. The distance between the reach curves and the expectation gives the margin in terms of efficiency losses or lower running time. The horizontal grid lines indicate a change of a factor of two in statistics. The plot on the right side gives a comparison to the expectations for CDF (RUN II).*

Table 66: *Numerical values of the background term for different signal-to-background ratios. In this study the signal-to-background ratio is estimated to be* $\simeq 20$*.*

S/B	50	20	10	5	2	1	0.5
$\ln(2\,(1+B/S))$	0.71	0.74	0.79	0.88	1.10	1.39	1.79

CDF provides the most convincing example for the use of hadron accelerators as B factories. The CDF experiment is optimized towards the physics at large mass scale (i.e. physics in the central rapidity region), but has been upgraded with a Silicon vertex detector and a secondary vertex trigger for B physics, as well as a time of flight system. At present the time of flight system is installed, while the silicon detector is being produced to be installed in the next half year. On the right-hand plot of Fig. 174, the capabilities of CDF [274] are shown. The numbers taken are for CDF's "option A" and it is assumed that CDF's luminosity corresponds to 17.3 pb^{-1} collected per week or 1 fb^{-1} per year [275]. In CDF's "option B", the integrated luminosity is doubled, but the number of reconstructed B_s^0 mesons is lower, so that both options give roughly the same number of B_s^0 mesons per year. The RUN IIb "option C" gives fewer recorded B_s^0 decays. The parabolic curves give the proper time resolution with (0.045 ps) and without (0.060 ps) installation of the layer I of the silicon detector, which is currently still under question. The largest uncertainties in their estimates might come from the performance of the upgraded Tevatron and the new and challenging vertex trigger.

In conclusion, in one year of operation at 20 MHz interaction rate HERA – B can make an observation of B_s^0 oscillations at a $3\,\sigma$ level in the range of the oscillation parameter x_s allowed by the Standard Model. Moreover it is possible to increase the x_s reach by increasing the track reconstruction efficiency, tagging power, background rejection and by using semi-leptonic B_s^0 decays and B_s^0 decay modes with neutral pions. Although this reach is worse than that projected for the Fermilab RUN II program, the measurement of x_s is still very likely if standard model expectations hold. Of course, the measurement is technically demanding since, besides a fully efficient FLT system, it needs all three pretrigger systems, including the high-p_T pretrigger, performing to design. However, already for a reduced HERA – B performance there exists a significant potential to measure the mixing parameter x_s.

5.4.3 Measurement of CKM Angles α and γ

The measurement of CKM angles α and γ has long been recognized as challenging. We focus our discussion on the two-body decays $B^0 \to \pi^+\pi^-$, $B^0 \to K^+\pi^-$, and $B_s^0 \to K^+K^-$; for these modes the high-p_T pretrigger should have high efficiency. As there are only two tracks in the final state, the OTR tracking and FLT mass cut efficiencies should also be high. In addition, the momentum spectrum of the daughter tracks is well-matched to the capabilities of the RICH detector, and thus we expect good π/K discrimination. Such discrimination is crucial for separating $\pi^+\pi^-$ final states from $K^+\pi^-$ final states, as the difference between pion and kaon masses is not sufficient to distinguish the two decays by kinematics alone. Such separation is important as they have similar branching fractions but different lifetime distributions, and thus it could prove difficult to extract the time dependence of $B^0 \to \pi^+\pi^-$ or $B^0 \to K^+\pi^-$ decays from the lifetime distribution of a combined sample.

The number of events expected are listed in Tab. 67. For this table we assume an interaction rate of 20 MHz, which was achieved for short periods during the 2000 run. We take the branching fraction for $B^0 \to \pi^+\pi^-$ to be that presented by the BaBar collaboration at ICHEP'00 in Osaka [276]. This sample is the world's largest to-date. The tracking efficiency is assumed to be 0.95 per track[67] and the vertexing efficiency is assumed to be 0.90. The geometric acceptance is defined as the fraction of decays in which both tracks traverse all three high-p_T trigger chambers, the RICH, and the TC2 chambers. From Monte Carlo simulation we find this fraction to be $\simeq 0.5$. We also assume a lifetime cut of $0.5\,\tau_B$; this corresponds to a separation between primary and secondary vertices of about 6 mm, which is ten times the expected vertex resolution and is similar to the vertex separation cuts used by experiments at Fermilab to select charm decays [277]. The table lists the yields only for B^0 decays; the yields for $\overline{B^0}$ decays depend on the time-integrated CP asymmetry and is considered later. The final tagged samples are $\simeq 100$ events/year. The yield for $B^0 \to \pi^+\pi^-$ is similar to that expected by the BaBar experiment, which recently recorded 30 events based on $\simeq 10\,\text{fb}^{-1}$ of data (the nominal data rate of BaBar corresponds to $30\,\text{fb}^{-1}$ per year) [276].

Extracting γ from $B^0 \to K^+\pi^-$ Decays

The mode $B^0 \to K^+\pi^-$ can be used to measure γ simply by measuring the branching fractions of the two charge-conjugate modes [278]. From these values one calculates the decay amplitudes and constructs two triangles in the complex plane as shown in Fig. 175. The angle between the two vectors $\vec{d}$ and $\vec{e}$ is $\pm 2\gamma$. While experimentally straightforward, this method suffers from theoretical uncertainty arising from electroweak penguin diagrams and final-state interactions. In addition,

[67] The time available for the completion of this report did not allow to analyze a more conservative scenario with a reduced track reconstruction efficiency around 80%.

Table 67: *The number of reconstructed and tagged events for two-body charm-less decays. The two left-most columns correspond to* B^0 *decays only; the right-most column corresponds to (untagged)* B_s^0 *and* $\overline{B_s^0}$ *decays combined.*

	$\varepsilon_{\pi\pi}$	$N_{\pi\pi}$ (1 year)	$\varepsilon_{K\pi}$	$N_{K\pi}$ (1 year)	ε_{KK}	N_{KK} (1 year)
$\sigma_{b\overline{b}}$ (nb)	12		12		12	
interaction rate (MHz)	20		20		20	
$b\overline{b}$ rate (Hz)	19	1.9×10^8	19	1.9×10^8	19	1.9×10^8
$b\overline{b} \to B^0 X$ or $B_s^0 X$ or $\overline{B_s^0} X$	0.4	7.6×10^7	0.4	7.6×10^7	0.2	3.8×10^7
$Br(B^0 \to h^+h^-) \times 10^{-5}$	1.0	760	1.5	1140	1.5	570
geometric acceptance	0.5	380	0.5	570	0.5	285
pretrigger + FLT + SLT efficiency	0.6	228	0.6	342	0.6	171
tracking efficiency	0.9	205	0.9	308	0.9	154
vertexing efficiency	0.9	185	0.9	277	0.9	139
$t_{\mathrm{vertex}} > 0.5\,\tau_B$	0.61	113	0.61	169	0.61	84
tagging fraction	0.7	79	0.7	118	–	84
Total in three years	240		350		250	

the color-allowed "tree" amplitude contributing to $B^0 \to K^+\pi^-$ must be calculated, which introduces theoretical model-dependence. For a detailed discussion of these uncertainties see Refs. [279] and [280].

The ability of HERA – B to measure a difference between the branching fractions for $B^0 \to K^+\pi^-$ and $\overline{B^0} \to K^-\pi^+$ has been studied in ref. [281]. This study found that the experiment could determine the asymmetry parameter $\mathcal{A} = [Br(K^+\pi^-) - Br(K^-\pi^+)]/[Br(K^+\pi^-) + Br(K^-\pi^+)]$ with a statistical precision of 7.5% in two years of running at an interaction rate of 20 MHz. This result was obtained assuming a signal-to-background ratio (S/B) of unity; for $S/B \simeq 1/5$, the statistical error increases to 12%.

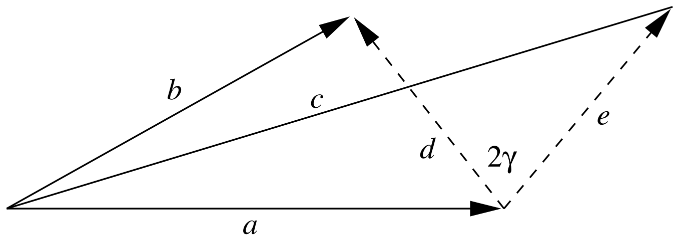

Figure 175: *$SU(2)$ isospin relations (in the complex plane) among amplitudes for* $B^+ \to \pi^+K^0$, $B^0 \to K^+\pi^-$, *and their charge conjugates. The labels are explained in the text. The interior angle between vectors* $\vec{d}$ *and* $\vec{e}$ *is* 2γ.

Extracting γ from $B^0 \to \pi^+\pi^-$ and $B_s^0 \to K^+K^-$ Decays

The modes $B^0 \to \pi^+\pi^-$ and $B_s^0 \to K^+K^-$ can be used to measure γ with relatively little theoretical uncertainty [282]. For these modes one plots the lifetime distributions and constructs the observable

$$A_f(t) \equiv \frac{\Gamma(B^0 \to f) - \Gamma(\overline{B^0} \to \overline{f})}{\Gamma(B^0 \to f) + \Gamma(\overline{B^0} \to \overline{f})} \quad . \tag{51}$$

This observable receives contributions from both CP violation due to $B^0 - \overline{B^0}$ mixing and direct CP violation in the decay amplitudes. The time dependence has the form

$$A_f(t) \;=\; \mathcal{A}_{\rm CP}^{\rm dir}\cos(\Delta m\, t) + \mathcal{A}_{\rm CP}^{\rm mix}\sin(\Delta m\, t) \quad , \tag{52}$$

where

$$\mathcal{A}_{\rm CP}^{\rm dir} \;=\; -\left[\frac{2d\sin\theta\sin\gamma}{1-2d\cos\theta\cos\gamma+d^2}\right] \quad , \tag{53}$$

$$\mathcal{A}_{\rm CP}^{\rm mix} \;=\; \eta\left[\frac{\sin(2\beta+2\gamma)-2d\cos\theta\sin(2\beta+\gamma)+d^2\sin(2\beta)}{1-2d\cos\theta\cos\gamma+d^2}\right] \quad , \tag{54}$$

and η is the CP eigenvalue of the final state (+1 for $\pi^+\pi^-$). In these expressions the parameters d and θ are the magnitude and phase of the ratio of a penguin decay amplitude to the sum of penguin and tree amplitudes, scaled by several CKM matrix elements. If the penguin amplitude is negligibly small, then $d = 0$, $\mathcal{A}_{\rm CP}^{\rm dir} = 0$, and $\mathcal{A}_{\rm CP}^{\rm mix} = +\sin(2\beta+2\gamma) = -\sin 2\alpha$. The objective is then to measure the two quantities $\mathcal{A}_{\rm CP}^{\rm dir}$ and $\mathcal{A}_{\rm CP}^{\rm mix}$ for both $B^0 \to \pi^+\pi^-$ and $B_s^0 \to K^+K^-$ decays; this yields four measurements for four unknowns (d, θ, β, γ) and γ can be determined. This method assumes d and θ are the same for both $B^0 \to \pi^+\pi^-$ and $B_s^0 \to K^+K^-$, i.e., that strong decay amplitudes remain unchanged under exchange of all d and s quarks. This assumption is referred to as "U-spin" symmetry and has been shown [282] to be valid within the "Bander-Silverman-Soni" mechanism [283]. Certain non-factorizable U-spin-breaking corrections have been studied in ref. [284] and found to be small; it is argued that remaining corrections are suppressed by $\Lambda_{\rm QCD}/m_b$.

Experimentally, it is probably not feasible for HERA – B to measure the observables $\mathcal{A}_{\rm CP}^{\rm dir}$ and $\mathcal{A}_{\rm CP}^{\rm mix}$ for $B_s^0 \to K^+K^-$, as the sample of tagged B_s^0 decays is expected to be only $\simeq 60$ events per year and the oscillations are rapid (current world limit: $\Delta m_s > 15\,{\rm ps}^{-1}$ [285]). However, the branching fraction for $B_s^0 \to K^+K^-$ can also be expressed in terms of d, θ, β, γ and should be measured with good precision at HERA – B, as no tagging or lifetime distribution is required. Once β is well-measured, the problem is reduced to three observables and three unknowns. The third observable is defined as

$$K \;\equiv\; -\left(\frac{1}{\epsilon}\right)\frac{\mathcal{A}_{\rm CP}^{\rm dir}(B^0\to\pi^+\pi^-)}{\mathcal{A}_{\rm CP}^{\rm dir}(B_s^0\to K^+K^-)} \;=\; \frac{1+2d\cos\theta\cos\gamma+d^2}{1-2d\cos\theta\cos\gamma+d^2} \tag{55}$$

$$=\; \left(\frac{1}{\epsilon}\right)\left|\frac{\mathcal{C}}{\mathcal{C}'}\right|^2\left[\frac{m_{B_s^0}}{m_{B^0}}\,\frac{\Phi(m_\pi/m_{B^0}, m_\pi/m_{B^0})}{\Phi(m_K/m_{B_s^0}, m_K/m_{B_s^0})}\,\frac{\tau_{B^0}}{\tau_{B_s^0}}\right]\left[\frac{{\rm Br}(B_s^0\to K^+K^-)}{{\rm Br}(B^0\to\pi^+\pi^-)}\right] \tag{56}$$

$$\simeq\; \left(\frac{1}{\epsilon}\right)\frac{1}{1.56}\left[\frac{{\rm Br}(B_s^0\to K^+K^-)}{{\rm Br}(B^0\to\pi^+\pi^-)}\right] \quad , \tag{57}$$

where

$$\epsilon \;=\; \frac{|V_{us}|^2}{1-|V_{us}|^2} \quad .$$

Combining eqs. (55) and (57) gives us the needed relationship among d, θ, and γ. In eq. (56), the factor $|\mathcal{C}/\mathcal{C}'|$ is a ratio of hadronic matrix elements which equals 1 in the limit of exact U-spin symmetry. Corrections to this have been calculated within a factorization model and found to be small. The factor $\Phi(x,y)$ is the two-body phase space function $([1-(x+y)^2][1-(x-y)^2])^{1/2}$.

In practice, the three observables $\mathcal{A}_{\rm CP}^{\rm dir}$, $\mathcal{A}_{\rm CP}^{\rm mix}$, and K are related to d, θ, and γ by using one observable to eliminate θ and using the other two to provide two relations for d as a function of

γ. These relations can be plotted as contours in the γ-d plane, and the points where the contours intersect yield the allowed values for γ. Explicitly, the relation resulting from $\mathcal{A}_{\rm CP}^{\rm dir}$ and $\mathcal{A}_{\rm CP}^{\rm mix}$ is:

$$d = \sqrt{\frac{\ell \pm \sqrt{\ell^2 - hk}}{k}} \quad , \tag{58}$$

where

$$\begin{aligned} h &= u^2 + D(1 - u\cos\gamma)^2 &(59)\\ k &= v^2 + D(1 - v\cos\gamma)^2 &(60)\\ \ell &= 2 - uv - D(1 - u\cos\gamma)(1 - v\cos\gamma) &(61)\end{aligned}$$

and $u,\ v,\ D$ are

$$u = \frac{\mathcal{A}_{\rm CP}^{\rm mix}({\rm B}^0 \to \pi^+\pi^-) - \sin(2\beta + 2\gamma)}{\mathcal{A}_{\rm CP}^{\rm mix}({\rm B}^0 \to \pi^+\pi^-)\cos\gamma - \sin(2\beta + \gamma)} \tag{62}$$

$$v = \frac{\mathcal{A}_{\rm CP}^{\rm mix}({\rm B}^0 \to \pi^+\pi^-) - \sin(2\beta)}{\mathcal{A}_{\rm CP}^{\rm mix}({\rm B}^0 \to \pi^+\pi^-)\cos\gamma - \sin(2\beta + 2\gamma)} \tag{63}$$

$$D = \left[\frac{\mathcal{A}_{\rm CP}^{\rm dir}({\rm B}^0 \to \pi^+\pi^-)}{\sin\gamma}\right]^2 \quad . \tag{64}$$

The relation resulting from the observable K is

$$d = \sqrt{\frac{\epsilon^2(K-1) - \epsilon(1+\epsilon K)u\cos\gamma}{1 - \epsilon^2 K + \epsilon(1+\epsilon K)v\cos\gamma}} \quad . \tag{65}$$

In summary, for HERA – B the relevant observables are $\mathcal{A}_{\rm CP}^{\rm dir}$ and $\mathcal{A}_{\rm CP}^{\rm mix}$ for the decay ${\rm B}^0 \to \pi^+\pi^-$, and the branching fractions ${\rm Br}({\rm B}^0 \to \pi^+\pi^-)$ and ${\rm Br}({\rm B}_{\rm s}^0 \to {\rm K}^+{\rm K}^-)$. These four observables together with the measured value of β allow a determination of the angle γ. The issue to be addressed is whether the number of ${\rm B}^0 \to \pi^+\pi^-$ events listed in Tab. 67 allows HERA – B to measure the asymmetry $A_{\pi^+\pi^-}(t)$ with sufficient precision to determine $\mathcal{A}_{\rm CP}^{\rm dir}$ and $\mathcal{A}_{\rm CP}^{\rm mix}$, and, given the resultant uncertainties on $\mathcal{A}_{\rm CP}^{\rm dir}$ and $\mathcal{A}_{\rm CP}^{\rm mix}$, what this implies for the uncertainty on γ.

Measurement of $\mathcal{A}_{\rm CP}^{\rm dir}$ and $\mathcal{A}_{\rm CP}^{\rm mix}$ with No Background

To determine the accuracy with which HERA – B can measure $\mathcal{A}_{\rm CP}^{\rm dir}$ and $\mathcal{A}_{\rm CP}^{\rm mix}$, we choose values for these parameters and generate samples of ${\rm B}^0 \to \pi^+\pi^-$ and $\overline{{\rm B}^0} \to \pi^+\pi^-$ decays. We plot their lifetime distributions, construct the observable $A_{\pi^+\pi^-}(t)$, and fit this distribution to the function $x\cos(\Delta m\,t) + y\sin(\Delta m\,t)$, where x and y are free parameters. The fit returns central values for x and y as well as $1\,\sigma$ errors. The interval implied by these errors should include the generated values 68.3% of the time. We repeat this procedure for different values of $\mathcal{A}_{\rm CP}^{\rm dir}$ and $\mathcal{A}_{\rm CP}^{\rm mix}$ to determine how well HERA – B can measure these parameters for various possibilities. When constructing the lifetime distributions, the number of ${\rm B}^0 \to \pi^+\pi^-$ decays generated is $237/0.61 = 388$, corresponding to the tagged sample before the lifetime cut listed in Tab. 67. The number of $\overline{{\rm B}^0} \to \pi^+\pi^-$ decays is given by $(1-\xi)/(1+\xi) \times N_{{\rm B}^0}$, where $\xi = (\mathcal{A}_{\rm CP}^{\rm dir} + x\,\mathcal{A}_{\rm CP}^{\rm mix})/(1+x^2)$ and x is the ${\rm B}^0 - \overline{{\rm B}^0}$ mixing parameter. This number of $\overline{{\rm B}^0} \to \pi^+\pi^-$ decays accounts for the time-integrated CP asymmetry predicated by the values of $\mathcal{A}_{\rm CP}^{\rm dir}$ and $\mathcal{A}_{\rm CP}^{\rm mix}$. When fitting the distributions, we do not include the first bin ($\tau < 0.50\,\tau_{\rm B}$), as these events would be removed by the lifetime cut needed to distinguish secondary vertices from primary vertices. Finally, when constructing the distributions we smear the generated lifetimes by the expected resolution, about $0.05\,\tau_B$. We do not yet include background or mistagging.

The results of the fitting procedure are listed in Tab. 68. The left-most columns list the chosen values of $\mathcal{A}_{\rm CP}^{\rm dir}$ and $\mathcal{A}_{\rm CP}^{\rm mix}$; the next two columns list the number of decays generated, and the right-most columns list the results of the fit. The table also denotes whether the original values of $\mathcal{A}_{\rm CP}^{\rm dir}$ and $\mathcal{A}_{\rm CP}^{\rm mix}$ are within $1.64\,\sigma$ intervals around the central values returned by the fit. We observe that they are within this interval 78% of the time for $\mathcal{A}_{\rm CP}^{\rm dir}$ and 86% of the time for $\mathcal{A}_{\rm CP}^{\rm mix}$. This is roughly consistent with our use of $1.64\,\sigma$, which corresponds to a 90% confidence interval. The fits themselves are shown in Figs. 176–178.

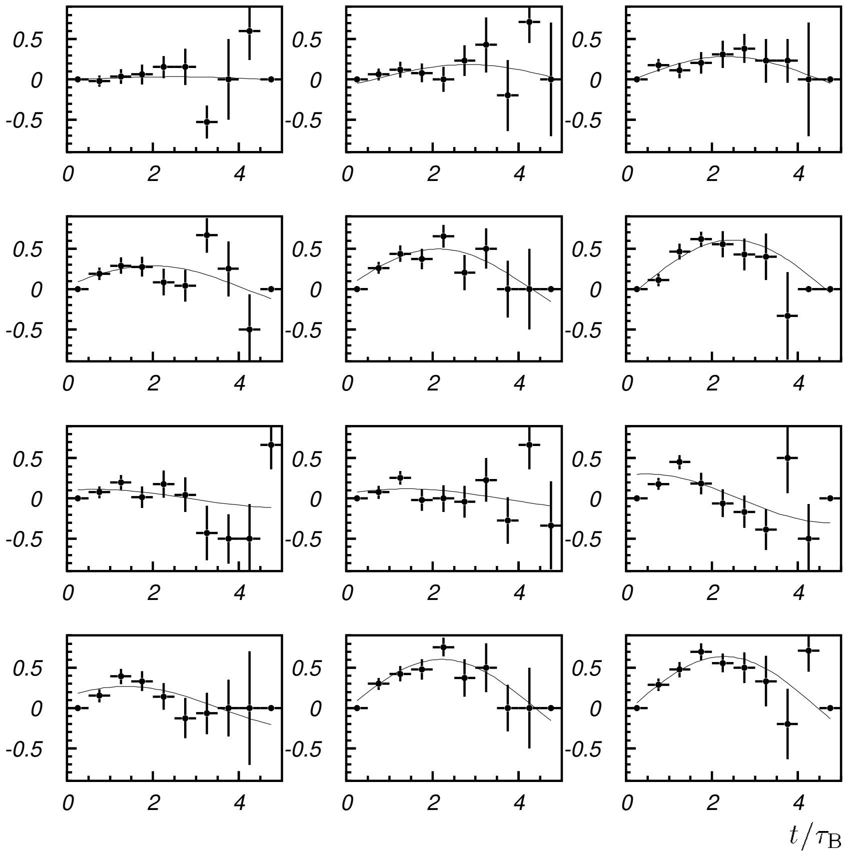

Figure 176: *Fit results for the reconstructed asymmetry $A_{\pi^+\pi^-}$ for the assumptions $\mathcal{A}_{\rm CP}^{\rm dir} = 0$ (top two rows) and $\mathcal{A}_{\rm CP}^{\rm dir} = 0.10$ (bottom two rows). For each pair of rows, $\mathcal{A}_{\rm CP}^{\rm mix} = 0$, 0.10, 0.20, 0.30, 0.40, and 0.50. The first (left-most) bin is not used in the fit as these events would be removed by the lifetime cut needed to distinguish primary vertices from secondary vertices.*

We insert the fit values for $\mathcal{A}_{\rm CP}^{\rm dir}$ and $\mathcal{A}_{\rm CP}^{\rm mix}$ into eqs. (62)–(64) and calculate u, v, and D. Using these values we plot the contours of d as a function of γ given by eqs. (58) and (65). The point(s) where the contours intersect denote the measured value for γ. To illustrate this procedure, we consider the case $\gamma = 76°$, $2\beta = 53°$, $d = 0.3$, and $\theta = 210°$, as chosen in ref. [282]. These choices lie within the currently allowed ranges for these parameters, and they give $\mathcal{A}_{\rm CP}^{\rm dir} = 0.2394$ and $\mathcal{A}_{\rm CP}^{\rm mix} = 0.04366$. These values imply that for $N_{{\rm B}^0\to\pi\pi} = 388$, $N_{\overline{{\rm B}^0}\to\pi\pi} = 271$. Fitting to such samples yields: $\mathcal{A}_{\rm CP}^{\rm dir} = 0.292 \pm 0.089$ and $\mathcal{A}_{\rm CP}^{\rm mix} = 0.064 \pm 0.082$. The fit is shown in Fig. 179, and the resultant γ-d contours are shown in Fig. 180. The plot on the left shows the contours resulting only from the central values of the fit. These contours intersect at two points; i.e., there is a two-fold

Table 68: *The results of fits to Monte Carlo distributions for the asymmetry function $A(t)$. The two left-most columns list the values of $\mathcal{A}_{\rm CP}^{\rm dir}$ and $\mathcal{A}_{\rm CP}^{\rm mix}$ used to generate the decay distributions. The right-most column lists whether the fit central values (columns 6, 7) are within $1.64\,\sigma$ of the true values: "badd" indicates $\mathcal{A}_{\rm CP}^{\rm dir}$ did not match, "badm" indicates $\mathcal{A}_{\rm CP}^{\rm mix}$ did not match, and "baddm" indicates neither matched. No background is included.*

$\mathcal{A}_{\rm CP}^{\rm dir}$	$\mathcal{A}_{\rm CP}^{\rm mix}$	$\pi\pi$ Decays of B^0	$\overline{B^0}$	χ^2	$\mathcal{A}_{\rm fit}^{\rm dir}$	$\mathcal{A}_{\rm fit}^{\rm mix}$	$< 1.64\,\sigma$?
0.00	0.00	388	388	1.906	-0.008 ± 0.081	0.032 ± 0.075	
0.00	0.10	388	353	1.239	-0.083 ± 0.086	0.165 ± 0.078	
0.00	0.20	388	321	0.367	-0.033 ± 0.084	0.282 ± 0.079	
0.00	0.30	388	291	1.549	0.040 ± 0.085	0.285 ± 0.078	
0.00	0.40	388	264	0.691	0.016 ± 0.087	0.496 ± 0.078	
0.00	0.50	388	239	1.054	-0.128 ± 0.093	0.595 ± 0.076	
0.10	0.00	388	340	1.840	0.100 ± 0.087	0.054 ± 0.084	
0.10	0.10	388	309	1.628	0.062 ± 0.085	0.102 ± 0.079	
0.10	0.20	388	281	2.073	0.288 ± 0.088	0.099 ± 0.081	badd
0.10	0.30	388	254	0.832	0.148 ± 0.092	0.224 ± 0.083	
0.10	0.40	388	230	0.673	-0.018 ± 0.085	0.603 ± 0.073	badm
0.10	0.50	388	208	1.466	-0.052 ± 0.085	0.637 ± 0.069	baddm
0.20	0.00	388	298	1.265	0.058 ± 0.086	0.064 ± 0.080	badd
0.20	0.10	388	270	0.373	0.135 ± 0.094	0.177 ± 0.084	
0.20	0.20	388	245	0.977	0.178 ± 0.092	0.275 ± 0.088	
0.20	0.30	388	221	0.226	0.233 ± 0.092	0.314 ± 0.087	
0.20	0.40	388	199	3.373	-0.006 ± 0.083	0.603 ± 0.068	baddm
0.20	0.50	388	179	0.593	0.118 ± 0.091	0.615 ± 0.078	
0.30	0.00	388	260	0.151	0.093 ± 0.090	0.093 ± 0.082	badd
0.30	0.10	388	236	1.207	0.357 ± 0.084	0.122 ± 0.081	
0.30	0.20	388	213	0.193	0.337 ± 0.091	0.213 ± 0.085	
0.30	0.30	388	191	1.169	0.375 ± 0.089	0.247 ± 0.084	
0.30	0.40	388	172	0.979	0.163 ± 0.095	0.451 ± 0.080	
0.30	0.50	388	153	0.348	0.088 ± 0.097	0.625 ± 0.083	badd
0.40	0.00	388	227	0.387	0.534 ± 0.085	-0.105 ± 0.081	
0.40	0.10	388	204	0.373	0.503 ± 0.090	0.054 ± 0.087	
0.40	0.20	388	184	0.656	0.394 ± 0.092	0.226 ± 0.085	
0.40	0.30	388	164	0.541	0.325 ± 0.090	0.335 ± 0.084	
0.40	0.40	388	146	1.239	0.281 ± 0.092	0.561 ± 0.084	badm
0.40	0.50	388	129	0.996	0.426 ± 0.091	0.509 ± 0.084	
0.50	0.00	388	196	0.939	0.514 ± 0.088	0.008 ± 0.087	
0.50	0.10	388	176	1.896	0.661 ± 0.092	-0.005 ± 0.084	badd
0.50	0.20	388	157	1.718	0.443 ± 0.092	0.234 ± 0.087	
0.50	0.30	388	140	1.093	0.288 ± 0.093	0.485 ± 0.082	baddm
0.50	0.40	388	123	1.505	0.492 ± 0.091	0.457 ± 0.077	
0.50	0.50	388	108	1.132	0.601 ± 0.085	0.460 ± 0.087	

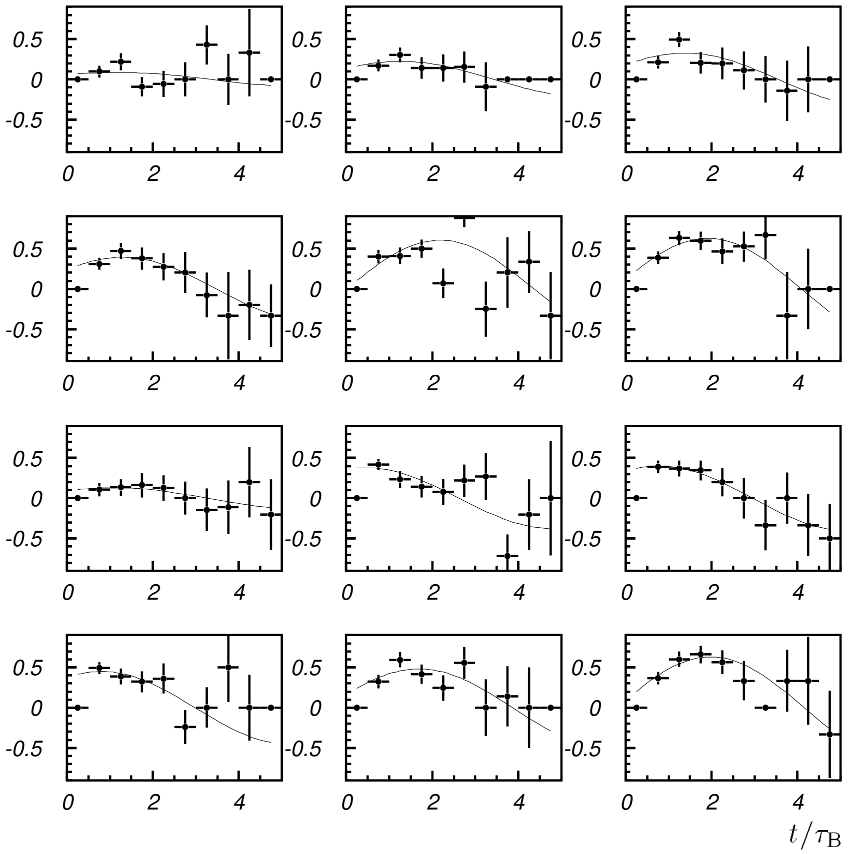

Figure 177: *Fit results for the reconstructed asymmetry* $A_{\pi^+\pi^-}$ *for the assumptions* $\mathcal{A}_{\mathrm{CP}}^{\mathrm{dir}} = 0.20$ *(top two rows) and* $\mathcal{A}_{\mathrm{CP}}^{\mathrm{dir}} = 0.30$ *(bottom two rows). For each pair of rows,* $\mathcal{A}_{\mathrm{CP}}^{\mathrm{mix}} = 0$, 0.10, 0.20, 0.30, 0.40, *and* 0.50. *The first (left-most) bin is not used in the fit as these events would presumably be eliminated by the lifetime cut needed to distinguish primary vertices from secondary vertices.*

ambiguity in determining γ. The two points are 54° and 74°, with the latter being very close to the true value. The plot on the right shows several contours resulting from setting $\mathcal{A}_{\mathrm{CP}}^{\mathrm{dir}}$ and $\mathcal{A}_{\mathrm{CP}}^{\mathrm{mix}}$ equal to values $1.64\,\sigma$ above and below the central values returned by the fit. This gives a conservative range for γ as it neglects correlations in the errors for $\mathcal{A}_{\mathrm{CP}}^{\mathrm{dir}}$ and $\mathcal{A}_{\mathrm{CP}}^{\mathrm{mix}}$. The plot shows that the lowest point where the contours intersect is 49° and the highest point is 80°; thus a 90% confidence interval for γ is 49°–80°. This measurement could be the first direct constraint upon γ, and the range of 30° is smaller than the current allowed range for γ – inferred indirectly – of $38° \leq \gamma \leq 81°$ [286]. Note that there exist contours which intersect at much higher values of γ; these would imply $\gamma > 120°$, which is strongly disfavored by current data [286] and in the future may be excluded. For other values of $\mathcal{A}_{\mathrm{CP}}^{\mathrm{dir}}$ and $\mathcal{A}_{\mathrm{CP}}^{\mathrm{mix}}$ we expect similar results, as the mean errors (values of σ) for $\mathcal{A}_{\mathrm{CP}}^{\mathrm{dir}}$ and $\mathcal{A}_{\mathrm{CP}}^{\mathrm{mix}}$ returned by the fit are 0.089 and 0.081 (see Tab. 68), which are the same as the values used above.

Measurement of $\mathcal{A}_{\mathrm{CP}}^{\mathrm{dir}}$ and $\mathcal{A}_{\mathrm{CP}}^{\mathrm{mix}}$ with Background

To include the effect of background, we assume that the background under the $\mathrm{B}^0 \to \pi^+\pi^-$ mass peak is the same as that comprising the sidebands next to the $\pi^+\pi^-$ peak. In this case both the approximate number of background events in the $\mathrm{B}^0 \to \pi^+\pi^-$ sample and their lifetime distribution can be determined. The $\mathrm{B}^0 \to \pi^+\pi^-$ and $\overline{\mathrm{B}^0} \to \pi^+\pi^-$ lifetime distributions can then be corrected before the asymmetry parameter $A(t)$ is calculated. After $A(t)$ is calculated the analysis proceeds

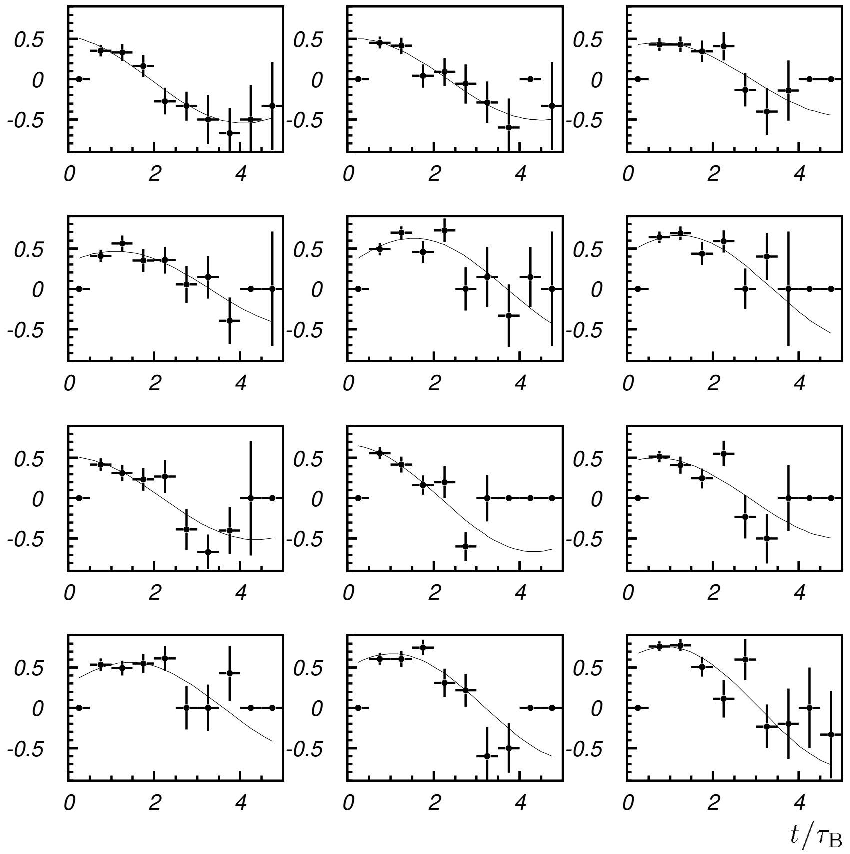

Figure 178: *Fit results for the reconstructed asymmetry $A_{\pi^+\pi^-}$ for the assumptions $\mathcal{A}_{\rm CP}^{\rm dir} = 0.40$ (top two rows) and $\mathcal{A}_{\rm CP}^{\rm dir} = 0.50$ (bottom two rows). For each pair of rows, $\mathcal{A}_{\rm CP}^{\rm mix} = 0$, 0.10, 0.20, 0.30, 0.40, and 0.50. The first (left-most) bin is not used in the fit as these events would presumably be eliminated by the lifetime cut needed to distinguish primary vertices from secondary vertices.*

as before. Due to statistical fluctuations in the background, the uncertainties on $\mathcal{A}_{\rm CP}^{\rm dir}$ and $\mathcal{A}_{\rm CP}^{\rm mix}$ returned by the fit will be larger, and the confidence interval for γ correspondingly larger.

To study this effect we generate two lifetime distributions for background events: one corresponding to $\rm B^0 \to \pi^+\pi^-$ decays and one corresponding to $\overline{\rm B^0} \to \pi^+\pi^-$ decays. The number of background events is taken to equal the number of $\rm B^0 \to \pi^+\pi^-$ decays, i.e., $S/B = 1$. The mean lifetime of the background is for simplicity taken to be $\tau_{\rm B}/3$, corresponding to the $\rm D^0$ lifetime. The lifetime distributions for background are then added to those for $\rm B^0 \to \pi^+\pi^-$ and $\overline{\rm B^0} \to \pi^+\pi^-$. The resultant distributions represent data as recorded, and they are subsequently corrected for background bin-by-bin by utilizing the knowledge that $N_{\rm bkg} \simeq N_{\rm B^0 \to \pi\pi}$ and $\tau_{\rm bkg} \simeq 0.3\tau_{\rm B}$. Specifically, the background estimate for a bin spanning the lifetime range $t_{\rm low}$–$t_{\rm high}$ is

$$N_{\rm bkg} = N_{\rm B^0 \to \pi\pi} \times \left[e^{-3\, t_{\rm low}/\tau_{\rm B}} - e^{-3\, t_{\rm high}/\tau_{\rm B}} \right]. \tag{66}$$

From this point the analysis proceeds as before. For the case considered above ($\gamma = 76°$, $2\beta = 53°$, $d = 0.3$, and $\theta = 210°$), the fit for $A(t)$ yields: $\mathcal{A}_{\rm CP}^{\rm dir} = 0.329 \pm 0.108$ and $\mathcal{A}_{\rm CP}^{\rm mix} = 0.143 \pm 0.087$. The fit function is shown in Fig. 181 and the γ-d contours are shown in Fig. 182. The plot on the right shows the contours resulting from setting $\mathcal{A}_{\rm CP}^{\rm dir}$ and $\mathcal{A}_{\rm CP}^{\rm mix}$ equal to values $1.64\,\sigma$ above and below the central values returned by the fit. The lowest point at which the contours intersect is 47° and the highest point is 78°; i.e., the 90% confidence interval is 47°–78°, which is very similar to the range found without background. It may seem surprising that the shifted values and errors for $\mathcal{A}_{\rm CP}^{\rm dir}$

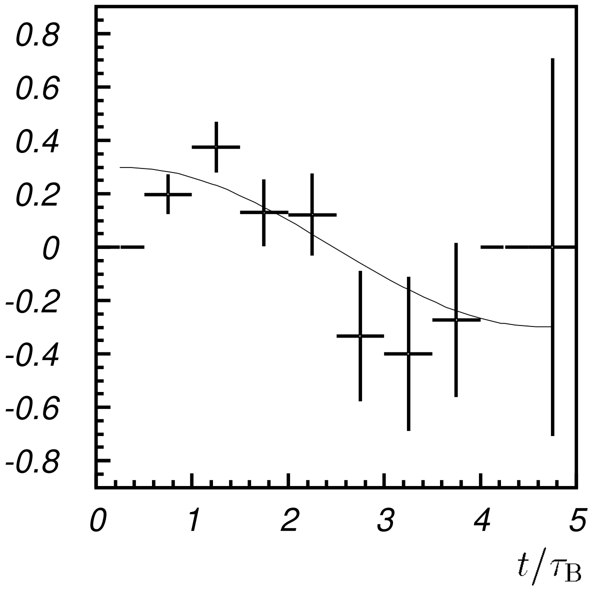

Figure 179: *Fit results for the reconstructed asymmetry $A_{\pi^+\pi^-}$ for the assumptions $\mathcal{A}_{\mathrm{CP}}^{\mathrm{dir}} = 0.2394$ and $\mathcal{A}_{\mathrm{CP}}^{\mathrm{mix}} = 0.04366$, which correspond to $\gamma = 76°$, $2\beta = 53°$, $d = 0.3$, and $\theta = 210°$. There is no background included here.*

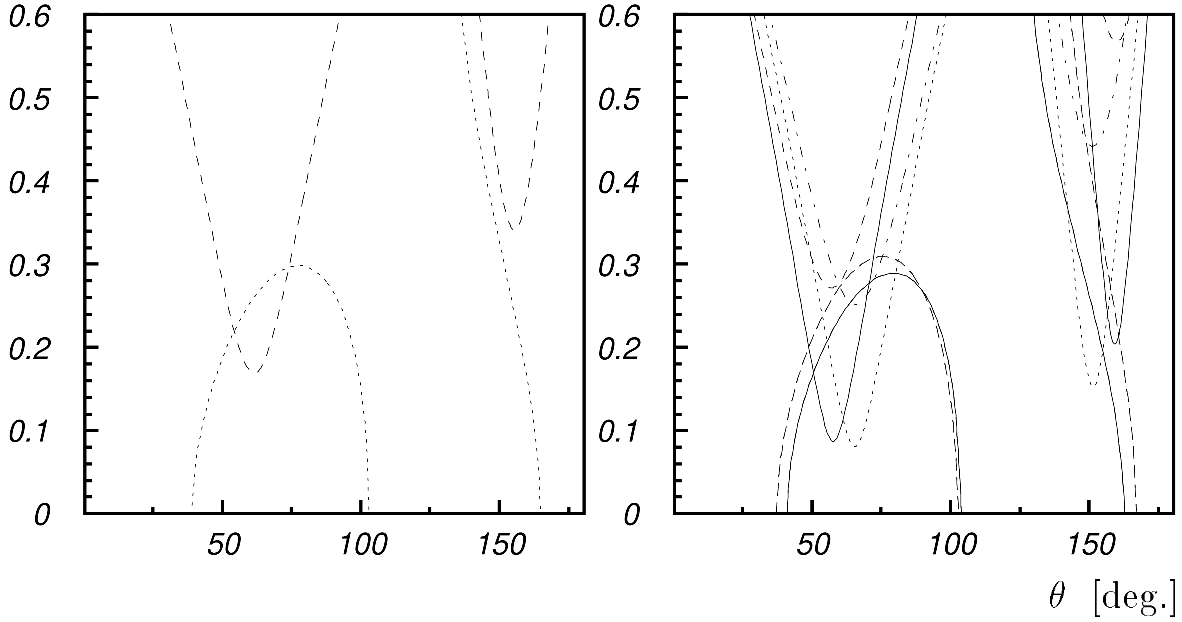

Figure 180: *The γ-d contours resulting from the measurements $\mathcal{A}_{\mathrm{CP}}^{\mathrm{dir}} = 0.292 \pm 0.089$ and $\mathcal{A}_{\mathrm{CP}}^{\mathrm{mix}} = 0.064 \pm 0.082$. The plot on the left shows the contours resulting only from the central values; the plot on the right shows the contours resulting from choosing $\mathcal{A}_{\mathrm{CP}}^{\mathrm{dir}}$ and $\mathcal{A}_{\mathrm{CP}}^{\mathrm{mix}}$ both higher and lower than their central values by $1.64\,\sigma$. No background is included here.*

and $\mathcal{A}_{\mathrm{CP}}^{\mathrm{mix}}$ result in such a small shift for γ; this is presumably due to the "steepness" of the γ-d contours, i.e., a small shift in γ results in a large shift in the intersection point of the two curves. Thus, interpreting this in reverse, a modest shift in the intersection points – as results from shifts in $\mathcal{A}_{\mathrm{CP}}^{\mathrm{dir}}$ and $\mathcal{A}_{\mathrm{CP}}^{\mathrm{mix}}$ – corresponds to a slight shift in γ.

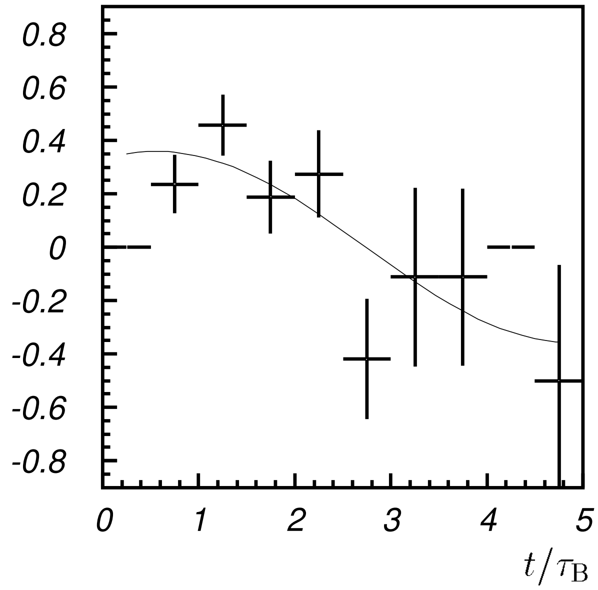

Figure 181: *Fit results for the reconstructed asymmetry $A_{\pi^+\pi^-}$ for the assumptions $\mathcal{A}_{\mathrm{CP}}^{\mathrm{dir}} = 0.2394$ and $\mathcal{A}_{\mathrm{CP}}^{\mathrm{mix}} = 0.04366$, which correspond to $\gamma = 76°$, $2\beta = 53°$, $d = 0.3$, and $\theta = 210°$. Background is included here for $S/B = 1$.*

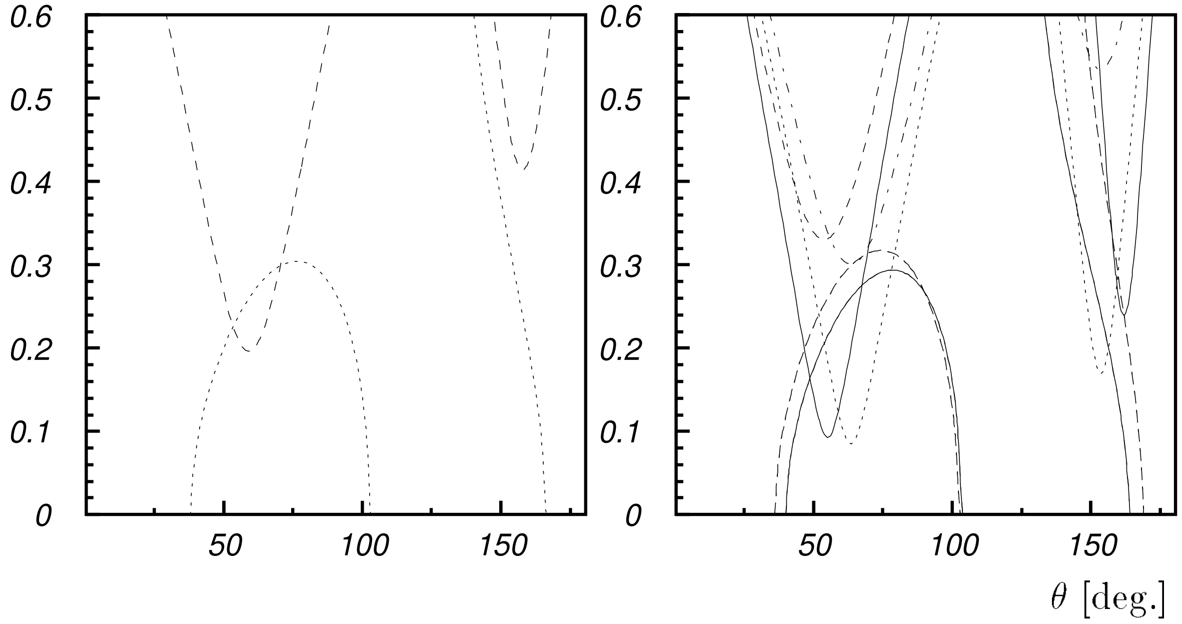

Figure 182: *The γ-d contours resulting from the measurements $\mathcal{A}_{\mathrm{CP}}^{\mathrm{dir}} = 0.329 \pm 0.108$ and $\mathcal{A}_{\mathrm{CP}}^{\mathrm{mix}} = 0.143 \pm 0.087$. The plot on the left shows the contours resulting only from the central values; the plot on the right shows the contours resulting from choosing $\mathcal{A}_{\mathrm{CP}}^{\mathrm{dir}}$ and $\mathcal{A}_{\mathrm{CP}}^{\mathrm{mix}}$ both higher and lower than their central values by $1.64\,\sigma$. Background is included here.*

For completeness we list the fit results for all values of $\mathcal{A}_{\mathrm{CP}}^{\mathrm{dir}}$ and $\mathcal{A}_{\mathrm{CP}}^{\mathrm{mix}}$ in Tab. 69. The table shows that the true values of $\mathcal{A}_{\mathrm{CP}}^{\mathrm{dir}}$ and $\mathcal{A}_{\mathrm{CP}}^{\mathrm{mix}}$ are within $1.64\,\sigma$ of the central values returned by the fit 89% of the time for $\mathcal{A}_{\mathrm{CP}}^{\mathrm{dir}}$ and 75% of the time for $\mathcal{A}_{\mathrm{CP}}^{\mathrm{mix}}$. The mean uncertainties on $\mathcal{A}_{\mathrm{CP}}^{\mathrm{dir}}$ and $\mathcal{A}_{\mathrm{CP}}^{\mathrm{mix}}$ (Tab. 69) are 0.109 and 0.086, respectively, which are somewhat larger than those obtained when background was neglected.

Table 69: *The results of fits to Monte Carlo distributions for the asymmetry function $A(t)$. The two left-most columns list the values of $\mathcal{A}_{\rm CP}^{\rm dir}$ and $\mathcal{A}_{\rm CP}^{\rm mix}$ used to generate the decay distributions. The right-most column lists whether the fit central values (columns 6, 7) are within $1.64\,\sigma$ of the true values: "*badd*" indicates $\mathcal{A}_{\rm CP}^{\rm dir}$ did not match, "*badm*" indicates $\mathcal{A}_{\rm CP}^{\rm mix}$ did not match, and "*baddm*" indicates neither matched. Background is included in the lifetime distributions.*

$\mathcal{A}_{\rm CP}^{\rm dir}$	$\mathcal{A}_{\rm CP}^{\rm mix}$	**$\pi\pi$ Decays of** B^0	$\overline{\mathrm{B}^0}$	χ^2	$\mathcal{A}_{\rm fit}^{\rm dir}$	$\mathcal{A}_{\rm fit}^{\rm mix}$	**$< 1.64\,\sigma$?**
0.00	0.00	388	388	0.689	0.076 ± 0.098	0.073 ± 0.079	
0.00	0.10	388	353	2.383	-0.072 ± 0.095	0.158 ± 0.079	
0.00	0.20	388	321	0.210	-0.108 ± 0.102	0.177 ± 0.081	
0.00	0.30	388	291	1.897	-0.105 ± 0.103	0.167 ± 0.081	badm
0.00	0.40	388	264	0.638	-0.072 ± 0.108	0.402 ± 0.088	
0.00	0.50	388	239	1.735	0.087 ± 0.101	0.491 ± 0.077	
0.10	0.00	388	340	0.189	0.235 ± 0.099	-0.133 ± 0.083	
0.10	0.10	388	309	1.399	0.153 ± 0.103	0.052 ± 0.087	
0.10	0.20	388	281	0.059	0.141 ± 0.104	0.230 ± 0.088	
0.10	0.30	388	254	0.816	0.335 ± 0.101	0.150 ± 0.087	baddm
0.10	0.40	388	230	0.693	0.069 ± 0.114	0.443 ± 0.082	
0.10	0.50	388	208	1.310	0.269 ± 0.107	0.491 ± 0.085	
0.20	0.00	388	298	0.787	0.227 ± 0.098	-0.019 ± 0.087	
0.20	0.10	388	270	2.509	0.362 ± 0.096	-0.121 ± 0.079	baddm
0.20	0.20	388	245	0.460	0.312 ± 0.110	0.136 ± 0.089	
0.20	0.30	388	221	1.717	0.207 ± 0.123	0.323 ± 0.087	
0.20	0.40	388	199	1.547	0.315 ± 0.104	0.394 ± 0.082	
0.20	0.50	388	179	0.984	0.163 ± 0.114	0.704 ± 0.076	badm
0.30	0.00	388	260	0.740	0.152 ± 0.106	0.185 ± 0.089	badm
0.30	0.10	388	236	1.070	0.460 ± 0.107	0.071 ± 0.092	
0.30	0.20	388	213	0.213	0.407 ± 0.116	0.144 ± 0.089	
0.30	0.30	388	191	0.075	0.356 ± 0.111	0.244 ± 0.092	
0.30	0.40	388	172	1.449	0.253 ± 0.105	0.379 ± 0.087	
0.30	0.50	388	153	1.134	0.373 ± 0.120	0.455 ± 0.091	
0.40	0.00	388	227	1.211	0.247 ± 0.096	0.221 ± 0.084	badm
0.40	0.10	388	204	0.630	0.378 ± 0.116	0.139 ± 0.086	
0.40	0.20	388	184	0.310	0.423 ± 0.118	0.122 ± 0.085	
0.40	0.30	388	164	0.799	0.370 ± 0.115	0.420 ± 0.085	
0.40	0.40	388	146	0.723	0.421 ± 0.105	0.437 ± 0.088	
0.40	0.50	388	129	3.189	0.689 ± 0.121	0.350 ± 0.089	baddm
0.50	0.00	388	196	0.262	0.467 ± 0.109	-0.065 ± 0.087	
0.50	0.10	388	176	0.927	0.629 ± 0.108	0.087 ± 0.090	
0.50	0.20	388	157	1.361	0.287 ± 0.113	0.358 ± 0.089	baddm
0.50	0.30	388	140	1.428	0.666 ± 0.121	0.181 ± 0.087	
0.50	0.40	388	123	0.703	0.453 ± 0.128	0.394 ± 0.095	
0.50	0.50	388	108	0.783	0.649 ± 0.122	0.343 ± 0.093	badm

Measurement of $\mathcal{A}_{\rm CP}^{\rm dir}$ and $\mathcal{A}_{\rm CP}^{\rm mix}$ with Background and Mistagging

Finally we include the effects of mistagging. This is achieved by assuming a mistagging fraction f and moving events from the $\mathrm{B}^0 \to \pi^+\pi^-$ lifetime distribution to the $\overline{\mathrm{B}^0} \to \pi^+\pi^-$ lifetime distribution and vice-versa. The number of events moved is $f \cdot N_{\mathrm{B}^0}$ and $f \cdot N_{\overline{\mathrm{B}^0}}$, respectively. The time-integrated asymmetry $\int A(t)\,dt = (N - \overline{N})/(N + \overline{N})$ is diluted by the well-known factor $1 - 2f$. While we can correct the amplitude of the measured $A(t)$ distribution by this factor, the “statistical smearing” in lifetime for mistagged events remains; i.e., mistagged events are not distributed smoothly among bins of lifetime, and thus applying a global adjustment over-corrects some bins and under-corrects others. The situation would be improved by correcting the lifetime distributions event-by-event rather than bin-by-bin; i.e., weighting events with dubious tags less than events with good tags. This calls for an *unbinned* maximum likelihood (ML) fit with the probability density function (pdf) for the tagging variable(s) included in the likelihood function. We suspect this would return smaller fitting errors for $\mathcal{A}_{\rm CP}^{\rm dir}$ and $\mathcal{A}_{\rm CP}^{\rm mix}$ than those obtained from a binned maximum likelihood fit using a simple yes/no ($\mathrm{B}^0/\overline{\mathrm{B}^0}$) tag. We are currently pursuing such a study, i.e., using an unbinned ML fit. Below we present results for a binned ML fit using a simple $\mathrm{B}^0/\overline{\mathrm{B}^0}$ tag.

For the example case of $\gamma = 76°$, $2\beta = 53°$, $d = 0.3$, $\theta = 210°$, and a mistagging fraction $f = 0.10$, the fit for $A(t)$ yields: $\mathcal{A}_{CP}^{\rm dir} = 0.440 \pm 0.132$ and $\mathcal{A}_{CP}^{\rm mix} = 0.098 \pm 0.107$. The fitted function is shown in Fig. 183 and the γ-d contours are shown in Fig. 184. In the latter figure, the plot on the right shows the contours resulting from setting $\mathcal{A}_{\rm CP}^{\rm dir}$ and $\mathcal{A}_{\rm CP}^{\rm mix}$ equal to values $1.64\,\sigma$ above and below the central values returned by the fit. The lowest point at which the contours intersect is 48° and the highest point is 80°; i.e., the 90% confidence interval is 48°–80°. This is only slighly worse than the case with no mistagging because many of the contours do not intersect, i.e., some combinations of $\mathcal{A}_{\rm CP}^{\rm dir}$ and $\mathcal{A}_{\rm CP}^{\rm mix}$ do not yield a viable solution for γ. The effect is explicitly shown in Fig. 185, which displays the pairs of contours contributing to Fig. 184 (plot on the right). The plots shown in Fig. 185 correspond to $\mathcal{A}_{\rm CP}^{\rm dir}$ and $\mathcal{A}_{\rm CP}^{\rm mix}$ each varying over the three values $\mathcal{A}_{\rm fit} - 1.64\,\sigma$, $\mathcal{A}_{\rm fit}$, and $\mathcal{A}_{\rm fit} + 1.64\,\sigma$.

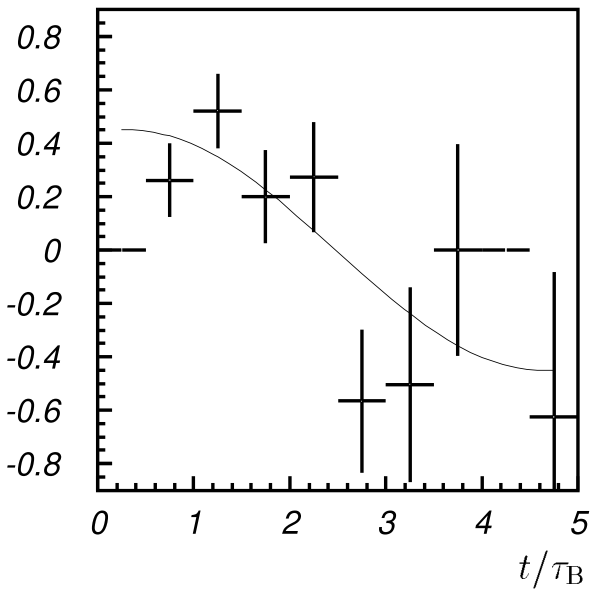

Figure 183: *Fit results for* $\mathcal{A}_{\rm CP}^{\rm dir} = 0.2394$ *and* $\mathcal{A}_{\rm CP}^{\rm mix} = 0.04366$*, which correspond to* $\gamma = 76°$, $2\beta = 53°$, $d = 0.3$, *and* $\theta = 210°$. *Both background and mistagging* ($f_{\rm mistag} = 0.10$) *are included.*

We have repeated the above analysis for different values of the mistagging fraction f. Our results

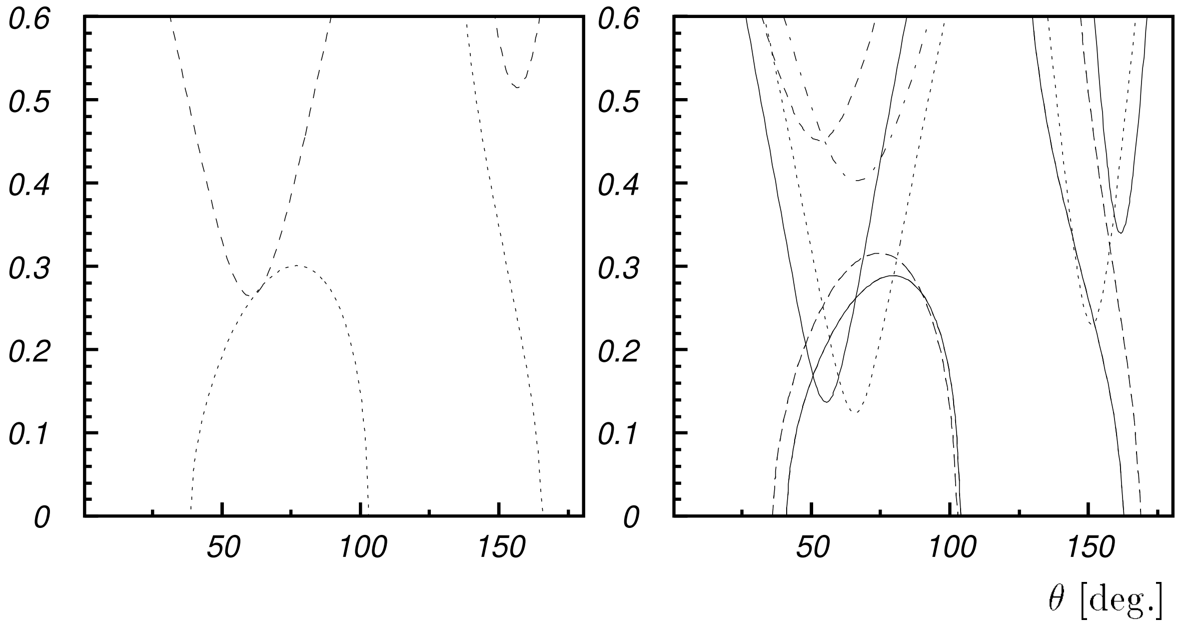

Figure 184: *The γ-d contours resulting from the measurements $\mathcal{A}_{\rm CP}^{\rm dir} = 0.440 \pm 0.132$ and $\mathcal{A}_{\rm CP}^{\rm mix} = 0.098 \pm 0.107$. Both background and mistagging ($f_{\rm mistag} = 0.10$) are included.*

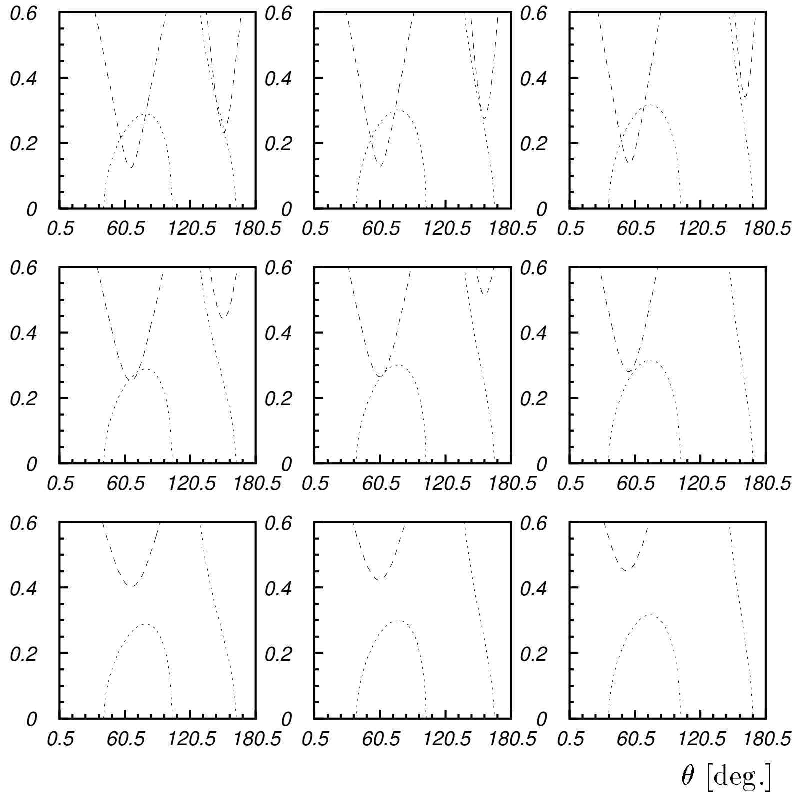

Figure 185: *The nine sets of γ-d contours corresponding to $\mathcal{A}_{\rm CP}^{\rm dir}$ and $\mathcal{A}_{\rm CP}^{\rm mix}$ varying over the values $\mathcal{A}_{\rm fit} - 1.64\,\sigma$, $\mathcal{A}_{\rm fit}$, and $\mathcal{A}_{\rm fit} + 1.64\,\sigma$. The central values and standard deviations returned by the fitting procedure are $\mathcal{A}_{CP}^{\rm dir} = 0.440 \pm 0.132$ and $\mathcal{A}_{CP}^{\rm mix} = 0.098 \pm 0.107$. Contours which do not intersect do not correspond to a viable value of γ.*

are summarized in Fig. 186, which shows the mean value of σ returned by the fits for $\mathcal{A}_{\rm CP}^{\rm dir}$ and $\mathcal{A}_{\rm CP}^{\rm mix}$ as a function of f. From this plot we see that $\langle\sigma\rangle$ increases significantly for $f_{\rm mistag} \gtrsim 0.2$, and thus it is desirable to keep the mistagging fraction below this value. To discern small values of $\mathcal{A}_{\rm CP}^{\rm dir}$ or $\mathcal{A}_{\rm CP}^{\rm mix}$, it may be necessary to keep the mistagging fraction $\lesssim 0.10$. Whether this can be achieved while obtaining good tagging efficiency requires further study with real data. We expect that an analysis using an unbinned ML fit may allow for a higher mistag fraction f.

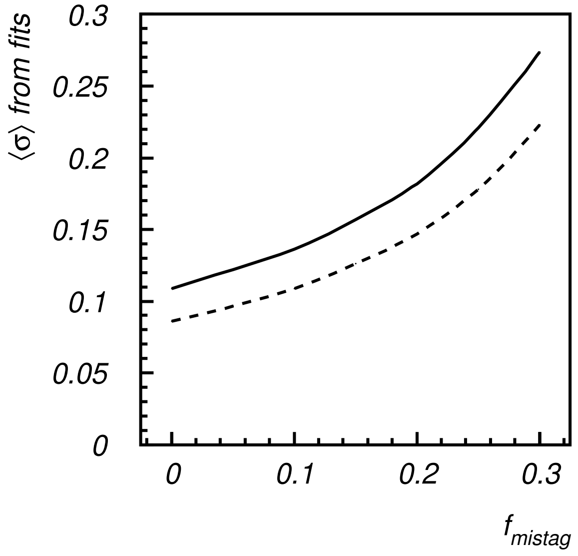

Figure 186: *The mean value of σ returned by the fits for $\mathcal{A}_{\rm CP}^{\rm dir}$ (solid curve) and $\mathcal{A}_{\rm CP}^{\rm mix}$ (dashed curve), as a function of the mistagging fraction f.*

Summary

HERA – B has the potential to measure CP asymmetries in two body hadronic decays of neutral B mesons, allowing sensitive probes of the angles γ and α of the unitarity triangle. A discrepancy between the range of γ inferred from all available data [286] and a direct measurement from HERA – B could indicate new physics; in fact the measured values of $\mathcal{A}_{\rm CP}^{\rm dir}$ and $\mathcal{A}_{\rm CP}^{\rm mix}$ may not even yield a solution for γ. Since flavor-changing neutral-current penguin amplitudes play an important role in these decays, these channels provide a promising way to search for new physics [287].

The event numbers and sensitivities are comparable to those of the e^+e^- factories. During RUN II, the Fermilab collider experiments are expected to acquire an order of magnitude higher statistics but, due to much weaker particle identification, $\pi^+\pi^-$, $K^+\pi^-$ and K^+K^- final states have to be analyzed on a statistical basis using maximum likelihood methods applied to the invariant mass spectra (assuming pion masses). Preliminary studies [288] indicate that the asymmetries could be measured with a precision comparable to that of HERA – B.

5.4.4 Hadronic Rare B Decays

Recent improvements in experimental sensitivity made less favored B decay modes become accessible. These include (i) $b \to u$ tree diagram quark transitions that are suppressed by the small CKM matrix element $V_{\rm ub}$, (ii) flavor changing neutral current (FCNC) decays $b \to s$ that are described by loop diagrams and (iii) decays to charm-less hadrons. In what follows we consider radiative decays belonging to (ii) and hadronic charm-less decays (iii).

Radiative Hadronic B Decays:

The most important $\mathrm{B} \to V\gamma$ channels, where V stands for the vector mesons $\mathrm{K}^*, \rho, \omega, \phi$, are listed in Tab. 70, together with the SM expectations. The CLEO observation of $\mathrm{B} \to \mathrm{K}^*\gamma$, at the level expected in the SM, has provided important constraints on many models of new physics. Note that preliminary results obtained by Belle [293] and BABAR [295] already compete in sensitivity. At the quark level the decays $\mathrm{B} \to V\gamma$ are dominated by $\mathrm{b} \to \mathrm{s}\gamma$ and $\mathrm{b} \to \mathrm{d}\gamma$ flavor changing neutral current (FCNC) transitions. The measured $\mathrm{b} \to \mathrm{s}\gamma$ inclusive branching fractions of $(3.11 \pm 0.80 \pm 0.72) \times 10^{-4}$ and $(3.15 \pm 0.35 \pm 0.32 \pm 0.26) \times 10^{-4}$ from ALEPH [289] and CLEO [290], respectively, are in good agreement with the SM calculation at next-to-leading order of $(3.28 \pm 0.33) \times 10^{-4}$ [291, 292]. More recently, Belle announced a preliminary result [293] of $(3.34 \pm 0.50^{+0.34+0.26}_{-0.37-0.28}) \times 10^{-4}$.

The radiative decay dominated by weak annihilation, $\mathrm{B}^0_\mathrm{s} \to \mathrm{J}/\psi\gamma$, could be interesting for HERA – B due to the presence of the J/ψ meson. The branching ratio is expected to be about $(1-10) \times 10^{-6}$. As the corresponding decay $\mathrm{B}^0 \to \mathrm{J}/\psi\gamma$ is CKM suppressed,

$$\frac{\mathrm{BR}(\mathrm{B}^0 \to \mathrm{J}/\psi\gamma)}{\mathrm{BR}(\mathrm{B}^0_\mathrm{s} \to \mathrm{J}/\psi\gamma)} \simeq \left(\frac{V_\mathrm{cd}}{V_\mathrm{cs}}\right)^2 \quad ,$$

it is not needed to distinguish B^0 from B^0_s. Notice that this radiative decay offers an interesting (and yet unexplored) possibility to measure CP violation in the same way as in the golden mode.

Table 70: *Branching ratios, scaled by* 10^{-5}*, on FCNC Radiative* B *Decays* $\mathrm{B} \to V\gamma$*. The theoretical predictions have uncertainties of* $\pm 40\% \pm 10\%$.

Reaction	CLEO [294, 296, 297]	Belle [293]	BABAR [295]	Prediction
$\mathrm{B}^0 \to \mathrm{K}^{*0}\gamma$	$4.55^{+0.72}_{-0.68} \pm 0.34$	$4.94 \pm 0.93^{+0.55}_{-0.52}$	$5.42 \pm 0.82 \pm 0.47$	~ 4.4 [298]
$\mathrm{B}^+ \to \mathrm{K}^{*+}\gamma$	$3.76^{+0.89}_{-0.83} \pm 0.28$	$2.87 \pm 1.20^{+0.55}_{-0.40}$		~ 4.4 [298]
$\mathrm{B} \to \mathrm{K}^*_2\gamma$	$1.7 \pm 0.6 \pm 0.1$			~ 4.4 [298]
$\mathrm{B}^0_\mathrm{s} \to \phi\gamma$	< 3.9 (CDF) [299]			~ 3.7 [300]
$\mathrm{B}^0_\mathrm{s} \to \overline{\mathrm{K}}^{*0}\gamma$	–			~ 0.05 [300]
$\mathrm{B}^+ \to \rho^+\gamma$	< 1.3	< 2.27		~ 0.09 [300]
$\mathrm{B}^0 \to \rho^0\gamma$	< 1.7	< 0.56		~ 0.09 [300]
$\mathrm{B}^0 \to \omega\gamma$	< 0.92			
$\mathrm{B}^0 \to \overline{\mathrm{D}^{*0}}\gamma$	< 5.0			~ 0.1 [300]

With 10^{11} $\mathrm{b\overline{b}}$ pairs, produced yearly, CDF expects to trigger on ≈ 2500 out of $\approx 3 \times 10^6$ expected radiative decays $\mathrm{B}^0 \to \mathrm{K}^{*0}\gamma$. Assuming a trigger efficiency of 10%, HERA – B (with 1.8×10^8 $\mathrm{b\overline{b}}$ per year) could record ≈ 700 events. This requires, of course, a good performance of the high-p_T pretrigger. HERA – B will have the advantage of good K/π separation, such that radiative decay channels not involving π^0 mesons should be observed and studied. Detailed simulations are, however, necessary, especially on the possibility to separate the isolated photon from the more abundant π^0 background.

Charm-less Hadronic B Decays:

Charm-less hadronic B decays offer prospects for the observation of direct CP violation. They are a sensitive probe of γ, the phase of the CKM matrix element $V_{\rm ub}^*$, due to the interference of tree and penguin diagrams. Tab. 71 summarizes charm-less hadronic branching ratios or upper limits at 90% CL measured by CLEO, BaBar and Belle, together with SM expectations. The entire CLEO data sample consists of 9.7×10^6 $\rm B\overline{B}$ pairs, whereas BaBar and Belle analyzed 8.6×10^6 and 6.2×10^6 pairs, respectively. The smallness of the $\pi^+\pi^-$ branching ratio relative to the $\rm K^+K^-$ branching ratio indicates that the penguin contribution is significant. Only an upper limit exists for the $\pi^0\pi^0$ branching ratio. The decay $\rm B_d \to \rho\pi$ has been proposed as an alternative to the decay $\rm B^0 \to \pi^+\pi^-$ to extract the angle α [301]. One method to extract the angle γ, is based on the rate measurements for the two-body decays $\rm B \to K\pi$ [302] and the use of U-spin symmetry to relate the decays $\rm B^0 \to \pi^+\pi^-$ and $\rm B_s^0 \to K^+K^-$ [282]. Note that the latter channel has not yet been observed. For details refer to section 5.4.3.

Table 71: *Branching ratios for charm-less* B *decays (scaled by* 10^{-5}*).*

Reaction	CLEO [303, 306, 308]	BaBar [304]	Belle [305]	Prediction
$\rm B^0 \to K^+\pi^-$	$1.72^{+0.25}_{-0.24} \pm 0.12$	$1.25^{+0.30+0.13}_{-0.26-0.17}$	$1.74^{+0.51}_{-0.46} \pm 0.34$	0.7 – 2.4 [307]
$\rm B^+ \to K^+\pi^0$	$1.16^{+0.30+0.14}_{-0.27-0.13}$		$1.88^{+0.55}_{-0.49} \pm 0.23$	0.3 – 1.5 [307]
$\rm B^+ \to K^0\pi^+$	$1.82^{+0.46}_{-0.40} \pm 0.16$		$1.66^{+0.98+0.22}_{-0.78-0.24}$	1.4 – 2.2 [307]
$\rm B^0 \to \pi^+\pi^-$	$0.43^{+0.16}_{-0.14} \pm 0.05$	$0.93^{+0.26+0.12}_{-0.23-0.14}$	$0.63^{+0.39}_{-0.35} \pm 0.16$	0.8 – 2.6 [307]
$\rm B^+ \to \pi^+\pi^0$	< 1.27		< 1.01	0.3 – 2.0 [307]
$\rm B^+ \to \pi^0\pi^0$	< 0.57			
$\rm B^+ \to K^0\overline{K^0}$	< 1.7			
$\rm B^0 \to K^+K^-$	< 0.19	< 0.66	< 0.6	
$\rm B^+ \to K^0K^+$	< 0.51		< 0.8	0.07 – 0.15 [307]
$\rm B^0 \to K^0\pi^0$	$1.46^{+0.59+0.44}_{-0.51-0.33}$		$2.10^{+0.93+0.25}_{-0.78-0.23}$	0.3 – 0.9 [307]
$\rm B^0 \to \rho^+K^-$	< 3.2			0.0 – 1.2 [309]
$\rm B^+ \to \rho^0K^+$	< 1.7	< 2.9		0.0 – 0.61 [309]
$\rm B^+ \to \omega K^+$	< 0.79			0.02 – 1.40 [309]
$\rm B^0 \to \rho^+\pi^-$	$2.76^{+0.84}_{-0.74} \pm 0.42$	$4.85 \pm 1.34^{+0.58}_{-0.52}$		1.2 – 9.3 [309]
$\rm B^+ \to \rho^0\pi^+$	$1.04 \pm 0.33 \pm 0.21$	< 3.9		0.04 – 1.3 [309]
$\rm B^+ \to \omega\pi^+$	$1.13^{+0.33}_{-0.29} \pm 0.14$			0.06 – 2.40 [309]

BaBar, HERA – B and CDF expect to reconstruct 64, 270 and 4700 decays $\rm B^0 \to \pi^+\pi^-$, respectively, assuming a branching ratio of 4.7×10^{-6} [311]. Again, the good particle identification of HERA – B compensates partly the higher rates at the Tevatron II. Possible contribution of HERA – B can be expected on channels without π^0 mesons.

Recently, CLEO [306] announced the observation of the decay $\rm B \to \Phi K$, mediated by a pure gluonic penguin diagram, sensitive to $\sin(2\beta)$. The preliminary results $\rm BR(B^- \to \Phi K^-) = (6.4^{+2.5+0.5}_{-2.1-2.0})\times 10^{-6}$ and $\rm BR(B^0 \to \Phi K^0) = (5.9^{+4.0+1.1}_{-2.0-0.9})\times10^{-6}$ lead to a combined branching ration of $\rm BR(B \to \Phi K) = (6.2^{+2.0+0.7}_{-1.8-1.7})\times 10^{-6}$, consistant with theoretical expectations of $(0.6-2.0)\times10^{-5}$. Belle [305] measured $\rm BR(B^- \to \Phi K^-) = (1.72^{+0.67}_{-0.54} \pm 0.18)\times 10^{-5}$, where the lower limit is higher than the central value from CLEO.

Hadronic 2-body B decays involving $\eta^{(\prime)}$ and $\rm K^{(*)}$ mesons could facilitate the quantitative understanding of the amplitudes that are essential to the interpretation of future CP measurements. Table 72 shows results obtained by CLEO. The interpretation of the results is far from being clarified. Two approaches have been proposed. Interference between two penguin diagrams could be constructive for η'K and ηK* and destructive for ηK and η'K* [312]. A $c\bar{c}$ component of the η' meson may be the reason for the large η'K rates [313, 314].

Table 72: *CLEO results for* $\mathrm{B} \to \eta(')\mathrm{K}^*$.

Reaction	BR ($\times 10^{-5}$)	Prediction ($\times 10^{-5}$)
$\mathrm{B}^+ \to \eta'\mathrm{K}^+$	$8.0^{+1.0}_{-0.9} \pm 0.7$ [310]	0.7 – 6.5 [315, 316]
$\mathrm{B}^0 \to \eta'\mathrm{K}^0$	$8.9^{+1.8}_{-1.6} \pm 0.9$ [310]	0.9 – 5.9 [315, 316]
$\mathrm{B}^+ \to \eta'\mathrm{K}^{*+}$	< 3.5 [310]	0.1 – 0.37 [315, 316]
$\mathrm{B}^0 \to \eta'\mathrm{K}^{*0}$	< 2.4 [310]	0.01 – 0.80 [315, 316]
$\mathrm{B}^+ \to \eta\mathrm{K}^+$	< 0.69 [310]	0.02 – 0.50 [315, 316]
$\mathrm{B}^0 \to \eta\mathrm{K}^0$	< 0.93 [310]	0.01 – 0.30 [315, 316]
$\mathrm{B}^+ \to \eta\mathrm{K}^{*+}$	$2.64^{+0.96}_{-0.82} \pm 0.33$ [310]	0.02 – 0.82 [315, 316]
$\mathrm{B}^0 \to \eta\mathrm{K}^{*0}$	$1.38^{+0.55}_{-0.46} \pm 0.16$ [310]	0.01 – 0.89 [315, 316]
$\mathrm{B}^+ \to \eta'\pi^+$	< 1.2 [310]	0.1 – 2.3 [315, 316]
$\mathrm{B}^0 \to \eta'\pi^0$	< 0.57 [310]	0.01 – 1.4 [315, 316]
$\mathrm{B}^+ \to \eta'\rho^+$	< 3.3 [310]	0.3 – 2.4 [315, 316]
$\mathrm{B}^0 \to \eta'\rho^0$	< 1.2 [318]	0.01 – 1.1 [315, 316]
$\mathrm{B}^+ \to \eta\pi^+$	< 0.57 [310]	0.19 – 0.74 [315, 316]
$\mathrm{B}^0 \to \eta\pi^0$	< 0.29 [310]	0.02 – 0.43 [315, 316]
$\mathrm{B}^+ \to \eta\rho^+$	< 1.5 [310]	0.4 – 1.7 [315, 316]
$\mathrm{B}^0 \to \eta\rho^0$	< 1.0 [310]	0.01 – 0.65 [315, 316]

Another hadronic rare B decay interesting for HERA – B involves the process $\mathrm{b} \to \mathrm{ss\bar{d}}$ which is expected to be small in the SM, of the order of 10^{-11} [319]. However, significant enhancement can be produced within supersymmetric models [319] or two-Higgs doublet models [320]. OPAL [321] searched for the decay $\mathrm{B}^+ \to \mathrm{K}^+\mathrm{K}^-\pi^-$ and obtained the 90% CL upper limits $\mathrm{BR}(\mathrm{B}^+ \to \mathrm{K}^+\mathrm{K}^-\pi^-) < 1.29 \times 10^{-4}$ or 8.79×10^{-4} if they assume that the decay is not via a K* resonance. With the estimate

$$\frac{\mathrm{B}^+ \to \mathrm{K}^+\mathrm{K}^-\pi^-}{\mathrm{b} \to \mathrm{ss\bar{d}}} \simeq \frac{1}{4} \quad ,$$

OPAL could put new limits on the contribution of R-parity violating couplings in this process.

CP Asymmetries:

Additional sensitivity to new physics can be provided by measuring CP rate asymmetries in (pure and radiative) hadronic B decays. Some non-SM predictions give asymmetries as large as 40% for the process $\mathrm{b} \to \mathrm{s}\gamma$ [322, 323], whereas no asymmetry is expected in the SM. CLEO [290] measured the quantity

$$A_{CP} \equiv \frac{\mathrm{BR}(\mathrm{b} \to \mathrm{s}\gamma) - \mathrm{BR}(\bar{\mathrm{b}} \to \bar{\mathrm{s}}\gamma)}{\mathrm{BR}(\mathrm{b} \to \mathrm{s}\gamma) + \mathrm{BR}(\bar{\mathrm{b}} \to \bar{\mathrm{s}}\gamma)}$$

and obtained the 90% CL range of $-0.22 < A_{CP} < +0.09$. The corresponding asymmetry for the exclusive decay $\mathrm{B} \to \mathrm{K}^*\gamma$ is measured to be $A_{CP} = +0.008 \pm 0.13 \pm 0.03$ [296].

CP asymmetries are expected to be large in most of the hadronic exclusive channels listed in Tables 71 and 72. CLEO [324] has performed first measurements of the asymmetry

$$A_{CP} \equiv \frac{\mathrm{BR}(\mathrm{b} \to f) - BR(\overline{\mathrm{b}} \to \overline{f})}{\mathrm{BR}(\mathrm{b} \to f) + \mathrm{BR}(\overline{\mathrm{b}} \to \overline{f})}$$

for five charm-less two-body final states. The results are compared to the SM expectations of reference [325] in Tab. 73.

Table 73: *CP asymmetries: CLEO data [324] and SM predictions from reference [325].*

Mode	Measured Asymmetry	90% CL	SM Prediction
$\mathrm{B}^+ \to \mathrm{K}^+\pi^0$	$-0.29 \pm 0.23 \pm 0.05$	$[-0.70, 0.16]$	$[0.026, 0.092]$
$\mathrm{B}^+ \to \mathrm{K}^0\pi^+$	$+0.18 \pm 0.24 \pm 0.05$	$[-0.27, 0.61]$	0.015
$\mathrm{B}^0 \to \mathrm{K}^+\,\pi^-$	$-0.04 \pm 0.16 \pm 0.05$	$[-0.35, 0.27]$	$[0.037, 0.106]$
$\mathrm{B}^+ \to \eta'\mathrm{K}^+$	$+0.03 \pm 0.12 \pm 0.05$	$[-0.22, 0.28]$	$[0.020, 0.061]$
$\mathrm{B}^+ \to \omega\pi^+$	$-0.34 \pm 0.25 \pm 0.05$	$[-0.80, 0.12]$	$[-0.120, 0.024]$

To summarize, rare decays are sensitive to new physics. There is a chance that HERA – B can make contributions to some of the channels listed above, especially the ones involving B_s^0 mesons, as the latter are not accessible at the currently running B factories. It is clear, however, that any claim of a physics case for HERA – B in this field has to await a detailed assessment of efficiencies and backgrounds. It is also obvious that HERA – B can only hope to contribute in a significant way if the complete detector, including the full trigger chain and the high-p_T pretrigger are operating at design performance.

References

[1] E.Hartouni et al., HERA – B : Design Report, **DESY-PRC 95/01** (1995).

[2] M. Leuthold, *Untersuchung zur Effizienz der Rekonstruktion des Zerfalls* $B^0 \to J/\psi\, K^0_S$ *im HERA – B Experiment anhand vollständig simulierter Modellereignisse*, Diploma Thesis, Humboldt University, Berlin (1997).

[3] R. Mankel and A. Spiridonov, HERA – B internal notes 98-154 and 98-206, 99-111.

[4] M. Langer, *Bestimmung der Beauty-Quantenzahl bei HERA – B mit Hilfe Neutronaler Netze*, Diploma Thesis, Humboldt University, Berlin (1998).

[5] J. Ivarsson, *Potential for B-physics measurements with a fixed-target proton-collision experiment*, Ph.D. thesis, Lund University (1999); internal HERA – B note 99-105.

[6] J. Ivarsson, private communication.

[7] T. Lohse, HERA – B internal note 97-085.

[8] D. Samtleben, HERA – B internal note 98-080.

[9] F. Abe et al., Phys. Rev. **D59** (1999) 032001.

[10] T. Affolder et al., Phys. Rev. **D61** (2000) 072005.

[11] T. Alexopoulos et al.(E771), Phys. Rev. Lett. **82** (1999) 41, (hep-ex/9906022).

[12] D.M. Jansen et al.(E789), Phys. Rev. Lett. **74** (1995) 3118.

[13] The BABAR Physics Book, **SLAC-R-504** (1998). The error is 0.12/year.

[14] Belle Technical Design Report, KEK Report 95-1 (1995). The error is 0.11/year.

[15] The CDF-II Collaboration, Fermilab-Proposal-909 (1998). The error is 0.10/year

[16] D. Hitlin, ICHEP2000 conference in Osaka, Japan, preprint *hep-ex/0008048*.

[17] H. Aihara, ICHEP2000 conference in Osaka, Japan.

[18] A. Ali, Patricia Ball, L.T. Handoko and G. Hiller, Phys. Rev. D61 (2000) 074024. (hep-ph/9910221).

[19] A. Ali and G. Hiller, Phys. Rev. D60 (1999) 034017. (hep-ph/9807418).

[20] V. Egorytchev, V. Saveliev, P. Schlein, HERA-B 00-146 (4 October, 2000).

[21] G.Hiller, "$b \to s l^+ l^-$ decays in and beyond the Standard Model", SLAC-PUB-8851, Aug 2000.

[22] The BABAR Physics Book, *Physics at an Asymmetric B Factory*, eds. P.F. Harrison and H.R. Quinn, SLAC-R-504 (1998).

[23] F. Ferrarotto, F. Ferroni, M. Rotondo, BABAR note 432 (May 5, 1998).

[24] K.T. Pitts, *CP Violation, Mixing and Rare Decays at the Tevatron Now and in Run II*, Proc. 4th Conference on Heavy Quarks at Fixed Target, Batavia, IL, USA, 10 - 12 Oct 1998, AIP conf. proc. 459 (1998) 55-65.

[25] D.J. Jaffe, *Recent Results on Rare b Decays*, presented at 8th International Symposium on Heavy Flavor Physics (Heavy Flavors 8), Southampton, England, 25-29 Jul 1999, hep-ex/9910055.

[26] T. Lohse et al., *An Experiment to Study CP Violation in the B System Using an Internal Target at the HERA Proton Ring*, Proposal, **DESY-PRC 94/02** (1994).

[27] Particle Data Group, Review of Particle Properties, Eur. Phys. J. **C15** (2000).

[28] P. Nason, S. Dawson and K.R. Ellis, Nucl. Phys. **B303** (1988) 607; **B327** (1989) 49; **B335** (1990) 260.

[29] E. Lohrmann and M. Seidel, *Study of Background Caused by Scattering at the HERA-B Wire Target*, **DESY HERA 95-04** (1995).

[30] K. Ehret, *Performance of the HERA-B Target and Interference with HERA operation*, International Symposium on Near Beam Physics, FNAL Batavia, Proceedings (1997) 33. `http://www-ap.fnal.gov/NEARBEAM/proceedings/ehret.ps.gz`.

[31] Y. Vassiliev et al., *Multi Target Operation at the HERA-B Experiment*, STORI99, Bloomington, Indiana, US, (1999), Proceedings published: Nuclear Physics at Storage Rings 359.

[32] C. Hast et al., Nucl. Instr. Methods **A354** (1995) 224.

[33] K. Ehret et al., *Observation of Coasting Beam at the HERA Proton-Ring*, **DESY 00-018** (2000) (hep-ex/0002002).

[34] K. Ehret, Nucl. Instr. Methods **A446** (2000) 190.

[35] S. Spratte, *Untersuchung zu den Eigenschaften eines internen Drahttargets für das HERA-B Experiment*, Diplomarbeit, University of Dortmund (1996), **DESY F15 96-01**.

[36] S. Issever, *Vorbereitende Untersuchungen für das HERA-B Experiment*, Diplomarbeit, University of Dortmund (1996).

[37] M. Bräuer, *Aufbau und Untersuchung der Eigenschaften des Targets für den HERA-B Detektor*, Diplomarbeit, University of Dortmund (1997).

[38] S. Schaller, *Untersuchung der Beiträge einzelner Protonbündel zur Wechselwirkungsrate des HERA-B Experiments*, Diplomarbeit University of Heidelberg (1998).

[39] T. Jagla, *Untersuchung der Target-Strahl Wechselwirkungen im HERA-B Target*, Diplomarbeit, University of Dortmund (1998), **DESY-THESIS 1999-007**.

[40] M. Funcke, *Alignment der HERA-B Targetmechanik*, Diplomarbeit, University of Dortmund (1999).

[41] M. Symalla, *Vorbereitende Untersuchungen zur Bestimmung der Wechselwirkungsraten und deren Zeitstruktur ...*, Diplomarbeit, University of Dortmund (1999).

[42] Chr. Knierim, *Messung und Analyse von Ratenfluktuationen am HERA-B-Target*, Diplomarbeit, University of Dortmund (2000).

[43] G. Baki, *Untersuchungen der Wechselwirkungen einzelner Protonenbunche mit dem HERA-B Drahttarget*, Diplomarbeit, University of Dortmund (2000).

[44] S. Spratte, *Bestimmung der Wechselwirkungsrate des HERA-B Targets und Untersuchung des Coasting Beams am HERA Protonenring*, PhD Thesis, University of Dortmund (2000).

[45] S. Issever, PhD Thesis - under preparation

[46] F. Benotto et al., *The LPS Trigger System*, **DESY 96-045** (1996).

[47] S. Karstensen, *The H1 Proton Pick Up (LOPEZ Monitor)*,
`http://www-h1.desy.de/~sven/ppu/ppu.html`
and W. Kriens (MSK-DESY) - private communication.

[48] C. Kleinwort, *Summary of the Cohabitation Task Force*, HERA Coordination Meeting, April 12th, 2000.

[49] G.H. Hoffstaetter (ed.), *HERA accelerator studies 1999*, **DESY HERA 00-02** (2000).

[50] C.Bauer, I.Baumann, M.Bräuer, M.Eberle, W.Fallot-Burghardt, E.Grigoriev, W.Hofmann, A.Hüpper, F.Klefenz, K.T.Knöpfle, G.Leffers, T.Perschke, J.Rieling, M.Schmelling, B.Schwingenheuer, E.Sexauer, L.Seybold, J.Spengler, R.St.Denis, U.Trunk, R.Wanke, I.Abt, H.Fox, B.Moshous, K.Riechmann, M.Rietz, R.Ruebsam, W.Wagner, Nucl. Instr. Methods **A418** (1998) 65.

[51] C.Bauer, M.Bräuer, T.Glebe, W.Hofmann, K.T.Knöpfle, V.Pugatch, M.Schmelling, B.Schwingenheuer, E.Sexauer, L.Seybold, U.Trunk, R.Wanke, I. Abt, M.Dressel, S.Masciocchi, B.Moshous, T.Perschke, K.Riechmann, M.Sang, S.Schaller, W.Wagner, M.Merk, M.Mevius, T.van den Brink, Nucl. Instr. Methods **A447** (2000) 61.

[52] M.Schmelling, *The HOLMES Program Package*, HERA-B note 99-086.

[53] I. Kisel, S. Masciocchi, *CATS - A Cellular Automaton for Tracking in Silicon for the HERA-B Vertex Detector* HERA-B note 99-242.

[54] D. Emeliyanov, I. Kisel, *CATS Track fitting Algorithm based on the discrete Kalman Filter*, HERA-B note 00-032.

[55] V.Pugatch, I.Abt, C.Bauer, M.Bräuer, M.Dressel, T.Glebe, W.Hofmann, K.T.Knöpfle, S.Masciocchi, B.Moshous, Th.Perschke, K.Riechmann, S.Schaller, M.Schmelling, B.Schwingenheuer, E.Sexauer, U.Trunk, R.Wanke, W.Wagner, and F.Zurheide, *Nuovo Cimento* **112A** (1999) 1383-1389.

[56] M. Capeáns, Nucl. Instr. Methods **A446** (2000) 317.

[57] M. Capeáns, C. Padilla, C. Stegmann, Module Production Guide, Version 1.2, December 1998.

[58] R. Mankel, 'A concurrent track evolution algorithm for pattern recognition in the HERA-B main tracking system', Nucl. Instr. Methods **A395** (1997) 169.

R. Mankel and A. Spiridonov, 'The concurrent track evolution algorithm: Extension for track finding in the inhomogeneous magnetic field of the HERA-B spectrometer', Nucl. Instr. Methods **A426** (1999) 268.

[59] R. Mankel, '*ranger* - a Pattern Recognition Algoritm for the HERA-B Main Tracking System. Part I : The HERA-B Pattern Tracker' HERA-B note 97-082 (1997).

R. Mankel and A. Spiridonov, '*ranger* - ... Part II : The HERA-B Magnet Tracker' HERA-B note 98-154 (1998).

R. Mankel and A. Spiridonov, '*ranger* - ... Part III : Tracking in Trigger Chamb ers' HERA-B note 98-206 (1998).

R. Mankel, '*ranger* - ... Part IV : The Object-Oriented Track Fit' HERA-B note 98-079 (1998).

R. Mankel and A. Spiridonov, '*ranger* - ... Part V : Compatibility Analysis' HERA-B note 99-101 (1999).

[60] K. Berkhan et al., 'Large System Experience with the ASD-8 Chip in the HERA-B Experiment', Proc. of the 5th Workshop on Electronics for LHC EXperiments, Snowmass, Co., USA, 1999, p. 564.

[61] V. Balagura et al., Nucl. Instr. Methods **A368** (1995) 252.

V. Balagura et al., Nucl. Instr. Methods **A379(3)** (1996) 404.

[62] C. Leonidopoulos, C. Lu, and A. J. Schwartz, Nucl. Instr. Methods **A427** (1999) 465.

[63] J. A. Kadyk, Nucl. Instr. Methods **A300** (1991) 436.

[64] D. Dujmić, R. Eckmann, K. Reeves, R.F. Schwitters, HERA-B Note 00-020, DESY, Hamburg (2000).

[65] D. Škrk, Doctoral Thesis, University of Ljubljana, Ljubljana (1999).

[66] D. Dujmić, R. Eckmann, R.F. Schwitters, HERA-B Note 00-019, DESY, Hamburg (2000).

[67] M. Starič, P. Križan, HERA-B Note 00-002, DESY, Hamburg (2000).

[68] D. Dujmić, HERA-B Note 00-016, DESY, Hamburg (2000).

[69] D. Dujmić, R. Eckmann, HERA-B Note 00-004, DESY, Hamburg (2000).

[70] D. Dujmić, R. Eckmann, K. Reeves, R.F. Schwitters, HERA-B Note 99-100, DESY, Hamburg (1999).

[71] I. Arinyo, L. Garrido, HERA-B Note 99-108, DESY, Hamburg (1999).

[72] M. Starič, P. Križan, Nucl. Instr. Methods **A433** (1999) 279.

[73] B.A.Dolgoshein, Nucl. Instr. Methods **A326** (1993) 434.

[74] V.Saveliev, Nucl. Instr. Methods **A408** (1998) 289.

[75] ATLAS Technical Proposal, CERN/LHCC/94-43,1994

[76] B.Bevensee, F.M.Newcommer. et al., An Amplifier Shaper Discriminator with Baseline Restoration, IEEE Transaction NS V43, 1996.

[77] M. Schmelling, *Evidence for Heavy Flavours in the 99 Magnet-Off Data*, HERA – B note 99-176, Physics 99-037.

[78] I. Matchikhilian et al., *HERA – B ECAL monitoring system and calibration procedures overview*, Proceeding of the VIII Conf. on Calorimetry in HEP, Lisbon, Portugal, World Scientifics (1999), pp 411-416.

[79] O. Igonkina et al., *Online π^0 calibration of ECAL*, HERA – B note 00-103, ECAL 00-005.

[80] M. Villa, *ECAL Analysis Status update*, HERA – B note 99-138, ECAL 99-005.

[81] F.M. Newcomer et al., IEEE Trans. Nucl. Sci. **NS-40** (1993) 630-6

[82] M. Buchler et al., IEEE Trans. Nucl. Sci. **NS-46** (1999) 126-132

[83] S. Nam, HERA-B Note 00-004.

[84] T. Fuljahn et al., Xth IEEE Real Time conference, 1997, pp 77.

[85] E. Gerndt, "The HERA-B Hardware Trigger in 1999", to be published in Nucl. Instr. and Meth. (2000).

[86] E. Gerndt, S. Xella, Nucl. Instr. Methods **A446** (2000) 264.

[87] D. Reßing, Nucl. Instr. Methods **A384** (1996) 131.

[88] H. D. Schulz, Nuclear Physics B (Proc. Suppl.) 44 (1995), 441-447.

[89] T. Fuljahn, DESY-THESIS-1999-016, May 1999.

[90] Joachim Gläß, "Message transfer module LVDS", Mannheim University note, February 11 2000.
http://www-li5.ti.uni-mannheim.de/mass_par/doc/messlvds.ps

[91] "Mapping of the OTR and the MUON detectors for the First level Trigger", I. Négri, FLT note, April 15 2000.
http://www-hera-b.desy.de/subgroup/flt/links_to_notes.html

[92] Technical specifications FLT Track Finding Unit V.4.2, Mannheim University.
http://www-li5.ti.uni-mannheim.de/mass_par/doc/tfudocu.ps.

[93] Technical specifications FLT Track Parameter Unit V.1.1, Mannheim University.
http://www-li5.ti.uni-mannheim.de/mass_par/doc/tpudocu.ps.

[94] J. Flammer, "TPU documentation", FLT note, September 26 2000.
http://www-hera-b.desy.de/subgroup/flt/tpu/tpu.html

[95] E. Gerndt, "HERA-B pretrigger and FLT latency", Hera-B note 00-013, Febrary 2000.

[96] A. Benedettini et al., *The Electromagnetic Calorimeter of the HERA-B Experiment*, proceedings of the *VI Conference on Calorimetry in High Energy Physics - Frascati, June 8-14, 1996* Frascati Physics Series Vol. VI, p. 817.

[97] M. Bruschi et al., Nucl. Instr. Methods **A409** (1998) 643.

[98] V. Alberico et al., Il Nuovo Cimento, **110A** (1997) 1453.

[99] S. Shuvalov et al., *HERA-B Electromagnetic Calorimeter*, Proceedings of *CALOR99 - The VIII International Conference on Calorimetry in High Energy Physics; June 13-19, 1999, Lisbon, Portugal*, p. 511, Ed. G. Barreira et al., World Scientific.

[100] D. Galli et al., *DAQ, Pretrigger and Remote Display System of the HERA-B Electromagnetic Calorimeter*, Proceedings of *CALOR99 - The VIII International Conference on Calorimetry in High Energy Physics; June 13-19, 1999, Lisbon, Portugal*, p. 611, Ed. G. Barreira et al., World Scientific.

[101] I. Matchikhilian et al., *HERA-B ECAL Monitoring System and Calibration Procedures*, Proceedings of *CALOR99 - The VIII International Conference on Calorimetry in High Energy Physics; June 13-19, 1999, Lisbon, Portugal*, p. 411, Ed. G. Barreira et al., World Scientific.

[102] B. Giacobbe et al., *First Results with the Electron Pretrigger System of the HERA-B Experiment*, Proceedings of *CALOR99 - The VIII International Conference on Calorimetry in High Energy Physics; June 13-19, 1999, Lisbon, Portugal*, p. 598, Ed. G. Barreira et al., World Scientific.

[103] A. Zoccoli et al., Nucl. Instr. Methods **A446** (2000) 246.

[104] Altera^{TM} Corp. "FLEX 10K Embedded Programmable Logic Family", *Data sheet* Ver.3, January (1998)

[105] Motorola^{TM} Inc. "AutoBahn^{TM} Spanceiver^{TM}", *Data sheet* Rev.0, June (1987)

[106] J. Gläß, A. Wurz, "Detector Data Transmission to the First Level Trigger of HERA – B", HERA – B *Internal Note* 97-011, January (1997)

[107] M. Adams, *private communication*, April (2000)

[108] V.Popov et al., *Proceedings of the Forth Workshop on Elecronics for LHC Experiments*, Rome, Sep.1998, CERN/LHCC/98-36 p.447-451

[109] H.Riege et al., Proceedings of the Fifth Workshop on Elecronics for LHC Experiments, Snowmass USA, Sep.1999, CERN/LHCC/99-09 p.557-561

[110] M. Medinnis et al., Real Time Conference 1997

[111] M. Medinnis, D. Ressing, Hera-B Note 96-247 (1996) 30.

[112] U. Schwanke, *Trigger and Reconstruction Farms in the HERA – B Experiment and Algorithms for a Third Level Trigger*, Doctoral Thesis, Humboldt-University Berlin (2000).

[113] A. Gellrich et al., *The Processor Farm for Online Triggering and Full Event Reconstruction of the HERA – B Experiment at HERA*,
Proceedings of CHEP '95, 18-22 Sep 1995, Rio de Janeiro, Brazil (1995).

[114] A. Gellrich et al., *A Test System for the HERA – B Online Trigger and Reconstruction Farm*, Poster presented at DAQ96, 13-15 Nov 1996, Osaka, Japan (1996).

[115] A. Gellrich et al., *A Prototype System for the Processor Farm of the HERA – B Experiment at HERA*,
Proceedings of CHEP '97, 4-11 April 1997, Berlin, Germany (1997).

[116] H. Leich et al., *Large Farms for Level 3 and 4 of the HERA – B Experiment*,
Poster presented at IEEE Real Time Conference, 22-26 Sep 1997, Beaune, France (1997).

[117] A. Gellrich et al., *HERA – B Higher-Level Triggers, Architecture and Software*,
Talk given at Beauty '97, 13-17 October 1997, Los Angeles, USA, published in **NIM A 408** (1998) 173-180

[118] A. Gellrich et al., *The Fourth Level Trigger Online Reconstruction Farm of HERA – B* ,
Proceedings of CHEP '98, 31 Aug - 4 Sep 1998, Chicago, USA (1998).

[119] A. Gellrich et al., *A Linux-PC Farm for Online Event Reconstruction at HERA – B* ,
Talk at IEEE NPSS Real-Time 1999, 14-18 June 1999, Santa Fe, USA (1999).

[120] A. Gellrich et al., *The Linux-PC Farm for Online Event Reconstruction of HERA – B* ,
Talk given at 1st LCB Event Filter Farms Workshop, 28 Sep - 1 Oct 1999, Marseille, France (1999).

[121] A. Gellrich et al., *Full Online Event Reconstruction at HERA – B* , Proceedings of CHEP2000, 7-11 Feb 2000, Padova, Italy (2000).

[122] HERA-B Collaboration, "DAQ Online Software and the Run Control System in the HERA-B Experiment". Proceedings CHEP 98 conference, Chicago, September 98.

[123] A.Gellrich et al. "The Fourth level Trigger Online Reconstruction Farm for HERA-B". Proceedings CHEP 98 conference, Chicago, September 98.

[124] Mogens Dam, "Second and Third Level Trigger Systems for the HERA-B Experiment". Proceedings CHEP 98 conference, Chicago, September 98.

[125] K.H.Sulanke and I.C.Legrand,"Fast PCI Communication Interfaces for On-Line distributed processing Systems". Proceedings CHEP 98 conference, Chicago, September 98.

[126] G.Wagner, "Aufbau und Test der mit Digitalen Signal Prozessoren realisierten Komponenten des Datennahmesystems von HERA-B". Ph.D.Dissertation, Universität Hamburg, 2000.

[127] A. Somov, *HERA-B rate calibration and luminosity determination using ECAL energy sum*, HERA-B internal note, General 00-076.

[128] M. Bargiotti et al., *Measurement of the mean interaction rate at HERA-B using the ECAL energy spectrum*, HERA-B internal note, Physics 00-134

[129] T. Perschke, PhD thesis, München, 2000.

[130] I. Arinyo, PhD thesis, Barcelona, in preparation.

[131] A. Breakstone at al., Z. Phys. **C69** (1995) 55.

[132] J. Cronin et al., Phys. Rev. **D11** (1975) 3105.

[133] D. Antreasyan et al., Phys. Rev. **D19** (1979) 764.

[134] C.N. Brown et al., Phys. Rev. **C54** (1996) 3195.

[135] B. Alper et al., Phys. Lett. **B44** (1973) 521.

[136] P.B. Straub et al., Phys. Rev. Lett. **68** (1992) 452.

[137] A. Sambamurti et al., Phys. Rev. **D41** (1990) 1371.

[138] R. Gomez et al., Phys. Rev. **D35** (1987) 2736.

[139] J. Crittenden et al., Phys. Rev. **D34** (1986) 2584.

[140] Y.B. Hsiung et al., Phys. Rev. Lett. **55** (1985) 457.

[141] A. Breakstone et al., Phys. Rev. **D30** (1984) 528.

[142] W. Bell et al., Phys. Lett. **B128** (1983) 349.

[143] A. Breakstone et al., Nuovo Cim. **A102** (1989) 1199.

[144] A. Breakstone et al., Z. Phys. **C33** (1987) 333.

[145] A. Breakstone et al., Phys. Lett. **B183** (1987) 227.

[146] L. Van Hove, Phys. Lett. **B130** (1982) 138.

[147] E.V. Shuryak, Phys. Rep. **61** (1980) 71.

[148] T. Akesson et al., Phys. Lett. **B129** (1983) 269.

[149] T. Akesson et al., Phys. Lett. **B155** (1985) 128.

[150] A. Breakstone, Phys. Lett. **B162** (1985) 400.

[151] K. Braune et al., Phys. Lett. **B123** (1983) 467.

[152] S. Barshay and W.Troost, Phys. Lett. **B73** (1978) 437.

[153] R. Hagedorn, Riv. Nuovo Cimento **6** (1984) 1.

[154] M. Banner et al., Phys. Lett. **B44** (1973) 537.

[155] P.W. Büsser et al., Phys. Lett. **B46** (1973) 471.

[156] D. Drijard et al., Nucl. Phys. **B155** (1979) 269.

[157] W. Bell et al., Z. Phys. **C22** (1984) 109.

[158] A. Breakstone et al., Mod. Phys. Lett. **A6** (1991) 2785.

[159] W. Bell et al., Z. Phys. **C32** (1986) 335.

[160] M.G. Albrow et al., Phys. Lett. **B65** (1975) 349.

[161] G.J. Bobbink et al., Nucl. Phys. **B204** (1982) 173.

[162] A. Breakstone et al., Z. Phys. **C23** (1984) 1.

[163] A. Breakstone et al., Phys. Lett. **B248** (1990) 220.

[164] M. Glück, L.E. Gordon, E. Reya, and W. Vogelsang, Phys. Rev. Lett. **73** (1994) 388.

[165] A.D. Martin et al., Eur. Phys. J. **C4** (1998) 463.

[166] R.P. Feynman and R.D. Field, Nucl. Phys. **B136** (1978) 1.

[167] B.L. Combridge et al., Phys. Lett. **B70** (1977) 234.

[168] R. Cutler and D. Sivers, Phys. Rev. **D16** (1977) 679.

[169] J.F. Owens, Rev. Mod. Phys. **59** (1987) 465.

[170] P. Aurenche et al., Phys. Lett. **B140** (1984) 87.

[171] E.L. Berger and J. Qiu, Phys. Rev. **D44** (1991) 2002.

[172] F. Aversa et al., Nucl. Phys. **B327** (1989) 105.

[173] M. Della Negra et al., Nucl. Phys. **B127** (1977) 1.

[174] A. Breakstone et al., Phys. Lett. **B135** (1984) 505.

[175] L. Apanasevich et al., Phys. Rev. Lett. **81** (1998) 2642.

[176] E. Bonvin et al., Phys. Lett. **B236** (1990) 523.

[177] A. Breakstone et al., Z. Phys. **C52** (11991) 551.

[178] P. Chiappetta et al., Phys. Lett. **B348** (1995) 646.

[179] A. Breakstone et al., Z. Phys. **C33** (1987) 475.

[180] E.L. Berger and M. Klasen, Nucl. Phys. Proc. Suppl. **82** (2000) 179.

[181] A. Breakstone et al., Z. Phys. **C25** (1984) 21.

[182] A. Breakstone et al., Z. Phys. **C27** (1985) 205.

[183] A. Breakstone et al., Z. Phys. **C36** (1987) 567.

[184] A. Breakstone et al., Phys. Lett. **B135** (984) 510.

[185] A. Breakstone et al., Phys. Lett. **B147** (984) 237.

[186] P.B. Straub et al., Phys. Rev. **D45** (1992) 3030.

[187] A. Breakstone et al., Z. Phys. **C28** (1985) 335.

[188] S. Ekelin and S. Fredriksson, Phys. Lett. **B149** (1984) 509.

[189] A.M. Smith et al., Phys. Lett. **B184** (1987) 293.

[190] A. Breakstone et al., Z. Phys. **C43** (1989) 185.

[191] D. Drijard et al., Nucl. Phys. **B156** (1979) 309.

[192] D. Drijard et al., Nucl. Phys. **B166** (1980) 233.

[193] M.W. Buchler, Int. Rep. $\mathsf{HERA-B}$ 97-151.

[194] J. Ivarsson and A. Somov, Int. Rep. $\mathsf{HERA-B}$ 97-166.

[195] J. Ivarsson, Thesis, University of Lund (1999).

[196] A. Brandenburg, O. Nachtmann and E. Mirkes, Z. Phys. **C60** (1993) 697.

[197] C.S. Lam and Wu-Ki Tung, Phys. Rev. **D21** (1980) 2712.

[198] S. Falciano et al., NA10 Coll.: Z. Phys. **C31** (1986) 513.

[199] M. Guanziroli et al., NA10 Coll.: Z. Phys. **C37** (1988) 545.

[200] W.J. Stirling and M.R. Walley, J. Phys. G: Nucl. Part. Phys. **19** (1993) D1.

[201] Ting-Hua Chang, Thesis, New Mexico State University (1999).

[202] T. Matsui, H. Satz, Phys. Lett. **B178** (1986) 416.

[203] R. Baier, R. Ruckl, Z. Phys. **C19** (1983) 251.

[204] G.A. Schuler, **CERN-TH.7170/94** (hep-ph/9403387) and references therein.

[205] F. Abe et al., Phys. Rev. Lett. **79** (1997) 578.

[206] G.T. Bodwin, E. Braaten and G.P. Lepage, Phys. Rev. **D51** (1995) 1125.

[207] M. Cacciari and M. Kramer, Phys. Rev. Lett. **76** (1996) 4128.

[208] T. Carli, *Latest Highlights from the H1 Collaboration*, hep-ph/9906540.

[209] T. Alexopoulos et al., Phys. Rev. **D62** (2000) 032006.

[210] M. Stancari, Nucl. Phys. Proc. Suppl. **82** (2000) 306.

[211] T.A. Armstrong et al., Phys. Rev. Lett. **69** (1992) 2337.

[212] L. Antoniazzi et al., Phys. Rev. **D50** (1994) 4258.

[213] C.-F. Qiao and C. Yuan, **DESY 00-081**, hep-ph/0005317.

[214] M.C. Abreu et al., Nucl. Phys. **A661** (1999) 93.

[215] R. Vogt, Phys. Rep. **310** (1999) 197.

[216] M.J. Leitch et al., Phys. Rev. Lett. **84** (2000) 3256.

[217] M. Glück, E. Reya, and M. Stratmann, Nucl. Phys. **B422** (1994) 37.

[218] S. Frixione et. al., **CERN-TH/97-16 (1997)** and references therein.

[219] A.B. Carter and A.I. Sanda, Phys. Rev. Lett. **45** (1980) 952; Phys. Rev. **D23** (1981) 1567; I.I. Bigi and A.I. Sanda, Nucl. Instr. Methods **B193** (1981) 85.

[220] A.J. Buras, Nucl. Instr. Methods **A368** (1995) 1.

[221] A.J. Buras and R. Fleischer, hep-ph/9704376.

[222] A.S. Dighe, I. Dunietz and R. Fleischer, Eur. Phys. J. **C6** (1999) 647.

[223] P. Conde, HERA – B internal note.

[224] F. Abe et al., Phys. Rev. Lett. **77** (1996) 1945.

[225] G. Bellini, I. Bigi and P. Dornan, Phys. Rep. **289** (1997) 1.

[226] C. Caso et al., Eur. Phys. J. **C3** (1998) 1.

[227] I. Bigi et al., hep-ph/9401298;
M. Beneke, G. Buchalla and I. Dunietz, Phys. Rev. **D54** (1996) 4419;
S. Hashimoto et al., hep-ph/9912318.

[228] M. Beneke et al., Phys. Lett. **B459** (1999) 631.

[229] B. Becirevic et al., hep-ph/0006135.

[230] V. Gimenez and J. Reyes, hep-lat/0009007.

[231] F. Abe et al., Phys. Rev. **D57** (1998) 5382.

[232] C.M.E. Paus, *Summary on* B *Mixing and Lifetimes*, Working Group 3, B Workshop, Fermilab, Feb. 2000.

[233] P. Ball et al., *B Decays at the LHC*, preprint hep-ph/0003238.

[234] A.J. Buras and R. Fleischer, *Quark Mixing, CP Violation and Rare Decays After the Top Quark Discovery*, in: Heavy Flavour II, eds. A.J. Buras and M. Linder, World Scientific (1997), 65-238.

[235] G. Buchalla and A.J. Buras, Nucl. Phys. **B548** (1999) 309.

[236] M. Gronau and D. London, Phys. Rev. **D55** (1997) 2845.

[237] X. Zhenjun et al., Chin. Phys. Lett. **16** (1999) 88, hep-ph/9903345;
X. Zhenjun et al., hep-ph/9903346.

[238] H.E. Logan and U. Nierste, hep-ph/0004139.

[239] F. Abe et al., Phys. Rev. **D57** (1988) 3811.

[240] L. Del Debbio et al, Phys. Lett. **B416** (1998) 392.

[241] P. Colangelo et al., hep-ph/9809372.

[242] P. Ball and V.M. Braun, hep-ph/9805422.

[243] D. Melikhov, *Long-Distance Contributions to Exclusive Rare Decays of Heavy Hesons in Quark Model*, Proc. 32nd Rencontres de Moriand 'Electroweak Interactions', Les Arcs, France, March 1997;
D. Melikhov, N. Nikitin and S. Simula, Phys. Rev. **D57** (1998) 6814.

[244] G. Hiller, *Improved QCD Perturbative Contributions And Power Corrections In Radiative And Semileptonic Rare B Decays*, PhD thesis, hep-ph/9809505.

[245] A. Ali, hep-ph/9606324.

[246] T.M. Aliev, M. Savcı and A. Özpineci, hep-ph/9704323.

[247] T.M. Aliev, A. Özpineci and M. Savcı, hep-ph/0002061.

[248] G. Burdman, M.C. Gonzalez-Garcia and S.F. Novaes, hep-ph/9906329.

[249] G. Burdman, Phys. Rev. **D59** (1999) 035001.

[250] E. Lunghi and I. Scimemi, Nucl. Phys. **B574** (2000) 43.

[251] Q.-S. Yan et al., hep-ph/0004262.

[252] S. Fukae et al., Phys. Rev. **D59** (1999) 074013.

[253] S. Fukae, C.S. Kim and T. Yoshikawa, hep-ph/0003053.

[254] T. Affolder et al., Phys. Rev. Lett. **83** (1999) 3378.

[255] B. Abbott et al., Phys. Lett. **B423** (1998) 419.

[256] S. Glenn et al, Phys. Rev. Lett. **80** (1998) 2289.

[257] F. Abe et al., Phys. Rev. **D60** (1999) 051101.

[258] T. Oest, talk, HERA-B Physics Prospects, BMBF, (1997).

[259] H.-G. Moser and A. Roussarie, Nucl. Instr. Methods **A384** (1997) 491.

[260] For a recent compilation on the predictons, see H. Nelson, Compilation of $D^0 \to \overline{D^0}$ Mixing Predictions, UCSB HEP 99-08, hep-ex/9908021, May, 2000.

[261] P. Sheldon, *Charm Mixing and Rare Decays*, in proceedings of *Heavy Flavors 8*, Southampton, UK, 1999.

[262] S. Bianco, *Charm Overview*, in proceedings of *XIX Physics in Collision*, University of Michigan at Ann Arbor, June, 1999.

[263] E. M. Aitala et al., Phys. Rev. Lett. **77** (1996) 2384.

[264] R. Godang et al., *Search for* D^0-$\overline{D}^0$, **CLNS 99/1659**.

[265] G. Blaylock, A. Seiden and Y. Nir, Phys. Lett. **B355** (1995) 555; see also T. Liu, *An Overview of DD Mixing Search Techniques*, Proceedings of FCNC97, Santa Monica, February 1997; D. Cline ed., World Scientific, Singapore 63 (1997) and references therein.

[266] J.M. Link et al., *A Measurement of Lifetime Differences in Nautral D-Meson System*, **Fermilab-Pub-00/091-E**, May, 2000, submitted to Phys. Lett. **B**.

[267] T. Alexopoulos et al., Phys. Rev. Lett. **77** (1996) 2380.

[268] J. Thom, Diploma Thesis, Hamburg 1997.

[269] T. Oest, HERA-B Physics Meeting, Zeuthen, May 1998, HERA – B Note.

[270] S.L. Glashow, J. Iliopoulos, and L. Maiani, Phys. Rev. **D2** (1970) 1285.

[271] S. Pakvasa, **Fermilab-Conf-94/190**.

[272] See, for example, L. Hall and S. Weinberg, Phys. Rev. **D48** (1993) R979; S. Pakvasa and H. Sugawara, Phys. Lett. **B73** (1978) 61.

[273] See, e.g., R.A. Bertlmann and A. Martin, Nucl. Phys. **B168** (1980) 111.

[274] The CDF II Collaboration, *The CDF II Detector Technical Design Report*, **FERMILAB–Pub–96/390–E.**;
Proposal for Enhancement of the CDF II Detector: An Inner Silicon Layer and A Time of Flight Detector;
Update to Proposal P–909: Physics Performance of the CDF II Detector with An Inner Silicon Layer and A Time of Flight Detector.

[275] Fermilab Accelerator Devision, *Run II Handbook.*

[276] See `http://ichep2000.hep.sci.osaka-u.ac.jp/scan/0731/pl/hitlin/index.html`.

[277] E. Aitala et al., Phys. Rev. **D57** (1998) 13.

[278] R. Fleischer, Phys. Lett. **B365** (1996) 399.

[279] R. Fleischer, Eur. Phys. J. **C6** (1999) 451.

[280] A. Buras and R. Fleischer, Eur. Phys. J. **C11** (1999) 93.

[281] V. Balagura et al., ITEP-3-99 (1999).

[282] R. Fleischer, Phys. Lett. **B459** (1999) 306; Eur. Phys. J. **C16** (2000) 87.

[283] M. Bander, D. Silverman and A. Soni, Phys. Rev. Lett. **43** (1979) 242.

[284] M. Beneke, B. Buchalla, Neubert, and C. T. Sachrajda, Phys. Rev. Lett. **83** (1999) 1914.

[285] See `http://lepbosc.web.cern.ch/LEPBOSC/combined_results/sept_2000/`.

[286] A. Ali and D. London, hep-ph/0002167 (2000).

[287] R. Fleischer and J. Matias, Phys. Rev. **D61** (2000) 074004.

[288] F. Wurthwein, CDF internal note 5271 (2000), unpublished.

[289] R. Barate et al., Phys. Lett. **B429** (1998) 169.

[290] S. Ahmed et al., hep-ex/990822v2 (1999).

[291] K. Chetykin et al., Phys. Lett. **B400** (1997) 206.

[292] A. Kagan and M. Neubert, Eur. Phys. J. **C7** (1999) 5.

[293] M. Nakao, **ICHEP, Osaka, Japan** (2000).

[294] T.E. Coan et al., Phys. Rev. Lett. **84** (2000) 5283.

[295] C. Jessop et al., ICHEP, Osaka, Japan (2000).

[296] T.E. Coan et al., ICHEP, Osaka, Japan (2000).

[297] M. Artuso et al., Phys. Rev. Lett. **84** (2000) 4292.

[298] P. Ball et al., hep-ph/0003238 (2000).

[299] J. Tseng et al., *Rare* B *decays, mixing and CP violation at Fermilab Tevatron*, **FERMILAB-Conf-99/355-E**.

[300] A. Khodjamirian, *Decays of Heavy flavoured hadrons accessible at* $HERA-B$, in preparation.

[301] A.E. Snyder and H.R. Quinn, Phys. Rev. **D48** (1993) 2139.

[302] R. Fleischer and T. Mannel, Phys. Rev. **D57** (1998) 2752.

[303] D. Cronin-Hennessy et al., Phys. Rev. Lett. **85** (2000) 515.

[304] T.T. Champion et al., ICHEP, Osaka, Japan (2000).

[305] P. Chang et al., ICHEP, Osaka, Japan (2000).

[306] R. Stroynowski et al., ICHEP, Osaka, Japan (2000).

[307] A. Ali et al., Phys. Rev. **D58** (1998) 094009.

[308] C.P. Jessop et al., hep-ex/0006008 (2000).

[309] Y-H. Chen et al., Phys. Rev. **D60** (1999) 094014.

[310] S.J. Richichi et al., Phys. Rev. Lett. **85** (2000) 520.

[311] P. Eerola, *Beauty'99 conference summary*, hep-ex/9910067 (1999).

[312] H.J. Lipkin, Phys. Lett. **B254** (1991) 247.

[313] H-Y. Cheng and B. Tseng, Phys. Lett. **B415** (1997) 263.

[314] M. Ciuchini et al., Nucl. Phys. **B512** (1998) 3.

[315] L.L. Chau et al., Phys. Rev. **D43** (1991) 2176; Phys. Rev. **D58** (1998) 19902.

[316] D. Du and L. Guo, Z. Phys. **C75** (1997) 9.

[317] Y. Gao and F.Wurthwein, hep-ex/9904008v2 (1999).

[318] B.H. Behrends et al., Phys. Rev. Lett. **80** (1998) 3710.

[319] K. Huitu et al., Phys. Rev. Lett. **81** (1998) 4313.

[320] K. Huitu et al., Phys. Lett. **B445** (1999) 394.

[321] G. Abbiendi et al., **CERN-EP/99-179** (1999).

[322] A. Kagan and M. Neubert, Phys. Rev. **D58** (1998) 094012.

[323] M. Aoki et al., Phys. Rev. **D60** (1999) 035004.

[324] T.E. Coan et al., hep-ex/9908039 (1999).

[325] A. Ali et al., Phys. Rev. **D59** (1999) 014005.